MPhil Thesis

Production of Weak Bosons in Association with Jets at Hadron Colliders

(April 2013)

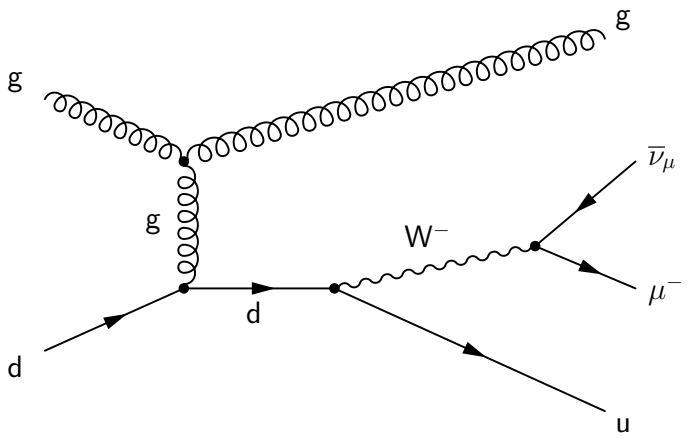

M. Stephan Tietz

Stephan.Tietz.2009@live.rhul.ac.uk

Centre for Particle Physics at Royal Holloway, University of London
NExT Institute for Particle Physics Phenomenology

Supervisor

Dr Nikolas Kauer

N.Kauer@rhul.ac.uk

Royal Holloway, University of London
NExT Institute

Royal Holloway University of London

NExT

SEPnet South East Physics Network

Declaration of Authorship

I, M. Stephan Tietz hereby declare that this thesis and the work presented in it is entirely my own. Where I have cited information or ideas taken or derived from the work of others, this is always clearly stated and corresponding bibliographical references are provided.

Egham, 21 April 2013

Abstract

This thesis investigates integrated and differential leading-order cross-sections for the production of weak bosons with up to two associated jets and leptonic decays at hadron colliders, i.e. $p^{(}\overline{p}^{)} \to (W^- \to \ell^-\overline{\nu}_\ell) + n\ jets$, $p^{(}\overline{p}^{)} \to (W^+ \to \ell^+\nu_\ell) + n\ jets$, $p^{(}\overline{p}^{)} \to (Z \to \ell^-\ell^+) + n\ jets$ and $p^{(}\overline{p}^{)} \to (Z \to \sum_{\ell=\tau,\mu,e} \nu_\ell\overline{\nu}_\ell) + n\ jets$. All cross-sections are calculated for accelerator setups Tevatron Run II, LHC with 7 TeV and 14 TeV, and PDF sets MSTW2008LO (90% C.L.) and CTEQ6L1. In all cases three different scale choices, static $\mu_0 = M_V$, dynamic E_T^V and $\hat{H}_T$, with a variation by a factor of four have been considered. Additionally, PDF uncertainties have been determined for the MSTW2008LO results. All results have been calculated using an amended version of the MCFM 6.0 package and custom Python scripts.

The ratio between the integrated cross-sections for W^+ and W^- production with leptonic decay and the ratio between the integrated cross-sections for the two studied decays of the Z production have been calculated. I find that both are very stable for all scale choices. In contrast, for the Berends-Giele scaling a dependence on the choice of static/dynamic scale was observed.

Furthermore a variety of differential cross-sections have been calculated. This includes transverse momentum p_T and rapidity y for charged leptons and jets, missing transverse momentum $p_{T,miss}$, rapidity separation Δy, separation in transverse angle $\Delta\phi$ and ΔR. The distance observables use p_T-ordered jets, charged leptons and missing momentum. For zero-jet processes the PDF and scale uncertainties decrease in the large invariant mass tails and for one and two-jet processes the uncertainties become larger in the tails. The latter was also observed for transverse momentum distributions.

The differential cross-sections are compared for the different scales and I find that different choices do not change the position of peaks or general features of the curves, but tails can differ. I show that varying the static scale by a factor of four is not always sufficient to cover the central values for dynamic scale choices. For invariant mass distributions, I show that the dynamic scale results are smaller than the static scale predictions and normally fall within the uncertainty envelope. Further, rapidity distributions are very stable with respect to different scale choices and only differ by a constant factor. The dynamic scales are well within the uncertainty envelope of the static scale. Comparisons with respect to different PDF sets showed a simple scaling for transverse observables. The PDF uncertainties for MSTW2008LO (90% C.L.) were large enough to encompass the deviation between the two studied PDF sets for zero and one-jet processes, but not for two associated jets. For rapidity distributions, no uniform behaviour of CTEQ6L1 versus MSTW2008LO was observed. CTEQ6L1 can give a larger cross-section in the central/forward region, and the MSTW2008LO error underestimated this deviation.

Contents

List of Tables

List of Figures

Chapter 1

Introduction

These are certainly exciting times for particle physics, with the Large Hadron Collider (LHC) at the CERN in Switzerland having delivered almost two years worth of data. Whilst not yet having achieved its design centre-of-mass energy and luminosity, the LHC has already surpassed previous records set by Tevatron at Fermilab. It has collected an integrated luminosity of over $5\,\mathrm{fb}^{-1}$ per experiment at a collision energy of 7 TeV [1] and has recently restarted data taking with 8 TeV [2]. It is the only operating high-energy hadron collider, as the Tevatron collider ceased operation in September 2011.

The LHC was built with the main purpose of pushing the energy and luminosity barrier, probing high-energy physics at the TeV scale. This will allow particle physicists to test predictions of the Standard Model (SM) of particle physics and established beyond SM (BSM) theories like Supersymmetry (SUSY). This could yield answers to open questions like the excess of dark matter in the universe (measured indirectly by astrophysical experiments) and the existence of massive neutrinos (observed by neutrino oscillation experiments). But the LHC might also observe New Physics (NP) phenomena, which could help physicists understand the nature of the four fundamental forces. We already know that the electromagnetic and weak nuclear forces are manifestations of one electroweak force. In turn it might itself be unifiable with the strong nuclear force as suggested by Grand Unification Theories (GUTs). Furthermore, gravity, the fourth fundamental force, is orders of magnitude weaker than the other three forces. This is known as the Hierarchy problem.

The LHC builds on the legacy of its predecessor, the Large Electron-Positron Collider (LEP) and Tevatron's Run II. Both have been extremely successful experiments. For example, both have measured and constrained a variety of SM parameters, most notably for the weak bosons at LEP and the top quark at Tevatron. Furthermore, they have both set limits on the mass of the hypothesized Higgs boson, which provides mass to particles via electro-weak symmetry breaking. The LEP may have seen glimpses of the Higgs boson at 115 GeV [3, 4] and excluded masses below 113 GeV. The Tevatron has excluded masses between 147 GeV to 180 GeV and has seen a small excess in the region

between 115 GeV to 135 GeV [5].

The four experiments at the LHC are looking for:

- the existence (and mass) of the Higgs boson
- the existence of a large number of supersymmetric particles predicted by SUSY
- the origin of the antimatter-matter asymmetry[1]
- a possible fourth generation of quarks and leptons
- additional weak bosons
- the nature of the quark-gluon plasma present in super-dense astronomical objects[2] and the early universe
- the existence of extra dimensions as required by String theory

Most measurements have confirmed the SM and are excluding possible extensions like the Constrained Minimal Supersymmetric SM (CMSSM) and minimal Super Gravity (mSUGRA). Only very few tentative hints have been found for BSM physics. Some of the most notable results are:

- 5.0σ observation of a SM Higgs-like boson with a mass 126 GeV by ATLAS [6] and CMS [7] (both used a combination of $H \to \gamma\gamma$ and $H \to ZZ \to 4\ell$ channels)
- lower boundaries for the masses of supersymmetric particles [8, 9], excluding large parts of the parameter space of more constraint supersymmetric models like CMSSM [10] and mSUGRA
- CMS observed a ridge-like structure when plotting the two particle correlation function of a gluon-quark plasma against pseudo-rapidity and azimuthal angle [11]
- confirmation of the SM predictions for the rare B_s^0 meson decay into two muons at the LHCb [12], which contradicts previous Tevatron results [13]
- discovery of the χ_b quarkonium state (P-wave of the $b\overline{b}$ system) by ATLAS [14]

To interpret measured data one has to compare it with theoretical predictions. Experimental results are associated with a broad range of uncertainties. At hadron colliders these uncertainties come from the operation of the accelerator, the detectors and the limitations of the data acquisition itself. At accelerator level there are uncertainties in the luminosity of colliding proton beams coming from both the number of protons as well as the proton energy distribution in each bunch. Furthermore, the different detector elements (calorimeters, pixel detector etc.) have a finite resolution with respect to energy, momentum and position. They also only cover a finite solid angle as they cannot, for example, penetrate the beam axis. Finally, the number of events happening at high luminosities is extremely large making it impossible to store all this data in real time.

[1] The observable universe consists almost exclusively of matter, though the Big Bang should have created equal amounts of antimatter and matter.

[2] Black holes are an example of super-dense astronomical objects.

Hence, event triggers are used to cut down the data stream. Because this is a lossy process, it is another cause for errors, especially considering the possibility of pile up events interfering with events of interest. From the recorded data, events are reconstructed giving a number of final state particles and their kinematical properties[3].

On the theoretical side there are also plenty of aspects that introduce uncertainties. The foremost problem is that the SM is a relativistic quantum field theory (QFT), which does not allow us to obtain exact solutions for the equation of motion (EOM) of particles. We resolve this by using perturbation theory, which can lead to divergences. These are taken care of via renormalisation which also introduces uncertainties. Furthermore, for hadron collider predictions we need to take care of the proton structure. This is done using parton distribution functions (PDFs), which are fitted to experimental data. These introduce uncertainties due to the nature of the experimental data as well as the underlying theory requiring the introduction of factorisation scales to cut out divergences. In the end one obtains a prediction for total and differential cross-sections as a function of properties of final state particles such that the predictions can be compared to data.

Both the unfolding of detector effects as well as the calculation of theoretical cross-sections require numerical integrations, usually using the Monte Carlo (MC) method. Finally, experimental and theoretical results can be compared as shown in Figure 1.1. This is possibly one of the biggest challenges facing experimentalists and theorists, because both sides can contribute errors of tens of percent. Sometimes errors can be minimised by collecting more data, determining the collider luminosity more precisely or calculating higher order predictions. All these, however, have limiting factors such as experimental resolution and computational time. Furthermore, only recently have theoretical errors for hadronic reactions been explored in more detail, as methods of estimating PDF uncertainties have been developed. Moreover, scale uncertainties are more important at higher energies and are acceptably small for next-to-leading (NLO) order predictions.

The precise computation of theoretical uncertainties is one field where phenomenologists are demanded. Furthermore they can help in this discourse by finding observables and making estimates that naturally minimise the uncertainties. This is particularly important for processes, which are used for testing the SM and/or are major backgrounds. Figure 1.2 shows how a variety of the largest cross-sections develop with respect to the centre-of-mass energy of a proton-proton collider. One can see that apart from $\mathrm{b\bar{b}}$ pair production and production of hard jets, the production of $\mathrm{W}^{\pm}$ bosons with leptonic decay is the third largest at the LHC. This means that the production of $\mathrm{W}^{\pm}$ is both one of the standard candles at the LHC as well as one of the major backgrounds at the LHC.

That means that the SM and its input parameters can be tested by comparing the-

[3]Some kinematical properties like energy E, transverse momentum p_T and rapidity η are defined in Chapter 6.

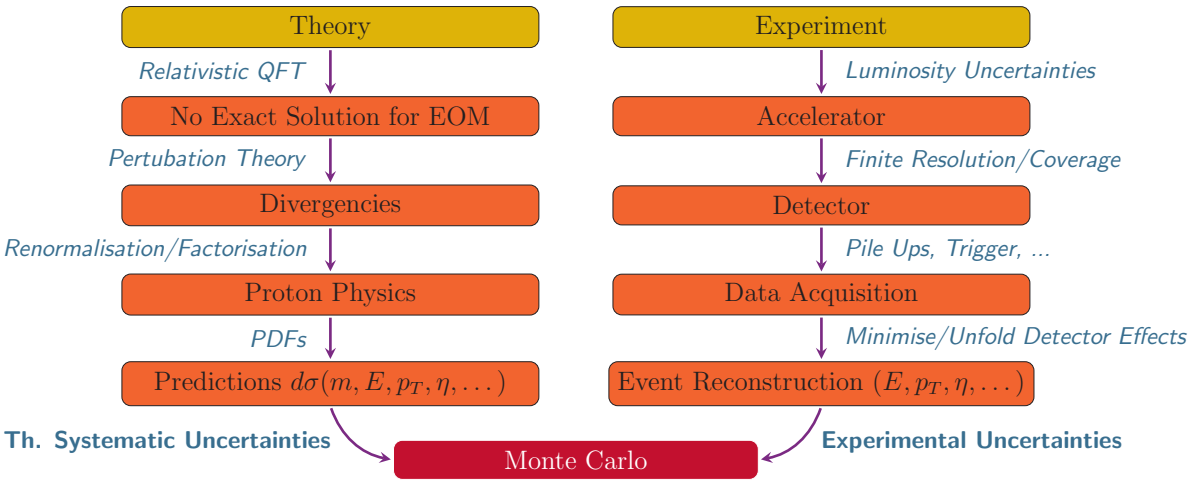

Figure 1.1: Overview of theoretical predictions for hadron colliders and experimental measurements being compared via MC simulations. To minimise uncertainties inherent to both sides is one aspect of Phenomenology. Adapted from Moretti [15] and Kauer [16].

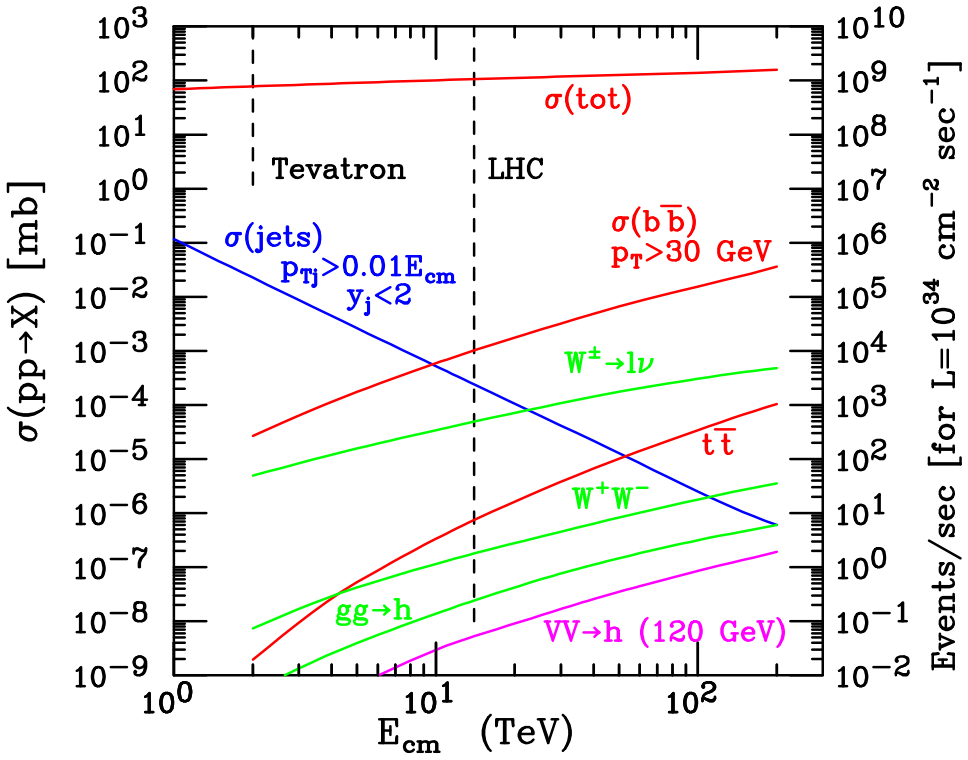

Figure 1.2: Scattering cross-sections versus centre-of-mass energy for the SM processes in proton-proton collisions. [17]

oretical predictions of production cross-section for weak bosons with measurements. For example, the transverse mass of the $W^{\pm}$ boson and the invariant mass of the Z boson provide a benchmark for electro-weak parameters and the decay of the weak bosons depend on their branching ratios. Moreover, the ratios between the total production cross-sections of W^+ and W^- can be used to probe proton PDFs, because the electro-weak

kinematics of W^+ and W^- are very similar and many sources for error like uncertainties of the beam luminosity are minimised.

Some BSM theories introduce additional weak bosons or other NP signatures with decay products which are the same as for the SM bosons. Hence, a precise knowledge of the expected SM differential cross-sections can help to find deviations. Production of weak bosons with leptonic decay is particularly interesting, because leptons can be easily tagged and are therefore part of many search signatures. As such the production of $W^\pm$ and Z is a background for many SM measurements and BSM searches. Precise predictions of both integrated and differential SM cross-sections are necessary to subtract them from measurements revealing the desired signals.

At the LHC not only $W^\pm$ and Z bosons have large production cross-sections, but also weak boson production with multiple associated jets due to the high centre-of-mass energy. Therefore, the object of the work presented is to calculate a wide range of observables for different $V + n\ jets$ processes at hadron colliders, providing integrated leading-order (LO) cross-sections and differential distributions for further analysis of both the SM measurements and BSM searches. For these calculations the MCFM software package (see Section 4.1) and a variety of custom Python scripts were used. Both PDF uncertainties for MSTW (Martin-Stirling-Thorne-Watt Parton Distribution Functions) and scale uncertainties for a variation by a factor of four have been considered.

Before presenting my results for integrated and differential cross-sections in Chapter 7, I will introduce the necessary theoretical background. I will start with the basics of QFT and SM required to calculate cross-sections at hadron colliders in Chapter 2. At the end of this chapter I will also discuss the MC method used for numerical integration and the motivation for selection cuts applied during the integration. In Chapter 3, I will introduce and discuss statistical, scale and PDF uncertainties, which form the main aspect of my investigations. How all this has been implemented into MCFM, the program used for calculating cross-sections and a variety of custom scripts are presented in Chapter 4.

Chapter 5 gives an overview of the investigated processes and presents their Feynman diagrams. Chapter 6 introduces the observables investigated using differential cross-sections. This concludes the necessary theoretical background and after presenting my results, I will discuss them in Chapter 8. This includes a comparison of the ratios between the integrated cross-sections of W^+ and W^- production, ratios between integrated cross-sections of Z production with decay into charged leptons and neutrinos and Berends-Giele scaling. These include PDF and scale uncertainties. Moreover, the PDF and scale uncertainties for different differential cross-sections are compared to find out how they depend on certain observables. Finally, I will compare distributions of differential cross-sections with respect to both different static/dynamic scales and PDF sets. A summary of my dissertation can be found in Chapter 9.

Chapter 2

Theoretical Framework

Firstly, I will introduce the SM of particle physics (Section 2.1), which describes the interactions of the fundamental particles and how it can be used to calculate differential and integrated cross-sections at hadron colliders (Section 2.2).

Secondly, I will introduce the MC method (Section 2.3) used for the numerical integration of calculated cross-sections and give a description of selection cuts (Section 2.4), which are required for physical reasons and for mirroring the geometry and acceptance of detectors.

2.1 Standard Model

The SM as proposed in 1978 is the theory of electromagnetic, weak and strong interactions and the elementary particles which take part in these interactions. The next section will introduce these particles. I will also summarise very quickly how the SM is expressed in term of group theory symmetries and how the Higgs mechanism is required to generate masses for particles. [18]

2.1.1 Leptons, Quarks and Force Mediators

There are three kinds of elementary particles: leptons, quarks and force mediators. There are six leptons which are classified according to their charge (Q) and mass. They naturally order into pairs of a charged lepton and a neutrino in three generations (electron, muon and tauon). Each generation contains two particles and two antiparticles: a massive and singly negatively charged lepton, its antilepton with the same mass but opposite charge, a (near to) massless neutral neutrino and its antineutrino. Hence, there are, in all, 12 leptons.

Furthermore, there are six flavours of quarks: down, up, strange, charm, bottom (or beauty) and top (or truth). They are classified according to their charge and mass. They fall into pairs of quarks (with charges $-1/3$ and $+2/3$) and anti-quarks (opposite charges)

Generation	**Leptons**		**Quarks**	
First	e^-	ν_e	d	u
Second	μ^-	ν_μ	s	c
Third	τ^-	ν_τ	b	t
Charge	-1	0	$-1/3$	$2/3$

Table 2.1: SM fermions arranged by generation and charge. (Antifermions and quark colours are not shown.)

Force mediators			
γ	$W^\pm$	Z	g

Table 2.2: SM gauge bosons. (Colours of the gluon are not shown.)

in three generations. Additionally every quark comes in three colours. In total there are 36 quarks.

Leptons and quarks are fermions, i.e. they have a spin of $1/2$. Table 2.1 lists an overview of the fermions (excluding antifermions and colours).

Finally, every interaction has its mediator: the photon (γ) for the electromagnetic force, two $W^\pm$ bosons and one Z boson for the weak force and eight gluons (g). This sums up to 12 mediators. These gauge bosons (excluding colours) are listed in Table 2.2. As we will see later, at least one Higgs boson is needed for the SM to be consistent. So, we have at least 61 elementary particles[1] in the SM. To date, all experimental tests of the three forces described by the SM have agreed with its predictions.

2.1.2 Local Gauge Invariance

Since the early twentieth century, symmetries have played an important role in the advance of theoretical physics, e.g. from the symmetry of space-time (special relativity) up to the internal and gauge invariances. This is summarised by Emmy Noether's theorem: "If an action is invariant under some group of transformations (symmetry), then there exist one or more conserved quantities (constants of motion) which are associated to these transformations." Or in other words, symmetries imply conservation laws. [19]

Indeed, Quantum Electrodynamics (QED) has been built on this idea. To date, it is the most precise theory ever built to describe nature. In QED the existence, and some of the properties of the gauge fields (e.g. the photon), follow from assuming invariance under local gauge transformations. This has become a prototype of the successful quantum field theory (QFT), which generalises the gauge principle for strong and weak interactions.

[1] There are only $6 + 6 + 5 + 1 = 18$ elementary particles if anti-particles and colours are not counted. Otherwise one gets $2 \cdot 6$ leptons, $3 \cdot 2 \cdot 6 = 36$ quarks, one photon, three weak bosons, eight gluons and one Higgs.

Spin	Field	Kinetic Term	Mass Term	Particle
0	scalar ϕ	$1/2\,(\partial_\mu\phi)\,(\partial^\mu\phi)$	$-1/2 m^2\phi^2$	Higgs boson
$1/2$	spinor ψ	$i\bar{\psi}\gamma^\mu\partial_\mu\psi$	$-m\psi\bar{\psi}$	fermions
1	gauge A^μ	$-1/16\pi\,(\partial^\mu A^\nu - \partial^\nu A^\mu)\,(\partial_\mu A_\nu - \partial_\nu A_\mu)$	$1/8\pi m^2 A^\nu A_\nu$	gauge boson

Table 2.3: Examples of kinetic and mass terms in the free Lagrangian of spin 0, spin $1/2$ and spin 1 particles. [23]

Lie Algebra is used to express the SM in terms of unitary groups and their symmetries, i.e. a $U(1)$ gauge field B_μ with coupling g' and weak hypercharge Y, an $SU(2)$ gauge field W_μ with coupling g and weak isospin I, and finally an $SU(3)$ gauge field G_μ with coupling g_s representing colour. Choosing a particular representation for each of these symmetry groups relates to a set of fermions and their generators relate to the gauge bosons. In $SU(3)$ quarks are represented by a triplet, leptons by a singlet and the eight generators represent the gluon. In $SU(2)$ left-handed[2] particles are represented as doublets, right-handed particles as a singlet and there are three generators. In $U(1)$ each particle has a hypercharge and there is exactly one generator. [20, 21]

Using this notation we can write down the Lagrangian consisting of a propagation and a mass term for each particle as shown in Table 2.3. By requiring the conservation of local gauge invariance, i.e. applying the covariant derivative, we get all the interaction terms required for the SM. For example the requirement of local gauge invariance, applied to the free Dirac Lagrangian (spin $1/2$ particle, e.g. electron), generates all of electrodynamics and specifies the current produced by spin $1/2$ particles. That is because one is forced to introduce a massless vector field (A^μ, i.e. the photon), which represents the electromagnetic potential. In summary we find that the photon couples to all charged particles, the weak bosons couple to all fermions and each other, the W boson also couples to itself and finally the gluon couples only to quarks and itself. [22]

2.1.3 Spontaneous Symmetry Breaking

I have already mentioned that $SU(2)_I$ has three massless gauge bosons and $U(1)_Y$ has one, i.e. so far there are no massive gauge bosons in the SM described. However, we know that heavy gauge bosons (e.g. W^+, W^- and Z) exist, and therefore a massive vector field is needed. But the incorporation of mass terms for gauge bosons and for fermions leads to a manifest breakdown of gauge invariance. The most popular resolution is the Higgs-Brout-Englert-Guralnik-Hagen-Kibble mechanism of spontaneous symmetry

[2] Handedness refers to the orientation of a particles spin with respect to its direction of propagation. This is related to the concept of helicity, which is the projection of a particle's spin onto the direction of its momentum. If the spin and velocity are parallel then the particle is right-handed and has a helicity of $+1$. If they are anti-parallel then the particle is left-handed and has helicity of -1. In the SM left-handed particles are equal to right-handed anti-particles and vice versa.

breaking (i.e. Higgs mechanism). An $SU(2)$ doublet with a $U(1)$ hypercharge and non-zero vacuum expectation value is introduced. This breaks $SU(2)_I \times U(1)_Y$ down to $SU(2)_{weak} \times U(1)_{em}$. This process provides mass terms for three gauge bosons, i.e. our weak bosons, and leaves one massless Goldstone boson, i.e. the photon. In fact it can be shown that the Higgs mechanism also provides mass terms for all fermions and itself (via self-coupling). [24]

2.2 General Cross-sections for Hadron Collisions

In the next step, we want to use the SM to make numerical predictions for the likelihood of interactions happening (i.e. cross-sections) at hadron colliders. First, we are going to look at the general formula used to calculate exact LO cross-sections for the collision of two hadron beams that result in the production of a weak boson with associated jets $V + n\ jets$ and the subsequent decay of the weak boson. In particular I am looking at hadron colliders, which means that I am interested in processes with two initial protons, e.g. $\mathrm{p}_a\mathrm{p}_b \to V + n\ jets + X$. [25]

I assume that the hard scattering process consists of two partons q_a, q_b, which can be quarks, anti-quarks or gluons. Since the incoming hadrons contain a mix of different types of partons, the final state can be produced via different reactions with different partonic initial states. The total differential cross-section $d\sigma$ is simply the sum of all the differential cross-sections of these subprocesses $d\sigma_{sub}$ weighted by the differential probability dF that the corresponding initial states occur in the incoming hadrons:

$$d\sigma = \sum dF(\mathrm{p}_a, q_a, \mathrm{p}_b, q_b, \mu_f)\ d\sigma_{sub}(q_a, q_b, \mu_r, \mu_f)$$

The differential probability dF depends only on the factorisation scale and the differential cross-section $d\sigma_{sub}$ depends on the renormalisation and factorisation scale[3]. Exact theoretical predictions, however, must be independent of arbitrary scale choices. The differential probability is approximated by:

$$dF(\mathrm{p}_a, q_a, \mathrm{p}_b, q_b, \mu_f) = f_{\mathrm{p}_a \to q_a}(x_a, \mu_f)\ dx_a\ f_{\mathrm{p}_b \to q_b}(x_b, \mu_f)\ dx_b$$

Here $0 \leq x_a, x_b \leq 1$ are the longitudinal fractions[4] of the proton momenta carried by the initial state quarks. PDFs, $f_{\mathrm{p} \to q}(x, \mu_f)$, are the probability densities of finding a given quark carrying a momentum fraction x at a squared energy scale $\mu_f = Q^2$. They are obtained by fitting experimental data from deep inelastic scattering of charged leptons

[3] A little more detail about scales can be found in Section 3.2.

[4] The partons cannot acquire a large transverse momentum because α_s is small at large momentum scales and hence the exchange of hard gluons is suppressed.

of hadrons (i.e. protons or anti-protons) and evolving the partonic structure obtained at these low energies (e.g. 100 GeV) to higher energies[5]. They are distributed by several collaborations using electronic formats suitable for numerical computations.

For the case of a symmetric proton-proton collision, the quark can come from the first or the second proton and *vice versa* for the anti quark. Hence, the differential probability in terms of the PDFs is given by:

$$\begin{aligned} dF(\mathrm{p}_a, q_a, \mathrm{p}_b, q_b, \mu_f) &= \big[f_{\mathrm{p}_a \to q_a}(x_a, \mu_f) \cdot f_{\mathrm{p}_b \to q_b}(x_b, \mu_f) + \\ &\qquad f_{\mathrm{p}_a \to q_b}(x_a, \mu_f) \cdot f_{\mathrm{p}_b \to q_a}(x_b, \mu_f)\big] \; dx_a \, dx_b \\ &= F_q(x_a, x_b, \mu_f) \, dx_a \, dx_b \end{aligned}$$

Now, let us consider the differential cross-section for a specific subprocesss. It is given by:

$$\begin{aligned} d\sigma_{sub} &= \frac{1}{2} \cdot \frac{1}{\lambda^{1/2}(\hat{s}, m_a^2, m_b^2)} \cdot S \cdot \left[d\Phi_n \, \overline{\sum} |\mathcal{M}|^2 \right] \\ &= \frac{1}{2\hat{s}} \cdot S \cdot \left[d\Phi_n \, \overline{\sum} |\mathcal{M}|^2 \right] \end{aligned}$$

$\hat{s} = E_{p,cms}^2$ is the square of the total energy in the parton centre-of-system, $\lambda(\hat{s}, m_a^2, m_b^2) = \hat{s}^2 + m_a^2 + m_b^2 - 2\hat{s}m_a^2 - 2\hat{s}m_b^2 - 2m_a^2 m_b^2$ and the symmetry factor $S = 1/n!$ for n identical particles in the final state. The symmetry factor avoids double counting of final states when integrating the phase space. I also assumed that the masses of the incoming partons m_a and m_b are negligible at the LHC, so that $\lambda^{1/2}(\hat{s}, m_a^2, m_b^2) \approx \hat{s}$.

The general form of the n-dimensional phase space element can be found in Peskin and Schroeder [23]:

$$d\Phi_n = \left(\prod_f \frac{d^3 p_f}{(2\pi)^3} \cdot \frac{1}{2E_f} \right) (2\pi)^4 \delta^{(4)}(\sum p_i - \sum p_f)$$

Furthermore, one needs the mod-squared matrix element, $|\mathcal{M}|^2$, summed and averaged overall initial and final states:

$$\overline{\sum} |\mathcal{M}|^2 = \overline{\sum} | \sum_i \mathcal{M}_i |^2$$

where $\mathcal{M}_i$ is the matrix element for each subprocess. They can be calculated using Feynman diagrams[6] and rules.

[5] The number of partons goes up at low x with Q^2 and falls at high x. At low Q^2 the three valence quarks become more dominant in the proton. At higher Q^2 there are more sea quarks (quark anti-quark pairs) which carry a low momentum fraction x and gluons which have a large x.

[6] Feynman diagrams are pictorial representations of the interactions of fundamental particles according to the SM. They can be used to calculate the matrix element. An introduction to Feynman rules and diagrams can be found in Griffiths [26].

The incoming beams of hadron collider experiments are usually unpolarised. Hence, one has to sum and average over all possible spin states for each fermion $s = \{1/2, -1/2\}$ and colour combination of the initial state partons in order to take all contributions into account. We know that the detectors at the LHC do not have polarisation preferences. That means one also has to sum over all possible polarisations of the final state.

In order to calculate these matrix elements, one has to investigate the possible hard scattering subprocesses. The easiest and most common way is to use Feynman rules to write down the possible matrix elements. I will discuss the respective Feynman graphs used in Chapter 5.

For the complete calculation of cross-sections for hadron collisions, I will only consider $q = \{\mathrm{d}, \mathrm{u}, \mathrm{s}, \mathrm{c}, \mathrm{b}\}$, because the probability of finding t in the initial state is negligible. Furthermore, I am going to ignore the parton quark mass ($M_q = 0$), because the centre-of-mass energy will be much larger then the mass of the quarks. Hence, the general expression for calculating the total cross-section is:

$$\sigma(\mathrm{p}_a\mathrm{p}_b \to (V \to \ell\bar{\ell}) + n\ jets + X, \mu_f, \mu_r) = \sum_{q=\{\mathrm{d,u,s,c,b}\}} F_q(x_a, x_b, \mu_f)\ \sigma(q_a q_b \to (V \to \ell\bar{\ell}) + n\ jets, \mu_r, \mu_f)\ dx_a\ dx_b$$

2.3 Monte Carlo Integration

I would like to present the general numerical method used to calculate such cross-sections, which is known as Monte Carlo (MC) integration [27]. Consider the integral of a function $f(\vec{x})$ for m variables $\vec{x} = \{x_1, x_2, .., x_m\}$ over an integration volume Ω:

$$I = \int_\Omega f(\vec{x}) d\vec{x} \tag{2.1}$$

During the MC integration the whole phase space is sampled, i.e. n points $\vec{x}_i$ are randomly selected from a uniform distribution of points in Ω. So, the integral can be approximated by:

$$X^{(1)} = \frac{1}{n} \sum_{i=1}^{n} f(\vec{x}_i) \tag{2.2}$$

An improvement for MC integrations are adaptive MC methods like Vegas [28], which use importance sampling. These provide faster and/or more precise computational algorithms. In contrast to the standard MC method, the points $\vec{x}_i$ are not uniformly distributed across the integration volume. Subregions with larger contributions are over represented and weighted with respect to their relative contribution using a probability

density function $p(\vec{x})$.[7] In this case the integral is approximated by [29, 30]:

$$X^{(1)} = \frac{1}{n}\sum_{i=1}^{n}\frac{f(\vec{x}_i)}{p(\vec{x}_i)} \tag{2.3}$$

The quantity $X^{(1)} \to I$ as $n \to \infty$. It is expected to fluctuate around the exact values of the integral as different sets of random points[8] are used. The variance of this fluctuation can be estimated:

$$\Delta X^2 = \frac{1}{n}\left[\int_\Omega \frac{f^2(\vec{x})}{p(\vec{x})}d\vec{x} - \left(\int_\Omega f(\vec{x})d\vec{x}\right)^2\right] \tag{2.4}$$

And for large n this quantity can be approximated by:

$$\Delta X^2 \simeq \frac{X^{(2)} - (X^{(1)})^2}{n} \qquad \text{with} \qquad X^{(2)} = \frac{1}{n}\sum_{i=1}^{n}\left(\frac{f(\vec{x}_i)}{p(\vec{x}_i)}\right)^2 \tag{2.5}$$

and hence:

$$\Delta X = \frac{1}{\sqrt{n}}\cdot\sqrt{\frac{1}{n}\sum_{i=1}^{n}\left(\frac{f(\vec{x}_i)}{p(\vec{x}_i)}\right)^2 - \frac{1}{n^2}\left(\sum_{i=1}^{n}\frac{f(\vec{x}_i)}{p(\vec{x}_i)}\right)^2} \tag{2.6}$$

This statistical uncertainty is discussed in more detail in Section 3.1.

2.4 Selection Cuts

Selection cuts are restrictions of the phase space, i.e. the integration domain. They can be easily implemented for MC integrations using additional acceptance tests. There are two types of cuts required: general acceptance cuts and physics-motivated cuts.

The former mirror the finite acceptance and resolution of the detectors at the LHC and Tevatron as I am interested in calculating cross-sections which only correspond to the region of phase space where experimental measurements can be made. These selection cuts are on the transverse momentum[9] and rapidity of both leptons and jets. The rapidity cut mirrors the finite size of the central detector and the forward detectors. The cuts on the transverse momentum represent the precision of the calorimeters. The cuts for leptons and jets can be different, because the coverage and precision of the electro-magnetic and the hadronic calorimeter are normally non-identical.

When calculating the process $q\overline{q} \to \mathrm{Z} \to \ell^+\ell^-$ one has to also consider $q\overline{q} \to \gamma^* \to$

[7] The probability density function is normalised $\int_\Omega p(\vec{x})d\vec{x} = 1$.

[8] It is impossible to computationally generate truly random numbers. Instead pseudo-random and quasi-random numbers are used by MC programs like MCFM. The latter guarantee a more uniform spread of points across the phase-space while still approximating all the necessary properties of randomness. [31]

[9] All physical quantities mentioned in this section are defined in Chapter 6.

$\ell^+\ell^-$ (s-channel), because both the Z boson and a virtual photon couple to the quarks and can decay into two leptons. Furthermore, the photon is massless and hence its propagator becomes infinite for small energies. Hence, a cut on the di-lepton invariant mass for two charged leptons from a Z decay has to be introduced to cut out the singularity at $\sqrt{s} = 0$ arising from the virtual photon.

For processes with leptonic decay of a W boson, $\mathrm{W} \to \ell\nu_\ell$, we have only one detectable, charged lepton. A cut on the transverse mass of a W boson ($M_{T,\mathrm{W}}$) can be used to improve signal-to-background selection, because it indirectly requires the invariant mass of the charged lepton and the neutrino to exceed a minimal value, making it more likely for them to come from W decay. Furthermore, a cut on the missing transverse momentum is also used to increase the likelihood of a neutrino in the final state.

Chapter 3

Uncertainties of Perturbative Theoretical Predictions

I have shown how to calculate the central value for integrated and differential cross-sections in Chapter 2. I will now present how to estimate the uncertainties associated with pertubative theoretical predictions. There are three sources of uncertainties: statistics, scales and PDFs.

3.1 Statistical Uncertainties

The first source of uncertainty originates from the use of the MC method to calculate cross-sections. The MC method has been described in Section 2.3. We have seen that the statistical error of an observable X is given by:

$$\Delta X = \frac{1}{\sqrt{n}} \cdot \sqrt{\frac{1}{n}\sum_{i=1}^{n} X_i^2 + \frac{1}{n^2}\left(\sum_{i=1}^{n} X_i\right)^2} \tag{3.1}$$

where X_i is the value[1] of a given sampling point i and n is the total number of points used for the MC integration.

It is obvious that theoretically this error can be minimised as much as needed by increasing the number of sampling points, i.e. quadrupling the number of points generally halves the statistical uncertainties. In practice this is not always viable due to computational limitations as discussed in Section 4.4.

[1]This is a short hand with respect to Section 2.3. For comparison: $X_i = {}^{f(\vec{x}_i)}/_{p(\vec{x}_i)}$, e.g. the value at a point $\vec{x}_i$ divided by a given probability distribution. This is equal to the integrand of a given shot multiplied by its weight.

3.2 Scale Uncertainties

It is the nature of perturbation theory that quantities can only be calculated to a given order. The deviations due to missing higher order terms are referred to as scale uncertainties, because they can be approximated by varying the scale. There are two types of scales: the factorisation scale and renormalisation scale. These provide an infra-red and an ultraviolet cut-off, respectively. This separates the hard scattering process that I am interested in from the underlying event in the detector.

A massless parton with p can emit soft radiation with four-momentum k. In the collinear limit $k \to 0$, which leads to an infra-red singularity $p^2 \to 0$ for massless propagators, because the relative momentum of the initial and the parton after emission is very small. This implies a strong interaction between the two, which is beyond the reach of pertubative calculations. A factorisation procedure absorbs these incalculable effects into the PDFs, which introduces the dependence on an arbitrary factor known as the factorisation scale μ_f. One can think of this scale splitting the process into a soft process, setting up the initial hadron system, and the hard scattering process. [32]

Moreover, one gets large contributions from introducing perturbative loop corrections to massless propagators in Feynman diagrams. These cause ultraviolet singularities, because there is no upper limit to the momentum of these loops. These can be avoided by choosing an arbitrary momentum scale μ_r, which cuts off higher orders of the perturbation theory. In practice this is done by absorbing these ultraviolet divergences into the strong coupling constant, which makes it depend on the renormalisation scale. This process is known as renormalisation. Using the $\overline{MS}$ renormalisation scheme gives the following equation for the *running* of the strong coupling constant [33]:

$$\alpha_s(\mu_r) = \frac{4\pi}{\beta_0}\left[\frac{1}{\ln\left(\frac{\mu_r}{\Lambda^2}\right)} - \frac{\beta_1}{\beta_0^2}\cdot\frac{\ln\left(\ln\left(\frac{\mu_r}{\Lambda^2}\right)\right)}{\ln^2\left(\frac{\mu_r}{\Lambda^2}\right)} + O\left\{\frac{1}{\ln^3\left(\frac{\mu_r}{\Lambda^2}\right)}\right\}\right] \tag{3.2}$$

For a given number of quark flavours, n_f, and three quark colours, $\beta_0 = {}^{33-2n_f}/_3$ and $\beta_1 = {}^{102-38n_f}/_3$. $\Lambda = \mu_{r,0}e^{-2\pi/\beta_0\cdot\alpha_s(\mu_{r,0})}$ with $\alpha_s(\mu_{r,0})$ being a constant. This means that the strong coupling varies with the energy scale becoming weaker as the energy increases.

Using perturbation theory, an observable, X, as a function of the square of the total energy, $\hat{s}$, and the strong coupling is given by [33, 23]:

$$X(\hat{s}, \alpha_s(\mu_r)) = a_0\cdot\frac{\alpha_s(\mu_r)}{\hat{s}} + a_1\cdot\frac{\alpha_s^2(\mu_r)}{\hat{s}}\cdot\left[b_0 + b_1\ln\left(\frac{\hat{s}}{\mu_r}\right)\right] + O\left\{\alpha_s^3(\mu_r)\right\} \tag{3.3}$$

where a_0, a_1, b_0 and b_1 are constants. It can be seen that at LO X is directly proportional to α_s and hence varying μ_r purely probes the dependence of observables on the strong coupling, unless the scale is chosen depending on the kinematics of the specific event.

These dynamic scales will be discussed below. At NLO additional terms partially cancel contributions from the leading order term, which makes NLO predictions generally more stable with respect to the scale.

Ideally cross-section predictions are independent of the choice of scale, but this is rarely the case. There is no theoretical relation between these two scales that justifies them to be either identical or different. However, varying them independently means that the number of calculations increases quadratically and that the results become much more complex. Hence, I will choose the factorisation and renormalisation scale to be equal to each other:

$$\mu_0 = \mu_r = \mu_f \tag{3.4}$$

That also means that the energy scale at which the PDFs are evaluated and the energy scale to which the strong coupling is evaluated are identical, which is phenomenologically appealing.

There are two fundamentally different ways of setting scales. The first one fixes the scale to a single value which is equal for all events calculated. This is known as static scale. For vector boson production, the invariant mass of the vector boson $\mu_0 = M_V$ is a popular choice for such a scale and I will be using it myself in Chapter 7. The second class is called dynamic scale, because it sets the scale depending on the final state kinematics of a specific event.

I will be using two different types of dynamic scales for my calculations: the transverse energy of the vector boson $\mu_0 = E_T^V := \sqrt{M_V^2 + p_{T,V}^2}$ (compare with Equation 6.6 defining the transverse energy E_T) and the sum of the transverse energies of all final state partons (including the decay products of, but not the vector boson itself) $\mu_0 = \hat{H}_T := \sum_{i=final} E_{T,i}$. It is clear that these are not necessarily observable quantities, because the required kinematics might not be experimentally accessible[2].

The scale uncertainties for an observable, X, can be estimated by calculating the cross-sections for different scales. The envelope around the central value defines the symmetric scale uncertainty [34]:

$$\Delta X_{scl} := \frac{1}{2} \cdot [X_{\max}(\mu_i) - X_{\min}(\mu_i)] \tag{3.5}$$

Here, $X_{\max}(\mu_i)$ and $X_{\min}(\mu_i)$ are the respective maximal and minimal value of an observable X for a scale $\mu_i = f_i \cdot \mu_0$, where f_i can be any numerical factor between zero and infinity. Furthermore, I will be looking at $X_{\max}(\mu_i)$ and $X_{\min}(\mu_i)$ separately as the divergences from the central value can be vastly asymmetric.

Most commonly, a scale variation by a factor of two is used to obtain scale uncertainties of NLO predictions, but the precise choice will depend strongly on the investigated

[2]Some of the processes I am going to investigate include neutrinos in the final state.

process. Furthermore, it is the nature of perturbation theory that the correction to the leading order will be larger than the one at next-to-leading order. I will be using $\mu_i = \mu_0 \cdot (\sqrt{2})^i$ with $i = \{-4, -3, -2, \ldots, 4\}$ which gives $0.25\mu_0 \leq \mu_i \leq 4\mu_0$. A comparison with Campbell and Ellis [35, 36] suggests that this is a good choice.

3.3 Parton Distribution Function Uncertainties

In the past PDF uncertainties could not be estimated as PDF sets were obtained by only finding a global minimum χ^2_0 to a set of experimental data from deep inelastic scattering events of charged leptons off hadrons. The partonic structure obtained for low energies at hadron-lepton colliders has to be evolved to the much larger centre-of-mass energies of hadron colliders. Both, the experimental input data as well as the assumption of a theoretical model for the evolution to higher energies give rise to uncertainties.

The need to quantify theoretical data has given rise to the development of PDF error sets. They are obtained using the Hessian [37] or the Lagrange [38] method. The former enables the characterisation of the behaviour of the χ^2 function in the neighbourhood of the global minimum[3], which makes it possible to determine the PDF uncertainties for any observables. The latter method allows for determining the exact χ^2 profile for a given observable. However it is much more time intensive and requires original data at runtime, so is seldom used.

The Hessian method gives one PDF set for the best fit, S_0, and $2N$ eigenvector basis sets (in the plus/minus directions along each eigenvector), S_i^+/S_i^-. The observables need to be calculated for each of the subsets. In the case of MSTW2008LO (90% C.L.) there are 41 subsets. The PDF uncertainty of an observable X can be calculated using one of two widely used methods. More commonly used is the symmetric definition, which gives a single measure for the uncertainties [39]:

$$\Delta X_{pdf} = \frac{1}{2} \cdot \sqrt{\sum_{i=1}^{N} \left[X(S_i^+) - X(S_i^-)\right]^2} \tag{3.6}$$

This adds all the differences between the positive and negative contributions along each eigenvector in quadrature. However, Campbell et al. [40] advise using an asymmetric definition, because some of the directions of the smaller eigenvectors are poorly

[3]The Hessian matrix is determined assuming a Gaussian distribution around the minimum and then diagonalised, while the eigenvectors are rescaled to adapt the natural size to natural scale.

determined, leading to deviations from the central value which are not symmetric:

$$\Delta X^{+}_{\mathrm{max}} = \sqrt{\sum_{i=1}^{N} \left[\max(X(S_i^{+}) - X(S_0), X(S_i^{-}) - X(S_0), 0)\right]^2} \tag{3.7}$$

$$\Delta X^{-}_{\mathrm{max}} = \sqrt{\sum_{i=1}^{N} \left[\max(X(S_0) - X(S_i^{+}), X(S_0) - X(S_i^{-}), 0)\right]^2} \tag{3.8}$$

In this case $\Delta X^{+}_{\mathrm{max}}$ sums in quadrature the PDF uncertainty contributions that lead to an increase in the observable X and $\Delta X^{-}_{\mathrm{max}}$ sums negative contributions. Normally, $X(S_i^{+}) - X(S_0)$ is positive and $X(S_i^{-}) - X(S_0)$ is negative. Hence, it is obvious which term will be included in each sum. Plus and minus contributions, however, may be in the same direction. The asymmetric definition will include the most positive and negative term for $\Delta X^{+}_{\mathrm{max}}$ and $\Delta X^{-}_{\mathrm{max}}$, respectively. That means there may be fewer than N terms for either the positive or negative directions.

Chapter 4

Computational Methods and Tools

We have seen in Chapter 2 how cross-sections at hadron colliders can be calculated. Most of these integrals cannot be solved analytically due to their mathematical complexity. Further complications can arise due to the necessity of numerical inputs like PDFs. Hence, numerical methods have to be used. I have discussed the MC method, which randomly samples the whole phase space and only accepts points which are inside the integrand, in Section 2.3.

In Section 4.1, I will introduce MCFM, the software package used to calculate the integrated and differential cross-sections and in Section 4.2 I will describe my modifications to MCFM. These are fixing the statistical errors for histograms, inclusion of arbitrary factors for scales, inclusion of PDF and scale uncertainties for histograms, implementation of custom cuts and histograms, and output customisations.

Section 4.3 describes the scripts used to combine the results of sub-processes and different scale factors. It also gives a quick overview of the analysis scripts used to compare static and dynamic scales, as well as different PDF sets.

Finally, I will show how all this has been automated and run on a Beowulf cluster at the Centre for Particle Physics at Royal Holloway. In particular, Section 4.4.3 shows how the number of shots[1] used in the MC integration has been tuned in order to obtain precise results for all calculations while trying to keep total computational time low.

4.1 MCFM Software Package

The *Monte Carlo for Femtobarn processes at Hadron Colliders* software package (MCFM) has been chosen for cross-section calculations. It is written in Fortran and maintained by Campbell and Ellis [41, 42]. It provides matrix elements for all investigated processes and has the ability to calculate both integrated, as well as differential cross-sections.

MCFM uses the Vegas MC method [43], which includes importance sampling as described in Section 2.3. In order to achieve this MCFM splits the phase space into a

[1] A shot is a set of random numbers generated to calculate one point in the MC phase space.

subregions and performs the MC integration with fewer shots than will be used for the final run. During this conditioning run the relative contributions to the total integral of each of the subregions is determined and all other results are disregarded. For subregions which contribute more towards the total integral a larger proportion of shots will be used during the final run and their contributions will be weighted accordingly to compensate for this oversampling.

The MCFM package provides a number of preset PDF sets, but it also allows the incorporation of any set of PDFs by using the LHAPDF package [44]. For my LO level calculation I used CTEQ6L1 and MSTW2008LO (90% C.L.). The latter comes with several eigenvector subsets in order to calculate the PDF uncertainties.

For this, the cross-section has to be calculated for each of the eigenvector subsets (see Section 3.3). This can either be achieved by invoking MCFM for each subset or by using the ability of MCFM to cycle through the PDF sets by itself. The latter cuts down the total run time, because the calculated matrix element for each shot can be reused.

4.2 Custom MCFM Modifications

Some modifications to MCFM have been necessary: fixing a bug in the calculation of statistical errors for differential distributions, implementing the ability for arbitrary dynamical scale factors, implementing custom cuts, implementing custom histograms which include PDF uncertainties and adding outputs which can be used for a complete analysis. I will discuss all five of these in turn.

The modifications have been developed and tested for MCFM 5.8 and MCFM 6.0. All final calculations have been run on the modified version of MCFM 6.0.

4.2.1 Fixing the Statistical Error in Histograms

I implemented a fix for the calculation of integration errors in histograms. I became aware of this issue when I compared the differential cross-section of the ZZ production at hadron colliders, which I had calculated in a test project, with the output of MCFM 5.8. The latter seemed to overestimates the statistical errors by a factor of 10 to 40. Furthermore, comparing the smoothness of the MCFM graphs for a variety of processes in comparison to the statistical error bars also yielded a discrepancy. Again one could see that MCFM was overestimating the statistical errors massively.

This is obviously problematic when calculating PDF and scale uncertainties with a high precision, as one has no way of accurately determining the ratio between the integration error and the PDF/scale uncertainties (see Section 4.4.3). MCFM calculates the integration error in each bin using Equation 3.1 and the total number of shots N for calculating the mean of an observable X and its square, X^2. However, it only divides by

the square root of the number of shots in each bin n_{bin} to normalise the integration error per bin:

$$\Delta X_{bin} = \frac{1}{\sqrt{n_{bin}}} \cdot \sqrt{\frac{1}{N}\sum_{i=1}^{n} X_i^2 + \frac{1}{N^2}\left(\sum_{i=1}^{n} X_i\right)^2}\Bigg|_{bin} \tag{4.1}$$

Sampling the phase space outside of each bin contributes towards minimising the overall statistical uncertainty as well as the error for each bin. Hence, the normalisation has to happen with respect to the total number of shots used including phase space points outside the width of the histogram. The correct statistical uncertainty for each bin is given by:

$$\Delta X_{bin} = \frac{1}{\sqrt{N}} \cdot \sqrt{\frac{1}{N}\sum_{i=1}^{n} X_i^2 + \frac{1}{N^2}\left(\sum_{i=1}^{n} X_i\right)^2}\Bigg|_{bin} \tag{4.2}$$

My implementation[2] has been tested by replacing the integrand with $f(r_i) = r_i$, where r_i are the pseudo-random numbers. Some quick test results can be found in Appendix A.1.[3]

4.2.2 Implementing Numerical Factors for Scales

An important part of this project is to be able to vary the renormalisation scale and factorisation scale by factors of $\sqrt{2}^i$. This is easily done for fixed scales by manually multiplying the factor and scale beforehand, but for dynamic scales it has to be implemented at run time. MCFM has some predefined factors for some of the dynamic scales, but unfortunately, these did not provide the correct steps nor a large enough variation.

I extended MCFM to read in the two factors f_r (for renormalisation scale) and f_f (for factorisation scale) from the input file and then to calculate $\mu_{r/f} = f_{r/f} \cdot \mu_{0,r/f}$, either at the beginning for static scales or before each shot for dynamic scales. My implementation allows for any numerical factor between zero and infinity. Furthermore, I had to thoroughly test it, especially as Ellis and Campbell have not always written their program in the most straightforward way[4]. The test results can be found in Appendix A.2.

[2] My supervisor and I have made the authors aware of this bug and fix in October 2010. As of March 2012 newer versions of MCFM (i.e. 6.0 and 6.1) still include this bug or an incorrect fix.

[3] There is still an error for NLO calculations. Single bins of the output histograms suffer from abnormally large errors, i.e. errors being 10 to 1000 times larger than errors in other bins. This error originates when the dipole contributions are summed up and binned. The latter can lead to an disproportional inflation of the sum of the squared contribution for the error in individual bins giving a false value for the total uncertainty in this bin. No fix could be found by the end of my project.

[4] For example, some function definitions are not consistently used throughout the code. Rather the code has been inserted directly in places.

4.2.3 Implementation of Cuts

I programmed my own routines for the calculation of all observables. The used definitions can be found in Chapter 6. All implementations have been checked against the MCFM presets or manually calculated results.

Furthermore, I developed routines for the standard LHC and Tevatron selection cuts. These include both general acceptance cuts and physics-motivated cuts:

- transverse momentum p_T of charged leptons
- rapidity y of charged leptons
- missing transverse momentum $p_{T,miss}$
- transverse momentum p_T of jets
- rapidity y of jets
- di-lepton invariant mass for two charged leptons from a Z decay
- transverse mass of the W

These were described in Section 2.4. All cuts are automatically chosen, depending on the centre-of-mass energy, the hadron collider setup ($p\overline{p}$ or pp) and the production process chosen in the input file for MCFM. This avoids the need for changing too many input parameters in the input file for each run. The correct implementation of these cuts has been checked using the respective histograms.

4.2.4 Implementation of Histograms Including PDF Uncertainties

Excluding histograms of non-physical observables, the following set of histograms has been implemented[5]:

- transverse momentum for p_T-ordered charged leptons
- rapidity y distribution for p_T-ordered charged leptons
- missing transverse momentum
- transverse momentum distribution for p_T-ordered jets
- rapidity y distribution for p_T-ordered jets
- transverse mass distributions for W^+ and W^- bosons
- invariant mass distribution for Z boson
- two-particle invariant mass for lepton-lepton, lepton-jet and jet-jet
- two-particle rapidity separation between lepton-lepton, lepton-jet and jet-jet
- two-particle azimuthal opening angle between lepton-lepton, lepton-jet and jet-jet
- two-particle separation ΔR between lepton-lepton, lepton-jet and jet-jet

MCFM only calculates the statistical error for each bin in the histogram and PDF uncertainties for the integrated cross-section only. I have extended MCFM by implementing routines which calculate the symmetric and asymmetric PDF uncertainties for each bin.

[5]Giving a total of approximately 30 histograms for the two-jet processes.

4.2.5 Numerical Output

In order to combine separately calculated gluon and quark-quark contributions and to combine different scale factors, it was necessary to output all the numerical values for the integrated cross-sections and distributions with maximum precision[6] so that they could be used by my Python scripts for analysis. Hence all the raw data was written to ASCII files. Their format is described in Appendix A.3.

4.3 Custom Scripts

Not all requirements for calculating PDF and scale uncertainties for investigated processes at different accelerators and for different scales could be implemented by modifying MCFM. Furthermore, some of the analysis is better done independently of MCFM. For this reason I developed a variety of bash and Python scripts customised to solving these specific tasks. These custom scripts are introduced below.

4.3.1 Implementation and Test of Sub-process Summation

MCFM splits processes with two LO jets in the final states into quark-quark and gluon contributions. Using the output data as described in Section 4.2.5 the full integrated and differential cross-sections can be found by simply adding the contributions.[7] Statistical uncertainties have been propagated correctly[8].

A custom Python script has been used to combine raw data files. This script has been checked in a variety of ways, for example by manually calculating for single bins and testing that the output is equal to the input when run on single files. It also catches empty and invalid data for each of the hundreds of subprocesses that cannot all be checked manually for each run.

4.3.2 Combining Scale Uncertainties

An important part of the implementation of scale uncertainties is to calculate scale uncertainties per bin. This process has been automated using my own Python script. This vastly simplifies computing the scale uncertainties for the 48 different total cross-sections and the corresponding histograms. Both symmetric and asymmetric scale uncertainties were obtained. They are discussed in Chapter 8. The resulting distributions including statistical, PDF and scale uncertainties were plotted using gnuplot [45].

[6] Outputting all the significant digits of the Fortran *double precision* data type is required.

[7] This is very similar to computing the matrix element for the virtual and real contributions of NLO processes separately.

[8] A standard error propagation as given in Equation 8.3 has been used.

4.3.3 Comparing PDFs and Scales

Having a final data set for each process, including statistical, PDF and scale uncertainties, it is possible to compare the influence of different PDF sets (e.g. MSTW2008LO (90% C.L.) and CTEQ6L1) as well as different scales (e.g. static scale M_V, dynamic scales E_T^V and $\hat{H}_T$). The required ratios were calculated using a Python script. The resulting distributions including statistical, PDF and scale uncertainties were plotted.

4.4 Computational Requirements and Automation

Preliminary runs have shown that any of the 18 different processes run for up to a few minutes (0 jets), hours (1 jets) or days (2 jets) each. The two jet events are particularly problematic. Each of them has to be calculated in two separate calculations. Hence, the calculation of all these processes on a single processor would take weeks. To overcome this problem all major calculations were done on a Beowulf cluster at the Centre for Particle Physics at Royal Holloway (Section 4.4.2) and the number of shots used for each run has been carefully tuned (Section 4.4.3). Furthermore, a large number of MCFM input files, which are later submitted to the cluster, needed to be written. This has been done with a bash script as described in Section 4.4.1.

4.4.1 Generating Input Files

My modifications of MCFM mean that it is straightforward to calculate different cross-sections, including PDF uncertainties (Section 4.2.4) for different processes, different scale factors (Section 4.2.2) and different accelerators (Section 4.2.3).

It is still necessary, however, to perform separate calculations for the different accelerators, processes (including the separation in quark-quark and gluon contributions for two-jet processes), scales, scale factors and PDF sets. For each of these one needs to rewrite the input file for MCFM. I wrote a bash script to take care of this job. It cycles over all the parameters mentioned and outputs the appropriate input file which it then submits to the cluster.

The same script can also be used to tune the number of shots required (Section 4.4.3) by reading in the appropriate number of shots for each process from a text file.

4.4.2 Computer Cluster Usage

I used the Beowulf cluster at the Centre for Particle Physics at Royal Holloway to calculate all subprocesses separately, using the prepared input files that I described above. The cluster consists of 42 nodes with 4 processors each and 10 nodes with 6 processors each.

It uses PBS for job submission and Torque as a scheduler. After overcoming several problems with the scheduler[9], the final set of calculations has taken less than a week.

The combination of quark-quark and gluon contributions and all the calculations for analysis were done on my local machine afterwards. The time needed for this step is approximately half a day.

4.4.3 Tuning the Number of Shots

After all this preliminary work, it is now necessary to set the number of shots in such a way that the integration error in each bin is at most 10% of the PDF error in each bin ($\Delta\sigma_{bin}^{MC} \approx 0.1\Delta\sigma_{bin}^{PDF}$). Obviously such a task is extremely labour intensive given the large amount of data, i.e. several thousand sets with dozens of histograms each.

I can simplify this task by assuming that the PDF error in each histogram bin is approximately equal to the PDF error of the total cross-section ($\Delta\sigma_{tot}^{PDF} := 0.1\Delta\sigma_{bin}^{PDF}$). All my histograms have approx. 40 bins, hence the statistical error per bin can be related to the statistical error of the cross-section ($\Delta\sigma_{tot}^{MC} \simeq {}^{1}/\sqrt{40}\Delta\sigma_{bin}^{MC}$). So I find that:

$$\Delta\sigma_{tot}^{MC} \simeq \frac{0.1}{\sqrt{40}}\Delta\sigma_{tot}^{PDF} \approx 0.0158\Delta\sigma_{tot}^{PDF} \tag{4.3}$$

I have fully calculated all the simulations for 10*10000 shots in the preliminary run and 10*1000000 shots in the final run[10]. Assuming that the Vegas grid is fully adapted, the MC error should be indirectly proportional to the square root of the number of shots used. Hence, I can estimate how many shots are required to obtain the required accuracy. The final number of shots have been chosen in such a way that the relative statistical error is smaller than 0.1% and does not exceed 1.58% of the PDF uncertainties.

[9]The scheduler does not allow pausing of large jobs to quickly process short jobs. Hence, I had to write my own script which gradually releases my jobs keeping some percentage of the farm free for other members of the group to use.

[10]On a single processor the total computational time would be 4 days for all LO calculations. Hence, the total walltime on the farm is less than one week.

Chapter 5

Weak Boson Production in Association with Jets

In Chapter 2 I showed how one can calculate SM cross-sections at hadron colliders. I have investigated the associated theoretical uncertainties in Chapter 3 and gave a quick overview of the computational tools used in Chapter 4. Now, I want to introduce the specific processes which I have investigated. These are:

- $\mathrm{p}^{(}\overline{\mathrm{p}}^{)} \to (\mathrm{W}^+ \to \ell^+\nu_\ell) + X$
- $\mathrm{p}^{(}\overline{\mathrm{p}}^{)} \to (\mathrm{W}^+ \to \ell^+\nu_\ell) + 1\ jet + X$
- $\mathrm{p}^{(}\overline{\mathrm{p}}^{)} \to (\mathrm{W}^+ \to \ell^+\nu_\ell) + 2\ jets + X$
- $\mathrm{p}^{(}\overline{\mathrm{p}}^{)} \to (\mathrm{W}^- \to \ell^-\overline{\nu}_\ell) + X$
- $\mathrm{p}^{(}\overline{\mathrm{p}}^{)} \to (\mathrm{W}^- \to \ell^-\overline{\nu}_\ell) + 1\ jet + X$
- $\mathrm{p}^{(}\overline{\mathrm{p}}^{)} \to (\mathrm{W}^- \to \ell^-\overline{\nu}_\ell) + 2\ jets + X$
- $\mathrm{p}^{(}\overline{\mathrm{p}}^{)} \to (\mathrm{Z} \to \ell^-\ell^+) + X$
- $\mathrm{p}^{(}\overline{\mathrm{p}}^{)} \to (\mathrm{Z} \to \ell^-\ell^+) + 1\ jet + X$
- $\mathrm{p}^{(}\overline{\mathrm{p}}^{)} \to (\mathrm{Z} \to \ell^-\ell^+) + 2\ jets + X$
- $\mathrm{p}^{(}\overline{\mathrm{p}}^{)} \to (\mathrm{Z} \to \sum_{\ell=\mathrm{e},\mu,\tau} \nu_\ell\overline{\nu}_\ell) + X$
- $\mathrm{p}^{(}\overline{\mathrm{p}}^{)} \to (\mathrm{Z} \to \sum_{\ell=\mathrm{e},\mu,\tau} \nu_\ell\overline{\nu}_\ell) + 1\ jet + X$
- $\mathrm{p}^{(}\overline{\mathrm{p}}^{)} \to (\mathrm{Z} \to \sum_{\ell=\mathrm{e},\mu,\tau} \nu_\ell\overline{\nu}_\ell) + 2\ jets + X$

where X are partons from the initial protons, which do not participate in the hard scattering event. Future use of these equations will omit $+X$.

I will first discuss the production and decay of weak bosons without associated jets. I will show all possible subprocesses for the production of W bosons decaying into a charged lepton and a neutrino, and for the production of Z bosons with decay into charged leptons or invisible decay. I will consider W^+ and W^- at the same time as both processes are quite similar. My introduction for processes including one associated jet is slightly more generic as I will only present Feynman diagrams for general weak boson production without decay. Finally, I will present the possible types of Feynman diagrams for the production with two associated jets.

5.1 No Associated Jets

At tree level the simplest production process for weak bosons with subsequent leptonic decay has no associated jets. Firstly, I will look at the production of $W^{\pm}$ bosons and subsequently the production of Z bosons.

5.1.1 $W^{\pm}$ Production and Decay into Charged Leptons

In the case of W^+ and W^- bosons we have only s-channel contributions with a quark-antiquark initial state, i.e. one up-type quark and one down-type quark. I am only interested in leptonic decays of the $W^{\pm}$ boson, i.e. the decay into a charged lepton and a neutrino. There is only one basic Feynman diagram for each as shown in Figure 5.1.

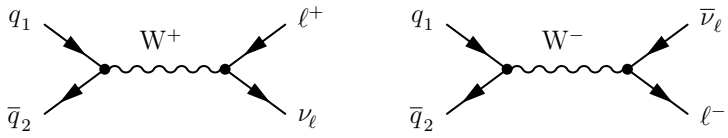

Figure 5.1: Feynman diagrams for $W^{\pm}$ production with leptonic decay at hadron colliders: $q_1\overline{q}_2 \to W^+ \to \ell^+\nu$ (left) and $q_1\overline{q}_2 \to W^- \to \ell^-\overline{\nu}$ (right). For possible q_1q_2 pairs see Table 5.1.

For the presented diagrams there are only two possible initial states, e.g. $u\overline{d}$ and $c\overline{s}$ for W^+. Two more diagrams exist, because each of the quarks can come from either of the colliding protons (which in this case is identical to reversing the direction of the fermion line), e.g. $\overline{d}u$ and $\overline{s}c$ for W^+. There is no initial state involving bottom quarks, because it would require a top quark, which are too heavy to be produced in an important amount. Moreover, there are three final states corresponding to the three generations of leptons. Hence there are twelve subprocesses for the production of each of the W bosons. The possible fermion lines, final states and number of subprocesses are summarised in Table 5.1.

5.1.2 Z Production with Decay into Charged Leptons or Neutrinos

The initial state for the Z production is a simple quark-antiquark pair of the same flavour. In contrast to W^+ production there are ten possible initial states: these are five possible quark-antiquark pairs ($u\overline{u}$, $c\overline{c}$, $d\overline{d}$, $s\overline{s}$ and $b\overline{b}$) and five corresponding antiquark-quark pairs. Again, I am not considering top quarks.

I am also only considering leptonic decays of Z bosons. These can either be pairs of oppositely-charged leptons or pairs of a neutrino and antineutrino. The former is also known as Drell–Yan process and the propagator between the quark pair and the lepton pair can also be a virtual photon γ^*. This process will be included in all calculated cross-sections, because it is not possible to distinguish the experimental measurements for each propagator from each other. [46]

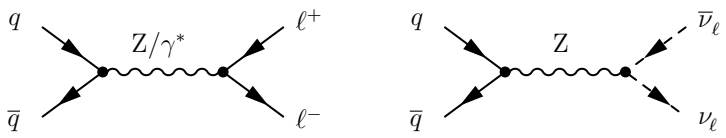

Figure 5.2: Feynman diagrams for Z production at hadron colliders with decay into charged leptons $q\overline{q} \to \mathrm{Z}/\gamma^* \to \ell^+\ell^-$ (left) and invisible decay $q\overline{q} \to \mathrm{Z} \to \overline{\nu}_\ell\nu_\ell$ (right). For possible $q\overline{q}$ pairs see Table 5.1

For both the decay in charged leptons and the decay into neutrinos there are three possible decays corresponding to three generations of leptons. I already mentioned in Section 2.4 that, for the decay into two charged leptons, the propagator can also be a virtual photon and it is experimentally impossible to determine the propagator of a given final state. Hence, all my calculated cross-sections are a summation of both processes, even if it is not explicitly stated in later chapters.

The corresponding Feynman diagrams are shown in Figure 5.2 and all the possible initial states and final states are listed in Table 5.1.

5.2 One Associated Jet

I will now consider weak boson production with one associated jet. It is clear that neither the final state charged lepton nor the neutrino can emit a gluon, the only source for an additional jet for the zero-jet process is from initial state radiation of either quark. This is shown in Figure 5.3. Similar to the W boson production without associated jets, there are two possible quark-antiquark pairs (one up-type quark and one down-type quark) for the initial state and the quarks can be contributed by either proton. So for the two Feynman diagrams and three possible decays there are 24 subprocesses for $\mathrm{W}^\pm$ production with an quark-quark initial state.

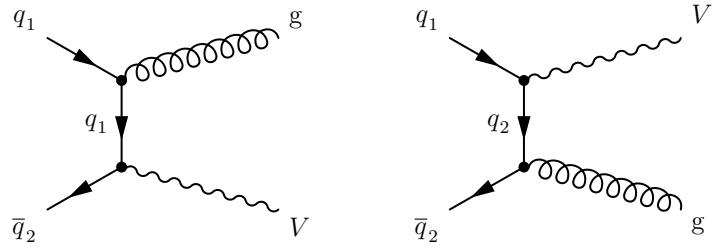

Figure 5.3: Feynman diagrams for vector boson production with one associated gluon from quark-quark initial state: $q_1\overline{q}_2 \to V\mathrm{g}$. For possible $q_1\overline{q}_2$ pairs see Table 5.1.

In addition to the quark-quark initial state there is also the possibility of a gluon-quark initial state for which there is an s-channel and a t/u-channel contribution, depending where along the fermion line the weak boson is emitted. This is recorded in Figure 5.4. There are four possible fermion lines, e.g. du, sc, $\overline{\mathrm{u}}\overline{\mathrm{d}}$ and $\overline{\mathrm{c}}\overline{\mathrm{s}}$ for W^+ where the latter two reverse the fermion line with respect to the diagrams in the figure. Additionally, the

initial gluon could come from either proton and there are three possible decays of the W boson. This gives 48 subprocesses for $W^{\pm}$ production with a gluon-quark initial state. In total there are 72 subprocesses for each of the W bosons.

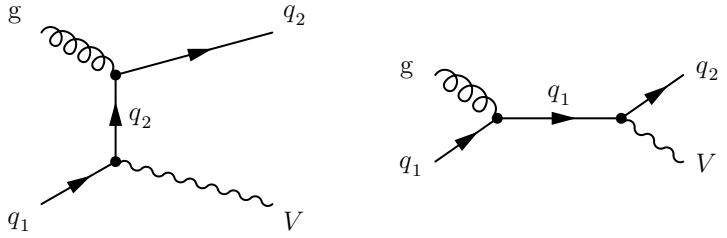

Figure 5.4: Feynman diagrams for vector boson production with one associated quark from gluon-quark initial state: $gq_1 \to Vq_2$. For possible q_1q_2 pairs see Table 5.1.

There are even more possible subprocesses for Z production. For the quark-antiquark initial state we have five possible quark pairs, as seen for the 0-jet production. This gives 60 subprocesses for the two diagrams. The gluon-quark initial state allows any quark to form the fermion line (apart from the t and $\bar{t}$), which means there are 120 possible subprocesses. In total there are 180 subprocesses for the Z production with one associated jet for either a decay into charged leptons or an invisible decay. A summary of possible fermion lines, initial and final states, and the resulting number of subprocesses is shown in Table 5.1.

5.3 Two Associated Jets

As previously, we can have a quark-quark and gluon-quark initial state. But for processes involving two associated jets, gluon-gluon initial states are also possible. This is particularly important for hadron colliders with large centre-of-mass energies like the LHC, where such initial states are much more likely. [35, 36]

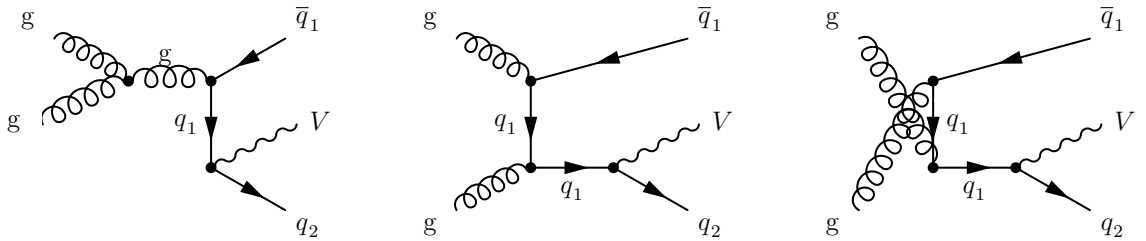

Figure 5.5: Feynman diagrams for vector boson production with two associated quarks from a gluon-gluon initial state: $gg \to V\overline{q}_1q_2$. The two right hand graphs represent two different kinematic configurations of the initial state. All three diagrams show a q_1q_2 fermion line with the strong vertices before the weak vertex. Swapping the vertices gives two independent diagrams for the left graph and three independent diagrams for each of the right hand graphs. For possible q_1q_2 pairs see Table 5.2.

The gluons can fuse to a single gluon, which then in turn couples to the fermion line which emits the weak boson. The weak vertex can be before or after the gluon vertex.

Alternatively, both gluons can couple to the fermion line separately and there are two possible initial states depending on which proton contributes which gluon. The weak boson is emitted from the fermion line before, in between or after these strong vertices. Hence, there are eight possible diagrams. Three of these (neglecting the order of strong and weak couplings) are shown in Figure 5.5. There are only two possible fermion lines for $W^{\pm}$ production, but ten for Z production. Including the three possible leptonic decays, we have 48 and 120 possible subprocesses, respectively.

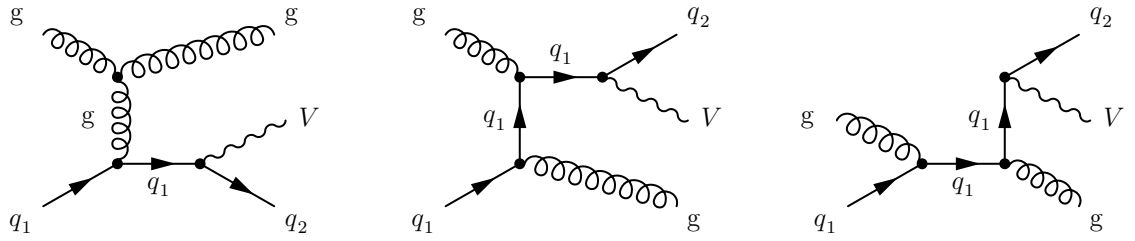

Figure 5.6: Feynman diagrams for vector boson production with one associated gluon and one associated quark from a gluon-quark initial state: $gq_1 \to Vgq_2$. Both diagrams show a q_1q_2 fermion line with the strong vertices before the weak vertex. Swapping the vertices gives two independent diagrams for the left graph and three independent diagrams for each of the right hand graphs. For possible q_1q_2 pairs see Table 5.2.

For 1-jet diagrams with a gluon-quark initial state, either a quark or the initial gluon could radiate an additional gluon giving a second jet in the final state. This is recorded in Figure 5.6. Taking the order of weak and strong couplings into account gives eight independent diagrams. So after considering contributions from both protons and the three possible final lepton states gives 192 subprocesses for $W^{\pm}$ production and 480 for Z production. There are only four possible fermion lines for W bosons, but ten for the Z boson.

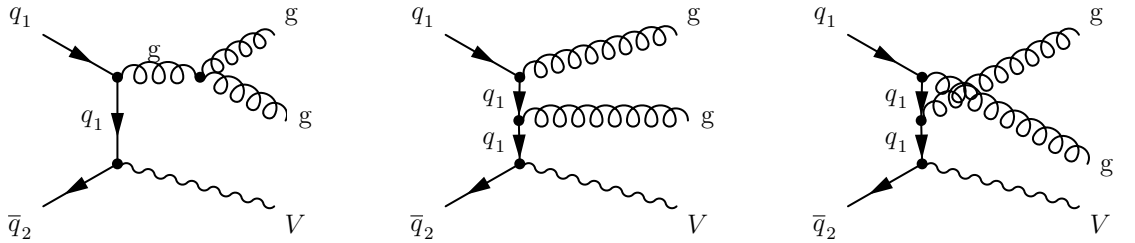

Figure 5.7: Feynman diagrams for vector boson production with two associated gluons from a quark-quark initial state: $q_1\overline{q}_2 \to Vgg$. The two right hand graphs represent two different kinematic configurations of the final state. All three diagrams show a q_1q_2 fermion line with the gluon vertex before the weak vertex. Swapping the vertices gives two independent diagrams for the left graph and three independent diagrams for each of the right hand graphs. For possible q_1q_2 pairs see Table 5.2.

Building on the 1-jet diagrams with quark-quark initial states, a second gluon can be emitted from the fermion line or the first emitted gluon could split into two. This is shown in Figure 5.7. Swapping the strong and weak vertices around gives eight possible

diagrams. There are two possible choices for the quark-quark initial state for $W^{\pm}$ production and five different ones for Z production. Together with the lepton final states and the possibility of quarks being contributed by either proton there are 96 and 240 subprocesses for $W^{\pm}$ and Z, respectively.

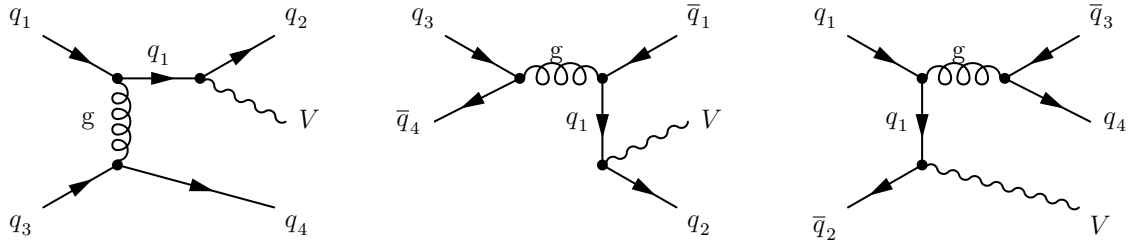

Figure 5.8: Feynman diagrams for vector boson production with two associated quarks from a quark-quark initial state: $q_1q_3 \to Vq_2q_4$ (left), $q_3\overline{q}_4 \to V\overline{q}_1q_2$ (middle) and $q_1\overline{q}_2 \to V\overline{q}_3q_4$ (right). All three diagrams show a q_1q_2 fermion line with the gluon vertex before the weak vertex. Swapping the vertices gives two independent diagrams for each of the three graphs. For possible q_1q_2 and q_3q_4 pairs see Table 5.2.

There is another group of quark-quark initial states, where a gluon is either exchanged between the two incoming quarks (t/u-channel) or the two quarks annihilate by forming a gluon, which itself decays into a quark pair (s-channel). In the latter case the weak boson can be emitted by the initial state quark pair or the final state pair. These contributions are sketched in Figure 5.8.

Swapping the order of the strong vertices gives two possible contributions each. The t/u-channel contribution has four possible choices for the fermion line emitting the W boson and ten for the other fermion line, which gives a total of 528 possible subprocesses. Eight of these subprocesses are due to final states with two quarks of identical flavour which can occur in two possible kinematic states. In contrast, if a Z boson is emitted, there are ten different choices for the emitting fermion line, which gives 1320 possible subprocesses counting all possible kinematic arrangements.

The s-channel contributions each have two possible choices of quark pairs for the fermion line emitting the W boson and five for the other fermion line. Including final states and allowing for quarks to come from either proton there are 120 subprocesses each. In case of an emission of a Z boson there are 5 corresponding fermion lines, giving 300 subprocesses for each of the shown diagrams.

In total there are 1104 possible subprocesses for $W^{\pm}$ production and 2760 possible subprocesses for Z. An overview of all the possible initial states, final states and fermion lines is given in Table 5.2.

Table 5.1: Shown are all possible q_1q_2 pairs for the fermion line in Figures 5.1 to 5.3. Some listed quark pairs invert the direction of the fermion line. Initial states of the quarks or gluons, number of independent diagrams, possible decays of the weak boson (lepton final states) and the total number of subprocesses are also recorded.

Process	**Initial States**	**Indep. Diag.**	q_1q_2	**Lepton Final States**	**No. of Processes**
$q_1\overline{q}_2 \to (W^+ \to \ell^+\nu)$	$q_1\overline{q}_2$,$\overline{q}_2q_1$	1	$u\overline{d}$,$c\overline{s}$		$1 \cdot 2 \cdot 2 \cdot 3 = 12$
$gq_1 \to (W^+ \to \ell^+\nu)\ q_2$	gq_1,q_1g	2	ud,cs,$\overline{d}\overline{u}$,$\overline{s}\overline{c}$	$e^+\nu_e$,$\mu^+\nu_\mu$,$\tau^+\nu_\tau$	$2 \cdot 2 \cdot 4 \cdot 3 = 48$
$q_1\overline{q}_2 \to (W^+ \to \ell^+\nu)\ g$	$q_1\overline{q}_2$,$\overline{q}_2q_1$	2	$u\overline{d}$,$c\overline{s}$		$2 \cdot 2 \cdot 2 \cdot 3 = 24$
$q_1\overline{q}_2 \to (W^- \to \ell^-\overline{\nu})$	$q_1\overline{q}_2$,$\overline{q}_2q_1$	1	$d\overline{u}$,$s\overline{c}$		$1 \cdot 2 \cdot 2 \cdot 3 = 12$
$gq_1 \to (W^- \to \ell^-\overline{\nu})\ q_2$	gq_1,q_1g	2	du,sc,$\overline{u}\overline{d}$,$\overline{c}\overline{s}$	$e^-\overline{\nu}_e$,$\mu^-\overline{\nu}_\mu$,$\tau^-\overline{\nu}_\tau$	$2 \cdot 2 \cdot 4 \cdot 3 = 48$
$q_1\overline{q}_2 \to (W^- \to \ell^-\overline{\nu})g$	$q_1\overline{q}_2$,$\overline{q}_2q_1$	2	$d\overline{u}$,$s\overline{c}$		$2 \cdot 2 \cdot 2 \cdot 3 = 24$
$q\overline{q} \to (Z/\gamma^* \to \ell^+\ell^-)$	$q\overline{q}$,$\overline{q}q$	1	$u\overline{u}$,$c\overline{c}$,$d\overline{d}$,$s\overline{s}$,$b\overline{b}$		$1 \cdot 2 \cdot 5 \cdot 3 = 30$
$gq_1 \to (Z/\gamma^* \to \ell^+\ell^-)\ q_2$	gq_1,q_1g	2	uu,cc,dd,ss,bb, $\overline{u}\overline{u}$,$\overline{c}\overline{c}$,$\overline{d}\overline{d}$,$\overline{s}\overline{s}$,$\overline{b}\overline{b}$	e^+e^-,$\mu^+\mu^-$,$\tau^+\tau^-$	$2 \cdot 2 \cdot 10 \cdot 3 = 120$
$q_1\overline{q}_2 \to (Z/\gamma^* \to \ell^+\ell^-)\ g$	$q_1\overline{q}_2$,$\overline{q}_2q_1$	2	$u\overline{u}$,$c\overline{c}$,$d\overline{d}$,$s\overline{s}$,$b\overline{b}$		$2 \cdot 2 \cdot 5 \cdot 3 = 60$
$q\overline{q} \to (Z \to \overline{\nu}_\ell\nu_\ell)$	$q\overline{q}$,$\overline{q}q$	1	$u\overline{u}$,$c\overline{c}$,$d\overline{d}$,$s\overline{s}$,$b\overline{b}$		$1 \cdot 2 \cdot 5 \cdot 3 = 30$
$gq_1 \to (Z \to \overline{\nu}_\ell\nu_\ell)\ q_2$	gq_1,q_1g	2	uu,cc,dd,ss,bb, $\overline{u}\overline{u}$,$\overline{c}\overline{c}$,$\overline{d}\overline{d}$,$\overline{s}\overline{s}$,$\overline{b}\overline{b}$	$\overline{\nu}_e\nu_e$,$\overline{\nu}_\mu\nu_\mu$,$\overline{\nu}_\tau\nu_\tau$	$2 \cdot 2 \cdot 10 \cdot 3 = 120$
$q_1\overline{q}_2 \to (Z \to \overline{\nu}_\ell\nu_\ell)\ g$	$q_1\overline{q}_2$,$\overline{q}_2q_1$	2	$u\overline{u}$,$c\overline{c}$,$d\overline{d}$,$s\overline{s}$,$b\overline{b}$		$2 \cdot 2 \cdot 5 \cdot 3 = 60$

Table 5.2: Shown are all possible q_1q_2 and q_3q_4 pairs for the fermion lines in Figures 5.5 to 5.8. Some listed quark pairs invert the direction of the fermion line. Initial states of the quarks or gluons, number of independent diagrams, possible decays of the weak boson (lepton final states) and the total number of subprocesses are also recorded.

Process	Initial States	Indep. Diag.	q_1q_2	q_3q_4	Lepton Final States	No. of Processes
$gg \to W^+ \; \bar{q}_1 q_2$	gg	8	$\bar{u}d$,$\bar{c}s$	-		$1 \cdot 8 \cdot 2 \cdot 3 = 48$
$gq_1 \to W^+ \; gq_2$	gq,qg	8	ud,cs,$\bar{d}\bar{u}$,$\bar{s}\bar{c}$	-		$2 \cdot 8 \cdot 4 \cdot 3 = 192$
$q_1\bar{q}_2 \to W^+ \; gg$	$q_1\bar{q}_2$,$\bar{q}_2q_1$	8	$u\bar{d}$,$c\bar{s}$	-	$e^+\nu_e$,$\mu^+\nu_\mu$,$\tau^+\nu_\tau$ for $W^+ \to \ell^+\nu_\ell$	$2 \cdot 8 \cdot 2 \cdot 3 = 96$
$q_1q_3 \to W^+ \; q_2q_4$	q_3q_1,q_1q_3	2	ud,cs,$\bar{d}\bar{u}$,$\bar{s}\bar{c}$	uu,cc,dd,ss,bb, $\bar{u}\bar{u}$,$\bar{c}\bar{c}$,$\bar{d}\bar{d}$,$\bar{s}\bar{s}$,$\bar{b}\bar{b}$		$2 \cdot 2 \cdot (4 \cdot 10 + 4) \cdot 3 = 528$ [a]
$q_3\bar{q}_4 \to W^+ \; \bar{q}_1q_2$	$q_3\bar{q}_4$,$\bar{q}_4q_3$	2	$u\bar{d}$,$c\bar{s}$	$u\bar{u}$,$c\bar{c}$,$d\bar{d}$,$s\bar{s}$,$b\bar{b}$		$2 \cdot 2 \cdot (2 \cdot 5) \cdot 3 = 120$
$q_1\bar{q}_2 \to W^+ \; \bar{q}_3q_4$	$q_1\bar{q}_2$,$\bar{q}_2q_1$	2	$u\bar{d}$,$c\bar{s}$	$u\bar{u}$,$c\bar{c}$,$d\bar{d}$,$s\bar{s}$,$b\bar{b}$		$2 \cdot 2 \cdot (2 \cdot 5) \cdot 3 = 120$
$gg \to W^- \; \bar{q}_1q_2$	gg	8	$\bar{d}u$,$\bar{s}c$	-		$1 \cdot 8 \cdot 2 \cdot 3 = 48$
$gq_1 \to W^- \; gq_2$	gq,qg	8	du,sc,$\bar{u}\bar{d}$,$\bar{c}\bar{s}$	-		$2 \cdot 8 \cdot 4 \cdot 3 = 192$
$q_1\bar{q}_2 \to W^- \; gg$	$q_1\bar{q}_2$,$\bar{q}_2q_1$	8	$d\bar{u}$,$s\bar{c}$	-	$e^-\bar{\nu}_e$,$\mu^-\bar{\nu}_\mu$,$\tau^-\bar{\nu}_\tau$ for $W^- \to \ell^-\bar{\nu}_\ell$	$2 \cdot 8 \cdot 2 \cdot 3 = 96$
$q_1q_3 \to W^- \; q_2q_4$	q_3q_1,q_1q_3	2	du,sc,$\bar{u}\bar{d}$,$\bar{c}\bar{s}$	uu,cc,dd,ss,bb, $\bar{u}\bar{u}$,$\bar{c}\bar{c}$,$\bar{d}\bar{d}$,$\bar{s}\bar{s}$,$\bar{b}\bar{b}$		$2 \cdot 2 \cdot (4 \cdot 10 + 4) \cdot 3 = 528$ [b]
$q_3\bar{q}_4 \to W^- \; \bar{q}_1q_2$	$q_3\bar{q}_4$,$\bar{q}_4q_3$	2	$d\bar{u}$,$s\bar{c}$	$u\bar{u}$,$c\bar{c}$,$d\bar{d}$,$s\bar{s}$,$b\bar{b}$		$2 \cdot 2 \cdot (2 \cdot 5) \cdot 3 = 120$
$q_1\bar{q}_2 \to W^- \; \bar{q}_3q_4$	$q_1\bar{q}_2$,$\bar{q}_2q_1$	2	$d\bar{u}$,$s\bar{c}$	$u\bar{u}$,$c\bar{c}$,$d\bar{d}$,$s\bar{s}$,$b\bar{b}$		$2 \cdot 2 \cdot (2 \cdot 5) \cdot 3 = 120$
$gg \to Z \; \bar{q}_1q_2$	gg	8	$\bar{u}u$,$\bar{c}c$,$\bar{d}d$,$\bar{s}s$,$\bar{b}b$	-		$1 \cdot 8 \cdot 5 \cdot 3 = 120$
$gq_1 \to Z \; gq_2$	gq,qg	8	uu,cc,dd,ss,bb, $\bar{u}\bar{u}$,$\bar{c}\bar{c}$,$\bar{d}\bar{d}$,$\bar{s}\bar{s}$,$\bar{b}\bar{b}$	-	e^+e^-,$\mu^+\mu^-$,$\tau^+\tau^-$ for $Z/\gamma^* \to \ell^+\ell^-$	$2 \cdot 8 \cdot 10 \cdot 3 = 480$
$q_1\bar{q}_2 \to Z \; gg$	$q_1\bar{q}_2$,$\bar{q}_2q_1$	8	$u\bar{u}$,$c\bar{c}$,$d\bar{d}$,$s\bar{s}$,$b\bar{b}$	-	or	$2 \cdot 8 \cdot 5 \cdot 3 = 240$
$q_1q_3 \to Z \; q_2q_4$	q_3q_1,q_1q_3	2	uu,cc,dd,ss,bb, $\bar{u}\bar{u}$,$\bar{c}\bar{c}$,$\bar{d}\bar{d}$,$\bar{s}\bar{s}$,$\bar{b}\bar{b}$	uu,cc,dd,ss,bb, $\bar{u}\bar{u}$,$\bar{c}\bar{c}$,$\bar{d}\bar{d}$,$\bar{s}\bar{s}$,$\bar{b}\bar{b}$	$\bar{\nu}_e\nu_e$,$\bar{\nu}_\mu\nu_\mu$,$\bar{\nu}_\tau\nu_\tau$ for $Z \to \bar{\nu}_\ell\nu_\ell$	$2 \cdot 2 \cdot (10 \cdot 10 + 10) \cdot 3 = 1320$ [c]
$q_3\bar{q}_4 \to Z \; \bar{q}_1q_2$	$q_3\bar{q}_4$,$\bar{q}_4q_3$	2	$u\bar{u}$,$c\bar{c}$,$d\bar{d}$,$s\bar{s}$,$b\bar{b}$	$u\bar{u}$,$c\bar{c}$,$d\bar{d}$,$s\bar{s}$,$b\bar{b}$		$2 \cdot 2 \cdot (5 \cdot 5) \cdot 3 = 300$
$q_1\bar{q}_2 \to Z \; \bar{q}_3q_4$	$q_1\bar{q}_2$,$\bar{q}_2q_1$	2	$u\bar{u}$,$c\bar{c}$,$d\bar{d}$,$s\bar{s}$,$b\bar{b}$	$u\bar{u}$,$c\bar{c}$,$d\bar{d}$,$s\bar{s}$,$b\bar{b}$		$2 \cdot 2 \cdot (5 \cdot 5) \cdot 3 = 300$

[a] There are four additional diagrams due to the final states with dd, ss, $\bar{u}\bar{u}$ and $\bar{c}\bar{c}$ having two possible kinematic arrangements.
[b] There are four additional diagrams due to the final states with uu, cc, $\bar{d}\bar{d}$ and $\bar{s}\bar{s}$ having two possible kinematic arrangements.
[c] There are ten additional diagrams due to the final states with uu, cc, dd, ss, bb, $\bar{u}\bar{u}$, $\bar{c}\bar{c}$, $\bar{d}\bar{d}$, $\bar{s}\bar{s}$ and $\bar{b}\bar{b}$ having two possible kinematic arrangements.

Chapter 6

Observables

In Chapter 2 I have shown how to calculate integrated cross-sections at hadron colliders. The total cross-section is just one of many possible observables. Of particular interest to us are differential cross-sections as these help us to understand the kinematics of the scattering processes better.

While hadron colliders are excellent machines in the quest for pushing the energy and luminosity limits, they can only achieve these benefits by using compound particles, i.e. protons and anti-protons. Hence, the parton-parton centre-of-mass frame will be generally boosted in the forward/backward direction relative to the lab frame and this boost is different for each event. Therefore, hadron collider observables should be observables that are Lorentz-invariant under boost along the z-axis or alternatively observables that are additive.[1]

In this chapter I will introduce the ideas of invariant mass, transverse momentum, missing transverse momentum and transverse mass, which are all invariant with respect to z-boost. I will also mention rapidity and pseudo-rapidity. Finally, I will introduce distance observables which are invariant, i.e. separation in rapidity, azimuthal opening angle and the "lego plot" distance. More details on these observables can be found in the literature, for example: Han [17] and Krämer and Soler [47].

6.1 Invariant Mass

The invariant mass of n particles is defined via the sum of their four-momenta squared:

$$M^2 = p^2 = \left(\sum_{i=1}^{n} p_i \right)^2 \tag{6.1}$$

The invariant mass of multiple final state particles can be used to find mass resonances, if they originate from a decay. I have plotted multiple two-particle invariant masses for

[1] This requirement is not essential, but different hard scattering events are easier to compare to each other if the reference frame is the same.

the investigated processes. It is defined by:

$$\begin{aligned} M_{1,2}^2 = p_{1,2}^2 &= (p_1 + p_2)^2 \\ &= (E_1 + E_2)^2 - (\vec{p}_1 + \vec{p}_2)^2 \\ &= m_1^2 + m_2^2 + 2\left(E_1 E_2 - \vec{p}_1 \cdot \vec{p}_2\right) \end{aligned} \tag{6.2}$$

And for relativistic particles ($E >> m$):

$$M_{1,2} = \sqrt{2|\vec{p}_1||\vec{p}_2|\left(1 - \cos\Delta\theta_{1,2}\right)} \tag{6.3}$$

because $m_i \approx 0$, $E_i = p_i$ and $\vec{p}_1 \cdot \vec{p}_2 = |\vec{p}_1||\vec{p}_2| \cos\Delta\theta_{1,2}$ where $\Delta\theta_{1,2}$ is the opening angle between the two particles.

6.2 Transverse Momentum

The overall z-boost cannot be measured when particles escape detection, either due to small couplings (e.g. neutrinos) or due to the finite coverage of the solid angle by the detector (i.e. the beamline punctures the detector). Therefore, final state momenta cannot be transferred to the centre-of-mass frame of the scattering process.

In contrast, the transverse components of the three momentum are invariant. The transverse momentum can be calculated for one or more particle:

$$p_T := \sqrt{\left(\sum_i p_{x,i}\right)^2 + \left(\sum_i p_{y,i}\right)^2} \tag{6.4}$$

As mentioned above, some particles escape detection. Due to the nature of head-on collisions, one can assume that the total initial transverse momentum of the particles participating in the inelastic scattering is zero. Using momentum conservation on the transverse plane one can calculate the missing transverse momentum:

$$\begin{aligned} \vec{p}_T &= \vec{p}_{T,miss} + \vec{p}_{T,detected} = 0 \\ \vec{p}_{T,miss} &:= -\vec{p}_{T,detected} \end{aligned} \tag{6.5}$$

This observable is particularly useful for final states with one neutrino.

6.3 Transverse Energy

Using the invariant mass and the transverse momentum defined above, one can calculate the transverse energy of a particle:

$$E_T := \sqrt{M^2 + p_T^2} \tag{6.6}$$

I will not calculate any differential cross-sections for this observable, but it will be needed in the calculation of other observables as well as for calculating the dynamic scales.

6.4 Transverse Mass

In order to calculate the invariant mass one needs to know the kinematics of all of the particles. As just discussed, this is not possible if there are neutrinos in the final state. For example, if a W boson decays into a charged lepton and a neutrino, the transverse mass observable can be used. Using only the transverse components of the invariant mass of two particles (Equation 6.2):

$$M_{T,1,2}^2 = m_1^2 + m_2^2 + 2\left(E_{T,1}E_{T,2} - \vec{p}_{T,1} \cdot \vec{p}_{T,2}\right) \tag{6.7}$$

And for relativistic particles ($E >> m$):

$$M_{T,1,2} = \sqrt{2p_{T,1}p_{T,2}\left(1 - \cos\Delta\phi_{1,2}\right)} \tag{6.8}$$

because $m_i \approx 0$, $E_{T,i} = p_{T,i}$ and $\vec{p}_{T,1} \cdot \vec{p}_{T,2} = p_{T,1}p_{T,2}\cos\Delta\phi_{1,2}$ where $\Delta\phi_{1,2}$ is the azimuthal opening angle between the two particles.

For example, in case of a leptonic decay of the W boson one obtains:

$$\begin{aligned} M_{T,\ell,\nu} &= \sqrt{2 \cdot p_{T,\ell} \cdot p_{T,\nu} \cdot \left(1 - \cos\Delta\phi_{\ell,\nu}\right)} \\ &= \sqrt{2 \cdot p_{T,\ell} \cdot p_{T,miss} \cdot \left(1 - \cos\Delta\phi_{\ell,miss}\right)} := M_{T,\mathrm{W}} \end{aligned} \tag{6.9}$$

6.5 Rapidity

Rapidity is sometimes also called the hypercubic angle, because it provides the longitudinal projection of the transverse variables:

$$p = \begin{pmatrix} E \\ p_x \\ p_y \\ p_z \end{pmatrix} = \begin{pmatrix} m_T \cdot \cosh y \\ p_T \cdot \cos\phi \\ p_T \cdot \sin\phi \\ m_T \cdot \sinh y \end{pmatrix} \tag{6.10}$$

Hence, the rapidity y is given by:

$$y = \tanh^{-1}\left(\frac{p_z}{E}\right) = \ln\left(\frac{E+p_z}{m_T}\right) = \frac{1}{2}\ln\left(\frac{E+p_z}{E-p_z}\right) \tag{6.11}$$

In contrast, experimentalists often use pseudo-rapidity as it is based on the longitudinal angle and hence can be directly measured. It is defined by:

$$\eta = \frac{1}{2}\ln\left(\frac{|\vec{p}|+p_z}{|\vec{p}|-p_z}\right) = \frac{1}{2}\ln\left(\frac{1+\cos\theta}{1-\cos\theta}\right) = -\ln\tan\frac{\theta}{2} \tag{6.12}$$

It can be seen that $|\eta| \geq |y|$, because $E \geq |\vec{p}|$. This also means that rapidity and pseudo-rapidity are identical for massless particles, which is true for all the rapidities calculated in this report.

While neither rapidity nor pseudo-rapidity are invariant under z-boost, the difference between the rapidity of two particles is:

$$\Delta y = |y_1 - y_2| \tag{6.13}$$

This can be easily shown. A Lorentz boost in the z direction is given by:

$$\gamma = \cosh y_{boost} \qquad \beta\gamma = \sinh y_{boost} \tag{6.14}$$

and can be applied by:

$$\begin{aligned} E' &= +E\cdot\gamma - p_z\cdot\beta\gamma &&= E\cdot\cosh y_{boost} - p_z\cdot\sinh y_{boost} && p'_x = p_x \\ p'_z &= -E\cdot\beta\gamma + p_z\cdot\gamma &&= -E\cdot\sinh y_{boost} + p_z\cdot\cosh y_{boost} && p'_y = p_y \end{aligned} \tag{6.15}$$

Then the boosted rapidity is given by:

$$\begin{aligned} y' &= \ln\frac{E'+p'_z}{m'_T} \\ &= \ln\frac{E\cdot(\cosh y_{boost} - \sinh y_{boost}) + p_z\cdot(\sinh y_{boost} - \cosh y_{boost})}{m_T} \\ &= \ln\left[\frac{E+p_z}{m_T}\cdot(\cosh y_{boost} - \sinh y_{boost})\right] \\ &= ln\frac{E+p_z}{m_T} + \ln(\cosh y_{boost} - \sinh y_{boost}) \\ &= y + k \end{aligned} \tag{6.16}$$

Finally, one can show that the difference between the rapidities is the same in both frames:

$$\Delta y' = y'_2 - y'_1 = y_2 + k - y_1 - k = y_2 - y_1 = \Delta y \tag{6.17}$$

However, the difference between the pseudo-rapidity of two particles $\Delta\eta$ is not z-boost invariant for massive particles.

6.6 Azimuthal Opening Angle

The azimuthal opening angle between two particles is the smallest angle between the particles in the transverse plane, given by:

$$\Delta\phi = \min\left(|\phi_1 - \phi_2|, 2\pi - |\phi_1 - \phi_2|\right) \tag{6.18}$$

This observable is invariant under boost in the z-direction.

6.7 Separation R

The separation R between two particles is also known as the "lego plot" distance, because it is the distance between two particles in ϕ-η plots. It is defined as:

$$\begin{aligned} R &:= \sqrt{(\eta_1 - \eta_2)^2 + (\phi_1 - \phi_2)^2} \\ &= \sqrt{\Delta\eta^2 + \Delta\phi^2} \end{aligned} \tag{6.19}$$

This observable is invariant for massless particles and if one replaces pseudo-rapidity η with rapidity y, it is also invariant for massive particles. Because all my final state particles are relativistic both these definitions give identical results and I will use the following definition:

$$R = \sqrt{\Delta y^2 + \Delta\phi^2} \tag{6.20}$$

This observable has the interesting feature of a kinematic peak at $R = \pi$, because $0 \leq \Delta\phi \leq \pi$ while $0 \leq \Delta y \leq \infty$.

Chapter 7

Results

The following two sections detail the input parameters used by MCFM and the applied selection cuts. The final two sections list the calculated integrated cross-sections and give an overview of the differential cross-sections which have been obtained with respect to a variety of observables. All of the results are at LO only.

7.1 Input Parameters for MCFM

All the presented integrated and differential cross-sections have been calculated using MCFM, which requires a variety of input parameters. Firstly, one needs to define the electroweak scheme [48]:

$$\begin{array}{ccc} M_{\mathrm{Z}} = 91.187\,\mathrm{GeV} & M_{\mathrm{W}} = 80.410\,\mathrm{GeV} & G_F = 1.16639 \times 10 \times 10^{-5}\,\mathrm{GeV}^2 \\ \Gamma_{\mathrm{Z}} = 2.49\,\mathrm{GeV} & \Gamma_{\mathrm{W}} = 2.06\,\mathrm{GeV} & \alpha(M_{\mathrm{Z}})^{-1} = 128.89 \end{array} \tag{7.1}$$

The other electroweak parameters have been derived from these[1] [42]:

$$\begin{array}{ccc} g_e^2 = 0.0975 & M_{\mathrm{t}} = 149.248\,\mathrm{GeV} & M_{\mathrm{b}} = 4.750\,\mathrm{GeV} \\ \sin^2\theta_{\mathrm{W}} = 0.2285 & \Gamma_{\mathrm{t}} = 1.11\,\mathrm{GeV} & M_{\mathrm{c}} = 1.500\,\mathrm{GeV} \end{array} \tag{7.2}$$

Furthermore, the QCD parameters need to be defined. The strong coupling is selected by the PDF set chosen. CTEQ6L1 uses a LO $\alpha_s(M_{\mathrm{Z}}) = 0.129783$ [39] and MSTW2008LO (90% C.L.) uses a 1-loop evolution with $\alpha_s(M_{\mathrm{Z}}) = 0.13939$ [49]. By default MCFM only uses mixing of the two lightest generations of quarks, i.e. $\theta_{12} \approx 12.83°$ and $\theta_{13} = \theta_{23} = 0°$. [48] This leads to minor contributions from initial states not listed in Chapter 5. The

[1] The electro-weak scheme used is designated as '-1' by MCFM. The numerical values of the derived parameters stated are rounded.

following CKM mixing matrix has been used as the input:

$$\begin{pmatrix} |V_{\mathrm{ud}}| & |V_{\mathrm{us}}| & |V_{\mathrm{ub}}| \\ |V_{\mathrm{cd}}| & |V_{\mathrm{cs}}| & |V_{\mathrm{cb}}| \\ |V_{\mathrm{td}}| & |V_{\mathrm{ts}}| & |V_{\mathrm{tb}}| \end{pmatrix} = \begin{pmatrix} 0.9750 & 0.2220 & 0.0000 \\ 0.2220 & 0.9750 & 0.0000 \\ 0.0000 & 0.0000 & 1.0000 \end{pmatrix} \tag{7.3}$$

Initially all calculations have been done using ten runs with 10^4 shots each in the pre-conditioning (total of 10^5 shots) and ten runs with 10^6 shots each in the final run (total of 10 million shots). Only the second set of runs contributes towards the MC integration. If the statistical error exceeded 0.1% or 1.58% of the PDF uncertainties[2] then the number of shots has been increased until both quality criteria were satisfied. Some of the two jet processes required a total of 126 million shots.

7.2 Selection Cuts

As discussed in Section 2.4, I am choosing a number of selection cuts in order to mirror the basic acceptance region of the detectors. For the two multi-purpose detectors at the Tevatron, the selection cuts are [35]:

$$\begin{aligned} p_{T,j} &> 20\,\mathrm{GeV} & p_{T,\ell^\pm} &> 20\,\mathrm{GeV} \\ |y_j| &< 2 & |y_{\ell^\pm}| &< 1 \end{aligned} \tag{7.4}$$

And for ATLAS and CMS at the LHC [36]:

$$\begin{aligned} p_{T,j} &> 30\,\mathrm{GeV} & p_{T,\ell^\pm} &> 20\,\mathrm{GeV} \\ |y_j| &< 3 & |y_{\ell^\pm}| &< 2.5 \end{aligned} \tag{7.5}$$

Jets are collimated bunches of partons originating from hadronised final state quarks and gluons. Jet clustering algorithms are applied to recombine these final state partons to jets. They generally fall into two groups: cone and sequential clustering. The former group clusters hadrons within a separation R of the most energetic particles in the event. They are favoured by experimentalists, because they provide jets with cone-like boundaries. They do, however, generally struggle with high energy jets being emitted close to each other (collinear unsafe) and infra-red emissions from the underlying event blurring the direction of the jet's total momentum (infra-red unsafe). The second group of algorithms is based on separation in momentum space. It is favoured by theorists, because k_T distance measures are closely related to the structure of QCD divergences. Furthermore, these algorithms are collinear and infra-red safe, but normally do not give cone-like jet

[2] See Section 4.4.3 for a more detailed description.

boundaries. I have used the anti-k_T algorithm with:

$$k_T = 0.4 \tag{7.6}$$

for both accelerators, because it is collinear and infra-red safe while also providing cone-like jets in momentum space. [50]

The production of $W^{\pm}$ bosons yields an undetectable neutrino in the final state. Cuts on the missing transverse momentum and the approximated transverse mass of the W boson improve signal-to-background selection. That means that some events with similar final state signatures to the hard scattering event I am interested in will be discarded, which improves the overall sensitivity to final states originating from an actual $W^{\pm}$ decay. For both colliders the cuts are chosen to be:

$$\begin{aligned} p_{T,miss} \approx p_{T,\nu} &> 30\,\text{GeV} \\ M_{T,\text{W}} &> 20\,\text{GeV} \end{aligned} \tag{7.7}$$

Z production with decay into two charged leptons also requires a cut on the di-lepton mass to suppress contributions from the virtual photon. So, I am applying the following cut at both accelerators.

$$M_{\ell^+,\ell^-} > 15\,\text{GeV} \tag{7.8}$$

7.3 Integrated Cross-sections

LO cross-sections have been calculated for:

- twelve different processes: see Chapter 5
- three different accelerator setups: Tevatron Run II (1.96 TeV), LHC with 7 TeV and LHC with 14 TeV
- three different scale choices[3]: $\mu_0 = M_V$, E_T^V and $\hat{H}_T$
- two different PDF sets: CTEQ6L1 (no error sets) and MSTW2008LO (90% C.L.)

The CTEQ6L1 PDF set does not include eigenvector sets in order to calculate PDF uncertainties. The deviation from the integrated cross-sections for MSTW2008LO (90% C.L.) can be found in Table 7.4. The full results can be found in Appendix B.1. All calculated LO cross-sections for the MSTW2008LO (90% C.L.) PDF sets are listed in Table 7.1 for Tevatron Run II, Table 7.2 for LHC with 7 TeV and Table 7.3 for LHC with 14 TeV. The statistical error is quoted using bracket notation[4]. Both the asymmetric (plus/superscript and minus/subscript) as well as the symmetric deviations (in square

[3] These were defined in Section 3.2.

[4] In the bracket notation of errors the result is compressed, by giving the the result up to the most significant number and rounding the error up accordingly. For example: $276134 \pm 45 = 27613(5) \times 10^1$

brackets) for the PDF and scale uncertainties are listed as relative errors. They have been rounded up to the nearest percent. The scale uncertainties have been estimated using a conservative variation by a factor of 4.

One can observe that all cross-sections follow $\sigma(V) > \sigma(V + 1\ jet) > \sigma(V + 2\ jets)$. This is to be expected, because the available phase space in the final state for each particle is decreased for processes with additional jets. Furthermore, we can observe that the production cross-sections for the W^+ and W^- are almost identical for the Tevatron, but for the LHC the integrated cross-section for the W^+ is larger than for the W^-. This is due to the net charge in the initial state being positive due to the abundance of up quarks in the two protons. For the Tevatron the total net charge is zero, due to the opposite charge of the proton and the anti-proton. Comparing the production cross-sections for $Z \to \ell^+\ell^-$ and $Z \to \sum_\ell \nu_\ell \overline{\nu}_\ell$ shows that the latter is much larger for all accelerators and scales. This is in agreement with the relevant branching ratios.

The PDF uncertainties are less than 4% for all accelerators, scales and processes. The Tevatron has the largest PDF uncertainties, because the initial state antiquarks are sea quarks and their PDFs have a larger uncertainty with them than valence quarks. [49] All uncertainties are between 3 and 4%. For the LHC we get PDF uncertainties of about 3%. For a centre-of-mass energy of 7 TeV some of the uncertainties are lower and for 14 TeV some are higher. There seems to be no dependence on the number of jets involved.

The picture is more complex for the scale uncertainties. For the Tevatron the scale uncertainties are between 1 and 4 percent for the processes without jets, larger than 30% for the one jet and larger than 65% for two jets. Furthermore, one can observe that the scale uncertainties for the events with jets drop by up to 10% if one uses the dynamic scales. The dynamic scale $\hat{H}_T$ gives a larger improvement than E_T^V. At the LHC with 7 TeV the scale uncertainties are lower than at the LHC with 14 TeV for the processes without a jet, but larger for the processes with jets. For both centre-of-mass energies the uncertainties are lowest for the one jet processes. They are less than 10% for 14 TeV and less than 19% for 7 TeV, but both are larger than the corresponding Tevatron results. For the one jet events we get a minimal increase for the scale uncertainties at LHC with 7 TeV, but a three-fold increase for the LHC with 14 TeV. This is smaller than at the Tevatron. For two jets the scale uncertainties are smaller at the LHC than at the Tevatron, i.e less than 58% for 7 TeV and less than 38% for 14 TeV. Only for the two jet events have I found a significant decrease in the scale uncertainties when using the dynamic scales. $\hat{H}_T$ gives twice the improvement of the E_T^V scale.

Campbell and Ellis [35] have calculated total cross-sections for weak boson production at the Tevatron with $\sqrt{s} = 2$ TeV. They have used identical rapidity cuts, but have a lower cut for the minimum transverse momentum of jets and an additional cut for its maximum ($15\,\text{GeV} < p_{T,j} < 200\,\text{GeV}$). There is no requirement on the minimum missing

transverse momentum. Furthermore, they also use the k_T clustering algorithm with a larger cone size ($k = 0.7$). Hence, one would expect my predictions to be smaller as I am looking at a more restricted phase space.

Only results for one associated jet and two associated jets are provided. All of their predictions are in the same order of magnitude. As expected, for $W^{\pm}$ production with one jet, their cross-sections are up to twice as large as mine and for Z production with one associated jet approximately 50% larger. However, my predictions for two associated jets are approximately 20% to 50% lower. This is most likely due to the different clustering algorithm with a larger cone size and the cut off for jets with large transverse momentum. I will present differential cross-sections in the following section, which show that there is a sizeable proportion of jets that are close together and that there is a non-negligible proportion of jets that have a high transverse momentum.

Campbell and Ellis only investigated the dependence on a static scale $\mu = M_V$. Their finds, however, match mine. The total cross-section drops exponentially with increasing scale for both processes with one and two jets. This effect is larger for two jet events.

Another study by Campbell and Ellis [36] provides total cross-sections for the LHC with 14 TeV. Once again my phase space is more restricted. For weak boson production with no jets and two jets my predictions are 40 to 70% smaller for $W^{\pm}$ bosons and less than 5% smaller for Z bosons. This suggests that the cut on the missing transverse momentum has a large impact on the total cross-section. For one associated jet, my cross-sections are a third of that of Campbell and Ellis for $W^{\pm}$ bosons and half as large for Z bosons. Looking at differential cross-sections presented in the next section, the most likely explanation is my cut on the transverse momentum of the jets, i.e. my cut off $p_{T,j} > 30\,\text{GeV}$ versus 20 GeV. This cuts out a large proportion of the events.

The dependence of the integrated cross-section on the scale found by Campbell and Ellis agrees with my predictions. For events with no associated jet the cross-section increases with scale. For one associated jet the cross-section does not depend very strongly on the scale, but decreases with increasing scale. Finally, for two jets the cross-section quickly becomes smaller for larger scales.

It is worth noting that Ellis and Campbell found all LO cross-sections to be larger for zero and one jet events and smaller for weak boson production with two associated jets, but all deviations are less than 20% for the central values.

Table 7.1: LO integrated cross-sections for $V + jets$ production processes at the Tevatron Run II ($\sqrt{s} = 1.96\,\text{TeV}$) using the MSTW2008LO (90% C.L.) PDFs and three different scale choices. Selection cuts as given in Equations 7.5 to 7.8 have been applied. MCFM input parameters are listed in Equations 7.1 to 7.3. The procedure used to choose the number of shots is described in Section 4.4.3. The scale uncertainties have been estimated using a conservative variation by a factor of 4. The statistical uncertainties are listed using bracket notation. The asymmetric (superscript and subscript) as well as the symmetric deviations (square brackets) for the PDFs and scale (scl) are recorded as relative errors rounded up to the nearest percent. Errors are propagated using Equations 8.3 and 8.4.

Tevtron Run II:	$\boldsymbol{\mu_0 = M_V}$			$\boldsymbol{\mu_0 = E_T^V}$			$\boldsymbol{\mu_0 = \hat{H}_T}$		
	σ_{LO}	$\Delta\sigma_{pdf}$	$\Delta\sigma_{scl}$	σ_{LO}	$\Delta\sigma_{pdf}$	$\Delta\sigma_{scl}$	σ_{LO}	$\Delta\sigma_{pdf}$	$\Delta\sigma_{scl}$
$p\overline{p} \to$	[fb]	[%]	[%]	[fb]	[%]	[%]	[fb]	[%]	[%]
$(W^+ \to \ell^+\nu_\ell)$	$27613(5) \times 10^1$	$^{+4}_{-4}[\pm4]$	$^{+2}_{-6}[\pm4]$	$27613(5) \times 10^1$	$^{+4}_{-4}[\pm4]$	$^{+2}_{-6}[\pm4]$	$27548(5) \times 10^1$	$^{+4}_{-4}[\pm4]$	$^{+2}_{-6}[\pm4]$
$(W^+ \to \ell^+\nu_\ell) + 1\ jet$	$3034(1) \times 10^1$	$^{+3}_{-4}[\pm3]$	$^{+45}_{-22}[\pm33]$	$2943(1) \times 10^1$	$^{+3}_{-4}[\pm3]$	$^{+43}_{-21}[\pm32]$	$2759(1) \times 10^1$	$^{+3}_{-4}[\pm3]$	$^{+42}_{-21}[\pm31]$
$(W^+ \to \ell^+\nu_\ell) + 2\ jets$	$12148(4) \times 10^0$	$^{+3}_{-4}[\pm3]$	$^{+114}_{-38}[\pm76]$	$11028(4) \times 10^0$	$^{+3}_{-4}[\pm3]$	$^{+107}_{-37}[\pm72]$	$8480(4) \times 10^0$	$^{+3}_{-4}[\pm3]$	$^{+94}_{-35}[\pm64]$
$(W^- \to \ell^-\overline{\nu}_\ell)$	$27612(5) \times 10^1$	$^{+4}_{-4}[\pm4]$	$^{+2}_{-6}[\pm4]$	$27612(5) \times 10^1$	$^{+4}_{-4}[\pm4]$	$^{+2}_{-6}[\pm4]$	$27546(5) \times 10^1$	$^{+4}_{-4}[\pm4]$	$^{+2}_{-6}[\pm4]$
$(W^- \to \ell^-\overline{\nu}_\ell) + 1\ jet$	$3033(1) \times 10^1$	$^{+3}_{-4}[\pm3]$	$^{+45}_{-22}[\pm33]$	$2942(1) \times 10^1$	$^{+3}_{-4}[\pm3]$	$^{+43}_{-21}[\pm32]$	$2758(1) \times 10^1$	$^{+3}_{-4}[\pm3]$	$^{+42}_{-21}[\pm31]$
$(W^- \to \ell^-\overline{\nu}_\ell) + 2\ jets$	$12140(4) \times 10^0$	$^{+3}_{-4}[\pm3]$	$^{+114}_{-38}[\pm76]$	$11019(4) \times 10^0$	$^{+3}_{-4}[\pm3]$	$^{+107}_{-37}[\pm72]$	$8476(3) \times 10^0$	$^{+3}_{-4}[\pm3]$	$^{+94}_{-35}[\pm64]$
$(Z \to \ell^-\ell^+)$	$37406(7) \times 10^0$	$^{+4}_{-4}[\pm4]$	$^{+1}_{-4}[\pm3]$	$37406(7) \times 10^0$	$^{+4}_{-4}[\pm4]$	$^{+1}_{-4}[\pm3]$	$37225(7) \times 10^0$	$^{+4}_{-4}[\pm4]$	$^{+1}_{-5}[\pm3]$
$(Z \to \ell^-\ell^+) + 1\ jet$	$5591(3) \times 10^0$	$^{+3}_{-4}[\pm3]$	$^{+44}_{-21}[\pm33]$	$5436(2) \times 10^0$	$^{+3}_{-4}[\pm3]$	$^{+43}_{-21}[\pm32]$	$5100(2) \times 10^0$	$^{+3}_{-4}[\pm3]$	$^{+41}_{-20}[\pm31]$
$(Z \to \ell^-\ell^+) + 2\ jets$	$2285(1) \times 10^0$	$^{+4}_{-4}[\pm4]$	$^{+109}_{-37}[\pm73]$	$2077(1) \times 10^0$	$^{+4}_{-4}[\pm4]$	$^{+103}_{-36}[\pm70]$	$1631(1) \times 10^0$	$^{+4}_{-4}[\pm4]$	$^{+91}_{-34}[\pm63]$
$(Z \to \sum_{\ell=e,\mu,\tau} \nu_\ell\overline{\nu}_\ell)$	$108278(6) \times 10^1$	$^{+3}_{-4}[\pm3]$	$^{+1}_{-2}[\pm1]$	$108278(6) \times 10^1$	$^{+3}_{-4}[\pm3]$	$^{+1}_{-2}[\pm1]$	$107965(6) \times 10^1$	$^{+3}_{-4}[\pm3]$	$^{+0}_{-3}[\pm2]$
$(Z \to \sum_{\ell=e,\mu,\tau} \nu_\ell\overline{\nu}_\ell) + 1\ jet$	$12996(2) \times 10^1$	$^{+3}_{-3}[\pm3]$	$^{+47}_{-22}[\pm35]$	$12670(2) \times 10^1$	$^{+3}_{-3}[\pm3]$	$^{+46}_{-22}[\pm34]$	$12312(2) \times 10^1$	$^{+3}_{-3}[\pm3]$	$^{+45}_{-22}[\pm33]$
$(Z \to \sum_{\ell=e,\mu,\tau} \nu_\ell\overline{\nu}_\ell) + 2\ jets$	$4749(2) \times 10^1$	$^{+3}_{-3}[\pm3]$	$^{+114}_{-38}[\pm76]$	$4377(2) \times 10^1$	$^{+3}_{-3}[\pm3]$	$^{+109}_{-37}[\pm73]$	$35540(8) \times 10^0$	$^{+3}_{-3}[\pm3]$	$^{+98}_{-35}[\pm67]$

Table 7.2: LO integrated cross-sections for $V + jets$ production processes at the LHC with $\sqrt{s} = 7\,\text{TeV}$ using the MSTW2008LO (90% C.L.) PDFs and three different scale choices. See caption of Table 7.1 for applied selection cuts, MCFM input parameters and description of the uncertainties.

LHC with 7 TeV:	$\boldsymbol{\mu_0 = M_V}$			$\boldsymbol{\mu_0 = E_T^V}$			$\boldsymbol{\mu_0 = \hat{H}_T}$		
	σ_{LO}	$\Delta\sigma_{pdf}$	$\Delta\sigma_{scl}$	σ_{LO}	$\Delta\sigma_{pdf}$	$\Delta\sigma_{scl}$	σ_{LO}	$\Delta\sigma_{pdf}$	$\Delta\sigma_{scl}$
pp $\to$	[fb]	[%]	[%]	[fb]	[%]	[%]	[fb]	[%]	[%]
$(\text{W}^+ \to \ell^+\nu_\ell)$	$20644(3) \times 10^2$	$^{+3}_{-4}[\pm3]$	$^{+14}_{-24}[\pm19]$	$20644(3) \times 10^2$	$^{+3}_{-4}[\pm3]$	$^{+14}_{-24}[\pm19]$	$20343(3) \times 10^2$	$^{+3}_{-4}[\pm3]$	$^{+15}_{-25}[\pm20]$
$(\text{W}^+ \to \ell^+\nu_\ell) + 1\ jet$	$23523(7) \times 10^1$	$^{+2}_{-4}[\pm3]$	$^{+22}_{-14}[\pm18]$	$22730(6) \times 10^1$	$^{+2}_{-4}[\pm3]$	$^{+26}_{-14}[\pm18]$	$21558(6) \times 10^1$	$^{+2}_{-3}[\pm3]$	$^{+22}_{-14}[\pm18]$
$(\text{W}^+ \to \ell^+\nu_\ell) + 2\ jets$	$17520(5) \times 10^1$	$^{+2}_{-4}[\pm3]$	$^{+84}_{-33}[\pm58]$	$15686(4) \times 10^1$	$^{+2}_{-4}[\pm3]$	$^{+78}_{-31}[\pm55]$	$11842(3) \times 10^1$	$^{+2}_{-3}[\pm3]$	$^{+68}_{-29}[\pm49]$
$(\text{W}^- \to \ell^-\overline{\nu}_\ell)$	$14163(2) \times 10^2$	$^{+3}_{-4}[\pm3]$	$^{+15}_{-24}[\pm19]$	$14163(2) \times 10^2$	$^{+3}_{-4}[\pm3]$	$^{+15}_{-24}[\pm19]$	$13970(2) \times 10^2$	$^{+3}_{-4}[\pm3]$	$^{+15}_{-25}[\pm20]$
$(\text{W}^- \to \ell^-\overline{\nu}_\ell) + 1\ jet$	$14820(6) \times 10^1$	$^{+2}_{-5}[\pm3]$	$^{+22}_{-14}[\pm18]$	$14335(5) \times 10^1$	$^{+2}_{-4}[\pm3]$	$^{+22}_{-14}[\pm18]$	$13590(5) \times 10^1$	$^{+2}_{-4}[\pm3]$	$^{+22}_{-14}[\pm18]$
$(\text{W}^- \to \ell^-\overline{\nu}_\ell) + 2\ jets$	$10346(4) \times 10^1$	$^{+3}_{-4}[\pm3]$	$^{+84}_{-33}[\pm58]$	$9306(3) \times 10^1$	$^{+3}_{-4}[\pm3]$	$^{+79}_{-32}[\pm55]$	$7025(3) \times 10^1$	$^{+3}_{-4}[\pm3]$	$^{+69}_{-29}[\pm49]$
$(\text{Z} \to \ell^-\ell^+)$	$40462(6) \times 10^1$	$^{+2}_{-4}[\pm3]$	$^{+14}_{-23}[\pm19]$	$40462(6) \times 10^1$	$^{+2}_{-4}[\pm3]$	$^{+14}_{-23}[\pm19]$	$39097(6) \times 10^1$	$^{+2}_{-4}[\pm3]$	$^{+15}_{-25}[\pm20]$
$(\text{Z} \to \ell^-\ell^+) + 1\ jet$	$5902(2) \times 10^1$	$^{+2}_{-4}[\pm3]$	$^{+21}_{-14}[\pm17]$	$5737(2) \times 10^1$	$^{+2}_{-4}[\pm3]$	$^{+21}_{-14}[\pm17]$	$5482(2) \times 10^1$	$^{+2}_{-4}[\pm3]$	$^{+21}_{-13}[\pm17]$
$(\text{Z} \to \ell^-\ell^+) + 2\ jets$	$3899(1) \times 10^1$	$^{+2}_{-4}[\pm3]$	$^{+80}_{-32}[\pm56]$	$3528(1) \times 10^1$	$^{+2}_{-4}[\pm3]$	$^{+76}_{-31}[\pm53]$	$27423(7) \times 10^0$	$^{+2}_{-4}[\pm3]$	$^{+67}_{-29}[\pm48]$
$(\text{Z} \to \sum_{\ell=\text{e},\mu,\tau} \nu_\ell\overline{\nu}_\ell)$	$45498(3) \times 10^2$	$^{+2}_{-4}[\pm3]$	$^{+12}_{-21}[\pm16]$	$45498(3) \times 10^2$	$^{+2}_{-4}[\pm3]$	$^{+12}_{-21}[\pm16]$	$42835(3) \times 10^2$	$^{+2}_{-4}[\pm3]$	$^{+14}_{-24}[\pm19]$
$(\text{Z} \to \sum_{\ell=\text{e},\mu,\tau} \nu_\ell\overline{\nu}_\ell) + 1\ jet$	$59345(7) \times 10^1$	$^{+2}_{-3}[\pm2]$	$^{+23}_{-15}[\pm19]$	$57711(7) \times 10^1$	$^{+2}_{-3}[\pm2]$	$^{+23}_{-14}[\pm19]$	$55529(7) \times 10^1$	$^{+2}_{-3}[\pm2]$	$^{+23}_{-14}[\pm18]$
$(\text{Z} \to \sum_{\ell=\text{e},\mu,\tau} \nu_\ell\overline{\nu}_\ell) + 2\ jets$	$37476(8) \times 10^1$	$^{+2}_{-3}[\pm3]$	$^{+83}_{-33}[\pm58]$	$34160(8) \times 10^1$	$^{+2}_{-3}[\pm3]$	$^{+79}_{-32}[\pm55]$	$26733(7) \times 10^1$	$^{+2}_{-3}[\pm3]$	$^{+70}_{-30}[\pm50]$

Table 7.3: LO integrated cross-sections for $V + jets$ production processes at the LHC with $\sqrt{s} = 14\,\text{TeV}$ using the MSTW2008LO (90% C.L.) PDFs and three different scale choices. See caption of Table 7.1 for applied selection cuts, MCFM input parameters and description of the uncertainties.

LHC with 14 TeV:	$\mu_0 = M_V$			$\mu_0 = E_T^V$			$\mu_0 = \hat{H}_T$		
	σ_{LO}	$\Delta\sigma_{pdf}$	$\Delta\sigma_{scl}$	σ_{LO}	$\Delta\sigma_{pdf}$	$\Delta\sigma_{scl}$	σ_{LO}	$\Delta\sigma_{pdf}$	$\Delta\sigma_{scl}$
pp $\to$	[fb]	[%]	[%]	[fb]	[%]	[%]	[fb]	[%]	[%]
$(\text{W}^+ \to \ell^+\nu_\ell)$	$36439(6) \times 10^2$	$^{+3}_{-4}[\pm3]$	$^{+22}_{-32}[\pm27]$	$36439(6) \times 10^2$	$^{+3}_{-4}[\pm3]$	$^{+22}_{-32}[\pm27]$	$35688(6) \times 10^2$	$^{+3}_{-4}[\pm3]$	$^{+22}_{-33}[\pm28]$
$(\text{W}^+ \to \ell^+\nu_\ell) + 1\ jet$	$5230(2) \times 10^2$	$^{+2}_{-4}[\pm3]$	$^{+9}_{-8}[\pm9]$	$5110(2) \times 10^2$	$^{+2}_{-4}[\pm3]$	$^{+9}_{-8}[\pm9]$	$4952(2) \times 10^2$	$^{+2}_{-4}[\pm3]$	$^{+10}_{-9}[\pm9]$
$(\text{W}^+ \to \ell^+\nu_\ell) + 2\ jets$	$4623(1) \times 10^2$	$^{+2}_{-4}[\pm3]$	$^{+63}_{-28}[\pm46]$	$4161(1) \times 10^2$	$^{+2}_{-4}[\pm3]$	$^{+60}_{-27}[\pm43]$	$32706(6) \times 10^1$	$^{+2}_{-4}[\pm3]$	$^{+53}_{-25}[\pm39]$
$(\text{W}^- \to \ell^-\overline{\nu}_\ell)$	$28851(4) \times 10^2$	$^{+3}_{-5}[\pm4]$	$^{+22}_{-33}[\pm27]$	$28851(4) \times 10^2$	$^{+3}_{-5}[\pm4]$	$^{+22}_{-33}[\pm27]$	$28282(4) \times 10^2$	$^{+3}_{-5}[\pm4]$	$^{+23}_{-33}[\pm28]$
$(\text{W}^- \to \ell^-\overline{\nu}_\ell) + 1\ jet$	$3895(2) \times 10^2$	$^{+2}_{-5}[\pm3]$	$^{+8}_{-8}[\pm8]$	$3810(2) \times 10^2$	$^{+2}_{-4}[\pm3]$	$^{+9}_{-8}[\pm9]$	$3693(2) \times 10^2$	$^{+2}_{-4}[\pm3]$	$^{+10}_{-9}[\pm9]$
$(\text{W}^- \to \ell^-\overline{\nu}_\ell) + 2\ jets$	$3258(1) \times 10^2$	$^{+2}_{-5}[\pm3]$	$^{+63}_{-28}[\pm45]$	$29437(8) \times 10^1$	$^{+2}_{-5}[\pm3]$	$^{+59}_{-27}[\pm43]$	$23184(7) \times 10^1$	$^{+2}_{-4}[\pm3]$	$^{+53}_{-25}[\pm39]$
$(\text{Z} \to \ell^-\ell^+)$	$7830(2) \times 10^2$	$^{+3}_{-4}[\pm3]$	$^{+22}_{-32}[\pm27]$	$7830(2) \times 10^2$	$^{+3}_{-4}[\pm3]$	$^{+22}_{-32}[\pm27]$	$7457(2) \times 10^2$	$^{+3}_{-4}[\pm3]$	$^{+23}_{-34}[\pm28]$
$(\text{Z} \to \ell^-\ell^+) + 1\ jet$	$14542(5) \times 10^1$	$^{+2}_{-4}[\pm3]$	$^{+8}_{-8}[\pm8]$	$14279(5) \times 10^1$	$^{+2}_{-4}[\pm3]$	$^{+8}_{-8}[\pm8]$	$13905(5) \times 10^1$	$^{+2}_{-4}[\pm3]$	$^{+9}_{-8}[\pm9]$
$(\text{Z} \to \ell^-\ell^+) + 2\ jets$	$11409(4) \times 10^1$	$^{+2}_{-4}[\pm3]$	$^{+60}_{-27}[\pm44]$	$10399(3) \times 10^1$	$^{+2}_{-4}[\pm3]$	$^{+57}_{-26}[\pm42]$	$8384(2) \times 10^1$	$^{+2}_{-4}[\pm3]$	$^{+52}_{-25}[\pm38]$
$(\text{Z} \to \sum_{\ell=\text{e},\mu,\tau} \nu_\ell\overline{\nu}_\ell)$	$105083(6) \times 10^2$	$^{+3}_{-4}[\pm3]$	$^{+19}_{-29}[\pm24]$	$105083(6) \times 10^2$	$^{+3}_{-4}[\pm3]$	$^{+19}_{-29}[\pm24]$	$96455(5) \times 10^2$	$^{+3}_{-4}[\pm3]$	$^{+22}_{-32}[\pm27]$
$(\text{Z} \to \sum_{\ell=\text{e},\mu,\tau} \nu_\ell\overline{\nu}_\ell) + 1\ jet$	$16399(2) \times 10^2$	$^{+2}_{-4}[\pm3]$	$^{+10}_{-9}[\pm10]$	$16093(2) \times 10^2$	$^{+2}_{-4}[\pm3]$	$^{+10}_{-9}[\pm10]$	$15696(2) \times 10^2$	$^{+2}_{-4}[\pm3]$	$^{+11}_{-9}[\pm10]$
$(\text{Z} \to \sum_{\ell=\text{e},\mu,\tau} \nu_\ell\overline{\nu}_\ell) + 2\ jets$	$12498(4) \times 10^2$	$^{+2}_{-4}[\pm3]$	$^{+64}_{-28}[\pm46]$	$11476(3) \times 10^2$	$^{+2}_{-4}[\pm3]$	$^{+61}_{-27}[\pm44]$	$9267(3) \times 10^2$	$^{+2}_{-4}[\pm3]$	$^{+55}_{-26}[\pm41]$

Table 7.4: Dependence on scale μ_0 for CTEQ6L1/MSTW2008LO (90% C.L.) ratios of the LO cross-sections for $V + jets$ production processes. The statistical uncertainties are rounded up to the nearest percent.

Tevatron: $p\overline{p} \rightarrow$	$R(M_V)$ [%]	$R(E_T^V)$ [%]	$R(\hat{H}_T)$ [%]
$(W^+ \rightarrow \ell^+\nu_\ell)$	97(3)	97(3)	97(3)
$(W^+ \rightarrow \ell^+\nu_\ell) + 1\ jet$	95(5)	95(5)	96(5)
$(W^+ \rightarrow \ell^+\nu_\ell) + 2\ jets$	89(5)	90(6)	91(5)
$(W^- \rightarrow \ell^-\overline{\nu}_\ell)$	95(2)	95(2)	95(2)
$(W^- \rightarrow \ell^-\overline{\nu}_\ell) + 1\ jet$	93(5)	94(5)	94(5)
$(W^- \rightarrow \ell^-\overline{\nu}_\ell) + 2\ jets$	87(7)	87(7)	89(6)
$(Z \rightarrow \ell^-\ell^+)$	96(2)	96(2)	96(2)
$(Z \rightarrow \ell^-\ell^+) + 1\ jet$	95(4)	95(4)	95(4)
$(Z \rightarrow \ell^-\ell^+) + 2\ jets$	88(6)	89(6)	90(6)
$(Z \rightarrow \sum_{\ell=e,\mu,\tau} \nu_\ell\overline{\nu}_\ell)$	96(1)	96(1)	95(1)
$(Z \rightarrow \sum_{\ell=e,\mu,\tau} \nu_\ell\overline{\nu}_\ell) + 1\ jet$	95(2)	95(2)	95(2)
$(Z \rightarrow \sum_{\ell=e,\mu,\tau} \nu_\ell\overline{\nu}_\ell) + 2\ jets$	89(5)	90(5)	91(4)

LHC @ 7 TeV: $pp \rightarrow$	$R(M_V)$ [%]	$R(E_T^V)$ [%]	$R(\hat{H}_T)$ [%]
$(W^+ \rightarrow \ell^+\nu_\ell)$	98(2)	98(2)	98(2)
$(W^+ \rightarrow \ell^+\nu_\ell) + 1\ jet$	96(5)	96(5)	96(5)
$(W^+ \rightarrow \ell^+\nu_\ell) + 2\ jet$	89(5)	89(5)	91(5)
$(W^- \rightarrow \ell^-\overline{\nu}_\ell)$	95(2)	95(2)	95(2)
$(W^- \rightarrow \ell^-\overline{\nu}_\ell) + 1\ jet$	93(5)	93(5)	93(5)
$(W^- \rightarrow \ell^-\overline{\nu}_\ell) + 2\ jets$	86(6)	86(7)	88(6)
$(Z \rightarrow \ell^-\ell^+)$	97(2)	97(2)	97(2)
$(Z \rightarrow \ell^-\ell^+) + 1\ jet$	94(4)	94(4)	95(4)
$(Z \rightarrow \ell^-\ell^+) + 2\ jets$	87(6)	88(6)	89(5)
$(Z \rightarrow \sum_{\ell=e,\mu,\tau} \nu_\ell\overline{\nu}_\ell)$	97(1)	97(1)	97(1)
$(Z \rightarrow \sum_{\ell=e,\mu,\tau} \nu_\ell\overline{\nu}_\ell) + 1\ jet$	95(2)	95(2)	95(2)
$(Z \rightarrow \sum_{\ell=e,\mu,\tau} \nu_\ell\overline{\nu}_\ell) + 2\ jets$	89(4)	89(4)	90(4)

LHC @ 14 TeV: $pp \rightarrow$	$R(M_V)$ [%]	$R(E_T^V)$ [%]	$R(\hat{H}_T)$ [%]
$(W^+ \rightarrow \ell^+\nu_\ell)$	97(3)	97(3)	97(3)
$(W^+ \rightarrow \ell^+\nu_\ell) + 1\ jet$	93(6)	93(6)	94(6)
$(W^+ \rightarrow \ell^+\nu_\ell) + 2\ jets$	87(6)	87(6)	89(7)
$(W^- \rightarrow \ell^-\overline{\nu}_\ell)$	97(3)	97(3)	97(3)
$(W^- \rightarrow \ell^-\overline{\nu}_\ell) + 1\ jet$	93(6)	93(6)	94(6)
$(W^- \rightarrow \ell^-\overline{\nu}_\ell) + 2\ jets$	87(60	87(6)	89(6)
$(Z \rightarrow \ell^-\ell^+)$	98(3)	98(3)	98(3)
$(Z \rightarrow \ell^-\ell^+) + 1\ jet$	93(6)	94(6)	94(7)
$(Z \rightarrow \ell^-\ell^+) + 2\ jets$	87(6)	87(6)	89(6)
$(Z \rightarrow \sum_{\ell=e,\mu,\tau} \nu_\ell\overline{\nu}_\ell)$	100(1)	100(1)	99(1)
$(Z \rightarrow \sum_{\ell=e,\mu,\tau} \nu_\ell\overline{\nu}_\ell) + 1\ jet$	95(2)	95(2)	96(2)
$(Z \rightarrow \sum_{\ell=e,\mu,\tau} \nu_\ell\overline{\nu}_\ell) + 2\ jets$	88(3)	89(4)	90(3)

7.4 Distributions of Observables

I will now look at some observables in more detail by plotting distributions of differential cross-sections at LO, which I have calculated for:

- twelve different processes: see Chapter 5
- three different accelerator setups: Tevatron Run II, LHC with 7 TeV and 14 TeV
- three different scale choices: $\mu_0 = M_V$, E_T^V and $\hat{H}_T$

Because of the extent of the results produced[5], I will only reproduce a selection. Unless otherwise specified, I will concentrate my presentation on LHC with $\sqrt{s} = 7\,\text{TeV}$ using the static scale $\mu_0 = M_V$ and the MSTW2008LO (90% C.L.) PDF set with 90% CL as recommended by the PDF4LHC work group [51]. I will point out where the results differ for Tevatron Run II ($\sqrt{s} = 1.96\,\text{TeV}$) and LHC with $\sqrt{s} = 14\,\text{TeV}$, as well as the two dynamic scales E_T^V and $\hat{H}_T$. Some additional histograms are given in Appendix B.2. While distributions have also been calculated for CTEQ6L1, only differential cross-sections with respect to experimental observables[6] for MSTW2008LO (90% C.L.) will be presented.

7.4.1 $\mathrm{p}^{(}\overline{\mathrm{p}}^{)} \to (\mathrm{W}^+ \to \ell^+\nu_\ell) + n$ jets

In this section I will present results for the $\mathrm{p}^{(}\overline{\mathrm{p}}^{)} \to (\mathrm{W}^+ \to \ell^+\nu_\ell) + n\ jets$ process. This group of processes has a fairly rich phenomenology. The produced W^+ decays into one detectable charged lepton and an invisible neutrino. Theoretically, one can recover some of the lost information because the detected transverse momentum of reactions with a single neutrino is identical to the missing transverse momentum. Lacking knowledge about the total boost along the z-axis, however, requires the use of observables like $M_{T,\mathrm{W}}$.

7.4.1.1 $\mathrm{p}^{(}\overline{\mathrm{p}}^{)} \to (\mathrm{W}^+ \to \ell^+\nu_\ell)$

For the $\mathrm{p}^{(}\overline{\mathrm{p}}^{)} \to (\mathrm{W}^+ \to \ell^+\nu_\ell)$ process without jets there are only a very limited amount of observables, as there are no jets and the neutrino that the W^+ boson decays into can only be observed in the form of missing transverse momentum. Figure 7.1 shows the charged lepton and the missing transverse momentum. For the LHC at 14 TeV and the Tevatron I obtained the same shapes. The magnitude of the differential cross-sections are proportional to the integrated cross-sections, i.e. they increase with centre of mass energy. The uncertainties also vary as expected. The largest PDF errors occur in the distribution for the Tevatron, as it requires proton and anti-proton PDFs. The LHC results are a little smaller and identical to each other, as they only depend on the proton PDFs. The scale uncertainties on the other hand are very small for the Tevatron and

[5] Approximately 3000 histograms have been calculated and printed.

[6] The bin width for distributions of the transverse momentum p_T and masses M is 5 GeV. For rapidities y and separation R a bin width of 0.2 has been used. The azimuthal angles use $\Delta\phi = 5°$.

increase with centre of mass energy. As an example the distributions of the transverse momentum of the charged lepton at the Tevatron and the LHC at 14 TeV are shown in Figures 7.2. These results are almost identical for the other two scales I have investigated.

Furthermore, we can observe the rapidity of the charged lepton as shown in Figure 7.3. The final state charged lepton tends slightly towards an emission in the forward direction of the detector, which differs to the W^- production (see Section 7.4.2.1). In comparison the rapidity distribution for the LHC with 14 TeV is more stretched[7] and for the Tevatron there is a bias towards one side of the detector due to the $p\overline{p}$ asymmetry (see Figure 7.4). The two dynamic scales yield the same result.

The distribution for the azimuthal angle between the charged lepton and the missing momentum shows that the charged lepton and the neutrino are emitted back-to-back on the transverse plane[8]. This must be true for all colliders and scales. The last observable for this process is the $M_{T,W}$ distribution and is shown in Figure 7.5. It can be observed that there is a threshold at 60 GeV and a peak at about 75 GeV to 80 GeV. One expects this distribution to have a threshold below the W mass and a peak just above. The shapes are the same for the other two accelerators and scales. Uncertainties and integrals vary according to the total cross-sections.

[7] See Figure B.1 in Appendix B.2.1.1.
[8] See Figure B.2 in Appendix B.2.1.1.

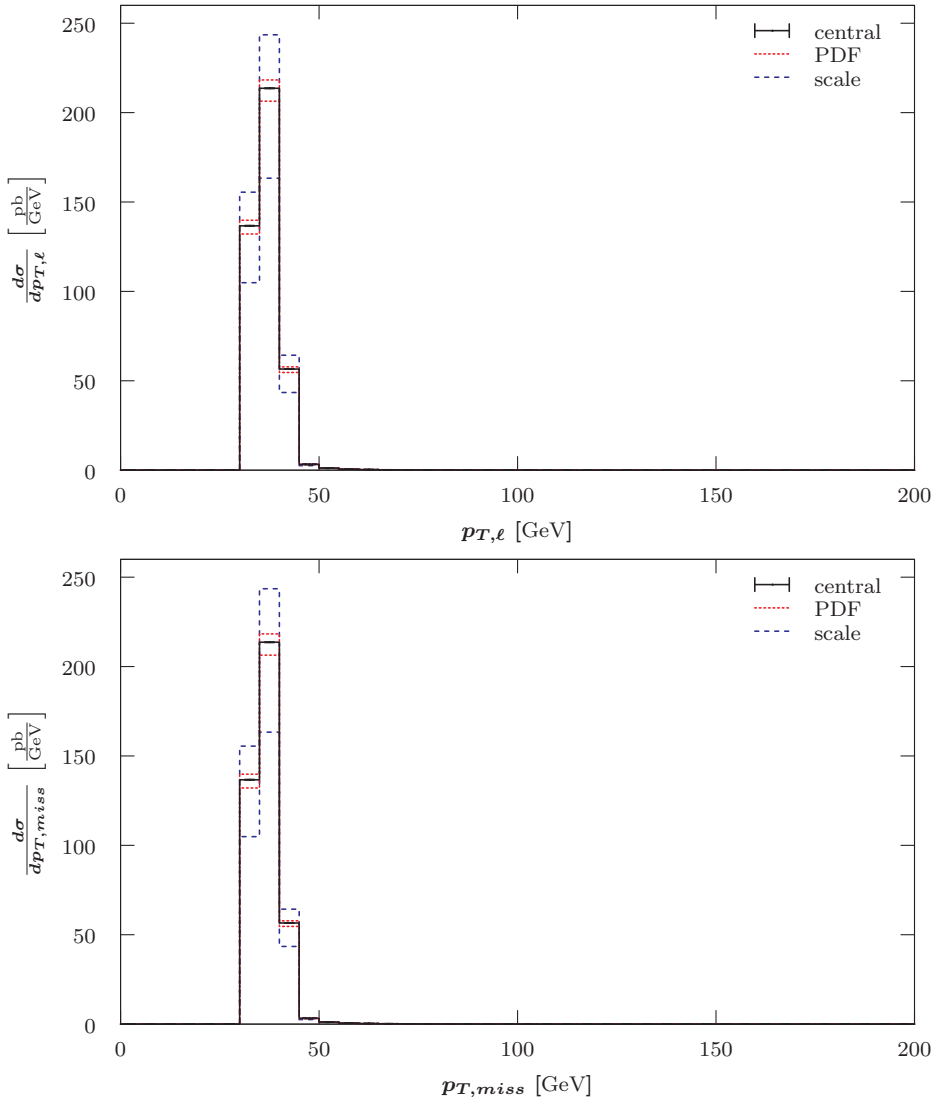

Figure 7.1: LO differential cross-section with respect to the charged lepton (top) and the missing (bottom) transverse momentum for the pp $\to$ ($W^+ \to \ell^+\nu_\ell$) process at the LHC with $\sqrt{s} = 7\,\text{TeV}$ using a fixed scale of $\mu_0 = M_W$ and MSTW2008LO (90% C.L.) PDFs. Selection cuts as given in Equations 7.5 to 7.8 have been applied. MCFM input parameters are listed in Equations 7.1 to 7.3. The procedure used to choose the number of shots is described in Section 4.4.3. The scale uncertainties have been estimated using a conservative variation by a factor of 4. The error bars for the statistical uncertainties are mostly too small to be visible or are only partially visible. Only the asymmetric deviations for the PDFs (red, dotted) and scale (blue, dashed) from the central value (black, solid) are given.

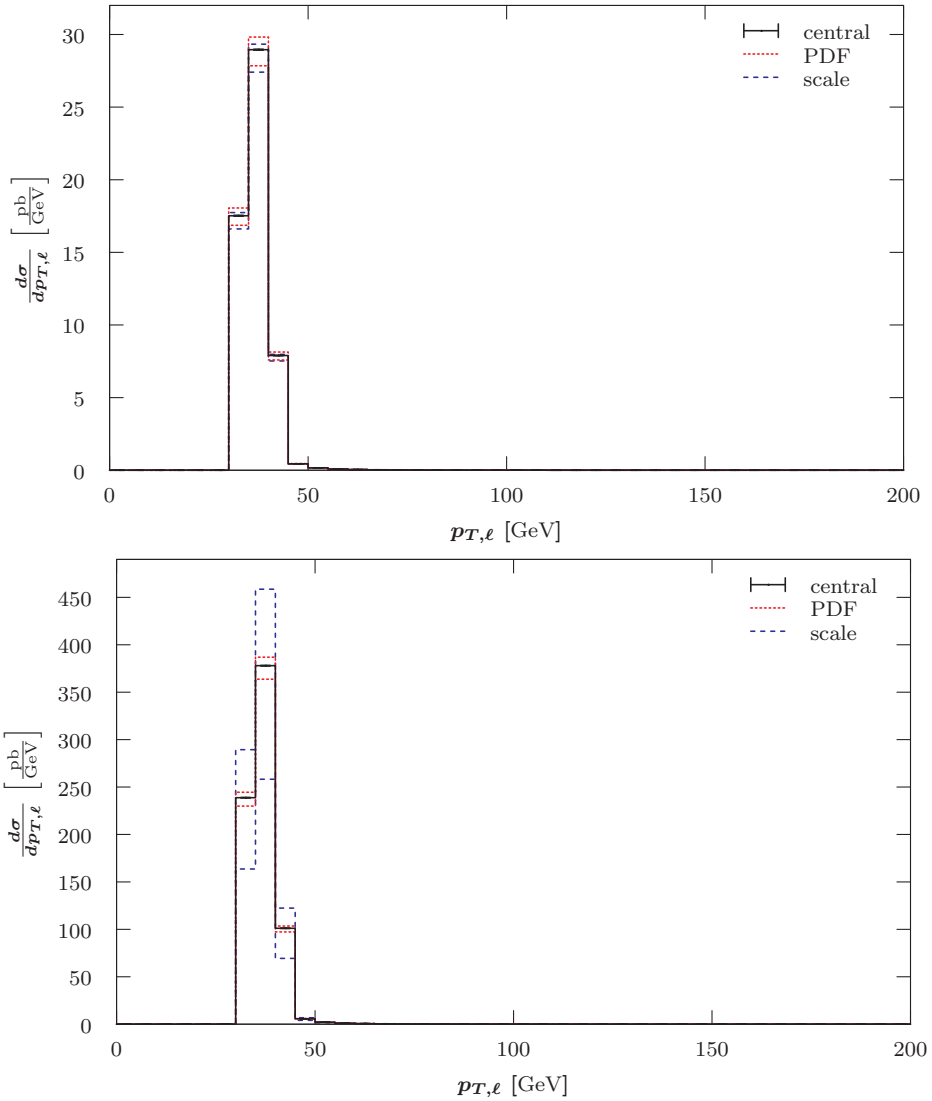

Figure 7.2: LO differential cross-section with respect to transverse momentum of to the charged lepton for the $p^{(}\overline{p}^{)} \to (W^+ \to \ell^+\nu_\ell)$ process at the Tevatron Run II (top) and the LHC with 14 TeV (bottom) using a fixed scale of $\mu_0 = M_W$. Additional details are given in the caption of Figure 7.1.

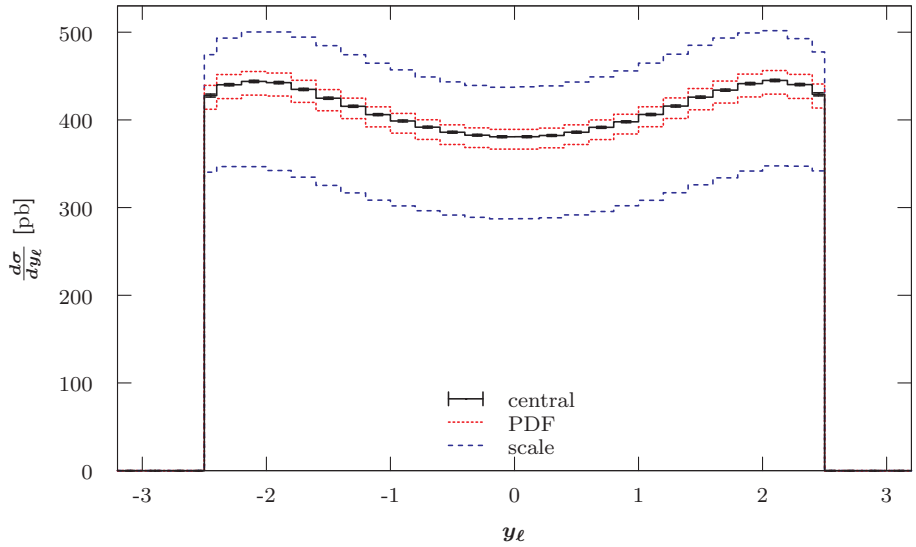

Figure 7.3: LO differential cross-section with respect to the charged lepton rapidity for the $pp \to (W^+ \to \ell^+\nu_\ell)$ process at the LHC with 7 TeV using a fixed scale of $\mu_0 = M_W$. The first and last filled bin are half-width due to the applied selection cut, $|y_\ell| < 2.5$. Additional details are given in the caption of Figure 7.1.

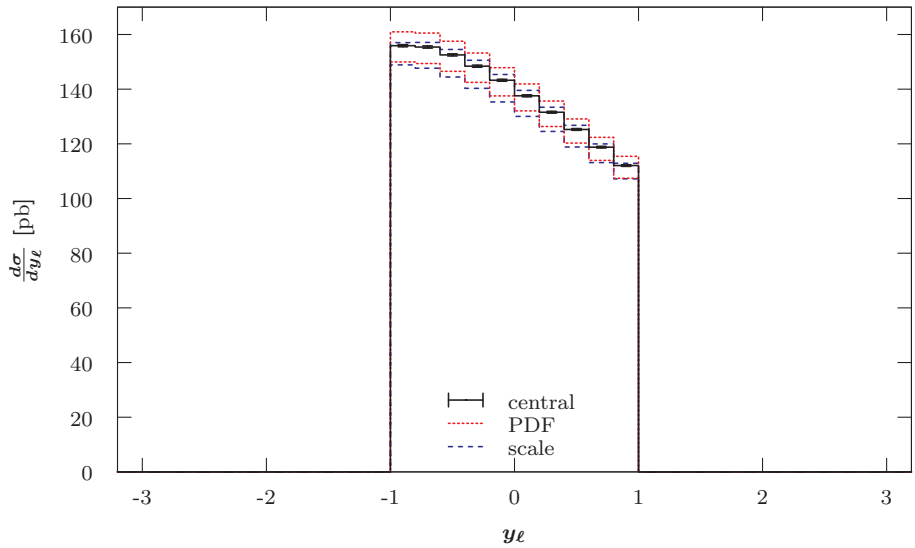

Figure 7.4: LO differential cross-section with respect to the charged lepton rapidity for the $p\overline{p} \to (W^+ \to \ell^+\nu_\ell)$ process at the Tevatron Run II using a fixed scale of $\mu_0 = M_W$. Additional details are given in the caption of Figure 7.1.

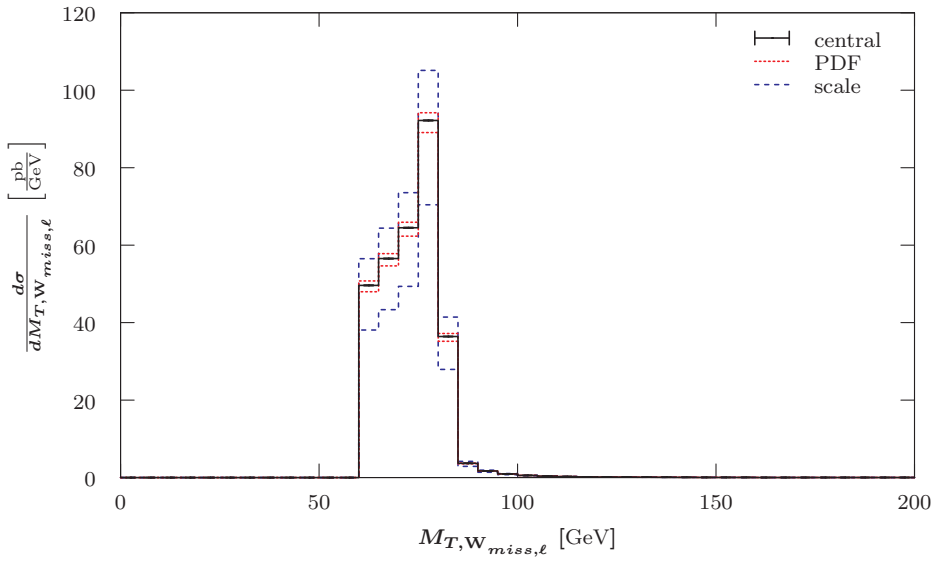

Figure 7.5: LO differential cross-section with respect to transverse mass $M_{T,\mathrm{W}}$ for the $\mathrm{pp} \to (\mathrm{W}^+ \to \ell^+\nu_\ell)$ process at the LHC with 7 TeV using a fixed scale of $\mu_0 = M_\mathrm{W}$. Additional details are given in the caption of Figure 7.1.

7.4.1.2 $p^{(}\overline{p}^{)} \to (W^+ \to \ell^+\nu_\ell) + 1$ jet

For the 1-jet process I will firstly look at the observables I have already mentioned above. Finally, I will present observables due to the additional jet. The differential cross-section with respect to the charged lepton and the transverse momentum is recorded in Figure 7.6. Both distributions are smeared out in comparison to the no jet event. This is due to final state radiation. The results for dynamical scales are very similar. The distributions for the Tevatron vary in shape (and magnitude) as can be seen in Figure 7.7. For the LHC with 14 TeV we obtain the same shape, while the integrated cross-section is larger and the scale uncertainties are smaller. This can be seen in Figure 7.8.

The next basic observable to look at is the rapidity distribution of the charged lepton. Figure 7.9 shows that the charged lepton tends to be emitted towards the forward/backward direction. The plots for the dynamic scales E_T^{W} and $\hat{H}_T$ have the same shape but a smaller magnitude as one would naïvely expect from the integrated cross-sections. The same holds true for the LHC with 14 TeV, though the distribution is much flatter and surprisingly the scale variation is much smaller (see Figure 7.11). The histogram for the Tevatron differs in so far that it shows a strong forward/backward asymmetry similar to the 0-jet case. The corresponding plot is given in Figure 7.10.

Figure 7.12 shows the difference between the azimuthal angle of the charged lepton and the missing momentum vector. We can see a broad distribution with a peak around 130° to 135°. The results for the dynamic scales are very similar, but smaller in magnitude as you would expect from the integrated cross-sections. The histogram for LHC with 14 TeV is very similar, though the scale uncertainties again are unexpectedly smaller (while the integral is larger)[9]. The distribution for the Tevatron is smaller in magnitude and the peak is shifted to 145° to 150° due to different cuts being applied[10]. The last observable known from the 0 jet event is the $M_{T,\mathrm{W}}$ distribution, shown in Figure 7.13. It is similar to the process without jets. Most notably there is no threshold and the peak is at the same position at about 75 GeV to 80 GeV. Results for the Tevatron and the LHC with 14 TeV are similar. Again, they differ in their magnitude according to the total cross-sections and the scale uncertainties for the LHC at higher energy is suppressed. Results for the two dynamic scaleS are proportional.

Now we can look at the jet distributions, namely the differential cross-sections with respect to the transverse momentum and the rapidity. They are both shown in Figure 7.14. The jet tends to be emitted at low transverse momentum and in the centre of the detector. For the Tevatron and the LHC with 14 TeV the magnitude increases with centre of mass energy and the scale uncertainties are decreasing[11]. Histograms for

[9] See Figure B.4 in Appendix B.2.1.2.
[10] See Figure B.3 in Appendix B.2.1.2.
[11] See Figures B.5 and B.6 in Appendix B.2.1.2, respectively.

dynamic scales are very similar.

Next, I present the distance observables between the jet and the charged lepton (or the missing momentum). Figure 7.15 shows the separation in azimuthal angle and rapidity between the jet and the charged lepton. The distribution stretches over the whole azimuthal angle and peaks around 135° to 140°. This is the same for the LHC with 14 TeV and for the Tevatron the peak is slightly lower at 130° to 135°.[12] Plots for dynamic scales are very similar. Additionally, I looked at the differential cross-sections with respect to the difference between the rapidities of the charged lepton and jet. It can be seen in Figure 7.16 that the jet and the charged lepton tend to have a similar rapidity. The usual differences for magnitude and uncertainties can be seen for other accelerator and dynamic scales. The separation R between the charged lepton and the jet can be found in Figure 7.17. It can be seen that it is very unlikely for the charged lepton and the jet to not be separated. The probability increases with separation up to a near back-to-back separation ($R \approx 3$), after which it drops rapidly. The results for the other two accelerator setups and the results for the dynamic scales are very similar, allowing for the obvious differences in the total cross-section and the size of the uncertainties. Figure 7.18 shows the differential cross-section with respect to the invariant mass of the charged lepton and the jet. One can observe a linear increase to a maximum at 75 GeV and then an exponential decays towards larger masses. This shape is similar for LHC with 14 TeV, but the integral is larger and there is a large decrease in the scale uncertainties down to twice the PDF uncertainties. This was already shown for other observables. For the Tevatron the peak is at 60 GeV to 54 GeV and a more rapid decrease towards larger masses can be observed[13]. The dynamic scales give the same shape and a minimal decrease of the scale uncertainties.

In comparison to the azimuthal angle between the jet and the charged lepton, I also looked at the angle between the jet and the missing transverse momentum vector as shown in Figure 7.19. This distribution stretches over the range of 40° to 180° and peaks at 155 GeV to 160 GeV. The same is true for the Tevatron and the LHC with 14 TeV.[14] The results for dynamic scales are very similar. Furthermore, one can construct a transverse mass out of the missing and the jet transverse momentum. This distribution is given in Figure 7.20. It starts of at almost zero up to 20 GeV after which it starts to increase exponentially. It peaks at 80 GeV to 85 GeV and then exponentially decays towards larger masses. The integrals and uncertainties for other accelerators and the dynamic scales behave similarly to what we have already seen. Only the shape for the Tevatron varies slightly as it does not start off flat[15].

[12] See Figures B.8 and B.7 in Appendix B.2.1.2.
[13] See Figure B.9 in Appendix B.2.1.2.
[14] See Figures B.10 and B.11 in Appendix B.2.1.2.
[15] See Figure B.12 in Appendix B.2.1.2.

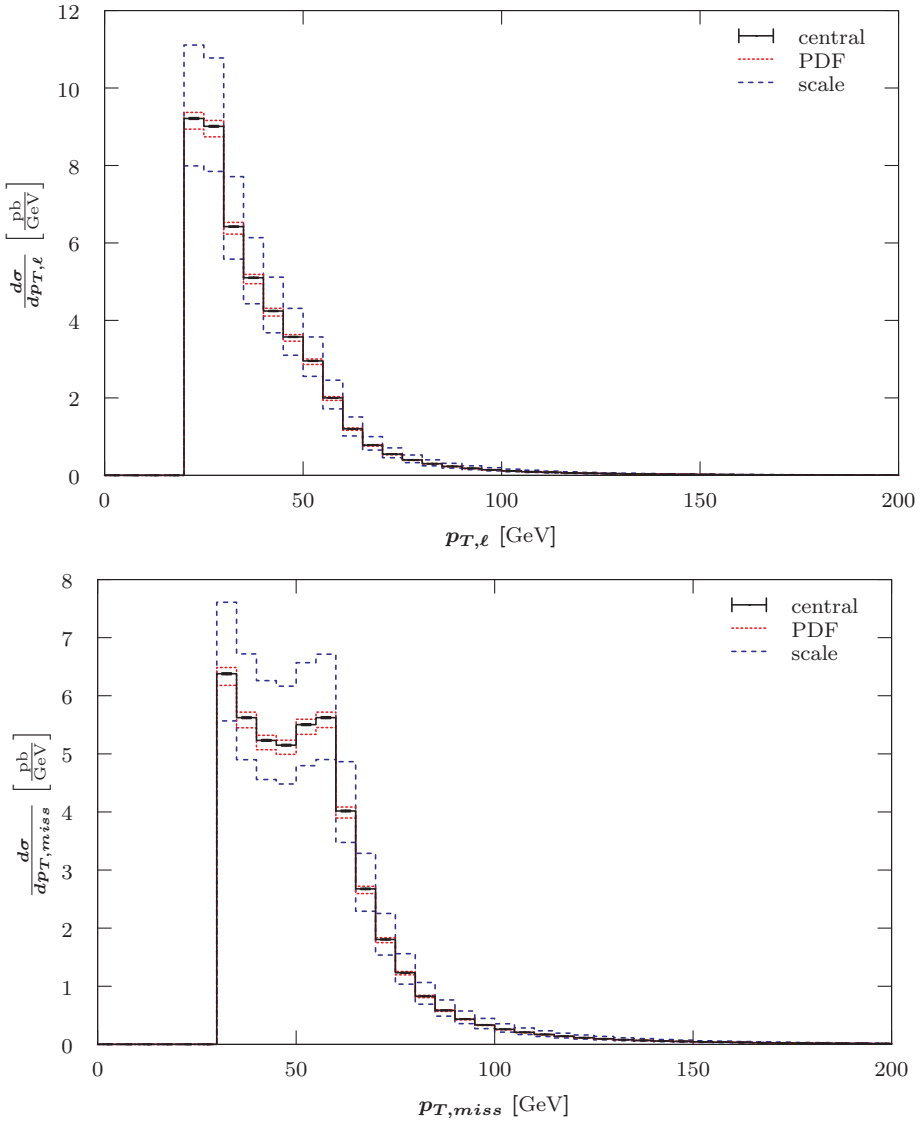

Figure 7.6: LO differential cross-section with respect to the charged lepton (top) and the missing (bottom) transverse momentum for the $pp \to (W^+ \to \ell^+\nu_\ell) + 1\ jet$ process at the LHC with 7 TeV using a fixed scale of $\mu_0 = M_W$. Additional details are given in the caption of Figure 7.1.

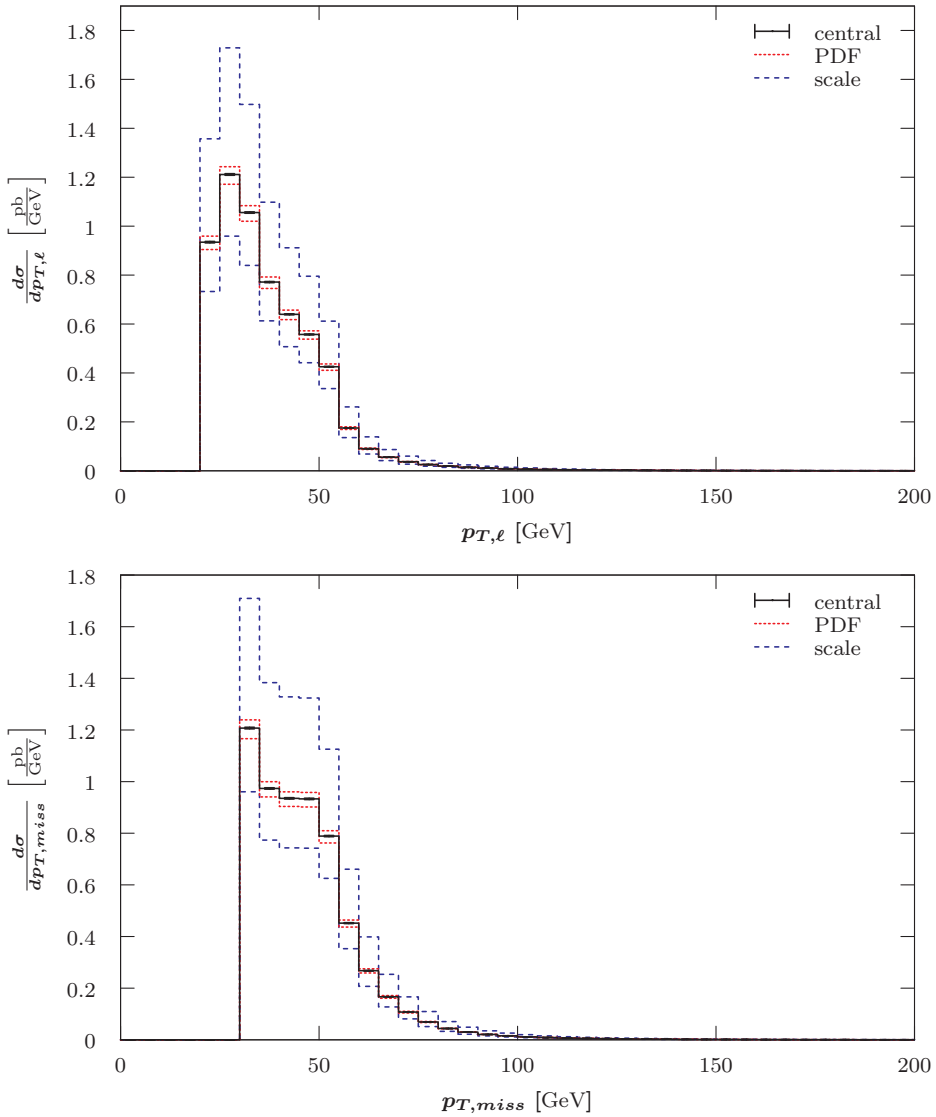

Figure 7.7: LO differential cross-section with respect to the charged lepton (top) and the missing (bottom) transverse momentum for the $p\bar{p} \to (W^+ \to \ell^+\nu_\ell) + 1\ jet$ process at the Tevatron Run II using a fixed scale of $\mu_0 = M_W$. Additional details are given in the caption of Figure 7.1.

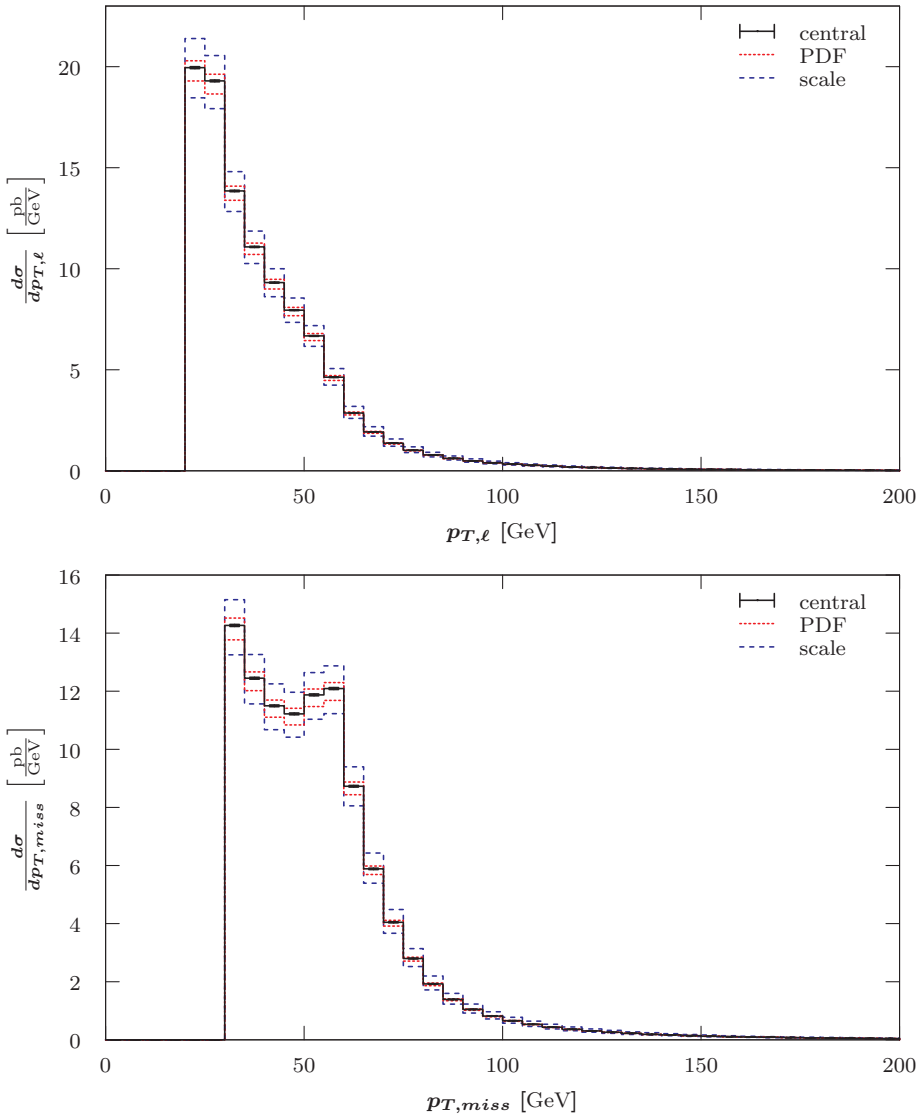

Figure 7.8: LO differential cross-section with respect to the charged lepton (top) and the missing (bottom) transverse momentum for the $pp \to (W^+ \to \ell^+\nu_\ell) + 1\ jet$ process at the LHC with 14 TeV using a fixed scale of $\mu_0 = M_W$. Additional details are given in the caption of Figure 7.1.

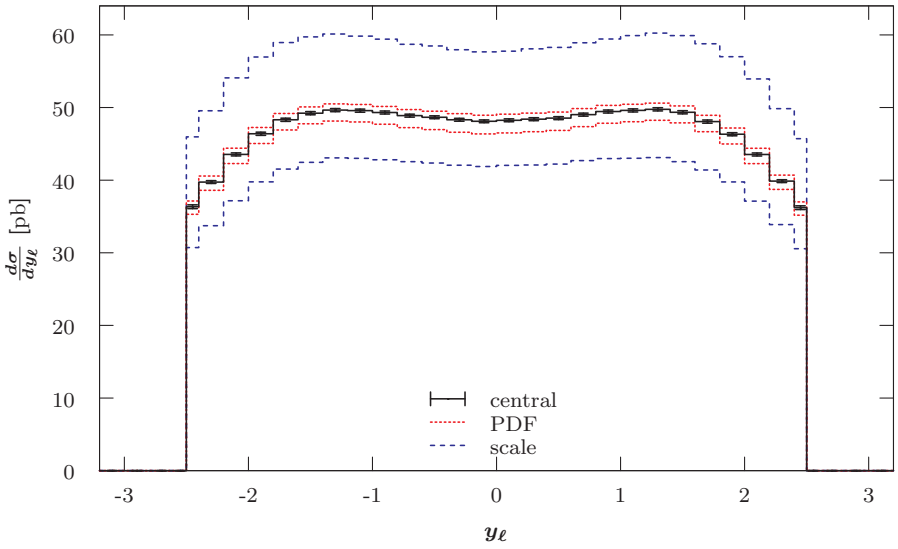

Figure 7.9: LO differential cross-section with respect to the charged lepton rapidity for the $pp \to (W^+ \to \ell^+\nu_\ell) + 1\ jet$ process at the LHC with 7 TeV using a fixed scale of $\mu_0 = M_W$. The first and last filled bin are half-width due to the applied selection cut, $|y_\ell| < 2.5$. Additional details are given in the caption of Figure 7.1.

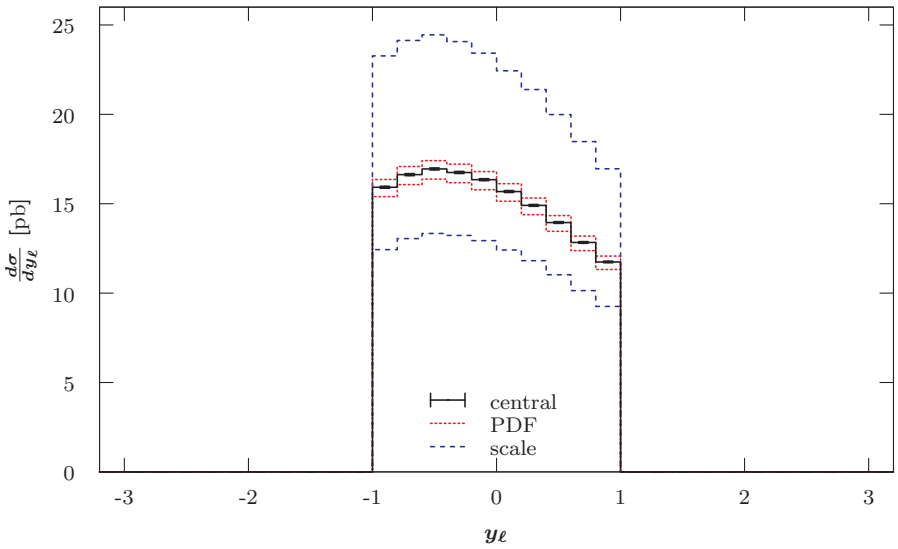

Figure 7.10: LO differential cross-section with respect to the charged lepton rapidity for the $p\overline{p} \to (W^+ \to \ell^+\nu_\ell) + 1\ jet$ process at the Tevatron Run II using a fixed scale of $\mu_0 = M_W$. Additional details are given in the caption of Figure 7.1.

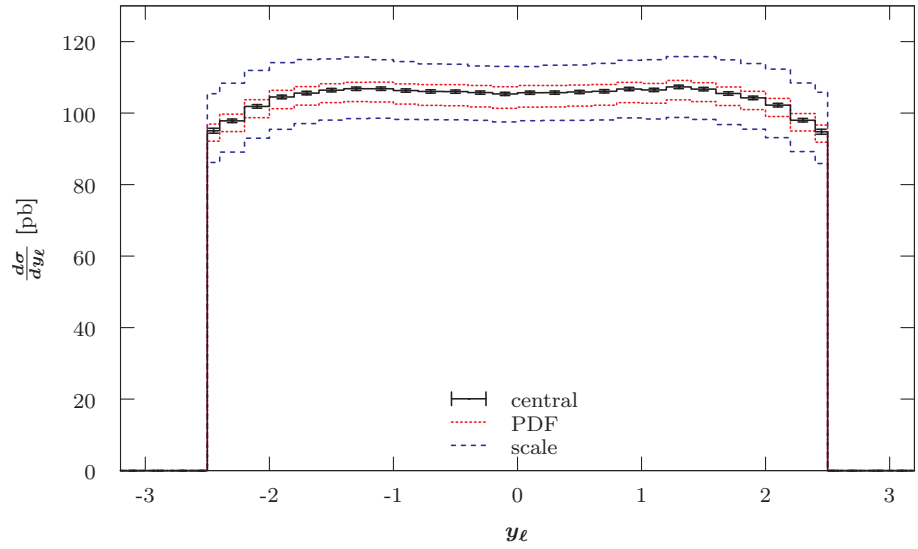

Figure 7.11: LO differential cross-section with respect to the charged lepton rapidity for the $pp \to (W^+ \to \ell^+\nu_\ell) + 1\ jet$ process at the LHC with 14 TeV using a fixed scale of $\mu_0 = M_W$. The first and last filled bin are half-width due to the applied selection cut, $|y_\ell| < 2.5$. Additional details are given in the caption of Figure 7.1.

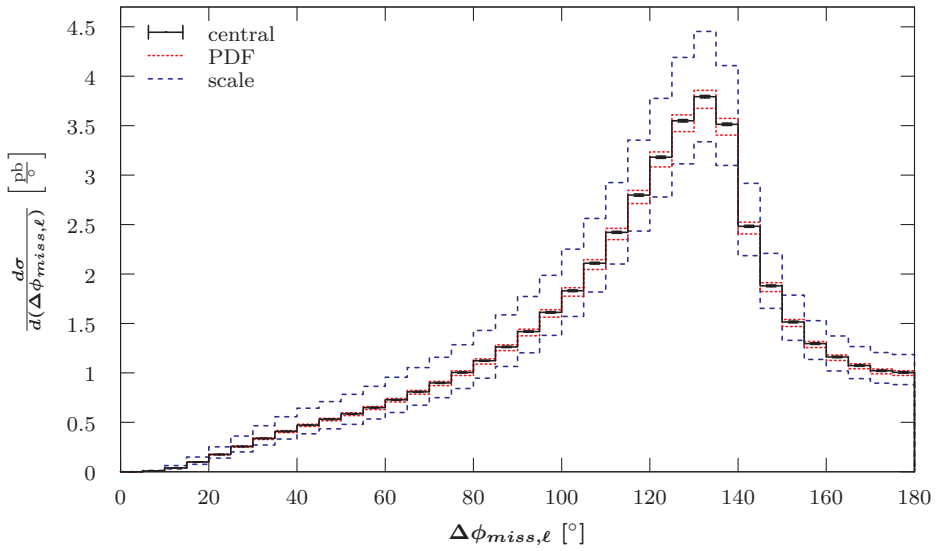

Figure 7.12: LO differential cross-section with respect to the azimuthal angle ϕ between the charged lepton and the missing transverse momentum for the $pp \to (W^+ \to \ell^+\nu_\ell) + 1\ jet$ process at the LHC with 7 TeV using a fixed scale of $\mu_0 = M_W$. Additional details are given in the caption of Figure 7.1.

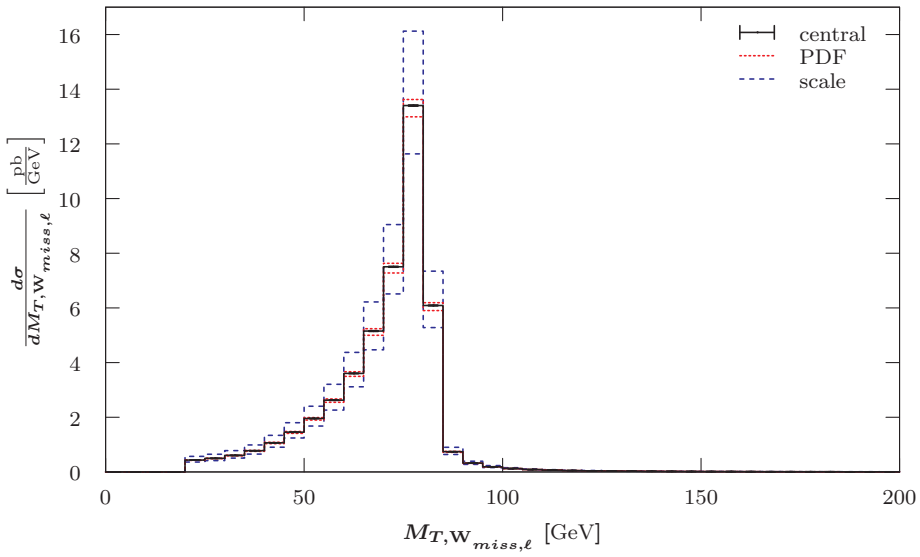

Figure 7.13: LO differential cross-section with respect to the transverse inavariant mass $M_{T,\mathrm{W}}$ for the pp $\to$ $(\mathrm{W}^+ \to \ell^+\nu_\ell) + 1$ *jet* process at the LHC with 7 TeV using a fixed scale of $\mu_0 = M_\mathrm{W}$. Additional details are given in the caption of Figure 7.1.

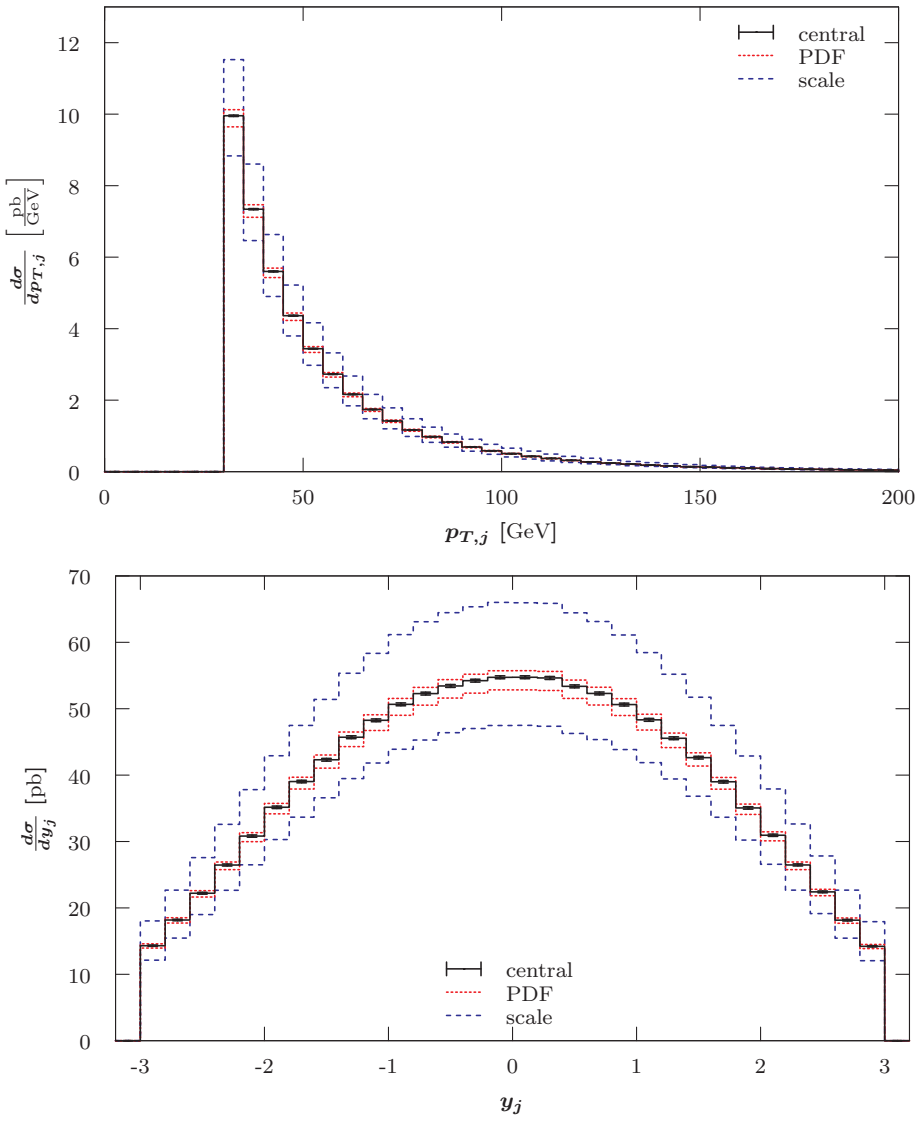

Figure 7.14: LO differential cross-section with respect to the jet transverse momentum (top) and the jet rapidity (bottom) for the $pp \to (W^+ \to \ell^+\nu_\ell) + 1\ jet$ process at the LHC with 7 TeV using a fixed scale of $\mu_0 = M_W$. Additional details are given in the caption of Figure 7.1.

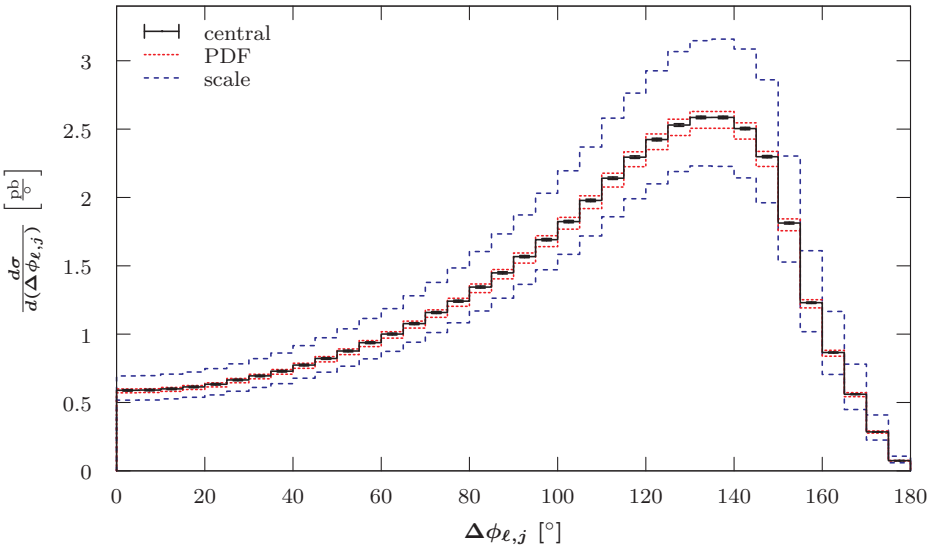

Figure 7.15: LO differential cross-section with respect to the azimuthal angle ϕ between the charged lepton and the jet for the $pp \to (W^+ \to \ell^+\nu_\ell) + 1\ jet$ process at the LHC with 7 TeV using a fixed scale of $\mu_0 = M_W$. Additional details are given in the caption of Figure 7.1.

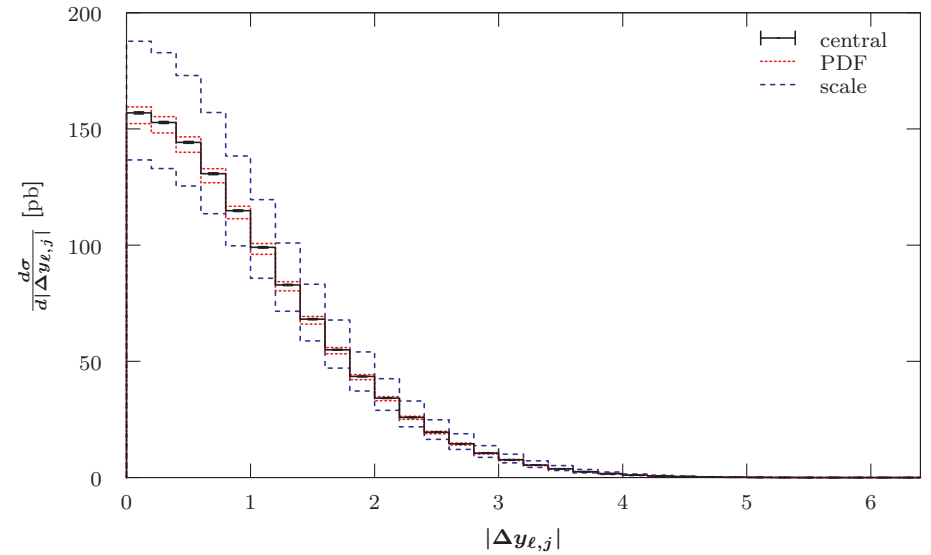

Figure 7.16: LO differential cross-section with respect to the difference in rapidity between the charged lepton and the jet for the $pp \to (W^+ \to \ell^+\nu_\ell) + 1\ jet$ process at the LHC with 7 TeV using a fixed scale of $\mu_0 = M_W$. Additional details are given in the caption of Figure 7.1.

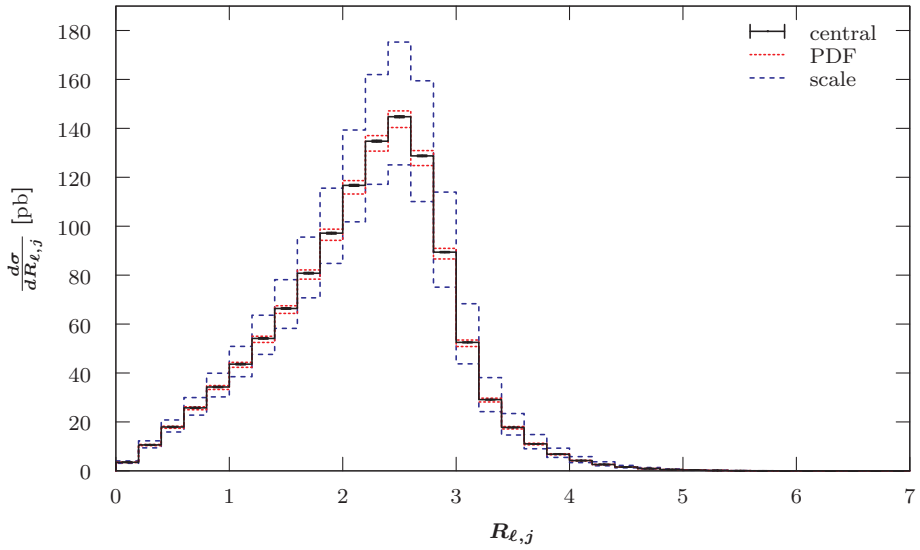

Figure 7.17: LO differential cross-section with respect to the separation between the charged lepton and the jet for the $pp \to (W^+ \to \ell^+\nu_\ell) + 1\ jet$ process at the LHC with 7 TeV using a fixed scale of $\mu_0 = M_W$. Additional details are given in the caption of Figure 7.1.

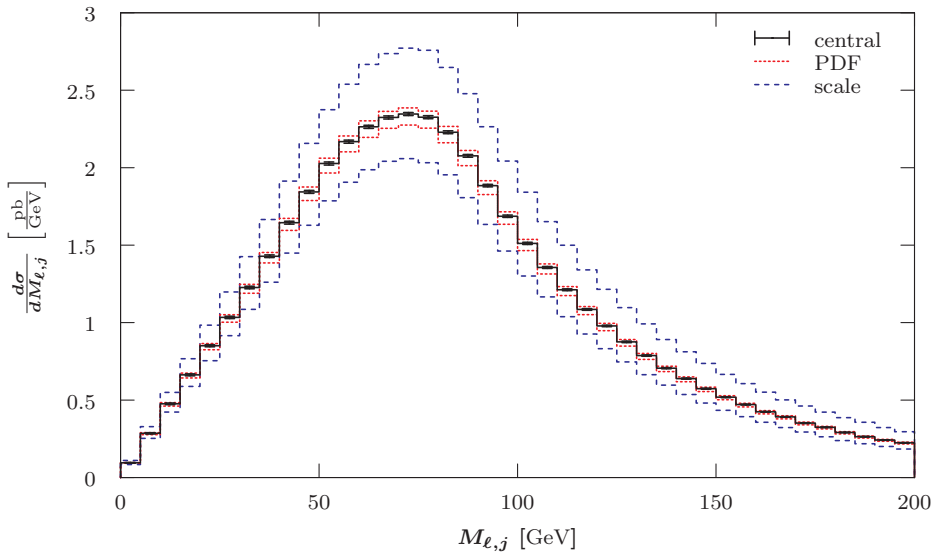

Figure 7.18: LO differential cross-section with respect to the invariant mass between the charged lepton and the jet for the $pp \to (W^+ \to \ell^+\nu_\ell) + 1\ jet$ process at the LHC with 7 TeV using a fixed scale of $\mu_0 = M_W$. Additional details are given in the caption of Figure 7.1.

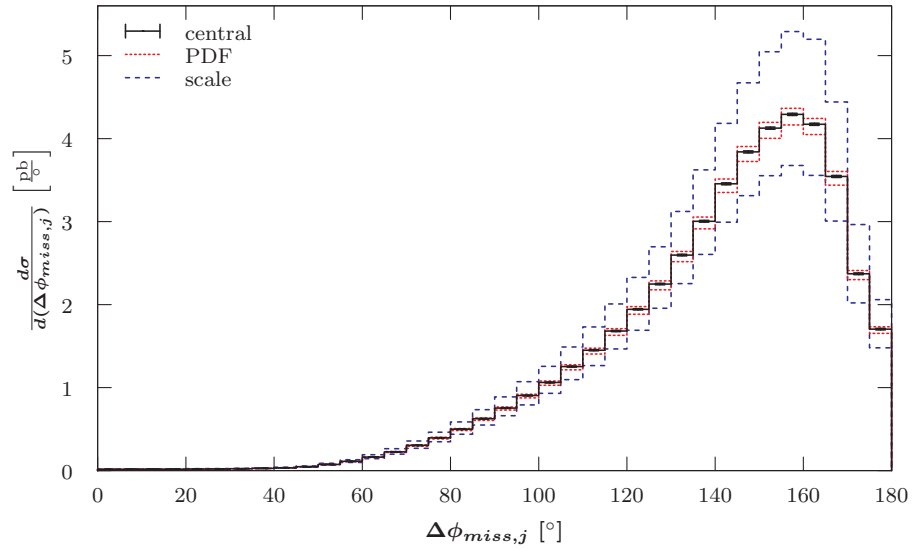

Figure 7.19: LO differential cross-section with respect to the azimuthal angle ϕ between the missing transverse momentum and the jet for the pp $\to (\mathrm{W}^+ \to \ell^+\nu_\ell) + 1\ jet$ process at the LHC with 7 TeV using a fixed scale of $\mu_0 = M_\mathrm{W}$. Additional details are given in the caption of Figure 7.1.

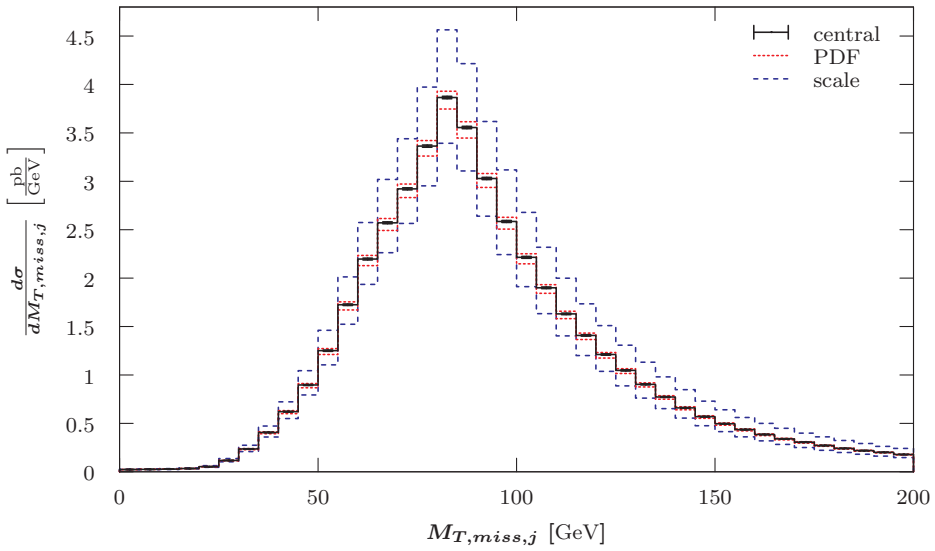

Figure 7.20: LO differential cross-section with respect to the transverse mass between the jet and missing transverse momentum vector for the pp $\to (\mathrm{W}^+ \to \ell^+\nu_\ell) + 1\ jet$ process at the LHC with 7 TeV using a fixed scale of $\mu_0 = M_\mathrm{W}$. Additional details are given in the caption of Figure 7.1.

7.4.1.3 $p^{(}\overline{p}^{)} \to (W^+ \to \ell^+\nu_\ell) + 2$ jets

The differential cross-sections for the 2-jet process with respect to the charged lepton and the transverse momentum are much more stable in comparison to the 1-jet calculations. The distributions for the transverse momentum of the charged lepton and the neutrino are recorded in Figure 7.21. Both distributions are very smooth and similar to each other. The results for the other two accelerators and the dynamic scales have similar shapes and are different in their integral, as one would expect from the integrated cross-sections. One can observe that the scale uncertainties decrease with the centre-of-mass energy of the collider. Furthermore, the scale uncertainties are also smaller for the dynamic scale E_T^{W} and even more suppressed for $\hat{H}_T$. This can be seen in more detail in distributions for the azimuthal angle between the charged lepton and the missing momentum[16].

Figure 7.22 shows the differential cross-sections with respect to the rapidity of the charged lepton. The distributions are very similar to the 1-jet event. The LHC with 14 TeV distribution in Figure 7.24 has a larger magnitude and is flatter. The Tevatron result is asymmetric as one would expect (see Figure 7.23). The results for the dynamic scales have smaller scale uncertainties.

As I did for processes with fewer jets, I will present the histograms for the azimuthal angles between the charged lepton and the missing transverse momentum vector. In Figure 7.25 one can see that the collinear case is strongly suppressed. One can also see a shoulder-like increase up to a local maximum around 95°. After a small dip, the differential cross-section increases linearly. The Tevatron results have a much more linear increase towards the local maximum at approximately 120°.[17] After a small dip it continues to rise linearly. For the LHC with 14 TeV the shoulder is much more pronounced[18]. For the dynamic scales the shoulder disappears almost completely and we can see a linear rise from zero to 180°, intercepted by a plateau from 90° to 120°, which makes them more similar to the Tevatron case[19]. An important observable for the charged lepton and the missing transverse momentum vector is the transverse mass $M_{T,\mathrm{W}}$. This distribution shows a sharp peak around 75 GeV to 80 GeV and can be found in Figure 7.26. The size of the integrals and the scale uncertainties for other accelerators and scales are similar to the ones seen in the $\Delta\phi$ histograms, i.e. largest integral for LHC with 14 TeV and smallest scale uncertainties for $\hat{H}_T$.

Now, I want to investigate the dynamic properties of the jets in more detail. In Figure 7.27 I show the differential cross-section with respect to the transverse momentum and the rapidity of the harder jet, j_{max}. The transverse momentum peaks near 50 GeV (35 GeV for the Tevatron) and exponentially decays towards larger momenta. The rapid-

[16] See Figure 7.25 as well as Figures B.14, B.15 and B.16 in Appendix B.2.1.3.
[17] See Figure B.13 in Appendix B.2.1.3.
[18] See Figure B.14 in Appendix B.2.1.3.
[19] See Figures B.15 and B.16 in Appendix B.2.1.3.

ity distribution shows that the jet is emitted closer to the transverse plane. The corresponding histograms for the softer jet, j_{min}, are given in Figure 7.28. It can be seen that the jet tends to be harder and to lie within the central region of the phase space. This is also true for the other two accelerators. In both cases one can observe that the rapidity distribution is more peaked in the central region for the dynamic scales[20].

Given that this process has two jets and a charged lepton in the final state, there are a variety of distance observables one can look at. Firstly, I present the azimuthal angle between the charged lepton and the harder jet as well as the charged lepton and the softer jet in Figure 7.29. Both distributions show that the jet and the missing transverse momentum are most likely back-to-back. For the harder jet the probability decreases towards 20° after which it is flat and non-zero. For the softer jet the plateau is wider (approximately from 0° to 100°) and higher. The Tevatron distribution differs from the LHC scenario, i.e. the hardest jet peaks around 150° to 155°. The histogram for the softer jet is not quite as flat for lower angles[21]. Histograms for LHC with 14 TeV and dynamic scales are as one would expect from the previous results, i.e. they have a larger integral and are flatter, respectively. The differential cross-section with respect to the rapidity difference between the charged lepton and the jets in Figure 7.30 shows that both jets tend to be emitted closer to the charged lepton. This is true for all accelerators and scales. The histograms of the separation between the charged lepton and the jets are given in Figure 7.31. It can be seen that both distributions increase towards $R = 3$, where they sharply decline (due to $\Delta\phi \leq \pi$). For the harder jet the increase is almost linear and for the softer jet it looks more shoulder like. Figure 7.32 shows the differential cross-section with respect to the invariant mass of the charged lepton and each of the jets. For the harder jet one can observe a linear increase towards a local maximum around 85 GeV to 90 GeV and for the softer jet one gets a slightly sharper peak around 70 GeV. For Tevatron, the peaks are shifted to 70 GeV and 60 GeV, respectively[22]. For the LHC with 14 TeV the results expectantly have a larger magnitude and slightly smaller scale uncertainties. For both the harder and softer jet, the shapes of the curves and the size of the errors are almost identical when using the dynamic scales.

In Figure 7.33 I am presenting the differential cross-section with respect to the azimuthal angle between the missing transverse momentum and the harder as well as the softer jet. The harder jet and the missing momentum vector tend to be not collinear. There is an almost linearly increase towards the back-to-back case. The distribution for the softer jet is almost flat with a small dip for smaller angles suggesting that there is little dependence between the emission of the jet and the neutrino. The result for the LHC with 14 TeV is very similar giving a larger magnitude and slightly reduced scale

[20] See Figures B.17, B.18, B.19 and B.20 in Appendix B.2.1.3.
[21] See Figure B.21 in Appendix B.2.1.3.
[22] See Figure B.22 in Appendix B.2.1.3.

uncertainties. The corresponding result for the Tevatron is flattening off towards larger angles for the harder jets and has an almost steady increase towards large angles for the softer jet[23]. The scale uncertainties are smaller for dynamic scales, similar to the above results. An interesting observable is the transverse mass of the missing transverse momentum vector and the transverse momentum of each jet. These graphs are recorded in Figure 7.34. For the harder jet there is a steep rise from zero mass to a peak at 90 GeV and a long tail. For the softer jet the differential cross-section is finite at zero mass and has a peak around 70 GeV, after which the distribution tails off. I obtained the same shapes, but slightly smaller scale uncertainties for the LHC with 14 TeV and the dynamic scales. For the Tevatron the peaks are steeper and at 70 GeV and 55 GeV to 60 GeV, respectively[24].

Finally, I have calculated the distance observables and the invariant mass for the two jets themselves. Figure 7.35 shows the azimuthal angle between the two jets. One can see that the jets are preferentially separated. There is a small peak at around 20°, which is more pronounced for the Tevatron[25]. This is true for all accelerators and dynamic scales. For the separation in rapidity one can also observe that there is a maximum at low rapidities (approximately 0.5) with a steady decline towards larger separations. The corresponding histogram is shown in Figure 7.36. This result is the same for the LHC with 14 TeV, the Tevatron[26] and the dynamic scales. Magnitudes and uncertainties relate as one would expect them to. The previous two distributions can be combined in the separation R as shown in Figure 7.37. One can observe a well defined peak just above $R = 3$, which means that the two jets tend to be emitted back-to-back. This result is the same for the LHC with 14 TeV and the dynamic scales. For the Tevatron the peak is less defined due to a secondary maximum at small separations (half the magnitude of the main peak)[27]. The last histogram I want to present for this process is the invariant mass of the two jets. One can observe a broad peak around 100 GeV. The slope of the lower flank steepens at 55 GeV. The plot is shown in Figure 7.38. At the Tevatron the peak is at 55 GeV to 60 GeV and the slope steepens at about 40 GeV.[28] The LHC with 14 TeV and dynamic scales are correlated in the usual way.

[23] See Figure B.23 in Appendix B.2.1.3.
[24] See Figure B.24 in Appendix B.2.1.3.
[25] See Figure B.25 in Appendix B.2.1.3.
[26] See Figure B.26 in Appendix B.2.1.3.
[27] See Figure B.27 in Appendix B.2.1.3.
[28] See Figure B.28 in Appendix B.2.1.3.

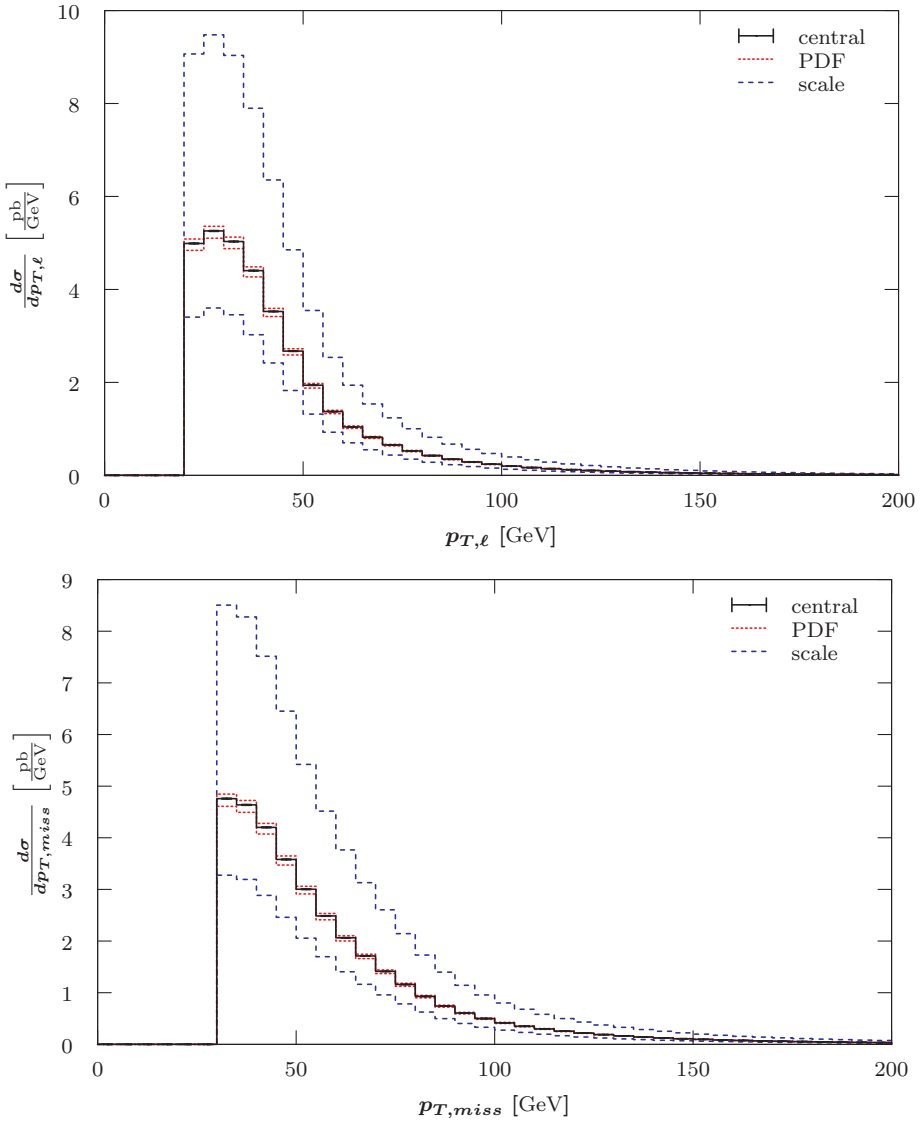

Figure 7.21: LO differential cross-section with respect to the charged lepton (top) and the missing (bottom) transverse momentum for the pp $\to$ ($\text{W}^+ \to \ell^+\nu_\ell$) + 2 *jets* process at the LHC with 7 TeV using a fixed scale of $\mu_0 = M_\text{W}$. Additional details are given in the caption of Figure 7.1.

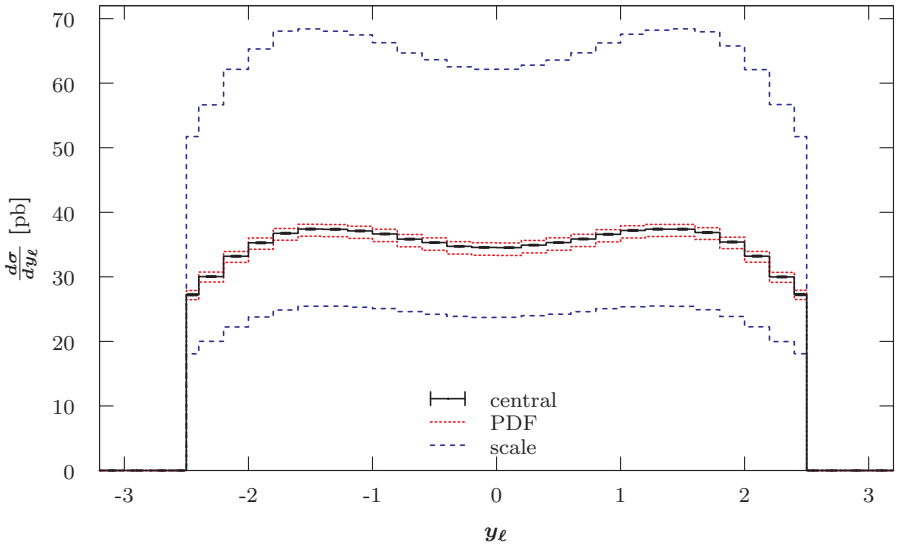

Figure 7.22: LO differential cross-section with respect to the charged lepton rapidity for the $pp \to (W^+ \to \ell^+\nu_\ell) + 2\ jets$ process at the LHC with 7 TeV using a fixed scale of $\mu_0 = M_W$. The first and last filled bin are half-width due to the applied selection cut, $|y_\ell| < 2.5$. Additional details are given in the caption of Figure 7.1.

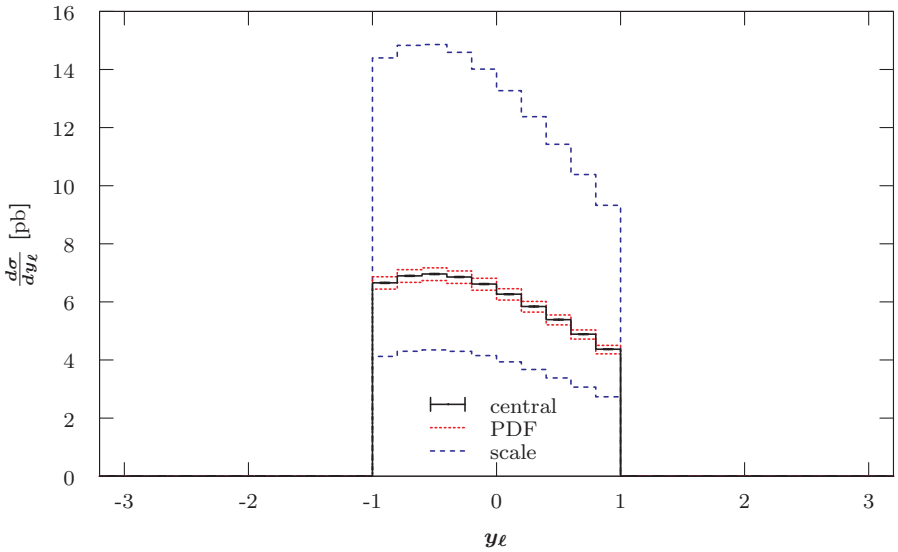

Figure 7.23: LO differential cross-section with respect to the charged lepton rapidity for the $p\overline{p} \to (W^+ \to \ell^+\nu_\ell) + 2\ jets$ process at the Tevatron Run II using a fixed scale of $\mu_0 = M_W$. Additional details are given in the caption of Figure 7.1.

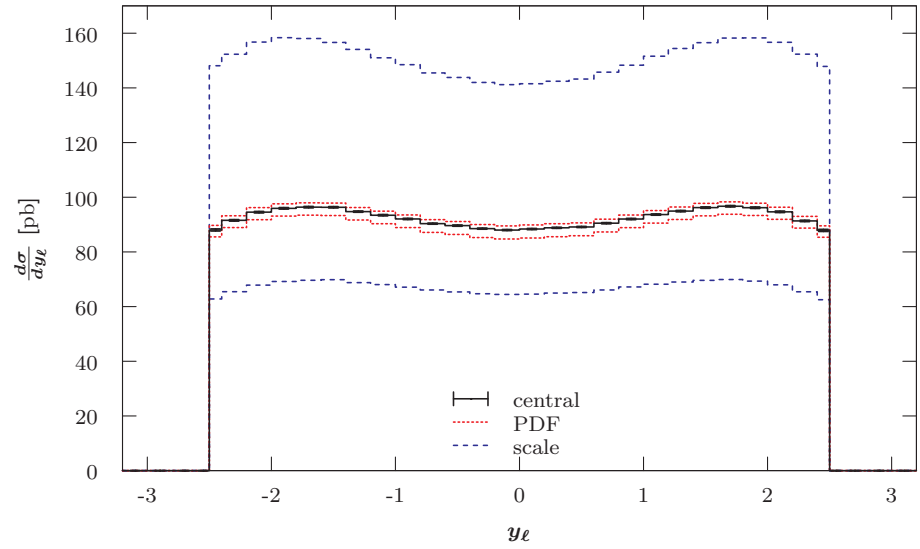

Figure 7.24: LO differential cross-section with respect to the charged lepton rapidity for the $pp \to (W^+ \to \ell^+\nu_\ell) + 2\ jets$ process at the LHC with 14 TeV using a fixed scale of $\mu_0 = M_W$. The first and last filled bin are half-width due to the applied selection cut, $|y_\ell| < 2.5$. Additional details are given in the caption of Figure 7.1.

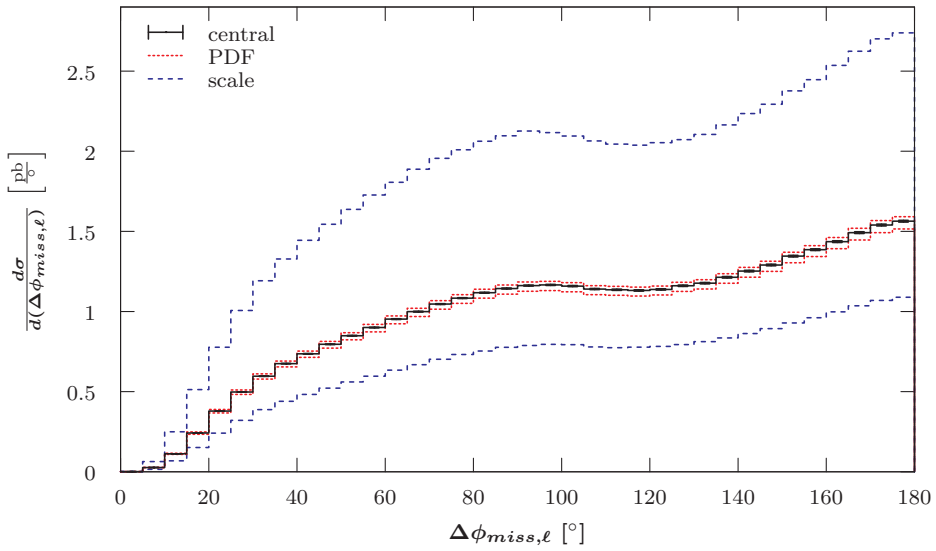

Figure 7.25: LO differential cross-section with respect to the azimuthal angle ϕ between the charged lepton and the missing transverse momentum for the $pp \to (W^+ \to \ell^+\nu_\ell) + 2\ jets$ process at the LHC with 7 TeV using a fixed scale of $\mu_0 = M_W$. Additional details are given in the caption of Figure 7.1.

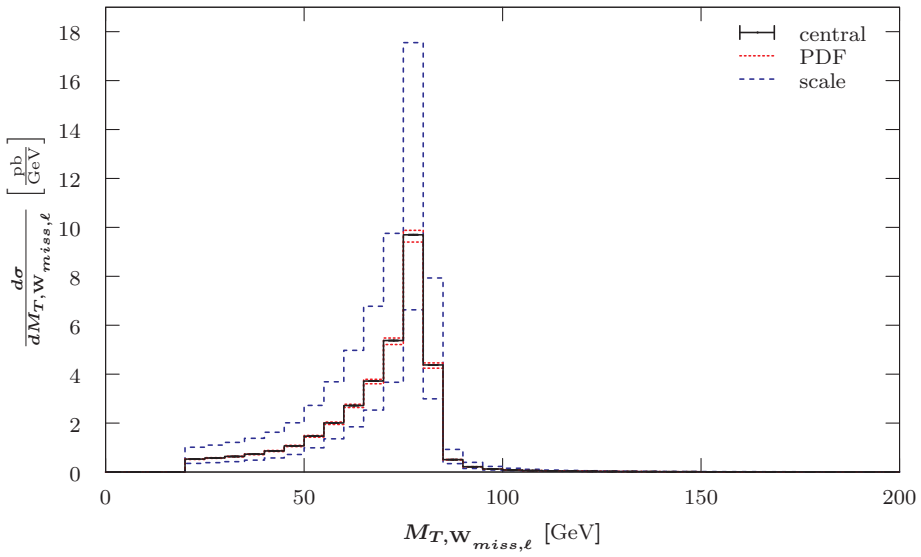

Figure 7.26: LO differential cross-section with respect to the transverse $pp \to (W^+ \to \ell^+\nu_\ell) + 2\ jets$ process at the LHC with 7 TeV using a fixed scale of $\mu_0 = M_W$. Additional details are given in the caption of Figure 7.1.

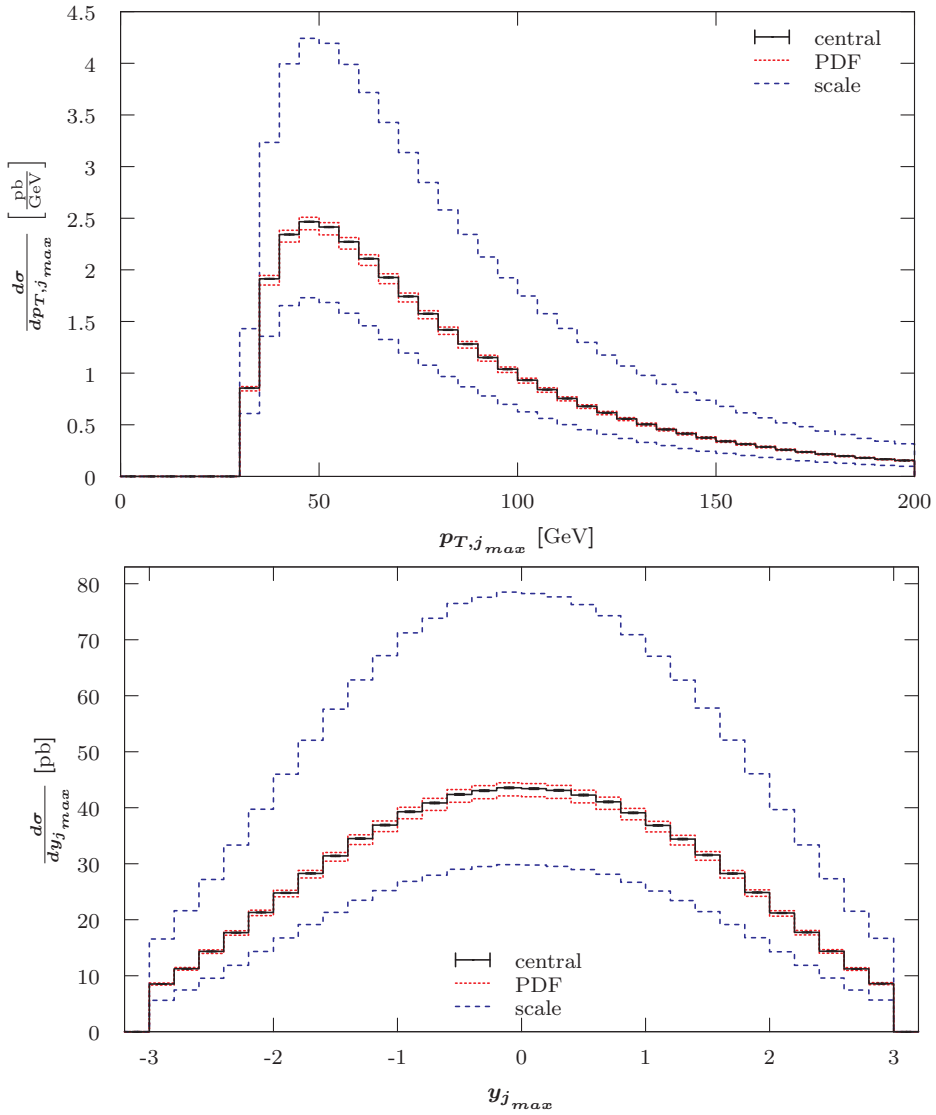

Figure 7.27: LO differential cross-section with respect to the transverse momentum (top) and the rapidity (bottom) of the harder jet j_{max} for the $pp \to (W^+ \to \ell^+\nu_\ell) + 2\ jets$ process at the LHC with 7 TeV using a fixed scale of $\mu_0 = M_W$. Additional details are given in the caption of Figure 7.1.

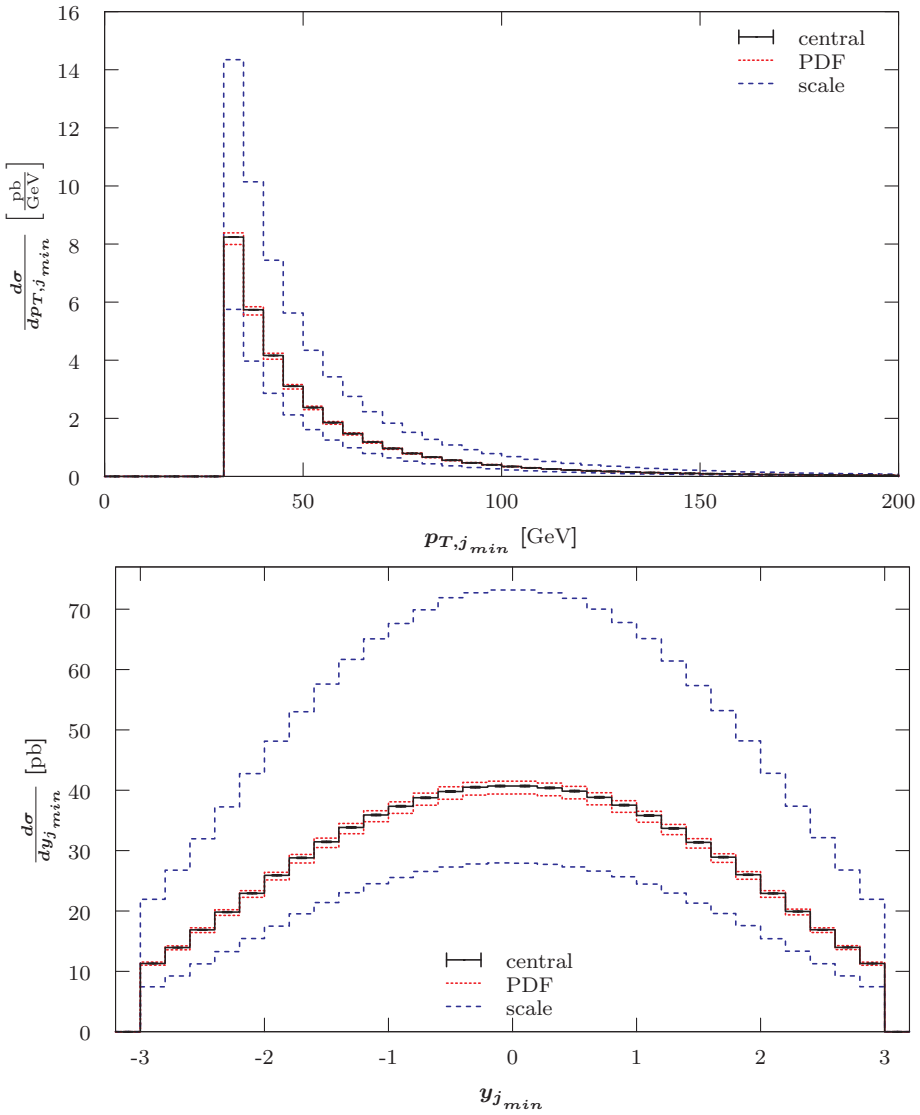

Figure 7.28: LO differential cross-section with respect to the transverse momentum (top) and the rapidity (bottom) of the softer jet j_{min} for the $pp \to (W^+ \to \ell^+\nu_\ell) + 2\ jets$ process at the LHC with 7 TeV using a fixed scale of $\mu_0 = M_W$. Additional details are given in the caption of Figure 7.1.

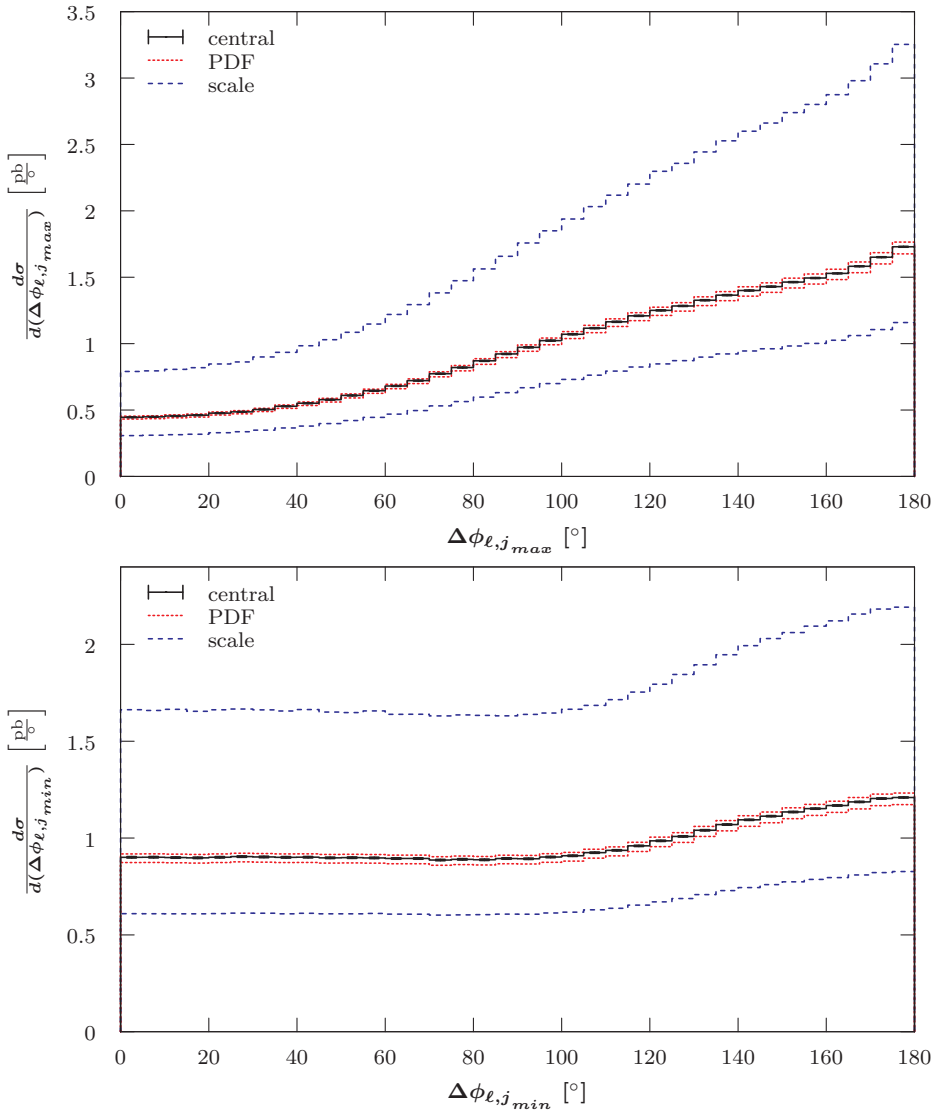

Figure 7.29: LO differential cross-section with respect to the azimuthal angle ϕ between the charged lepton and the harder (top) as well as the softer (bottom) jet for the pp $\to$ ($\text{W}^+ \to \ell^+\nu_\ell$)+2 *jets* process at the LHC with 7 TeV using a fixed scale of $\mu_0 = M_\text{W}$. Additional details are given in the caption of Figure 7.1.

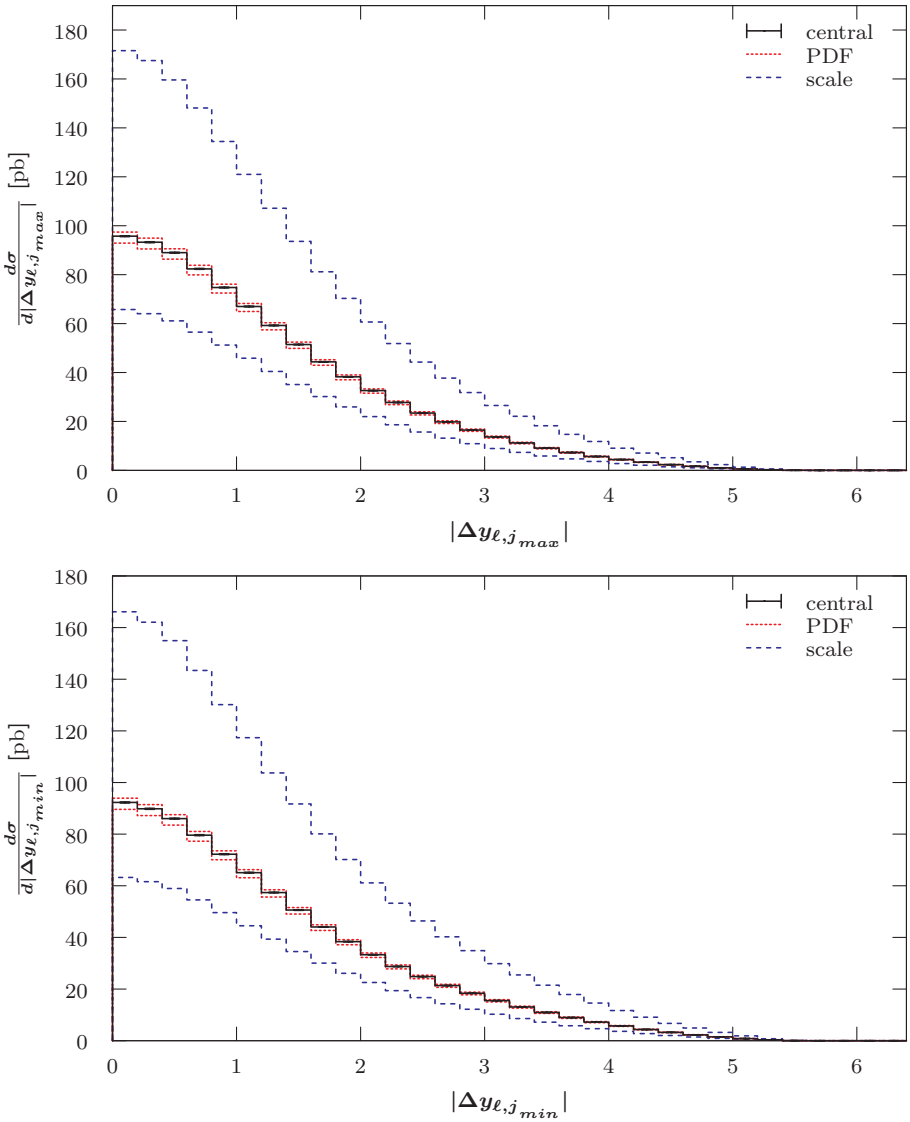

Figure 7.30: LO differential cross-section with respect to the difference in rapidity between the charged lepton and the harder (top) as well as softer (bottom) jet for the pp $\to$ ($W^+ \to \ell^+\nu_\ell$)+2 *jets* process at the LHC with 7 TeV using a fixed scale of $\mu_0 = M_W$. Additional details are given in the caption of Figure 7.1.

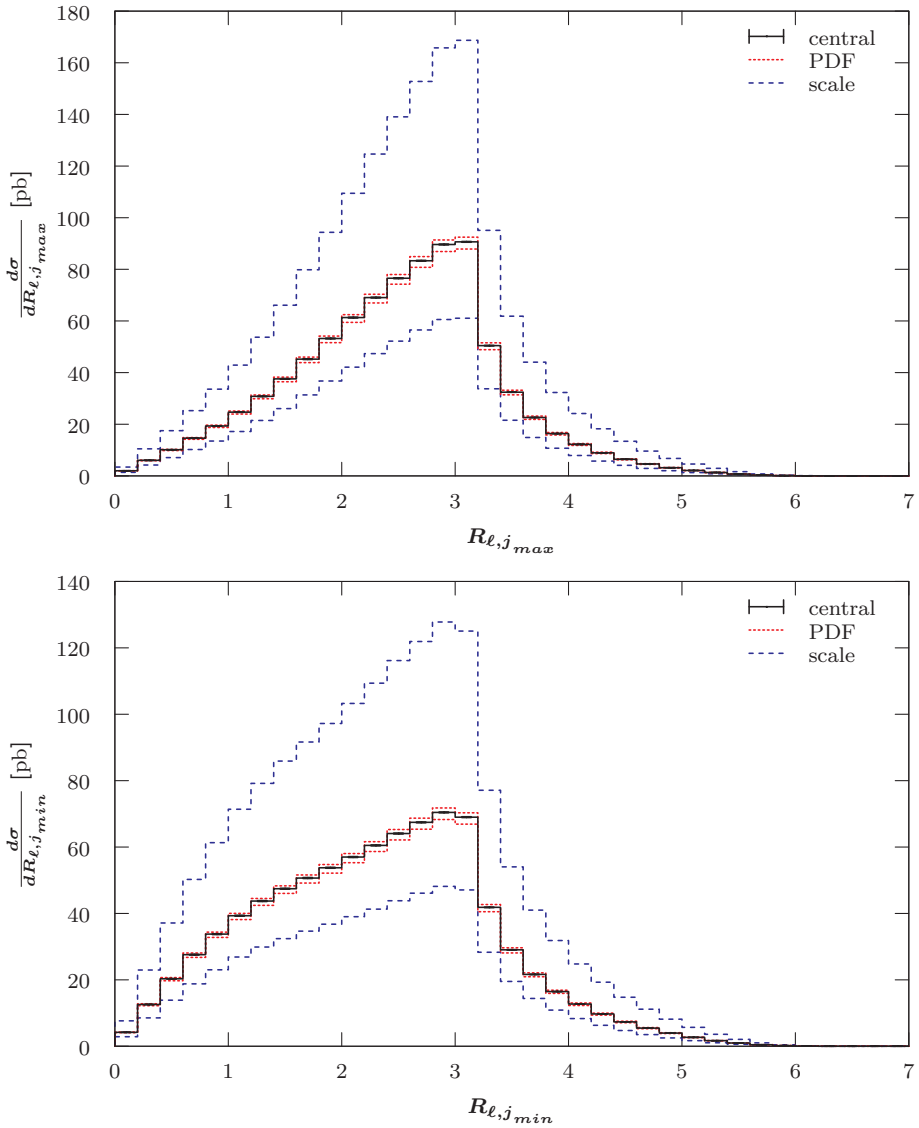

Figure 7.31: LO differential cross-section with respect to the separation between the charged lepton and the harder (top) as well as softer (bottom) jet for the $pp \to (W^+ \to \ell^+\nu_\ell) + 2\ jets$ process at the LHC with 7 TeV using a fixed scale of $\mu_0 = M_W$. Additional details are given in the caption of Figure 7.1.

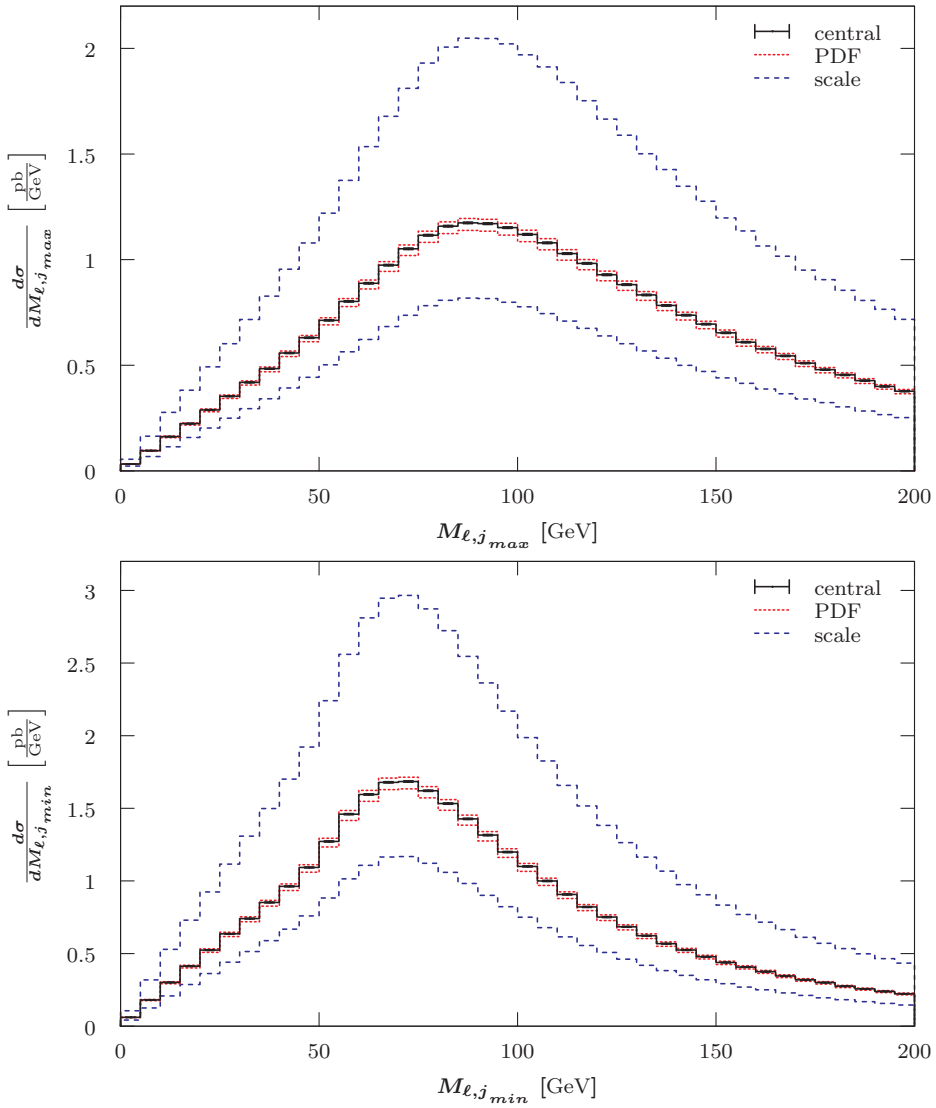

Figure 7.32: LO differential cross-section with respect to the invariant mass of the charged lepton and the harder (top) as well as softer (bottom) jet for the $pp \to (W^+ \to \ell^+\nu_\ell) + 2\ jets$ process at the LHC with 7 TeV using a fixed scale of $\mu_0 = M_W$. Additional details are given in the caption of Figure 7.1.

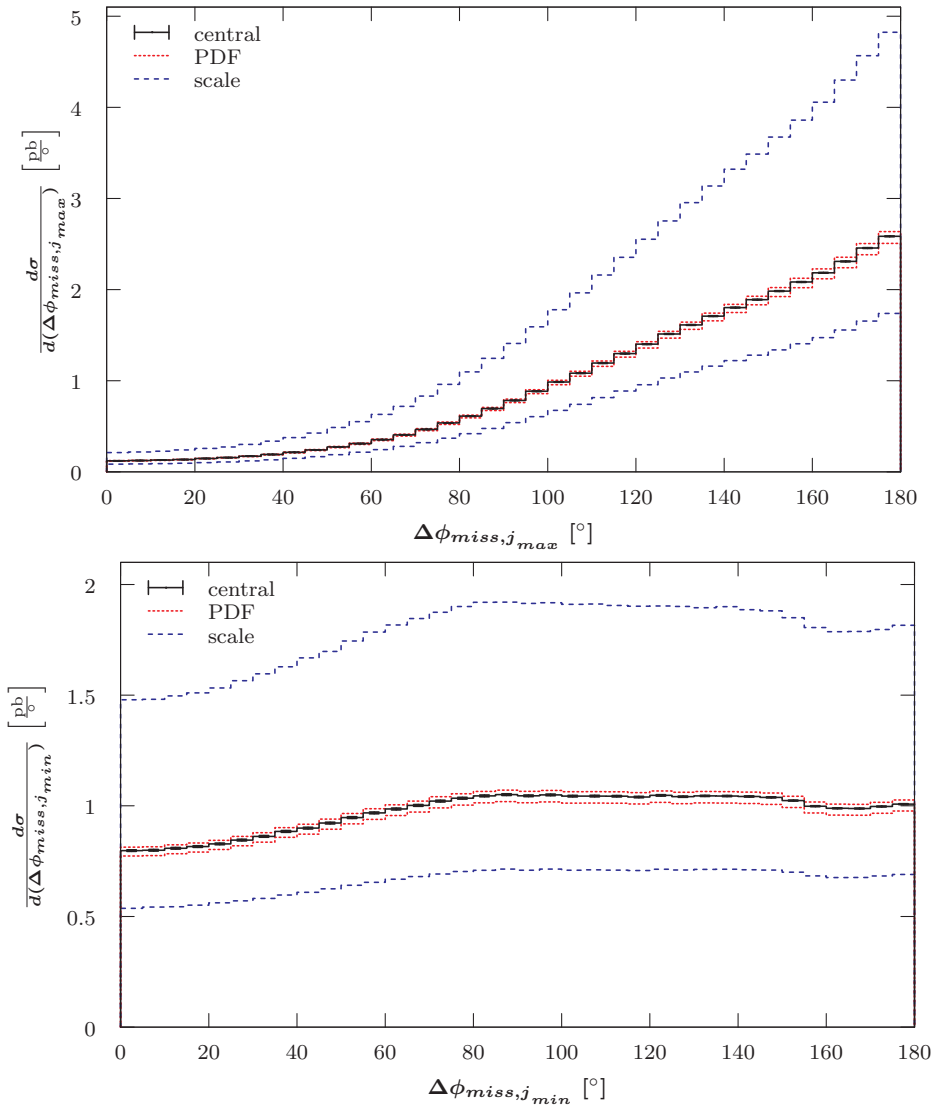

Figure 7.33: LO differential cross-section with respect to the azimuthal angle ϕ between the missing transverse momentum and the harder (top) as well as softer (bottom) jet for the $pp \to (W^+ \to \ell^+\nu_\ell)+2\,jets$ process at the LHC with 7 TeV using a fixed scale of $\mu_0 = M_W$. Additional details are given in the caption of Figure 7.1.

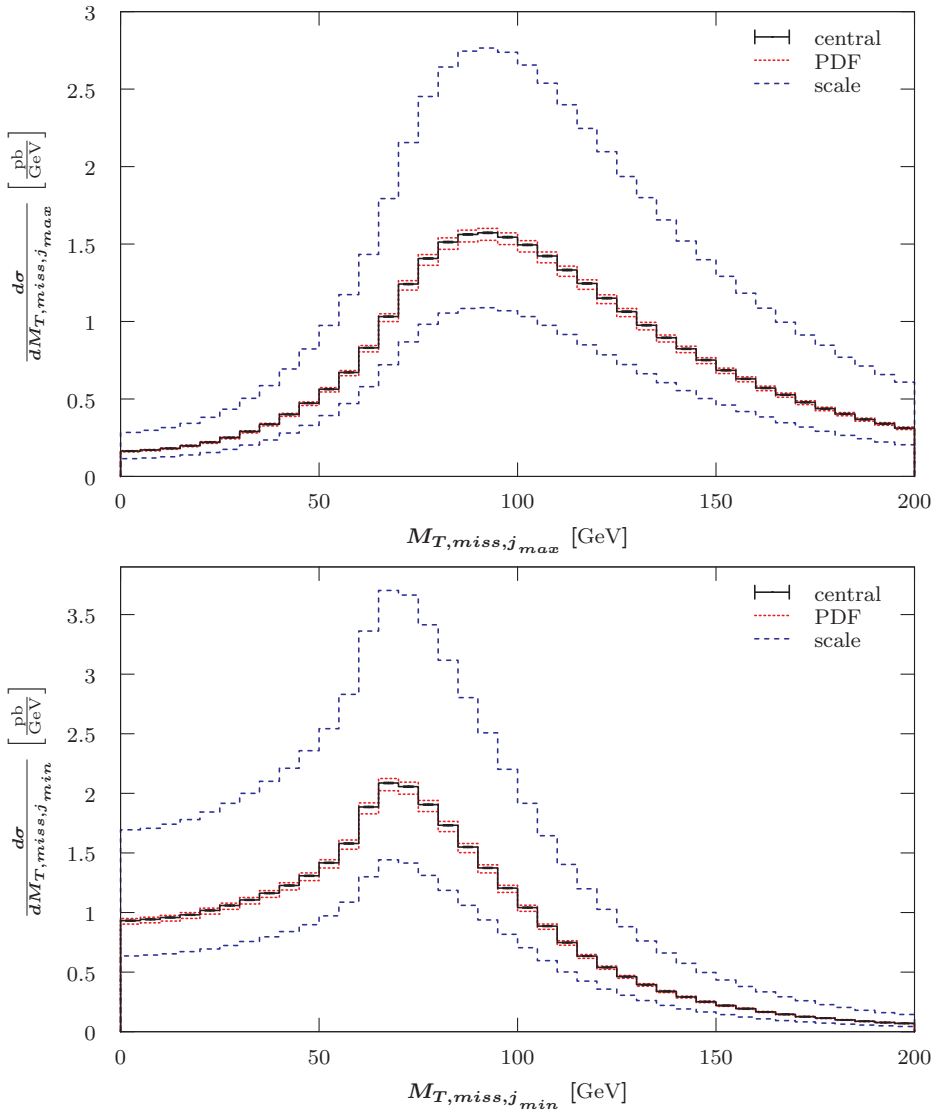

Figure 7.34: LO differential cross-section with respect to the transverse mass of the missing transverse momentum vector and the harder (top) as well as softer (bottom) jet for the $pp \to (W^+ \to \ell^+\nu_\ell)+2\,jets$ process at the LHC with 7 TeV using a fixed scale of $\mu_0 = M_W$. Additional details are given in the caption of Figure 7.1.

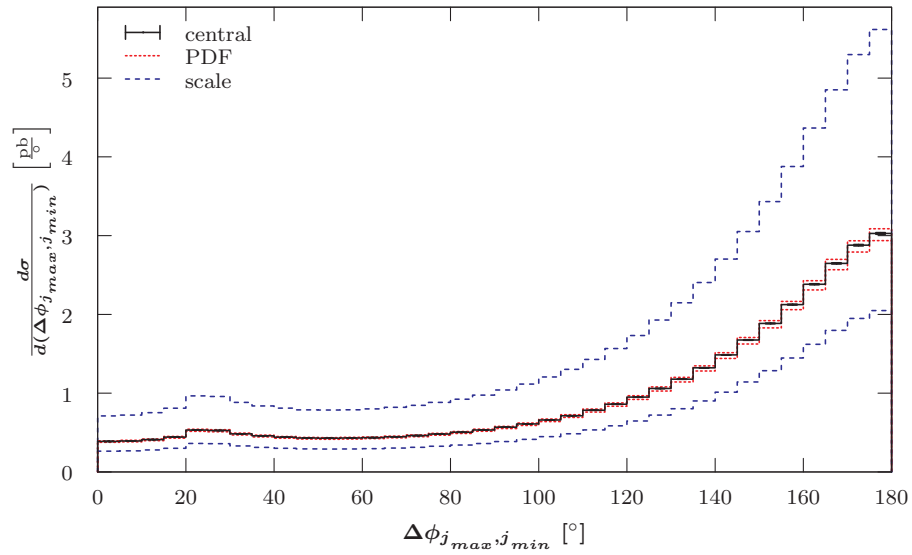

Figure 7.35: LO differential cross-section with respect to the azimuthal angle ϕ between the harder j_{max} and the softer jet j_{min} for the pp $\rightarrow$ ($W^+ \rightarrow \ell^+\nu_\ell$)+2 *jets* process at the LHC with 7 TeV using a fixed scale of $\mu_0 = M_Z$. Additional details are given in the caption of Figure 7.1.

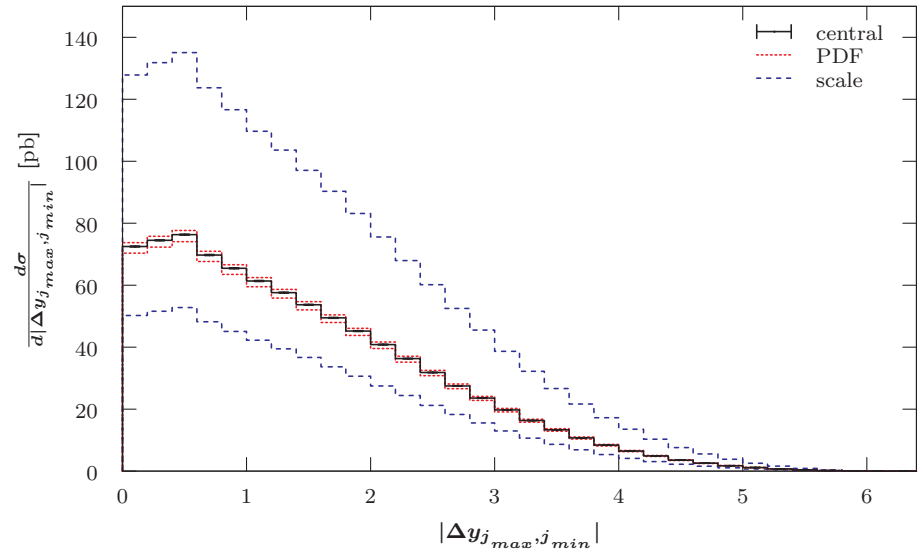

Figure 7.36: LO differential cross-section with respect to the difference in rapidity between the harder j_{max} and the softer jet j_{min} for the pp $\rightarrow$ ($W^+ \rightarrow \ell^+\nu_\ell$)+2 *jets* process at the LHC with 7 TeV using a fixed scale of $\mu_0 = M_Z$. Additional details are given in the caption of Figure 7.1.

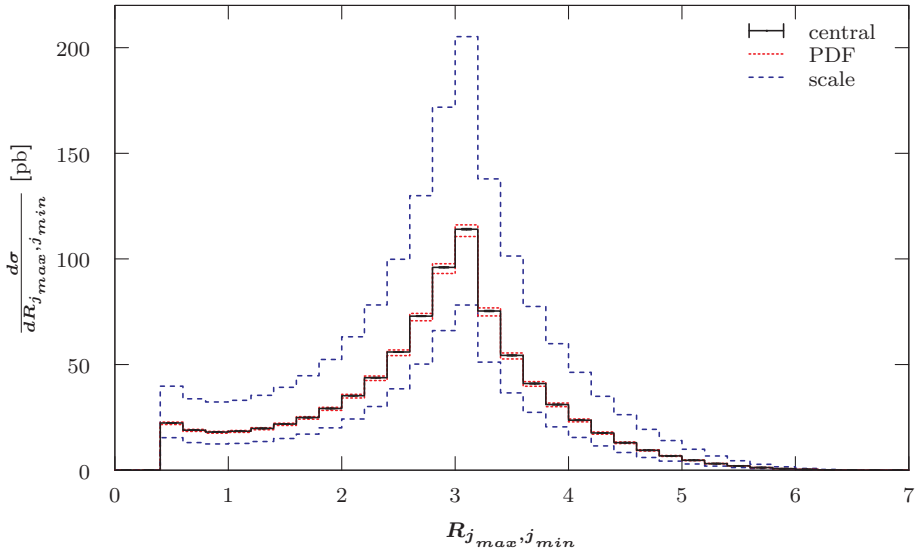

Figure 7.37: LO differential cross-section with respect to separation between the harder j_{max} and the softer j_{min} jet for the pp $\rightarrow$ ($W^+ \rightarrow \ell^+\nu_\ell$) + 2 *jets* process at the LHC with 7 TeV using a fixed scale of $\mu_0 = M_Z$. Additional details are given in the caption of Figure 7.1.

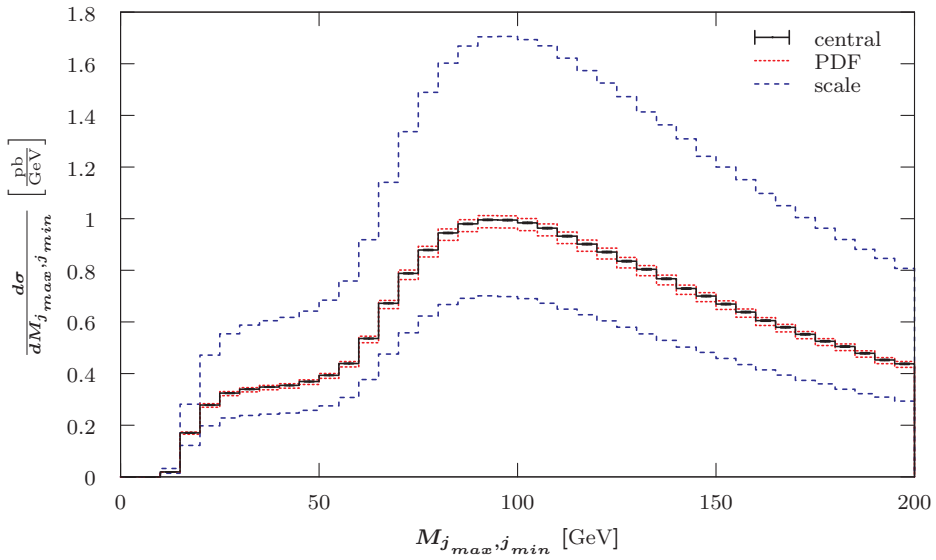

Figure 7.38: LO differential cross-section with respect to the inavaraitn mass of the harder j_{max} and the softer j_{min} jet for the pp $\rightarrow$ ($W^+ \rightarrow \ell^+\nu_\ell$) + 2 *jets* process at the LHC with 7 TeV using a fixed scale of $\mu_0 = M_Z$. Additional details are given in the caption of Figure 7.1.

7.4.2 $p^{(}\overline{p}^{)} \to (W^- \to \ell^-\overline{\nu}_\ell) + n$ jets

In this section I will show the differential cross-sections for the $p^{(}\overline{p}^{)} \to (W^- \to \ell^-\overline{\nu}_\ell) + n\ jets$. This process is very similar to $p^{(}\overline{p}^{)} \to (W^+ \to \ell^+\nu_\ell) + n\ jets$ (see Section 7.4.1). At LHC the integral will be smaller, because of the abundance of up quarks with respect to down quarks in the initial state. In contrast, for the Tevatron the integrals and shape of the distributions will be almost identical to the W^+ case, because the $p\overline{p}$ initial state leads to the integrated PDF function being the same for W^+ and W^- production.

7.4.2.1 $p^{(}\overline{p}^{)} \to (W^- \to \ell^-\overline{\nu}_\ell)$

Figure 7.39 presents the transverse momentum distribution for the charged lepton and the missing transverse momentum distribution. The plots relate to the W^+ histograms as expected. Distributions for the dynamic scales are very similar. The charged lepton transverse momentum for the Tevatron and the LHC with 14 TeV are shown in Figure 7.40. The total integral and the errors behave as one would expect from the total cross-sections.

For comparison to the W^+ process, I show the rapidity distribution for the final state charged lepton in Figure 7.41. It can be seen that the charged lepton tends to be emitted closer to the transverse plane. This is different to the W^+ case. In comparison the rapidity distribution for the LHC with 14 TeV is more stretched[29] and for the Tevatron there is a bias towards one side of the detector due to $p\overline{p}$ asymmetry (see Figure 7.42). A comparison with Figure 7.42 reveals that the charged lepton is biased in the opposite direction with respect to W^+ production. The two dynamic scales yield the same result.

The azimuthal angle between the neutrino and the charged lepton is 180°, as both particles are emitted back-to-back[30]. This is obviously true for all colliders and scales. Figure 7.43 shows the distribution of the transverse mass $M_{T,\mathrm{W}}$. It has the same shape but a lower magnitude than the W^+ equivalent. The shapes are the same for the other two colliders and dynamic scales. Uncertainties and integrals vary according to the total cross-sections.

[29] See Figure B.29 in Appendix B.2.2.1.
[30] See Figure B.30 in Appendix B.2.2.1.

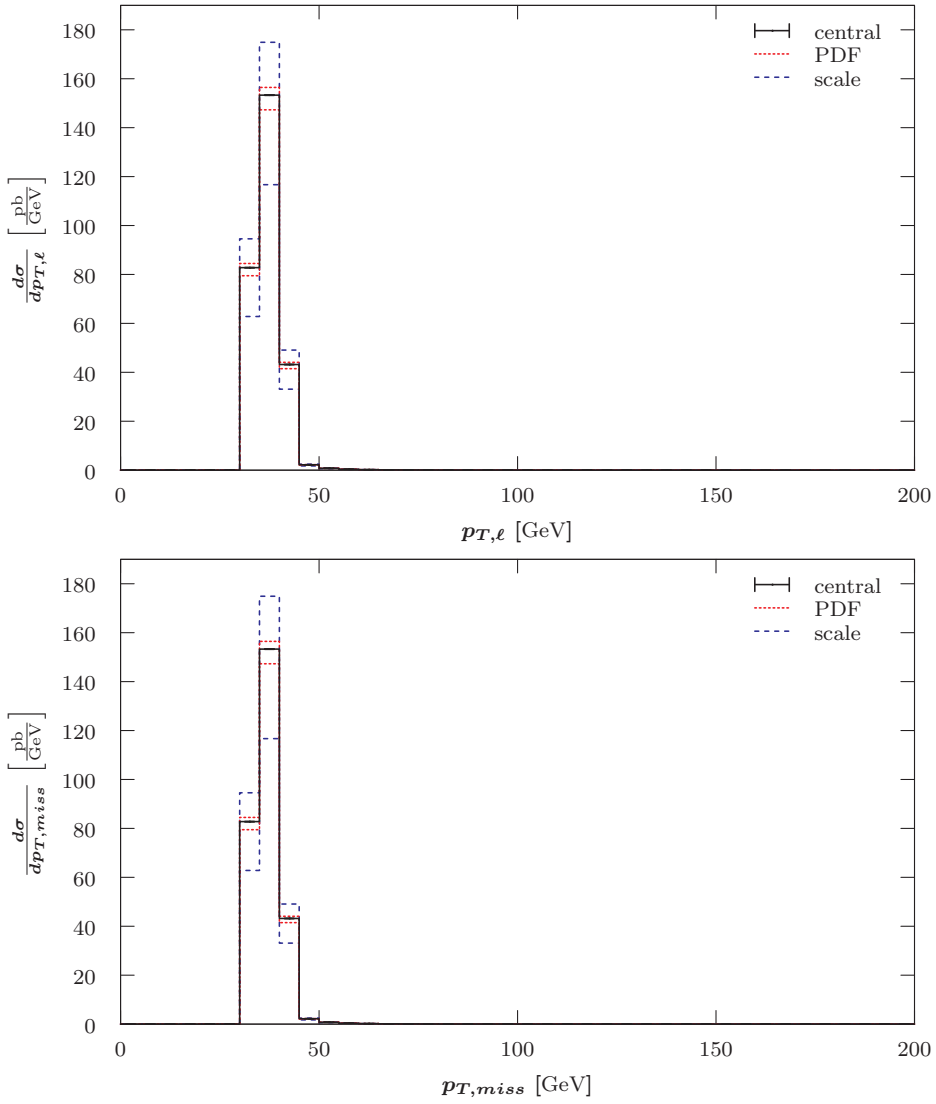

Figure 7.39: LO differential cross-section with respect to the charged lepton (top) and the missing (bottom) transverse momentum for the pp $\to$ ($W^- \to \ell^- \overline{\nu}_\ell$) process at the LHC with $\sqrt{s} = 7\,\text{TeV}$ using a fixed scale of $\mu_0 = M_W$ and MSTW2008LO (90% C.L.) PDFs. Selection cuts as given in Equations 7.5 to 7.8 have been applied. MCFM input parameters are listed in Equations 7.1 to 7.3. The procedure used to choose the number of shots is described in Section 4.4.3. The scale uncertainties have been estimated using a conservative variation by a factor of 4. The error bars for the statistical uncertainties are mostly too small to be visible or are only partially visible. Only the asymmetric deviations for the PDFs (red, dotted) and scale (blue, dashed) from the central value (black, solid) are given.

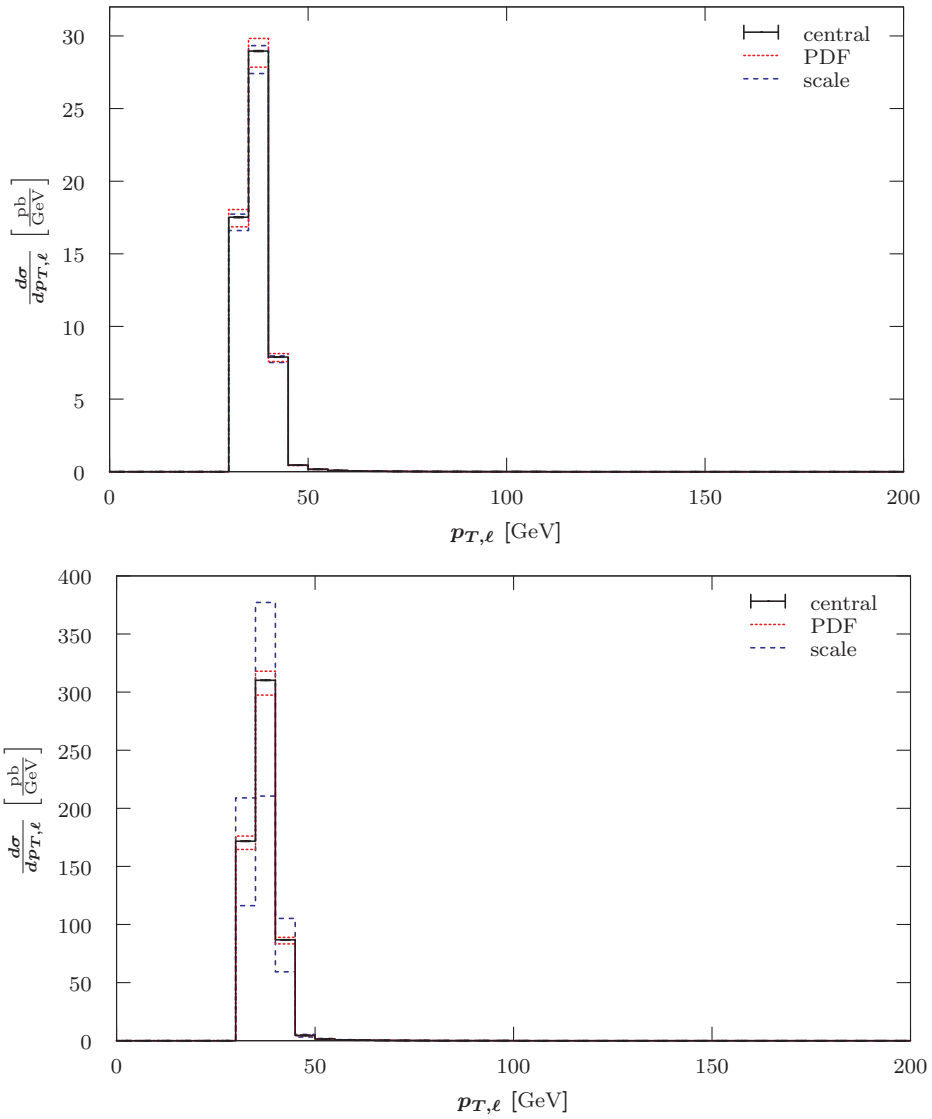

Figure 7.40: LO differential cross-section with respect to the charged lepton (top) and the missing (bottom) transverse momentum for the $\mathrm{p}^{(}\overline{\mathrm{p}}^{)} \to (\mathrm{W}^- \to \ell^- \overline{\nu}_\ell)$ process at the Tevatron Run II using a fixed scale of $\mu_0 = M_\mathrm{W}$. Additional details are given in the caption of Figure 7.39.

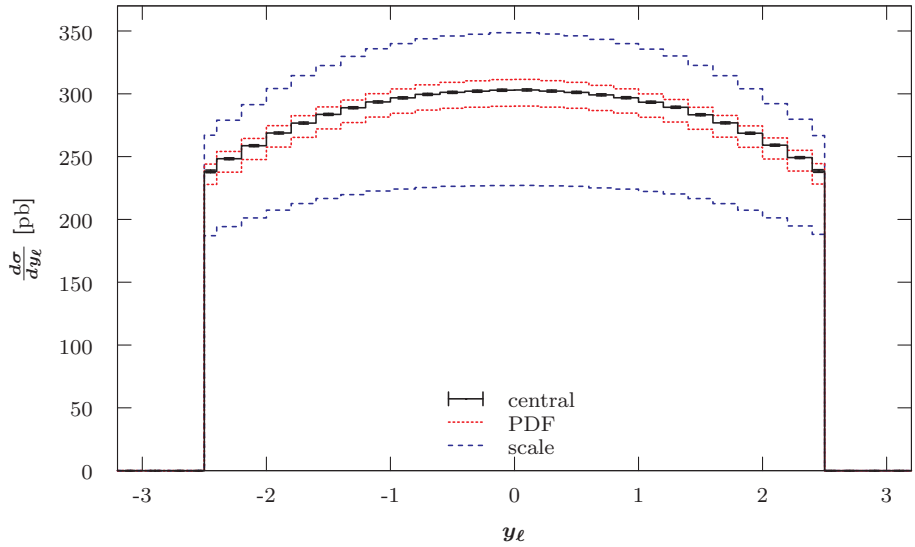

Figure 7.41: LO differential cross-section with respect to the charged lepton rapidity for the $pp \to (W^- \to \ell^- \overline{\nu}_\ell)$ process at the LHC with 7 TeV using a fixed scale of $\mu_0 = M_W$. The first and last filled bin are half-width due to the applied selection cut, $|y_\ell| < 2.5$. Additional details are given in the caption of Figure 7.39.

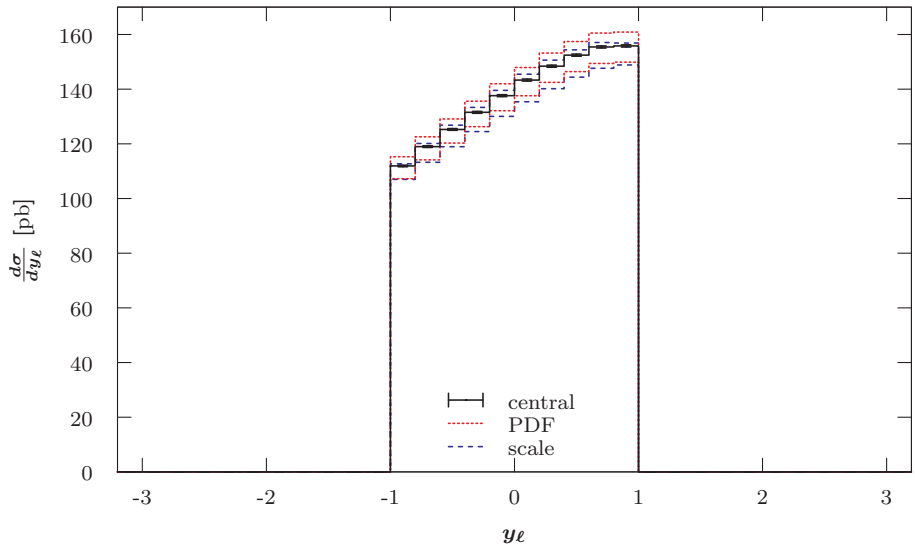

Figure 7.42: LO differential cross-section with respect to the charged lepton rapidity for the $p\overline{p} \to (W^- \to \ell^- \overline{\nu}_\ell)$ process at the Tevatron Run II using a fixed scale of $\mu_0 = M_W$. Additional details are given in the caption of Figure 7.39.

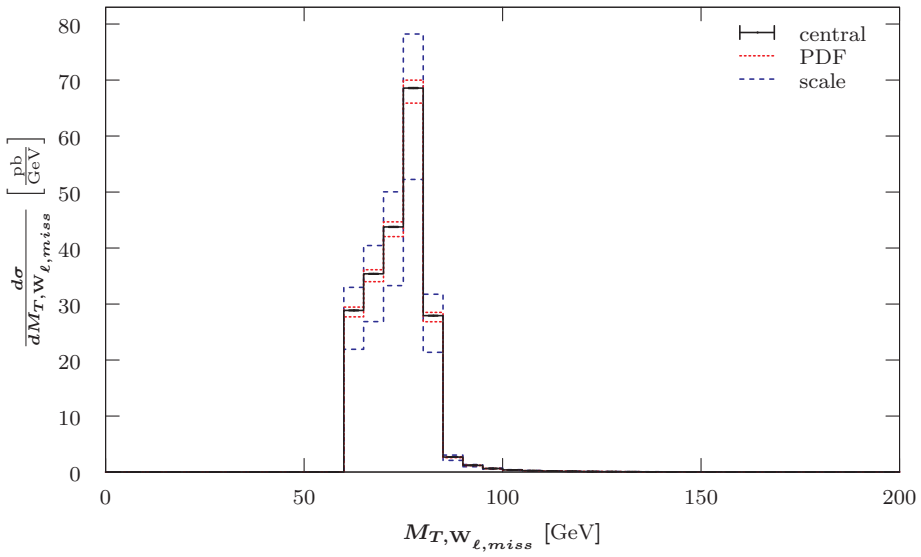

Figure 7.43: LO differential cross-section with respect to transverse inavariant mass $M_{T,\mathrm{W}}$ for the $\mathrm{pp} \to (\mathrm{W}^- \to \ell^- \overline{\nu}_\ell)$ process at the LHC with 7 TeV using a fixed scale of $\mu_0 = M_\mathrm{W}$. Additional details are given in the caption of Figure 7.39.

7.4.2.2 $p^{(}\overline{p}^{)} \to (W^- \to \ell^- \overline{\nu}_\ell) + 1$ jet

Similar to the W^+ case, the distributions for the 1-jet case vary widely. Figure 7.39 presents the transverse momentum distribution for the charged lepton and the missing transverse momentum distribution. The plots relate to the W^+ histograms as expected. Distributions for the dynamic scales are identical. The charged lepton transverse momentum for the Tevatron and the LHC with 14 TeV are shown in Figure 7.45 and 7.46, respectively. The total integrals behave as one would expect, but the scale uncertainties for the LHC with 14 TeV are smaller than one would naïvely expect.

The differential cross-section with respect to the the rapidity distribution of the charged lepton is shown in Figure 7.47. Opposing the W^+ case the charged lepton tends to be emitted in the central region of the detector. The same shapes, but with a smaller integral, are also obtained using dynamic scales. As already seen for W^+ case, one can observe a larger magnitude, but smaller scale uncertainties for the LHC with 14 TeV. This distribution is shown in Figure 7.49 and is also flatter than for the LHC with 7 TeV. In contrast, the rapidity distribution for the Tevatron is marked by a forward/backward asymmetry, which is flipped in comparison to the W^+ case (see Figure 7.48).

The difference between the azimuthal angle of the charged lepton and the missing momentum vector is shown in Figure 7.50. The distribution rises steadily to a peak at 130° to 135° and then decreases rapidly. I found the same shape for the LHC with 14 TeV. For the Tevatron the peak is shifted up to 145° to 150°.[31] One can observe that the scale uncertainties decrease with centre-of-mass energy, because the strong coupling also decreases[32]. At the LHC with 14 TeV the uncertainties are only twice the PDF uncertainties. The plots are all identical to the W^+ case. The transverse mass of the charged lepton and the missing transverse momentum $M_{T,\mathrm{W}}$ is shown in Figure 7.51. The distribution peaks at about 75 GeV to 80 GeV. Results for the Tevatron and the LHC with 14 TeV only differ in the integral. At the LHC with 14 TeV scale uncertainties are suppressed. Results for the two dynamic scales vary according to the total integral.

The differential cross-section with respect to the transverse momentum and the rapidity of the jet are both shown in Figure 7.52. One can observe that the jet tends to be emitted at low transverse momentum and in the centre of the detector. For the Tevatron and LHC with 14 TeV one can see that the magnitude increases according to the centre of mass energy and the scale uncertainty decreases[33]. Histograms for dynamic scales are very similar. These results are identical to the W^+ process.

As for the W^+ process I will present the distance observables between the jet and the charged lepton (or the neutrino). Figure 7.53 shows the difference of the azimuthal angle

[31] See Figures B.31 and B.32 in Appendix B.2.2.2.
[32] See Section 3.2
[33] See Figures B.33 and B.34 in Appendix B.2.2.2.

and the rapidity between the jet and the charged lepton. The azimuthal angle distribution peaks around 140° to 145°. For the LHC with 14 TeV the shape of the histogram is the same and for the Tevatron the peak is slightly lower at 135° to 140°.[34] These are slightly higher than for W^+ bosons. Plots for dynamic scales are very similar. The difference between the rapidities of the charged lepton and jet can be seen in Figure 7.54. One can see that the jet and the charged lepton tend to have a similar rapidity. The usual differences for magnitude and uncertainties can be seen for other accelerator and dynamic scales. The separation R between the charged lepton and the jet is shown in Figure 7.55. One can see that the charged lepton and the jet tend to be separated in the phase space. The histogram peaks at $R \approx 3$, after which it drops rapidly. The results for the other two accelerator setups and for the dynamic scales are very similar. They only vary in the obvious differences in the total cross-section and the size of the uncertainties. The histogram for the invariant mass of the charged lepton and the jet is given in Figure 7.56. One can observe a linear rise from zero mass to a maximum at 75 GeV after which it tails off exponentially. Apart from the larger integral and the decreased scale uncertainties (twice the PDF uncertainties) the distibution for the LHC with 14 TeV is the same. For Tevatron, however, the peak is positioned at 60 GeV to 65 GeV and there is a more rapid decrease towards larger masses[35]. The histograms for the dynamic scales have the same shape and yield a minimal decrease for the scale uncertainties. All these shapes are similar to the W^+ scenario.

Lastly, we can look at the combination between the missing transverse momentum and the jet. The azimuthal angle between the jet and the missing transverse momentum vector is shown in Figure 7.57. As in the W^+ case, this distribution starts rising above zero at 40° and peaks at 155° to 160°. For the Tevatron and the LHC with 14 TeV we can see the same type of plots.[36] The results for dynamic scales are very similar. In Figure 7.58 one can find the differential cross-section with respect to the transverse mass of the missing transverse momentum and the jet. For low masses up to 20 GeV the histogram is almost zero. There it starts to exponentially increase to a peak at 80 GeV to 85 GeV before it rapidly decays towards larger masses. The integrals and uncertainties are similar to what we have seen for other distributions like $M_{\ell,j}$. The shape for the Tevatron is slightly different, because it does not start off as flat[37].

[34] See Figures B.36 and B.35 in Appendix B.2.2.2.
[35] See Figure B.37 in Appendix B.2.2.2.
[36] See Figures B.36 and Figures B.38 and B.39.
[37] See Figure B.40 in Appendix B.2.2.2.

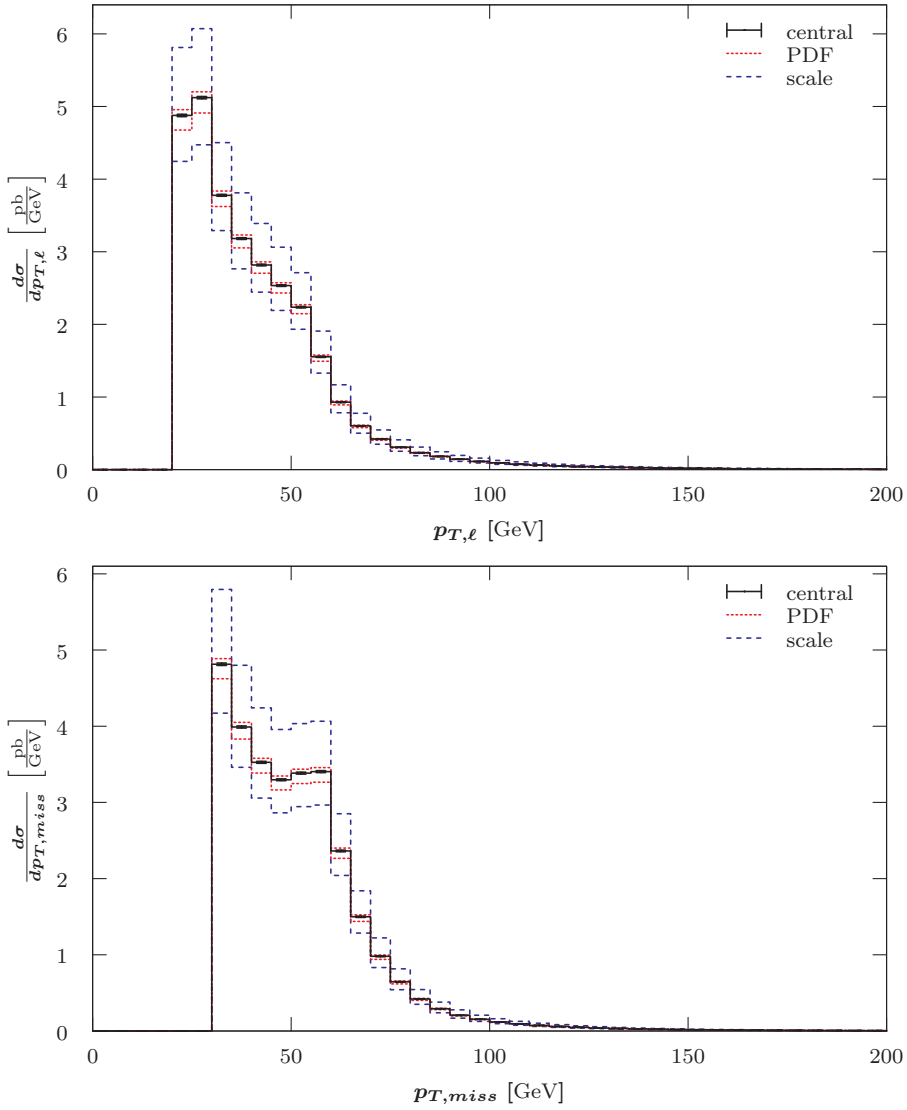

Figure 7.44: LO differential cross-section with respect to the charged lepton (top) and the missing (bottom) transverse momentum for the $pp \to (W^- \to \ell^- \overline{\nu}_\ell) + 1\ jet$ process at the LHC with 7 TeV using a fixed scale of $\mu_0 = M_W$. Additional details are given in the caption of Figure 7.39.

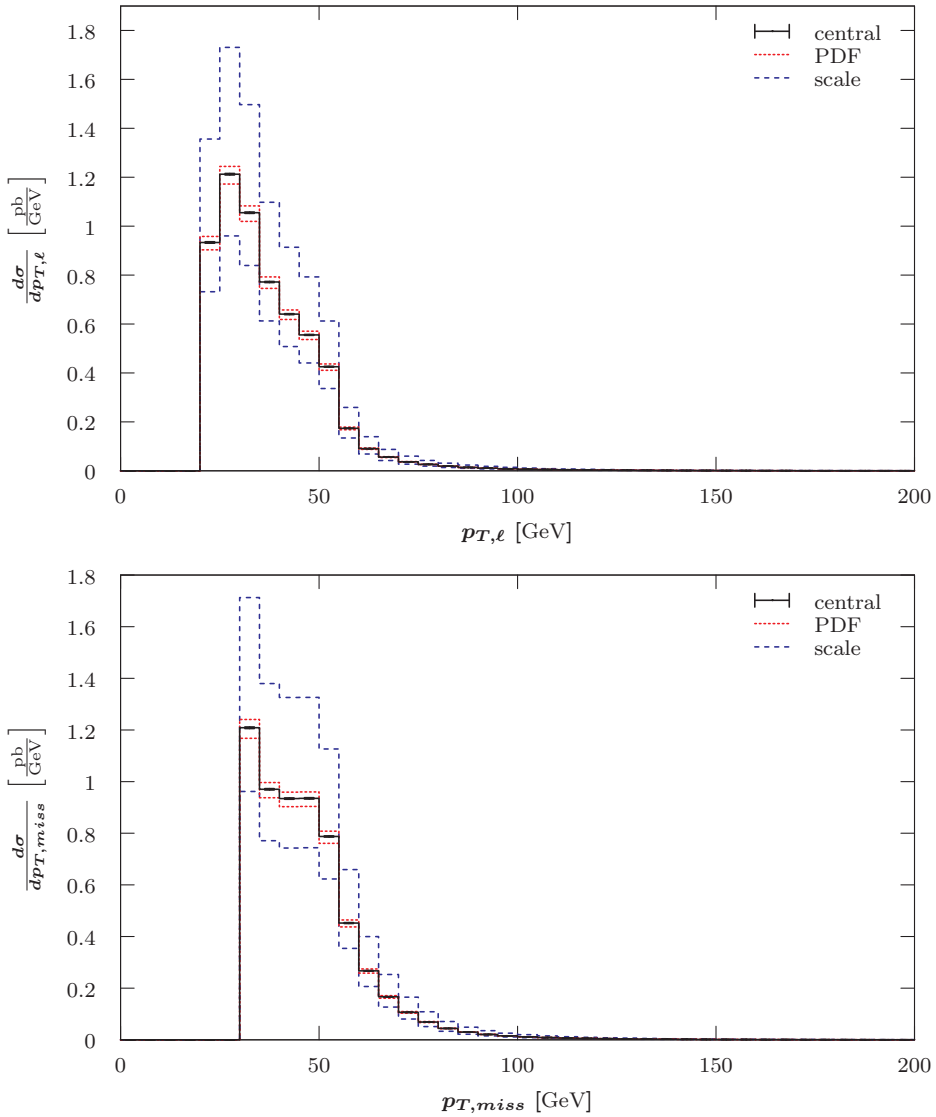

Figure 7.45: LO differential cross-section with respect to the charged lepton (top) and the missing (bottom) transverse momentum for the $p\bar{p} \to (W^- \to \ell^- \overline{\nu}_\ell) + 1\ jet$ process at the Tevatron Run II using a fixed scale of $\mu_0 = M_W$. Additional details are given in the caption of Figure 7.39.

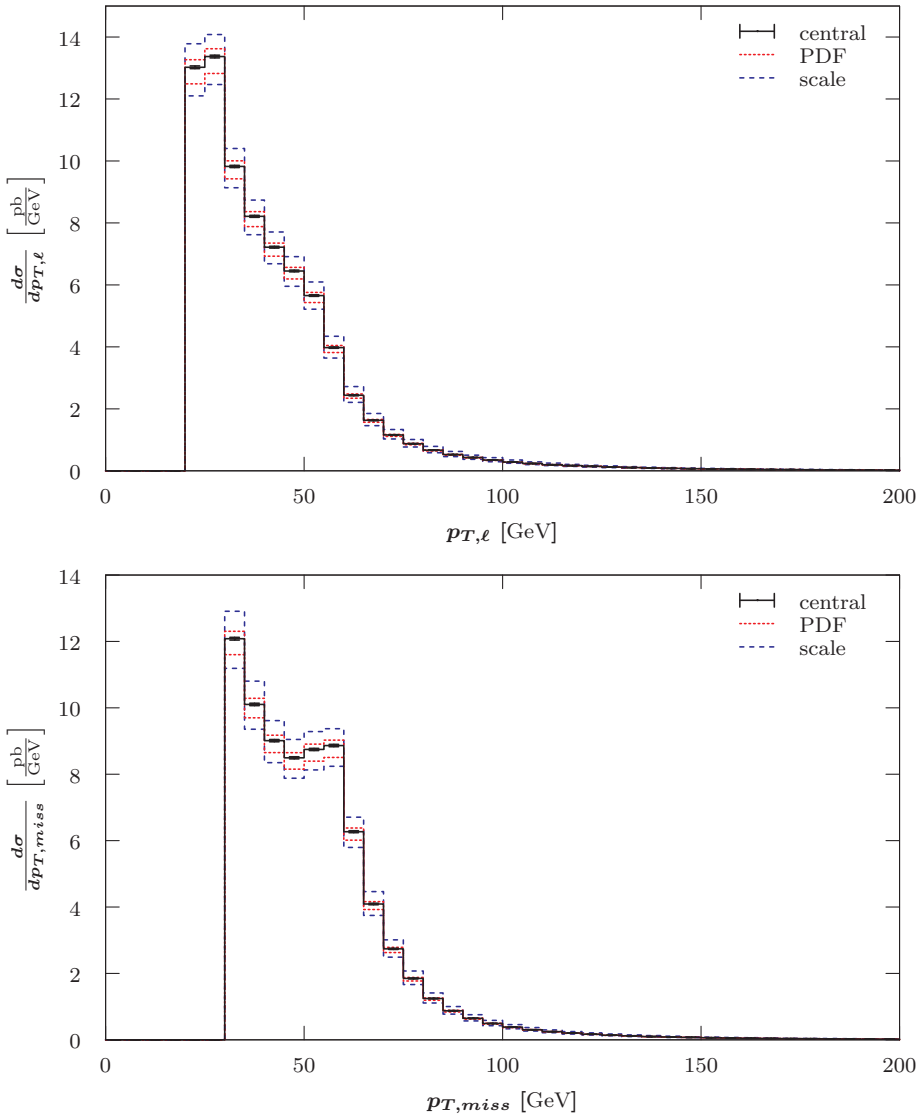

Figure 7.46: LO differential cross-section with respect to the charged lepton (top) and the missing (bottom) transverse momentum for the $pp \to (W^- \to \ell^- \overline{\nu}_\ell) + 1\ jet$ process at the LHC with 14 TeV using a fixed scale of $\mu_0 = M_W$. Additional details are given in the caption of Figure 7.39.

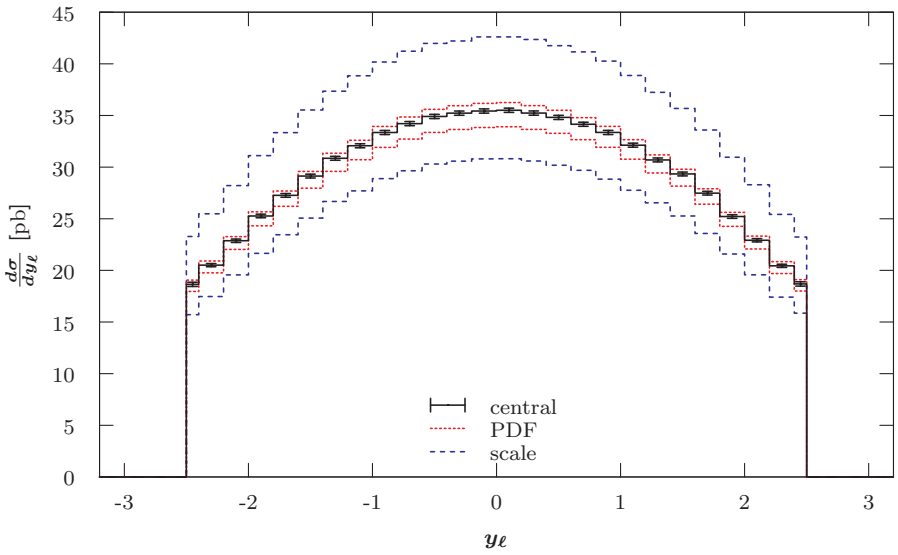

Figure 7.47: LO differential cross-section with respect to the charged lepton rapidity for the $pp \to (W^- \to \ell^- \overline{\nu}_\ell) + 1\ jet$ process at the LHC with 7 TeV using a fixed scale of $\mu_0 = M_W$. The rapidity cut goes through the middle of the first and last filled bin and hence should be twice the hight. Additional details are given in the caption of Figure 7.39.

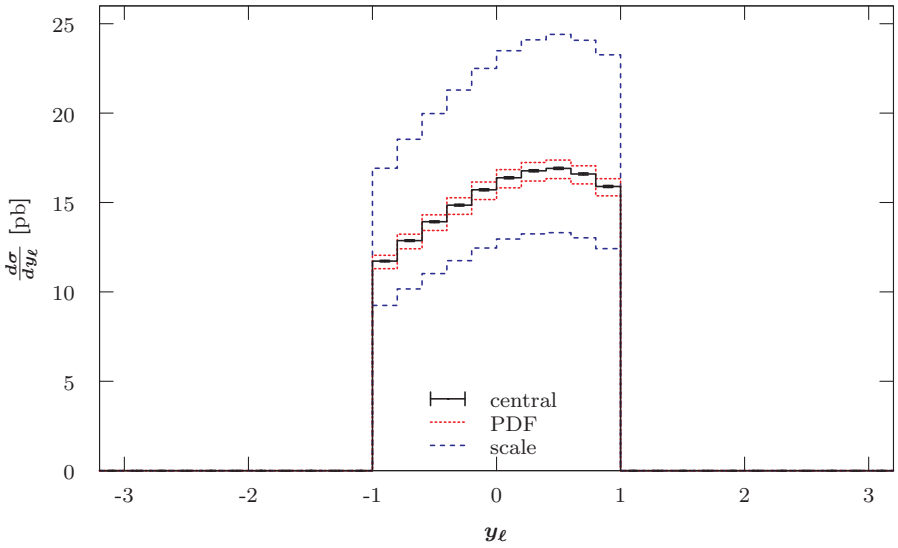

Figure 7.48: LO differential cross-section with respect to the charged lepton rapidity for the $p\overline{p} \to (W^- \to \ell^- \overline{\nu}_\ell) + 1\ jet$ process at the Tevatron Run II using a fixed scale of $\mu_0 = M_W$. Additional details are given in the caption of Figure 7.39.

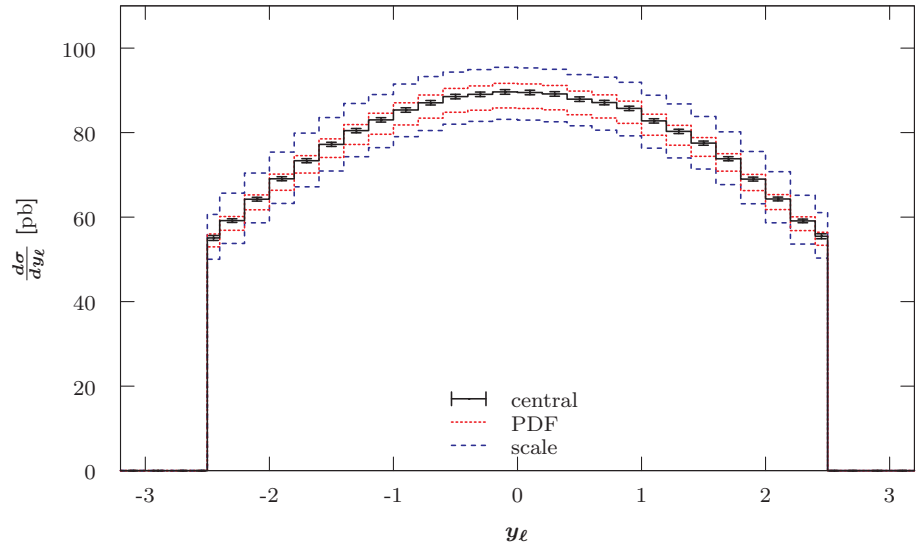

Figure 7.49: LO differential cross-section with respect to the charged lepton rapidity for the $pp \to (W^- \to \ell^- \overline{\nu}_\ell) + 1\ jet$ process at the LHC with 14 TeV using a fixed scale of $\mu_0 = M_W$. The first and last filled bin are half-width due to the applied selection cut, $|y_\ell| < 2.5$. Additional details are given in the caption of Figure 7.39.

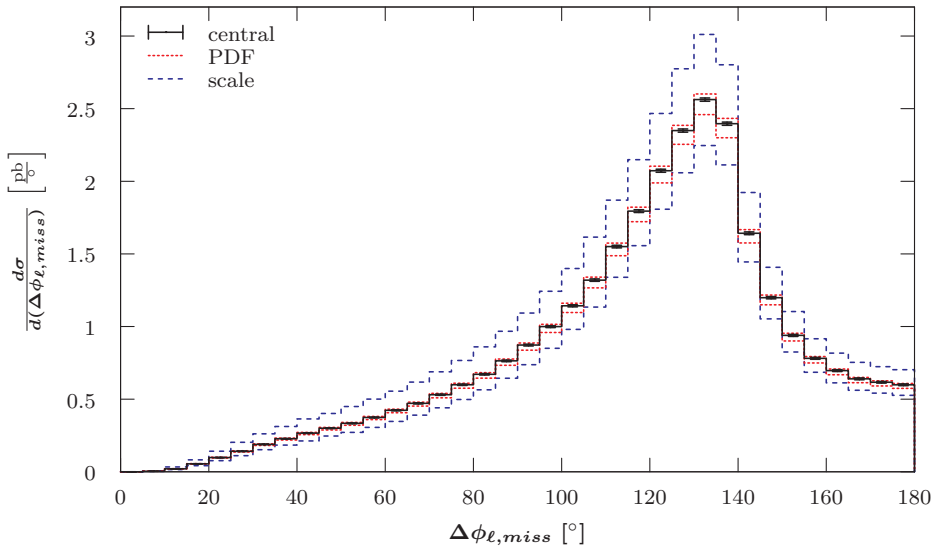

Figure 7.50: LO differential cross-section with respect to the azimuthal angle ϕ between the charged lepton and the missing transverse momentum for the $pp \to (W^- \to \ell^- \overline{\nu}_\ell) + 1\ jet$ process at the LHC with 7 TeV using a fixed scale of $\mu_0 = M_W$. Additional details are given in the caption of Figure 7.39.

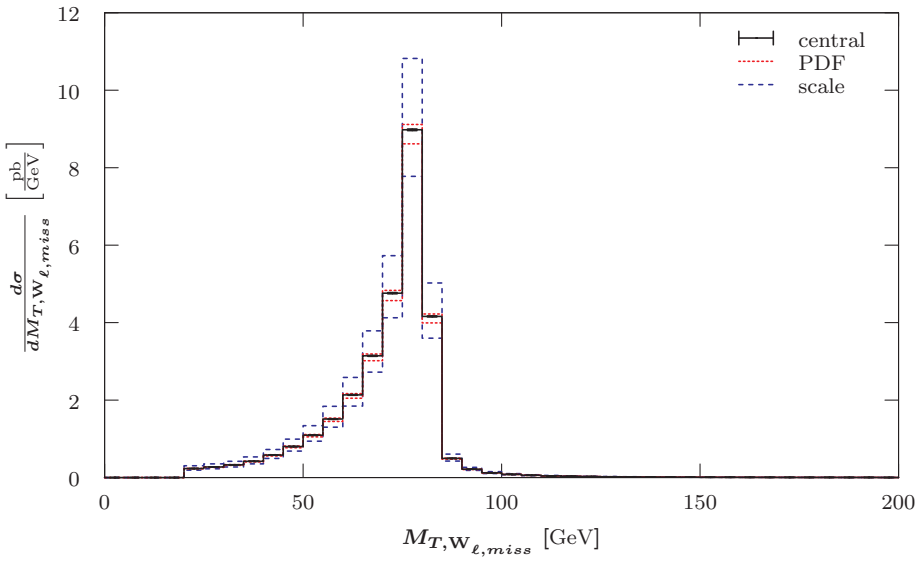

Figure 7.51: LO differential cross-section with respect to transverse inavariant mass $M_{T,\mathrm{W}}$ for the $\mathrm{pp} \to (\mathrm{W}^- \to \ell^- \overline{\nu}_\ell) + 1\ jet$ process at the LHC with 7 TeV using a fixed scale of $\mu_0 = M_\mathrm{W}$. Additional details are given in the caption of Figure 7.39.

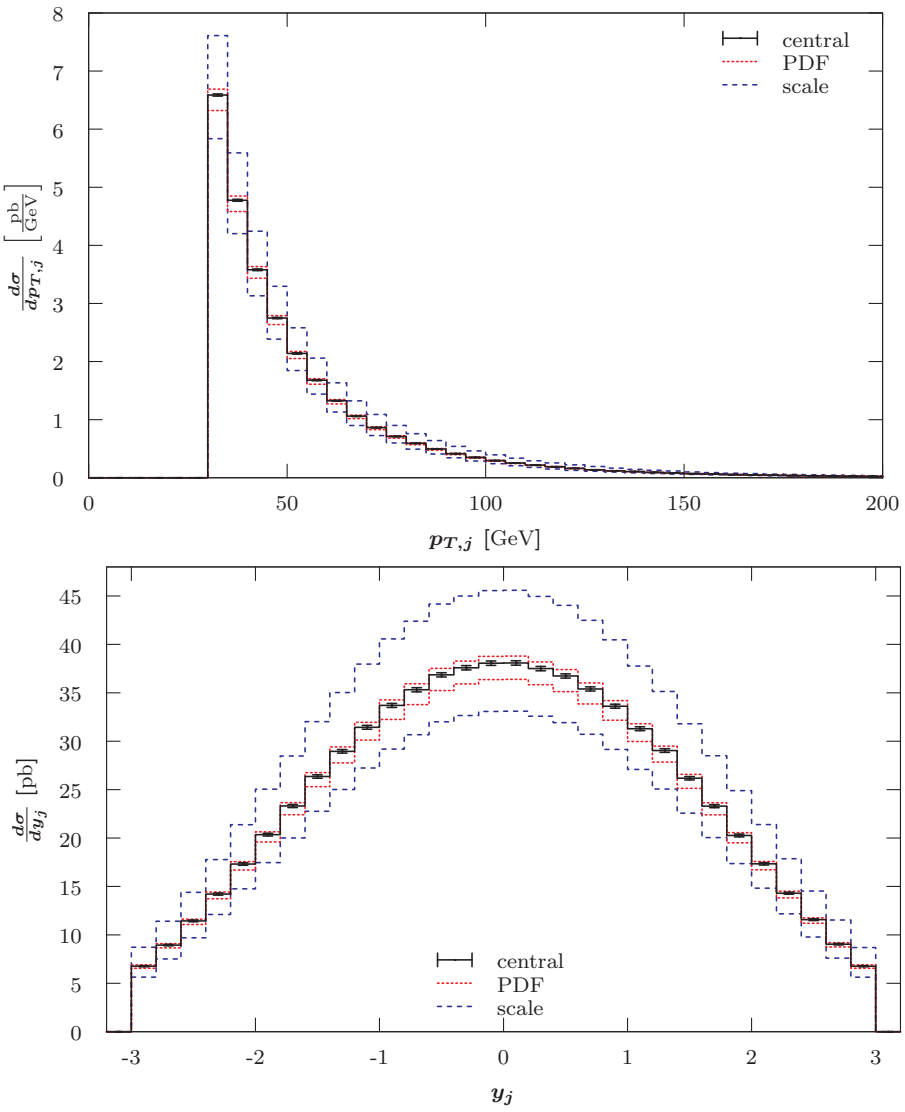

Figure 7.52: LO differential cross-section with respect to the jet transverse momentum (top) and the jet rapidity (bottom) for the pp $\to (\mathrm{W}^- \to \ell^- \overline{\nu}_\ell) + 1\ jet$ process at the LHC with 7 TeV using a fixed scale of $\mu_0 = M_\mathrm{W}$. Additional details are given in the caption of Figure 7.39.

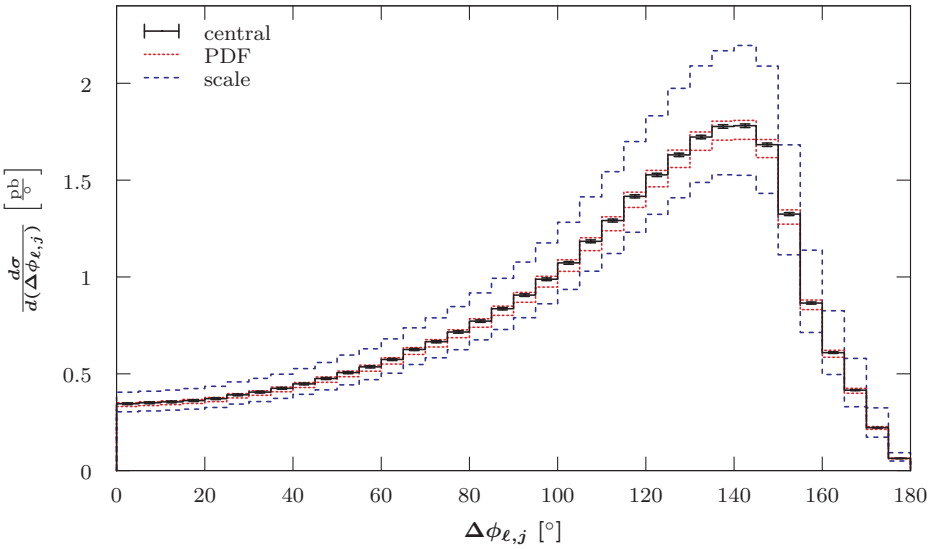

Figure 7.53: LO differential cross-section with respect to the azimuthal angle ϕ between the charged lepton and the jet for the $pp \to (W^- \to \ell^- \overline{\nu}_\ell) + 1\ jet$ process at the LHC with 7 TeV using a fixed scale of $\mu_0 = M_W$. Additional details are given in the caption of Figure 7.39.

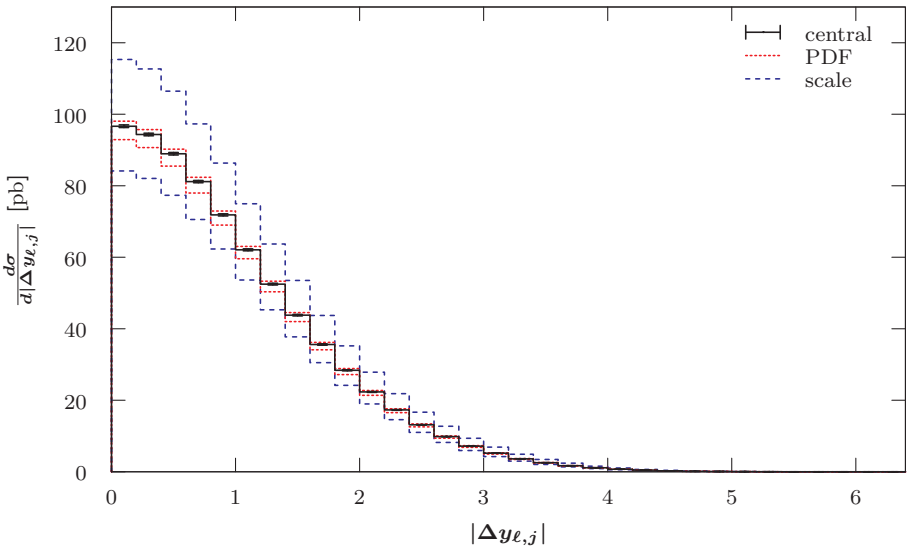

Figure 7.54: LO differential cross-section with respect to the difference in rapidity between the charged lepton and the jet for the $pp \to (W^- \to \ell^- \overline{\nu}_\ell) + 1\ jet$ process at the LHC with 7 TeV using a fixed scale of $\mu_0 = M_W$. Additional details are given in the caption of Figure 7.46.

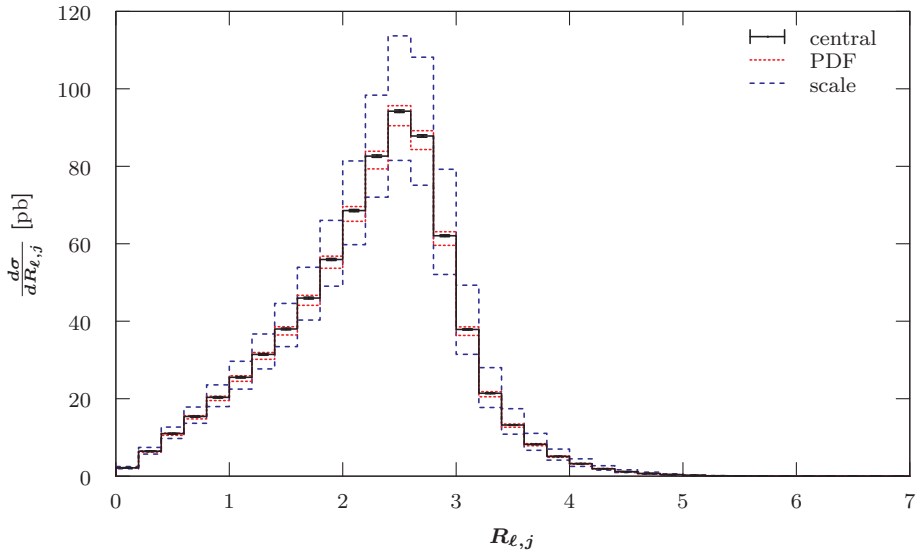

Figure 7.55: LO differential cross-section with respect to the separation between the charged lepton and the jet for the $pp \to (W^- \to \ell^- \overline{\nu}_\ell) + 1\ jet$ process at the LHC with 7 TeV using a fixed scale of $\mu_0 = M_W$. Additional details are given in the caption of Figure 7.46.

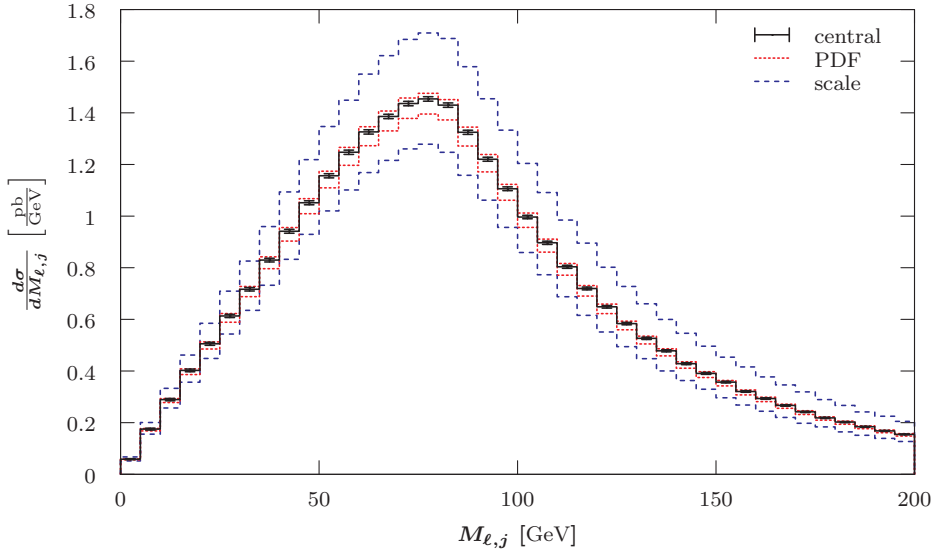

Figure 7.56: LO differential cross-section with respect to the transverse mass of the charged lepton and the jet for the $pp \to (W^- \to \ell^- \overline{\nu}_\ell) + 1\ jet$ process at the LHC with 7 TeV using a fixed scale of $\mu_0 = M_W$. Additional details are given in the caption of Figure 7.39.

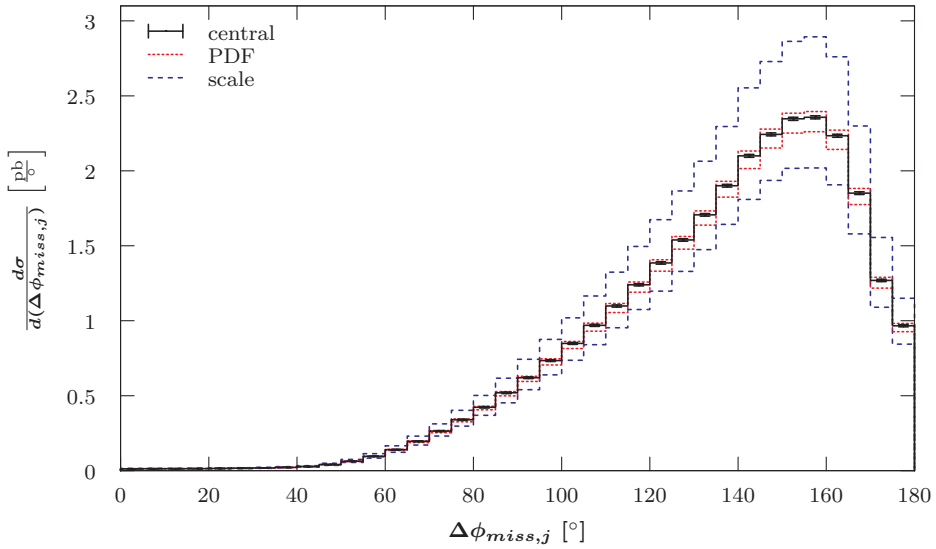

Figure 7.57: LO differential cross-section with respect to the azimuthal angle ϕ between the missing transverse momentum and the jet for the $pp \to (W^- \to \ell^- \overline{\nu}_\ell) + 1\ jet$ process at the LHC with 7 TeV using a fixed scale of $\mu_0 = M_W$. Additional details are given in the caption of Figure 7.39.

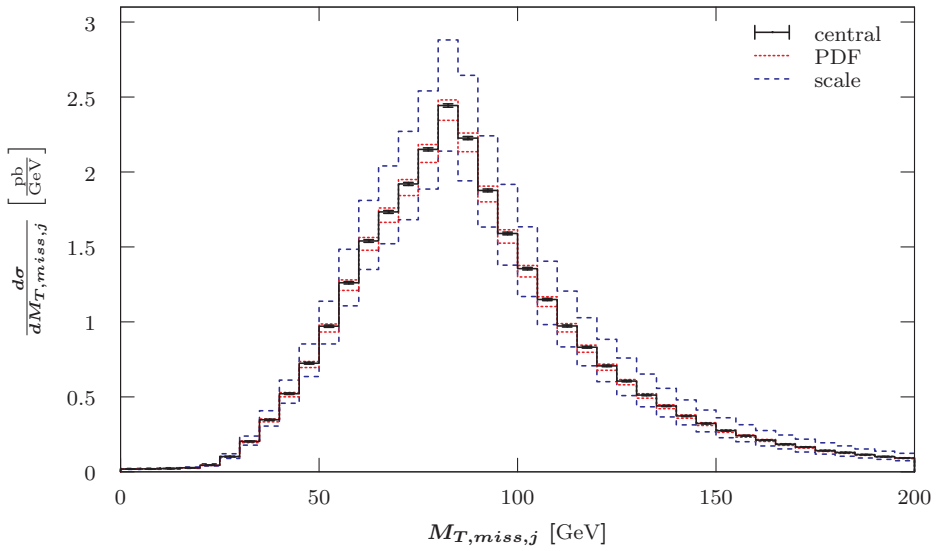

Figure 7.58: LO differential cross-section with respect to the transverse mass between the jet and missing transverse momentum vector for the $pp \to (W^- \to \ell^- \overline{\nu}_\ell) + 1\ jet$ process at the LHC with 7 TeV using a fixed scale of $\mu_0 = M_W$. Additional details are given in the caption of Figure 7.39.

7.4.2.3 $p^{(}\overline{p}^{)} \to (W^- \to \ell^-\overline{\nu}_\ell) + 2$ jets

The 2-jet case gives differential cross-sections which are more continuous than the 1-jet case. Figure 7.59 shows the transverse momentum distribution for the charged lepton and the missing transverse momentum distribution. The curves are very smooth and similar to the W^+ process. The calculated histograms for the two other accelerators and the dynamic scales have the same shapes and are different in their integral according to the total cross-section. Furthermore, the scale uncertainties decrease with the centre-of-mass energy of the collider. They are also smaller for the dynamic scale E_T^W and even more suppressed for $\hat{H}_T$. This behaviour is the same as in the W^+ case.

Figure 7.60 shows the charged lepton rapidity distribution. They are very similar to the distributions for W^- production with one associated jet as well as W^+ production with two associated jets. A larger integral can be observed for the LHC with 14 TeV distribution in Figure 7.62. The distribution is also flatter. The Tevatron histogram is asymmetric as in the 1 jet scenario and flipped in regards to the W^+ process (see Figure 7.61). The distributions for the dynamic scales have smaller scale uncertainties.

As for the previous processes, I will present the azimuthal angles between the charged lepton and the missing transverse momentum vector. Likewise to processes with fewer jets, the collinear emission is strongly suppressed. This can be seen in Figure 7.63. One can see a logarithmic-like increase up to a local maximum around 95° and a small dip before the differential cross-section increases linearly. For the Tevatron the local maximum is at approximately 120°, with a much more linear increase for smaller angles and for the LHC with 14 TeV I obtained a more logarithmic-like increase[38]. In contrast, the histograms for the dynamic scales have a linear rise from zero to 180°, which is only intercepted by a plateau from 90° to 120°.[39]. All these results are similar to the W^+ process. The distribution for the $M_{T,W}$ observable is given in Figure 7.64 The main feature is a sharp peak around 75 GeV to 80 GeV. The magnitude of the various distributions is largest for LHC with 14 TeV and the scale uncertainties are smallest for $\hat{H}_T$. This is similar to what we see for the $\Delta\phi$ histograms.

In Figure 7.65 one can see the dynamic properties of the harder jet. The transverse momentum peaks near 50 GeV (35 GeV for the Tevatron) and exponentially decays towards larger transverse momenta. The rapidity distribution shows that the jet tends to lie within the central region of the detector. Figure 7.66 shows the corresponding results for the softer jet. This jet is likely to have a small transverse momentum (exponential decay towards larger momenta) and likely to be in the central rapidity region. This behaviour is the same for the other two accelerators. For the dynamic scales, the rapidity

[38] See Figures B.41 and B.42 in Appendix B.2.2.3.
[39] See Figures B.43 and B.44 in Appendix B.2.2.3.

distribution is more biased towards the central region[40].

Now, I want to present the same distance observables that I have shown for the W^+ process. The azimuthal angle between the charged lepton and the jets can be found in Figure 7.67. The histograms are identical to what we have already seen, i.e. both jets are most likely to be back-to-back and they both level out towards lower angles. For the harder jet the plateau starts at 20°, for the softer jet at 100°. Deviating from the LHC results, the Tevatron distribution for the harder jet peaks around 150° to 155° and the softer jet is not quite as flat for lower angles[41]. For the dynamic scales the distributions are flatter. The rapidity differences between the charged lepton and the jets are shown in Figure 7.68. It can be seen that both jets tend to be emitted closer to the charged lepton. This holds for all accelerators and scales. The separations between the charged lepton and the jets are given in Figure 7.69. Both distributions increase towards $R = 3$. After that they sharply decline due to $\Delta\phi \leq \pi$. For the harder jet the increase is almost linear, but for the softer jet the increase from zero is more logarithmic. We have already seen this for the W^+ process. The differential cross-sections with respect to the invariant mass of the charged lepton and each of the jets is recorded in Figure 7.70. The shape of these results agrees with the W^+ plots. This means that for the harder jet there is a linear increase towards local maximum around 85 GeV to 90 GeV (70 GeV for the Tevatron) and for the softer jet there is a slightly sharper peak around 70 GeV (55 GeV to 60 GeV for the Tevatron)[42]. The scale uncertainties decrease towards higher centre-of-mass energies. For dynamic scales the shapes and the size of the scale error are almost identical.

The differential cross-section with respect to the azimuthal angle between the missing transverse momentum and the harder as well as the softer jet is shown in Figure 7.71. There is a small probability that the harder jet and the missing momentum vector are collinear, though the probability increases linearly towards back-to-back emission. For the softer jet we have an almost flat distribution with a small dip for smaller angles. Hence, there is little dependence between the emission of the softer jet and the neutrino. The result for the LHC with 14 TeV has a larger magnitude and slightly reduced scale uncertainties. The corresponding results for the Tevatron flatten off towards larger angles[43]. Similarly to previous results, one finds that the scale uncertainties are reduced for dynamic scales. Similar to the W^+ case, I present the transverse mass of the missing transverse momentum vector and each of the jets in Figure 7.72. Again, I obtained a broad peak at 90 GeV. For the softer jet I obtained a peak at 70 GeV which has a more quickly decreasing tail. This histogram also has a secondary maximum at low masses, which has approximately half the magnitude of the main peak. The scale uncertainties

[40] See Figures B.45, B.46, B.47 and B.48 in Appendix B.2.2.3.
[41] See Figure B.49 in Appendix B.2.2.3.
[42] See Figure B.50 in Appendix B.2.2.3.
[43] See Figure B.51 in Appendix B.2.2.3.

are slightly decreased for the LHC with 14 TeV and the dynamic scales. For the Tevatron the peaks are more pronounced and their position is shifted to 70 GeV and 55 GeV, respectively[44].

Lastly, I show the distance observables and the invariant mass for the two jets themselves. The azimuthal angle between the two jets is given in Figure 7.73. The jets are more likely to be separated. There is a small peak at low angles. This feature is more prominent for the Tevatron[45]. The shapes are the same for all accelerators and dynamic scales. The difference in rapidity of the two jets is shown in Figure 7.74. There is a local maximum at $\Delta y = 0.5$ and linear decrease for larger separations. The same qualitative result has been obtained for the LHC with 14 TeV and the Tevatron[46], as well as for the dynamic scales. Magnitudes and uncertainties behave as in previous distributions. The separation R between the jets is given in Figure 7.75. There is a peak just above $R = 3$ suggesting a back-to-back emission of the two jets. I found the same shape for the LHC with 14 TeV and the dynamic scales. For the Tevatron, however, there is a secondary maximum for small separations, which has half the magnitude of the main peak[47]. Figure 7.76 shows the invariant mass distribution of the two jets, which has a broad peak around 100 GeV. For the Tevatron the peak is at 55 GeV to 60 GeV.[48] Both shapes are the same as for the W^+ case.

[44] See Figure B.52 in Appendix B.2.2.3.
[45] See Figure B.53 in Appendix B.2.2.3.
[46] See Figure B.54 in Appendix B.2.2.3.
[47] See Figure B.55 in Appendix B.2.2.3.
[48] See Figure B.56 in Appendix B.2.2.3.

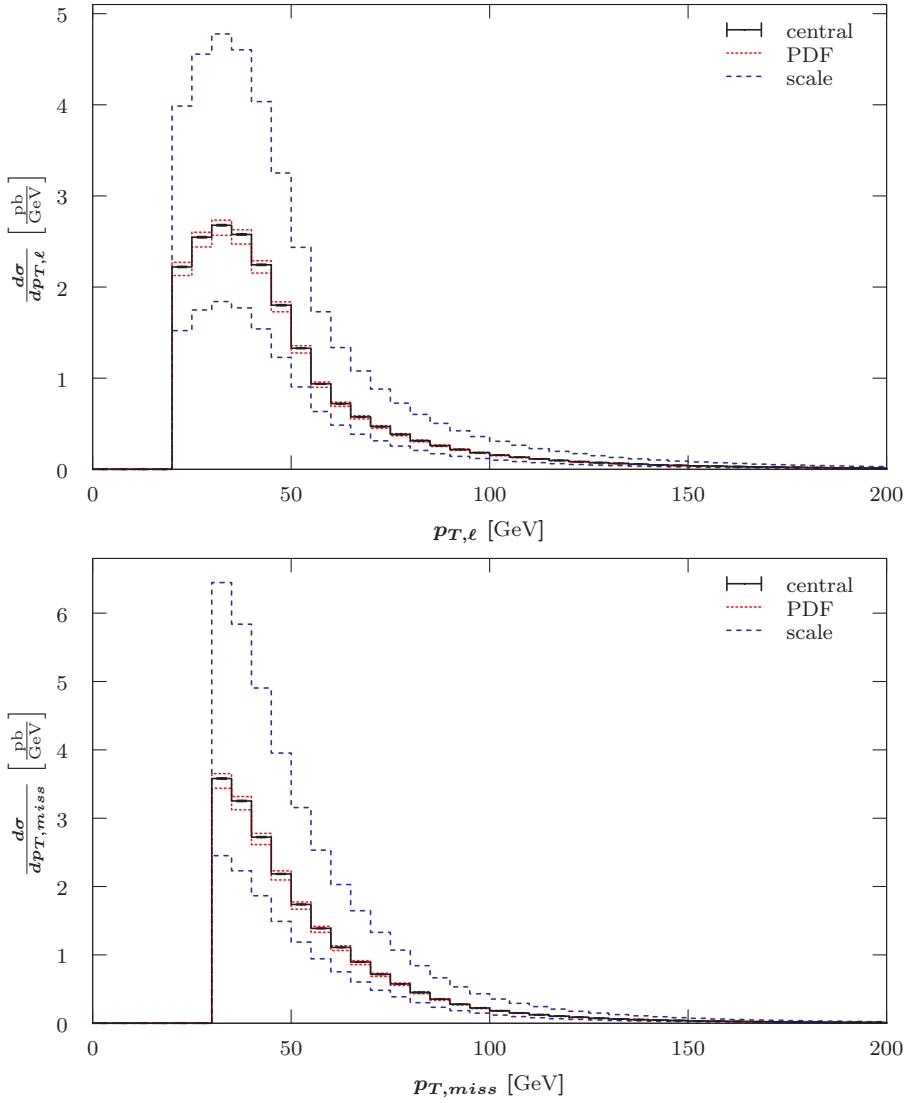

Figure 7.59: LO differential cross-section with respect to the charged lepton (top) and the missing (bottom) transverse momentum for the $pp \to (W^- \to \ell^- \overline{\nu}_\ell) + 2\ jets$ process at the LHC with 7 TeV using a fixed scale of $\mu_0 = M_W$. Additional details are given in the caption of Figure 7.39.

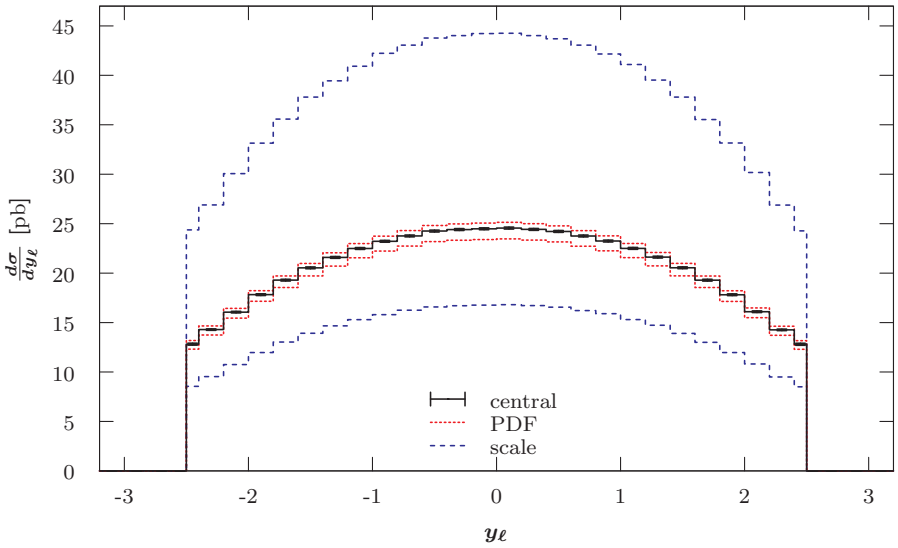

Figure 7.60: LO differential cross-section with respect to the charged lepton rapidity for the $pp \to (W^- \to \ell^- \overline{\nu}_\ell) + 2\ jets$ process at the LHC with 7 TeV using a fixed scale of $\mu_0 = M_W$. The first and last filled bin are half-width due to the applied selection cut, $|y_\ell| < 2.5$. Additional details are given in the caption of Figure 7.39.

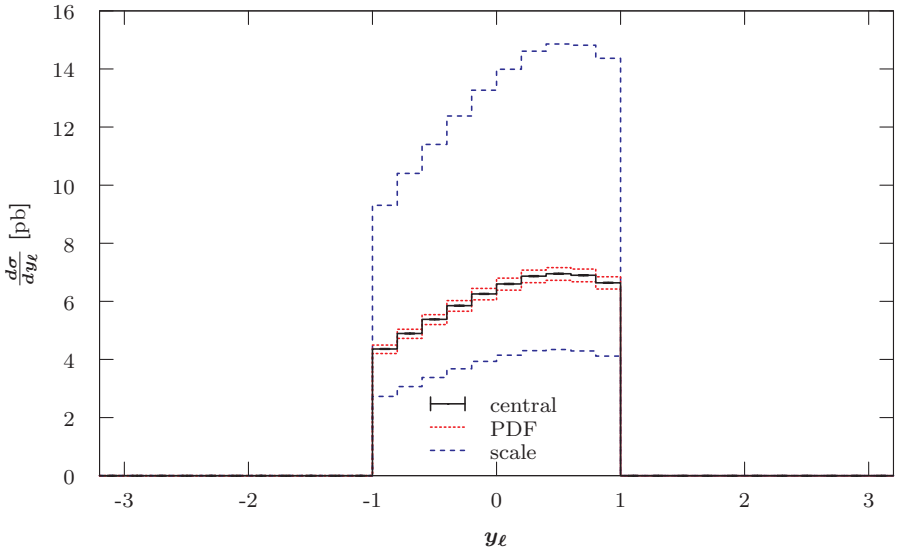

Figure 7.61: LO differential cross-section with respect to the charged lepton rapidity for the $p\overline{p} \to (W^- \to \ell^- \overline{\nu}_\ell) + 2\ jets$ process at the Tevatron Run II using a fixed scale of $\mu_0 = M_W$. Additional details are given in the caption of Figure 7.39.

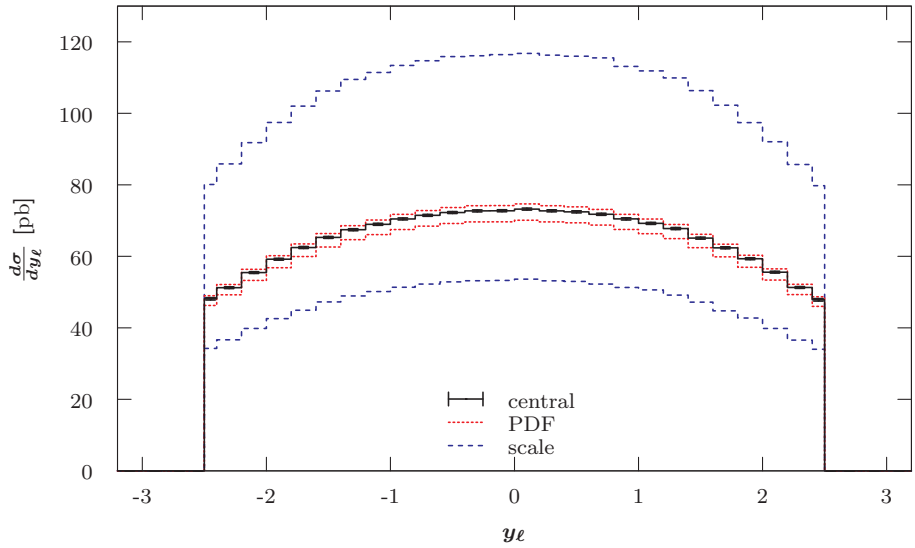

Figure 7.62: LO differential cross-section with respect to the charged lepton rapidity for the $pp \to (W^- \to \ell^- \overline{\nu}_\ell) + 2\ jets$ process at the LHC with 14 TeV using a fixed scale of $\mu_0 = M_W$. The first and last filled bin are half-width due to the applied selection cut, $|y_\ell| < 2.5$. Additional details are given in the caption of Figure 7.39.

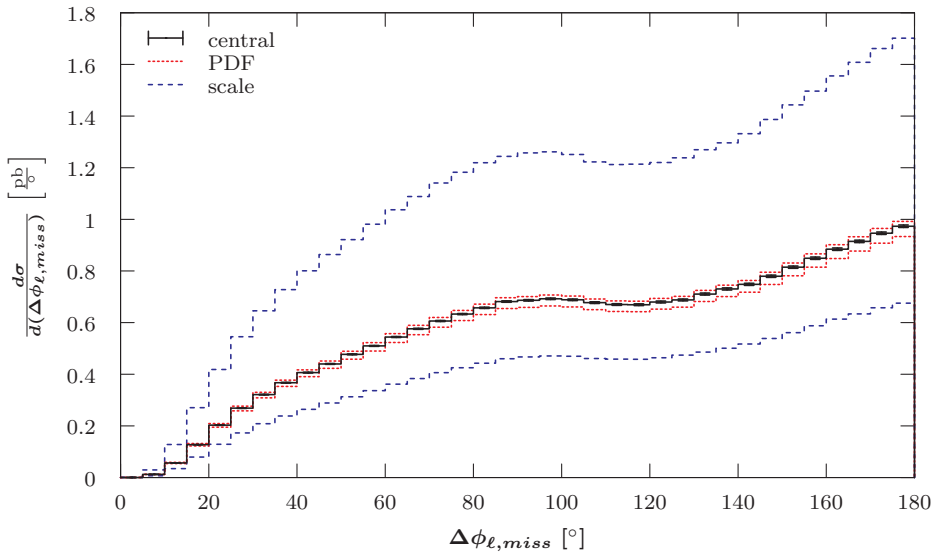

Figure 7.63: LO differential cross-section with respect to the azimuthal angle ϕ between the charged lepton and the missing transverse momentum for the $pp \to (W^- \to \ell^- \overline{\nu}_\ell) + 2\ jets$ process at the LHC with 7 TeV using a fixed scale of $\mu_0 = M_W$. Additional details are given in the caption of Figure 7.39.

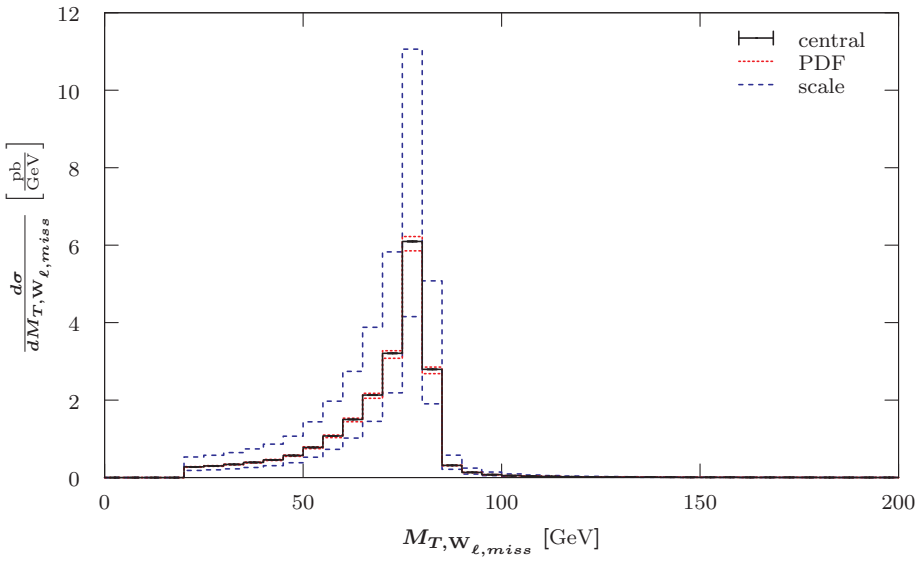

Figure 7.64: LO differential cross-section with respect to transverse mass $M_{T,\mathrm{W}}$ for the $\mathrm{pp} \to (\mathrm{W}^- \to \ell^- \overline{\nu}_\ell)$+2 *jets* process at the LHC with 7 TeV using a fixed scale of $\mu_0 = M_{\mathrm{W}}$. Additional details are given in the caption of Figure 7.39.

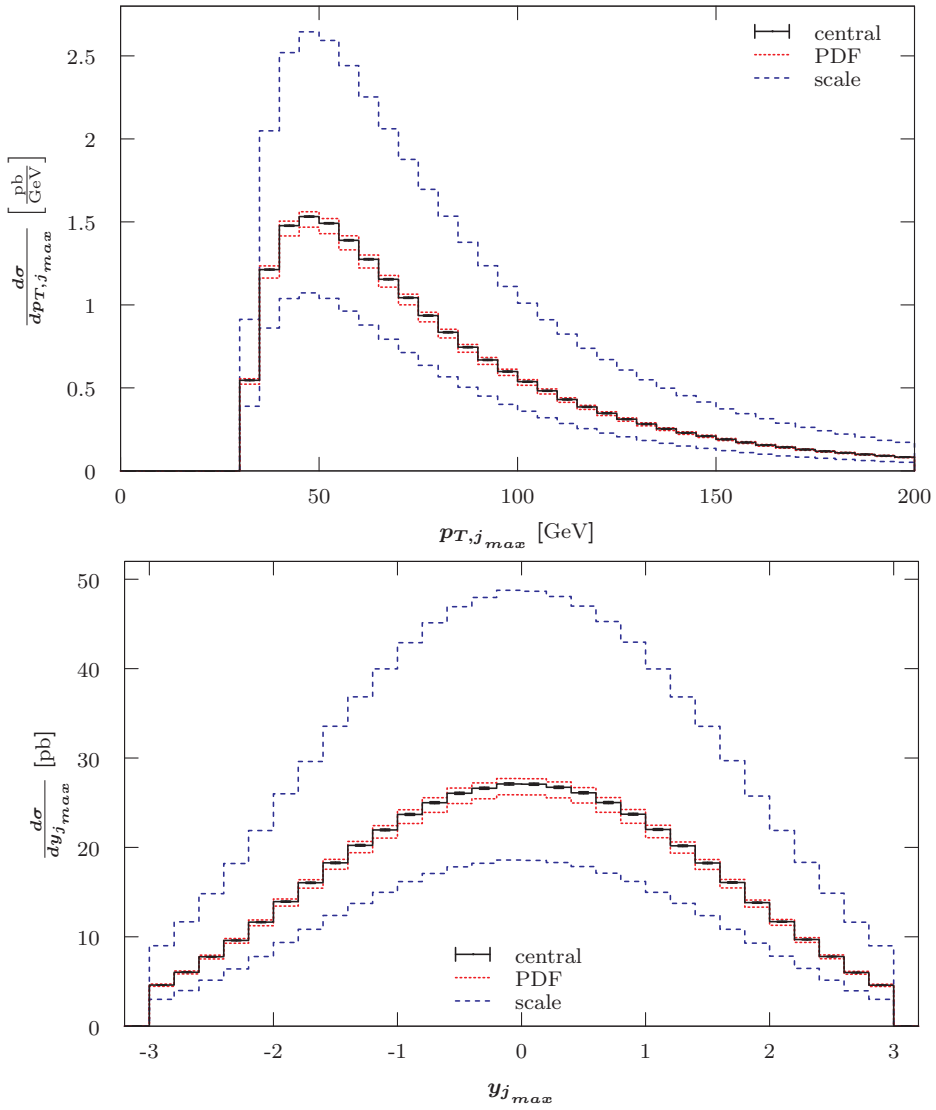

Figure 7.65: LO differential cross-section with respect to the transverse momentum (top) and the rapidity (bottom) of the harder jet j_{max} for the $pp \to (W^- \to \ell^- \overline{\nu}_\ell) + 2\ jets$ process at the LHC with 7 TeV using a fixed scale of $\mu_0 = M_W$. Additional details are given in the caption of Figure 7.39.

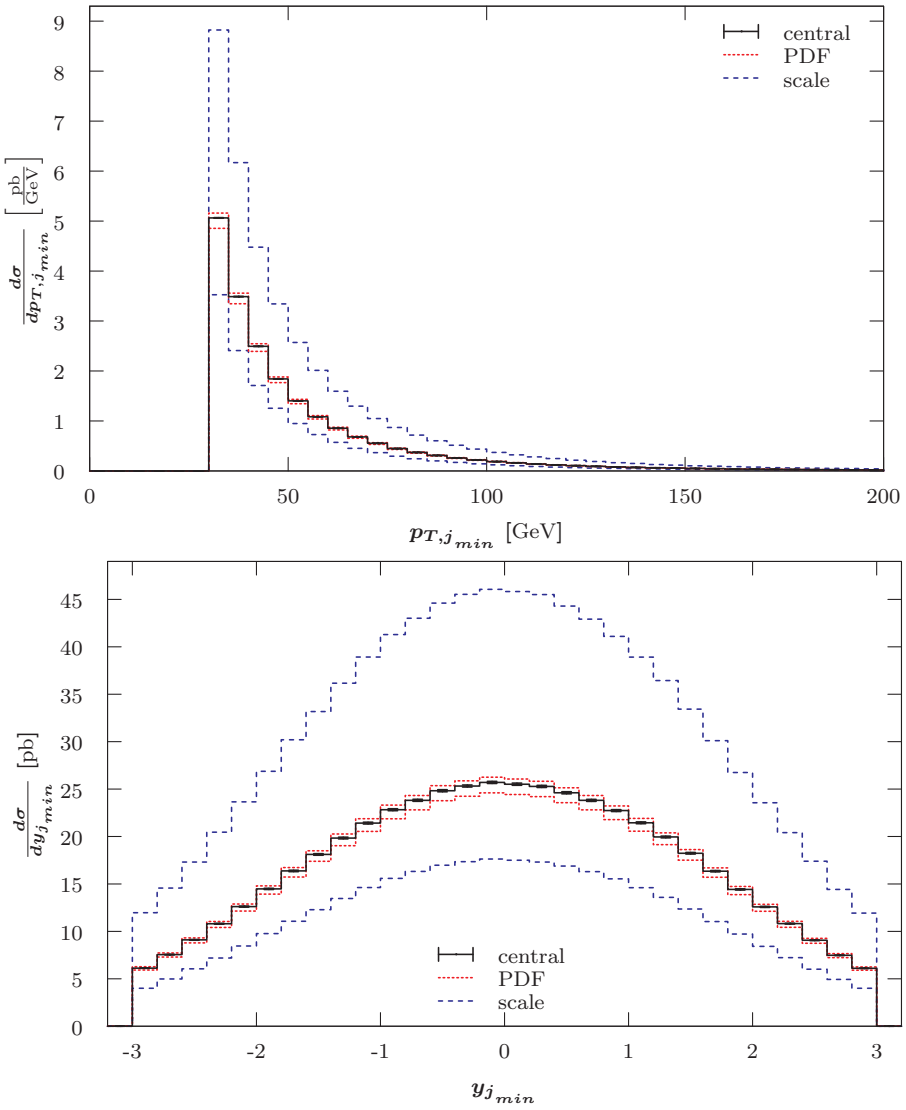

Figure 7.66: LO differential cross-section with respect to the transverse momentum (top) and the rapidity (bottom) of the softer jet j_{min} for the $pp \to (W^- \to \ell^- \overline{\nu}_\ell) + 2\ jets$ process at the LHC with 7 TeV using a fixed scale of $\mu_0 = M_W$. Additional details are given in the caption of Figure 7.39.

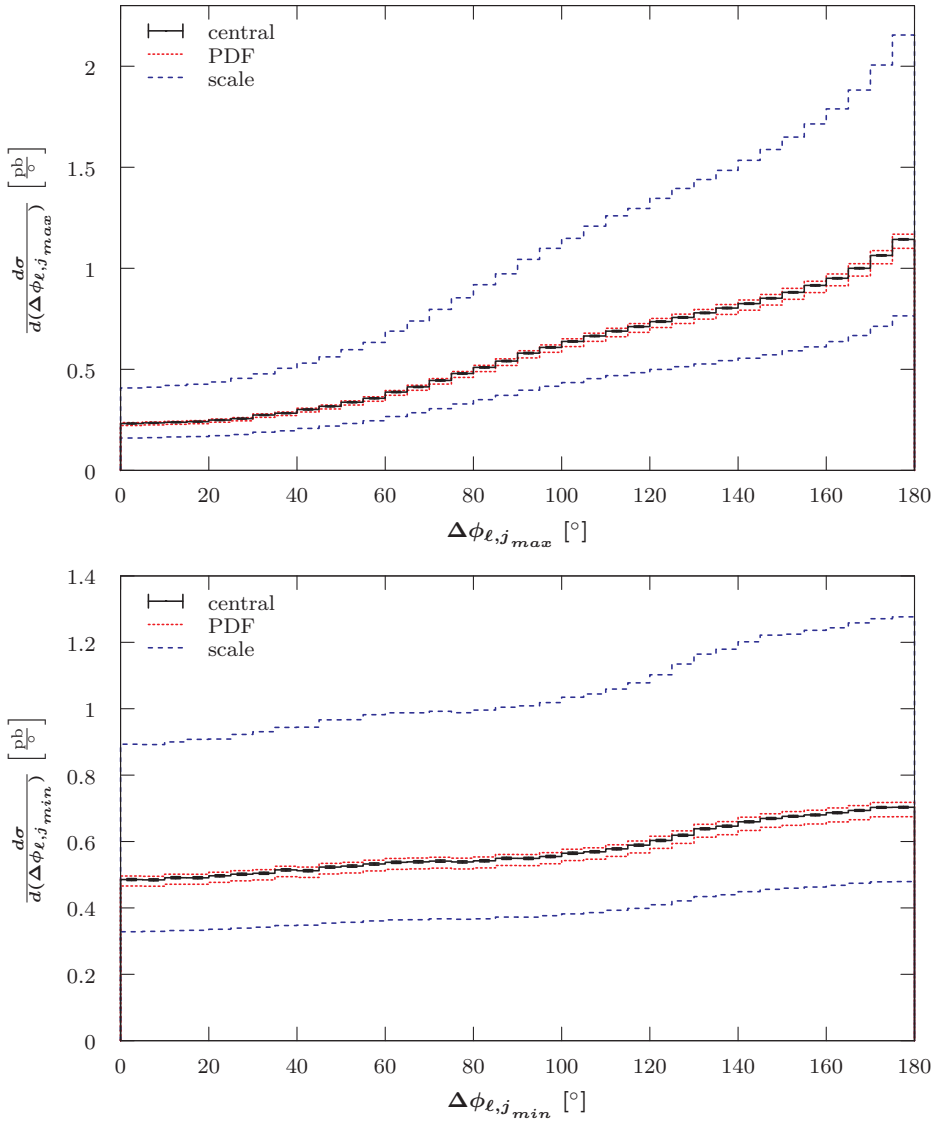

Figure 7.67: LO differential cross-section with respect to the azimuthal angle ϕ between the charged lepton and the harder (top) as well as the softer (bottom) jet for the pp $\to$ ($\text{W}^- \to \ell^-\overline{\nu}_\ell$) + 2 *jets* process at the LHC with 7 TeV using a fixed scale of $\mu_0 = M_\text{W}$. Additional details are given in the caption of Figure 7.39.

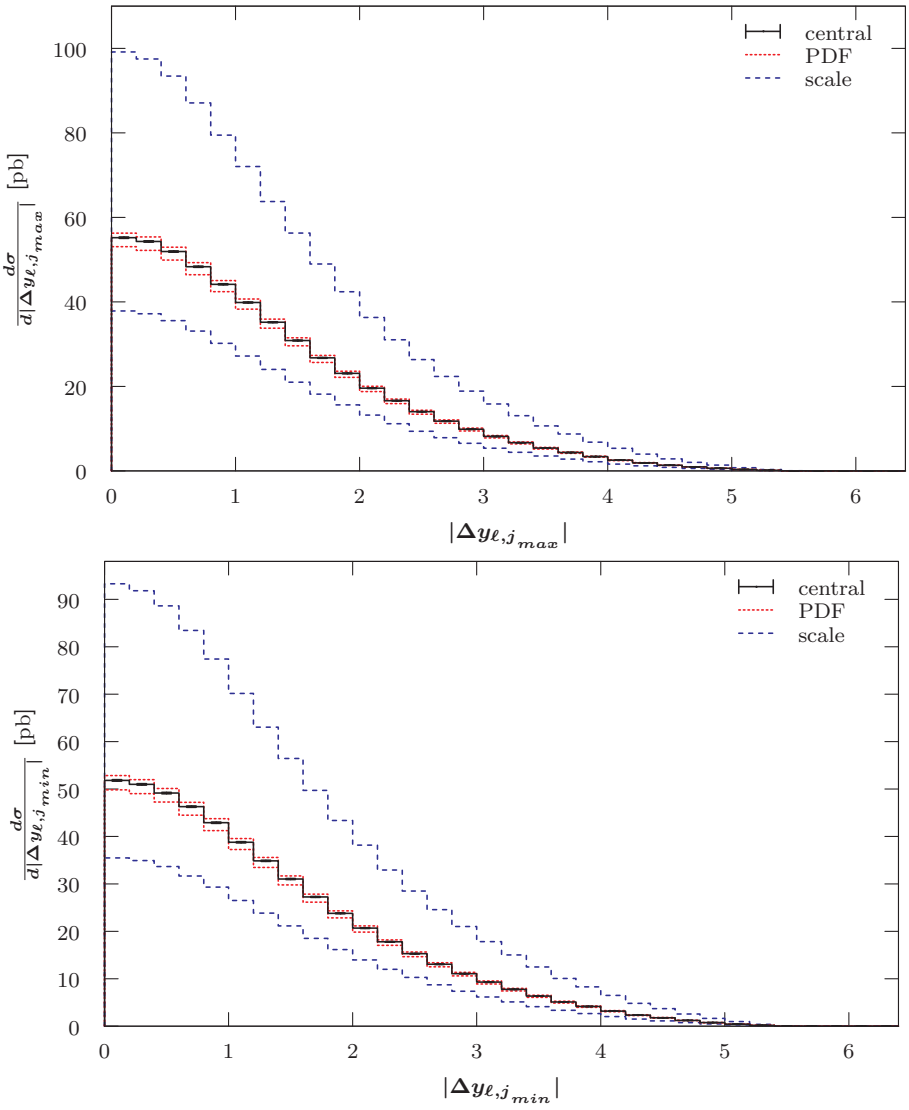

Figure 7.68: LO differential cross-section with respect to the difference in rapidity between the charged lepton and the harder (top) as well as softer (bottom) jet for the $pp \to (W^- \to \ell^- \overline{\nu}_\ell) + 2\ jets$ process at the LHC with 7 TeV using a fixed scale of $\mu_0 = M_W$. Additional details are given in the caption of Figure 7.46.

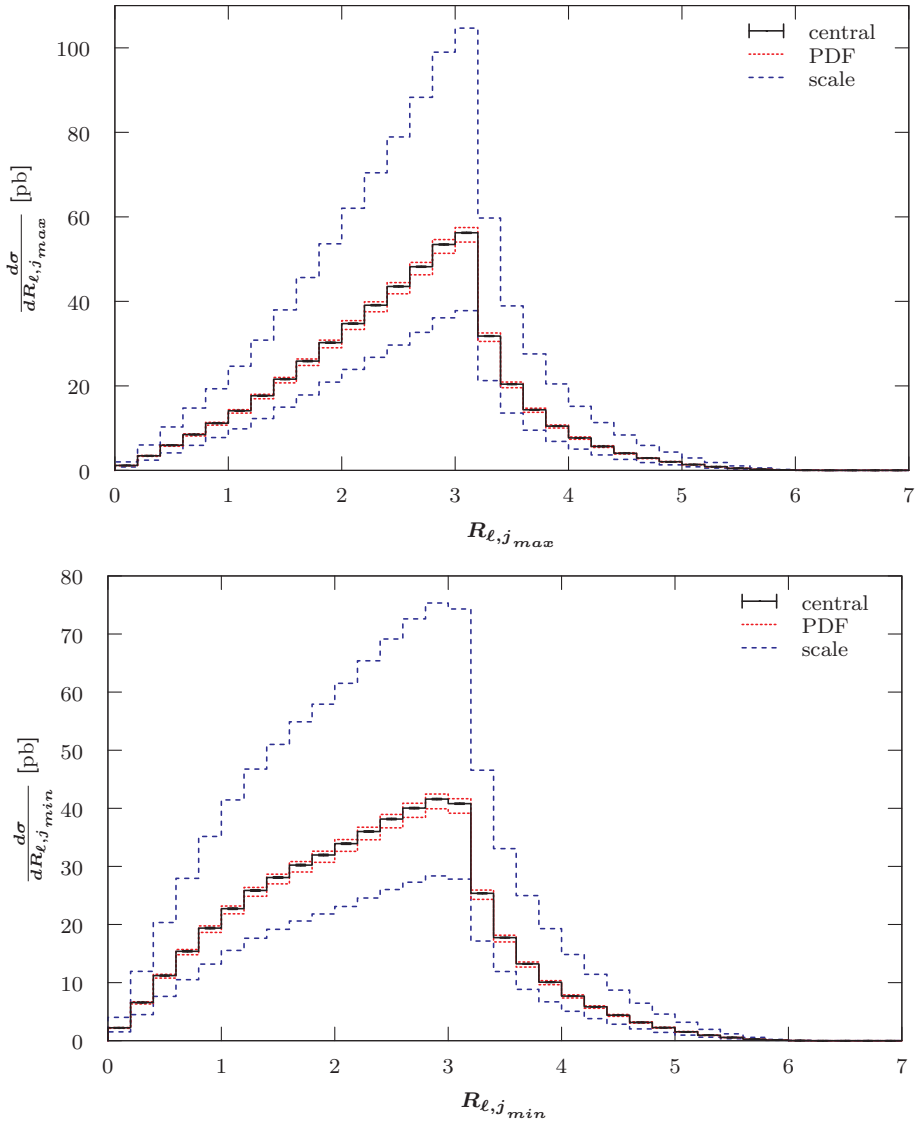

Figure 7.69: LO differential cross-section with respect to the separation between the charged lepton and the harder (top) as well as softer (bottom) jet for the $pp \to (W^- \to \ell^- \overline{\nu}_\ell) + 2\ jets$ process at the LHC with 7 TeV using a fixed scale of $\mu_0 = M_W$. Additional details are given in the caption of Figure 7.46.

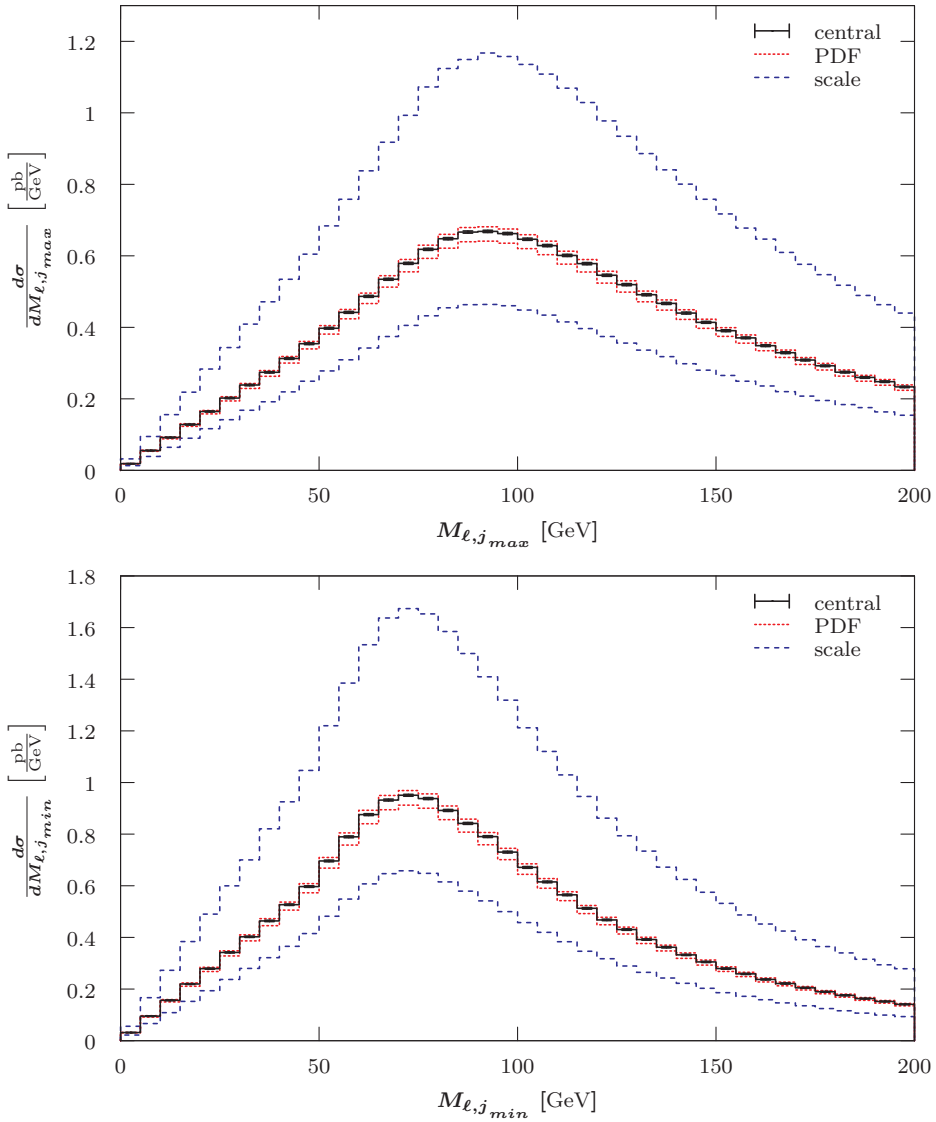

Figure 7.70: LO differential cross-section with respect to the invariant mass of the charged lepton and the harder (top) as well as softer (bottom) jet for the $pp \to (W^- \to \ell^- \overline{\nu}_\ell) + 2\ jets$ process at the LHC with 7 TeV using a fixed scale of $\mu_0 = M_W$. Additional details are given in the caption of Figure 7.46.

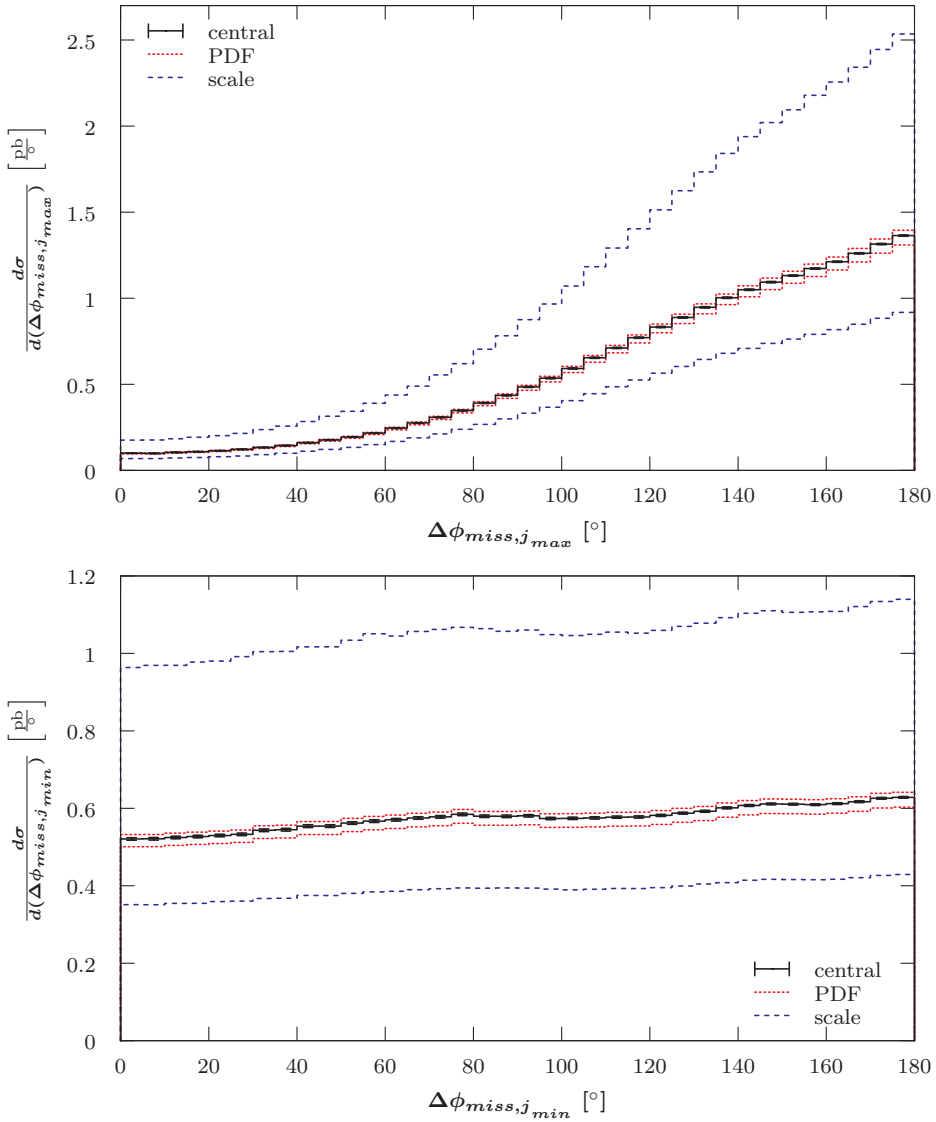

Figure 7.71: LO differential cross-section with respect to the azimuthal angle ϕ between the missing transverse momentum and the harder (top) as well as softer (bottom) jet for the $pp \to (W^- \to \ell^- \overline{\nu}_\ell)+2\,jets$ process at the LHC with 7 TeV using a fixed scale of $\mu_0 = M_W$. Additional details are given in the caption of Figure 7.39.

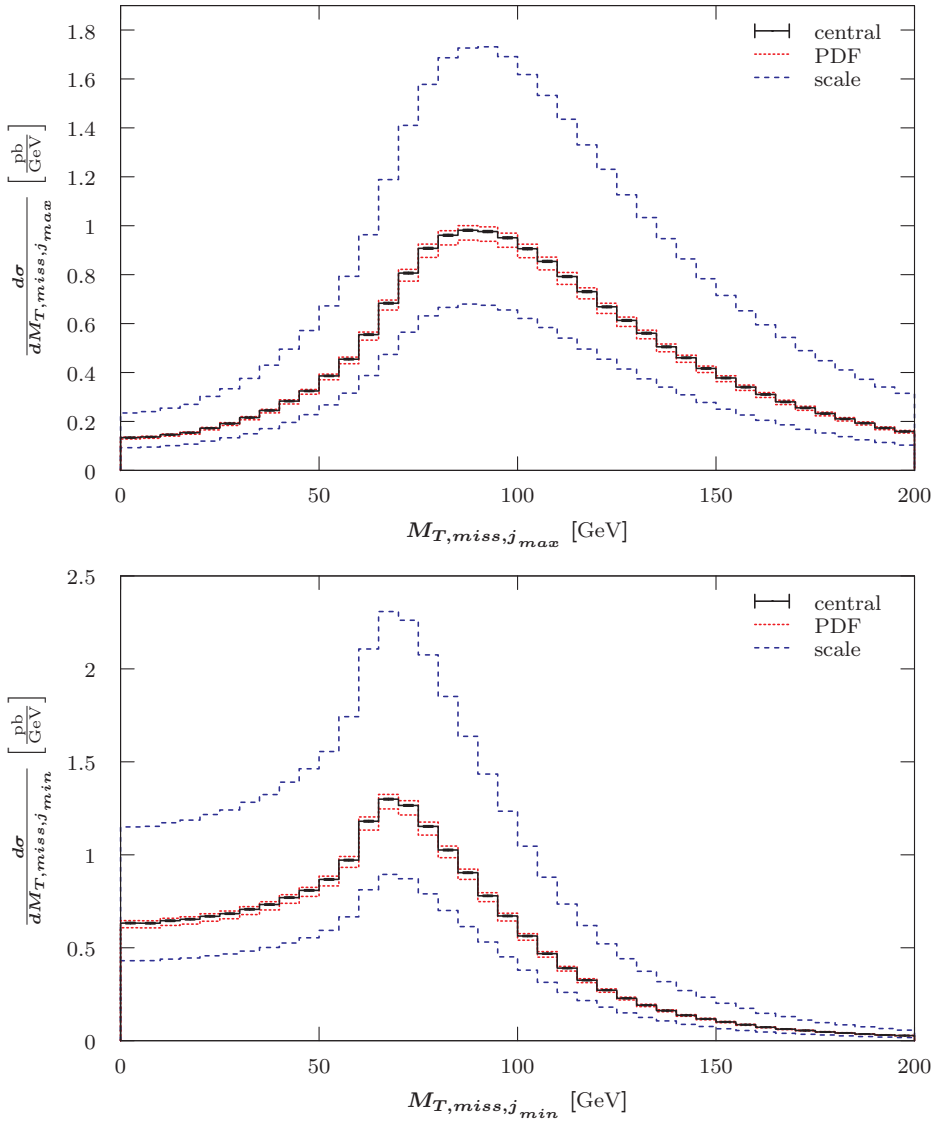

Figure 7.72: LO differential cross-section with respect to the transverse mass of the missing transverse momentum vector and the harder (top) as well as softer (bottom) jet for the $pp \to (W^- \to \ell^- \overline{\nu}_\ell)+2\,jets$ process at the LHC with 7 TeV using a fixed scale of $\mu_0 = M_W$. Additional details are given in the caption of Figure 7.39.

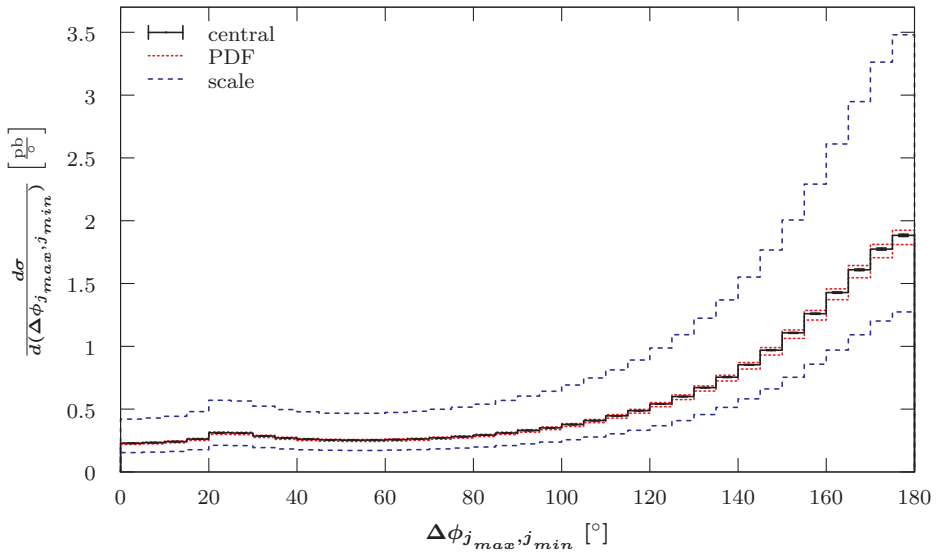

Figure 7.73: LO differential cross-section with respect to the azimuthal angle ϕ between the harder j_{max} and the softer jet j_{min} for the pp $\to$ ($\text{W}^- \to \ell^- \overline{\nu}_\ell$)+2 $jets$ process at the LHC with 7 TeV using a fixed scale of $\mu_0 = M_\text{Z}$. Additional details are given in the caption of Figure 7.39.

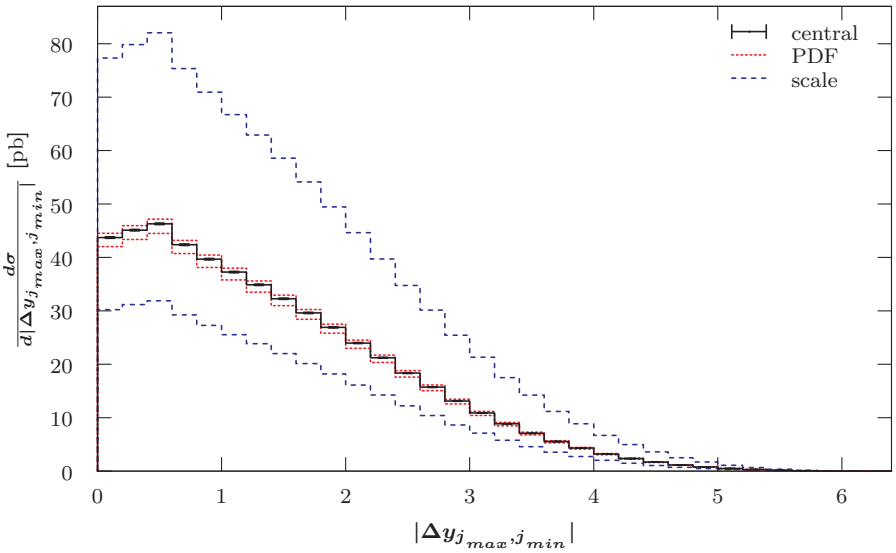

Figure 7.74: LO differential cross-section with respect to the difference in rapidity between the harder j_{max} and the softer jet j_{min} for the pp $\to$ ($\text{W}^- \to \ell^- \overline{\nu}_\ell$)+2 $jets$ process at the LHC with 7 TeV using a fixed scale of $\mu_0 = M_\text{Z}$. Additional details are given in the caption of Figure 7.39.

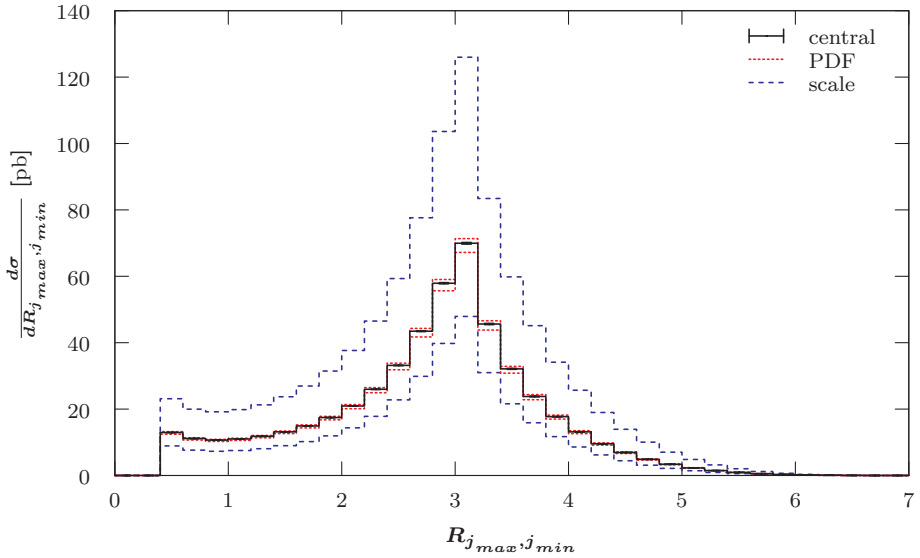

Figure 7.75: LO differential cross-section with respect to separation between the harder j_{max} and the softer j_{min} jet for the pp $\to (\mathrm{W}^- \to \ell^- \overline{\nu}_\ell) + 2\ jets$ process at the LHC with 7 TeV using a fixed scale of $\mu_0 = M_\mathrm{Z}$. Additional details are given in the caption of Figure 7.39.

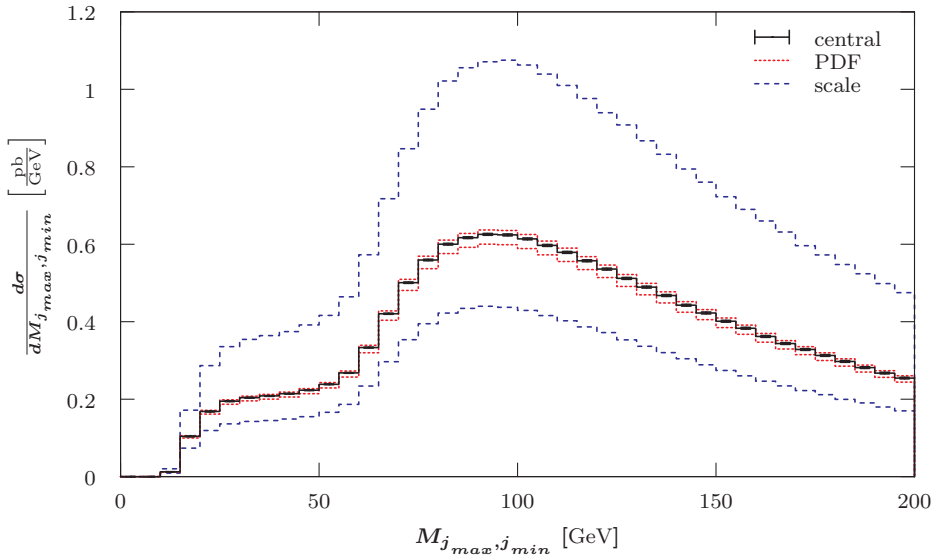

Figure 7.76: LO differential cross-section with respect to the invariant mass of the harder j_{max} and the softer j_{min} jet for the pp $\to (\mathrm{W}^- \to \ell^- \overline{\nu}_\ell) + 2\ jets$ process at the LHC with 7 TeV using a fixed scale of $\mu_0 = M_\mathrm{Z}$. Additional details are given in the caption of Figure 7.39.

7.4.3 $\mathrm{p}^{(}\overline{\mathrm{p}}^{)} \to (\mathrm{Z} \to \ell^-\ell^+) + n$ jets

For Z production with decay into two charged leptons there is a very large number of observables, because all the final state particles are detectable.

7.4.3.1 $\mathrm{p}^{(}\overline{\mathrm{p}}^{)} \to (\mathrm{Z} \to \ell^-\ell^+)$

Figure 7.77 shows the differential cross-section with respect to the transverse momentum for the harder (max) and the softer (min) charged lepton, respectively. They are identical, as one would expect, because there are only two final state particles[49]. The results for the other accelerators scale accordingly to the integrated cross-sections. The dynamic scales give the same results as no jets are involved[50]. At the two other accelerators magnitudes are as one would expect from the integrated cross-sections[51].

Figure 7.78 shows the differential cross-section with respect to rapidity for the two charged leptons. As expected, they are also identical and one can observe that the emission of the charged leptons happens mainly in the centre of the detector. These distributions are almost identical for the dynamic scales. For the LHC with 14 TeV the magnitude and the uncertainties are larger[52]. Figure 7.79 shows the rapidity distributions of the two charged leptons at the Tevatron. In stark contrast to the expectation, these distributions are forward/backward asymmetric. This is a glitch in the calculation originating in the $\mathrm{p}\overline{\mathrm{p}}$ asymmetry of the Tevatron. The two charged leptons always have the same momentum, but they are ordered by charge. In reality one would expect the distributions to be the same, i.e. the average of the two shown.

There are a couple of distance observables we can look at. Firstly, the difference in rapidity for the two charged leptons is shown in Figure 7.80. One can see that the two charged leptons tend to have a similar rapidity. Furthermore, we know that the two charged leptons are emitted back-to-back on the transverse plane[53]. This is true for all accelerators and scales. The result for LHC with 14 TeV has a larger integral and larger errors, and the Tevatron has a smaller integral and scale uncertainties[54]. The dynamic scales give almost identical result. The separation R between the two charged leptons is recorded in Figure 7.81. The offset at $R = 3$ is due to the back-to-back emission in the transverse plane and the smearing out towards larger R is due to different rapidities. For the Tevatron the distribution is less smeared out due to a smaller rapidity coverage of the Tevatron detectors and has a smaller integral as well as scale uncertainties[55]. The

[49] All ℓ_{max} and ℓ_{min} should be identical for zero associated jets.
[50] See Figure B.58 in Appendix B.2.3.1.
[51] See Figure B.57 in Appendix B.2.3.1.
[52] See Figure B.59 in Appendix B.2.3.1.
[53] See Figure B.61 in Appendix B.2.3.1.
[54] See Figures B.62 and B.60 in Appendix B.2.3.1.
[55] See Figure B.63 in Appendix B.2.3.1.

LHC with 14 TeV yields a larger integral and bigger scale uncertainties[56]. Finally, we can look at the invariant mass of the two charged leptons in Figure 7.82. A peak can be observed at the mass of the Z boson. Again he LHC with 14 TeV has a larger integral and larger scale uncertainties[57]. The histogram for the Tevatron has a smaller integral and scale uncertainties, which are smaller than the PDF uncertainties[58].

[56]See Figure B.64 in Appendix B.2.3.1.
[57]See Figure B.66 in Appendix B.2.3.1.
[58]See Figure B.65 in Appendix B.2.3.1.

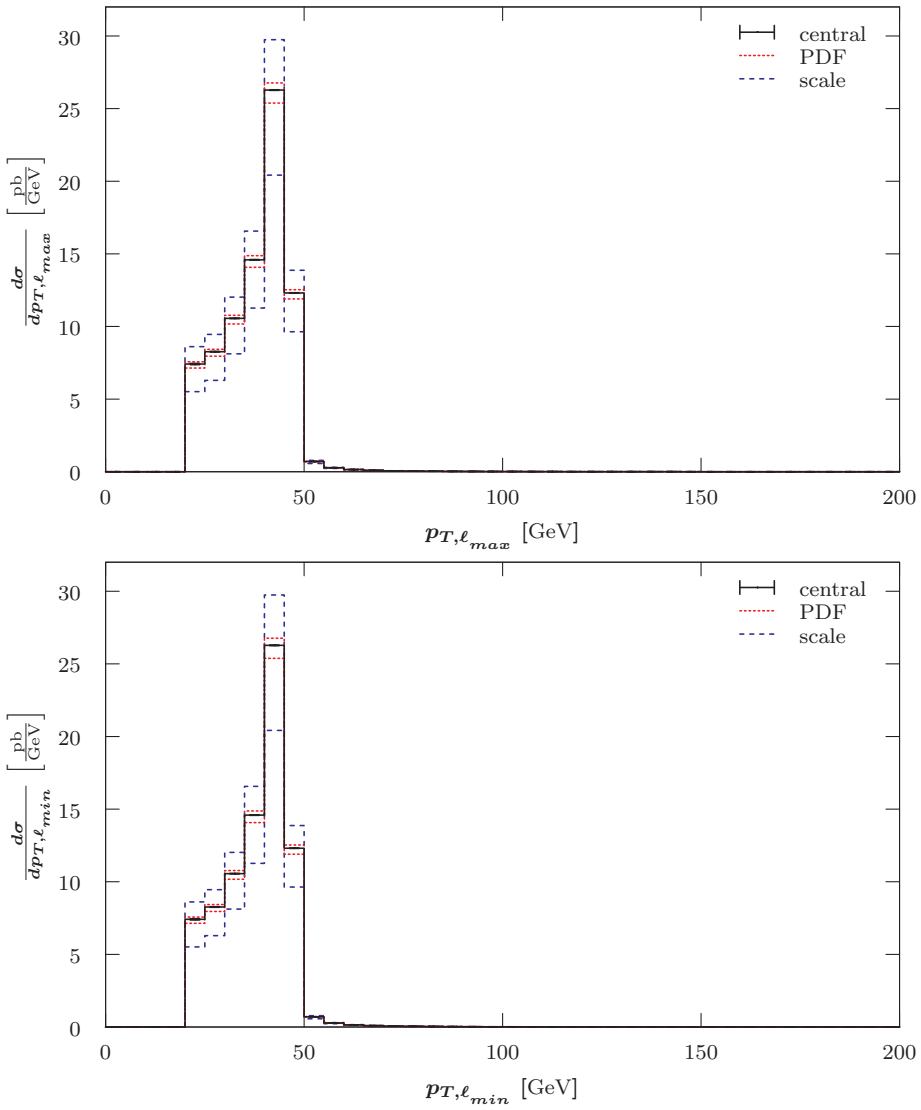

Figure 7.77: LO differential cross-section with respect to the harder ℓ_{max} (top) and the softer ℓ_{min} (bottom) charged lepton transverse momentum for the pp $\rightarrow$ (Z $\rightarrow \ell^-\ell^+$) process at the LHC with $\sqrt{s} = 7\,\text{TeV}$ using a fixed scale of $\mu_0 = M_\text{Z}$ and MSTW2008LO (90% C.L.) PDFs. Selection cuts as given in Equations 7.5 to 7.8 have been applied. MCFM input parameters are listed in Equations 7.1 to 7.3. The procedure used to choose the number of shots is described in Section 4.4.3. The scale uncertainties have been estimated using a conservative variation by a factor of 4. The error bars for the statistical uncertainties are mostly too small to be visible or are only partially visible. Only the asymmetric deviations for the PDFs (red, dotted) and scale (blue, dashed) from the central value (black, solid) are given.

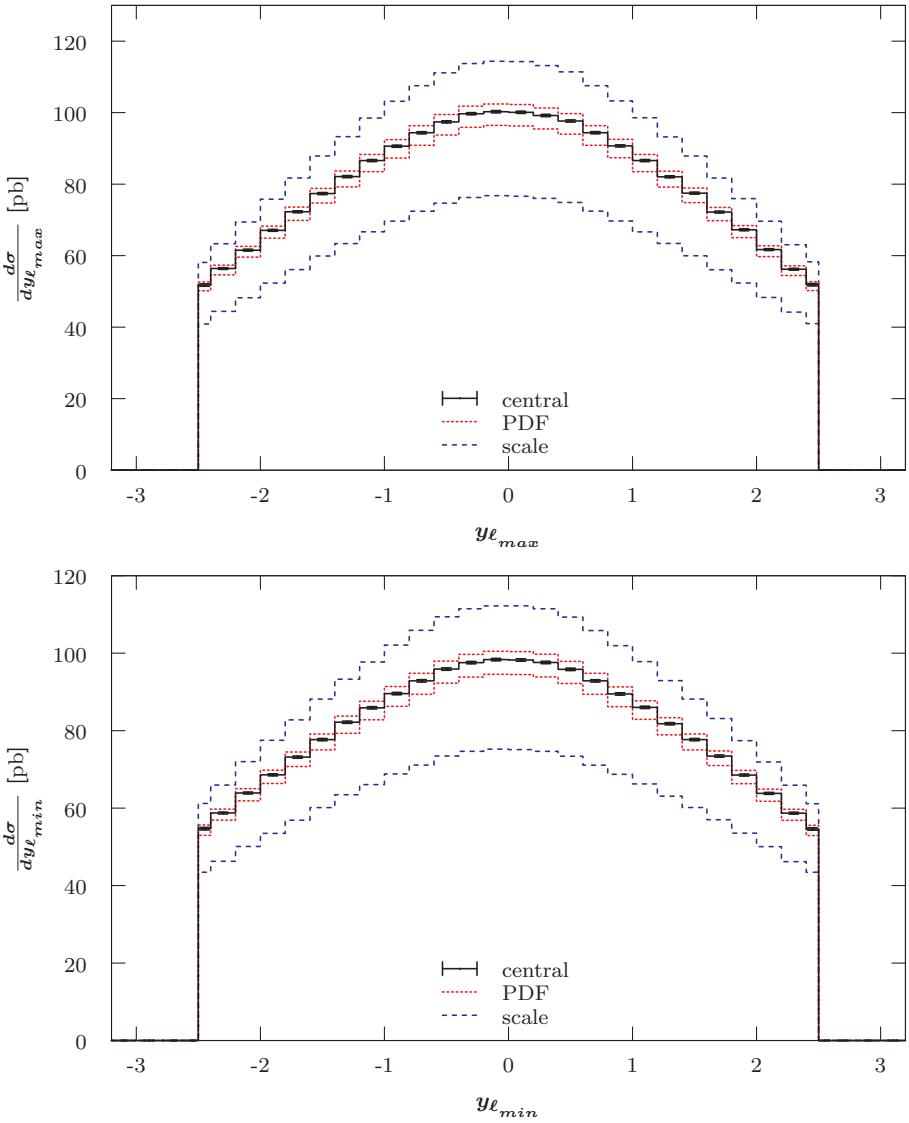

Figure 7.78: LO differential cross-section with respect to the rapidity of the harder ℓ_{max} (top) and the softer ℓ_{min} (bottom) charged lepton for the pp $\to$ (Z $\to \ell^-\ell^+$) process at the LHC with 7 TeV using a fixed scale of $\mu_0 = M_{\mathrm{Z}}$. The first and last filled bin are half-width due to the applied selection cut, $|y_\ell| < 2.5$. Additional details are given in the caption of Figure 7.77.

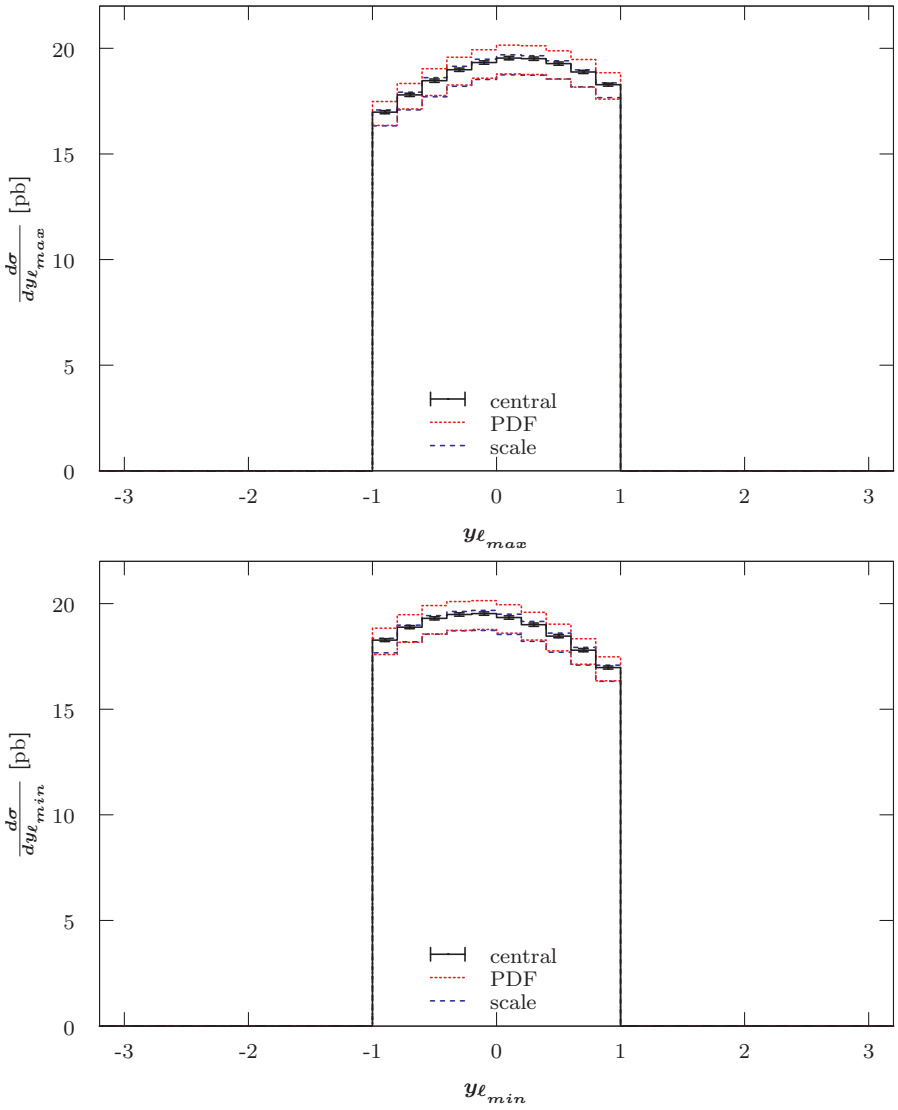

Figure 7.79: LO differential cross-section with respect to the rapidity of the harder ℓ_{max} (top) and the softer ℓ_{min} (bottom) charged lepton for the $p\overline{p} \to (Z \to \ell^-\ell^+)$ process at the Tevatron Run II using a fixed scale of $\mu_0 = M_Z$. A glitch in the calculation which makes these two distributions non-identical is explained in the main text. Additional details are given in the caption of Figure 7.77.

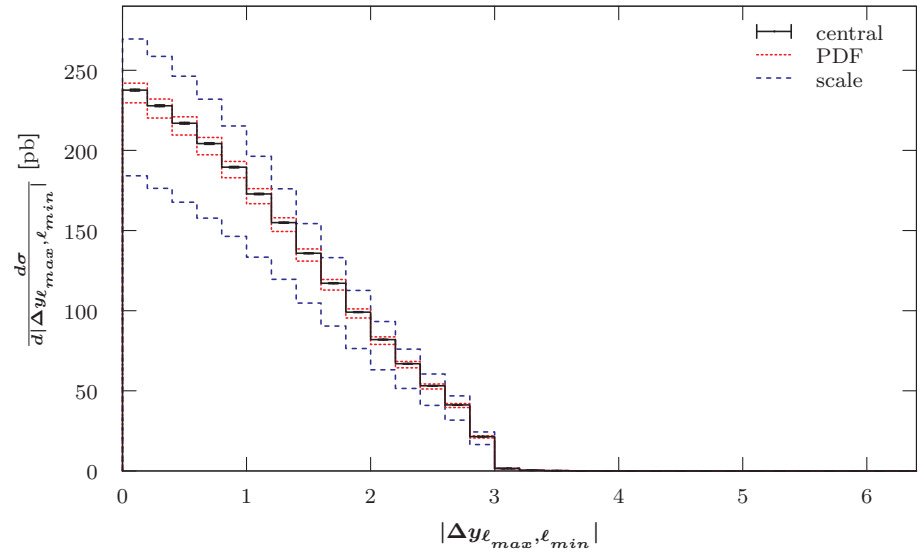

Figure 7.80: LO differential cross-section with respect to the difference in rapidity between the harder ℓ_{max} and the softer ℓ_{min} charged lepton for the pp $\to$ (Z $\to \ell^-\ell^+$) process at the LHC with 7 TeV using a fixed scale of $\mu_0 = M_{\mathrm{Z}}$. Additional details are given in the caption of Figure 7.77.

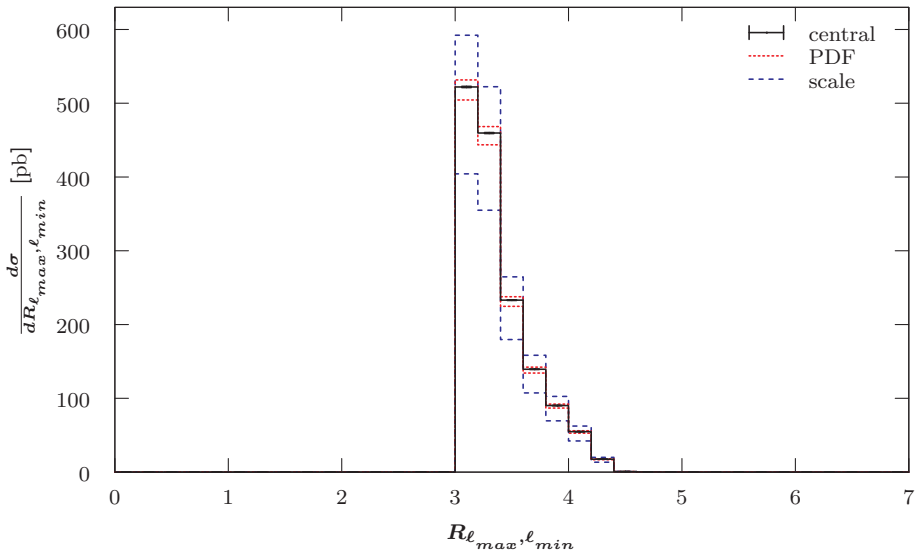

Figure 7.81: LO differential cross-section with respect to distance R between the harder ℓ_{max} and the softer ℓ_{min} charged lepton for the pp $\to$ (Z $\to \ell^-\ell^+$) process at the LHC with 7 TeV using a fixed scale of $\mu_0 = M_{\mathrm{Z}}$. Additional details are given in the caption of Figure 7.77.

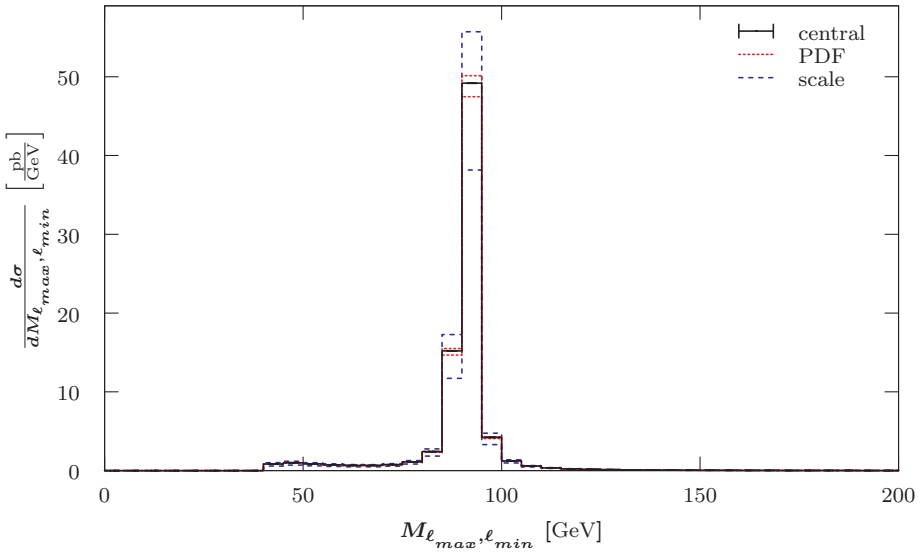

Figure 7.82: LO differential cross-section with to the invariant mass of the two charged leptons for the pp $\to$ (Z $\to \ell^-\ell^+$) process at the LHC with 7 TeV using a fixed scale of $\mu_0 = M_{\text{Z}}$. Additional details are given in the caption of Figure 7.77.

7.4.3.2 $p^{(}\overline{p}^{)} \to (Z \to \ell^-\ell^+) + 1$ jet

For the one jet process the differential cross-section with respect to the transverse momentum for the two charged leptons varies, as final state radiation causes the charged leptons to not be back-to-back. The histograms can be seen in Figure 7.83. At the Tevatron there are larger scale uncertainties and the shapes are slightly different as given in Figure 7.84. The LHC with 14 TeV has the same shape, greater total cross-section and smaller relative scale uncertainties[59]. The dynamic scales produce the same results[60].

Histograms obtained for the rapidity distribution of the harder and the softer charged lepton are shown in Figure 7.85. The charged leptons tend to be emitted in the central region of the detector. The same shapes, but with a smaller integral, are also obtained using dynamic scales. For the LHC with 14 TeV the overall cross-section is larger and the scale uncertainties are smaller, and for the Tevatron results are similar to the LHC with 7 TeV, though the rapidity coverage is much smaller and so is the integral[61]. The correlations between centre-of-mass energy and the size of the scale uncertainties can be seen more clearly in $\Delta\phi_{\ell_{max},\ell_{min}}$ histograms.

The difference in the rapidity of the two charged leptons is shown in Figure 7.86. One can see that the two charged leptons tend to lie close together. The distribution for the Tevatron is similar apart from spanning a smaller range due to tighter rapidity cuts[62] The scale uncertainties decrease with the centre-of-mass energy and are only twice the size of the PDF uncertainties for the LHC with 14 TeV. The separation in azimuthal angle between the two charged leptons is given in Figure 7.87. One can see that the charged leptons tend to be emitted further apart with a maximum at 135° to 140°. For the Tevatron the maximum is at 150° to 155°. Again, I found that the scale uncertainties are massively decreased for the LHC with 14 TeV, but the dynamical scales give only a very small improvement.[63] The last distance observable for the two charged leptons is the separation R as shown in Figure 7.88. The histogram peaks at $2.2-2.4$, which means that the charged leptons are not fully back-to-back. The results for the other accelerators have the same shape and the magnitudes and scale uncertainties vary as described above.[64] A very important observable for processes with two oppositely charged leptons is the invariant mass of the two charged leptons. This histogram is shown in Figure 7.89 and one can see the sharp peak at the Z mass. This is the same for all accelerators as well as the dynamic scales.

Figure 7.90 shows kinematic observables for the jet. It can be seen that the jet is

[59] See Figure B.67 in Appendix B.2.3.2.
[60] See Figure B.68 and B.69 in Appendix B.2.3.2.
[61] See Figures B.71 and Figure B.70 in Appendix B.2.3.2.
[62] See Figure 7.86 in Appendix B.2.3.2.
[63] See Figures B.73 and B.74 in Appendix B.2.3.2.
[64] See Figures B.75 and B.76 in Appendix B.2.3.2.

harder and tends to lie close to the transverse plane. This is true for all accelerator and dynamic scales. As seen before, the scale uncertainties are suppressed for the LHC with 14 TeV in comparison to the LHC with 7 TeV .

Now, I would like to present the distance observables between the jet and each of the charged leptons. Figure 7.91 shows the differential cross-section with respect to the difference in azimuthal angle between the harder charged lepton and the jet. One can see a linear increase from 100° peaking at 155° to 160°. For the Tevatron the peak is at 160° to 165°.[65] The magnitude and scales for the different accelerators and dynamic scales vary as described above. The difference in rapidity of the harder charged lepton and the jet is shown in Figure 7.92. It can be seen that both tend to lie close together. Moreover, their separation peaks around 3, as can be seen in Figure 7.93, suggesting that they are almost back-to-back. The invariant mass of the harder charged lepton and the jet has a well defined peak at 90 GeV. This can be seen in Figure 7.94. For the Tevatron the peak is at 70 TeV.[66]

After I looked at the combinations of the harder charged lepton and the jet, I want to look at the softer charged lepton and the jet. Figure 7.95 shows the difference in azimuthal angle between the jet and the softer charged lepton. There is a maximum at 110° and the magnitude of the differential cross-section is larger at zero degree than for 180°. As before we obtain larger scale uncertainties for the Tevatron[67] and massively smaller ones for the LHC with 14 TeV. The rapidity difference between the softer charged lepton and the jet shows that they tend to lie close together. The corresponding graph is shown in Figure 7.96. Figure 7.97 shows the separation R between the softer charged lepton and the jet. This distribution has a maximum around $R = 2$, which means that both are separated but not opposite to each other. The shapes for the other accelerator and the dynamic scales are very similar. Finally, Figure 7.98 shows the invariant mass of the softer charged lepton and the jet. A well defined peak at 55 GeV to 60 GeV can be observed. This peak is shifted to 45 GeV to 50 GeV for the Tevatron[68]. Otherwise the shapes are the same for all accelerators and dynamic scales. The magnitude and scale uncertainties behave as one would expect from the previous histograms.

[65] See Figure B.77 in Appendix B.2.3.2.
[66] See Figure B.78 in Appendix B.2.3.2.
[67] See Figure B.79 in Appendix B.2.3.2.
[68] See Figure B.80 in Appendix B.2.3.2.

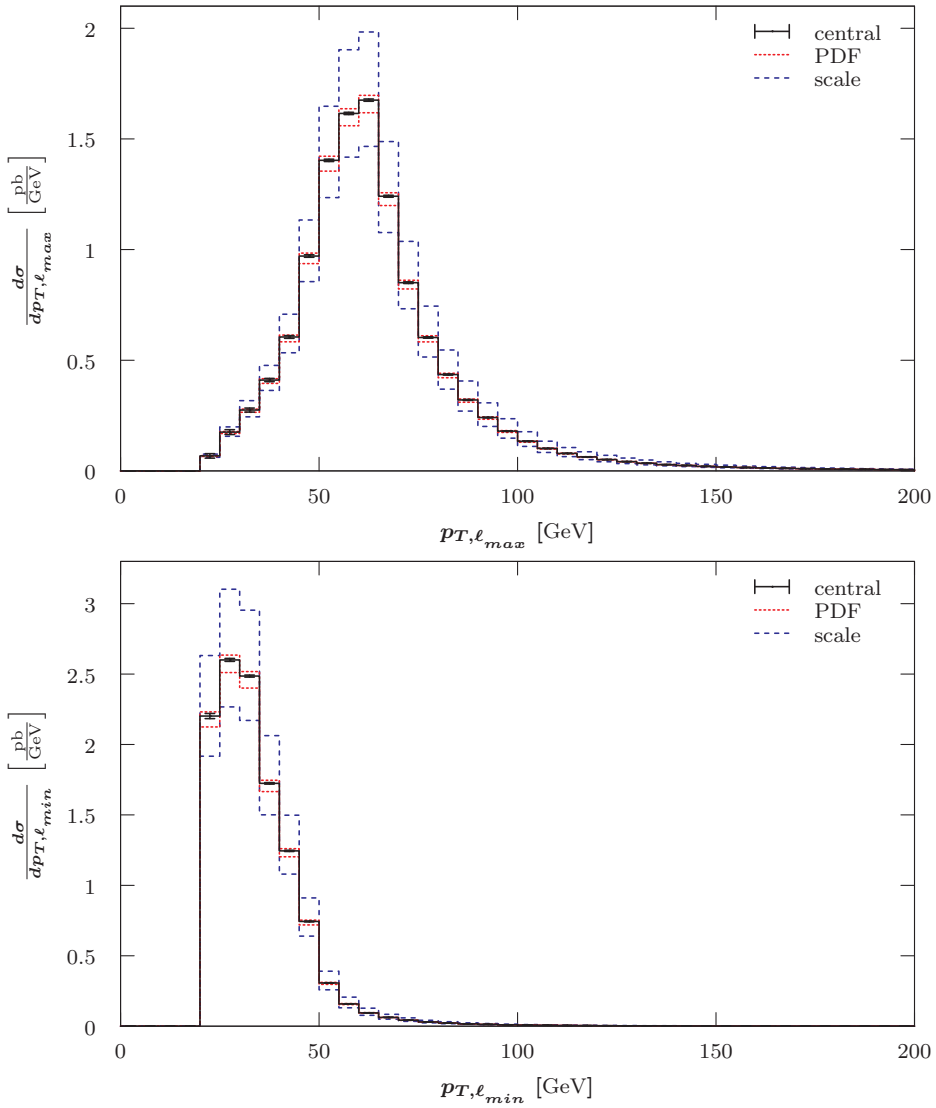

Figure 7.83: LO differential cross-section with respect to the harder ℓ_{max} (top) and the softer ℓ_{min} (bottom) charged lepton transverse momentum for the $pp \to (Z \to \ell^-\ell^+) + 1\ jet$ process at the LHC with 7 TeV using a fixed scale of $\mu_0 = M_Z$. Additional details are given in the caption of Figure 7.77.

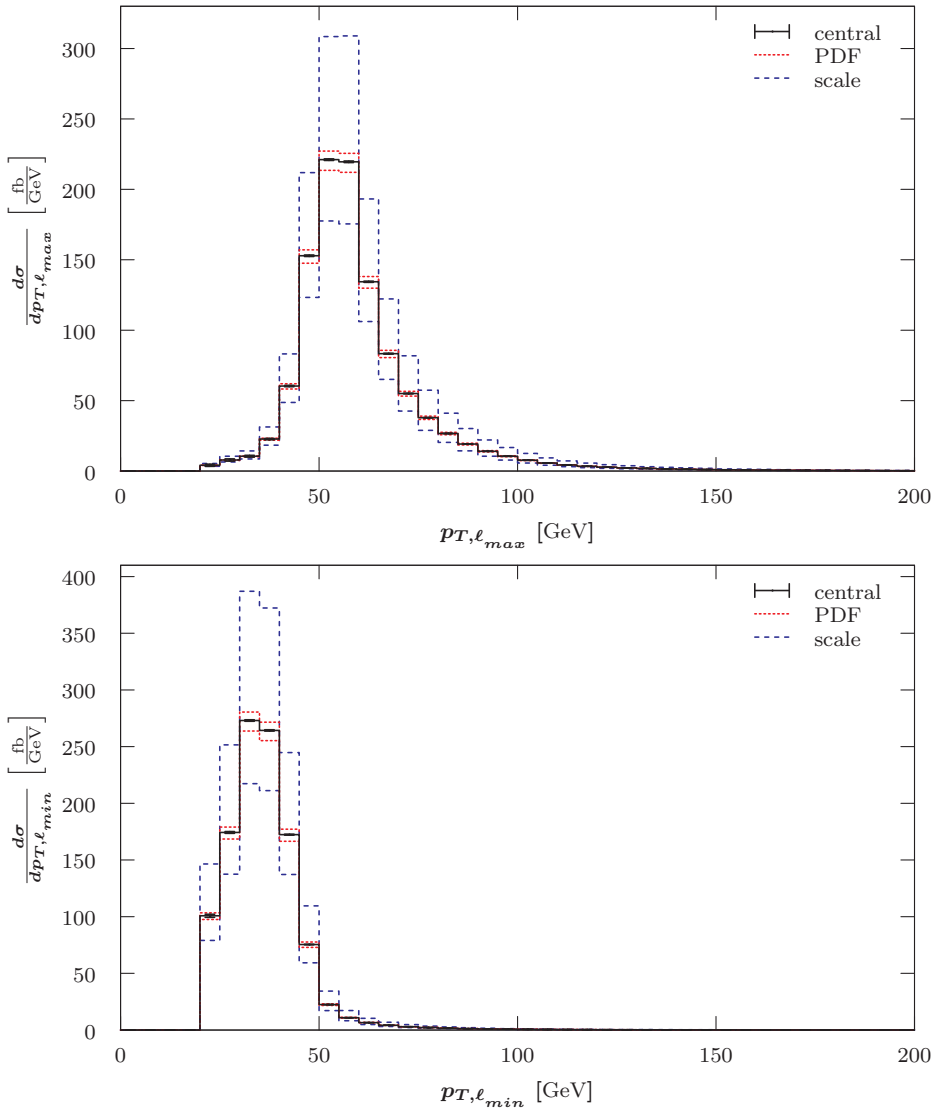

Figure 7.84: LO differential cross-section with respect to the harder ℓ_{max} (top) and the softer ℓ_{min} (bottom) charged lepton transverse momentum for the $p\overline{p} \to (Z \to \ell^-\ell^+) + 1\ jet$ process at the Tevatron Run II using a fixed scale of $\mu_0 = M_Z$. Additional details are given in the caption of Figure 7.77.

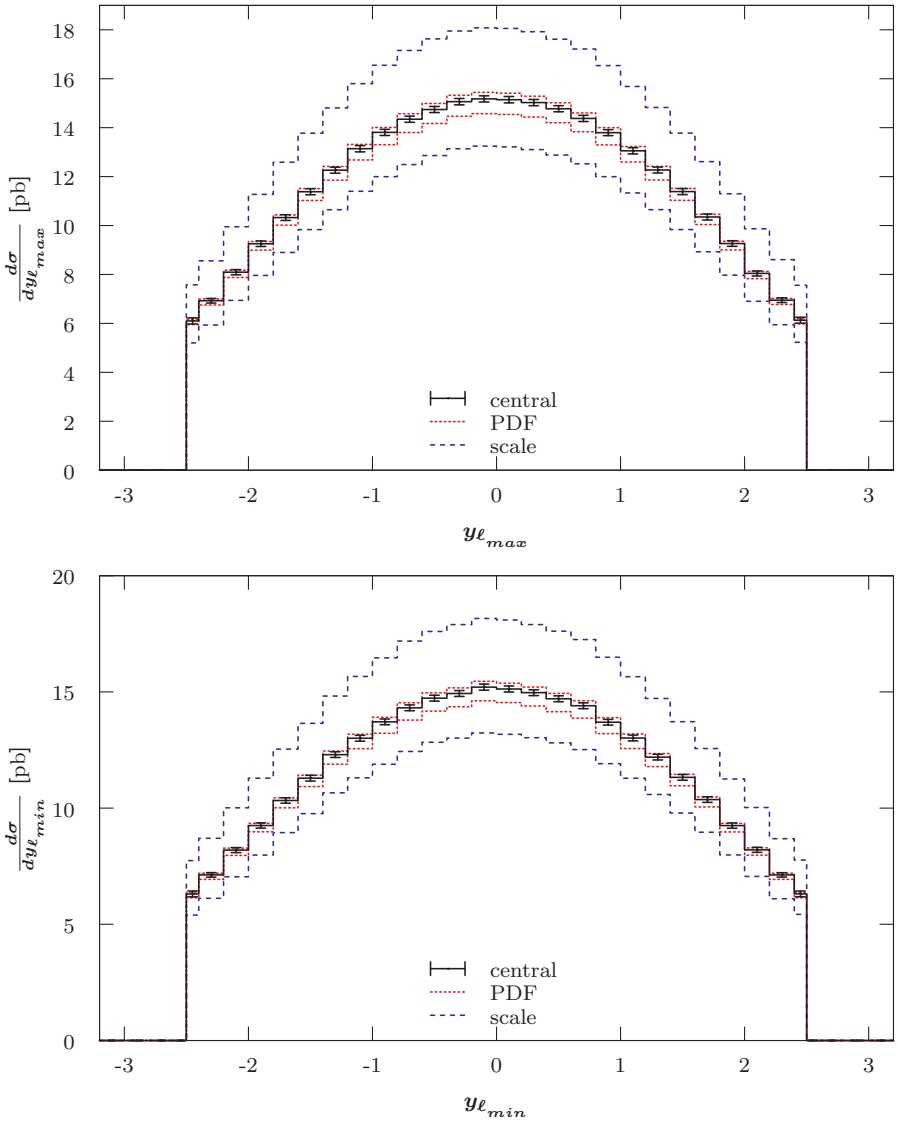

Figure 7.85: LO differential cross-section with respect to the harder ℓ_{max} (top) and the softer ℓ_{min} (bottom) charged lepton rapidity for the pp $\to$ (Z $\to \ell^-\ell^+$) + 1 *jet* process at the LHC with 7 TeV using a fixed scale of $\mu_0 = M_Z$. The first and last filled bin are half-width due to the applied selection cut, $|y_\ell| < 2.5$. Additional details are given in the caption of Figure 7.77.

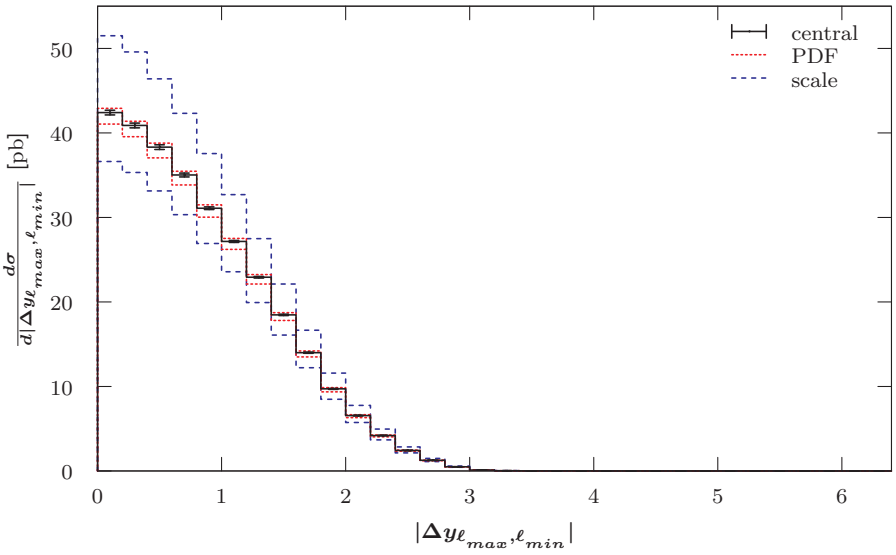

Figure 7.86: LO differential cross-section with respect to the difference in rapidity between the harder ℓ_{max} and the softer ℓ_{min} charged lepton for the pp $\to$ (Z $\to \ell^-\ell^+$) + 1 *jet* process at the LHC with 7 TeV using a fixed scale of $\mu_0 = M_{\mathrm{Z}}$. Additional details are given in the caption of Figure 7.77.

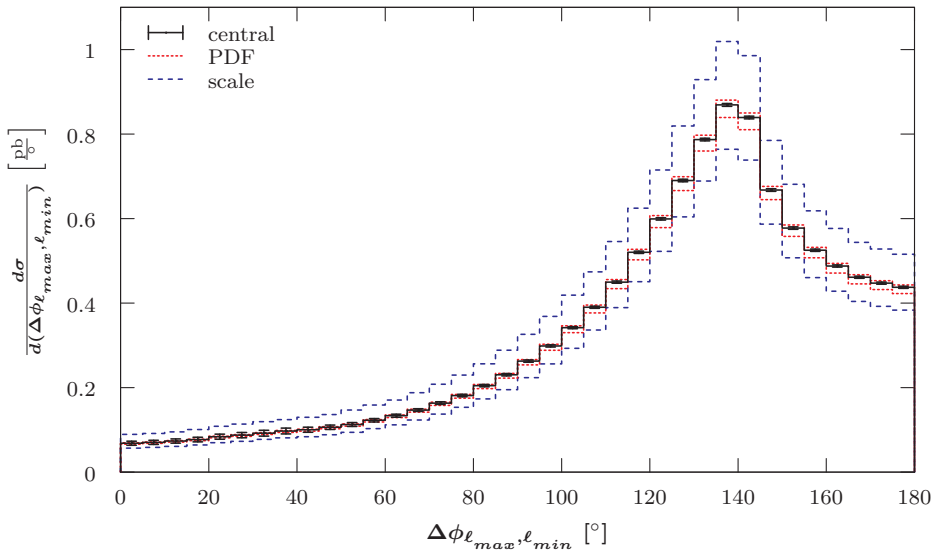

Figure 7.87: LO differential cross-section with respect to rapidity difference between the two charged leptons for the pp $\to$ (Z $\to \ell^-\ell^+$) + 1 *jet* process at the LHC with 7 TeV using a fixed scale of $\mu_0 = M_{\mathrm{Z}}$. Additional details are given in the caption of Figure 7.77.

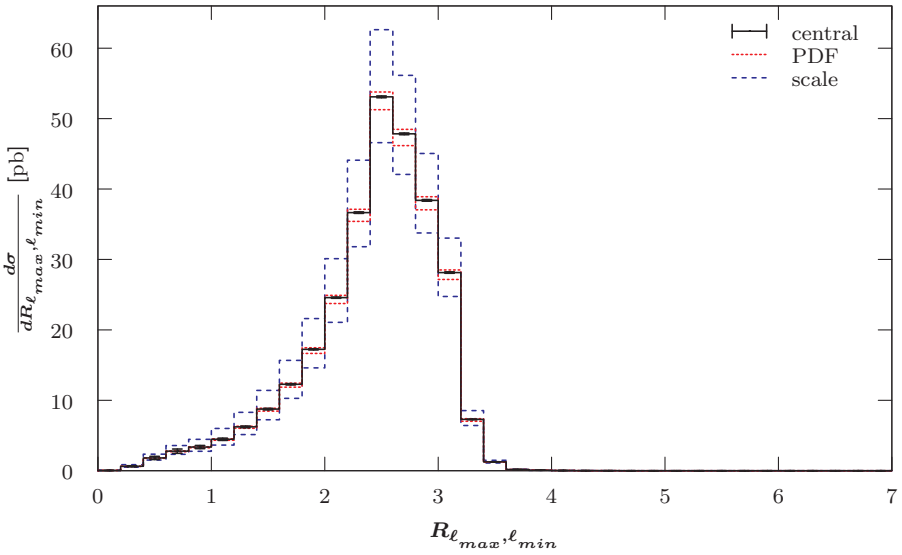

Figure 7.88: LO differential cross-section with respect to separation between the two charged leptons for the pp $\to$ (Z $\to \ell^-\ell^+$) + 1 *jets* process at the LHC with 7 TeV using a fixed scale of $\mu_0 = M_Z$. Additional details are given in the caption of Figure 7.77.

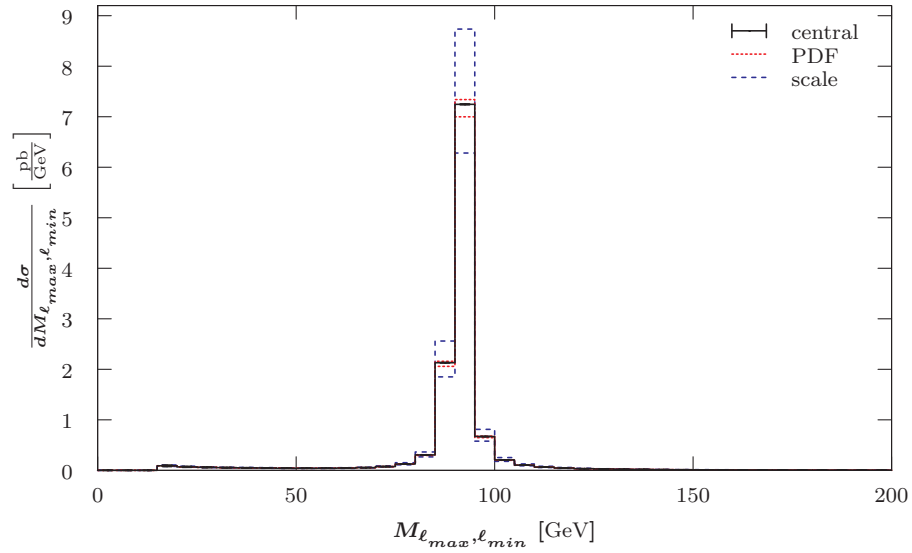

Figure 7.89: LO differential cross-section with respect to the invariant mass of the two charged leptons for the pp $\to$ (Z $\to \ell^-\ell^+$) + 1 *jets* process at the LHC with 7 TeV using a fixed scale of $\mu_0 = M_Z$. Additional details are given in the caption of Figure 7.77.

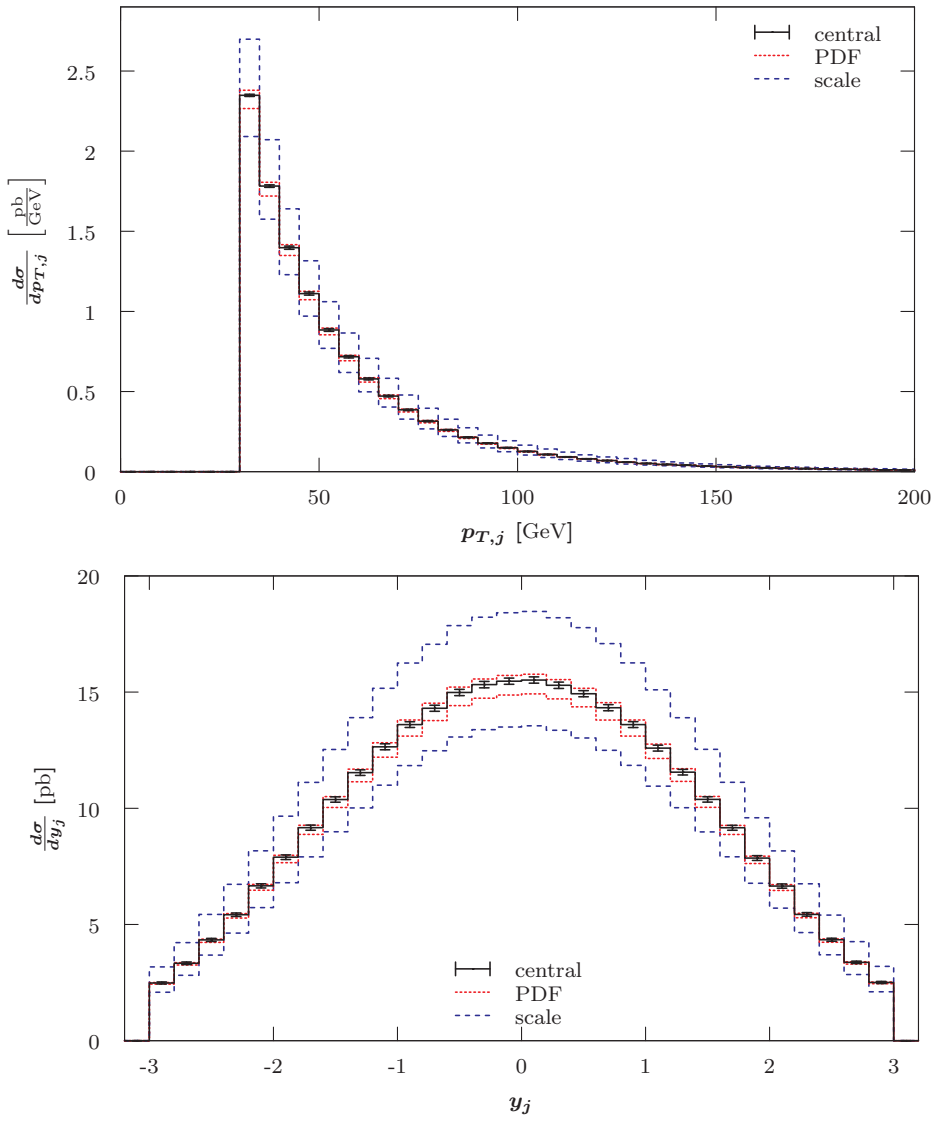

Figure 7.90: LO differential cross-section with respect to the transverse momentum (top) and the rapidity (bottom) of the jet for the pp $\to$ (Z $\to \ell^-\ell^+$) + 1 *jet* process at the LHC with 7 TeV using a fixed scale of $\mu_0 = M_Z$. Additional details are given in the caption of Figure 7.1.

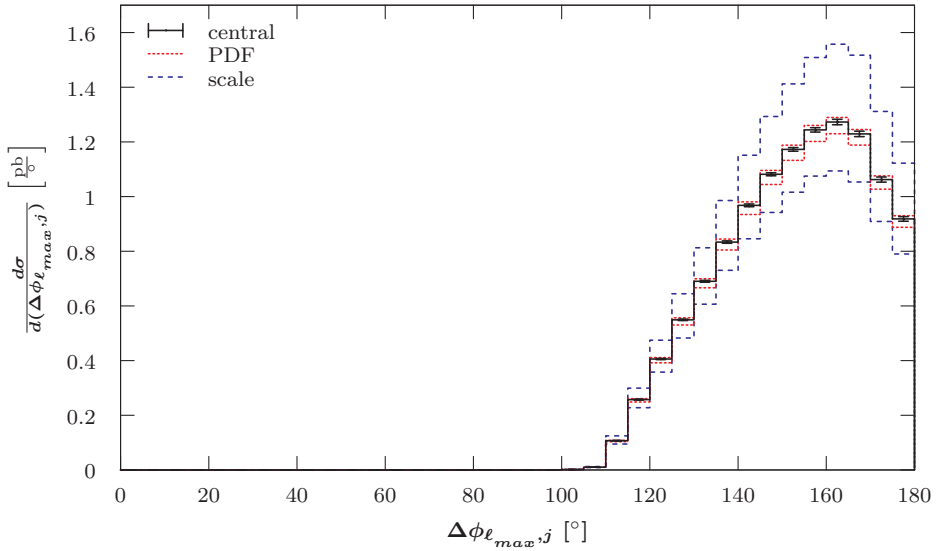

Figure 7.91: LO differential cross-section with respect to the rapidity difference between the harder charged lepton ℓ_{max} and the jet j for the pp $\rightarrow$ (Z $\rightarrow \ell^-\ell^+$) + 1 *jet* process at the LHC with 7 TeV using a fixed scale of $\mu_0 = M_{\text{Z}}$. Additional details are given in the caption of Figure 7.77.

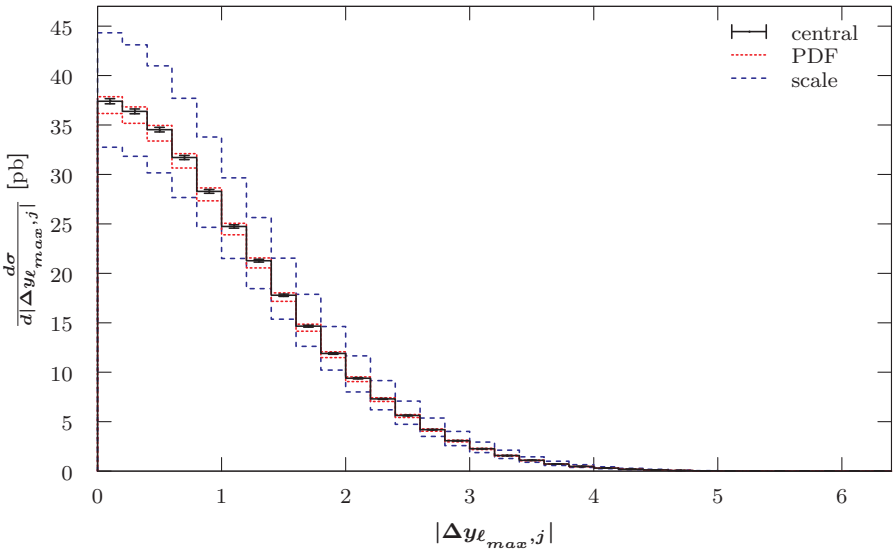

Figure 7.92: LO differential cross-section with respect to the difference in rapidity between the harder charged lepton ℓ_{max} and the jet j for the pp $\rightarrow$ (Z $\rightarrow \ell^-\ell^+$) + 1 *jet* process at the LHC with 7 TeV using a fixed scale of $\mu_0 = M_{\text{Z}}$. Additional details are given in the caption of Figure 7.77.

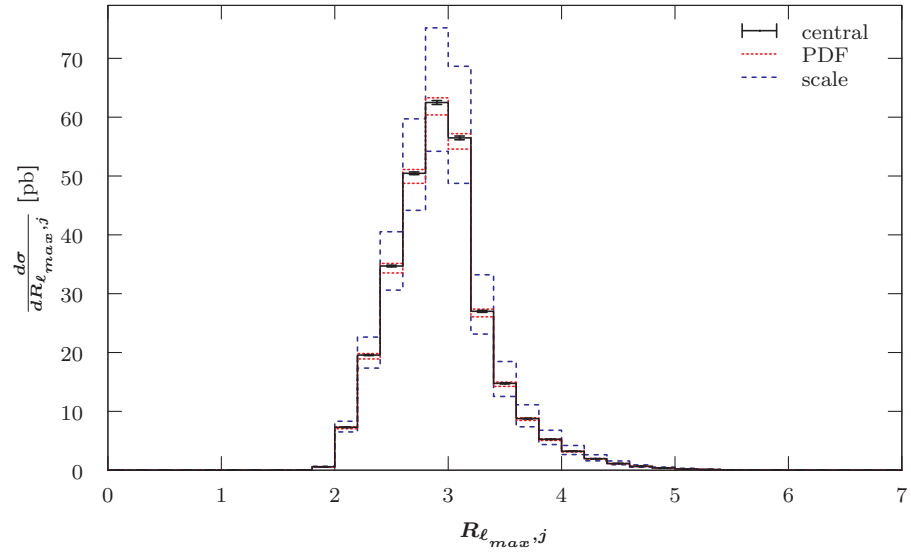

Figure 7.93: LO differential cross-section with respect to separation between the harder charged lepton ℓ_{max} and the jet j for the pp $\to$ (Z $\to \ell^-\ell^+$) + 1 *jet* process at the LHC with 7 TeV using a fixed scale of $\mu_0 = M_Z$. Additional details are given in the caption of Figure 7.77.

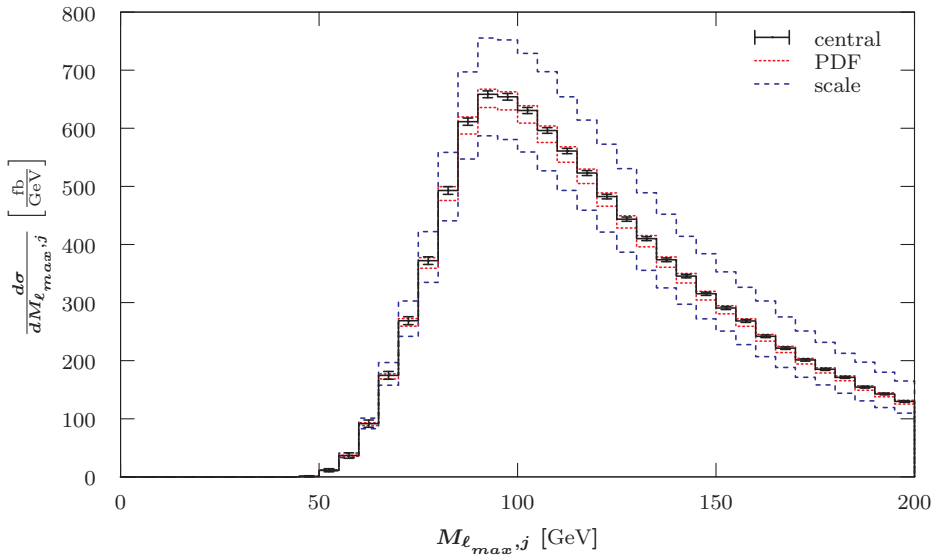

Figure 7.94: LO differential cross-section with respect to the invariant mass of the harder charged lepton ℓ_{max} and the jet j for the pp $\to$ (Z $\to \ell^-\ell^+$) + 1 *jet* process at the LHC with 7 TeV using a fixed scale of $\mu_0 = M_Z$. Additional details are given in the caption of Figure 7.77.

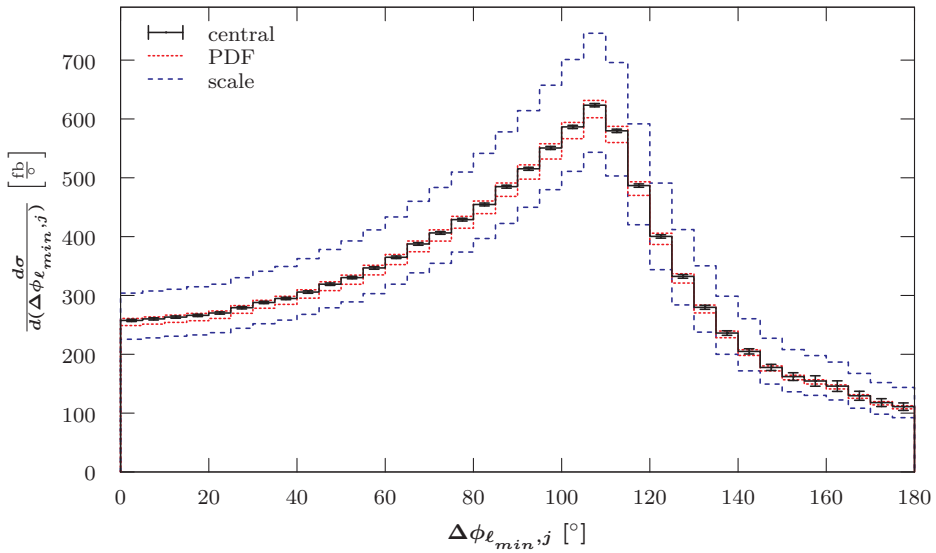

Figure 7.95: LO differential cross-section with respect to the rapidity difference between the softer charged lepton ℓ_{min} and the jet j for the pp $\to$ (Z $\to \ell^-\ell^+$) + 1 *jet* process at the LHC with 7 TeV using a fixed scale of $\mu_0 = M_\text{Z}$. Additional details are given in the caption of Figure 7.77.

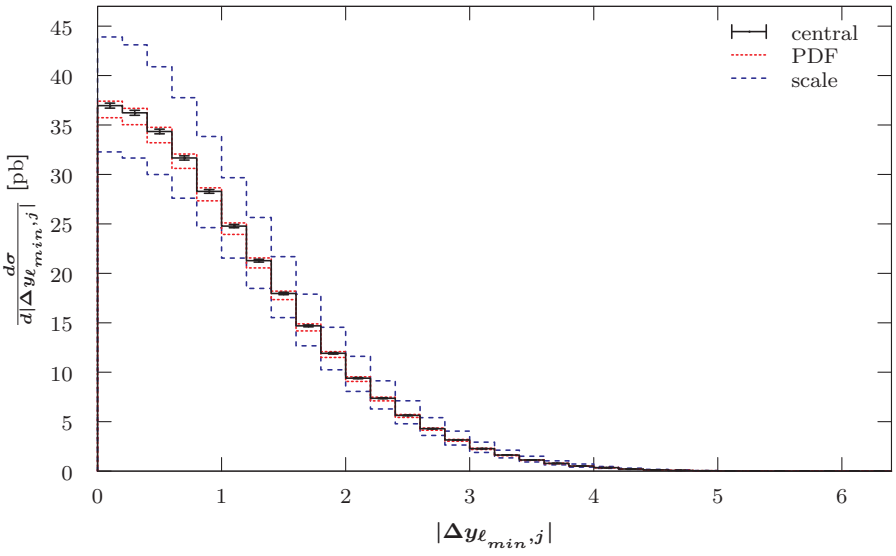

Figure 7.96: LO differential cross-section with respect to the difference in rapidity between the softer charged lepton ℓ_{min} and the jet j for the pp $\to$ (Z $\to \ell^-\ell^+$) + 1 *jet* process at the LHC with 7 TeV using a fixed scale of $\mu_0 = M_\text{Z}$. Additional details are given in the caption of Figure 7.77.

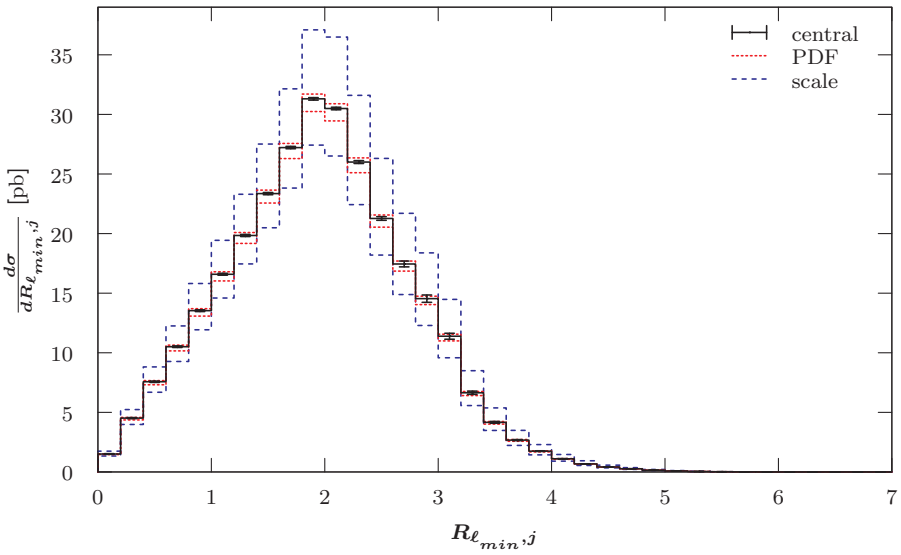

Figure 7.97: LO differential cross-section with respect to separation between the softer charged lepton ℓ_{min} and the jet j for the $pp \to (Z \to \ell^-\ell^+) + 1\ jet$ process at the LHC with 7 TeV using a fixed scale of $\mu_0 = M_Z$. Additional details are given in the caption of Figure 7.77.

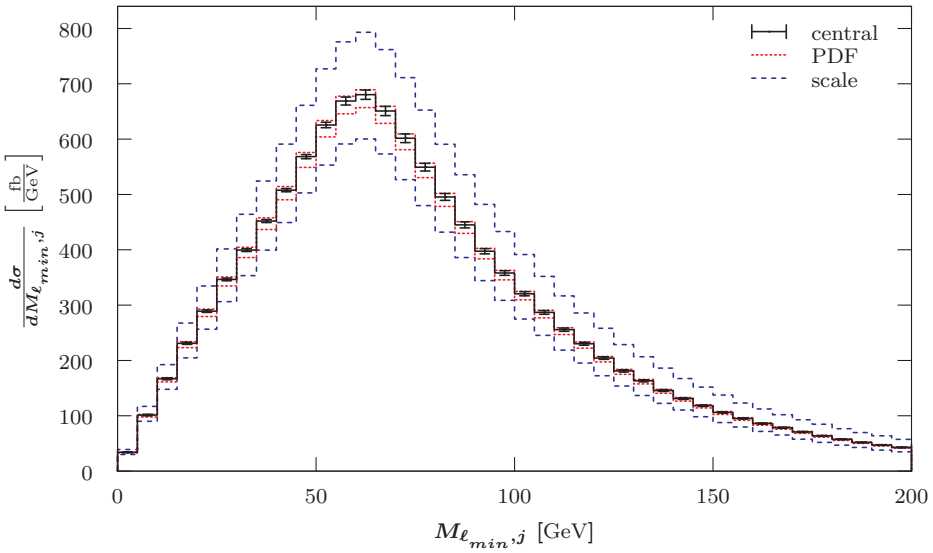

Figure 7.98: LO differential cross-section with respect to the invariant mass of the softer charged lepton ℓ_{min} and the jet j for the $pp \to (Z \to \ell^-\ell^+) + 1\ jet$ process at the LHC with 7 TeV using a fixed scale of $\mu_0 = M_Z$. Additional details are given in the caption of Figure 7.77.

7.4.3.3 $p^{(}\overline{p}^{)} \to (Z \to \ell^-\ell^+) + 2$ jets

Figure 7.99 shows the transverse momentum distribution for the two charged leptons. It can be seen that the harder charged lepton tends to have a transverse momentum larger then 45 GeV and the softer charged lepton tends to have one smaller than 45 GeV. The distributions for the other colliders and scales are very similar. Figure 7.100 shows the rapidity distributions of each of the charged leptons. One can see that both charged leptons tend to be in the central region of the detector. These distributions are even more central for the LHC with 14 TeV and the dynamic scales.

The difference in rapidity between the two charged leptons is given in Figure 7.101. One can see that both particles tend to lie close together. The graph for the Tevatron is slightly different, because it lacks the small tail[69]. The integrals of the distributions for different accelerators and scale choices behave as one would expect from the integrated cross-sections. The scale uncertainties, however, slightly decrease with centre-of-mass energy and for the dynamic scales. Figure 7.102 gives the difference in azimuthal angle between the two charged leptons. There is an almost linear increase towards 180° in the magnitude of the differential cross-section. The shapes for the other accelerators are very similar. For the Tevatron the histogram flattens off for larger angles[70]. The separation R between the two charged leptons is given in Figure 7.103. It can be seen that there is a peak at $R = 3$ and a sharp drop just beyond it. The increasing flank flattens just below $R = 2$. This kink is less pronounced for the Tevatron[71]. The invariant mass of the two charged leptons is shown in Figure 7.104. It has a very sharp peak at the Z mass. This is true for all accelerators and scales.

Next, I show the kinematic observables of the harder jet. Its transverse momentum and rapidity distribution are given in Figure 7.105. One can observe that the transverse momentum distribution peaks at 50 GeV and that the jet tends to be emitted in the central part of the detector. These results are true for all accelerators and scales. The corresponding histograms for the softer jet are given in Figure 7.106. This jet tends to have smaller transverse momentum exponentially tailing off for larger momentum. The rapidity distribution is very similar to the one we have seen for the harder jet. Again, the results for other colliders and scales are very similar.

The differential cross-section with respect to the difference in azimuthal angle between the harder charged lepton and the harder jet is given in Figure 7.107. The distribution increases from zero more and more rapidly towards larger angles. Showing that the harder jet and the harder charged lepton tend to be emitted in opposing hemispheres of the detector. The histogram for the Tevatron varies in so far that it flattens off for larger

[69] See Figure B.84 in Appendix B.2.3.3.
[70] See Figure B.81 in Appendix B.2.3.3.
[71] See Figure B.82 in Appendix B.2.3.3.

angles[72]. The difference in rapidity between the harder jet and the harder charged lepton is given in Figure 7.108. It can be seen that they tend to lie closer together. The previous two distributions can be combined to give the separation R as shown in Figure 7.109. A well defined peak just above $R = 3$ can be observed. The invariant mass of the harder jet and the harder charged lepton has a broad maximum at 120 GeV. The differential cross-section is close to zero for masses less than 50 GeV. This is recorded in Figure 7.110. For the Tevatron the peak is at 95 GeV to 100 GeV.[73]

Figure 7.111 shows the difference in azimuthal angle for the softer jet and the harder charged lepton. This distribution is very broad and flat. It has a very small maximum at 110°. For the Tevatron I obtained a more continuously increasing slope[74]. Also, the softer jet and the harder charged lepton tend to have similar rapidity. This can be seen in Figure 7.112. The separation R between the softer jet and the harder charged lepton is broader than for the harder jet. The differential cross-section increases logarithmically towards a maximum at $R = 2.8$. This is recorded in Figure 7.113. For the Tevatron the increase is linear[75]. The invariant mass of the harder charged lepton and the softer jet shows a broad peak with a linear rise from zero and a long tail (see Figure 7.114). For the Tevatron the peak is lower at approximately 85° to 90°.[76]

After having had an extensive look at the harder charged lepton, I will now look at the observables for the softer charged lepton and jets. Figure 7.115 shows the difference in azimuthal angle between the harder jet and the softer charged lepton. The histogram is very flat at lower angles and has a slight rise towards 180°. At the Tevatron, in contrast one can observe a maximum at 110° and a steep drop for larger angles[77]. As we have seen previously, also the softer charged lepton and the harder jet tend to be close together with respect to rapidity. The corresponding plot is shown in Figure 7.116. And the separation, again, shows a peak just below $R = 3$. This can be seen in Figure 7.117. For the Tevatron this peak is at $R = 2$.[78] Figure 7.118 shows the invariant mass of the harder jet and the softer charged lepton. One can observe a broad peak at 80 GeV to 85 GeV with a long tail. For the Tevatron the peak is at 60 GeV to 65 GeV.[79]

Figure 7.119 shows the azimuthal angle between the softer jet and the softer charged lepton. Again, we have a very flat distribution with a slight increase towards 180°. The Tevatron results flatten off towards 180°.[80] The difference in rapidity between the softer jet and the softer charged lepton is shown in Figure 7.120. It can be seen that they tend

[72]See Figure B.83 in Appendix B.2.3.3.
[73]See Figure B.85 in Appendix B.2.3.3.
[74]See Figure B.86 in Appendix B.2.3.3.
[75]See Figure B.87 in Appendix B.2.3.3.
[76]See Figure B.88 in Appendix B.2.3.3.
[77]See Figure B.89 in Appendix B.2.3.3.
[78]See Figure B.90 in Appendix B.2.3.3.
[79]See Figure B.91 in Appendix B.2.3.3.
[80]See Figure B.92 in Appendix B.2.3.3.

to have a similar boost. Figure 7.121 shows the differential cross-section with respect to separation R between the softer charged lepton and the softer jet. A steady increase from zero leads to a peak at $R = 3$. For the Tevatron the maximum is below $R = 2.5$.[81] The invariant mass of the softer jet and the softer charged lepton has a broad peak at 55 GeV to 60 GeV, as shown in Figure 7.122. The Tevatron peaks at 50 GeV to 60 GeV.[82]

The last set of histograms is the combination of the harder and the softer jet. Figure 7.123 shows the azimuthal angle between the two jets. The distribution is quite flat up to 80° apart from a small peak at 25°. After the plateau the distribution increases towards 180°. The mentioned peak is more pronounced for the Tevatron[83]. The difference in rapidity for the two jets is listed in Figure 7.124. The two jets generally tend to lie close together. There is a small local maximum at 0.5. The separation R between the two jets is shown in Figure 7.125. We can see that the histogram sharply peaks around $R = 3$ suggesting that they tend to be emitted back-to-back. For the Tevatron there is a secondary peak at 0.4 GeV, which coincides with the onset of the cut[84]. Figure 7.126, finally, shows the invariant mass of the two jets. There is a broad peak at 100 GeV. This peak has a long tail to the right. From the left the differential cross-section starts relatively flat and then steepens around 60 GeV. For the Tevatron the peak is at 55 GeV to 60 GeV.[85]

[81] See Figure B.93 in Appendix B.2.3.3.
[82] See Figure B.94 in Appendix B.2.3.3.
[83] See Figure B.95 in Appendix B.2.3.3.
[84] See Figure B.96 in Appendix B.2.3.3.
[85] See Figure B.97 in Appendix B.2.3.3.

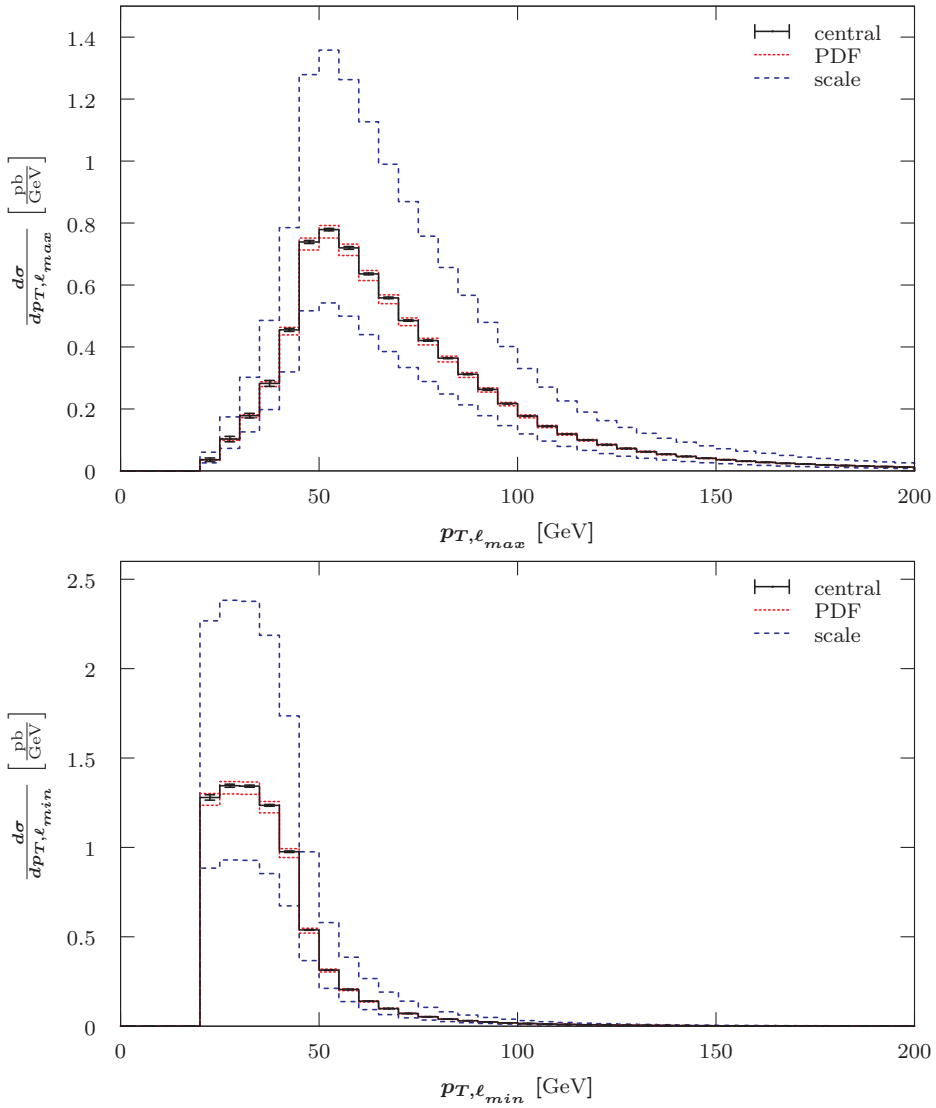

Figure 7.99: LO differential cross-section with respect to the harder ℓ_{max} (top) and the softer ℓ_{min} (bottom) charged lepton transverse momentum for the $pp \to (Z \to \ell^-\ell^+) + 2\ jets$ process at the LHC with 7 TeV using a fixed scale of $\mu_0 = M_Z$. Additional details are given in the caption of Figure 7.77.

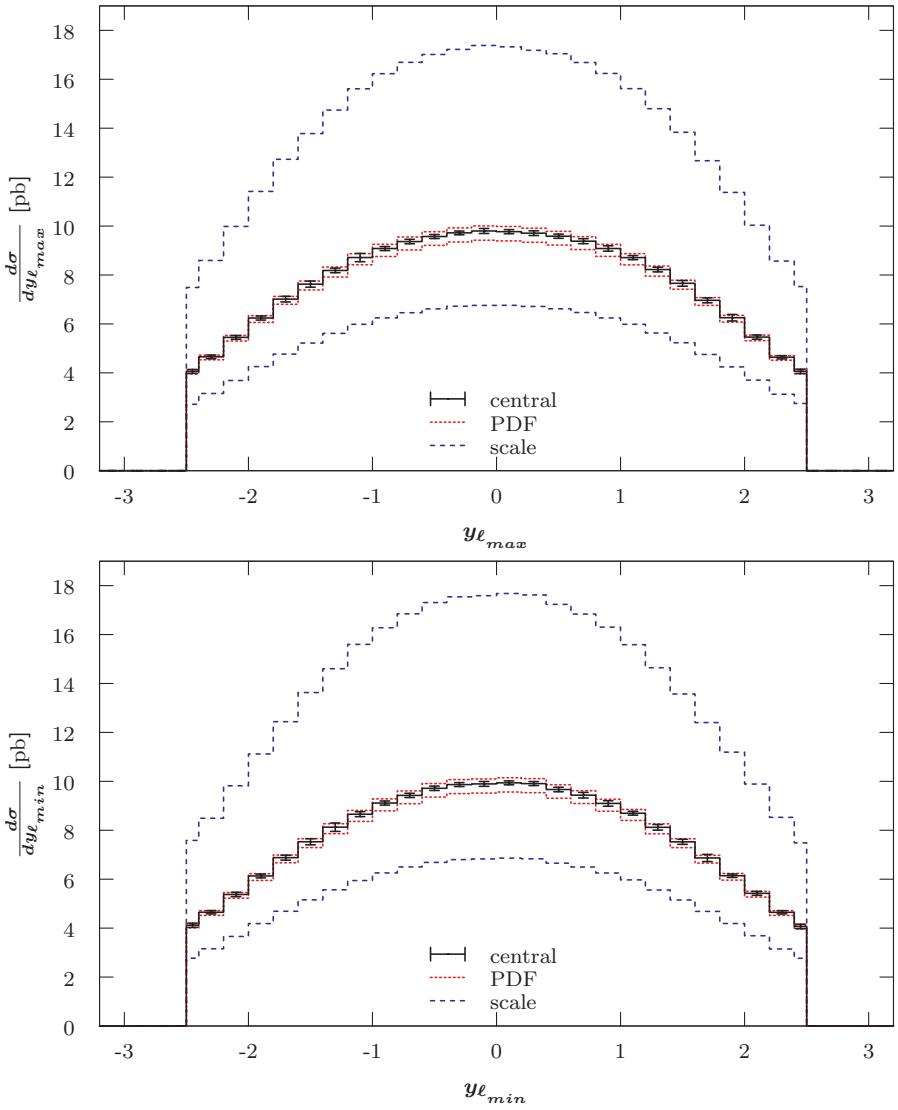

Figure 7.100: LO differential cross-section with respect to the harder ℓ_{max} (top) and the softer ℓ_{min} (bottom) charged lepton rapidity for the pp $\to$ (Z $\to \ell^-\ell^+$) + 2 *jets* process at the LHC with 7 TeV using a fixed scale of $\mu_0 = M_{\mathrm{Z}}$. The first and last filled bin are half-width due to the applied selection cut, $|y_\ell| < 2.5$. Additional details are given in the caption of Figure 7.77.

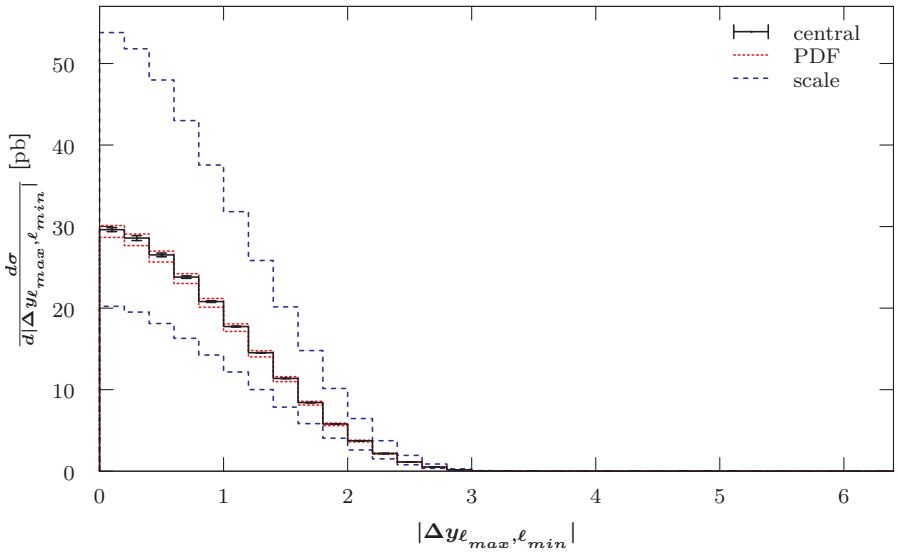

Figure 7.101: LO differential cross-section with respect to the difference in rapidity between the harder ℓ_{max} and the softer ℓ_{min} charged lepton for the $pp \to (Z \to \ell^-\ell^+) + 2\ jets$ process at the LHC with 7 TeV using a fixed scale of $\mu_0 = M_Z$. Additional details are given in the caption of Figure 7.77.

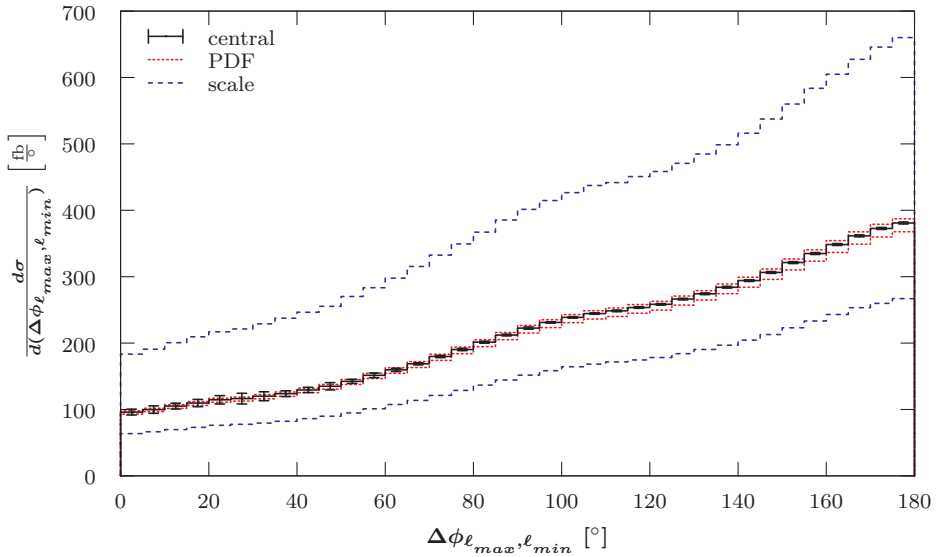

Figure 7.102: LO differential cross-section with respect to the azimuthal angle ϕ between the two charged leptons for the $pp \to (Z \to \ell^-\ell^+) + 2\ jets$ process at the LHC with 7 TeV using a fixed scale of $\mu_0 = M_Z$. Additional details are given in the caption of Figure 7.77.

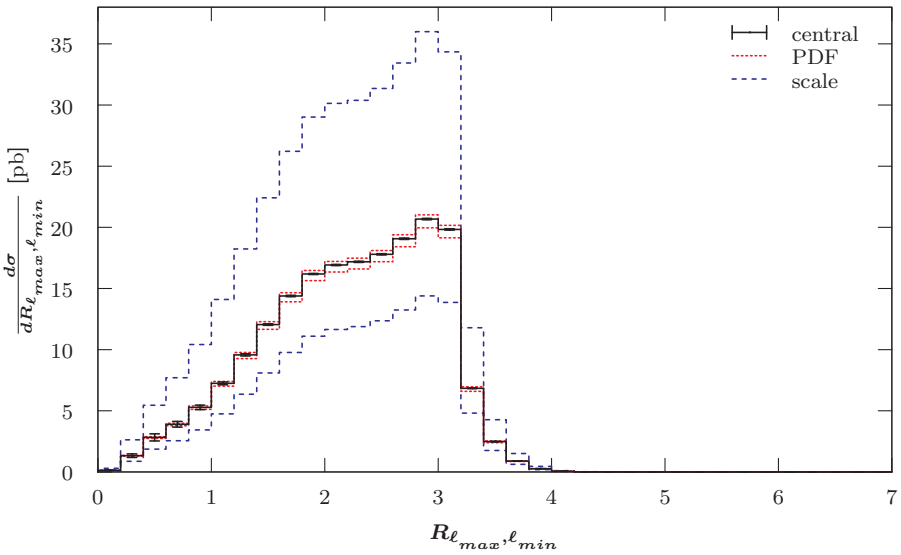

Figure 7.103: LO differential cross-section with respect to the separation between the two charged leptons for the pp $\to (\mathrm{Z} \to \ell^-\ell^+) + 2\ jets$ process at the LHC with 7 TeV using a fixed scale of $\mu_0 = M_\mathrm{Z}$. Additional details are given in the caption of Figure 7.77.

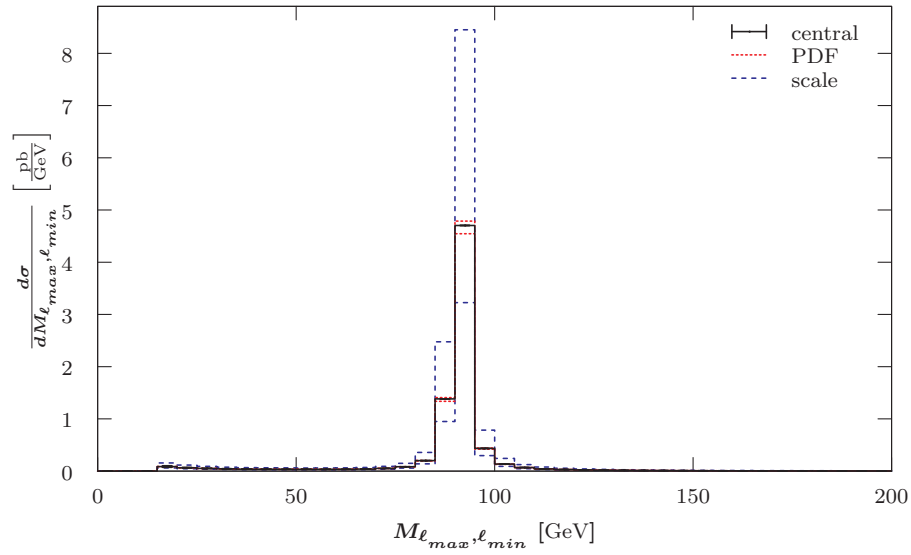

Figure 7.104: LO differential cross-section with respect to the invariant mass of the two charged leptons for the pp $\to (\mathrm{Z} \to \ell^-\ell^+) + 2\ jets$ process at the LHC with 7 TeV using a fixed scale of $\mu_0 = M_\mathrm{Z}$. Additional details are given in the caption of Figure 7.77.

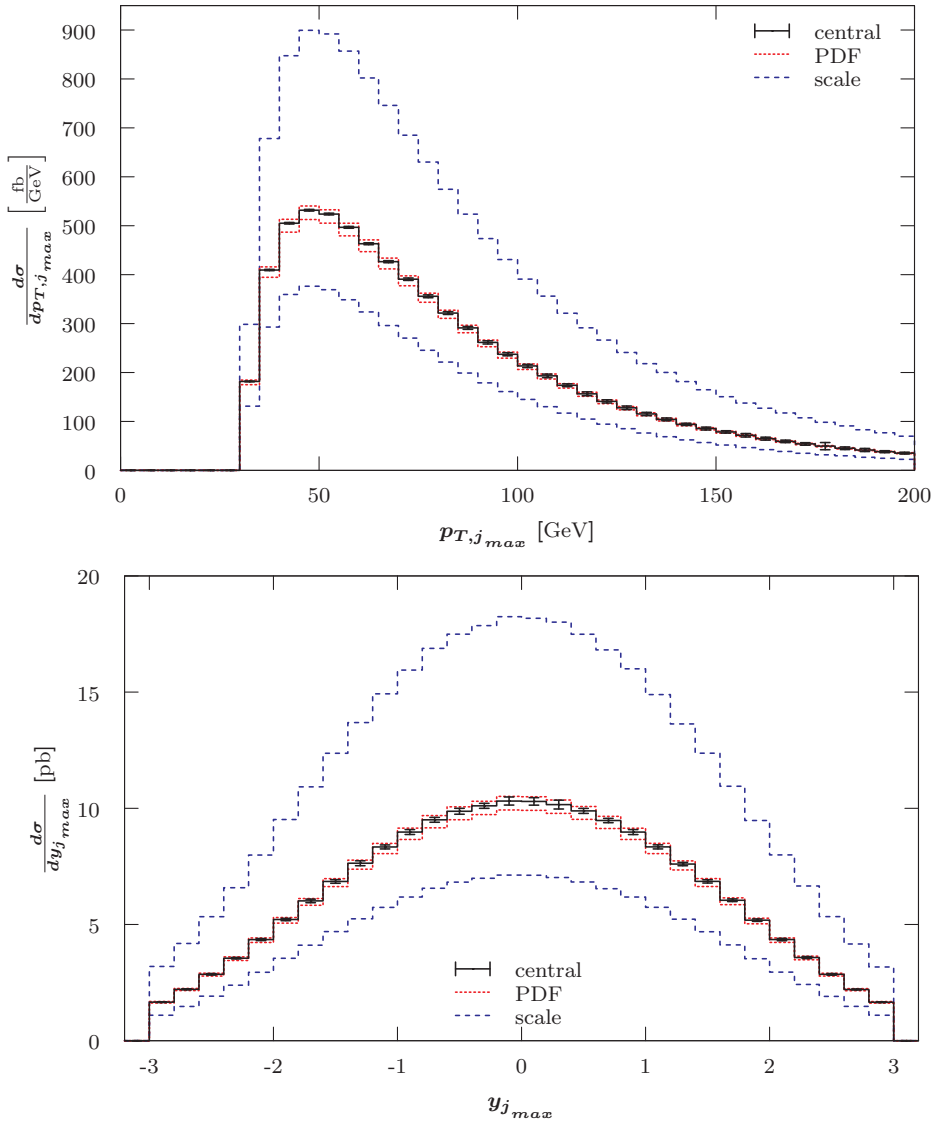

Figure 7.105: LO differential cross-section with respect to the transverse momentum (top) and the rapidity (bottom) of the harder jet j_{max} for the pp $\rightarrow$ (Z $\rightarrow \ell^-\ell^+$) + 2 *jets* process at the LHC with 7 TeV using a fixed scale of $\mu_0 = M_Z$. Additional details are given in the caption of Figure 7.1.

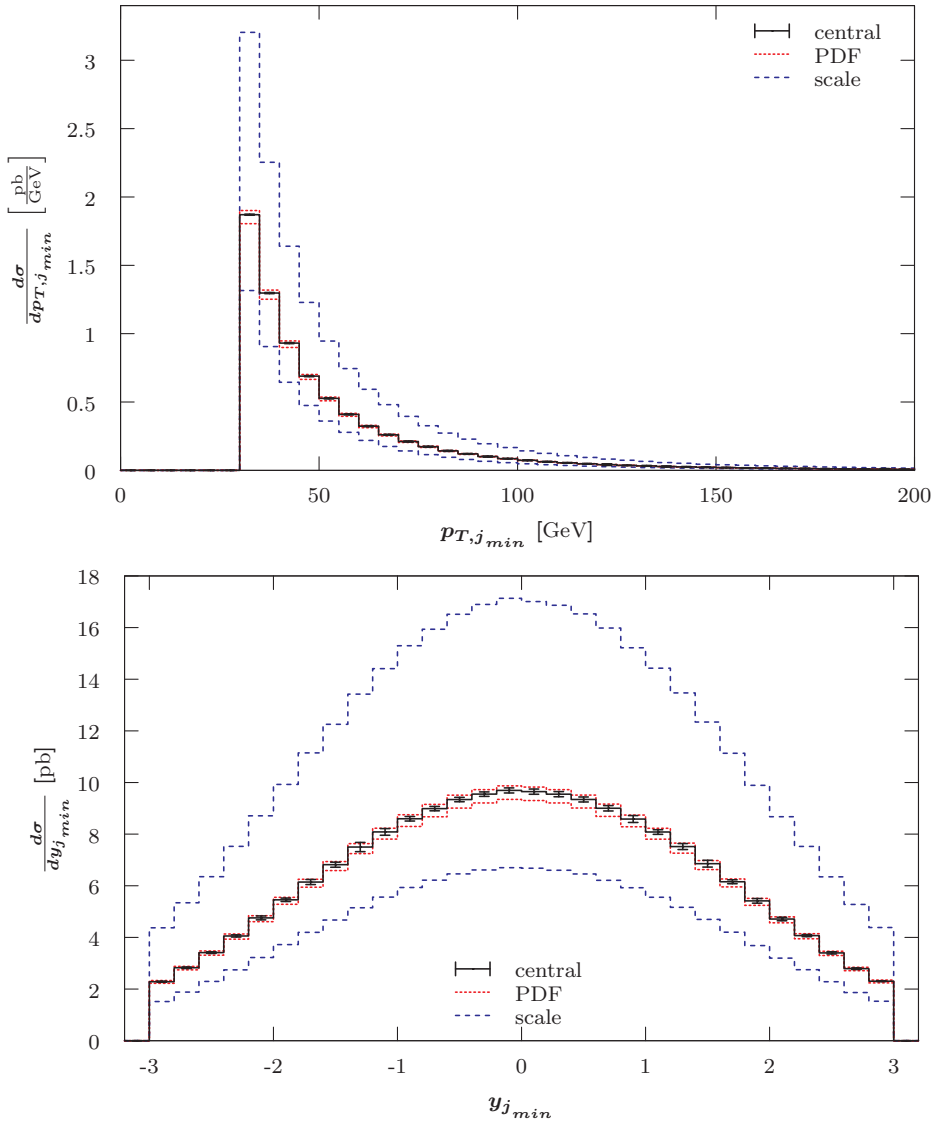

Figure 7.106: LO differential cross-section with respect to the transverse momentum (top) and the rapidity (bottom) of the softer jet j_{min} for the pp $\to$ (Z $\to \ell^-\ell^+$) + 2 *jets* process at the LHC with 7 TeV using a fixed scale of $\mu_0 = M_{\text{Z}}$. Additional details are given in the caption of Figure 7.1.

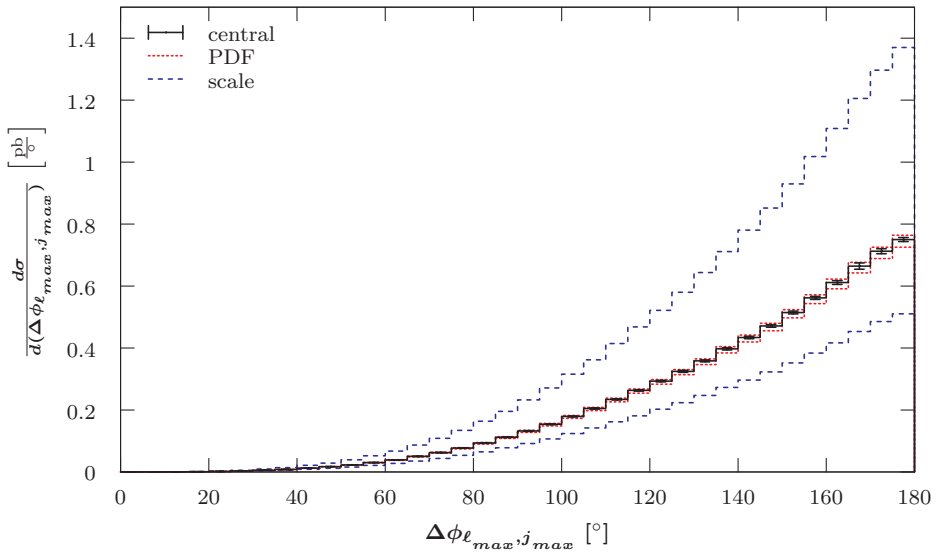

Figure 7.107: LO differential cross-section with respect to the azimuthal angle ϕ between the harder charged lepton ℓ_{max} and the harder jet j_{max} for the pp $\to$ (Z $\to \ell^-\ell^+$) + 2 *jets* process at the LHC with 7 TeV using a fixed scale of $\mu_0 = M_Z$. Additional details are given in the caption of Figure 7.77.

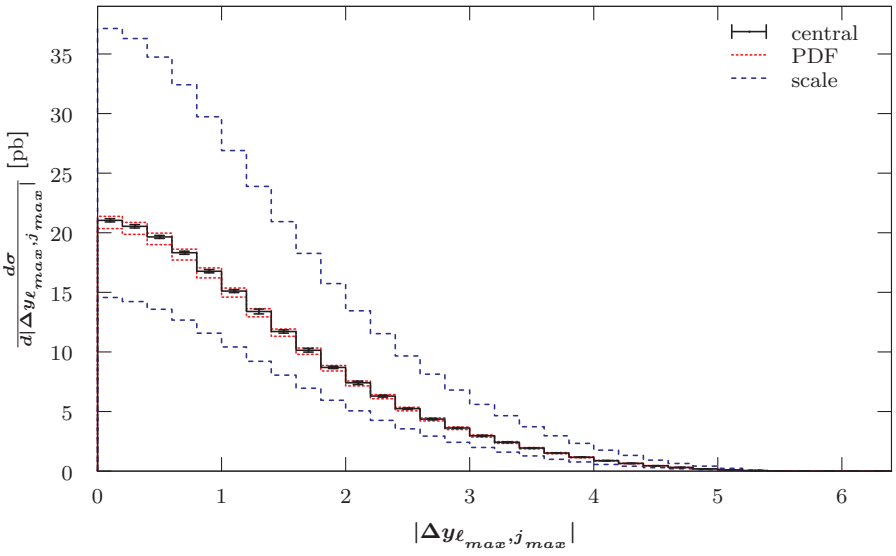

Figure 7.108: LO differential cross-section with respect to the difference in rapidity between the harder charged lepton ℓ_{max} and the harder jet j_{max} for the pp $\to$ (Z $\to \ell^-\ell^+$) + 2 *jets* process at the LHC with 7 TeV using a fixed scale of $\mu_0 = M_Z$. Additional details are given in the caption of Figure 7.77.

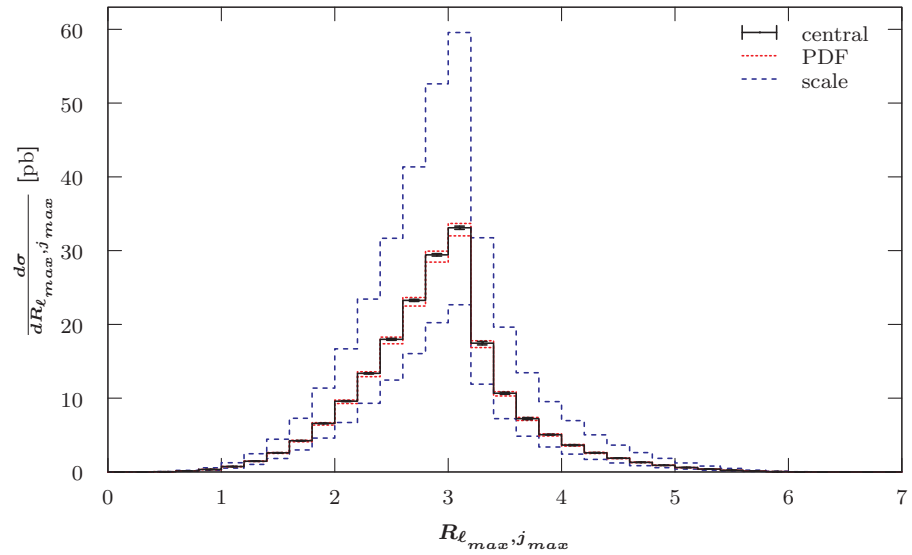

Figure 7.109: LO differential cross-section with respect to the separation between the harder charged lepton ℓ_{max} and the harder jet j_{max} for the $pp \to (Z \to \ell^-\ell^+) + 2\ jets$ process at the LHC with 7 TeV using a fixed scale of $\mu_0 = M_Z$. Additional details are given in the caption of Figure 7.77.

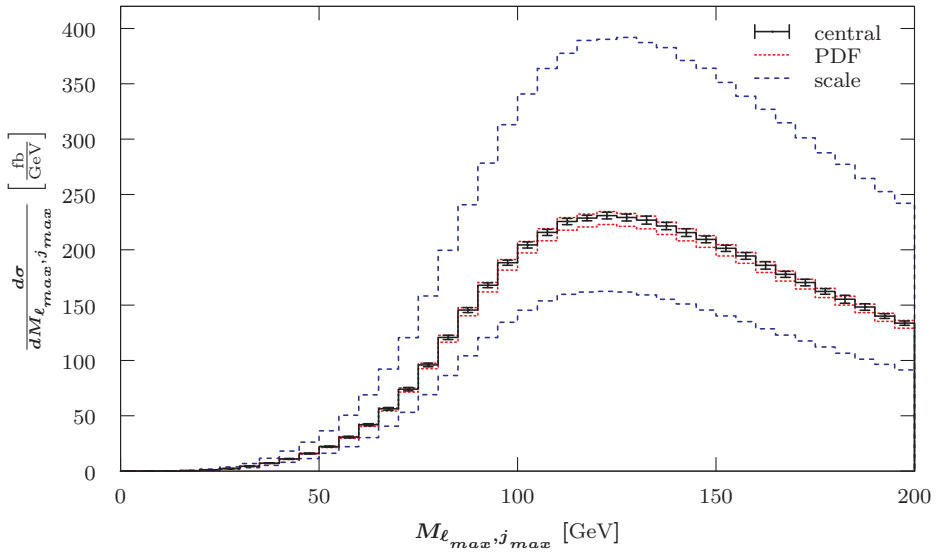

Figure 7.110: LO differential cross-section with respect to the invariant mass of the harder charged lepton ℓ_{max} and the harder jet j_{max} for the $pp \to (Z \to \ell^-\ell^+) + 2\ jets$ process at the LHC with 7 TeV using a fixed scale of $\mu_0 = M_Z$. Additional details are given in the caption of Figure 7.77.

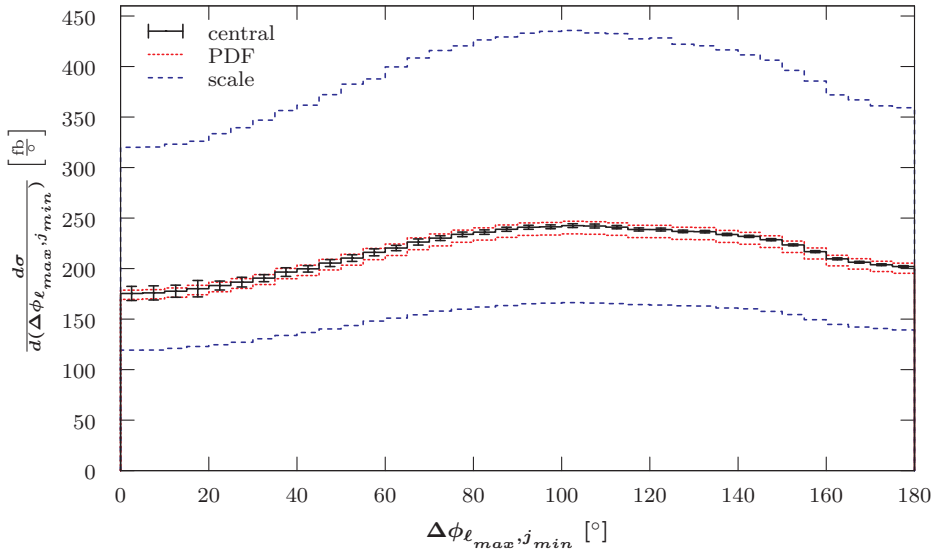

Figure 7.111: LO differential cross-section with respect to the azimuthal angle ϕ between the harder charged lepton ℓ_{max} and the softer jet j_{min} for the pp $\to$ (Z $\to \ell^-\ell^+$) + 2 *jets* process at the LHC with 7 TeV using a fixed scale of $\mu_0 = M_\text{Z}$. Additional details are given in the caption of Figure 7.77.

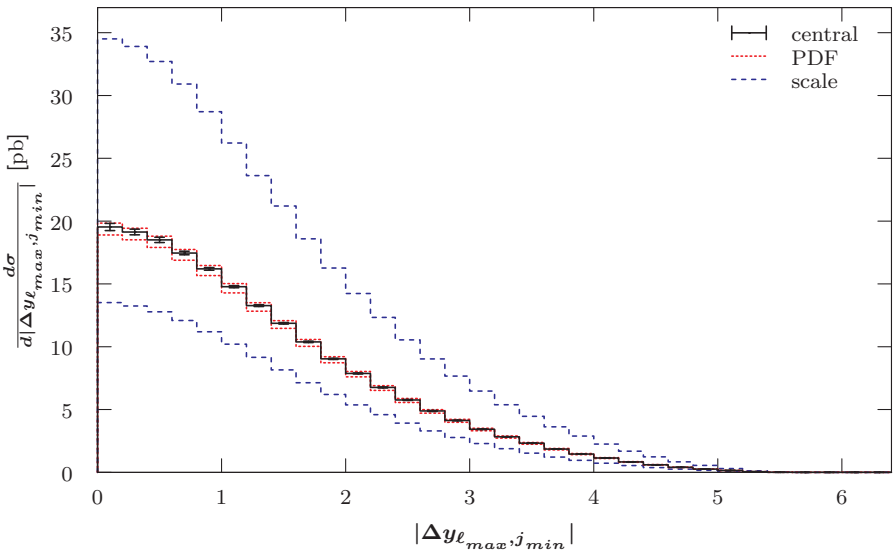

Figure 7.112: LO differential cross-section with respect to the difference in rapidity between the harder charged lepton ℓ_{max} and the softer jet j_{min} for the pp $\to$ (Z $\to \ell^-\ell^+$) + 2 *jets* process at the LHC with 7 TeV using a fixed scale of $\mu_0 = M_\text{Z}$. Additional details are given in the caption of Figure 7.77.

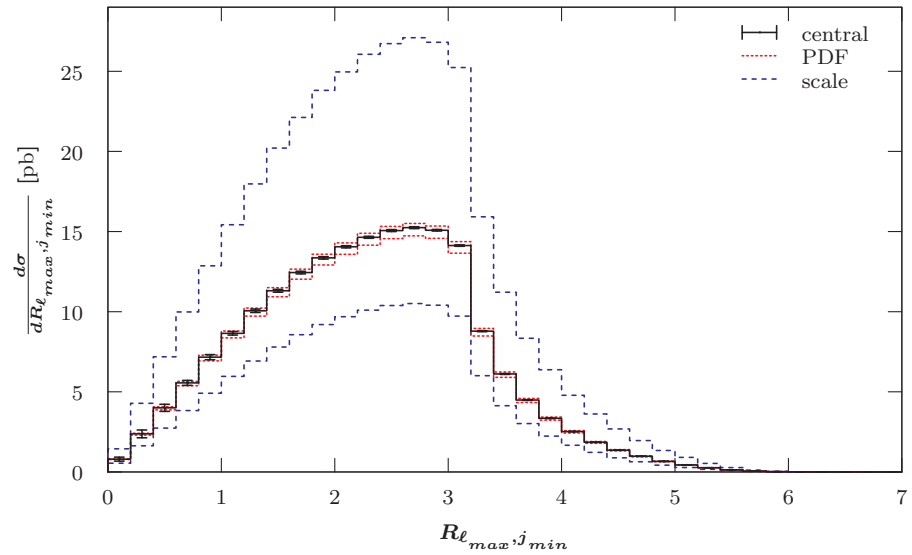

Figure 7.113: LO differential cross-section with respect to the separation between the harder charged lepton ℓ_{max} and the softer jet j_{min} for the $pp \to (Z \to \ell^-\ell^+) + 2\ jets$ process at the LHC with 7 TeV using a fixed scale of $\mu_0 = M_Z$. Additional details are given in the caption of Figure 7.77.

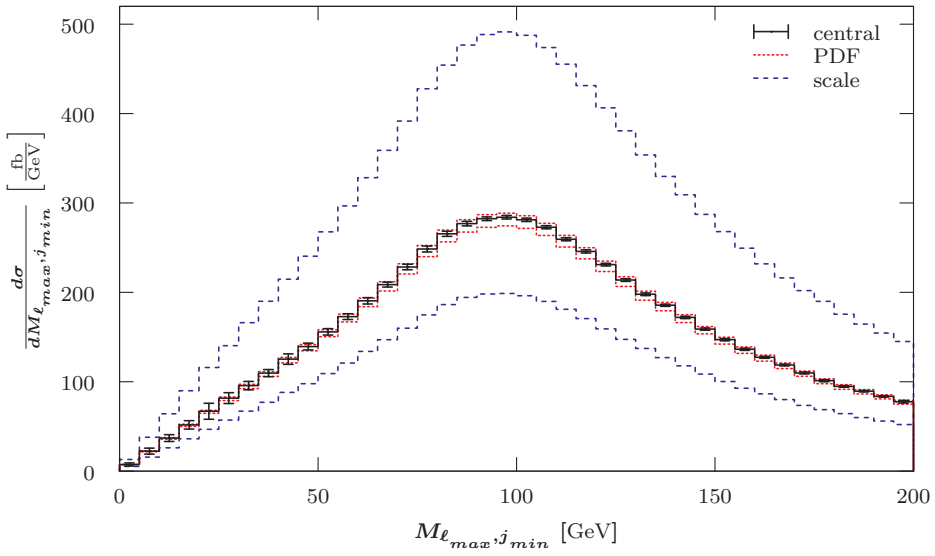

Figure 7.114: LO differential cross-section with respect to the invariant mass of the harder charged lepton ℓ_{max} and the softer jet j_{min} for the $pp \to (Z \to \ell^-\ell^+) + 2\ jets$ process at the LHC with 7 TeV using a fixed scale of $\mu_0 = M_Z$. Additional details are given in the caption of Figure 7.77.

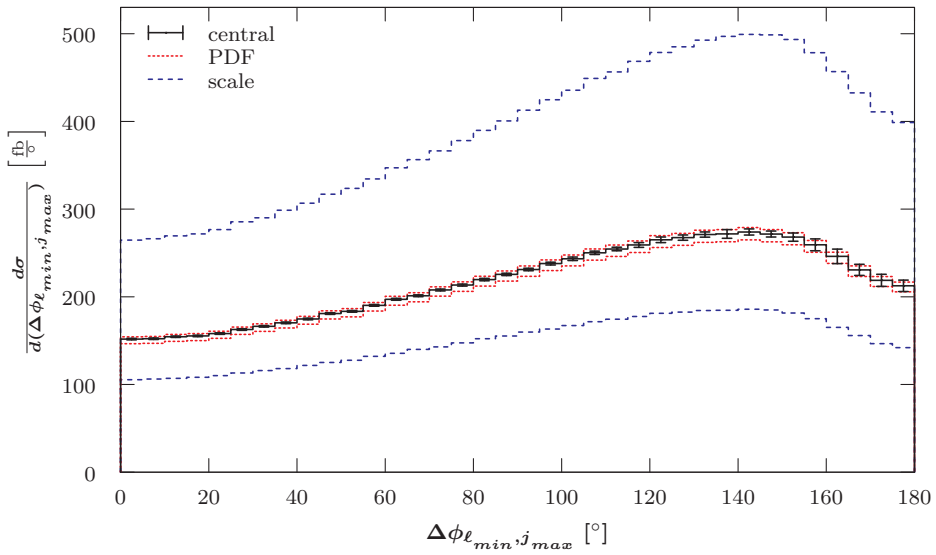

Figure 7.115: LO differential cross-section with respect to the azimuthal angle ϕ between the softer charged lepton ℓ_{min} and the harder jet j_{max} for the pp $\rightarrow$ (Z $\rightarrow \ell^-\ell^+$) + 2 *jets* process at the LHC with 7 TeV using a fixed scale of $\mu_0 = M_{\text{Z}}$. Additional details are given in the caption of Figure 7.77.

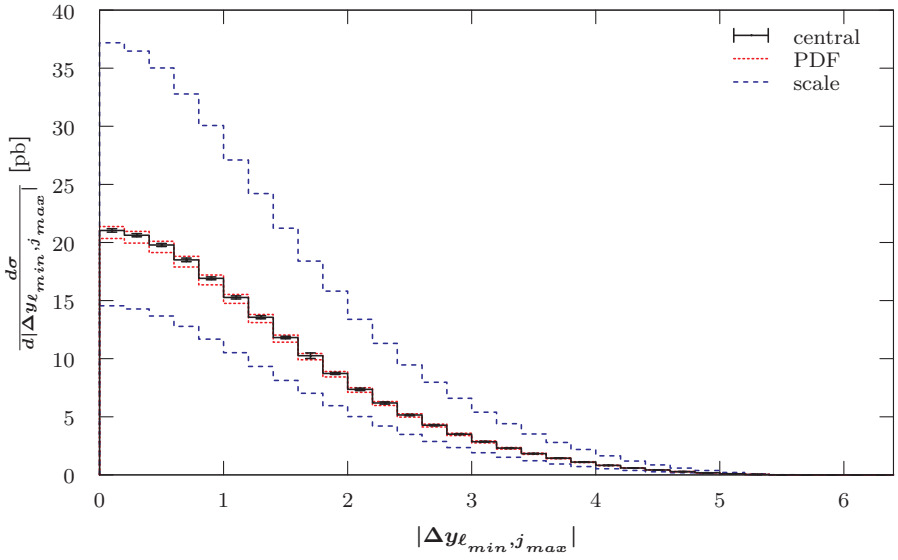

Figure 7.116: LO differential cross-section with respect to the difference in rapidity between the softer charged lepton ℓ_{min} and the harder jet j_{max} for the pp $\rightarrow$ (Z $\rightarrow \ell^-\ell^+$) + 2 *jets* process at the LHC with 7 TeV using a fixed scale of $\mu_0 = M_{\text{Z}}$. Additional details are given in the caption of Figure 7.77.

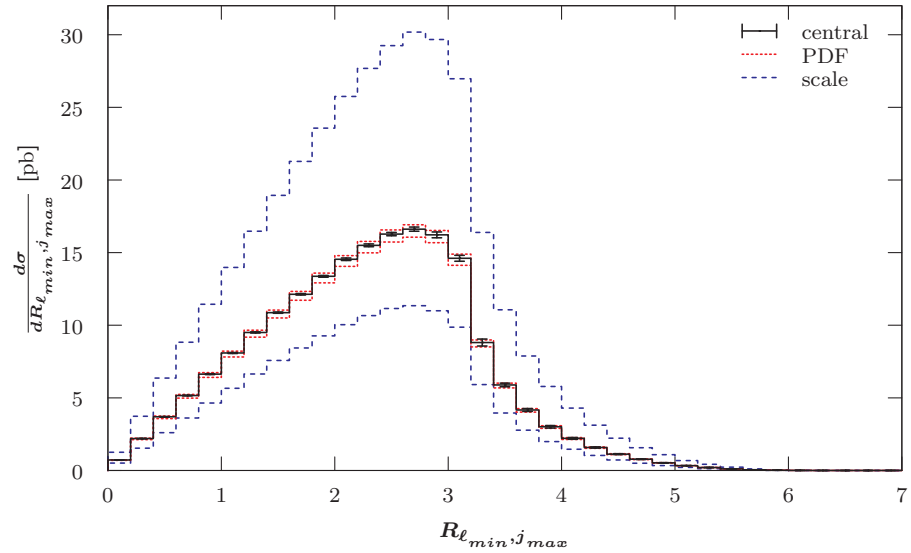

Figure 7.117: LO differential cross-section with respect to the separation between the softer charged lepton ℓ_{min} and the harder jet j_{max} for the pp $\to$ (Z $\to \ell^-\ell^+$) + 2 *jets* process at the LHC with 7 TeV using a fixed scale of $\mu_0 = M_{\mathrm{Z}}$. Additional details are given in the caption of Figure 7.77.

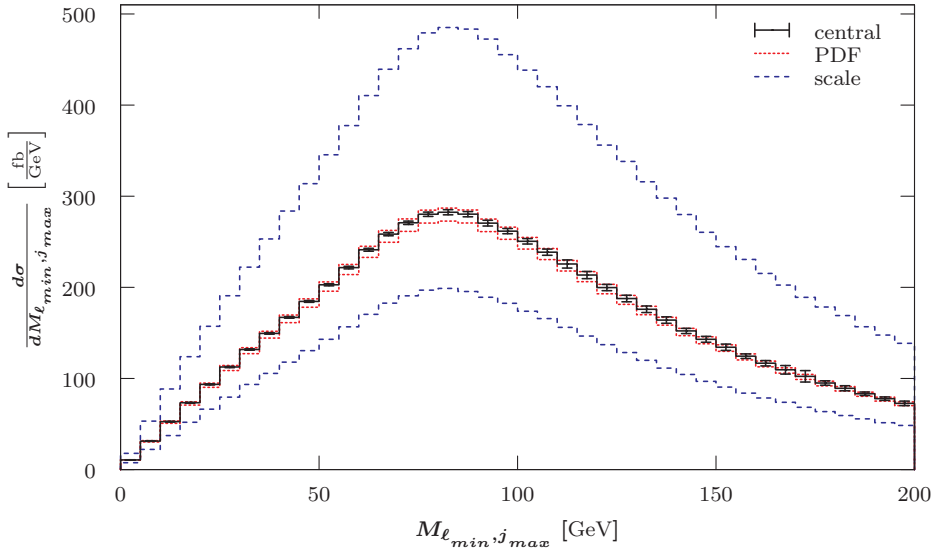

Figure 7.118: LO differential cross-section with respect to the invariant mass of the softer charged lepton ℓ_{min} and the harder jet j_{max} for the pp $\to$ (Z $\to \ell^-\ell^+$) + 2 *jets* process at the LHC with 7 TeV using a fixed scale of $\mu_0 = M_{\mathrm{Z}}$. Additional details are given in the caption of Figure 7.77.

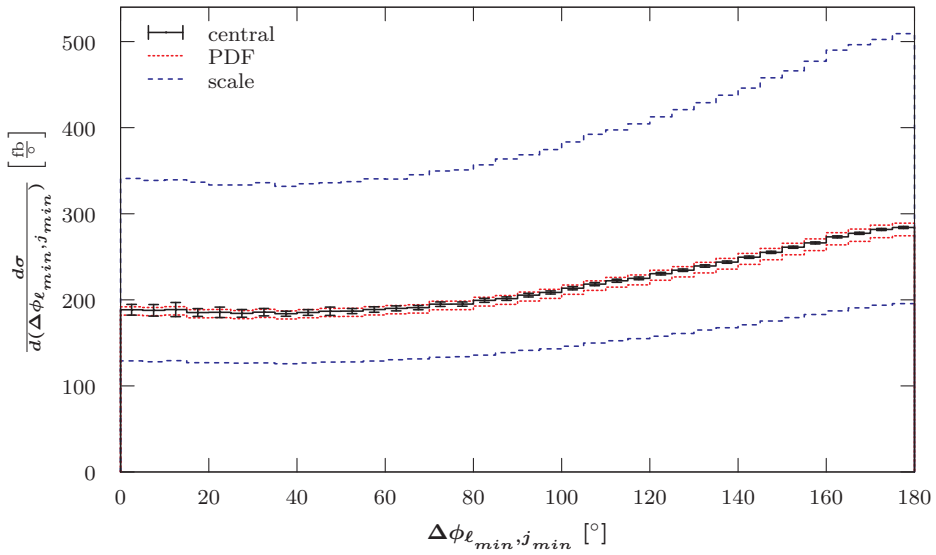

Figure 7.119: LO differential cross-section with respect to the azimuthal angle ϕ between the softer charged lepton ℓ_{min} and the softer jet j_{min} for the pp $\rightarrow$ (Z $\rightarrow \ell^-\ell^+$) + 2 *jets* process at the LHC with 7 TeV using a fixed scale of $\mu_0 = M_Z$. Additional details are given in the caption of Figure 7.77.

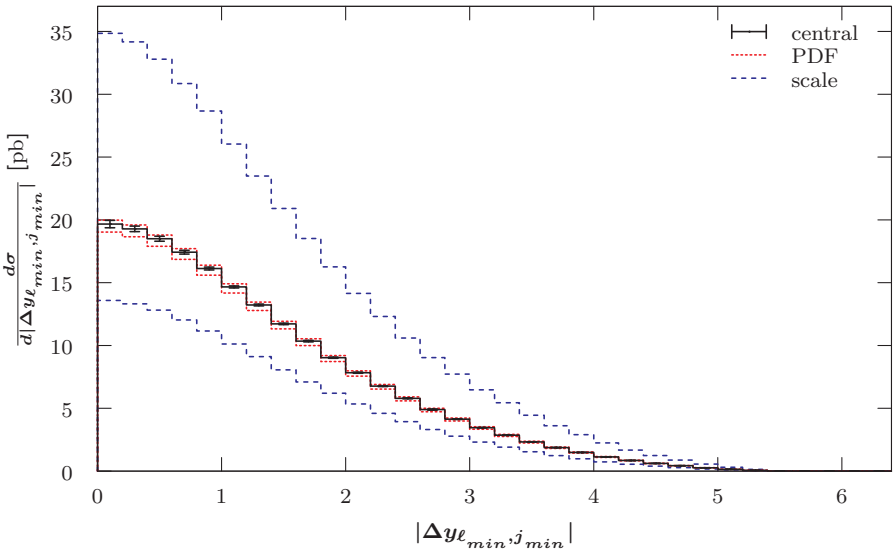

Figure 7.120: LO differential cross-section with respect to the difference in rapidity between the softer charged lepton ℓ_{min} and the softer jet j_{min} for the pp $\rightarrow$ (Z $\rightarrow \ell^-\ell^+$) + 2 *jets* process at the LHC with 7 TeV using a fixed scale of $\mu_0 = M_Z$. Additional details are given in the caption of Figure 7.77.

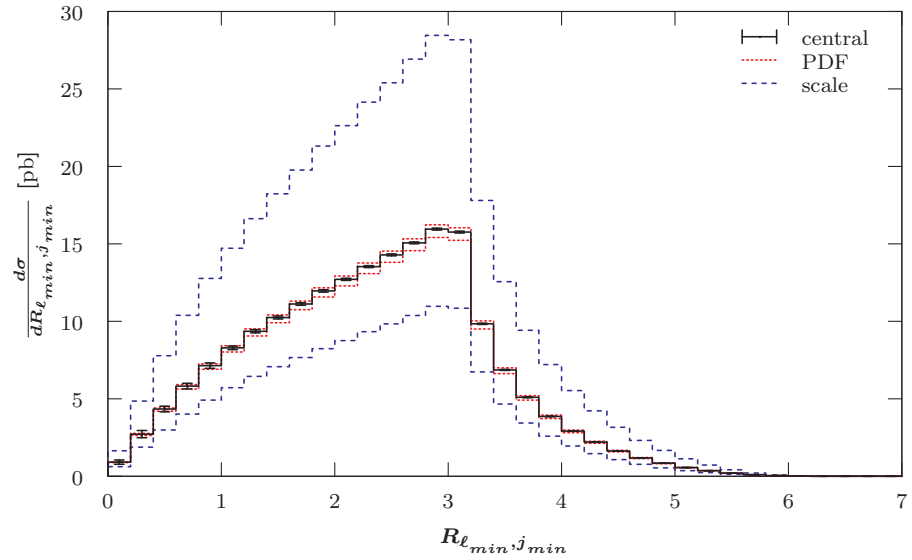

Figure 7.121: LO differential cross-section with respect to the separation between the softer charged lepton ℓ_{min} and the softer jet j_{min} for the $pp \to (Z \to \ell^-\ell^+) + 2\ jets$ process at the LHC with 7 TeV using a fixed scale of $\mu_0 = M_Z$. Additional details are given in the caption of Figure 7.77.

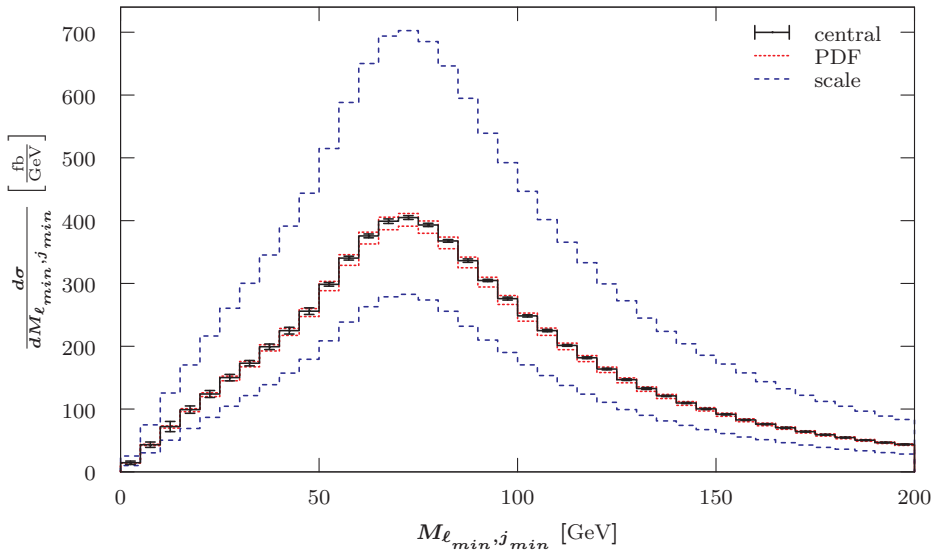

Figure 7.122: LO differential cross-section with respect to the invariant mass of the softer charged lepton ℓ_{min} and the softer jet j_{min} for the $pp \to (Z \to \ell^-\ell^+) + 2\ jets$ process at the LHC with 7 TeV using a fixed scale of $\mu_0 = M_Z$. Additional details are given in the caption of Figure 7.77.

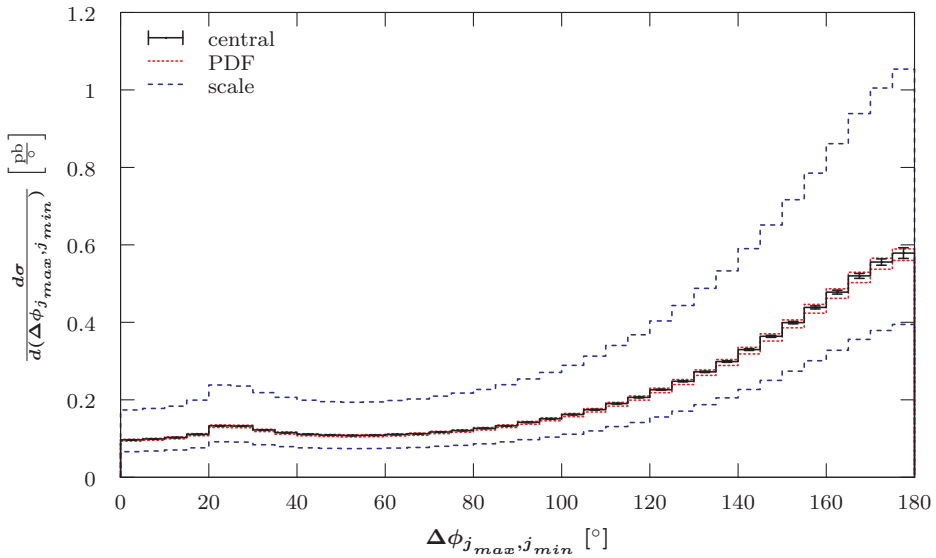

Figure 7.123: LO differential cross-section with respect to the azimuthal angle ϕ between the harder j_{max} and the softer jet j_{min} for the pp $\to$ (Z $\to \ell^-\ell^+$) + 2 *jets* process at the LHC with 7 TeV using a fixed scale of $\mu_0 = M_\text{Z}$. Additional details are given in the caption of Figure 7.77.

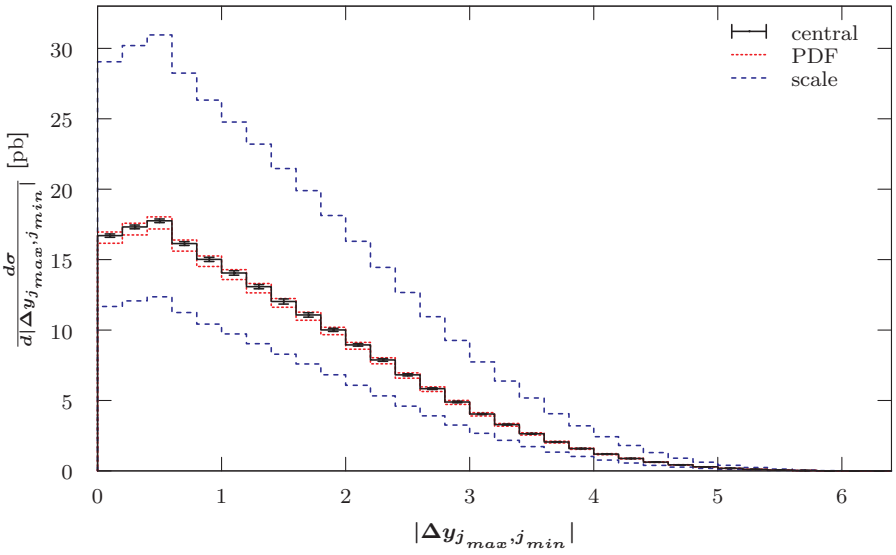

Figure 7.124: LO differential cross-section with respect to the difference in rapidity between the harder j_{max} and the softer jet j_{min} for the pp $\to$ (Z $\to \ell^-\ell^+$) + 2 *jets* process at the LHC with 7 TeV using a fixed scale of $\mu_0 = M_\text{Z}$. Additional details are given in the caption of Figure 7.77.

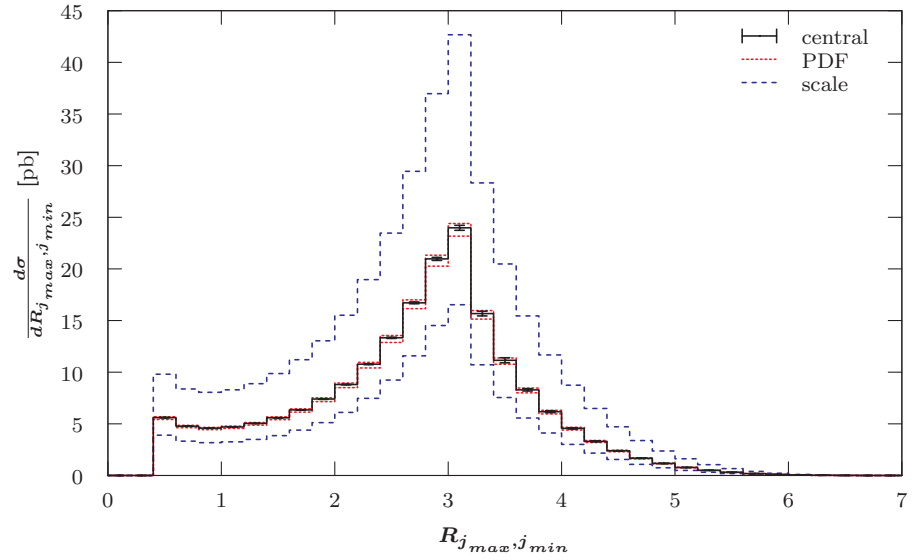

Figure 7.125: LO differential cross-section with respect to separation between the harder j_{max} and the softer j_{min} jet for the pp $\to$ (Z $\to \ell^-\ell^+$) + 2 *jets* process at the LHC with 7 TeV using a fixed scale of $\mu_0 = M_Z$. Additional details are given in the caption of Figure 7.77.

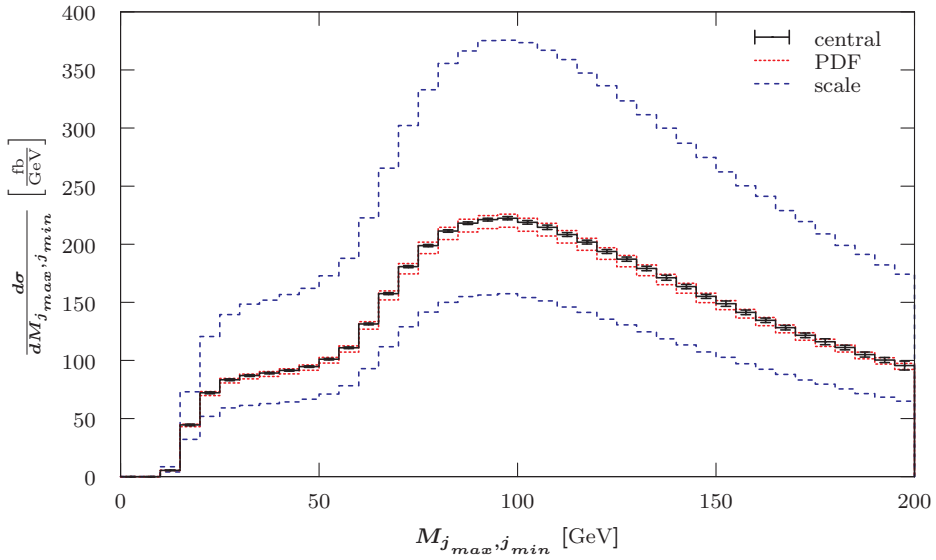

Figure 7.126: LO differential cross-section with respect to the invariant mass of the harder j_{max} and the softer j_{min} jet for the pp $\to$ (Z $\to \ell^-\ell^+$) + 2 *jets* process at the LHC with 7 TeV using a fixed scale of $\mu_0 = M_Z$. Additional details are given in the caption of Figure 7.77.

7.4.4 $p^{(}\overline{p}^{)} \to (Z \to \sum_{\ell=e,\mu,\tau} \nu_\ell \overline{\nu}_\ell) + n$ jets

The last group of processes I calculated is $p^{(}\overline{p}^{)} \to (Z \to \sum_{\ell=e,\mu,\tau} \nu_\ell \overline{\nu}_\ell) + n\ jets$. These have a poorer phenomenology, because in contrast to Z production with the decay into two charged leptons the Z production with decay into two neutrinos means that the decay products are invisible. One can only look at the differential cross-section with respect to missing transverse momentum and observables arising from the produced jets.

7.4.4.1 $p^{(}\overline{p}^{)} \to (Z \to \sum_{\ell=e,\mu,\tau} \nu_\ell \overline{\nu}_\ell)$

In this process all final state particles escape detection in the detector. Furthermore, the neutrinos are emitted back-to-back in the transverse plane, so that there is no missing momentum in the transverse plane[86].

7.4.4.2 $p^{(}\overline{p}^{)} \to (Z \to \sum_{\ell=e,\mu,\tau} \nu_\ell \overline{\nu}_\ell) + 1$ jet

For the production of the Z boson with an additional jets, the missing momentum distribution is more interesting due to final state radiation. The corresponding plot can be seen in Figure 7.127. It is a simple exponential decay starting above the missing transverse momentum cut at 30 GeV. For the dynamic scales the magnitudes and scale uncertainties behave as one expects it from the integrated cross-sections. For the other accelerators the integrals increase with the centre-of-mass energy, but the scale uncertainties are smallest for the LHC with 14 TeV. This is in stark contrast to the integrated cross-sections, but agrees with the $W^\pm$ and $Z \to \ell^+\ell^-$ histograms.

Figure 7.128 shows the transverse momentum and the rapidity distribution of the jet. The jet tends to have a large transverse momentum and to lie within the central region of the detector. For the LHC with 14 TeV the rapidity distribution is flatter and the scale uncertainties are largely suppressed (only of the order of twice the PDF uncertainties). As mentioned for the previous distribution the scale uncertainties are larger at the Tevatron and slightly decreased for the dynamic scales.[87]

[86] See Figure B.98 in Appendix B.2.4.1.
[87] See Figures B.99, B.100, B.101 and B.102 in Appendix B.2.4.2.

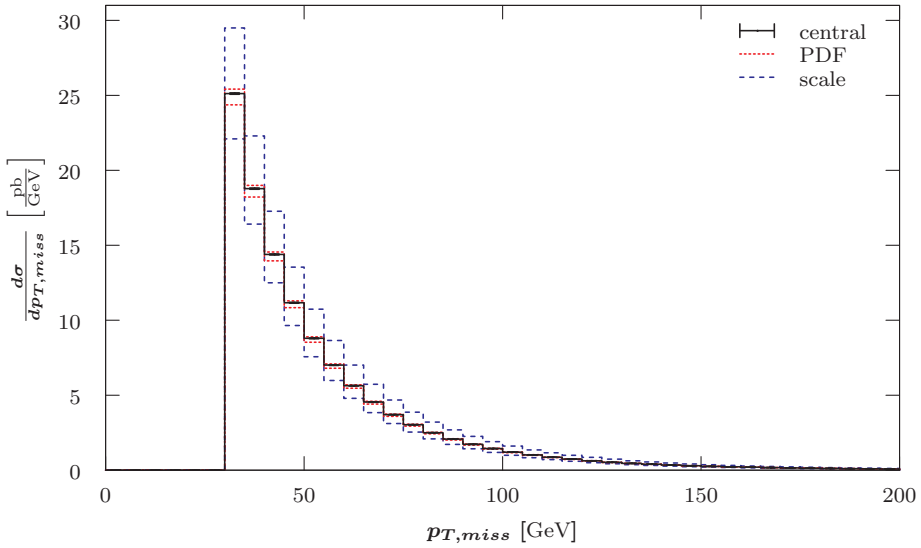

Figure 7.127: LO differential cross-section with respect to missing transverse momentum for the pp $\rightarrow$ (Z $\rightarrow \sum_{\ell=\text{e},\mu,\tau} \nu_\ell \overline{\nu}_\ell$) + 1 *jet* process at the LHC with $\sqrt{s} = 7\,\text{TeV}$ using a fixed scale of $\mu_0 = M_\text{Z}$ and MSTW2008LO (90% C.L.) PDFs. Selection cuts as given in Equations 7.5 to 7.8 have been applied. MCFM input parameters are listed in Equations 7.1 to 7.3. The procedure used to choose the number of shots is described in Section 4.4.3. The scale uncertainties have been estimated using a conservative variation by a factor of 4. The error bars for the statistical uncertainties are mostly too small to be visible or are only partially visible. Only the asymmetric deviations for the PDFs (red, dotted) and scale (blue, dashed) from the central value (black, solid) are given.

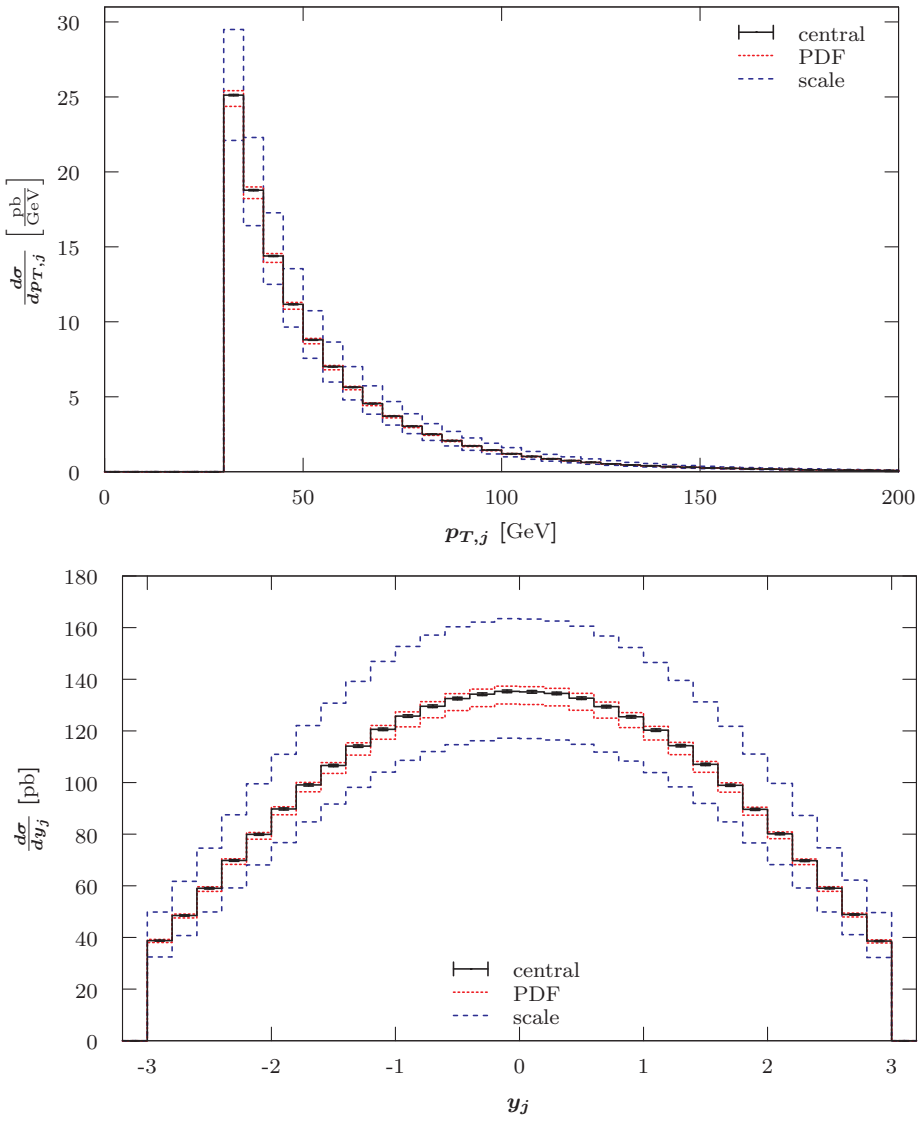

Figure 7.128: LO differential cross-section with respect to the transverse momentum (top) and the rapidity (bottom) of the jet for the pp $\to$ (Z $\to \sum \nu\bar{\nu}$)+1 *jet* process at the LHC with 7 TeV using a fixed scale of $\mu_0 = M_{\text{Z}}$. Additional details are given in the caption of Figure 7.127.

7.4.4.3 $p^{(}\overline{p}^{)} \to (Z \to \sum_{\ell=e,\mu,\tau} \nu_\ell \overline{\nu}_\ell) + 2$ jets

For the 2-jet process we are firstly looking at the missing transverse momentum in Figure 7.129. It can be seen that there is a maximum at 35 GeV and secondary local maximum at 70 GeV after which it tails off. This distribution has little experimental value, because a transverse momentum distribution for $Z \to \sum_{\ell=e,\mu,\tau} \nu_\ell \overline{\nu}_\ell$ is almost indistinguishable from the background.

The kinematic observables for the harder jet are given in Figure 7.130. The transverse momentum distribution has a maximum at 45 GeV to 50 GeV and then tails off. This distribution is more peaked for the Tevatron. The rapidity distribution reveals that the harder jet tends to be emitted in the central region of the detector. This distribution is flatter for the LHC with 14 TeV.

The corresponding plots for the softer jet are given in Figure 7.131. This jet also tends to be in the central region and it tends to have a small transverse momentum, i.e. the differential cross-section decreases towards larger momenta.

As for all 2-jet processes so far, I will look at the combinations of the two jets. Firstly, the difference in azimuthal angle between the two jets is given in Figure 7.132. There is a small local peak around 20° and a general increase towards 180°. The Tevatron distribution has a more pronounced peak and for the LHC with 14 TeV there is a steeper slope for larger angles[88].

The difference in rapidity for the two jets is given in Figure 7.133. It can be seen that the two jets prefer to lie close together. The decrease in differential cross-section towards larger angles is very linear. Furthermore, there is a local maximum at approximately 5°. This is likely an effect of the R cut.

The separation R between the two jets is given in Figure 7.134. There is a well defined peak at $R = 3$. The Tevatron has a secondary peak just above the R cut[89].

Finally, I show the invariant mass of the two jets in Figure 7.135. This distribution has a maximum at 90 GeV to 95 GeV. It is similar in shape to the corresponding $Z \to \ell^+\ell^-$ one. The Tevatron result has its maximum at 55 GeV to 60 GeV and another secondary one at 25 GeV to 30 GeV.[90]

[88] See Figures B.103 and B.104 in Appendix B.2.4.3.
[89] See Figure B.105 in Appendix B.2.4.3.
[90] See Figure B.106 in Appendix B.2.4.3.

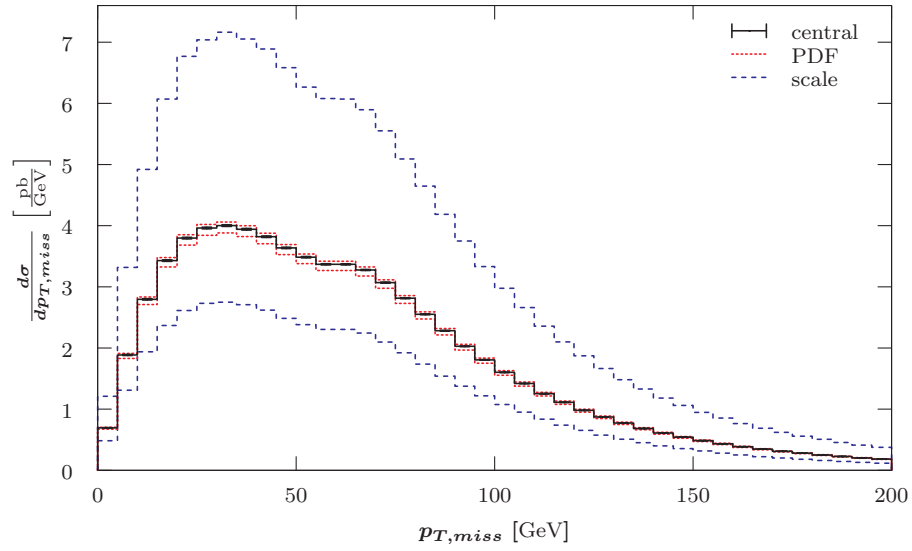

Figure 7.129: LO differential cross-section with respect to missing transverse momentum for the pp $\to$ (Z $\to \sum_{\ell=\text{e},\mu,\tau} \nu_\ell \overline{\nu}_\ell$) + 2 *jets* process at the LHC with 7 TeV using a fixed scale of $\mu_0 = M_\text{Z}$. Additional details are given in the caption of Figure 7.127.

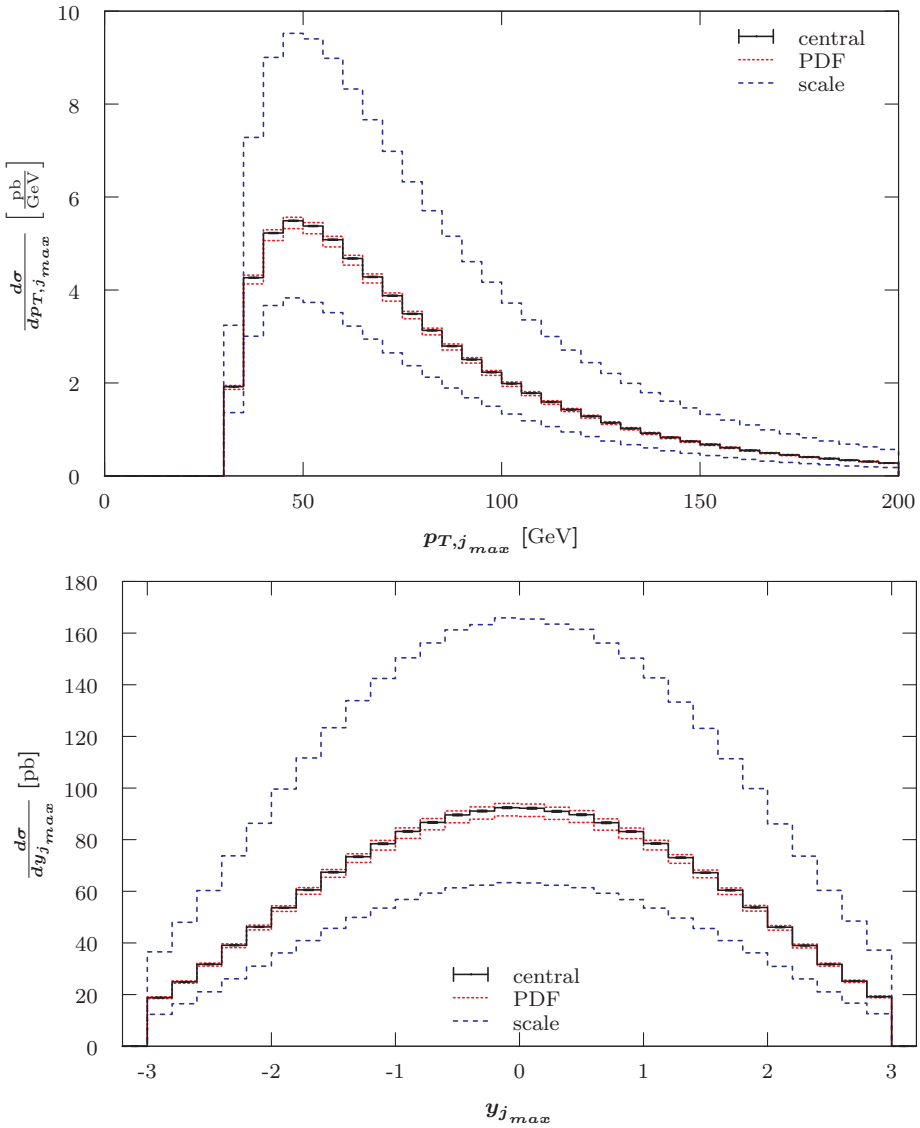

Figure 7.130: LO differential cross-section with respect to the transverse momentum (top) and the rapidity (bottom) of the harder jet j_{max} for the pp $\to$ (Z $\to \sum \nu\overline{\nu}$) + 2 *jets* process at the LHC with 7 TeV using a fixed scale of $\mu_0 = M_{\text{Z}}$. Additional details are given in the caption of Figure 7.127.

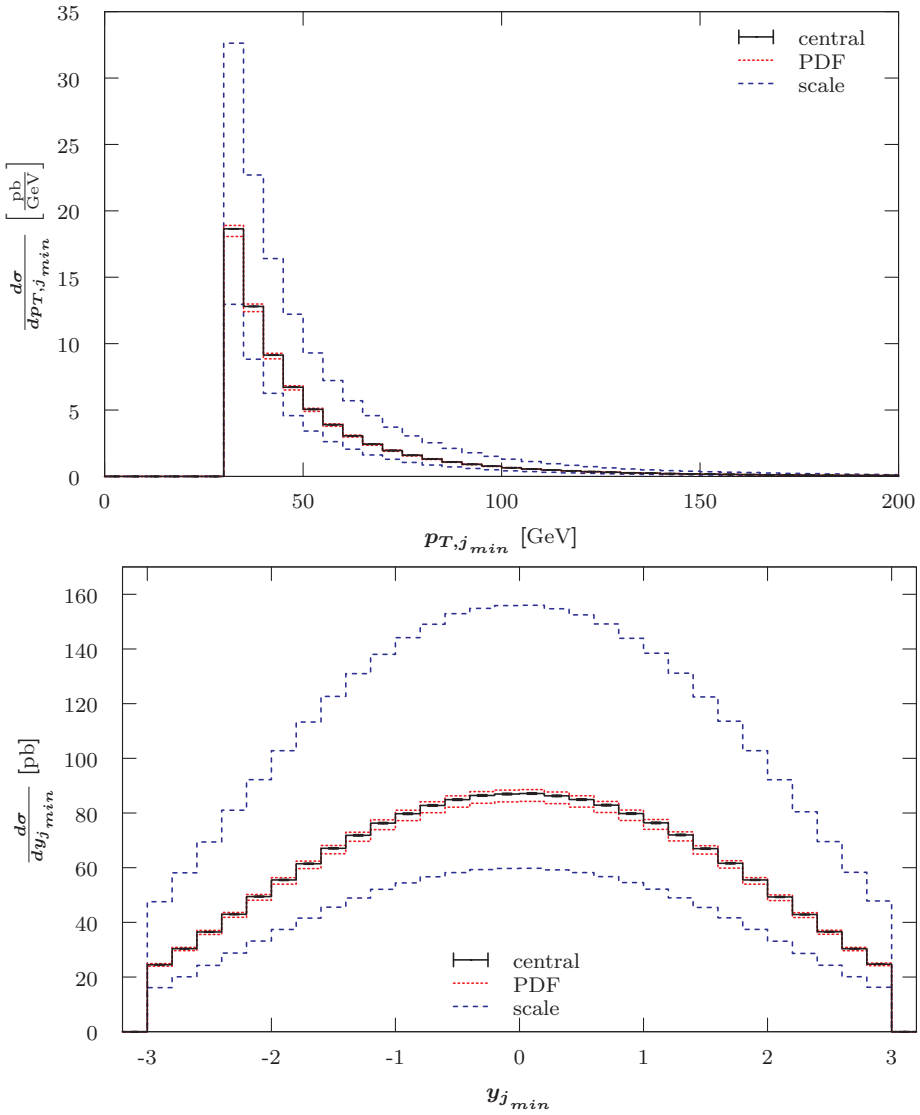

Figure 7.131: LO differential cross-section with respect to the transverse momentum (top) and the rapidity (bottom) of the softer jet j_{min} for the pp $\to$ (Z $\to \sum \nu\overline{\nu}$) + 2 *jets* process at the LHC with 7 TeV using a fixed scale of $\mu_0 = M_{\mathrm{Z}}$. Additional details are given in the caption of Figure 7.127.

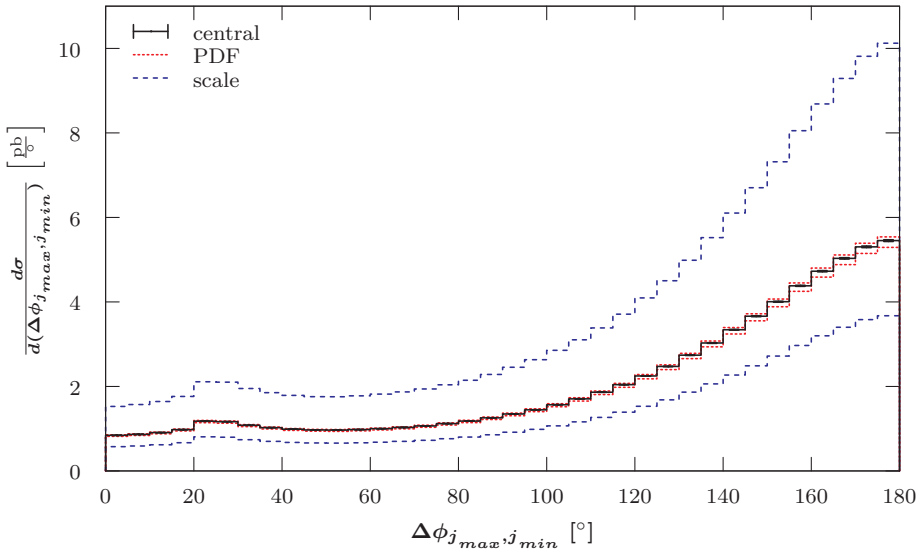

Figure 7.132: LO differential cross-section with respect to the azimuthal angle ϕ between the harder j_{max} and the softer jet j_{min} for the pp $\rightarrow$ (Z $\rightarrow \sum \nu\overline{\nu}$) + 2 *jets* process at the LHC with 7 TeV using a fixed scale of $\mu_0 = M_{\mathrm{Z}}$. Additional details are given in the caption of Figure 7.127.

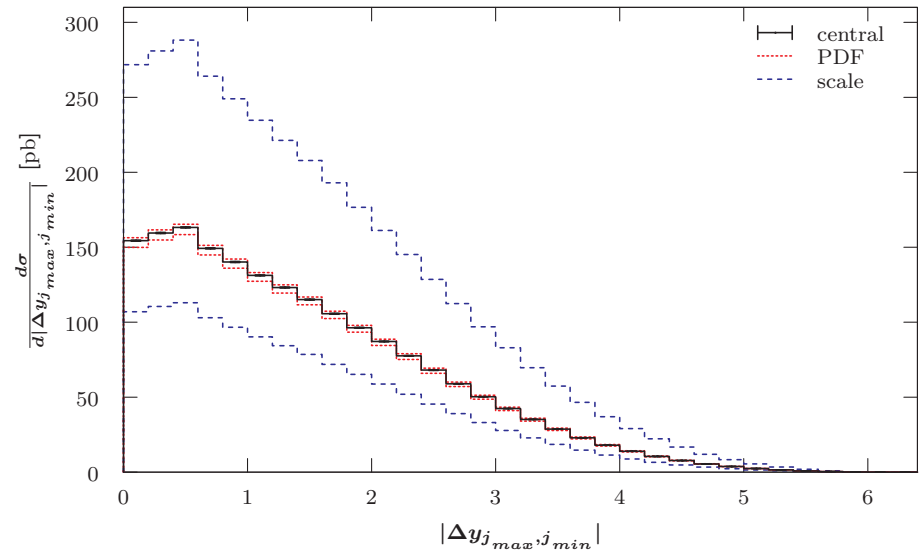

Figure 7.133: LO differential cross-section with respect to the difference in rapidity between the harder j_{max} and the softer jet j_{min} for the pp $\rightarrow$ (Z $\rightarrow \sum \nu\overline{\nu}$) + 2 *jets* process at the LHC with 7 TeV using a fixed scale of $\mu_0 = M_{\mathrm{Z}}$. Additional details are given in the caption of Figure 7.127.

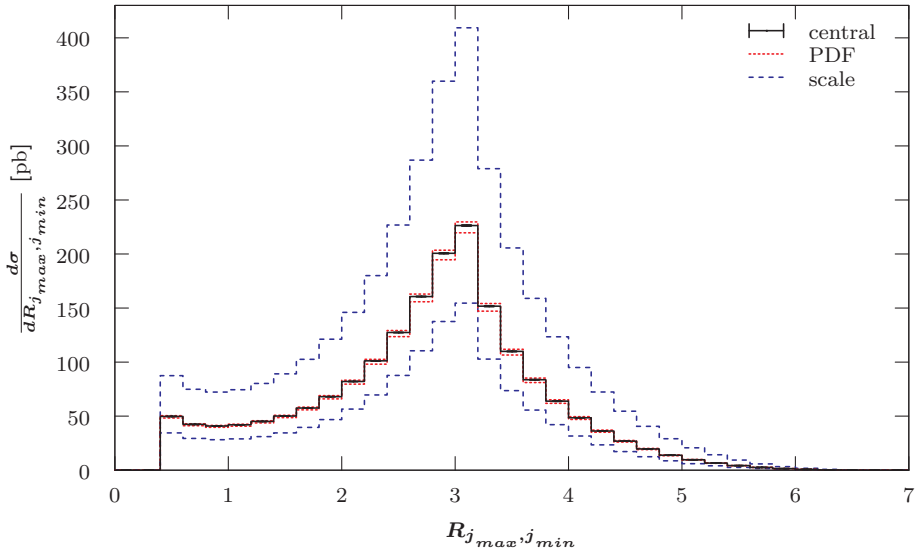

Figure 7.134: LO differential cross-section with respect to separation between the harder j_{max} and the softer j_{min} jet for the pp $\to$ (Z $\to \sum \nu\overline{\nu}$) + 2 *jets* process at the LHC with 7 TeV using a fixed scale of $\mu_0 = M_Z$. Additional details are given in the caption of Figure 7.127.

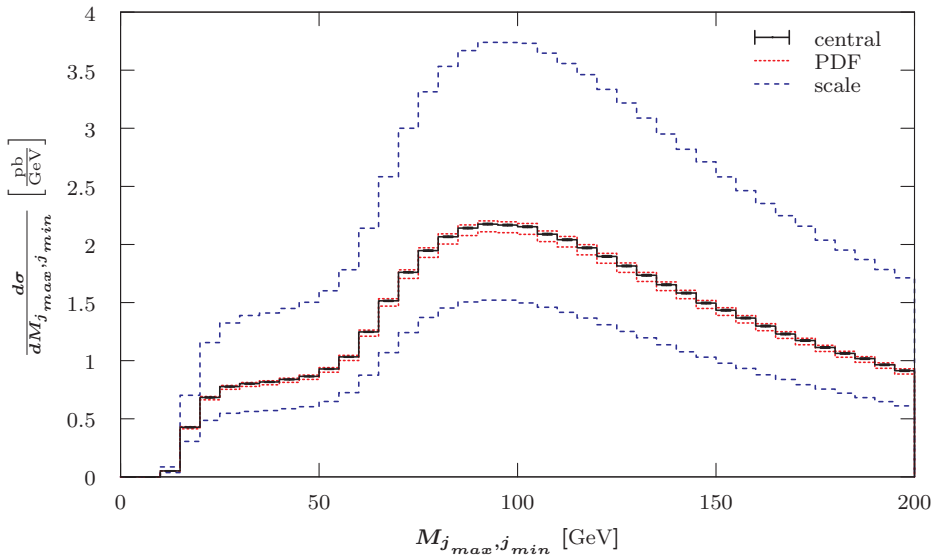

Figure 7.135: LO differential cross-section with respect to the inavaraitn mass of the harder j_{max} and the softer j_{min} jet for the pp $\to$ (Z $\to \sum \nu\overline{\nu}$) + 2 *jets* process at the LHC with 7 TeV using a fixed scale of $\mu_0 = M_Z$. Additional details are given in the caption of Figure 7.127.

Chapter 8

Physics Discussion

Production processes for vector bosons have one of the larger integrated cross-sections at hadron colliders. [17] Hence, they are both a good candidate for benchmark tests of the SM and one of the main sources of backgrounds in searches for NP. Therefore a precise knowledge of the magnitude of the integrated cross-sections and the associated uncertainties is crucial.

Testing of the SM can be achieved using observables comparing integrated cross-sections. I will present the ratios for W^+ and W^- production with leptonic decay (Section 8.1), the ratios between Z production with decay into charged leptons and neutrinos (Section 8.2) and the Berends-Giele scalings (Section 8.3). Ratios are generally more stable with respect to systematic uncertainties. For example hadron colliders suffer from relatively large luminosity uncertainties, which are suppressed in such ratios.

Next, I will give comparisons for a wide range of differential cross-sections, because in searches where weak boson production is a background, the shapes of the differential cross-sections are of particular importance. Concentrating on the LHC with 7 TeV I will study the variation of PDF and scale uncertainties over the range of the differential cross-sections to predict the behaviour of the total cross-sections with respect to changes in the selection cuts (Section 8.4). I will point out when selection cuts can be optimised by avoiding integration over regions with large uncertainties and regions where large uncertainties can provide issues for NP searches.

Finally, I will present differences between static and dynamic scales in Section 8.5; and I will discuss the impact of the two different PDF sets in Section 8.6.

8.1 Ratios between W^+ and W^- Production with Leptonic Decay

A very important phenomenological observable is the ratio between the W^+ and W^- production:

$$\begin{aligned} R_W &= \frac{\sigma^+}{\sigma^-} = \frac{\sigma(p^{(}\overline{p}^{)} \to W^+ + n\ jets)}{\sigma(p^{(}\overline{p}^{)} \to W^- + n\ jets)} \\ &= \frac{\sigma(p^{(}\overline{p}^{)} \to W^+ + n\ jets) \cdot BR(W^+ \to \ell^+\nu_\ell)}{\sigma(p^{(}\overline{p}^{)} \to W^- + n\ jets) \cdot BR(W^- \to \ell^-\overline{\nu}_\ell)} \\ &= \frac{\sigma(p^{(}\overline{p}^{)} \to (W^+ \to \ell^+\nu_\ell) + n\ jets)}{\sigma(p^{(}\overline{p}^{)} \to (W^- \to \ell^-\overline{\nu}_\ell) + n\ jets)} \end{aligned} \tag{8.1}$$

For quark-antiquark initial states W^+ bosons are produced from an up-type quark and a down-type anti-quark, and W^- from a down-type quark and an up-type antiquark. At Tevatron protons (2u and 1d) collide with antiprotons ($2\overline{u}$ and $1\overline{d}$). The PDFs for u/d in protons and $\overline{u}/\overline{d}$ in antiprotons are the same. Hence, for symmetry reasons[1] we expect this ratio to be equal to exactly 1 at Tevatron. In contrast, the LHC ratio should be larger than 1 due to the integrated net charge in the initial state. The two protons in the initial state provide four up quarks and two down quarks. Integrating the respective PDFs shows that there are more (positively charged) up quarks available in the initial state, making W^+ production more likely.

Moreover, there are mutual sources of uncertainties for the W^+ and W^- production. Particularly, experimental uncertainties in luminosity can be suppressed using the $W^\pm$ production ratio. Similarly, theoretical PDF and scale uncertainties can be treated in a way which minimises them.

Hence, this observable is ideal for testing SM predictions and deviations from it. In fact, Kom and Stirling [52] have provided a derived observable f_{NP} which compares experimental results with the theoretical calculations and gives an easy to use indicator for the presence of NP. Their observable allows for the detection of weakly interacting neutral particles (e.g. Z′) or processes which produce W^+ and W^- in equal amounts as this will shift the ratio R_W. It is defined as following:

$$\begin{aligned} f_{NP} = \frac{\sigma_{NP}}{\sigma_{SM}} &= \frac{2\left(\frac{\sigma^+_{SM}}{\sigma^-_{SM}} - \frac{\sigma^+_{SM}+\sigma^+_{NP}}{\sigma^-_{SM}+\sigma^-_{NP}}\right)}{\left(\frac{\sigma^+_{SM}}{\sigma^-_{SM}} + 1\right)\left(\frac{\sigma^+_{SM}+\sigma^+_{NP}}{\sigma^-_{SM}+\sigma^-_{NP}} - 1\right)} \\ &= \frac{2\,(R_{SM} - R_{exp})}{(R_{SM}+1)\,(R_{exp}-1)} \end{aligned} \tag{8.2}$$

where we used the sum of the W^+ and W^- SM prediction $\sigma_{SM} = \sigma^+_{SM} + \sigma^-_{SM}$, the NP cross-

[1] Similar arguments are true for initial states with gluons.

section $^1/_2\sigma_{NP} = \sigma^+_{NP} = \sigma^-_{NP}$ and the experimental measurements $\sigma^\pm_{exp} = \sigma^\pm_{SM} + \sigma^\pm_{NP}$.

In Table 8.1 I present all the ratios between the integrated cross-sections for $W^\pm$ production with leptonic decay for three different scales and the MSTW2008LO (90% C.L.) PDF set. Both, symmetric and asymmetric, PDF and scale uncertainties have been calculated. A standard error propagation has been done for the symmetric uncertainties $\Delta\sigma^+$ and $\Delta\sigma^-$ of the integrated cross-section of W^+ bosons σ^+ and W^- bosons σ^-, respectively:

$$\left(\frac{\Delta R}{R}\right)^2 = \left(\frac{\Delta\sigma^+}{\sigma^+}\right)^2 + \left(\frac{\Delta\sigma^-}{\sigma^-}\right)^2 - 2\rho\cdot\left(\frac{\Delta\sigma^+}{\sigma^+}\right)\left(\frac{\Delta\sigma^-}{\sigma^-}\right) \tag{8.3}$$

with the correlation efficient $\rho = 0$, i.e. I assume that the errors are not correlated[2]. I have not investigated the correlation for different PDFs and scales, as they can be very different for the investigated processes and accelerators. For example, the PDF uncertainties at the Tevatron[3] for $W^\pm$ are very correlated as they integrate over the same initial state, but at the LHC the contributions from the PDFs for W^- and W^+ production are very different, as can be seen in the rapidity distributions.

PDFs are based on experimental measurements using the Hessian method to determine their uncertainties. This means that they tend to be Gaussian. However, the same is not true for the scale uncertainties, because they are an approximation for the higher-order terms of the perturbation theory, i.e. for LO these depend on the strong scaling which decreases exponentially with respect to energy. Hence, the asymmetric uncertainties are probably a much better representation of the actual behaviour. I have defined the asymmetric error, $\Delta R_{max,min}$, of the ratio R to be:

$$\begin{aligned} R + \Delta R_{max} &= \frac{\sigma^+ + \Delta\sigma^+_{max}}{\sigma^- - \Delta\sigma^-_{min}} \\ R - \Delta R_{min} &= \frac{\sigma^+ - \Delta\sigma^+_{min}}{\sigma^- + \Delta\sigma^-_{max}} \end{aligned} \tag{8.4}$$

where the integrated cross-section for W^+ bosons is donated as σ^+ and for W^- as σ^-. The associated asymmetric errors are $\Delta\sigma^+_{max,min}$ and $\Delta\sigma^-_{max,min}$, respectively. This gives the widest spread and probably the safest option without estimating a likelihood function

[2]The uncertainties can be positively ($\rho > 0$) or a negatively ($\rho < 0$) correlated, which decreases or increases the uncertainty, respectively.

[3]For comparative reasons I have used the same calculation for the uncertainties at the Tevatron and the LHC. At the Tevatron we have $\sigma^+ \simeq \sigma^-$ and $\Delta\sigma^+ \simeq \Delta\sigma^-$ suggesting a strong correlation of $\rho = 1$. Using Equation 8.3 would give $^{\Delta R}/_R = 0$

for each cross-section[4].

One can observe that the ratios are very stable with respect to different static and dynamic scale choices. For zero and one jet process, the variation is of the order of the statistical error (i.e. less than 0.1%) at the LHC. For the two jet process at the LHC the ratio is up to 1% smaller for the two dynamic scales. At the Tevatron all the ratios are equal to 1 as expected. At the LHC the ratio depends on the centre-of-mass energy and the number of jets. It decreases with respect to the former and increases with respect to the latter. For the LHC with 14 TeV we have $1.26 < R_{\mathrm{W}} < 1.42$ and for the LHC with 7 TeV we have $1.46 < R_{\mathrm{W}} < 1.70$.

The increase of the ratio with respect to additional jets can be explained by the different rapidity distributions for the final state lepton. From the differential distributions presented in Section 7.4.1, it can be seen that the lepton tends to be emitted in the forward/backward direction of the detector for W^+ production. In contrast, final state leptons for W^- production are generally in the central region of the detector as it can be seen in Section 7.4.2. For both bosons, however, the emitted lepton is emitted more centrally for two associated jets than one jet and it is least central for no jets. Therefore, less phasespace is cut out for W^+ production with multiple jets in contrast to zero jet events, i.e. the nominator increases relative to the denominator for one and two jet events.

The associated symmetric scale uncertainties, however, are much larger. They are largest for processes with two associated jets and static scales ranging between 241% for the static scale at the Tevatron and 104% for the $\hat{H}_T$ scale at the LHC with 14 TeV. For the Tevatron they are approximately 80% for 1-jet events and less than 10% when jets are absent. At the LHC the 0-jets processes have a larger scale uncertainty (approx. 50% for 7 TeV and 80% for 14 TeV) than the 1-jet processes (approx. 43% for 7 TeV and 20% for 14 TeV). There is a general trend of errors becoming smaller when using dynamic scales.

The asymmetric scale uncertainties, however, are probably a better representation as they are directly related to the maximal and minimal scale variations calculated. They are also more stable and similar in magnitude to the scale uncertainties obtained for the integrated cross-sections. One can see that zero-jet processes at the Tevatron have a scale variation of less than 7%, increasing for one-jet (approx. 45%) and two-jet events (up to

[4]A narrower spread can be found using:

$$\begin{aligned} R + \Delta R_{max} &= \max\left[\frac{\sigma^+ + \Delta\sigma^+_{max}}{\sigma^- + \Delta\sigma^-_{max}}, \frac{\sigma^+ - \Delta\sigma^+_{min}}{\sigma^- - \Delta\sigma^-_{min}}\right] \\ R - \Delta R_{min} &= \min\left[\frac{\sigma^+ + \Delta\sigma^+_{max}}{\sigma^- + \Delta\sigma^-_{max}}, \frac{\sigma^+ - \Delta\sigma^+_{min}}{\sigma^- - \Delta\sigma^-_{min}}\right] \end{aligned} \tag{8.5}$$

For the Tevatron, $\sigma^+ \simeq \sigma^-$, $\Delta\sigma^+_{max} \simeq \Delta\sigma^-_{max}$ and $\Delta\sigma^+_{min} \simeq \Delta\sigma^-_{min}$, which makes both these asymmetric uncertainties zero. This is, however, not true for Equation 8.4 used in the main text.

107%). For the LHC the asymmetric scale uncertainties are smallest for one-jet events at larger energies, i.e. approx. 13%. These uncertainties are almost twice as large at the LHC with 7 TeV. The energy dependence is reverted for zero-jet events: approx. 41% for 14 TeV and 30% for 7 TeV. The two-jet processes have by far the largest uncertainties ranging from -51% for the dynamic scale $\hat{H}_T$ at the LHC with 14 TeV to +82% for the static scale at the LHC with 7 TeV.

The symmetric PDF uncertainties are between 6% and 8% and largest for zero jet processes. Asymmetric PDF uncertainties are generally smaller (down to 4%). There is a very small decrease of these errors for multi-jet events.

A comparison of my results with Kom and Stirling [52] shows that their use of different input parameters and cuts means that R_{W} values are different by as much as 15%. For both the LHC with 7 TeV and 14 TeV, ratios are higher for weak boson production with associated jets and lower for no associated jets. My cross-sections for zero jets use a cut on the missing transverse momentum, which reduces my available phase space. However, for events with associated jets I accept jets with larger rapidities and smaller transverse momentum. This gives me larger cross-sections especially for W^- production making the denominator relatively bigger.

It is worth noting that Kom and Stirling only present results for the dynamic scale $\hat{H}_T$, but they found that the ratio R_{W} tends to be smaller by only 5% for NLO in comparison to LO.

Table 8.1: Ratio R_{W} between the integrated cross-sections of $(\mathrm{W}^+ \to \ell^+\nu_\ell) + n\ jets$ and $(\mathrm{W}^- \to \ell^-\overline{\nu}_\ell) + n\ jets$ at all three accelerators using the MSTW2008LO (90% C.L.) PDFs and three different scale choices. Selection cuts as given in Equations 7.5 to 7.8 have been applied. MCFM input parameters are listed in Equations 7.1 to 7.3. The procedure used to choose the number of shots is described in Section 4.4.3. The scale uncertainties have been estimated using a conservative variation by a factor of 4. The statistical uncertainties are listed using bracket notation. The asymmetric (superscript and subscript) as well as the symmetric deviations (square brackets) for the PDFs and scale (scl) are recorded as relative errors rounded up to the nearest percent. Errors are propagated using Equations 8.3 and 8.4.

$R_{\mathrm{W}} = \frac{\sigma(\mathrm{p}^{(}\overline{\mathrm{p}}^{)} \to (\mathrm{W}^+ \to \ell^+\nu_\ell) + n\ jets)}{\sigma(\mathrm{p}^{(}\overline{\mathrm{p}}^{)} \to (\mathrm{W}^- \to \ell^-\overline{\nu}_\ell) + n\ jets)}$		$\mu_0 = M_V$			$\mu_0 = E_T^V$			$\mu_0 = \hat{H}_T$		
		R	ΔR_{pdf}	ΔR_{scl}	R	ΔR_{pdf}	ΔR_{scl}	R	ΔR_{pdf}	ΔR_{scl}
LHC @ 14 TeV	0 *jets*	1.263(1)	$^{+5}_{-7}[\pm 7]\%$	$^{+38}_{-44}[\pm 79]\%$	1.263(1)	$^{+5}_{-7}[\pm 7]\%$	$^{+38}_{-44}[\pm 79]\%$	1.262(1)	$^{+5}_{-7}[\pm 7]\%$	$^{+39}_{-45}[\pm 82]\%$
	1 *jet*	1.343(1)	$^{+4}_{-6}[\pm 6]\%$	$^{+12}_{-15}[\pm 18]\%$	1.341(1)	$^{+4}_{-5}[\pm 6]\%$	$^{+12}_{-16}[\pm 19]\%$	1.341(1)	$^{+4}_{-5}[\pm 6]\%$	$^{+13}_{-17}[\pm 20]\%$
	2 *jets*	1.419(1)	$^{+4}_{-5}[\pm 6]\%$	$^{+64}_{-56}[\pm 125]\%$	1.414(1)	$^{+4}_{-5}[\pm 6]\%$	$^{+61}_{-54}[\pm 117]\%$	1.411(1)	$^{+4}_{-5}[\pm 6]\%$	$^{+55}_{-51}[\pm 104]\%$
LHC @ 7 TeV	0 *jets*	1.458(1)	$^{+4}_{-6}[\pm 7]\%$	$^{+27}_{-33}[\pm 50]\%$	1.458(1)	$^{+4}_{-6}[\pm 7]\%$	$^{+27}_{-33}[\pm 50]\%$	1.456(1)	$^{+4}_{-6}[\pm 7]\%$	$^{+28}_{-34}[\pm 52]\%$
	1 *jet*	1.587(1)	$^{+4}_{-5}[\pm 6]\%$	$^{+25}_{-29}[\pm 41]\%$	1.586(1)	$^{+4}_{-5}[\pm 6]\%$	$^{+25}_{-29}[\pm 46]\%$	1.586(1)	$^{+4}_{-5}[\pm 6]\%$	$^{+25}_{-29}[\pm 40]\%$
	2 *jets*	1.693(1)	$^{+4}_{-6}[\pm 7]\%$	$^{+82}_{-63}[\pm 170]\%$	1.686(1)	$^{+4}_{-6}[\pm 7]\%$	$^{+78}_{-62}[\pm 159]\%$	1.686(1)	$^{+4}_{-6}[\pm 7]\%$	$^{+69}_{-58}[\pm 137]\%$
Tevatron Run II	0 *jets*	1.000(1)	$^{+5}_{-7}[\pm 8]\%$	$^{+5}_{-7}[\pm 7]\%$	1.000(1)	$^{+5}_{-7}[\pm 8]\%$	$^{+5}_{-7}[\pm 7]\%$	1.000(1)	$^{+5}_{-7}[\pm 8]\%$	$^{+5}_{-7}[\pm 8]\%$
	1 *jet*	1.000(1)	$^{+5}_{-6}[\pm 7]\%$	$^{+47}_{-46}[\pm 83]\%$	1.000(1)	$^{+5}_{-6}[\pm 7]\%$	$^{+46}_{-45}[\pm 81]\%$	1.000(1)	$^{+5}_{-6}[\pm 7]\%$	$^{+44}_{-44}[\pm 77]\%$
	2 *jets*	1.001(1)	$^{+5}_{-6}[\pm 7]\%$	$^{+107}_{-71}[\pm 241]\%$	1.001(1)	$^{+5}_{-6}[\pm 7]\%$	$^{+102}_{-70}[\pm 226]\%$	1.001(1)	$^{+5}_{-6}[\pm 7]\%$	$^{+91}_{-66}[\pm 194]\%$

8.2 Ratios between Z Production with Decay into Charged Leptons and Neutrinos

For the production of Z bosons, the ratio between the cross-sections of two decay channels integrated over the whole phase space is equal to the ratio between the respective decay widths. The branching ratios of the Z boson are well known. From Particle Data Group [48]:

$$BR(\mathrm{Z} \to \ell^-\ell^+) = (3.3658 \pm 0.0023)\% \qquad BR(\mathrm{Z} \to \sum_\ell \nu_\ell\overline{\nu}_\ell) = (20.00 \pm 0.06)\% \quad (8.6)$$

And therefore:

$$\begin{aligned} R_\mathrm{Z} &= \frac{\Gamma(\mathrm{Z} \to \ell^-\ell^+)}{\Gamma(\mathrm{Z} \to \sum_\ell \nu_\ell\overline{\nu}_\ell)} = \frac{\Gamma(\mathrm{Z} \to \ell^-\ell^+)}{\Gamma(\mathrm{Z})} \cdot \frac{\Gamma(\mathrm{Z})}{\Gamma(\mathrm{Z} \to \sum_\ell \nu_\ell\overline{\nu}_\ell)} \\ &= \frac{BR(\mathrm{Z} \to \ell^-\ell^+)}{BR(\mathrm{Z} \to \sum_\ell \nu_\ell\overline{\nu}_\ell)} \\ &= 0.16829 \pm 0.00052 \end{aligned} \quad (8.7)$$

This observable is identical to the ratio between the integrated cross-section of Z production with decay into charged leptons and decay into neutrinos:

$$\begin{aligned} R_\mathrm{Z} &= \frac{\sigma(\mathrm{p}^{(}\overline{\mathrm{p}}^{)} \to (\mathrm{Z} \to \ell^-\ell^+) + n\ jets)}{\sigma(\mathrm{p}^{(}\overline{\mathrm{p}}^{)} \to (\mathrm{Z} \to \sum_\ell \nu_\ell\overline{\nu}_\ell) + n\ jets)} \\ &= \frac{\sigma(\mathrm{p}^{(}\overline{\mathrm{p}}^{)} \to \mathrm{Z} + n\ jets) \cdot BR(\mathrm{Z} \to \ell^-\ell^+)}{\sigma(\mathrm{p}^{(}\overline{\mathrm{p}}^{)} \to \mathrm{Z} + n\ jets) \cdot BR(\mathrm{Z} \to \sum_\ell \nu_\ell\overline{\nu}_\ell)} \\ &= \frac{BR(\mathrm{Z} \to \ell^-\ell^+)}{BR(\mathrm{Z} \to \sum_\ell \nu_\ell\overline{\nu}_\ell)} \end{aligned} \quad (8.8)$$

The ratios for different scale choices and accelerators are recorded in Table 8.2. They have been calculated using the integrated cross-sections for MSTW2008LO (90% C.L.) It can be seen that all ratios are smaller than the expected R_Z. There are no selection cuts applied during the calculation of the $\mathrm{Z} \to \sum_\ell \nu_\ell\overline{\nu}_\ell$ process. However, a large portion of the populated phase space is cut out for the $\mathrm{Z} \to \ell^-\ell^+$ process by the applied rapidity, transverse momentum and invariant mass[5] cut. This makes the calculated cross-section smaller, which subsequently decreases R_Z. Moreover we can see that $R_\mathrm{Z}(0\ jet) < R_\mathrm{Z}(1\ jets) < R_\mathrm{Z}(2\ jets)$, which suggests that the emission of jets makes events with charged lepton decay more central.

The symmetric and asymmetric PDF as well as scale uncertainties have been calculated as described in the previous section. The behaviour and magnitude of the PDF

[5]The invariant mass cut, cuts out the photon singularity.

and scale uncertainties is almost identical to the ratio between the cross-sections for W^+ and W^- processes from Section 8.1.

Practically, these ratios can only be determined, by measuring both the width of the decay into charged leptons and the hadronic decay. Subtracting both from the total width of the Z boson, one obtains the width for decay into neutrinos. [53]

Table 8.2: Ratio R_Z between the integrated cross-sections of $(Z \to \ell^-\ell^+) + n\ jets$ and $(Z \to \sum_\ell \nu_\ell\overline{\nu}_\ell) + n\ jets$ at all three accelerators using the MSTW2008LO (90% C.L.) PDFs and three different scale choices. Selection cuts as given in Equations 7.5 to 7.8 have been applied. MCFM input parameters are listed in Equations 7.1 to 7.3. The procedure used to choose the number of shots is described in Section 4.4.3. The scale uncertainties have been estimated using a conservative variation by a factor of 4. The statistical uncertainties are listed using bracket notation. The asymmetric (superscript and subscript) as well as the symmetric deviations (square brackets) for the PDFs and scale (scl) are recorded as relative errors rounded up to the nearest percent. Errors are propagated using Equations 8.3 and 8.4.

$R_Z = \frac{\sigma(p^{(}\overline{p}^{)} \to (Z \to \ell^-\ell^+) + n\ jets)}{\sigma(p^{(}\overline{p}^{)} \to (Z \to \sum_\ell \nu_\ell\overline{\nu}_\ell) + n\ jets)}$		$\mu_0 = M_V$			$\mu_0 = E_T^V$			$\mu_0 = \hat{H}_T$		
		R	ΔR_{pdf}	ΔR_{scl}	R	ΔR_{pdf}	ΔR_{scl}	R	ΔR_{pdf}	ΔR_{scl}
LHC @ 14 TeV	0 *jets*	0.075(1)	$^{+4}_{-7}[\pm7]\%$	$^{+36}_{-43}[\pm70]\%$	0.075(1)	$^{+4}_{-7}[\pm7]\%$	$^{+36}_{-43}[\pm70]\%$	0.077(1)	$^{+5}_{-7}[\pm7]\%$	$^{+39}_{-45}[\pm80]\%$
	1 *jet*	0.089(1)	$^{+4}_{-5}[\pm6]\%$	$^{+12}_{-16}[\pm18]\%$	0.089(1)	$^{+4}_{-5}[\pm5]\%$	$^{+12}_{-16}[\pm18]\%$	0.089(1)	$^{+4}_{-5}[\pm5]\%$	$^{+13}_{-17}[\pm19]\%$
	2 *jets*	0.091(1)	$^{+4}_{-5}[\pm5]\%$	$^{+63}_{-56}[\pm121]\%$	0.091(1)	$^{+4}_{-5}[\pm5]\%$	$^{+60}_{-54}[\pm114]\%$	0.090(1)	$^{+4}_{-5}[\pm5]\%$	$^{+56}_{-52}[\pm103]\%$
LHC @ 7 TeV	0 *jets*	0.089(1)	$^{+4}_{-6}[\pm6]\%$	$^{+25}_{-31}[\pm43]\%$	0.089(1)	$^{+4}_{-6}[\pm6]\%$	$^{+25}_{-31}[\pm43]\%$	0.091(1)	$^{+4}_{-6}[\pm6]\%$	$^{+27}_{-34}[\pm50]\%$
	1 *jet*	0.099(1)	$^{+3}_{-5}[\pm5]\%$	$^{+25}_{-30}[\pm41]\%$	0.099(1)	$^{+3}_{-5}[\pm5]\%$	$^{+25}_{-29}[\pm40]\%$	0.099(1)	$^{+3}_{-5}[\pm5]\%$	$^{+25}_{-29}[\pm40]\%$
	2 *jets*	0.104(1)	$^{+4}_{-5}[\pm5]\%$	$^{+80}_{-63}[\pm165]\%$	0.103(1)	$^{+4}_{-5}[\pm5]\%$	$^{+77}_{-62}[\pm155]\%$	0.103(1)	$^{+4}_{-5}[\pm5]\%$	$^{+69}_{-58}[\pm136]\%$
Tevatron Run II	0 *jets*	0.035(1)	$^{+5}_{-7}[\pm7]\%$	$^{+3}_{-5}[\pm2]\%$	0.035(1)	$^{+5}_{-7}[\pm7]\%$	$^{+3}_{-5}[\pm2]\%$	0.034(1)	$^{+5}_{-7}[\pm7]\%$	$^{+3}_{-5}[\pm4]\%$
	1 *jet*	0.043(1)	$^{+4}_{-6}[\pm6]\%$	$^{+47}_{-47}[\pm84]\%$	0.043(1)	$^{+4}_{-6}[\pm6]\%$	$^{+46}_{-46}[\pm82]\%$	0.041(1)	$^{+4}_{-6}[\pm6]\%$	$^{+45}_{-45}[\pm79]\%$
	2 *jets*	0.048(1)	$^{+5}_{-6}[\pm7]\%$	$^{+105}_{-71}[\pm235]\%$	0.047(1)	$^{+5}_{-6}[\pm7]\%$	$^{+101}_{-70}[\pm221]\%$	0.046(1)	$^{+5}_{-6}[\pm7]\%$	$^{+91}_{-67}[\pm194]\%$

8.3 Berends-Giele Scaling

Berends et al. [54] have introduced the Berends-Giele scaling as an important phenomelogical observable for NP at hadron colliders. It has been and still is used to estimate these background processes quickly. I am using the following definition:

$$f(V,n,m) = \frac{\sigma(\mathrm{p}^{(}\overline{\mathrm{p}}^{)} \to V + n\ jets)}{\sigma(\mathrm{p}^{(}\overline{\mathrm{p}}^{)} \to V + m\ jets)} \tag{8.9}$$

The matrix element for one additional jet has an additional strong vertex. Hence, we expect the ratio between n jet events and $(n+1)$ jets events to be approximately equal to the strong coupling constant. This approximation ignores the reduced phase space in the final state as well as relative contributions due to different initial states, i.e. quark-antiquark, quark-gluon or gluon-gluon.

Table 8.3 shows the Berends-Giele scaling for the Tevatron using different scales and the MSTW2008LO (90% C.L.) PDF set, which uses a 1-loop evolution of the strong coupling constant of $\alpha_s(M_\mathrm{Z}) = 0.118$. The calculated ratios between one and zero-jet processes are surprisingly close to the coupling constant when using the static scale, e.g. 0.120 for $\mathrm{Z} \to \sum_\ell \nu_\ell \overline{\nu}_\ell$ and 0.110 for both W boson processes. In contrast, I obtained $f = 0.150$ for $\mathrm{Z} \to \sum \ell^+\ell^-$. Due to the the applied selection cuts, we are looking at the more central part of the detector. Therefore, we can conclude that the 1-jet process is more aligned with the transverse plane. The results for the E_T^V scale are approximately 4% smaller and for the $\hat{H}_T$ approximately 10% smaller.

The scaling for the two and one-jet processes are substantially larger. For the static scale they are 0.400 for W processes, 0.409 for $\mathrm{Z} \to \ell^+\ell^-$ and 0.365 for $\mathrm{Z} \to \sum_\ell \nu_\ell \overline{\nu}_\ell$. Using E_T^V and $\hat{H}_T$, the scaling drops by 8% and 20%, respectively.

An important observation is that the variation between the scaling for W^+ production and W^- production is less than the statistical error, i.e. they are identical. The same does not hold true for the Z boson processes. The Berends-Giele scaling for Z production with decay into charged leptons is generally larger.

The symmetric PDF uncertainties are 7% and the symmetric scale uncertainties are less than 52% for the 1/0-jets ratio and less than 174% for 2/1-jets ratio. Dynamic scales generally give smaller uncertainties. The asymmetric uncertainties are approximately half of the symmetric uncertainties.

Table 8.4 shows the corresponding results for the LHC with 7 TeV. Straight away one can observe that the scaling for W^+ and W^- are not identical anymore. The W^+ scaling is the larger one. For example the ratio between 1-jet production and 0-jet production is 0.114 for W^+ and 0.105 for W^-. Again, these numbers decrease for the E_T^V and $\hat{H}_T$ scales by approximately 4% and 10%, respectively. For the 2/1-scaling I calculated 0.745 and 0.698, with an approximate decrease of 8% and 20%.

For the Z production we get 1/0-ratio of 0.146 for decay into charged leptons and 0.130 for decay into neutrinos. The 2/1-ratios are 0.661 (charged leptons) and 0.632 (neutrinos). As in the Tevatron case, one can see that the $Z \to \ell^+\ell^-$ is slightly more central.

One can also see that the symmetric PDF uncertainties have slightly decreased (5%-7%). For the 1/0-ratio, the symmetric scale uncertainties are slightly larger (up to 61%) and for the 2/1-ratio the scale uncertainties are smaller (down to 94%). The asymmetric scale uncertainties are approximately half of the symmetric uncertainties.

All the scalings increase with an increase in centre-of-mass energy. The results for the LHC with 14 TeV are recorded in Table 8.5. The increase is in the order of 20-30% for all the scalings. While the scale uncertainties for the 1/0-scaling have hardly changed, one can observe a decrease in symmetric scale uncertainties where the 2/1-ratio is down to 79% or less. There has been no significant change in the PDF uncertainties.

Table 8.3: Berends-Giele scaling $f(V, n, m)$, given by the ratio between the integrated cross-sections of $V + n$ *jets* and $V + m$ *jets*, at the Tevatron Run II using the MSTW2008LO (90% C.L.) PDFs and three different scale choices. Selection cuts as given in Equations 7.5 to 7.8 have been applied. MCFM input parameters are listed in Equations 7.1 to 7.3. The procedure used to choose the number of shots is described in Section 4.4.3. The scale uncertainties have been estimated using a conservative variation by a factor of 4. The statistical uncertainties are listed using bracket notation. The asymmetric (superscript and subscript) as well as the symmetric deviations (square brackets) for the PDFs and scale (scl) are recorded as relative errors rounded up to the nearest percent. Errors are propagated using Equations 8.3 and 8.4.

Tevatron Run II:	$\mu_0 = M_V$			$\mu_0 = E_T^V$			$\mu_0 = \hat{H}_T$		
$f =$	f	Δf_{pdf}	Δf_{scl}	f	Δf_{pdf}	Δf_{scl}	f	Δf_{pdf}	Δf_{scl}
$\frac{\sigma_{LO}(p\bar{p}\to(W^+\to\ell^+\nu_\ell)+1\ jet)}{\sigma_{LO}(p\bar{p}\to(W^+\to\ell^+\nu_\ell))}$	0.1099(1)	$^{+5}_{-7}[\pm7]\%$	$^{+33}_{-23}[\pm52]\%$	0.1066(1)	$^{+5}_{-7}[\pm7]\%$	$^{+32}_{-22}[\pm51]\%$	0.1001(1)	$^{+5}_{-7}[\pm7]\%$	$^{+31}_{-22}[\pm50]\%$
$\frac{\sigma_{LO}(p\bar{p}\to(W^+\to\ell^+\nu_\ell)+2\ jets)}{\sigma_{LO}(p\bar{p}\to(W^+\to\ell^+\nu_\ell)+1\ jet)}$	0.4004(2)	$^{+5}_{-6}[\pm7]\%$	$^{+83}_{-57}[\pm171]\%$	0.3748(2)	$^{+5}_{-6}[\pm7]\%$	$^{+79}_{-56}[\pm162]\%$	0.3074(2)	$^{+5}_{-6}[\pm7]\%$	$^{+71}_{-54}[\pm143]\%$
$\frac{\sigma_{LO}(p\bar{p}\to(W^-\to\ell^-\bar{\nu}_\ell)+1\ jet)}{\sigma_{LO}(p\bar{p}\to(W^-\to\ell^-\bar{\nu}_\ell))}$	0.1098(1)	$^{+5}_{-7}[\pm7]\%$	$^{+33}_{-23}[\pm52]\%$	0.1066(1)	$^{+5}_{-7}[\pm7]\%$	$^{+32}_{-22}[\pm51]\%$	0.1001(1)	$^{+5}_{-7}[\pm7]\%$	$^{+31}_{-22}[\pm50]\%$
$\frac{\sigma_{LO}(p\bar{p}\to(W^-\to\ell^-\bar{\nu}_\ell)+2\ jets)}{\sigma_{LO}(p\bar{p}\to(W^-\to\ell^-\bar{\nu}_\ell)+1\ jet)}$	0.4003(2)	$^{+5}_{-6}[\pm7]\%$	$^{+83}_{-57}[\pm171]\%$	0.3745(2)	$^{+5}_{-6}[\pm7]\%$	$^{+79}_{-56}[\pm161]\%$	0.3073(2)	$^{+5}_{-6}[\pm7]\%$	$^{+71}_{-54}[\pm143]\%$
$\frac{\sigma_{LO}(p\bar{p}\to(Z\to\ell^-\ell^+)+1\ jet)}{\sigma_{LO}(p\bar{p}\to(Z\to\ell^-\ell^+))}$	0.1495(1)	$^{+5}_{-7}[\pm7]\%$	$^{+33}_{-22}[\pm50]\%$	0.1453(1)	$^{+5}_{-7}[\pm7]\%$	$^{+32}_{-22}[\pm49]\%$	0.1370(1)	$^{+5}_{-7}[\pm7]\%$	$^{+31}_{-21}[\pm47]\%$
$\frac{\sigma_{LO}(p\bar{p}\to(Z\to\ell^-\ell^+)+2\ jets)}{\sigma_{LO}(p\bar{p}\to(Z\to\ell^-\ell^+)+1\ jet)}$	0.4086(2)	$^{+5}_{-6}[\pm7]\%$	$^{+80}_{-56}[\pm164]\%$	0.3820(2)	$^{+5}_{-6}[\pm7]\%$	$^{+77}_{-55}[\pm156]\%$	0.3197(2)	$^{+5}_{-6}[\pm7]\%$	$^{+70}_{-53}[\pm139]\%$
$\frac{\sigma_{LO}(p\bar{p}\to(Z\to\sum_{\ell=e,\mu,\tau}\nu_\ell\bar{\nu}_\ell)+1\ jet)}{\sigma_{LO}(p\bar{p}\to(Z\to\sum_{\ell=e,\mu,\tau}\nu_\ell\bar{\nu}_\ell))}$	0.1200(1)	$^{+4}_{-6}[\pm7]\%$	$^{+35}_{-23}[\pm49]\%$	0.1170(1)	$^{+4}_{-6}[\pm7]\%$	$^{+34}_{-22}[\pm48]\%$	0.1140(1)	$^{+4}_{-6}[\pm7]\%$	$^{+33}_{-22}[\pm48]\%$
$\frac{\sigma_{LO}(p\bar{p}\to(Z\to\sum_{\ell=e,\mu,\tau}\nu_\ell\bar{\nu}_\ell)+2\ jets)}{\sigma_{LO}(p\bar{p}\to(Z\to\sum_{\ell=e,\mu,\tau}\nu_\ell\bar{\nu}_\ell)+1\ jet)}$	0.3654(1)	$^{+4}_{-6}[\pm7]\%$	$^{+83}_{-58}[\pm174]\%$	0.3455(1)	$^{+4}_{-6}[\pm7]\%$	$^{+81}_{-57}[\pm166]\%$	0.2887(1)	$^{+4}_{-6}[\pm7]\%$	$^{+74}_{-56}[\pm152]\%$

Table 8.4: Berends-Giele scaling $f(V,n,m)$, given by the ratio between the integrated cross-sections of $V+n$ *jets* and $V+m$ *jets*, at the LHC with 7 TeV using the MSTW2008LO (90% C.L.) PDFs and three different scale choices. See caption of Table 8.3 for applied selection cuts, MCFM input parameters and description of the uncertainties.

LHC with 7 TeV:	$\mu_0 = M_V$			$\mu_0 = E_T^V$			$\mu_0 = \hat{H}_T$		
$f =$	f	Δf_{pdf}	Δf_{scl}	f	Δf_{pdf}	Δf_{scl}	f	Δf_{pdf}	Δf_{scl}
$\frac{\sigma_{LO}(\mathrm{pp}\to(\mathrm{W}^+\to\ell^+\nu_\ell)+1\ jet)}{\sigma_{LO}(\mathrm{pp}\to(\mathrm{W}^+\to\ell^+\nu_\ell))}$	0.1139(1)	$^{+4}_{-6}[\pm6]\%$	$^{+26}_{-25}[\pm59]\%$	0.1101(1)	$^{+4}_{-6}[\pm6]\%$	$^{+26}_{-24}[\pm65]\%$	0.1060(1)	$^{+4}_{-6}[\pm6]\%$	$^{+26}_{-25}[\pm60]\%$
$\frac{\sigma_{LO}(\mathrm{pp}\to(\mathrm{W}^+\to\ell^+\nu_\ell)+2\ jets)}{\sigma_{LO}(\mathrm{pp}\to(\mathrm{W}^+\to\ell^+\nu_\ell)+1\ jet)}$	0.7448(3)	$^{+4}_{-5}[\pm6]\%$	$^{+61}_{-45}[\pm112]\%$	0.6901(3)	$^{+4}_{-5}[\pm6]\%$	$^{+58}_{-46}[\pm106]\%$	0.5493(2)	$^{+4}_{-5}[\pm6]\%$	$^{+52}_{-42}[\pm94]\%$
$\frac{\sigma_{LO}(\mathrm{pp}\to(\mathrm{W}^-\to\ell^-\overline{\nu}_\ell)+1\ jet)}{\sigma_{LO}(\mathrm{pp}\to(\mathrm{W}^-\to\ell^-\overline{\nu}_\ell))}$	0.1046(1)	$^{+4}_{-6}[\pm6]\%$	$^{+26}_{-25}[\pm60]\%$	0.1012(1)	$^{+4}_{-6}[\pm6]\%$	$^{+26}_{-25}[\pm59]\%$	0.0973(1)	$^{+4}_{-6}[\pm6]\%$	$^{+27}_{-25}[\pm61]\%$
$\frac{\sigma_{LO}(\mathrm{pp}\to(\mathrm{W}^-\to\ell^-\overline{\nu}_\ell)+2\ jets)}{\sigma_{LO}(\mathrm{pp}\to(\mathrm{W}^-\to\ell^-\overline{\nu}_\ell)+1\ jet)}$	0.6981(4)	$^{+4}_{-6}[\pm7]\%$	$^{+61}_{-45}[\pm113]\%$	0.6492(4)	$^{+4}_{-6}[\pm7]\%$	$^{+58}_{-44}[\pm106]\%$	0.5169(3)	$^{+4}_{-6}[\pm7]\%$	$^{+52}_{-42}[\pm95]\%$
$\frac{\sigma_{LO}(\mathrm{pp}\to(\mathrm{Z}\to\ell^-\ell^+)+1\ jet)}{\sigma_{LO}(\mathrm{pp}\to(\mathrm{Z}\to\ell^-\ell^+))}$	0.1459(1)	$^{+4}_{-6}[\pm5]\%$	$^{+25}_{-24}[\pm57]\%$	0.1418(1)	$^{+4}_{-6}[\pm5]\%$	$^{+25}_{-24}[\pm56]\%$	0.1402(1)	$^{+4}_{-6}[\pm5]\%$	$^{+26}_{-25}[\pm59]\%$
$\frac{\sigma_{LO}(\mathrm{pp}\to(\mathrm{Z}\to\ell^-\ell^+)+2\ jets)}{\sigma_{LO}(\mathrm{pp}\to(\mathrm{Z}\to\ell^-\ell^+)+1\ jet)}$	0.6606(3)	$^{+4}_{-5}[\pm6]\%$	$^{+59}_{-44}[\pm108]\%$	0.6149(3)	$^{+4}_{-5}[\pm6]\%$	$^{+56}_{-43}[\pm102]\%$	0.5003(2)	$^{+4}_{-5}[\pm6]\%$	$^{+51}_{-41}[\pm92]\%$
$\frac{\sigma_{LO}(\mathrm{pp}\to(\mathrm{Z}\to\sum_{\ell=\mathrm{e},\mu,\tau}\nu_\ell\overline{\nu}_\ell)+1\ jet)}{\sigma_{LO}(\mathrm{pp}\to(\mathrm{Z}\to\sum_{\ell=\mathrm{e},\mu,\tau}\nu_\ell\overline{\nu}_\ell))}$	0.1304(1)	$^{+3}_{-5}[\pm5]\%$	$^{+25}_{-24}[\pm54]\%$	0.1268(1)	$^{+3}_{-5}[\pm5]\%$	$^{+25}_{-23}[\pm54]\%$	0.1296(1)	$^{+4}_{-5}[\pm5]\%$	$^{+26}_{-24}[\pm59]\%$
$\frac{\sigma_{LO}(\mathrm{pp}\to(\mathrm{Z}\to\sum_{\ell=\mathrm{e},\mu,\tau}\nu_\ell\overline{\nu}_\ell)+2\ jets)}{\sigma_{LO}(\mathrm{pp}\to(\mathrm{Z}\to\sum_{\ell=\mathrm{e},\mu,\tau}\nu_\ell\overline{\nu}_\ell)+1\ jet)}$	0.6315(2)	$^{+3}_{-5}[\pm5]\%$	$^{+61}_{-45}[\pm113]\%$	0.5919(2)	$^{+3}_{-5}[\pm5]\%$	$^{+58}_{-44}[\pm108]\%$	0.4814(2)	$^{+3}_{-4}[\pm5]\%$	$^{+53}_{-43}[\pm97]\%$

Table 8.5: Berends-Giele scaling $f(V,n,m)$, given by the ratio between the integrated cross-sections of $V+n\ jets$ and $V+m\ jets$, at the LHC with 14 TeV using the MSTW2008LO (90% C.L.) PDFs and three different scale choices. See caption of Table 8.3 for applied selection cuts, MCFM input parameters and description of the uncertainties.

LHC with 14 TeV:	$\mu_0 = M_V$			$\mu_0 = E_T^V$			$\mu_0 = \hat{H}_T$		
$f =$	f	Δf_{pdf}	Δf_{scl}	f	Δf_{pdf}	Δf_{scl}	f	Δf_{pdf}	Δf_{scl}
$\frac{\sigma_{LO}(\mathrm{pp}\to(\mathrm{W}^+\to\ell^+\nu_\ell)+1\ jet)}{\sigma_{LO}(\mathrm{pp}\to(\mathrm{W}^+\to\ell^+\nu_\ell))}$	0.1435(1)	$^{+4}_{-6}$[±6]%	$^{+28}_{-25}$[±59]%	0.1402(1)	$^{+4}_{-6}$[±6]%	$^{+28}_{-25}$[±59]%	0.1387(1)	$^{+4}_{-6}$[±6]%	$^{+29}_{-25}$[±63]%
$\frac{\sigma_{LO}(\mathrm{pp}\to(\mathrm{W}^+\to\ell^+\nu_\ell)+2\ jets)}{\sigma_{LO}(\mathrm{pp}\to(\mathrm{W}^+\to\ell^+\nu_\ell)+1\ jet)}$	0.8840(3)	$^{+4}_{-5}$[±6]%	$^{+46}_{-34}$[±77]%	0.8143(3)	$^{+4}_{-5}$[±5]%	$^{+44}_{-33}$[±73]%	0.6605(3)	$^{+4}_{-5}$[±5]%	$^{+40}_{-32}$[±67]%
$\frac{\sigma_{LO}(\mathrm{pp}\to(\mathrm{W}^-\to\ell^-\overline{\nu}_\ell)+1\ jet)}{\sigma_{LO}(\mathrm{pp}\to(\mathrm{W}^-\to\ell^-\overline{\nu}_\ell))}$	0.1350(1)	$^{+5}_{-7}$[±7]%	$^{+28}_{-25}$[±59]%	0.1321(1)	$^{+5}_{-7}$[±7]%	$^{+28}_{-25}$[±60]%	0.1306(1)	$^{+5}_{-7}$[±7]%	$^{+29}_{-25}$[±64]%
$\frac{\sigma_{LO}(\mathrm{pp}\to(\mathrm{W}^-\to\ell^-\overline{\nu}_\ell)+2\ jets)}{\sigma_{LO}(\mathrm{pp}\to(\mathrm{W}^-\to\ell^-\overline{\nu}_\ell)+1\ jet)}$	0.8365(4)	$^{+4}_{-6}$[±6]%	$^{+46}_{-33}$[±77]%	0.7725(4)	$^{+4}_{-6}$[±6]%	$^{+44}_{-33}$[±73]%	0.6277(3)	$^{+4}_{-6}$[±6]%	$^{+40}_{-32}$[±67]%
$\frac{\sigma_{LO}(\mathrm{pp}\to(\mathrm{Z}\to\ell^-\ell^+)+1\ jet)}{\sigma_{LO}(\mathrm{pp}\to(\mathrm{Z}\to\ell^-\ell^+))}$	0.1857(1)	$^{+4}_{-6}$[±6]%	$^{+28}_{-24}$[±57]%	0.1824(1)	$^{+4}_{-6}$[±6]%	$^{+28}_{-24}$[±57]%	0.1865(1)	$^{+4}_{-6}$[±6]%	$^{+30}_{-25}$[±63]%
$\frac{\sigma_{LO}(\mathrm{pp}\to(\mathrm{Z}\to\ell^-\ell^+)+2\ jets)}{\sigma_{LO}(\mathrm{pp}\to(\mathrm{Z}\to\ell^-\ell^+)+1\ jet)}$	0.7845(4)	$^{+4}_{-6}$[±6]%	$^{+44}_{-32}$[±73]%	0.7282(3)	$^{+4}_{-6}$[±6]%	$^{+42}_{-32}$[±69]%	0.6029(3)	$^{+4}_{-6}$[±6]%	$^{+39}_{-31}$[±64]%
$\frac{\sigma_{LO}(\mathrm{pp}\to(\mathrm{Z}\to\sum_{\ell=\mathrm{e},\mu,\tau}\nu_\ell\overline{\nu}_\ell)+1\ jet)}{\sigma_{LO}(\mathrm{pp}\to(\mathrm{Z}\to\sum_{\ell=\mathrm{e},\mu,\tau}\nu_\ell\overline{\nu}_\ell))}$	0.1561(1)	$^{+4}_{-6}$[±5]%	$^{+26}_{-23}$[±53]%	0.1531(1)	$^{+4}_{-6}$[±5]%	$^{+26}_{-23}$[±54]%	0.1627(1)	$^{+4}_{-6}$[±5]%	$^{+28}_{-25}$[±62]%
$\frac{\sigma_{LO}(\mathrm{pp}\to(\mathrm{Z}\to\sum_{\ell=\mathrm{e},\mu,\tau}\nu_\ell\overline{\nu}_\ell)+2\ jets)}{\sigma_{LO}(\mathrm{pp}\to(\mathrm{Z}\to\sum_{\ell=\mathrm{e},\mu,\tau}\nu_\ell\overline{\nu}_\ell)+1\ jet)}$	0.7622(3)	$^{+3}_{-5}$[±5]%	$^{+47}_{-34}$[±79]%	0.7131(2)	$^{+3}_{-5}$[±5]%	$^{+45}_{-34}$[±76]%	0.5904(2)	$^{+3}_{-5}$[±5]%	$^{+42}_{-33}$[±70]%

8.4 PDF and Scale Uncertainties

Now that we have had a thorough look at the integrated cross-sections, I will investigate the differential cross-sections and their associated uncertainties in more detail. The knowledge about the development of uncertainties across the range of the distributions allows one to choose selection cuts in a way that minimises uncertainties and predicts possible issues for NP searches. For example, invariant mass distributions are used as primary observables in the search for heavier gauge bosons like W′ or Z′. The understanding of the tails in these histograms is therefore crucial to be able to subtract the SM background.

The relation between the relative PDF and scale uncertainties are as one would expect from the integrated cross-sections. The PDF uncertainties are vastly smaller than the scale uncertainties in all histograms. I have multiplied the relative PDF uncertainties by a factor of ten so that the variations of the PDF and scale uncertainties are visible in the same graph. These relative plots show the central value in each bin normalised to one, and the relative statistical, as well as relative asymmetric PDF and scale uncertainties. One should note, that the statistical uncertainties for the central value and the PDF envelope are zero (self-correlated[6]); the statistical uncertainties for the dynamic scales are propagated assuming that there is no correlation between the MC errors for the two calculations which gives an approximate increase by a factor of $\sqrt{2}$, because the relative error for the scale calculation is the same[7].

The behaviour of the different classes of distributions is similar for processes with the same number of associated jets. Firstly, I will look at the zero-jet processes. One of the most important distributions are the invariant mass distributions. Figures 8.1 and 8.2 show the mass peak for the W^+ and Z boson, respectively. One can see that for the W boson the scale uncertainties are a constant +15% and -25% at the peak region and then decrease steadily towards larger masses. In the Z case the scale uncertainties steadily decrease across the whole range, which suggest a higher selection cut for the di-lepton invariant mass in order to decrease the overall error. The smaller scale uncertainty in the high mass region is good news for searches for heavier weak bosons, because the SM background will give a small contribution to the overall uncertainties. The PDF uncertainties on the other hand have a tiny decrease with respect to small and large masses in the peak regions with an overall variation of less than 0.5%.

The histograms for transverse momenta of the (hard) charged lepton for these two processes is recorded in Figures 8.3 and 8.4. One can see that the scale uncertainties drop quickly after the peak. The increase in the PDF uncertainties towards larger momenta is up to 2% over the range of the histogram and hence bigger than in the previous

[6] Using $\Delta\sigma^+/\sigma^+ = \Delta\sigma^-/\sigma^- = \Delta\sigma/\sigma$ and $\rho = 1$ in Equation 8.3.

[7] Using $\Delta\sigma^+/\sigma^+ \approx \Delta\sigma^-/\sigma^- \approx \Delta\sigma/\sigma$ and $\rho = 0$ in Equation 8.3 gives $\Delta R/R = \sqrt{(2)} \cdot \Delta\sigma/\sigma$

distributions.

The corresponding rapidity distributions are shown in Figures 8.5 and 8.6. The scale uncertainties vary by less than 5% and the PDF uncertainties by less than 2% in both plots. All errors are largest in the central regions, which means that observables based on the rapidity separation (like R) for the two leptons in the Z process can benefit from cutting of low values.

In comparison, the process with one associated jet behaves very differently. I have observed that the PDF and scale uncertainties are increasing towards larger momenta or masses in the presence of an exponentially decreasing tail. This is of no concern when looking at SM predictions, because the contribution of the tails to the total integral is negligible. If one is only interested in the SM signal, more precise predictions can be made by applying harder cuts on the transverse momenta and the invariant masses. Searches for heavy weak bosons will, however, suffer from increased errors in these channels.

In particular the transverse mass of the missing transverse momentum and the charged lepton has the smallest scale and PDF uncertainties just around the peak, 60 GeV to 85 GeV, and the di-lepton invariant mass has up to two-fold larger errors below 85 GeV. The corresponding plots for the W^+ production and the $Z \to \ell^+\ell^-$ are shown in Figures 8.7 and 8.8. In the latter case the contributions to the total integral are very small, but for the former a selection cut of $65\,\text{GeV} < M_{T,\text{W}_{miss,\ell}} < 85\,\text{GeV}$ would decrease the uncertainties for the signal of the W^+ and the W^- boson.

The tails of the transverse momentum distributions suffer from an increase in the scale uncertainty of over 20% as shown in Figure 8.9 and 8.10 for the W^+ process and the Z process with decay into two charged leptons. Similarly, for distributions of the azimuthal angle between particles the uncertainties shoot up when the differential cross-section becomes small. For example, the azimuthal angle between the charged lepton and the jet for the W^+ production drops off lafter a peak at 135° and the scale uncertainty increases from +20% to over +40%. This region distributes about 25% to the integral and a cut could therefore improve the overall uncertainty. The corresponding plot is given in Figure 8.11. Similarly, the azimuthal angle between the two leptons for $(Z \to \ell^+\ell^-)+1\ jet$ has a peak at approximately 135° and an exponential decrease towards lower angles. In the same region the scale uncertainties increase from +18%/-12% to +30%/-18%.

For the above histograms the PDF uncertainties show the same basic behaviour, though it is about one order of magnitude smaller. In contrast, the rapidity distributions show an increase in the PDF uncertainties in the central region, while the scale uncertainties decrease. This is true for W (Figure 8.13) and Z processes (Figure 8.14). The scale variations are comparatively small (less then 5%), but the PDF uncertainties are comparatively large (up to 2%). For W processes it is worth mentioning that the overall increase in the PDF uncertainties in the central region is despite the positive PDF

deviation being larger in the forward direction than in the centre.

Finally, I am presenting some distributions for processes with 2 jets, for which especially the scale uncertainties are up to four times as large. The invariant mass and the transverse momentum distributions show a very similar behaviour to the 1-jet differential cross-sections, i.e. the uncertainties are smallest at the peak for the invariant mass and for the transverse momentum they get larger towards greater momenta. Because of these similarities, I will only show the distributions for the W^+ processes in Figures 8.15 and 8.16. The scale uncertainties are up to 80% in the regions with 'small' errors and increase by another 20% elsewhere. Hence, tight cuts, especially for the transverse momentum should give a big improvement for the total scale uncertainties.

The differential cross-sections with respect to the azimuthal angle between final state particles do not exert a consistent behaviour. Figure 8.17 shows the separation in azimuthal angle between the lepton and the harder jet for the W^+ process. The scale uncertainties increase with the angle. However, the angular separation between the two charged leptons for Z shows the opposite behaviour, i.e. the scale uncertainties decrease with larger angles and the scale uncertainties for angular separation between the two jets for the W^+ can even show no variation with respect to the angle. The respective plots can be found in Figures 8.18 and 8.19. In all three cases the asymmetric scale uncertainty spans from -30% to +80%.

The PDF uncertainties behave similarly to the scale uncertainties in all of these plots. As seen for the 1-jet distributions, this is not true for the rapidity distributions. I present only the rapidity distribution of the lepton for W^+ in Figure 8.20, because all rapidity distributions behave similarly to the 1-jet results. That means that the scale uncertainties are smallest in the central region and the PDF uncertainties are smallest in the forward direction of the detector.

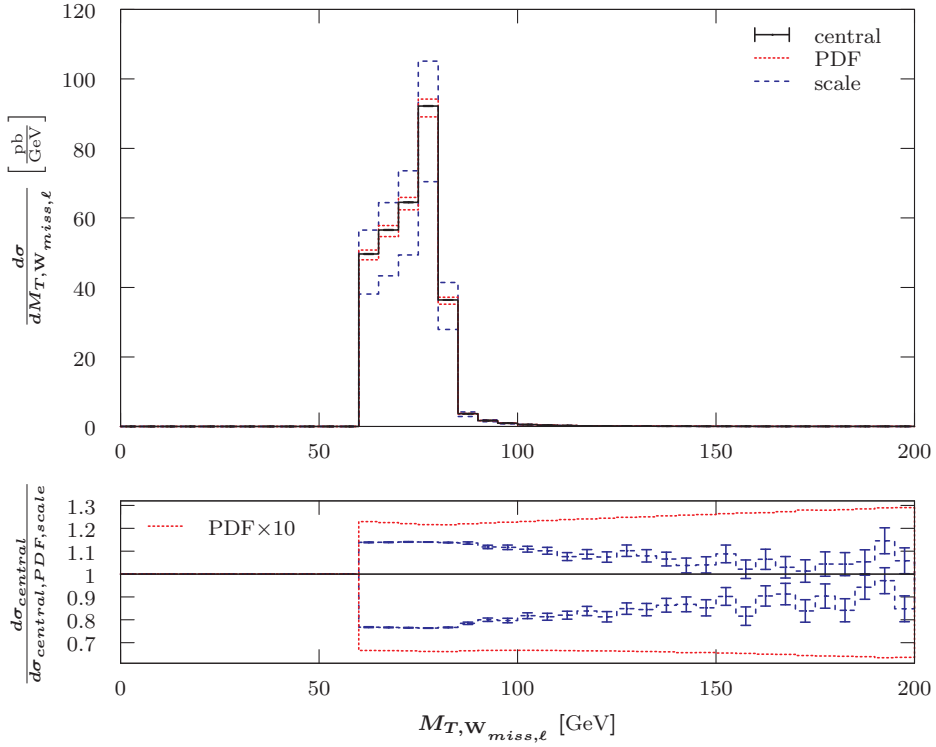

Figure 8.1: LO differential cross-section with respect to the transverse mass between the charged lepton and the missing transverse momentum for the $pp \to (W^+ \to \ell^+\nu_\ell)$ process at the LHC with 7 TeV using a fixed scale of $\mu_0 = M_W$ and MSTW2008LO (90% C.L.). The central value (black, solid) as well as the associated asymmetric deviations for the PDFs (red, dotted) and scale (blue, dashed) are shown (top) and compared (bottom). Selection cuts as given in Equations 7.5 to 7.8 have been applied. MCFM input parameters are listed in Equations 7.1 to 7.3. The procedure used to choose the number of shots is described in Section 4.4.3. The scale uncertainties have been estimated using a conservative variation by a factor of 4. The error bars for the statistical uncertainties are mostly too small to be visible or are only partially visible. The PDF uncertainties have been multiplied by a factor of ten in the bottom graph to make them more comparable to the scale uncertainties. Errors are propagated using Equations 8.3 and 8.4.

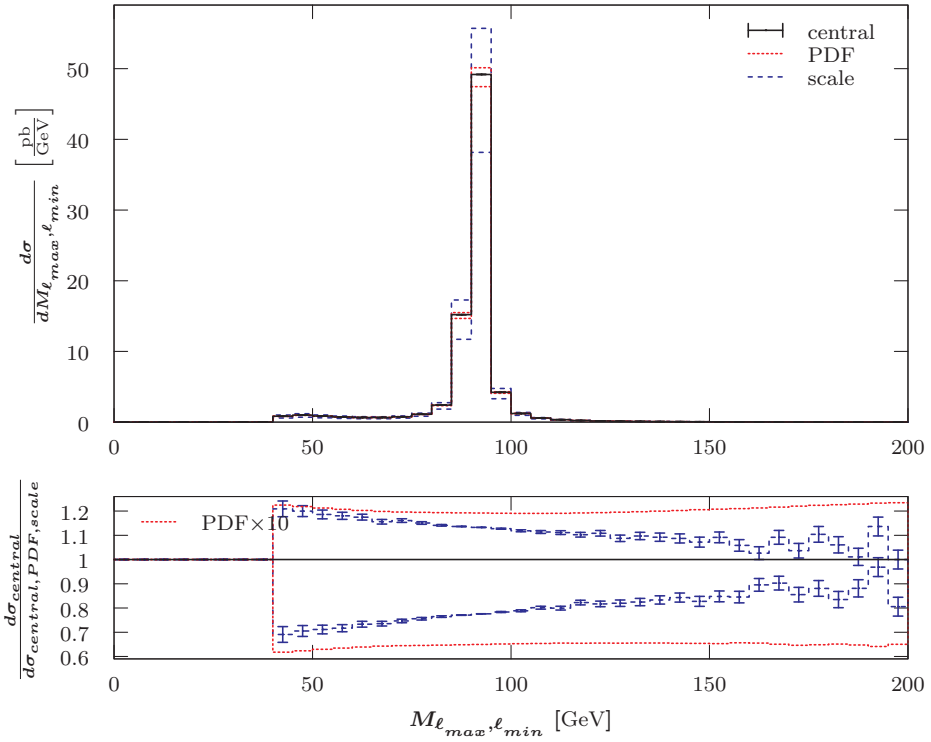

Figure 8.2: LO differential cross-section with respect to the invariant mass of the two charged leptons for the pp $\to$ (Z $\to \ell^-\ell^+$) process. Additional details are given in the caption of Figure 8.1.

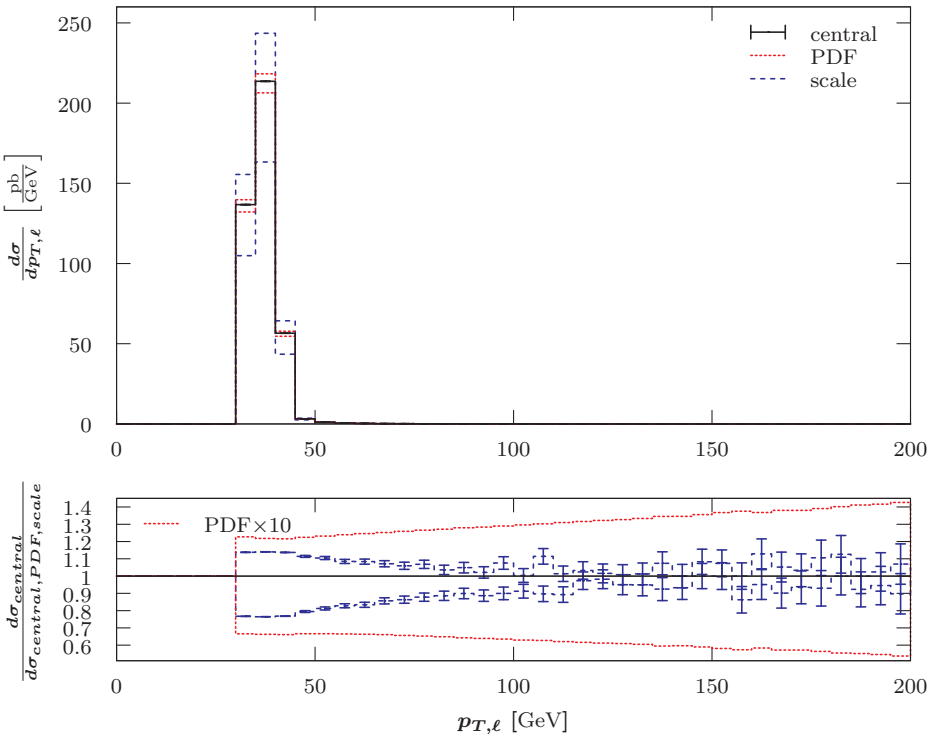

Figure 8.3: LO differential cross-section with respect to the transverse momentum of the charged lepton for the pp $\to$ (W$^+ \to \ell^+\nu_\ell$) process. Additional details are given in the caption of Figure 8.1.

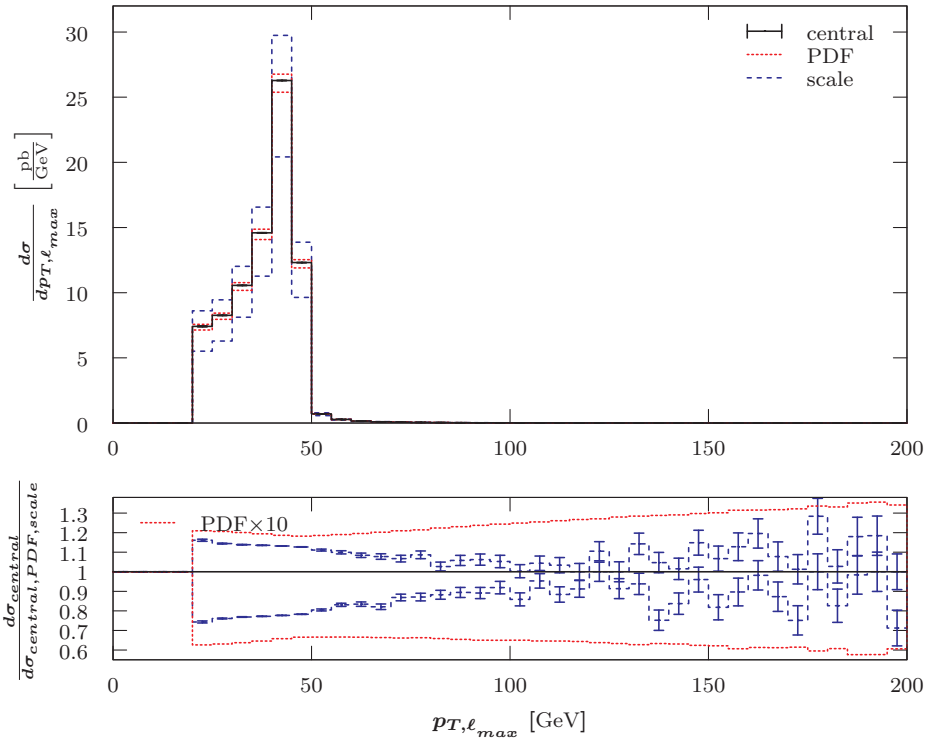

Figure 8.4: LO differential cross-section with respect to the transverse momentum of the harder charged lepton for the pp $\to$ (Z $\to \ell^-\ell^+$)process. Additional details are given in the caption of Figure 8.1.

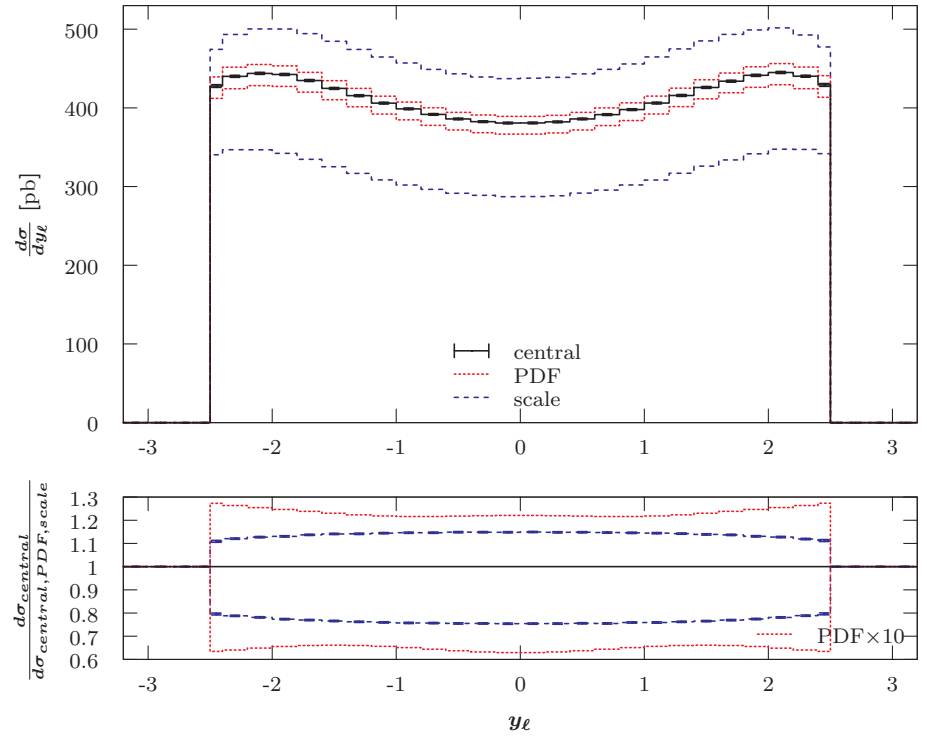

Figure 8.5: LO differential cross-section with respect to the rapidity of the charged lepton for the pp $\to$ (W$^+ \to \ell^+\nu_\ell$) process. The first and last filled bin are half-width due to the applied selection cut, $|y_\ell| < 2.5$. Additional details are given in the caption of Figure 8.1.

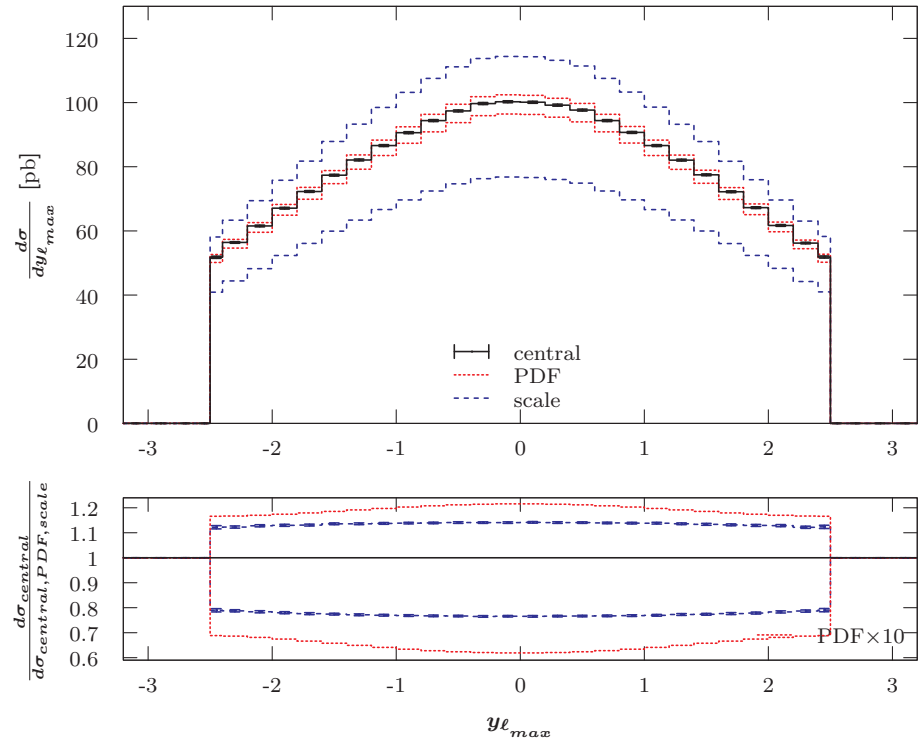

Figure 8.6: LO differential cross-section with respect to the rapidity of the harder charged lepton for the pp $\to$ (Z $\to \ell^-\ell^+$) process. The first and last filled bin are half-width due to the applied selection cut, $|y_\ell| < 2.5$. Additional details are given in the caption of Figure 8.1.

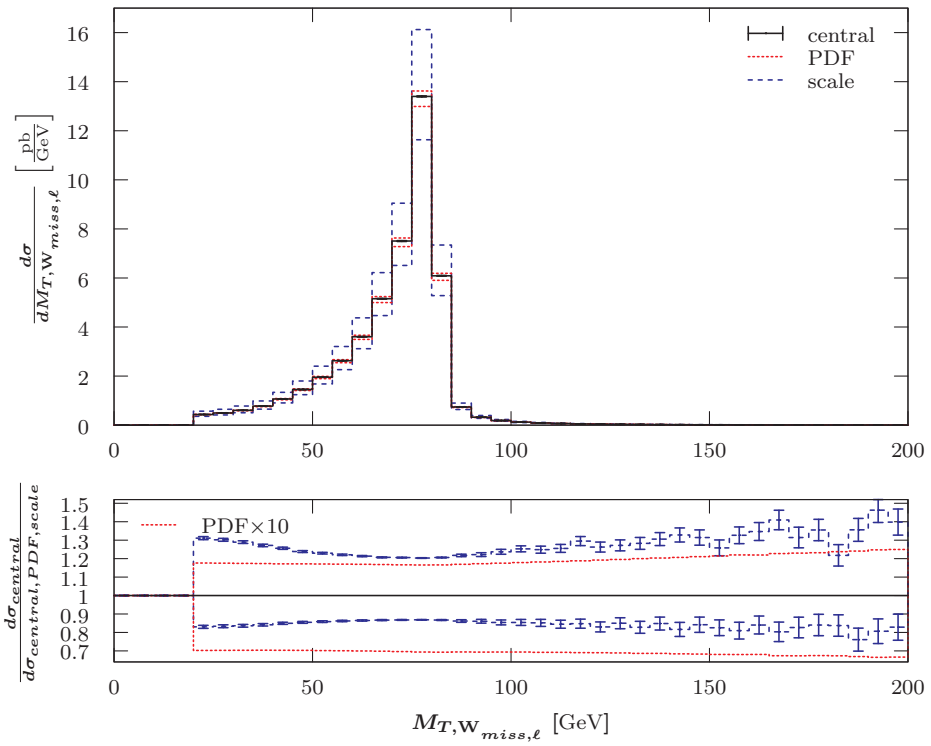

Figure 8.7: LO differential cross-section with respect to the transverse mass between the charged lepton and the missing transverse momentum for the pp $\to$ (W$^+ \to \ell^+\nu_\ell$) + 1 *jet* process. Additional details are given in the caption of Figure 8.1.

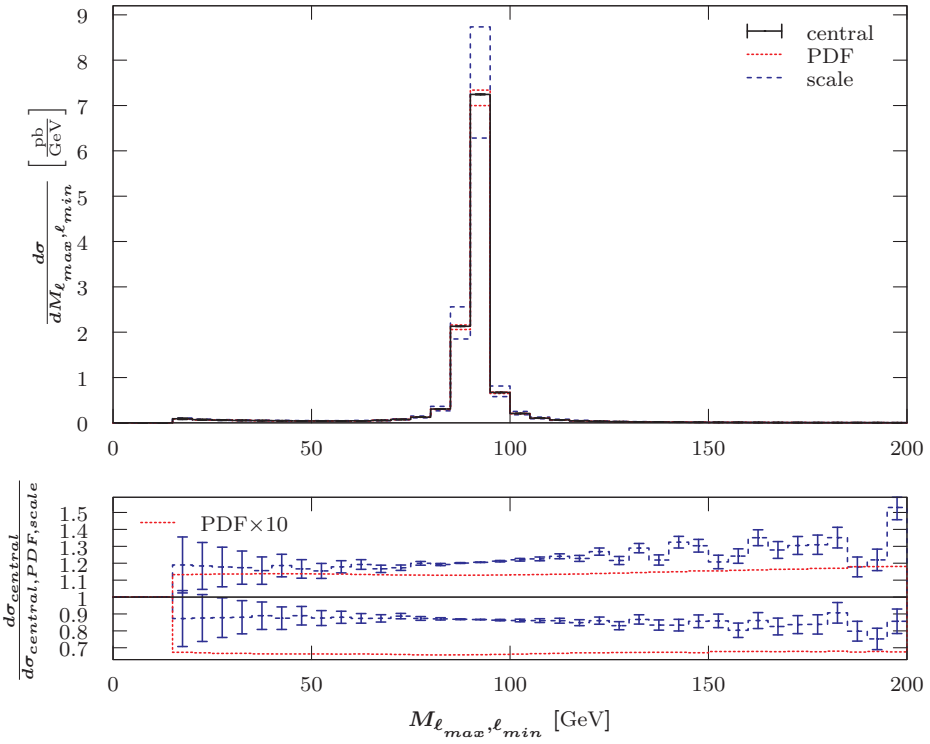

Figure 8.8: LO differential cross-section with respect to the invariant mass of the two charged lepton for the pp $\to$ (Z $\to \ell^-\ell^+$) + 1 *jet* process. Additional details are given in the caption of Figure 8.1.

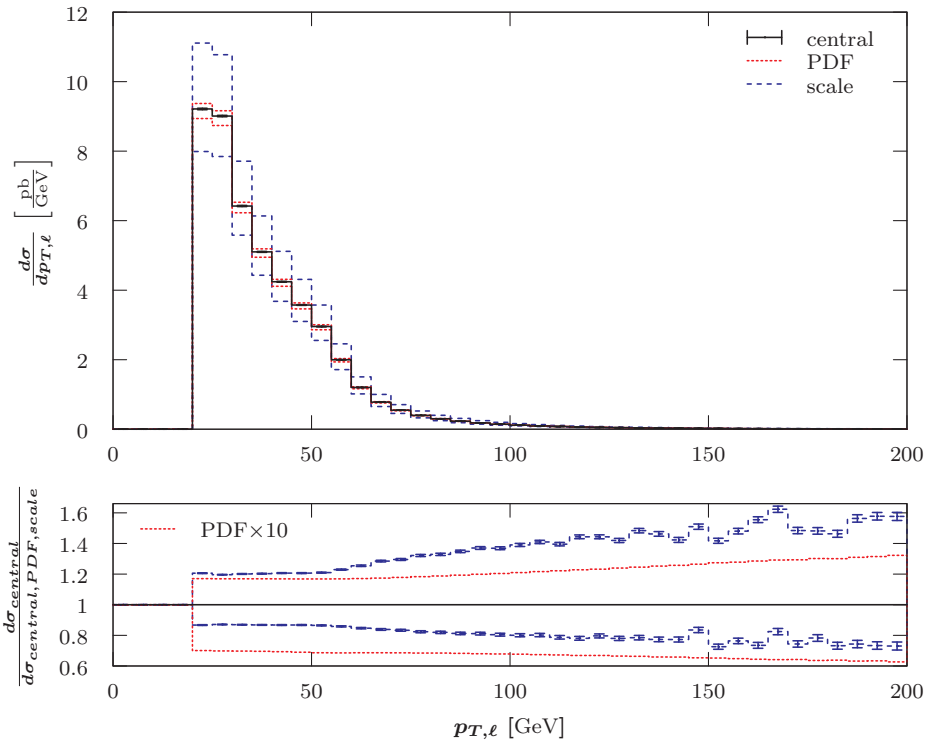

Figure 8.9: LO differential cross-section with respect to the transverse momentum of the charged lepton for the pp $\to$ (W$^+ \to \ell^+\nu_\ell$) + 1 *jet* process. Additional details are given in the caption of Figure 8.1.

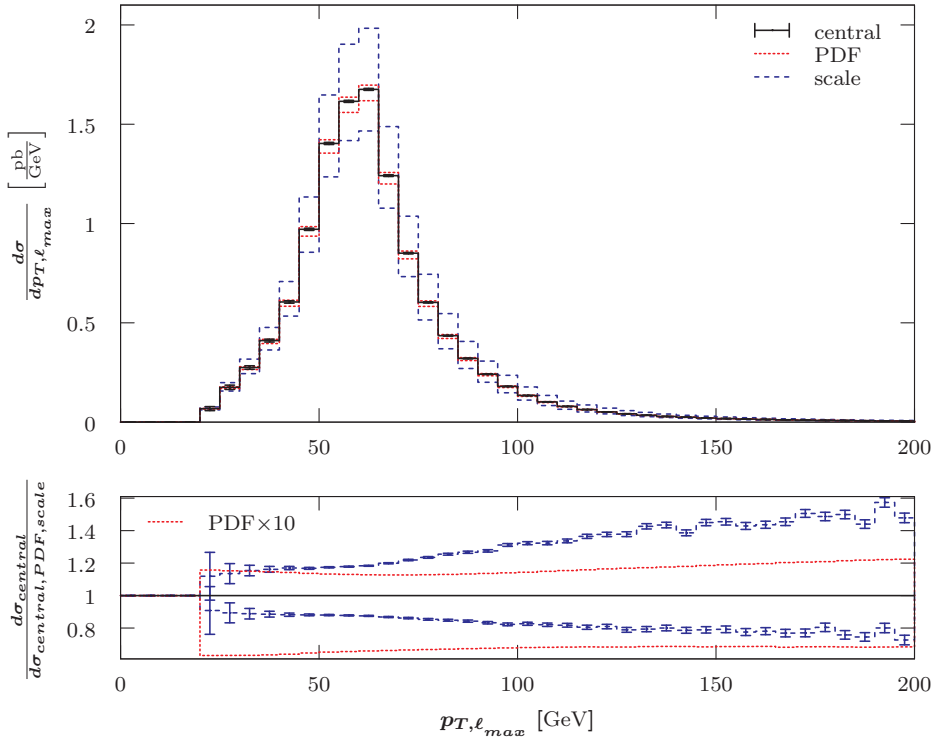

Figure 8.10: LO differential cross-section with respect to the transverse momentum of the harder charged lepton for the pp $\to$ (Z $\to \ell^-\ell^+$) + 1 *jet* process. Additional details are given in the caption of Figure 8.1.

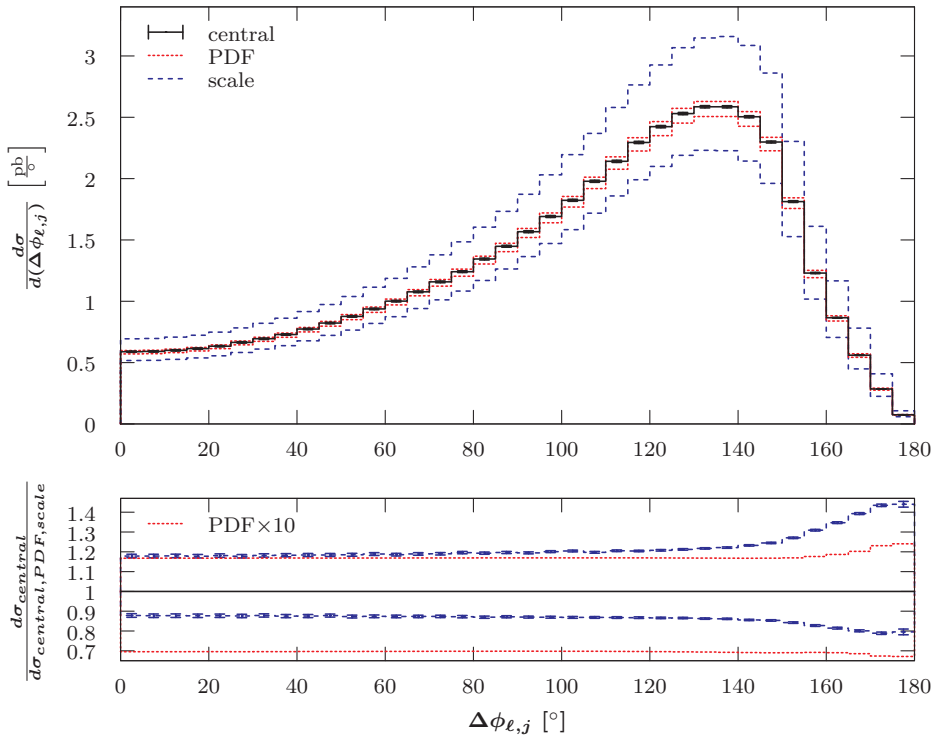

Figure 8.11: LO differential cross-section with respect to the azimuthal angle between the charged lepton and the jet for the pp $\to$ (W$^+ \to \ell^+\nu_\ell$) + 1 *jet* process. Additional details are given in the caption of Figure 8.1.

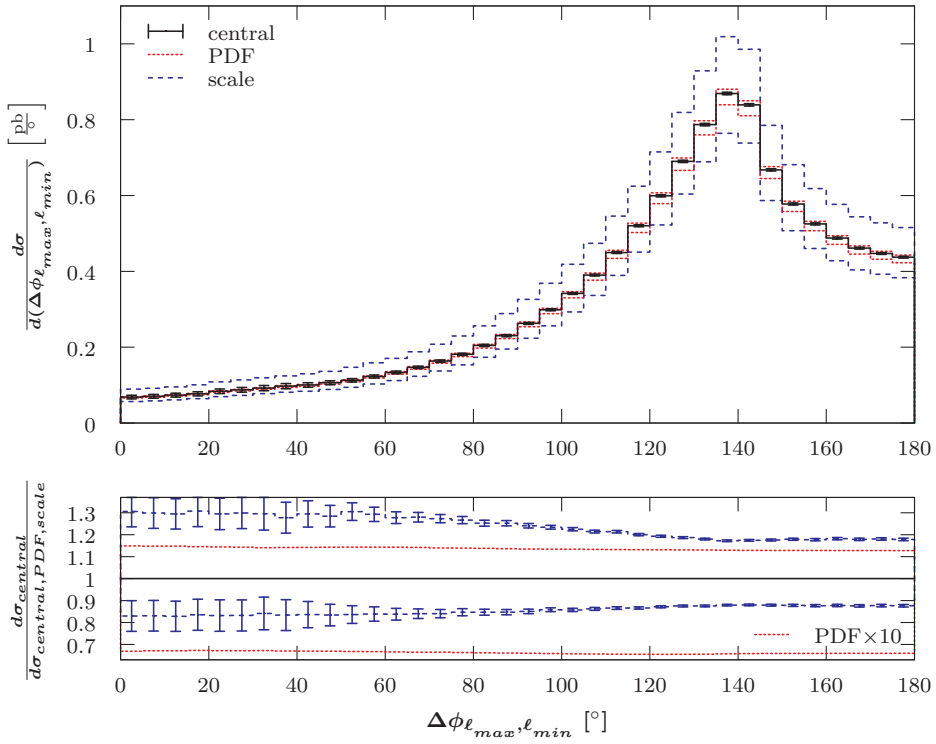

Figure 8.12: LO differential cross-section with respect to the azimuthal anglew between the two charged leptons for the pp $\to$ (Z $\to \ell^-\ell^+$) + 1 *jet* process. Additional details are given in the caption of Figure 8.1.

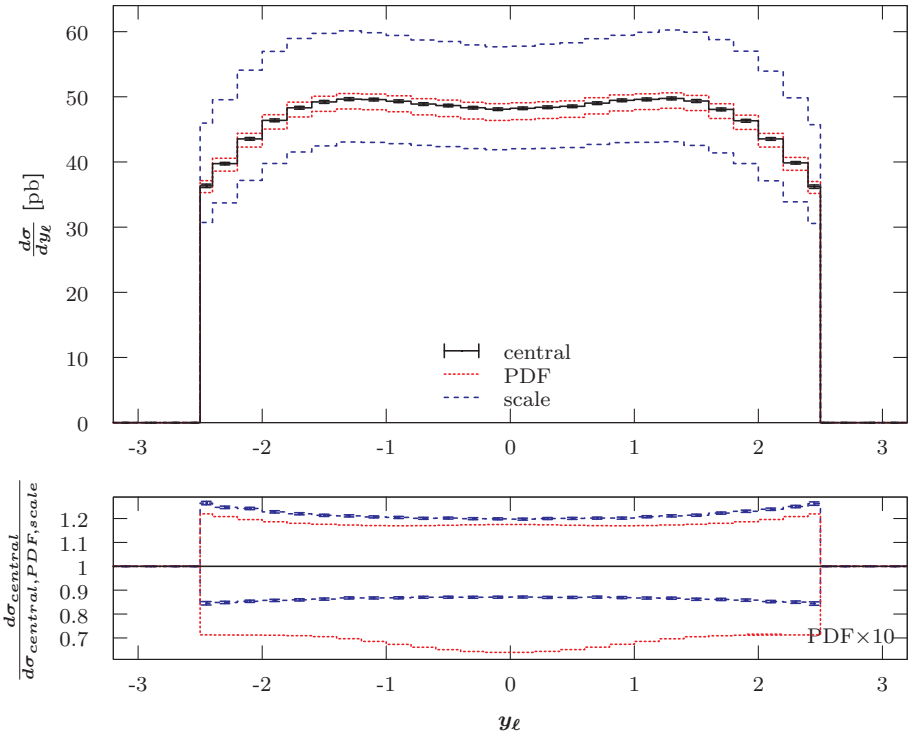

Figure 8.13: LO differential cross-section with respect to the rapidity of the charged lepton for the pp $\to$ (W$^+ \to \ell^+\nu_\ell$) + 1 *jet* process. The first and last filled bin are half-width due to the applied selection cut, $|y_\ell| < 2.5$. Additional details are given in the caption of Figure 8.1.

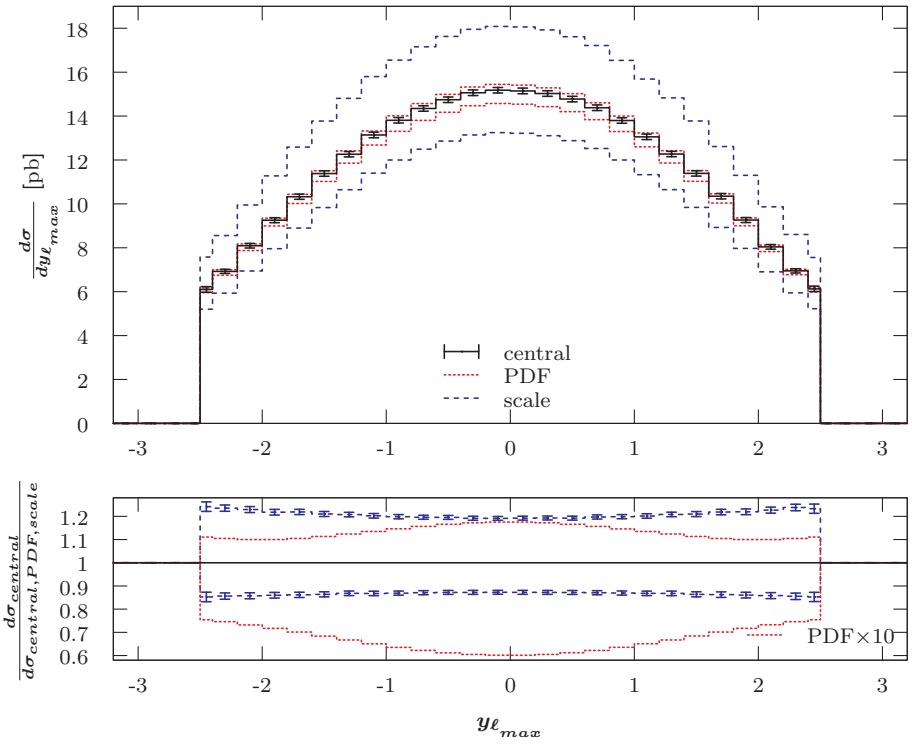

Figure 8.14: LO differential cross-section with respect to the rapidity of the harder charged lepton for the $pp \to (Z \to \ell^-\ell^+) + 1\ jet$ process. The first and last filled bin are half-width due to the applied selection cut, $|y_\ell| < 2.5$. Additional details are given in the caption of Figure 8.1.

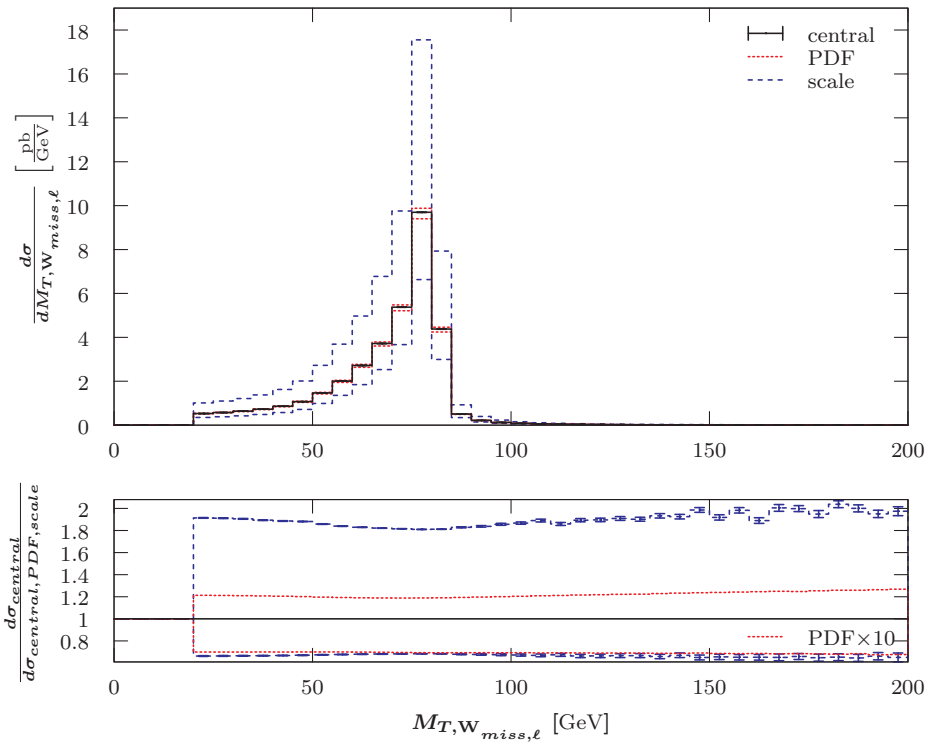

Figure 8.15: LO differential cross-section with respect to the transverse mass between the charged lepton and the missing transverse momentum for the $pp \to (W^+ \to \ell^+\nu_\ell) + 2\ jets$ process. Additional details are given in the caption of Figure 8.1.

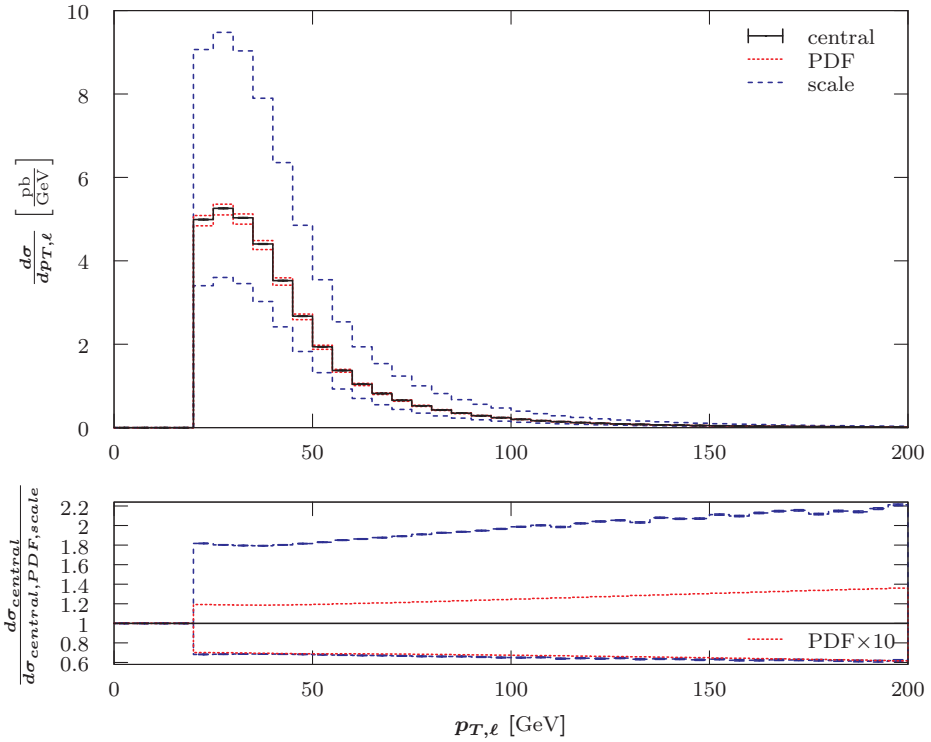

Figure 8.16: LO differential cross-section with respect to the transverse momentum of the charged lepton for the pp $\to (W^+ \to \ell^+\nu_\ell) + 2\ jets$ process. Additional details are given in the caption of Figure 8.1.

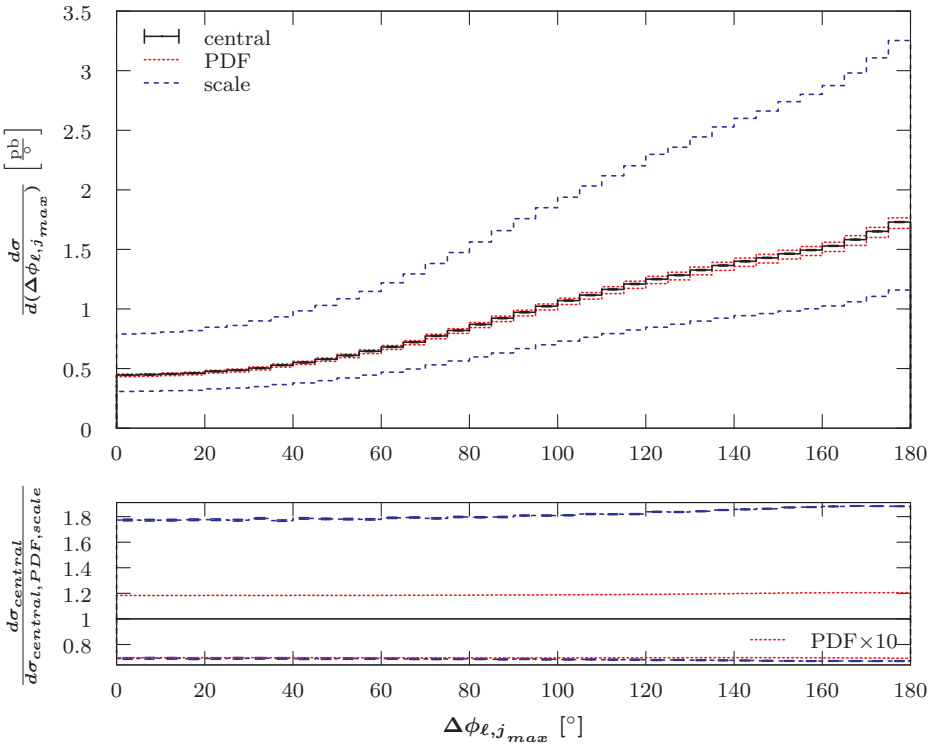

Figure 8.17: LO differential cross-section with respect to the azimuthal angle between the charged lepton and the harder jet for the pp $\to (W^+ \to \ell^+\nu_\ell) + 2\ jets$ process. Additional details are given in the caption of Figure 8.1.

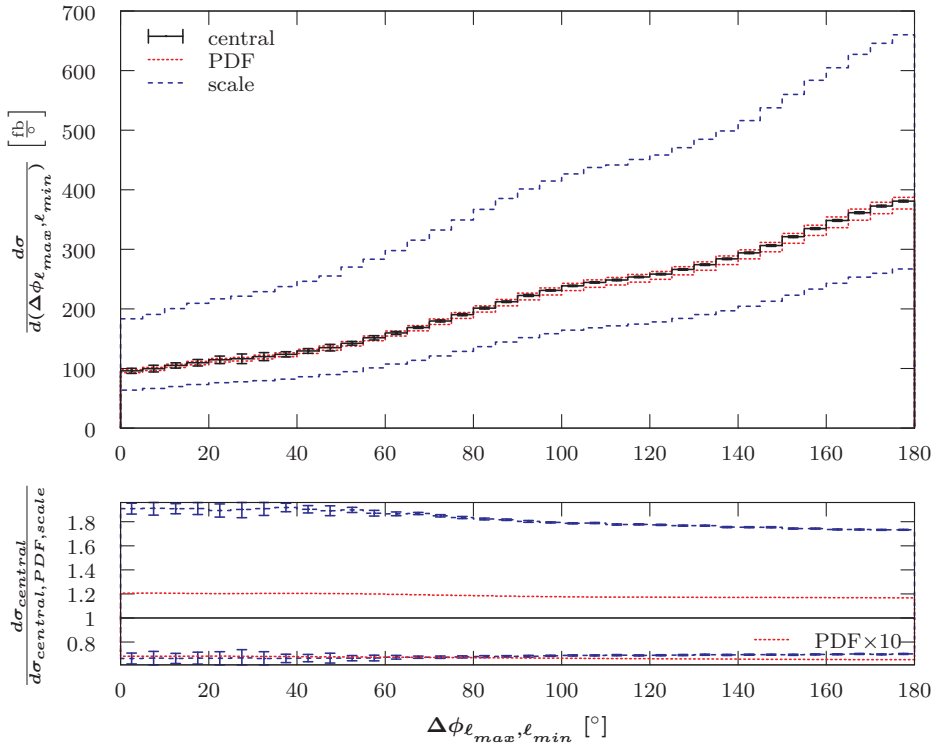

Figure 8.18: LO differential cross-section with respect to the tazimuthal angle between the two charged leptons for the pp $\to (\mathrm{Z} \to \ell^-\ell^+) + 2\ jets$ process. Additional details are given in the caption of Figure 8.1.

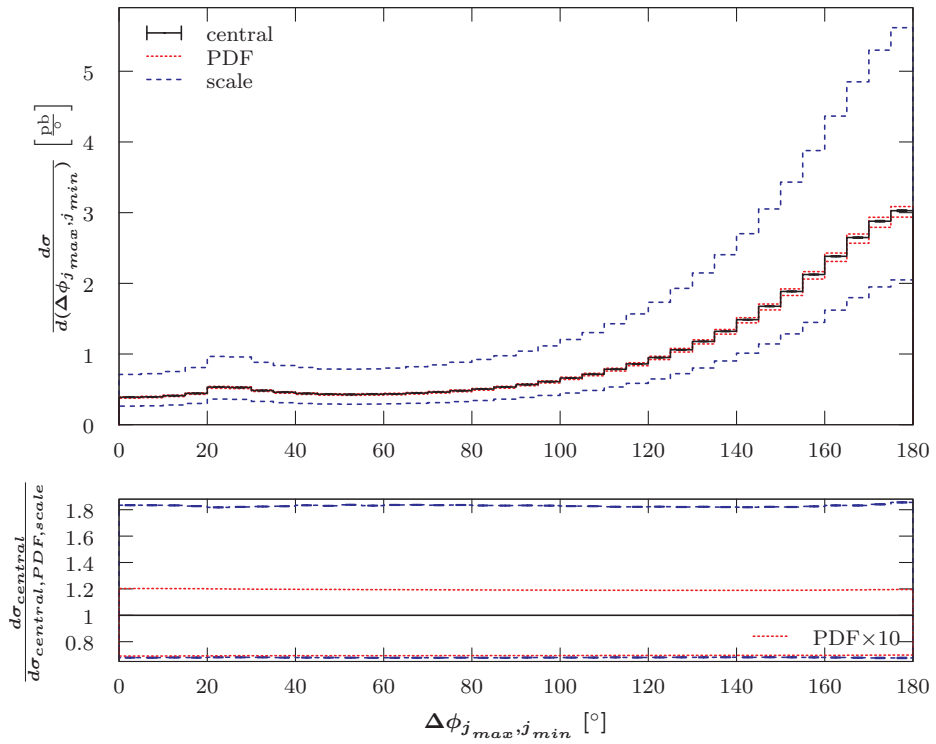

Figure 8.19: LO differential cross-section with respect to the azimuthal angle between the two jets for the pp $\to (\mathrm{W}^+ \to \ell^+\nu_\ell) + 2\ jets$ process. Additional details are given in the caption of Figure 8.1.

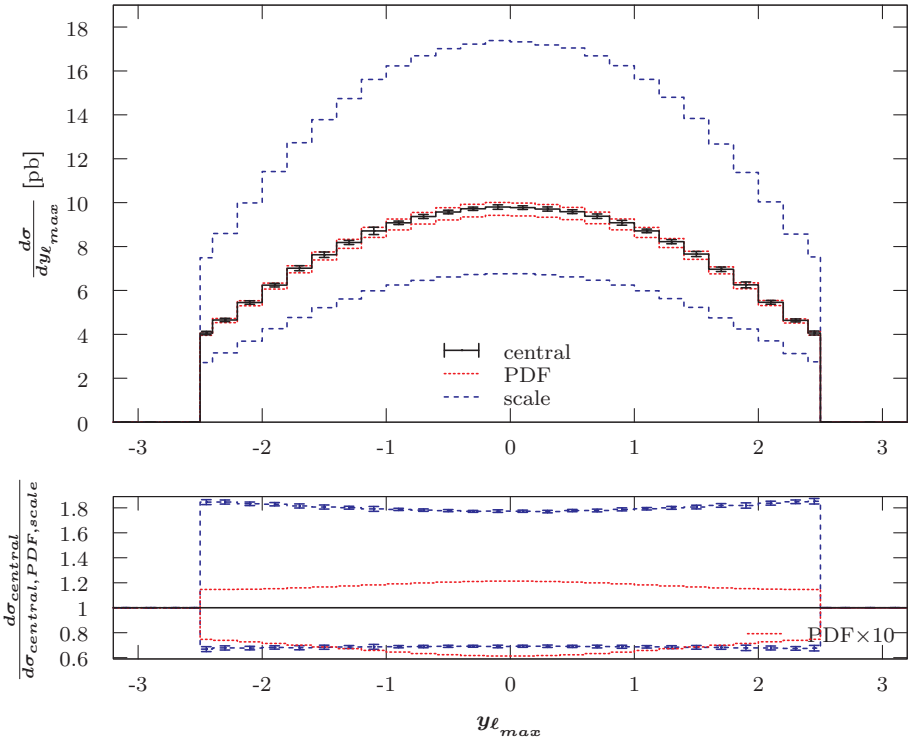

Figure 8.20: LO differential cross-section with respect to the rapidity of the harder charged lepton for the pp $\rightarrow$ (Z $\rightarrow \ell^-\ell^+$)+2 *jets* process. The first and last filled bin are half-width due to the applied selection cut, $|y_\ell| < 2.5$. Additional details are given in the caption of Figure 8.1.

8.5 Comparison between the Static and Dynamic Scales: M_V, E_T^V and $\hat{H}_T$

All theoretical predictions are based on pertubative quantum field theory, which introduces two arbitrary scales. The factorisation scale provides the energy scale at which the PDFs are evaluated and the renormalisation scale determines the energy scale to which the strong coupling is evaluated. These provide an infra-red and ultra-violet cut-off for the calculation of the hard scattering event one is interested in. While our theoretical calculations are dependent on scales, these are non-physical and one has to choose a scale which fits experimental results best. Hence, it is important to understand the impact different scale choices have on theoretical predictions. Comparison with future experimental results might allow us to decide which scale choice is most appropriate for calculating integrated and, more importantly, differential cross-sections for these processes.

For processes with no jets, the histograms for the static scale, M_V, and the dynamic scale, E_T^V, are identical because the transverse momentum of the weak boson is zero if no jets are emitted. The dynamic scale, $\hat{H}_T$ diverges from the former two by almost 5%, which is well within the error band for a scale variation by a factor of four (approx. 15%). As a representation for this behaviour I have given the transverse mass of the W^+ boson in Figure 8.21. The relative plots show the ratio between the differential cross-section for a given scale and the static scale, so that the M_V curve is a constant function equal to one and the curves for the dynamic scales show the relative deviation from the former. The relative asymmetric scale uncertainties and the statistical uncertainties are also given. One should note, that the statistical uncertainties for the static scale only applies to the envelope of the asymmetric scale uncertainty[8]; the statistical uncertainties for the dynamic scales are propagated assuming that there is no correlation between the MC errors for the two calculations, which gives an approximate increase by a factor of $\sqrt{2}$.[9]

The shape of the rapidity distributions is independent of the scale choice and the uncertainties are almost constant across the whole range (with small increases towards the tails). In Figures 8.22 and 8.23 we can see the histograms of the charged lepton rapidity for W^+ production with leptonic decay and associated production of one and two jets, respectively. In both cases, the histograms for the dynamic scales are scaled by a constant factor and lie within the error bands of the static scale. For the process with two jets the scale variation by a factor of four is just about enough. We can see the same behaviour for $Z + 2\ jets$ production with decay into two charged leptons as shown in Figure 8.24 and also for the rapidity of jets as recorded in Figure 8.25 for the Z process

[8]The statistical error for the central value is zero, because it is correlated to itself.
[9]The statistical errors are of the same size for two scales which are compared.

with one jet.

All histograms of the transverse momenta, the differences in azimuthal angle between two final state particles and the invariant masses show divergences from a constant scaling in the tails. In general, the histograms for the dynamic scales give a smaller contribution to the tails. For the transverse momentum this deviation is within the error band for the E_T^V scale, but exceeds it for $\hat{H}_T$. This can be seen in Figures 8.26 and 8.27 for the (hard) charged lepton of $(\mathrm{W}^+ \to \ell^+\nu) + 1\ jet$ and $(\mathrm{Z} \to \ell^+\ell^-) + 2\ jets$, respectively.

The uncertainty envelope for the static scale also covers the divergences of the dynamic scales for the difference between the azimuthal angles of final state particles. For example, the azimuthal angles between the two charged leptons in a one-jet process is given in Figure 8.28, and also for a the invariant mass distributions. Figure 8.30 presents the di-lepton invariant mass for the same process. The transverse mass of the charged lepton and the missing transverse momentum vector for W^+ production with one associated jet is given in Figure 8.29. Some of the two-jet observables can exceed the error bands, though there is no obvious pattern.

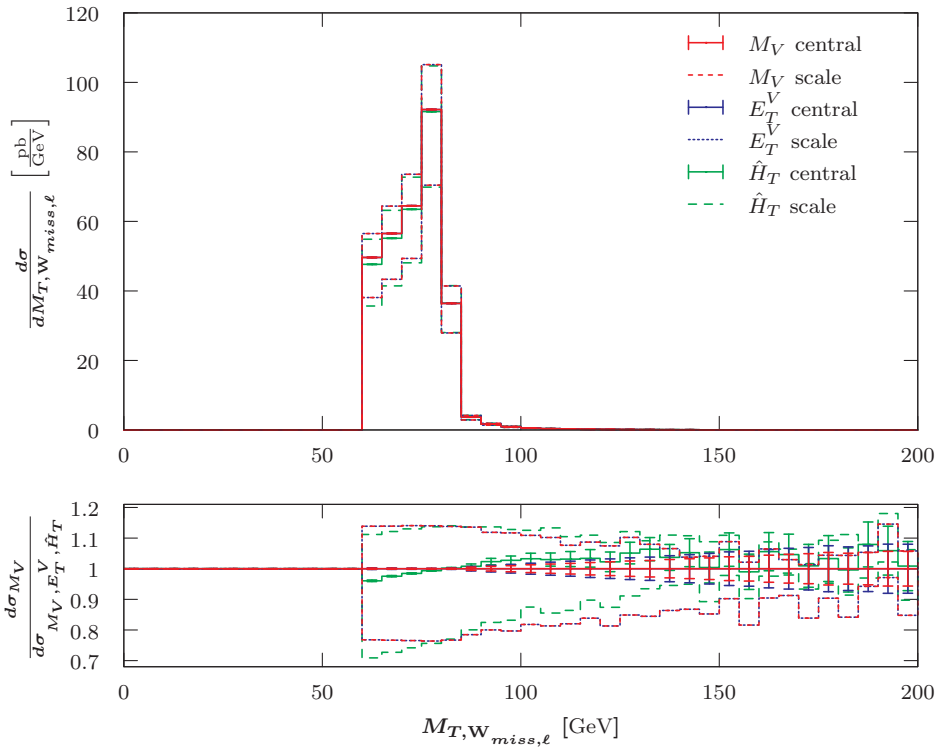

Figure 8.21: LO differential cross-section with respect to the transverse mass of the charged lepton and the missing transverse momentum for the pp $\rightarrow$ ($\mathrm{W}^+ \rightarrow \ell^+\nu_\ell$) process at the LHC with 7 TeV using MSTW2008LO (90% C.L.). Three results for the static scale M_V (red), the dynamic scale E_T^V (blue) and the dynamic scale $\hat{H}_T$ (green), are shown (top) and compared (bottom). Selection cuts as given in Equations 7.5 to 7.8 have been applied. MCFM input parameters are listed in Equations 7.1 to 7.3. The procedure used to choose the number of shots is described in Section 4.4.3. The scale uncertainties have been estimated using a conservative variation by a factor of 4. Only the asymmetric deviations for the scales (dotted/dashed) from the central value (solid) are given. Errors are propagated using Equations 8.3 and 8.4.

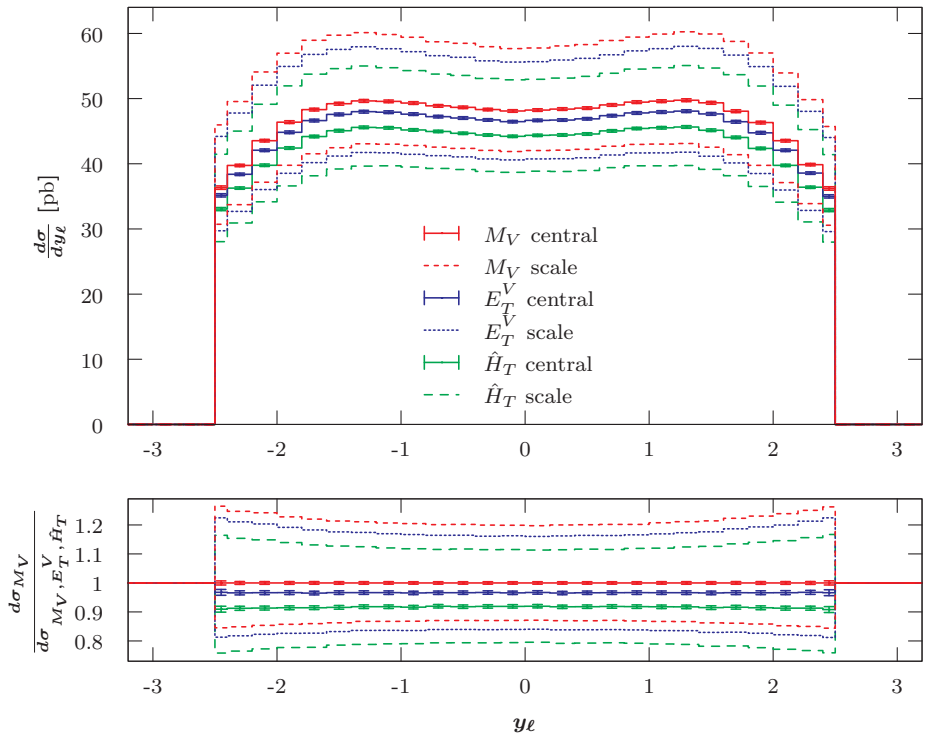

Figure 8.22: LO differential cross-section with respect to the rapidity of the charged lepton for the $pp \to (W^+ \to \ell^+\nu_\ell) + 1\ jet$ process. The first and last filled bin are half-width due to the applied selection cut, $|y_\ell| < 2.5$. Additional details are given in the caption of Figure 8.21.

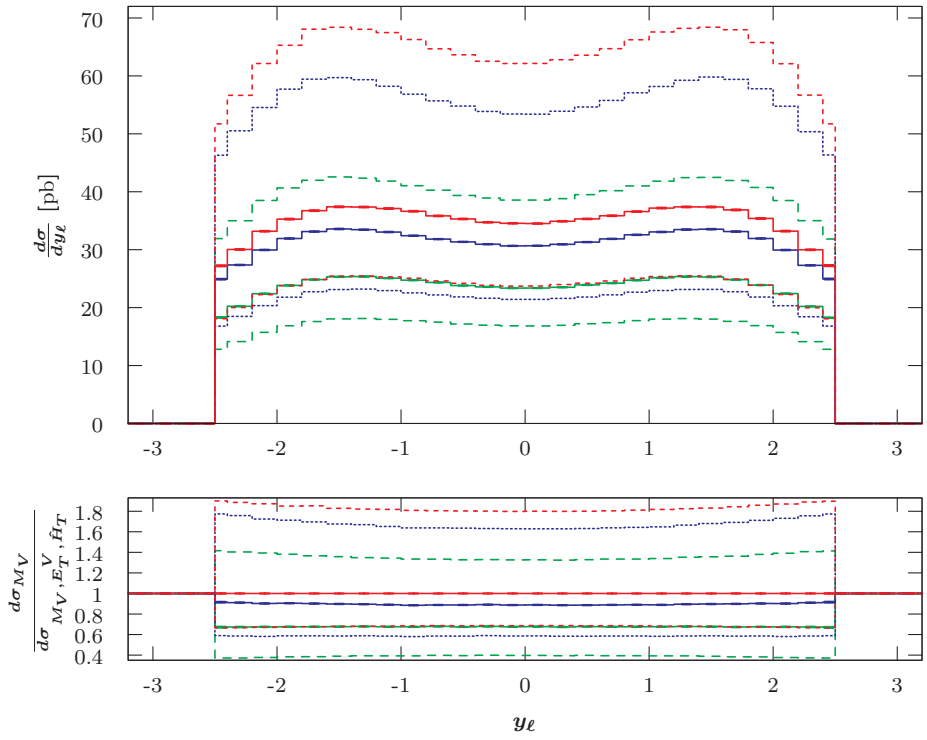

Figure 8.23: LO differential cross-section with respect to the rapidity of the charged lepton for the $pp \to (W^+ \to \ell^+\nu_\ell) + 2\ jets$ process. The first and last filled bin are half-width due to the applied selection cut, $|y_\ell| < 2.5$. The key is given in the previous histogram. Additional details are given in the caption of Figure 8.21.

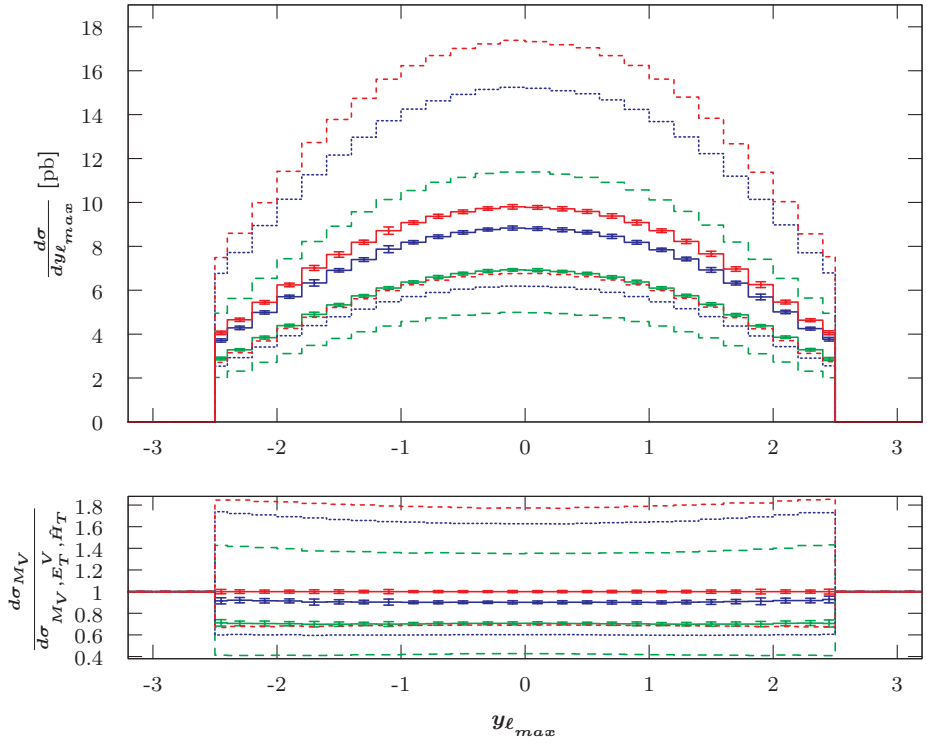

Figure 8.24: LO differential cross-section with respect to the rapidity of the harder charged lepton for the pp $\to$ (Z $\to \ell^-\ell^+$) + 2 *jets* process. The first and last filled bin are half-width due to the applied selection cut, $|y_\ell| < 2.5$. The key is given in the following histogram. Additional details are given in the caption of Figure 8.21.

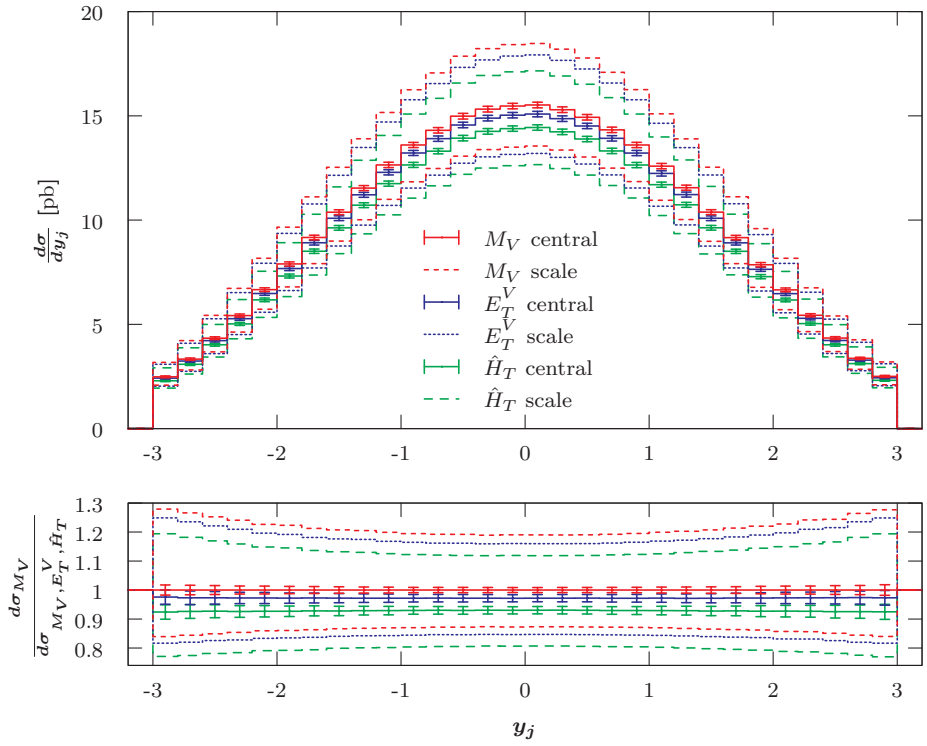

Figure 8.25: LO differential cross-section with respect to the rapidity of the jet for the pp $\to$ (Z $\to \ell^-\ell^+$) + 1 *jet* process. Additional details are given in the caption of Figure 8.21.

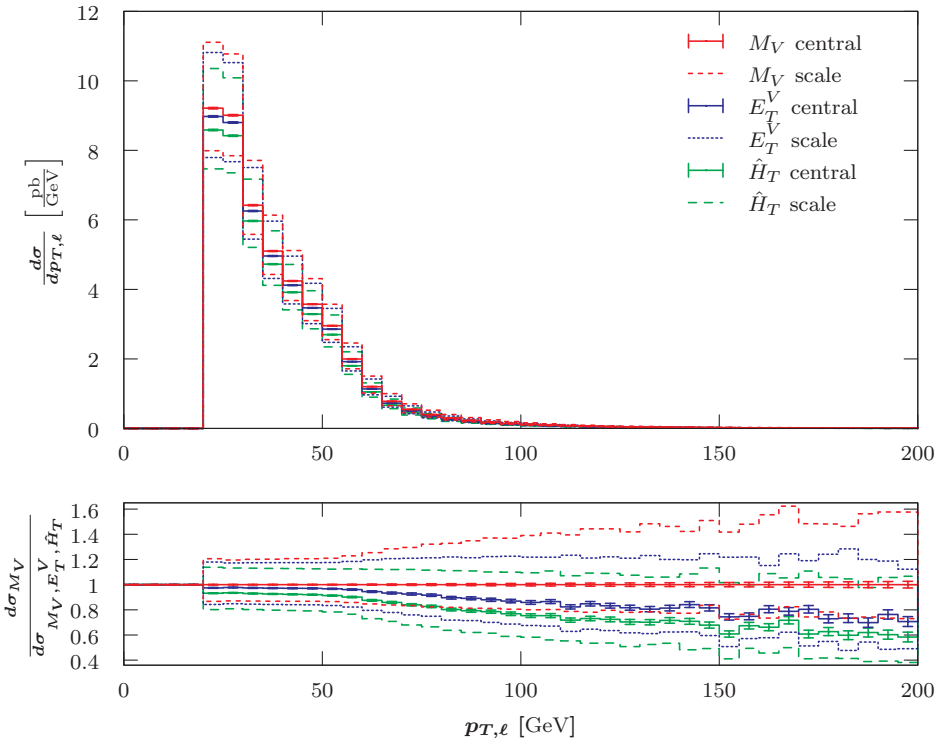

Figure 8.26: LO differential cross-section with respect to the transverse momentum of the charged lepton for the pp $\to (\mathrm{W}^+ \to \ell^+\nu_\ell) + 1\ jet$ process. Additional details are given in the caption of Figure 8.21.

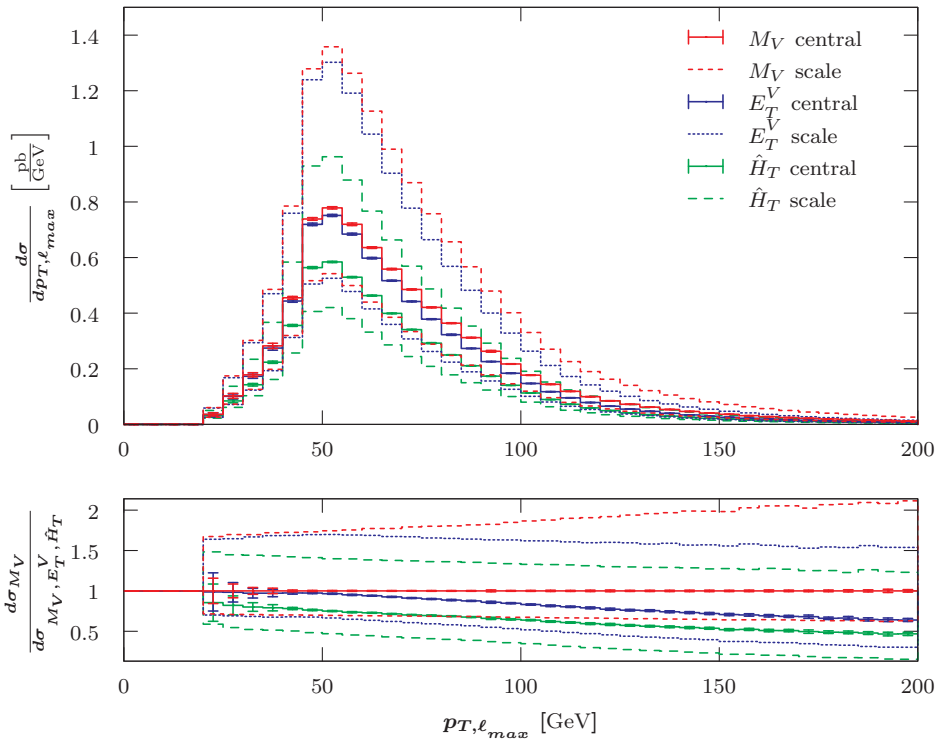

Figure 8.27: LO differential cross-section with respect to the transverse momentum of the harder charged lepton for the pp $\to (\mathrm{Z} \to \ell^-\ell^+) + 2\ jets$ process. Additional details are given in the caption of Figure 8.21.

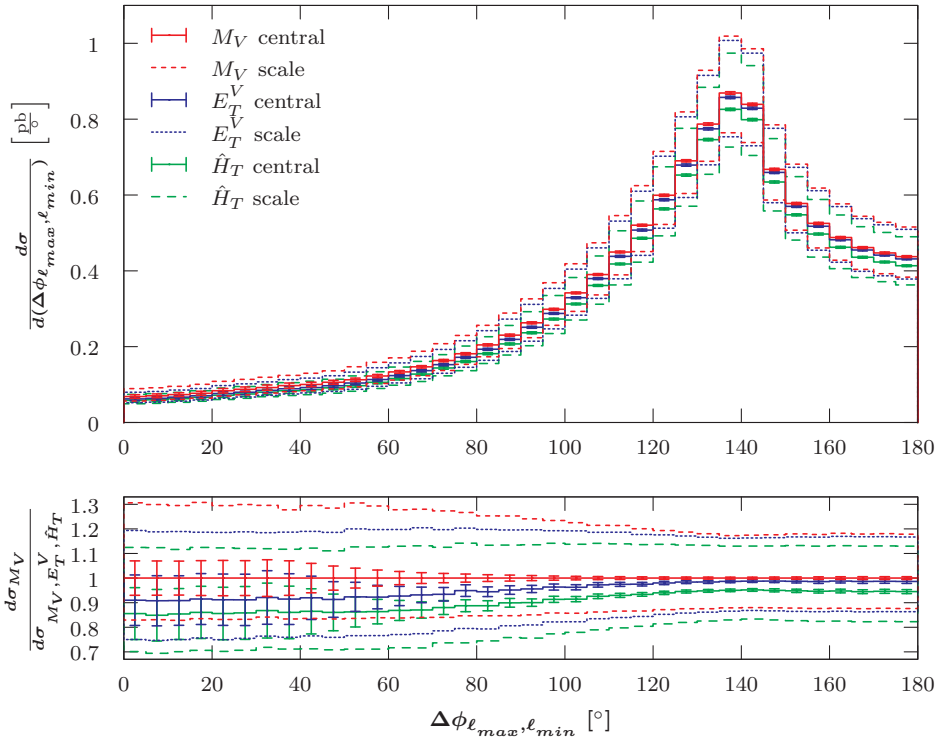

Figure 8.28: LO differential cross-section with respect to azimuthal angle between the two charged leptons for the pp $\to$ (Z $\to \ell^-\ell^+$) + 1 *jet* process. Additional details are given in the caption of Figure 8.21.

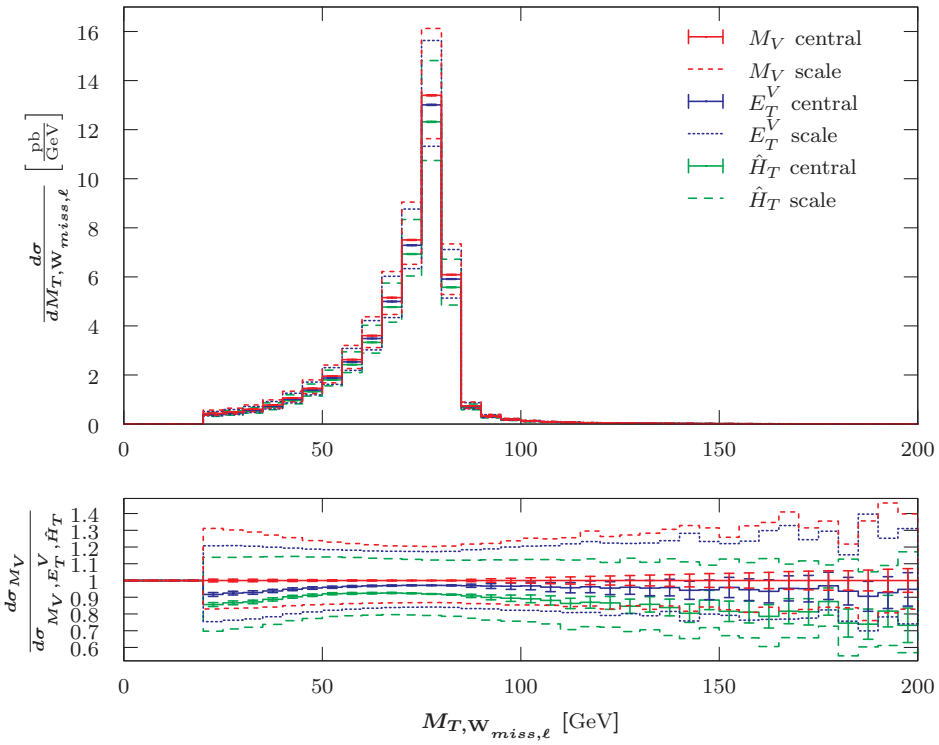

Figure 8.29: LO differential cross-section with respect to transverse mass of charged lepton and the missing transverse momentum for the pp $\to$ (W$^+ \to \ell^+\nu_\ell$) + 1 *jet* process. Additional details are given in the caption of Figure 8.21.

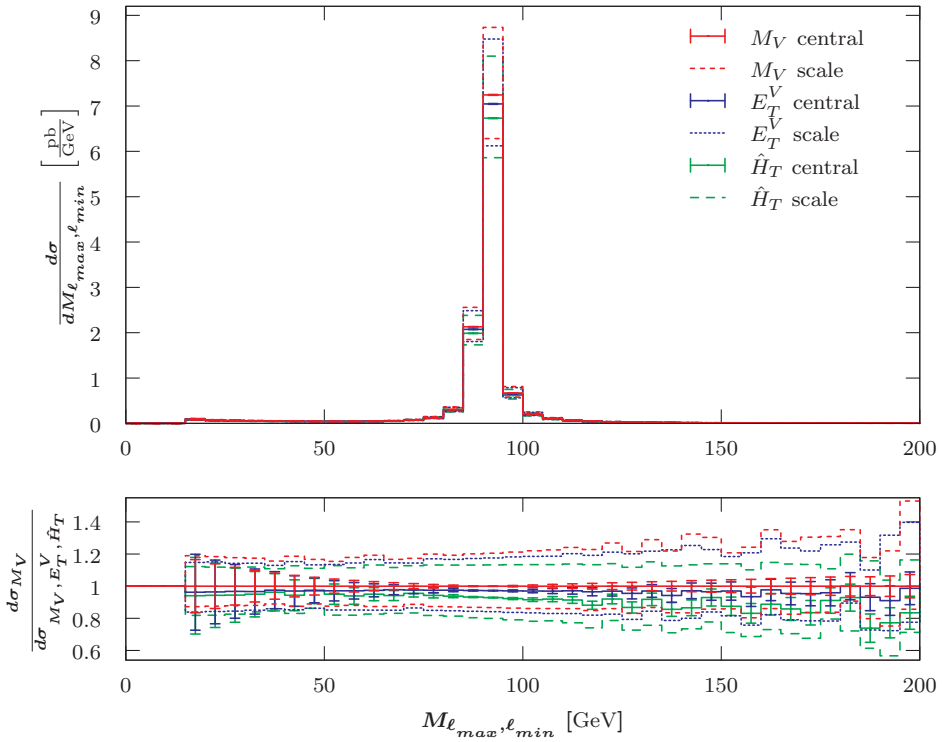

Figure 8.30: LO differential cross-section with respect to the transverse mass of the two leptons for the pp $\rightarrow$ (Z $\rightarrow \ell^-\ell^+$) + 1 *jet* process. Additional details are given in the caption of Figure 8.21.

8.6 Comparison between PDF Sets: MSTW2008LO (90% C.L.) and CTEQ6L1

I have already presented that the integrated cross-section for the presented processes is larger for the MSTW2008LO (90% C.L.) PDF set in comparison to the CTEQ6L1 PDF set. In summary, I found that the integrated cross-section using CTEQ6L1 falls within the errors of the MSTW2008LO (90% C.L.) for processes with no jets, within two to three error bars for one-jet processes and are more than 10% smaller for the processes with two jets.

In this section I want to summarise the influence of the different PDF sets for differential cross-sections. I have compared all the distributions for MSTW2008LO (90% C.L.) and CTEQ6L1 to see if the behaviour of the integrated cross-sections is similar to the behaviour of the differential cross-sections. I have also looked at changes to the shape of differential cross-sections, because these introduce a dependence on selection cuts that is not independent of the chosen PDF sets. This would influence other observables like the ratios discussed in previous sections.

I found that all differential cross-sections, with the exception of the rapidity distribution, behave as expected from the integrated cross-section. That means that the CTEQ6L1 distributions are consistently lower than MSTW2008LO (90% C.L.) distributions. For zero jet processes the deviation is within one error bar of MSTW2008LO (90% C.L.), for one jet process it is within two error bars and for two jet processes CTEQ6L1 predictions are much smaller than MSTW2008LO (90% C.L.) predictions. All the features are preserved and all positions of peaks are identical. This is most important for invariant mass observables.

To represent this observation I have recorded the transverse mass of the W^+ for the zero-jet process in Figure 8.31, the di-lepton invariant mass for $Z \to \ell^-\ell^+$ production with one associated jet in Figure 8.32 and the transverse mass of the W^- with two associated jets in Figure 8.33. All plots in this section are for the LHC with 7 TeV using a static scale M_V and the selection cuts given in Equations 7.5 to 7.8.

The relative plots show the ratio between the differential cross-section for the two PDF sets, so that the MSTW2008LO (90% C.L.) curve is a constant function equal to one and the CTEQ6L1 curve show the relative deviation from the former. The relative asymmetric PDF uncertainties and the statistical uncertainties are also given. One should note, that the statistical uncertainties for MSTW2008LO (90% C.L.) are zero (due to self-correlation); the statistical uncertainties for CTEQ6L1 are propagated assuming that there is no correlation between the MC errors for the two PDF sets.

One can also see that the distribution for CTEQ6L1 not only preserves the dominant features of the histogram, but is in fact just a scaled down version of the MSTW2008LO

(90% C.L.) plot with very small fluctuations in the peak regions. I have found that the same is true for transverse plane observables. This is particularly important for the transverse momentum of the charged lepton, the missing transverse momentum and the difference between azimuthal angles, as these are used for cuts. These fluctuations of the comparative plot are only in the order of the statistical error (less than 2%). Figure 8.34 and 8.35 show examples of the transverse momentum distribution of the charged lepton as well as the distribution of the azimuthal angle between the charged lepton and the jet for $(\mathrm{W}^+ \to \ell^+\nu_\ell) + 1\ jet$.

Last but not least, I want to present explicit examples that show that the above behaviour also holds true for associated jets. Figure 8.36 shows the invariant mass of the two jets for Z production with decay into two leptons and Figure 8.37 shows the transverse momenta of the harder jet for W^- production.

The rapidity distributions, however, are not just scaled down equally over the whole range. Figures 8.38 and 8.39 show the rapidity distribution of the charged lepton for W^+ production with no and two associated jets, respectively. One can see that there is a significantly larger contribution in the central region for the zero-jet scenario when one uses the CTEQ6L1 PDF set. Jet rapidity distributions behave similarly as shown in Figure 8.41 for the $(\mathrm{Z} \to \ell^+\ell^-) + 1\ jet$ process. For all processes involving jets the charged lepton rapidities are more dominant in the forward direction for CTEQ6L1 in comparision to MSTW2008LO (90% C.L.). The same is also true for the Z production as it can be seen in Figure 8.40, which shows the rapidity distribution of the harder charged lepton for the $(\mathrm{Z} \to \ell^-\ell^+) + 2\ jets$ process.

These differences disappear for the separation in rapidity and the separation $R < \pi$, i.e. for the region where there is a contribution from the azimuthal angle. Figure 8.42 gives the differential cross-section with respect to the separation R between the two associated jets for $(\mathrm{Z} \to \ell^-\ell^+)$.

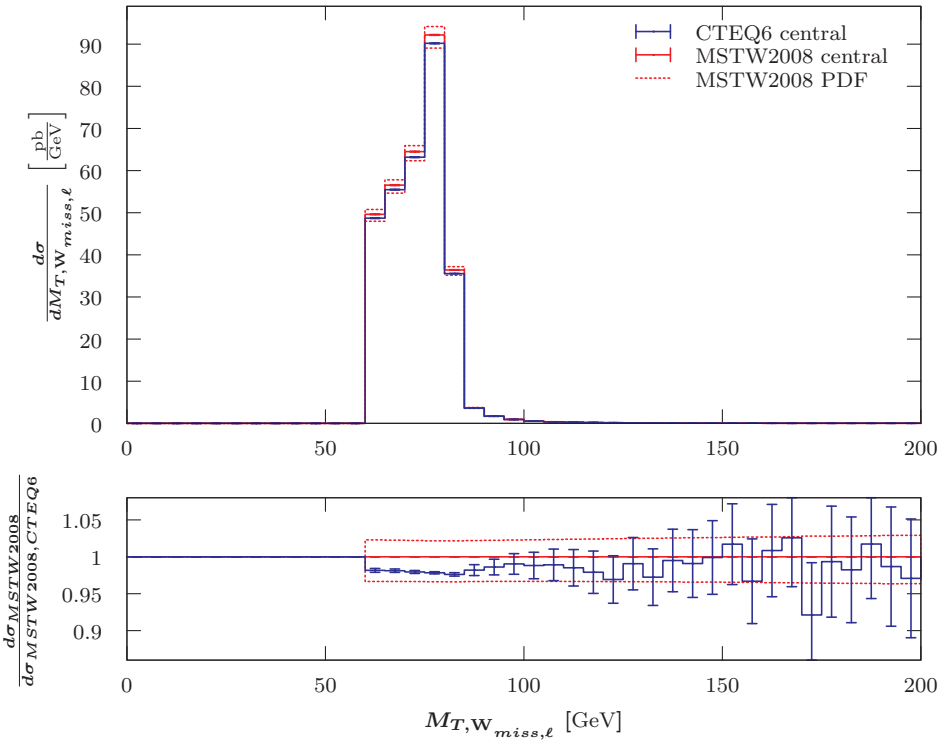

Figure 8.31: LO differential cross-section with respect to the transverse mass of the charged lepton and the missing transverse momentum for the $pp \to (W^+ \to \ell^+\nu_\ell)$ process at the LHC with 7 TeV using a fixed scale of $\mu_0 = M_W$. Results for two PDF sets, MSTW2008LO (90% C.L.) (red) and CTEQ6L1 (blue), are shown (top) and compared (bottom). Selection cuts as given in Equations 7.5 to 7.8 have been applied. MCFM input parameters are listed in Equations 7.1 to 7.3. The procedure used to choose the number of shots is described in Section 4.4.3. The scale uncertainties have been estimated using a conservative variation by a factor of 4. Only the asymmetric deviations for the PDFs (dashed) from the central value (solid) are given.Errors are propagated using Equations 8.3 and 8.4.

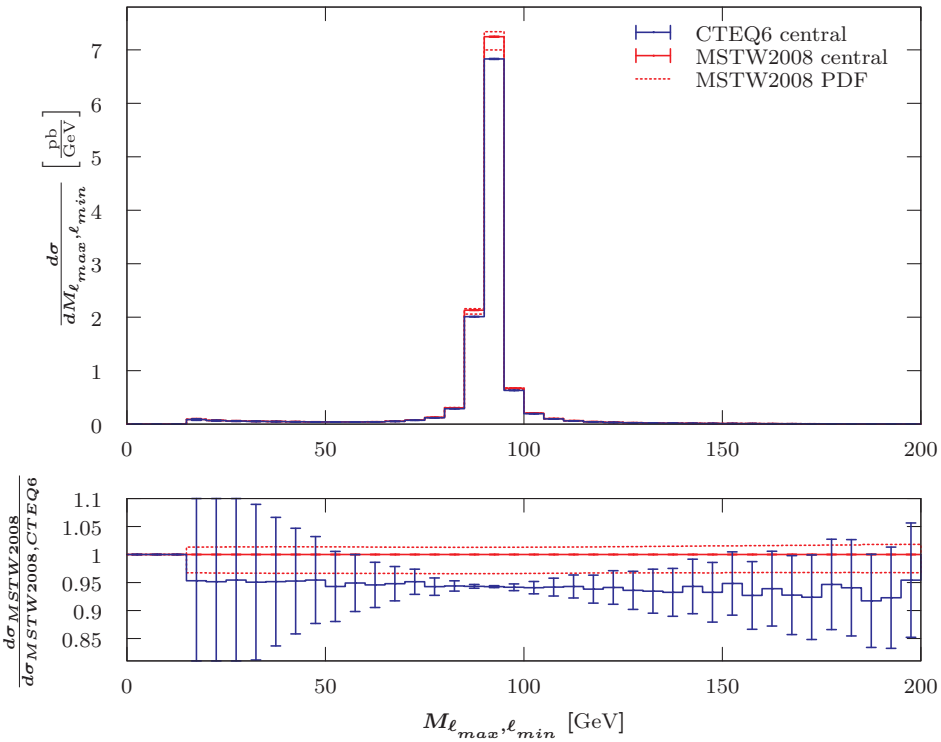

Figure 8.32: LO differential cross-section with respect to the di-lepton invariant mass for the $pp \to (Z \to \ell^-\ell^+) + 1\ jet$ process. Additional details are given in the caption of Figure 8.31.

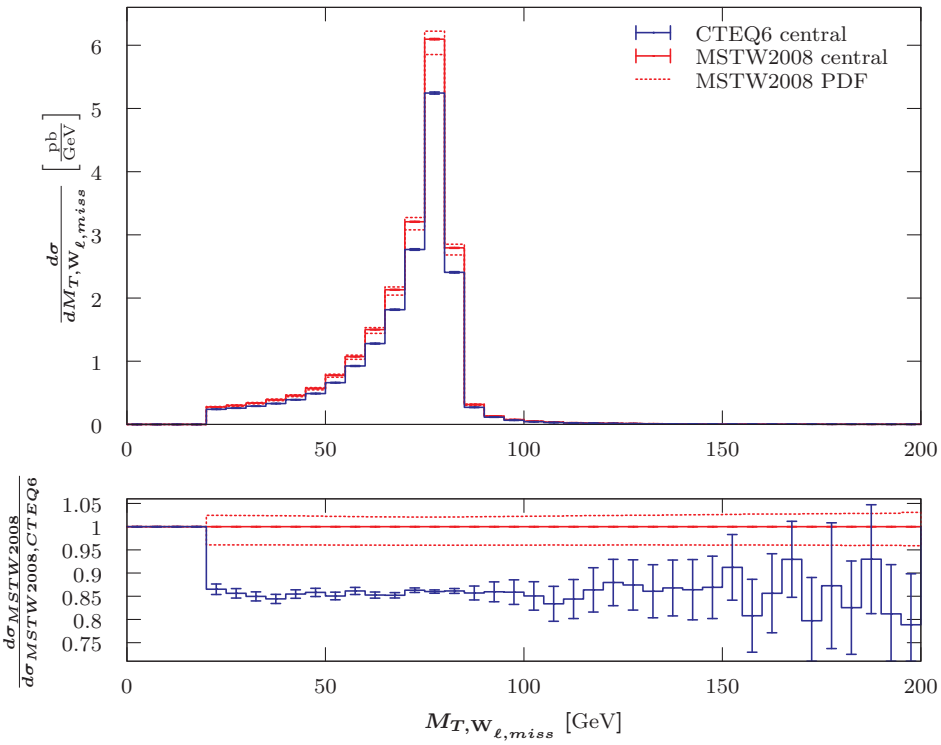

Figure 8.33: LO differential cross-section with respect to the transverse mass of the charged lepton and the missing transverse momentum for the $pp \to (W^- \to \ell^-\overline{\nu}_\ell) + 2\ jets$ process. Additional details are given in the caption of Figure 8.31.

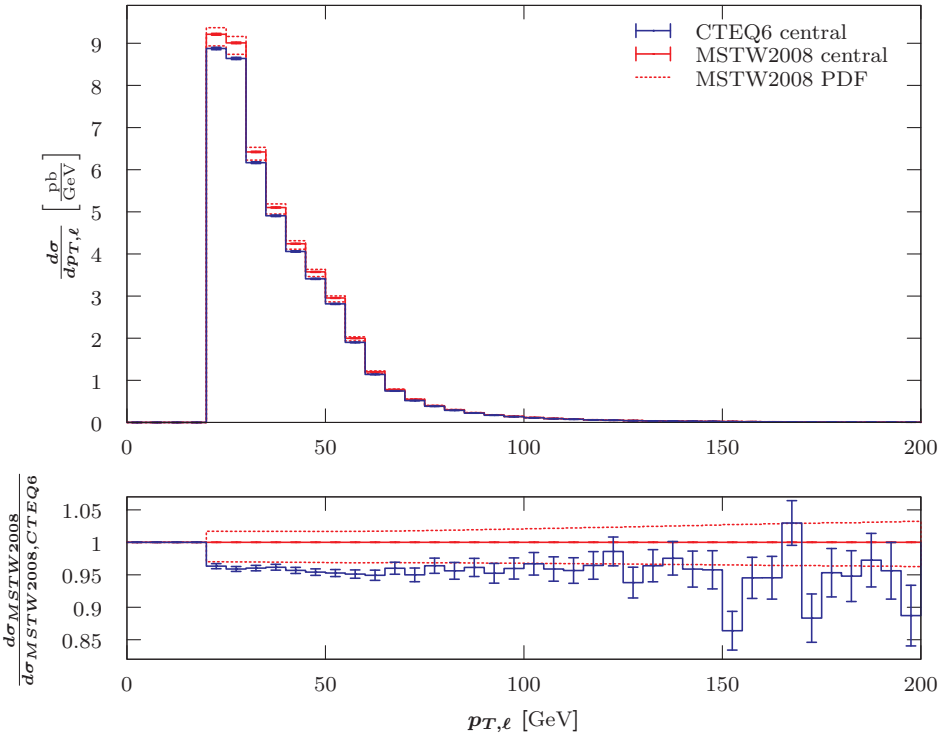

Figure 8.34: LO differential cross-section with respect to the transverse momentum of the charged lepton for the pp $\to (\mathrm{W}^+ \to \ell^+\nu_\ell) + 1\ jet$ process. Additional details are given in the caption of Figure 8.31.

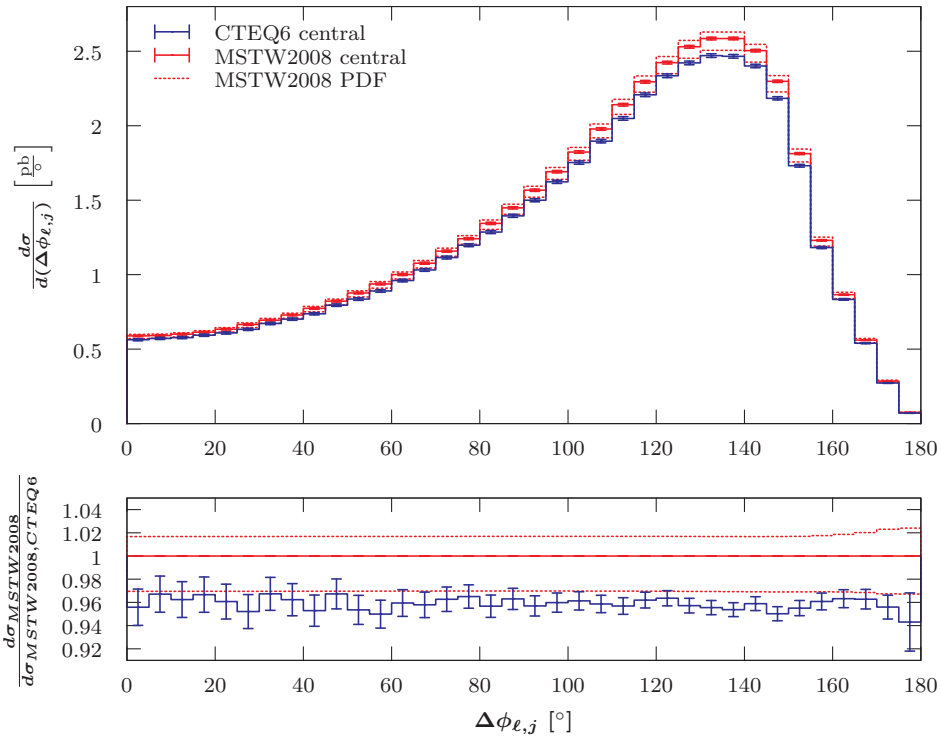

Figure 8.35: LO differential cross-section with respect to the azimuthal angle between the charged lepton and the jet for the pp $\to (\mathrm{W}^+ \to \ell^+\nu_\ell) + 1\ jet$ process. Additional details are given in the caption of Figure 8.31.

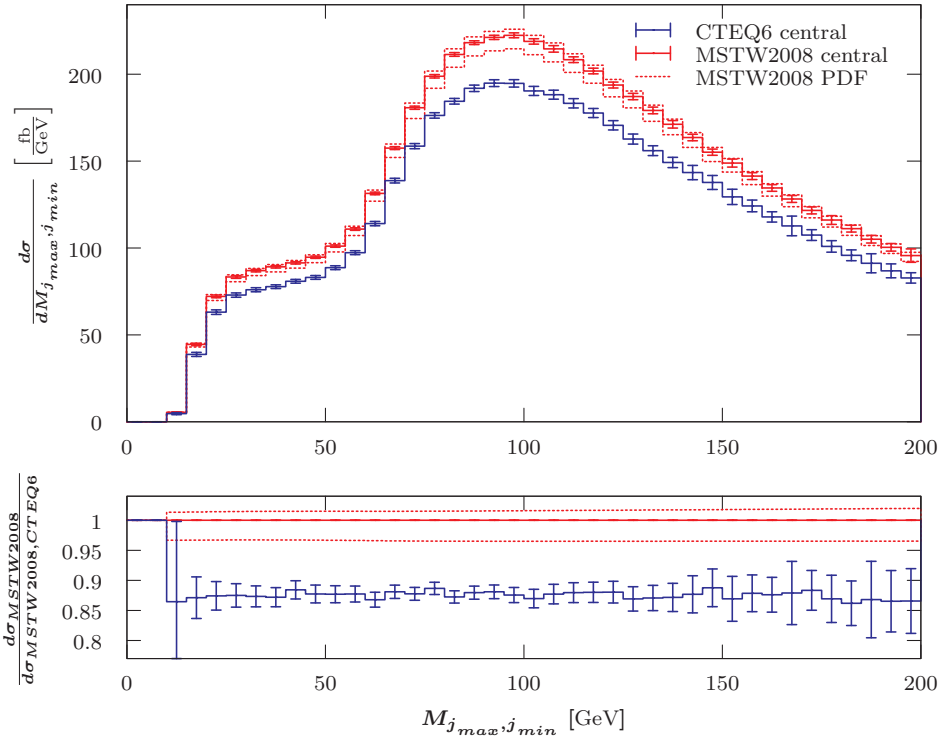

Figure 8.36: LO differential cross-section with respect to the invariant mass between the two jets for the pp $\to$ (Z $\to \ell^-\ell^+$) + 2 *jets* process. Additional details are given in the caption of Figure 8.31.

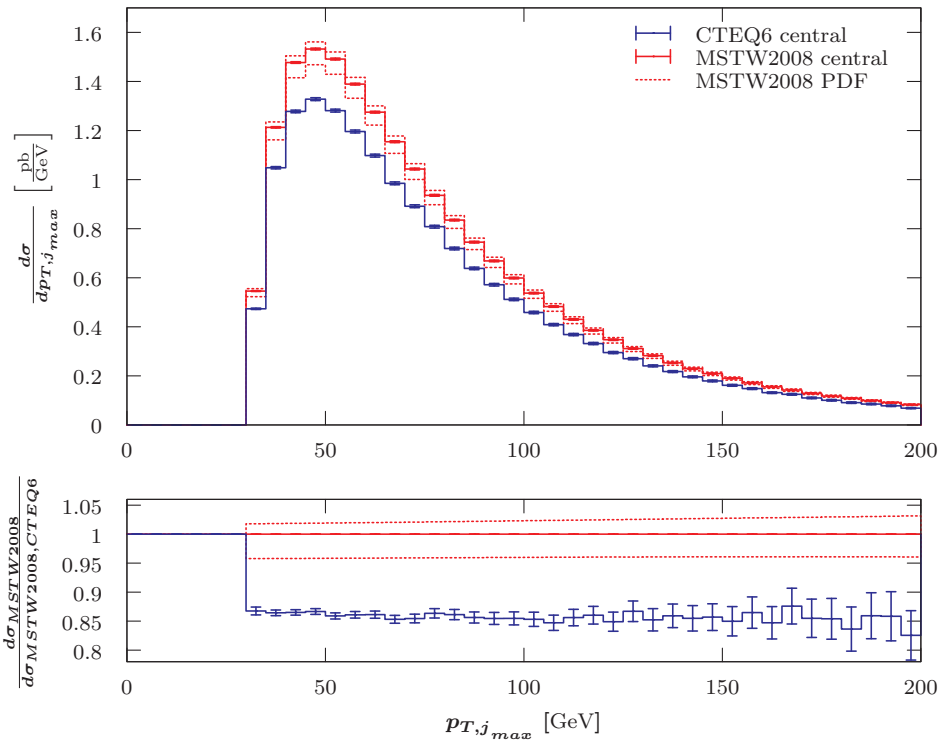

Figure 8.37: LO differential cross-section with respect to the transverse momentum of the harder jet for the pp $\to$ (W$^-$ $\to \ell^-\overline{\nu}_\ell$) + 2 *jets* process. Additional details are given in the caption of Figure 8.31.

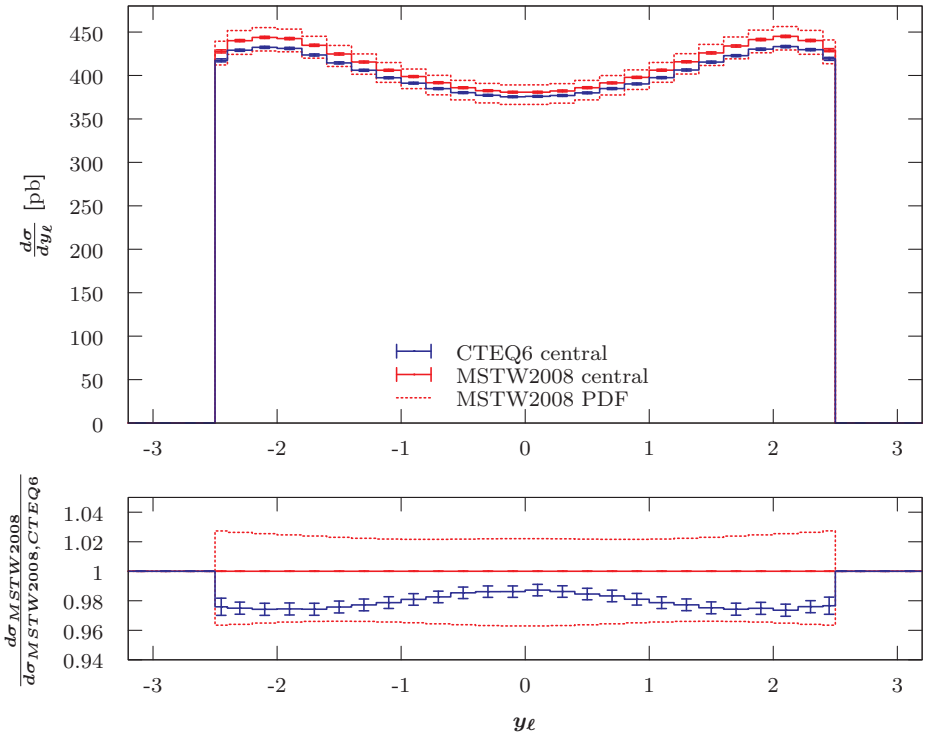

Figure 8.38: LO differential cross-section with respect to the rapidity of the charged lepton for the $pp \to (W^+ \to \ell^+\nu_\ell)$ process. The first and last filled bin are half-width due to the applied selection cut, $|y_\ell| < 2.5$. Additional details are given in the caption of Figure 8.31.

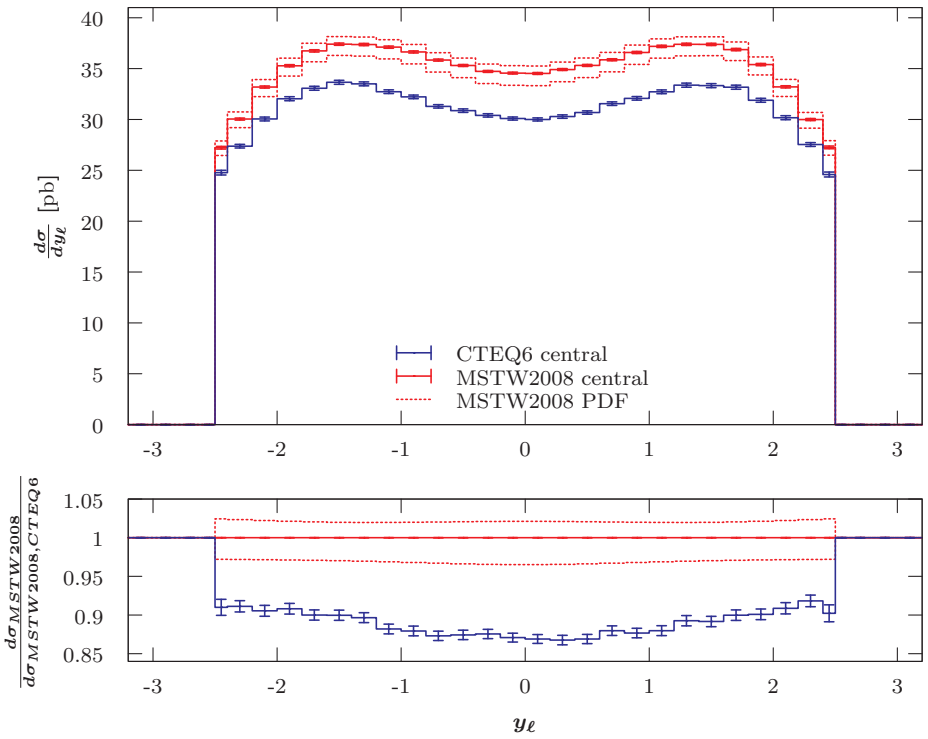

Figure 8.39: LO differential cross-section with respect to the rapidity of the charged lepton for the $pp \to (W^+ \to \ell^+\nu_\ell) + 2\ jets$ process. The first and last filled bin are half-width due to the applied selection cut, $|y_\ell| < 2.5$. Additional details are given in the caption of Figure 8.31.

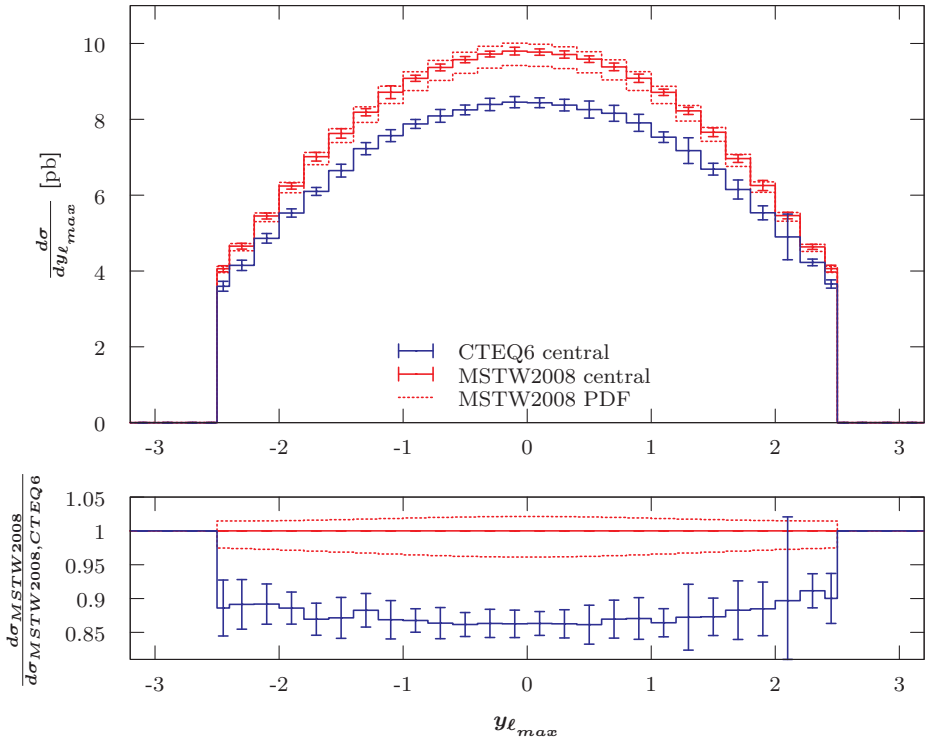

Figure 8.40: LO differential cross-section with respect to the rapidity of the harder charged lepton for the pp $\to$ (Z $\to \ell^-\ell^+$) + 2 *jets* process. The first and last filled bin are half-width due to the applied selection cut, $|y_\ell| < 2.5$. Additional details are given in the caption of Figure 8.31.

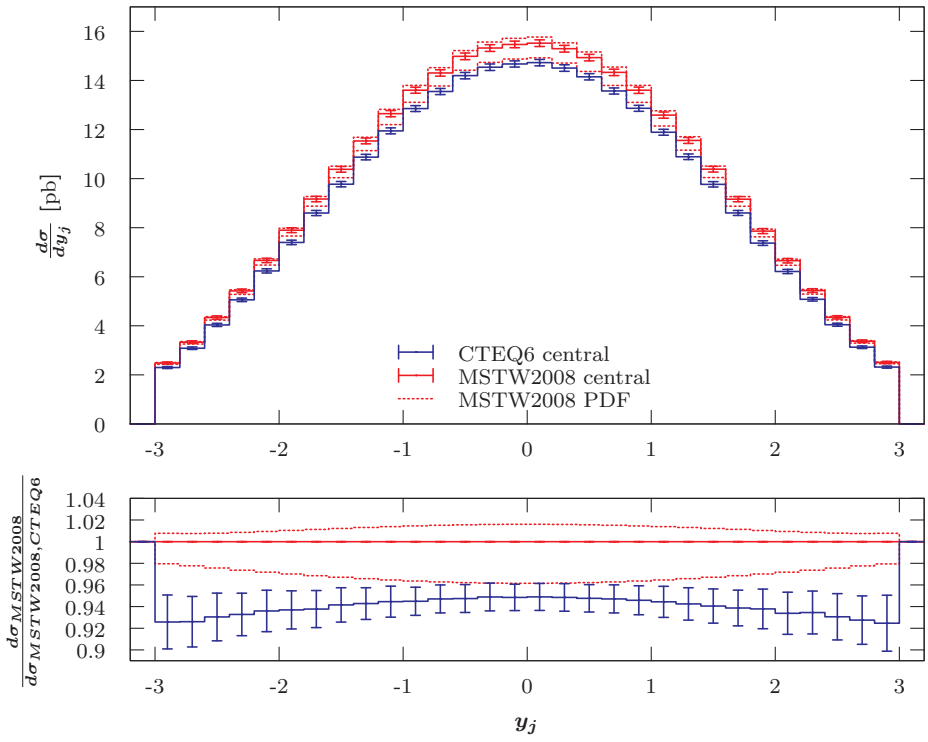

Figure 8.41: LO differential cross-section with respect to the rapidity of the jet for the pp $\to$ (Z $\to \ell^-\ell^+$) + 1 *jet* process. Additional details are given in the caption of Figure 8.31.

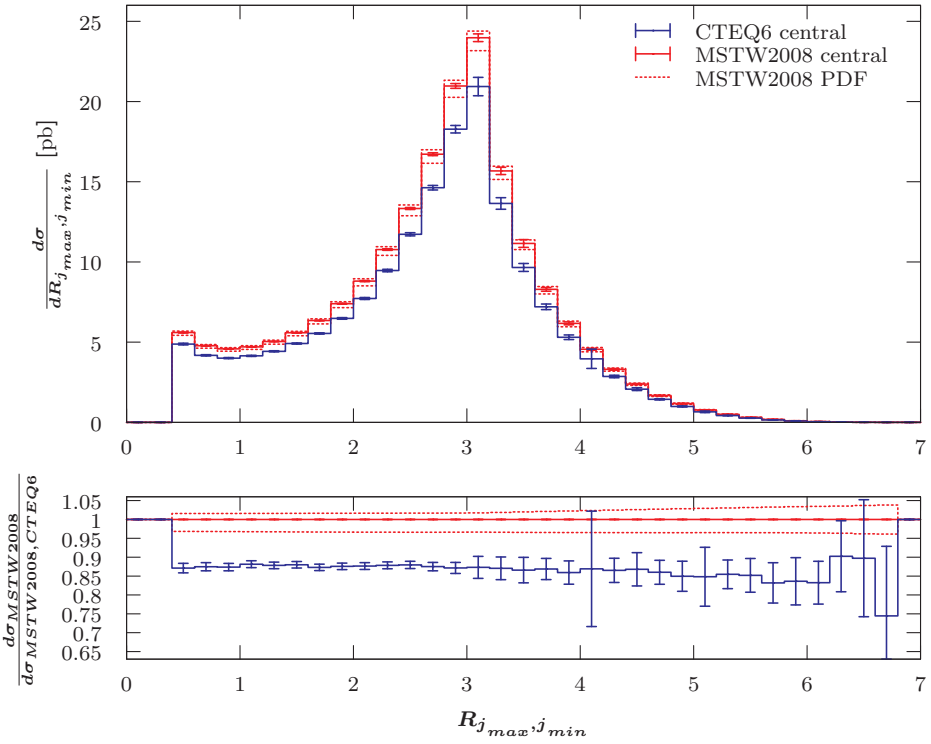

Figure 8.42: LO differential cross-section with respect to the separation R between the two jets for the pp $\rightarrow$ (Z $\rightarrow \ell^-\ell^+$) + 2 *jets* process. Additional details are given in the caption of Figure 8.31.

8.7 Conclusion

This work has found that the production processes for weak bosons with leptonic decay and associated jets provide a wide phenomenological spectrum. I have presented a variety of different observables for integrated and differential cross-sections.

The ratio between the total cross-section for W^+ and W^- production with leptonic decay has been proven to be very stable with respect to the static and dynamic scales. That means that it is a very good test for the SM, both at the Tevatron where the ratio is equal to one and at the the LHC where the ratio is expected to be larger than one. For the latter, the one-jet process has the smallest scale uncertainty, which makes it the best choice for such a test. Its scale uncertainties will be even smaller for the LHC running at 14 GeV.

I have also shown that processes producing equal amounts of W^+ and W^- will shift the $W^\pm$ ratio towards one. Hence, it can be used as an indicator for the presence of new, weakly interacting neutral particles. The observable $f_{NP} = {}^{2(R_{SM}-R_{exp})}/_{(R_{SM}+1)(R_{exp}-1)}$ gives an easy way of comparing the theoretical predictions and the experimental measurements.

Similarly, I have shown that the ratio between the total cross-sections for Z production with decay into charged leptons and with decay into neutrinos, is also a variable that is stable with respect to the choice of static and dynamic scales. This is, however, a very impractical observable, because the total cross-section for the decay into neutrinos cannot be measured directly. Only a very accurate measurement of the width of the Z boson decay into charged leptons and the width of the hardonic decay makes this channel accessible via a comparison to the total width of the Z boson.

The last observable constructed from integrated cross-sections which I looked at is the Berends-Giele scaling. I have shown that it changes depending on the use of static or different dynamic scales, though, it is a an observable which is widely used by experimentalists and could allow us to make a more educated decision about which scales are best used. Such knowledge would be very useful in order to calculate accurate profiles for differential cross-sections.

Though I have not shown it (as I have not calculated cross-sections for three associated jets), the Berends-Giele scaling is not the best way to predict cross-sections with more than four jets, as it cannot be calculate at (N)LO yet. The BFKL scaling which tries to estimate evolution of the gluon and the quark contributions towards the integrated cross-sections seems to be more promising [52].

Moreover, I have shown the scale and PDF uncertainties associated with differential cross-sections. I found that the zero-jet processes are probably the best to detect heavier weak bosons, because both sources of theoretical uncertainties decrease in the large mass tail. For one and two-jets processes the uncertainties became larger in the tails. I found

similar behaviour for transverse momentum distributions. Hence, I suggested the use of hard cuts around the W and Z peak of the (transverse) invariant mass, as well as hard cuts on the transverse momentum to improve the SM signal for processes with one or two associated jets. I hinted that the same might be possible for some of the separations in the azimuthal angle between the final state particles.

I also provided a comparison of differential cross-sections with respect to the use of the static scale M_V and the dynamic scales E_T^V and $\hat{H}_T$. I found that the choice of different scales does not change the position of peaks and general features of the curves, but often tails can be steeper or shallower.

As expected, I found that E_T^V provides the same result for the zero-jet distributions, but that the $\hat{H}_T$ scale can deviate by almost the full error band. One should be particularly careful when the tails of distributions for the transverse momentum or the separation in azimuthal angle are used to scale theoretical predictions in order to estimate backgrounds. This is likely to be imprecise, because even a scale variation of the static scale by a factor of four does not always cover the deviation of both of the dynamic scales for two-jet processes or at least the $\hat{H}_T$ scale deviations for one jet processes.

While the same warning should be given for invariant mass distributions, I have shown that the deviations are smaller and normally fall within the uncertainty of the static scale predictions. In contrast, rapidity distributions have been very stable with respect to different scale choices and only vary by a constant factor. The dynamic scales are well within the error envelope even for processes with two-jets.

Finally, I compared differential cross-sections with respect to different PDF sets. I used MSTW2008LO (90% C.L.) and CTEQ6L1. I found that the results for the latter are scaled down by constant factor for transverse observables. The PDF uncertainties for MSTW2008LO (90% C.L.) were large enough to cover the deviation for zero and one-jet processes, but not for two associated jets. This behaviour could be accurately predicted from the integrated cross-sections. For the rapidity distributions there were no uniform behaviours with respect to the deviations, i.e. the CTEQ6L1 could be more dominant in the central region or the forward regions. The deviation could even get larger in regions were the MSTW2008LO (90% C.L.) errors would suggest otherwise.

This does not fully coincide with observations made by Alekhin et al. [55]. They found that most theoretical predictions for different PDF sets are within the error bars of each other. I agree, however, that some PDF sets consistently yield larger or smaller cross-sections. This hints towards not only quantitative, but also qualitative differences. Comparison of these theoretical predictions with experimental measurements might be able to rule out some of the PDF sets. From my analysis I would suggest that rapidity distributions and the $W^{\pm}$ ratio are useful tools for such an analysis.

Chapter 9

Summary

I have investigated integrated and differential LO cross-sections for weak boson production with up to two associated jets ($n = \{0, 1, 2\}$) and leptonic decays at hadron colliders. Twelve processes have been investigated:

- $\mathrm{p}^{(}\overline{\mathrm{p}}^{)} \to (\mathrm{W}^+ \to \ell^+\nu_\ell) + n\ jets$
- $\mathrm{p}^{(}\overline{\mathrm{p}}^{)} \to (\mathrm{W}^- \to \ell^-\overline{\nu}_\ell) + n\ jets$
- $\mathrm{p}^{(}\overline{\mathrm{p}}^{)} \to (\mathrm{Z} \to \ell^-\ell^+) + n\ jets$
- $\mathrm{p}^{(}\overline{\mathrm{p}}^{)} \to (\mathrm{Z} \to \sum_{\ell=\mathrm{e},\mu,\tau} \nu_\ell\overline{\nu}_\ell) + n\ jets$

All results have been calculated using an amended version of the MCFM 6.0 package and custom Python scripts. MCFMs estimation of statistical uncertainties has been fixed and routines for cuts, histograms, scale and PDF uncertainties have been added. All raw data has been recorded in output files and are provided online[1]. Post-processing, including combination of gluon and quark-quark calculations as well as comparisons, has been done using Python scripts. All simulations have been run on a Beowulf cluster at the Centre of Particle Physics at Royal Holloway.

Total cross-sections and distributions have been calculated for the Tevatron Run II (1.96 TeV), and LHC with 7 TeV and 14 TeV. Basic kinematic cuts to mirror detector acceptance have been used. Some additional physics motivated cuts have been applied, namely invariant mass, transverse mass and missing transverse momentum. Cross-sections have been obtained for two different PDF sets, MSTW2008LO (90% C.L.) and CTEQ6L1, and three different scale choices: static $\mu_0 = M_V$, dynamic E_T^V and $\hat{H}_T$. For each setup and process up to 30 different observables have been calculated:

- integrated cross-sections
- transverse momentum for p_T-ordered charged leptons
- rapidity y distribution for p_T-ordered charged leptons
- missing transverse momentum
- transverse momentum distribution for p_T-ordered jets
- rapidity y distribution for p_T-ordered jets

[1] See `www.pp.rhul.ac.uk/~stietz/Vjets`.

- transverse mass distributions for W^+ and W^- bosons
- invariant mass distribution for Z boson
- two-particle invariant mass for lepton-lepton, lepton-jet and jet-jet
- two-particle rapidity separation between lepton-lepton, lepton-jet and jet-jet
- two-particle azimuthal opening angle between lepton-lepton, lepton-jet and jet-jet
- two-particle separation ΔR between lepton-lepton, lepton-jet and jet-jet

For all these observables, uncertainties, both for PDFs and scales, have been estimated. Symmetric and asymmetric PDF uncertainties have been determined for the MSTW2008 results using the provided eigenvector sets. The symmetric and asymmetric scale uncertainties for a variation by a conservative factor of four[2] have been obtained. Relative statistical uncertainties for all cross-sections are smaller than 0.1% and do not exceeded 1.58% of the PDF uncertainties.

The integrated cross-sections have been analysed using constructed observables, i.e. the ratio between the cross-sections for W^+ and W^- production with leptonic decay and the ratio between the cross-sections for the two studied decays of the Z production. Both have been calculated and I found that they are very stable for all scale choices. In contrast, the Berends-Giele scaling, which compares integrated cross-sections for weak boson production with different numbers of associated jets, strongly depends on the choice of static or dynamic scales.

Distributions of differential cross-sections have been compared with respect to different PDF and scale choices. For the former I found a simple scaling for transverse observables. The PDF uncertainties for MSTW2008LO (90% C.L.) were large enough to encompass the deviation between the two studied PDF sets for zero and one-jet processes, but not for two associated jets. Care has to be taken for rapidity distributions. The behaviour of CTEQ6L1 versus MSTW2008LO was unpredictable meaning that CTEQ6L1 can give a larger cross-section in the central or forward region, and the MSTW2008LO error underestimated this deviation. For differential cross-sections with respect to the invariant mass, the PDF and scale uncertainties decrease in the large invariant mass tails for zero-jet processes, but increase in the tails for one and two-jet processes. The latter could also be observed for transverse momentum distributions.

I saw that different scale choices do not change the position of peaks and general features of the curves, but tails can differ. Varying the static scale by a factor of four was not always sufficient to cover the central values for dynamic scale choices. The dynamic scale results for invariant mass distributions were smaller than the static scale predictions and normally fell within the uncertainty envelope. Rapidity distributions were very stable with respect to different scale choices and only differ by a constant factor and the dynamic scales are well within the uncertainty envelope of the static scale.

[2]Other values are available online.

Acknowledgements

I thank my supervisor Dr Nikolas Kauer for useful discussions. My work was supported by the Higher Education Funding Council for England and the Science and Technology Facilities Council under the SEPnet Initiative as part of the NExT institute.

Thanks and Dedication

I would like to thank my family, particularly my parents Michael and Kornelia who with their unconditional dedication and unbreakable optimism have supported me all the way since the beginning of my life, and I would like to dedicate this work to my late grandfather Günther Tietz and late grandmother Karin Freisleben, who both could not witness the completion of my thesis.

Special thanks goes to my girlfriend Heather Rumble who has been a great source of motivation and inspiration. I would especially like to thank her for proof reading seemingly meaningless long sentences containing dozens of cryptic equations and words made-up by particle physicists.

Finally, I would like to thank my friends who have been at my side during this adventure and who like me believe in the virtue of learning and teaching. If we don't who will?

Bibliography

[1] LHC Physics Centre at CERN. *LHC luminosity charts*. Website (**April 2012**). URL `http://lpcc.web.cern.ch/LPCC/index.php?page=luminosity_charts`.

[2] CERN Press Office. *LHC to run at 4 TeV per beam in 2012*. Website (**February 2012**). URL `http://press.web.cern.ch/press/PressReleases/Releases2012/PR01.12E.html`.

[3] M. Kado. *The Search for the Higgs Boson in the Four-Jet Channel at LEP*. Nucl. Phys. B - Proc. Sup., 109 (2-3) (2002) pp. 118. doi:10.1016/S0920-5632(02)01589-X.

[4] P. Teixeira-Dias. *Higgs boson searches at LEP* (**April 2008**). `arXiv:heo-ex/0804.4146v1`.

[5] Tevatron New Phenomena & Higgs Working Group. *Updated Combination of CDF and DZero's Searches for Standard Model Higgs Boson Production with up to* $10.0\,\mathrm{fb}^{-1}$ *of Data*. Website (**June 2012**). URL `http://tevnphwg.fnal.gov/results/SM_Higgs_Summer_12/index.html`.

[6] F. Gianotti. *Status of Standard Model Higgs searches in ATLAS*. Presentation Slides (**July 2012**). URL `http://indico.cern.ch/conferenceDisplay.py?confId=197461`.

[7] J. Incandela. *Status of the CMS SM Higgs Search*. Presentation Slides (**July 2012**). URL `http://indico.cern.ch/conferenceDisplay.py?confId=197461`.

[8] ATLAS Collaboration. *ATLAS Experiment - Public Results*. Website (**June 2012**). URL `https://twiki.cern.ch/twiki/bin/view/AtlasPublic`.

[9] CMS Collaboration. *CMS Physics Results*. Website (**June 2012**). URL `https://twiki.cern.ch/twiki/bin/view/CMSPublic/PhysicsResults`.

[10] C. Strege et al. *Updated global fits of the cMSSM including the latest LHC SUSY and Higgs searches and XENON100 data*. `arXiv:1112.4192v2[hep-ph]`.

[11] CMS Collaboration. *Observation of Long-Range Near-Side Angular Correlations in Proton-Proton Collisions at the LHC*. J. High Energy Phys., 10.1007 (2010) p. 091. `arXiv:1009.4122v1[hep-ex]`.

[12] LHCb Collaboration. *Rare Decays in LHCb*. `arXiv:1201.5359v1[hep-ex]`.

[13] CDF Collaboration. *Search for* $B_s^0 \to \mu^-\mu^+$ *and* $B^0 \to \mu^-\mu^+$ *Decays with CDF II*. Phys. Rev. Lett., 107. doi:10.1103/PhysRevLett.107.191801. `arXiv:1107.2304v2[hep-ex]`.

[14] ATLAS Collaboration. *Observation of a New χ_b State in Radiative Transitions to $\Upsilon(1S)$ and $\Upsilon(2S)$ at ATLAS.* Phys. Rev. Lett., 108 (2012) p. 2001. arXiv:1112.5154v5.

[15] S. Moretti. *Selected topics in Phenomenology.* Lecture Series (**February 2010**).

[16] N. Kauer. *Hadron Collider Phenomenology.* Lecture Series (**December 2010**).

[17] T. Han. *Collider Phenomenology (Basic Knowledge and Technics).* arXiv:hep-ph/0508097.

[18] D. Griffiths. *Introduction to Elementary Particles.* John Wiley & Sons, New York (**1987**). ISBN 0-471-60386-4.

[19] S. F. Novaes. *Standard Model: An Introduction* (**2000**). arXiv:hep-ph/0001283v1.

[20] I. J. R. Aitchison. *Introduction to Symmetries.* Lecture Notes (**2000**).

[21] H. Georgi. *Lie Algebras in Particle Physics (From Isospin to Unified Theories).* 2nd ed. Academic Press (**1999**). ISBN 978-0-7382-0233-4.

[22] D. H. Perkins. *Introduction to High Energy Physics.* 4th ed. Cambridge University Press, Cambridge (**2000**). ISBN 0-521-62196-8.

[23] M. E. Peskin and D. V. Schroeder. *An Introduction to Quantum Field Theory.* Westview Press (**1995**). ISBN 0-201-50397-2.

[24] A. Djouadi. *The Anatomy of Electro-Weak Symmetry Breaking. Tome II: The Higgs boson in the Standard Model* (**March 2005**). arXiv:hep-ph/0503172v2.

[25] N. Kauer. *Chapter 2: Cross Sections for $b\bar{b} \to W^-W^+(j)$ Production (PhD thesis).* Ph.D. thesis (**2001**).

[26] D. Griffiths. *Introduction to Elementary Particles.* Wiley VCH, Weinheim (**2008**). ISBN 978-3-527-40601-2.

[27] G. Cowan. *Statistical Data Analysis.* Oxford University Press, Oxford (**1998**). ISBN 0-19-850155-2.

[28] G. P. Lepage. *A New Algorithm for Adaptive Multidimensional Integration.* J. Compuut. Phys., 27 (1978) pp. 192.

[29] G. P. Lepage. *VEGAS - An Adaptive Multi-dimensional Integration Program.* Cornell preprint CLNS, 80/447 (1980) pp. 192.

[30] T. Hahn. *Cuba: a library for multidimensional numerical integration.* Website (**May 2010**). URL http://www.feynarts.de/cuba.

[31] F. James, J. Hoogland and R. Kleiss. *Multidimensional sampling for simulation and integration: measures, discrepancies, and quasi-random numbers.* Computer Physics Communications, 99 (2–3) (1997) pp. 180. doi:10.1016/S0010-4655(96)00108-7.

[32] I. J. R. Aitchison and A. J. G. Hey. *Gauge Theories in Particle Physics (Volume II: QCD and the Electroweak Theory.* 3rd ed. Taylor and Francis (**2004**). ISBN 978-0-7503-0950-9.

[33] G. Sterman et al. (CTEQ collaboration). *Handbook of perturbative QCD (Version 1.1).*

[34] N. Kauer. *Research Projet: $V + jets$ backgrounds to searches with jets and missing transverse energy at hadron colliders $V = W, Z$.* Project discription (**Dec 2010**).

[35] J. M. Campbell and R. K. Ellis. *NLO corrections to $W + 2j$ and $Z + 2j$ production at hadron colliders.* `arXiv:hep-ph/0202176`.

[36] J. M. Campbell and R. K. Ellis. *NLO QCD predictions for $W + 2j$ and $Z + 2j$ production at the CERNLHC.* `arXiv:hep-ph/0308195`.

[37] J. Pumplin et al. *Uncertainties of predictions from parton distribution functions. 2. The Hessian method.* Phys. Rev., D65 (2001) p. 014013. doi:10.1103/PhysRevD.65.014013. `arXiv:hep-ph/0101032`.

[38] D. Stump et al. *Uncertainties of Predictions from Parton Distribution Functions I: the Lagrange Multiplier Method.* doi:10.1103/PhysRevD.65.014012. `arXiv:hep-ph/0101051`.

[39] J. Pumplin et al. *New generation of parton distributions with uncertainties from global QCD analysis.* J. High Energy Phys., 07 (2002) p. 012. `arXiv:hep-ph/0201195`.

[40] J. M. Campbell, J. W. Huston and W. J. Stirling. *Hard Interactions of Quarks and Gluons: A Primer for LHC Physics.* Rept. Prog. Phys., 70 (2007) p. 89. doi:10.1088/0034-4885/70/1/R02. `arXiv:hep-ph/0611148`.

[41] J. M. Campbell and R. K. Ellis. *Monte Carlo for FeMtobarn processes (MCFM).* Website (**April 2012**). URL `http://mcfm.fnal.gov`.

[42] J. M. Campbell, R. K. Ellis and C. Williams. *MCFM v6.0 User Guide* (**May 2011**).

[43] W. H. Press et al. *Numerical Recipes in Fortran: The Art of Scientific Computing.* Cambridge University Press, Cambridge (**1992**). ISBN 0-521-43064-X.

[44] M. Whalley and A. Buckley. *Les Houches Accord PDF Interface (LHAPDF).* Website (**May 2011**). URL `http://lhapdf.hepforge.org`.

[45] *Gnuplot.* Website (**March 2012**). URL `http://www.gnuplot.info/`.

[46] S. Drell and T.-M. Yan. *Massive Lepton-Pair Production in Hadron-Hadron Collisions at High Energies.* Physical Review Letters, p. 316–320. doi:10.1103/PhysRevLett.25.316.

[47] M. Krämer and F. J. P. Soler (editors). *Large Hadron Collider Phenomenology (Scottish Graduate Series).* Institute of Physics (**2004**). ISBN 0-7503-0986-5.

[48] Particle Data Group. *2010 Review of Particle Physics* (**January 2010**). URL http://pdg.lbl.gov.

[49] A. Martin et al. *Parton distributions for the LHC*. arXiv:0901.0002v3[hep-ph].

[50] M. Cacciari, G. P. Salam and G. Soyez. *The anti-k_t jet clustering algorithm*. 0802.1189v2[hep-ph].

[51] M. Botje et al. *The PDF4LHC Working Group Interim Recommendations* (**January 2008**). arXiv:1101.0538v1[hep-ph].

[52] C. H. Kom and W. J. Stirling. *Charge asymmetry in W + jets production at the LHC*. arXiv:1004.3404v3[hep-ph].

[53] G. M. Dallavalle. *Review of Precision Determinations of the Accelerator Luminosity in LEP Experiments*. Acta Phys. Pol. A, 28 (1997) pp. 901.

[54] F. Berends et al. *Multijet production in W, Z events at pp colliders*. Phys. Lett. B, 224 (1-2) (1989) pp. 237 . doi:10.1016/0370-2693(89)91081-2.

[55] S. Alekhin et al. *The PDF4LHC Working Group Interim Report* (**January 2011**). arXiv:1101.0536v1[hep-ph].

Appendix A

Addendum to Custom MCFM Modifications

This appendix gives some of the results of the tests used to check on the customisation of MCFM 5.8 and 6.0.

A.1 Testing the Statistical Error in Histograms

The observed spread around the analytical function should follow a Gaussian distribution. Two runs for different numbers of shots have been done. The results for $N = 10^6$ shots can be seen in Table A.1 and for $N = 10^7$ shots in Table A.2 and Figure A.1. It can be seen that for the lower number of shots the share of points within 1 to 4 standard deviations was underestimated, regardless of the number of bins used. That means that the statistical error was slightly underestimated[1]. For the second case the share was overestimated, meaning the statistical error was overestimated. Though we cannot expect pseudo-random numbers to follow a perfect Gaussian distribution.

Table A.1: Shown are the ratio between shots within $1\sigma_{MC}$, $2\sigma_{MC}$, $3\sigma_{MC}$ and $4\sigma_{MC}$ deviation of $f(r_1) = r_1$ and the total number of shots ($N = 10^6$) for different numbers of bins. The expected ratios for the Gaussian distribution $\Phi(\mu = 0, \sigma^2)$ are given in the second column.

σ	$\Phi(\mu = 0, \sigma^2)$	$\Phi(100\ bins, \sigma^2)$	$\Phi(1000\ bins, \sigma^2)$
$1\sigma_{MC}$	0.682	0.670	0.608
$2\sigma_{MC}$	0.954	0.860	0.885
$3\sigma_{MC}$	0.996	0.960	0.956
$4\sigma_{MC}$	0.998	0.980	0.978

[1] That the statistical error is underestimated means that the actual variation might be larger then stated.

Table A.2: Shown are the ratio between shots within $1\sigma_{MC}$, $2\sigma_{MC}$, $3\sigma_{MC}$ and $4\sigma_{MC}$ deviation of $f(r_1) = r_1$ and the total number of shots ($N = 10^7$) for different numbers of bins. The expected ratios for the Gaussian distribution $\Phi(\mu = 0, \sigma^2)$ are given in the second column.

σ	$\Phi(\mu = 0, \sigma^2)$	$\Phi(100\ bins, \sigma^2)$	$\Phi(1000\ bins, \sigma^2)$
$1\sigma_{MC}$	0.682	0.720	0.757
$2\sigma_{MC}$	0.954	0.970	0.983
$3\sigma_{MC}$	0.996	1.000	1.000
$4\sigma_{MC}$	0.998	1.000	1.000

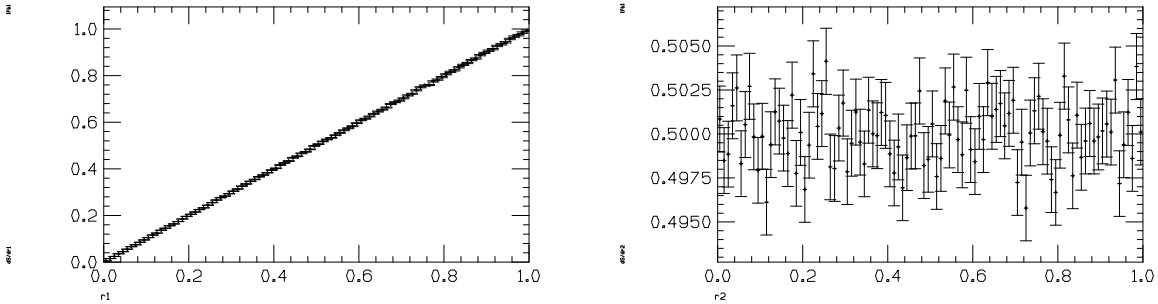

Figure A.1: Shown are histograms of the first pseudo-random number (left) and the second pseudo-random number (right) both with respect to the first pseudo-random number. Histograms have 100 bins and were filled with 10^7 shots.

A.2 Testing Numerical Factors for Scales

For the static case the testing was done by manually changing the scale and via the newly implemented method. In the dynamic case some of the hard coded dynamic scales were used for comparison. The calculated test cross-section are for the process $pp \to (W^+ \to \ell^+\nu_\ell) + 2jets$ at the LHC with 7 TeV and cuts similar to the once used in the final calculation. The results are recorded in Table A.3.

Table A.3: Comparison of test cross-sections for different numerical factors and scales.

Ren./Fac. scale	Numerical factor	σ [fb]
-1 (m_{Z})	0.5	1281161 ± 12922
-3 ($0.5m_{\mathrm{Z}}$)	1	1281161 ± 12922
80.410 (m_{Z})	1	1037780 ± 7458
-1 (m_{Z})	1	1037780 ± 7458
-1 (m_{Z})	2	865000 ± 5813
-6 ($2m_{\mathrm{Z}}$)	1	865000 ± 5813
$+7$ ($\hat{H}_T$)	0.5	1012077 ± 8630
$+22$ ($0.5\hat{H}_T$)	1	1012077 ± 8630
$+7$ ($\hat{H}_T$)	1	837462 ± 6133
$+24$ ($\hat{H}_T$)	1	837462 ± 6133
$+7$ ($\hat{H}_T$)	2	709870 ± 4820
$+25$ ($2\hat{H}_T$)	1	709870 ± 4820

A.3 File Format for Numerical Output and Input

Table A.4 gives an example of an ASCII file used to interface MCFM with my custom Python scripts in order to allow others to use my data for their own work. My raw data is available under `www.pp.rhul.ac.uk/~stietz/Vjets`.

Table A.4: Shown is an example of an ASCII file used to interface MCFM with my custom Python scripts. The file consist of different blocks, where each block consists of two header lines (starting with '#') followed by at least one data line. All values a re semicolon-separated. The first line in the header contains general information about the data in the block in a key-value format. The second line gives labels for each column of the following data. The first block contains the total cross-section and all following blocks contain differential distributions.

```
1  #title                  ;cross-section          ;total                  ;62914560               ;iterations             ;
   10,10                   ;shots/iteration        ;3145728,3145728        ;units                  ;fb
2  #S(PDFset/mu_fac=0)     ;S(avg)                 ;S2(avg)                ;S(PDFset= 1)           ;S(PDFset= 2)           ;
   S(PDFset= 3)            ;S(PDFset= 4)           ;S(PDFset= 5)           ;S(PDFset= 6)           ;S(PDFset= 7)           ;
   S(PDFset= 8)            ;S(PDFset= 9)           ;S(PDFset=10)           ;S(PDFset=11)           ;S(PDFset=12)           ;
   S(PDFset=13)            ;S(PDFset=14)           ;S(PDFset=15)           ;S(PDFset=16)           ;S(PDFset=17)           ;
   S(PDFset=18)            ;S(PDFset=19)           ;S(PDFset=20)           ;S(PDFset=21)           ;S(PDFset=22)           ;
   S(PDFset=23)            ;S(PDFset=24)           ;S(PDFset=25)           ;S(PDFset=26)           ;S(PDFset=27)           ;
   S(PDFset=28)            ;S(PDFset=29)           ;S(PDFset=30)           ;S(PDFset=31)           ;S(PDFset=32)           ;
   S(PDFset=33)            ;S(PDFset=34)           ;S(PDFset=35)           ;S(PDFset=36)           ;S(PDFset=37)           ;
   S(PDFset=38)            ;S(PDFset=39)           ;S(PDFset=40)           ;S(mu_fac=-4)           ;S(mu_fac=-3)           ;
   S(mu_fac=-2)            ;S(mu_fac=-1)           ;S(mu_fac=0)            ;S(mu_fac=1)            ;S(mu_fac=2)            ;
   S(mu_fac=3)             ;S(mu_fac=4)            ;statistical err.       ;sym.PDFerr.(del)       ;asym.PDFerr.(lo)       ;
   asym.PDFerr.(hi)        ;sym.scaleerr.(del,i=1) ;asym.scaleerr.(lo,i=1) ;asym.scaleerr.(hi,i=1) ;sym.scaleerr.(del,i=2) ;
   asym.scaleerr.(lo,i=2)  ;asym.scaleerr.(hi,i=2) ;sym.scaleerr.(del,i=3) ;asym.scaleerr.(lo,i=3) ;asym.scaleerr.(hi,i=3) ;
   sym.scaleerr.(del,i=4)  ;asym.scaleerr.(lo,i=4) ;asym.scaleerr.(hi,i=4)
3              103459.419339;            103462.134477;            35343748888.0; ...
4  #title                  ;pt(l-)                 ;entires                ;29575800               ;overflow               ;
   0                       ;underflow              ;2720768                ;units                  ;GeV                    ;
   integral                ;102749.046317          ;statistical error      ;18.0422843372
5  #X(PDFset=0)            ;dS/dX(PDFsset=0)       ;dS2/dX(avg)            ;dS/dX(PDFset= 1)       ;dS/dX(PDFset= 2)       ;
   dS/dX(PDFset= 3)        ;dS/dX(PDFset= 4)       ;dS/dX(PDFset= 5)       ;dS/dX(PDFset= 6)       ;dS/dX(PDFset= 7)       ;
   dS/dX(PDFset= 8)        ;dS/dX(PDFset= 9)       ;dS/dX(PDFset=10)       ;dS/dX(PDFset=11)       ;dS/dX(PDFset=12)       ;
   dS/dX(PDFset=13)        ;dS/dX(PDFset=14)       ;dS/dX(PDFset=15)       ;dS/dX(PDFset=16)       ;dS/dX(PDFset=17)       ;
   dS/dX(PDFset=18)        ;dS/dX(PDFset=19)       ;dS/dX(PDFset=20)       ;dS/dX(PDFset=21)       ;dS/dX(PDFset=22)       ;
   dS/dX(PDFset=23)        ;dS/dX(PDFset=24)       ;dS/dX(PDFset=25)       ;dS/dX(PDFset=26)       ;dS/dX(PDFset=27)       ;
   dS/dX(PDFset=28)        ;dS/dX(PDFset=29)       ;dS/dX(PDFset=30)       ;dS/dX(PDFset=31)       ;dS/dX(PDFset=32)       ;
   dS/dX(PDFset=33)        ;dS/dX(PDFset=34)       ;dS/dX(PDFset=35)       ;dS/dX(PDFset=36)       ;dS/dX(PDFset=37)       ;
   dS/dX(PDFset=38)        ;dS/dX(PDFset=39)       ;dS/dX(PDFset=40)       ;dS/dX(mu_fac=-4)       ;dS/dX(mu_fac=-3)       ;
   dS/dX(mu_fac=-2)        ;dS/dX(mu_fac=-1)       ;dS/dX(mu_fac=0)        ;dS/dX(mu_fac=1)        ;dS/dX(mu_fac=2)        ;
   dS/dX(mu_fac=3)         ;dS/dX(mu_fac=4)        ;statistical err.       ;sym.PDFerr.(del)       ;asym.PDFerr.(lo)       ;
   asym.PDFerr.(hi)        ;sym.scaleerr.(del,i=1) ;asym.scaleerr.(lo,i=1) ;asym.scaleerr.(hi,i=1) ;sym.scaleerr.(del,i=2) ;
   asym.scaleerr.(lo,i=2)  ;asym.scaleerr.(hi,i=2) ;sym.scaleerr.(del,i=3) ;asym.scaleerr.(lo,i=3) ;asym.scaleerr.(hi,i=3) ;
   sym.scaleerr.(del,i=4)  ;asym.scaleerr.(lo,i=4) ;asym.scaleerr.(hi,i=4)
6                    2.5;                    0.0;                    0.0; ...
7                    7.5;                    0.0;                    0.0; ...
... ...
45                 197.5;             13.522495655;             946777.24222; ...
46 #title                  ;pt(nbar_1)             ;entires                ; ...
47 #X(PDFset=0)            ;dS/dX(PDFsset=0)       ;dS2/dX(avg)            ; ...
48                   2.5;                    0.0;                    0.0; ...
... ...
```

Appendix B

Additional Results

This appendix holds some additional results. Firstly, I will list the integrated cross-sections for CTEQ6L1. Secondly, I will show some additional distributions for Tevatron Run II (1.96 TeV) and LHC with 14 TeV as well as for the two dynamic scales $\mu_0 = E_T^V$ and $\mu_0 = H_T$ for completeness. These plots are mostly identical to the results for LHC with 7 TeV and the static scale $\mu_0 = M_V$ which are listed in Chapter 7.4.

B.1 Integrated Cross-sections for CTEQ6L1

LO cross-sections for the CTEQ6L1 PDF sets are listed in Table B.1 for Tevatron Run II, Table B.2 for LHC at 7 TeV and Table B.3 for LHC at 14 TeV. The statistical error is quoted using bracket notation. Both the asymmetric as well as the symmetric deviations (in square brackets) for the scale uncertainties are listed as relative errors. They have been rounded up to the nearest percent. These responding results for MSTW2008 are recorded in Section 7.3 and comparison can be found in Table 7.4.

Table B.1: LO integrated cross-sections for $V + jets$ production processes at the Tevatron Run II ($\sqrt{s} = 1.96\,\text{TeV}$) using the CTEQ6L1 PDFs and three different scale choices. See caption of Table 7.1 for applied selection cuts, MCFM input parameters and description of the uncertainties.

Tevatron Run II:	$\boldsymbol{\mu_0 = M_V}$		$\boldsymbol{\mu_0 = E_T^V}$		$\boldsymbol{\mu_0 = \hat{H}_T}$	
$p\bar{p} \rightarrow$	σ_{LO} [fb]	$\Delta\sigma_{scl}$ [%]	σ_{LO} [fb]	$\Delta\sigma_{scl}$ [%]	σ_{LO} [fb]	$\Delta\sigma_{scl}$ [%]
$(W^+ \rightarrow \ell^+\nu_\ell)$	$26734(5) \times 10^1$	$^{+2}_{-7}[\pm 4]$	$26734(5) \times 10^1$	$^{+2}_{-7}[\pm 4]$	$26654(5) \times 10^1$	$^{+2}_{-7}[\pm 5]$
$(W^+ \rightarrow \ell^+\nu_\ell) + 1\ jet$	$2829(2) \times 10^1$	$^{+41}_{-20}[\pm 31]$	$2749(2) \times 10^1$	$^{+40}_{-20}[\pm 30]$	$2587(2) \times 10^1$	$^{+39}_{-20}[\pm 29]$
$(W^+ \rightarrow \ell^+\nu_\ell) + 2\ jets$	$10524(7) \times 10^0$	$^{+102}_{-36}[\pm 69]$	$9602(6) \times 10^0$	$^{+97}_{-35}[\pm 66]$	$7512(5) \times 10^0$	$^{+86}_{-33}[\pm 59]$
$(W^- \rightarrow \ell^-\overline{\nu}_\ell)$	$26730(5) \times 10^1$	$^{+2}_{-7}[\pm 4]$	$26730(5) \times 10^1$	$^{+2}_{-7}[\pm 4]$	$26649(5) \times 10^1$	$^{+2}_{-7}[\pm 5]$
$(W^- \rightarrow \ell^-\overline{\nu}_\ell) + 1\ jet$	$2829(2) \times 10^1$	$^{+41}_{-21}[\pm 31]$	$2749(2) \times 10^1$	$^{+40}_{-20}[\pm 30]$	$2587(2) \times 10^1$	$^{+39}_{-20}[\pm 29]$
$(W^- \rightarrow \ell^-\overline{\nu}_\ell) + 2\ jets$	$10512(7) \times 10^0$	$^{+102}_{-36}[\pm 69]$	$9597(6) \times 10^0$	$^{+97}_{-35}[\pm 66]$	$7504(5) \times 10^0$	$^{+86}_{-33}[\pm 59]$
$(Z \rightarrow \ell^-\ell^+)$	$36607(7) \times 10^0$	$^{+2}_{-5}[\pm 3]$	$36607(7) \times 10^0$	$^{+2}_{-5}[\pm 3]$	$36415(7) \times 10^0$	$^{+2}_{-6}[\pm 4]$
$(Z \rightarrow \ell^-\ell^+) + 1\ jet$	$5227(3) \times 10^0$	$^{+41}_{-20}[\pm 30]$	$5091(3) \times 10^0$	$^{+40}_{-20}[\pm 30]$	$4793(3) \times 10^0$	$^{+38}_{-19}[\pm 29]$
$(Z \rightarrow \ell^-\ell^+) + 2\ jets$	$1982(2) \times 10^0$	$^{+98}_{-35}[\pm 67]$	$1812(2) \times 10^0$	$^{+93}_{-34}[\pm 64]$	$1444(1) \times 10^0$	$^{+83}_{-32}[\pm 58]$
$(Z \rightarrow \sum_{\ell=e,\mu,\tau} \nu_\ell\overline{\nu}_\ell)$	$107991(6) \times 10^1$	$^{+0}_{-2}[\pm 1]$	$107991(6) \times 10^1$	$^{+0}_{-2}[\pm 1]$	$107366(6) \times 10^1$	$^{+1}_{-4}[\pm 2]$
$(Z \rightarrow \sum_{\ell=e,\mu,\tau} \nu_\ell\overline{\nu}_\ell) + 1\ jet$	$12384(2) \times 10^1$	$^{+44}_{-21}[\pm 32]$	$12091(2) \times 10^1$	$^{+43}_{-21}[\pm 32]$	$11765(2) \times 10^1$	$^{+42}_{-21}[\pm 31]$
$(Z \rightarrow \sum_{\ell=e,\mu,\tau} \nu_\ell\overline{\nu}_\ell) + 2\ jets$	$4202(1) \times 10^1$	$^{+103}_{-36}[\pm 70]$	$3893(1) \times 10^1$	$^{+99}_{-35}[\pm 67]$	$32015(8) \times 10^0$	$^{+90}_{-34}[\pm 62]$

Table B.2: LO integrated cross-sections for $V + jets$ production processes at the LHC with $\sqrt{s} = 7\,\text{TeV}$ using the CTEQ6L1 PDFs and three different scale choices. See caption of Table 7.1 for applied selection cuts, MCFM input parameters and description of the uncertainties.

LHC with 7 TeV:	$\boldsymbol{\mu_0 = M_V}$		$\boldsymbol{\mu_0 = E_T^V}$		$\boldsymbol{\mu_0 = \hat{H}_T}$	
pp $\rightarrow$	σ_{LO} [fb]	$\Delta\sigma_{scl}$ [%]	σ_{LO} [fb]	$\Delta\sigma_{scl}$ [%]	σ_{LO} [fb]	$\Delta\sigma_{scl}$ [%]
$(\text{W}^+ \rightarrow \ell^+\nu_\ell)$	$20209(3) \times 10^2$	$^{+15}_{-24}[\pm 19]$	$20209(3) \times 10^2$	$^{+15}_{-24}[\pm 19]$	$19907(3) \times 10^2$	$^{+15}_{-25}[\pm 20]$
$(\text{W}^+ \rightarrow \ell^+\nu_\ell) + 1\ jet$	$22551(9) \times 10^1$	$^{+21}_{-13}[\pm 17]$	$21827(9) \times 10^1$	$^{+20}_{-13}[\pm 17]$	$20763(8) \times 10^1$	$^{+20}_{-13}[\pm 17]$
$(\text{W}^+ \rightarrow \ell^+\nu_\ell) + 2\ jets$	$15574(8) \times 10^1$	$^{+77}_{-31}[\pm 54]$	$14030(8) \times 10^1$	$^{+72}_{-30}[\pm 51]$	$10747(5) \times 10^1$	$^{+64}_{-28}[\pm 46]$
$(\text{W}^- \rightarrow \ell^-\overline{\nu}_\ell)$	$13487(2) \times 10^2$	$^{+15}_{-25}[\pm 20]$	$13487(2) \times 10^2$	$^{+15}_{-25}[\pm 20]$	$13298(2) \times 10^2$	$^{+16}_{-26}[\pm 21]$
$(\text{W}^- \rightarrow \ell^-\overline{\nu}_\ell) + 1\ jet$	$13762(5) \times 10^1$	$^{+20}_{-13}[\pm 17]$	$13335(5) \times 10^1$	$^{+20}_{-13}[\pm 17]$	$12678(5) \times 10^1$	$^{+20}_{-13}[\pm 17]$
$(\text{W}^- \rightarrow \ell^-\overline{\nu}_\ell) + 2\ jets$	$8880(6) \times 10^1$	$^{+77}_{-31}[\pm 54]$	$8038(6) \times 10^1$	$^{+73}_{-30}[\pm 51]$	$6160(4) \times 10^1$	$^{+64}_{-28}[\pm 46]$
$(\text{Z} \rightarrow \ell^-\ell^+)$	$39179(6) \times 10^1$	$^{+15}_{-24}[\pm 19]$	$39179(6) \times 10^1$	$^{+15}_{-24}[\pm 19]$	$37823(6) \times 10^1$	$^{+16}_{-25}[\pm 20]$
$(\text{Z} \rightarrow \ell^-\ell^+) + 1\ jet$	$5565(2) \times 10^1$	$^{+20}_{-13}[\pm 16]$	$5416(2) \times 10^1$	$^{+20}_{-13}[\pm 16]$	$5187(2) \times 10^1$	$^{+19}_{-13}[\pm 16]$
$(\text{Z} \rightarrow \ell^-\ell^+) + 2\ jets$	$3403(2) \times 10^1$	$^{+74}_{-31}[\pm 52]$	$3095(2) \times 10^1$	$^{+70}_{-30}[\pm 50]$	$2439(2) \times 10^1$	$^{+63}_{-28}[\pm 45]$
$(\text{Z} \rightarrow \sum_{\ell=\text{e},\mu,\tau} \nu_\ell\overline{\nu}_\ell)$	$44340(3) \times 10^2$	$^{+13}_{-21}[\pm 17]$	$44340(3) \times 10^2$	$^{+13}_{-21}[\pm 17]$	$41674(3) \times 10^2$	$^{+15}_{-24}[\pm 19]$
$(\text{Z} \rightarrow \sum_{\ell=\text{e},\mu,\tau} \nu_\ell\overline{\nu}_\ell) + 1\ jet$	$56422(7) \times 10^1$	$^{+21}_{-14}[\pm 18]$	$54946(7) \times 10^1$	$^{+21}_{-14}[\pm 17]$	$52971(7) \times 10^1$	$^{+21}_{-13}[\pm 17]$
$(\text{Z} \rightarrow \sum_{\ell=\text{e},\mu,\tau} \nu_\ell\overline{\nu}_\ell) + 2\ jets$	$3319(2) \times 10^2$	$^{+77}_{-31}[\pm 54]$	$3042(2) \times 10^2$	$^{+73}_{-30}[\pm 52]$	$24113(9) \times 10^1$	$^{+66}_{-29}[\pm 47]$

Table B.3: LO integrated cross-sections for $V + jets$ production processes at the LHC with $\sqrt{s} = 14\,\text{TeV}$ using the CTEQ6L1 PDFs and three different scale choices. See caption of Table 7.1 for applied selection cuts, MCFM input parameters and description of the uncertainties.

LHC with 14 TeV:	$\boldsymbol{\mu_0 = M_V}$		$\boldsymbol{\mu_0 = E_T^V}$		$\boldsymbol{\mu_0 = \hat{H}_T}$	
pp $\to$	σ_{LO} [fb]	$\Delta\sigma_{scl}$ [%]	σ_{LO} [fb]	$\Delta\sigma_{scl}$ [%]	σ_{LO} [fb]	$\Delta\sigma_{scl}$ [%]
$(\text{W}^+ \to \ell^+\nu_\ell)$	$35197(6) \times 10^2$	$^{+22}_{-32}[\pm 27]$	$35197(6) \times 10^2$	$^{+22}_{-32}[\pm 27]$	$34460(6) \times 10^2$	$^{+23}_{-33}[\pm 28]$
$(\text{W}^+ \to \ell^+\nu_\ell) + 1\ jet$	$4982(2) \times 10^2$	$^{+8}_{-8}[\pm 8]$	$4876(2) \times 10^2$	$^{+8}_{-8}[\pm 8]$	$4737(2) \times 10^2$	$^{+9}_{-8}[\pm 9]$
$(\text{W}^+ \to \ell^+\nu_\ell) + 2\ jets$	$4123(3) \times 10^2$	$^{+58}_{-27}[\pm 43]$	$3730(3) \times 10^2$	$^{+55}_{-26}[\pm 40]$	$2970(2) \times 10^2$	$^{+50}_{-24}[\pm 37]$
$(\text{W}^- \to \ell^-\overline{\nu}_\ell)$	$27367(4) \times 10^2$	$^{+23}_{-33}[\pm 28]$	$27367(4) \times 10^2$	$^{+23}_{-33}[\pm 28]$	$26819(4) \times 10^2$	$^{+23}_{-34}[\pm 29]$
$(\text{W}^- \to \ell^-\overline{\nu}_\ell) + 1\ jet$	$3637(2) \times 10^2$	$^{+7}_{-8}[\pm 7]$	$3564(2) \times 10^2$	$^{+8}_{-8}[\pm 8]$	$3464(2) \times 10^2$	$^{+9}_{-8}[\pm 8]$
$(\text{W}^- \to \ell^-\overline{\nu}_\ell) + 2\ jets$	$2834(2) \times 10^2$	$^{+58}_{-27}[\pm 42]$	$2575(2) \times 10^2$	$^{+55}_{-26}[\pm 40]$	$2055(2) \times 10^2$	$^{+50}_{-24}[\pm 37]$
$(\text{Z} \to \ell^-\ell^+)$	$7554(2) \times 10^2$	$^{+22}_{-32}[\pm 27]$	$7554(2) \times 10^2$	$^{+22}_{-32}[\pm 27]$	$7188(2) \times 10^2$	$^{+24}_{-34}[\pm 29]$
$(\text{Z} \to \ell^-\ell^+) + 1\ jet$	$13762(5) \times 10^1$	$^{+6}_{-7}[\pm 7]$	$13529(4) \times 10^1$	$^{+7}_{-7}[\pm 7]$	$13203(4) \times 10^1$	$^{+8}_{-8}[\pm 8]$
$(\text{Z} \to \ell^-\ell^+) + 2\ jets$	$10065(6) \times 10^1$	$^{+56}_{-26}[\pm 41]$	$9209(6) \times 10^1$	$^{+53}_{-25}[\pm 39]$	$7521(5) \times 10^1$	$^{+48}_{-24}[\pm 36]$
$(\text{Z} \to \sum_{\ell=\text{e},\mu,\tau} \nu_\ell\overline{\nu}_\ell)$	$100471(6) \times 10^2$	$^{+20}_{-29}[\pm 24]$	$100471(6) \times 10^2$	$^{+20}_{-29}[\pm 24]$	$92083(5) \times 10^2$	$^{+22}_{-32}[\pm 27]$
$(\text{Z} \to \sum_{\ell=\text{e},\mu,\tau} \nu_\ell\overline{\nu}_\ell) + 1\ jet$	$15508(2) \times 10^2$	$^{+9}_{-8}[\pm 8]$	$15240(2) \times 10^2$	$^{+9}_{-8}[\pm 9]$	$14893(2) \times 10^2$	$^{+10}_{-8}[\pm 9]$
$(\text{Z} \to \sum_{\ell=\text{e},\mu,\tau} \nu_\ell\overline{\nu}_\ell) + 2\ jets$	$11136(5) \times 10^2$	$^{+59}_{-27}[\pm 43]$	$10271(5) \times 10^2$	$^{+56}_{-26}[\pm 41]$	$8389(4) \times 10^2$	$^{+52}_{-25}[\pm 38]$

B.2 More Distributions of Observables for Tevatron, LHC with 14 TeV and Dynamic Scales

For completeness, some additional distributions of differential cross-sections are given in this appendix. They are mostly for Tevatron Run II (1.96 TeV) and the LHC with 14 TeV as well as for the two dynamic scales $\mu_0 = E_T^V$ and $\mu_0 = H_T$ for completeness. These plots are often very similar to the result for the LHC with 7 TeV and the static scale $\mu_0 = M_V$ which were presented in Section 7.4.

B.2.1 $p^{(}\overline{p}^{)} \to (W^+ \to \ell^+\nu_\ell) + n$ jets

B.2.1.1 $p^{(}\overline{p}^{)} \to (W^+ \to \ell^+\nu_\ell)$

This section provides an additional rapidity distribution and an additional azimuthal angle distribution for the $pp \to (W^+ \to \ell^+\nu_\ell)$ process. Both were mentioned in Section 7.4.1.1.

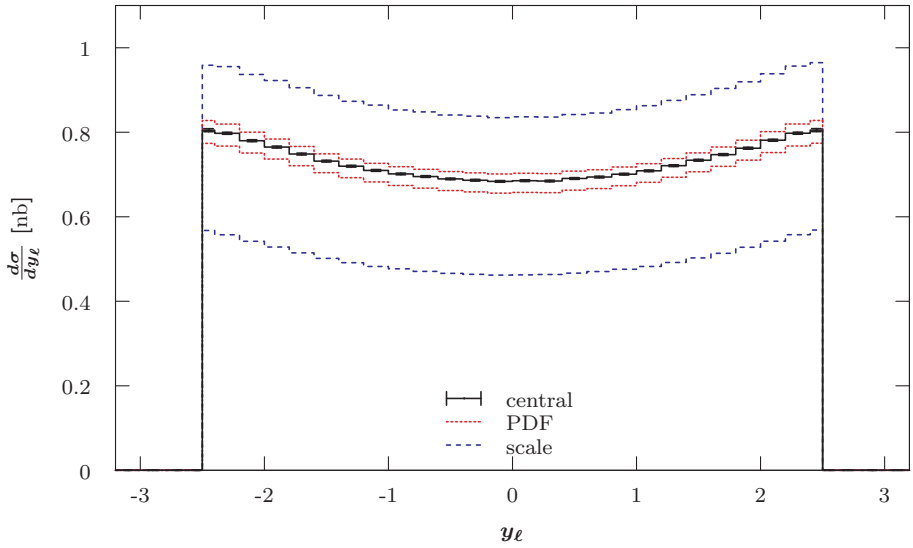

Figure B.1: LO differential cross-section with respect to the charged lepton rapidity for the $pp \to (W^+ \to \ell^+\nu_\ell)$ process at the LHC with 14 TeV using a fixed scale of $\mu_0 = M_W$. The first and last filled bin are half-width due to the applied selection cut, $|y_\ell| < 2.5$. Additional details are given in the caption of Figure 7.1.

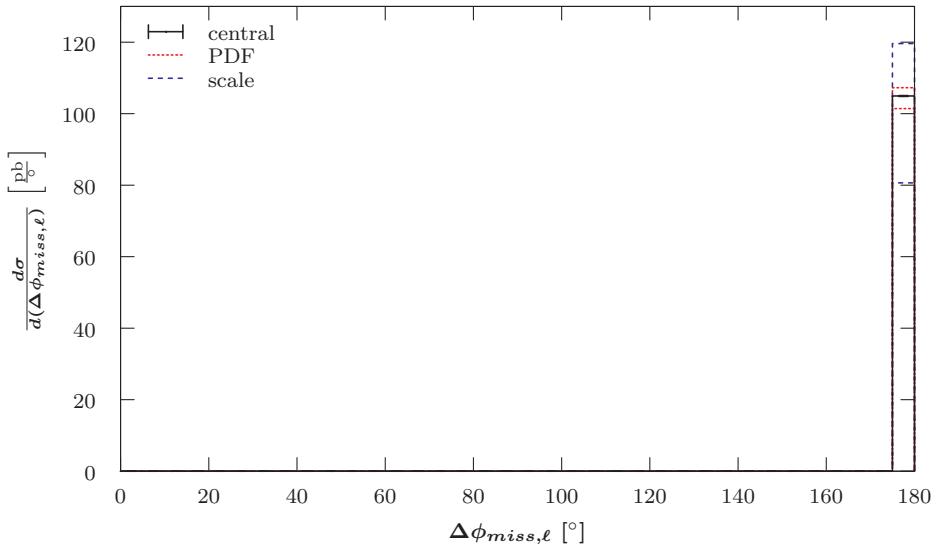

Figure B.2: LO differential cross-section with respect to the azimuthal angle ϕ between the charged lepton and the missing transverse momentum for the pp $\to$ ($\mathrm{W}^+ \to \ell^+\nu_\ell$) process at the LHC with 7 TeV using a fixed scale of $\mu_0 = M_\mathrm{W}$. Additional details are given in the caption of Figure 7.1.

B.2.1.2 $p^{(}\overline{p}^{)} \to (W^+ \to \ell^+\nu_\ell) + 1$ jets

This section provides some additional graphs for the $p^{(}\overline{p}^{)} \to (W^+ \to \ell^+\nu_\ell)+1\ jet$ process, which were mentioned in Section 7.4.1.2.

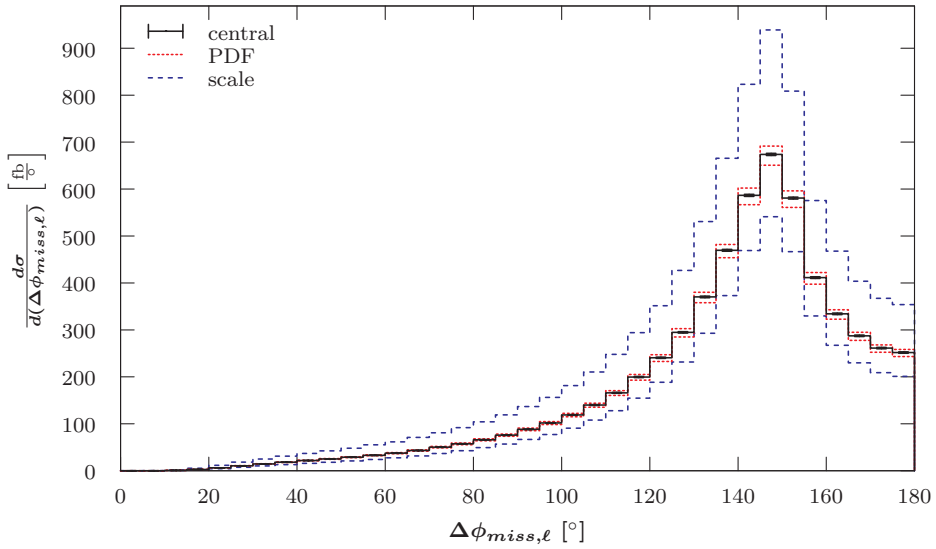

Figure B.3: LO differential cross-section with respect to the azimuthal angle ϕ between the charged lepton and the missing transverse momentum for the $p\overline{p} \to (W^+ \to \ell^+\nu_\ell) + 1\ jet$ process at the Tevatron Run II using a fixed scale of $\mu_0 = M_W$. Additional details are given in the caption of Figure 7.1.

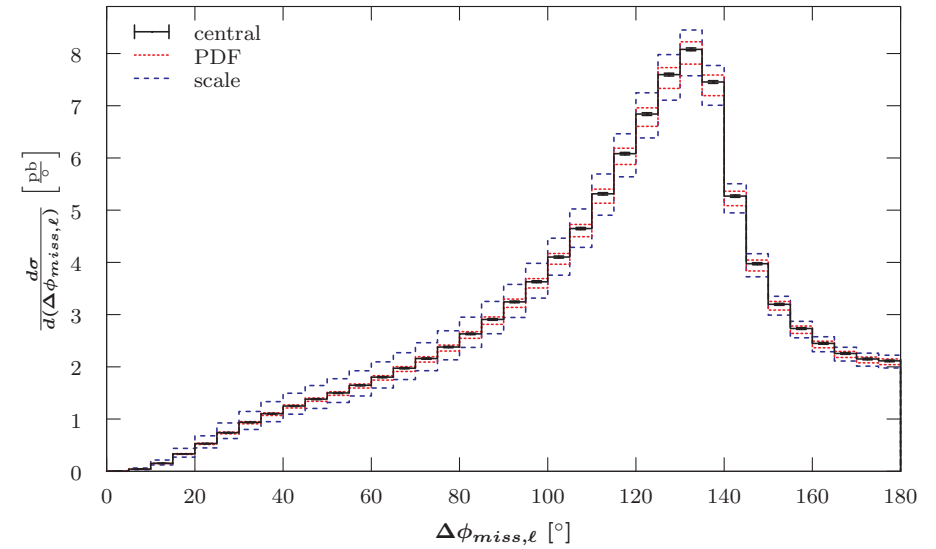

Figure B.4: LO differential cross-section with respect to the azimuthal angle ϕ between the charged lepton and the missing transverse momentum for the $pp \to (W^+ \to \ell^+\nu_\ell)+1\ jet$ process at the LHC with 14 TeV using a fixed scale of $\mu_0 = M_W$. Additional details are given in the caption of Figure 7.1.

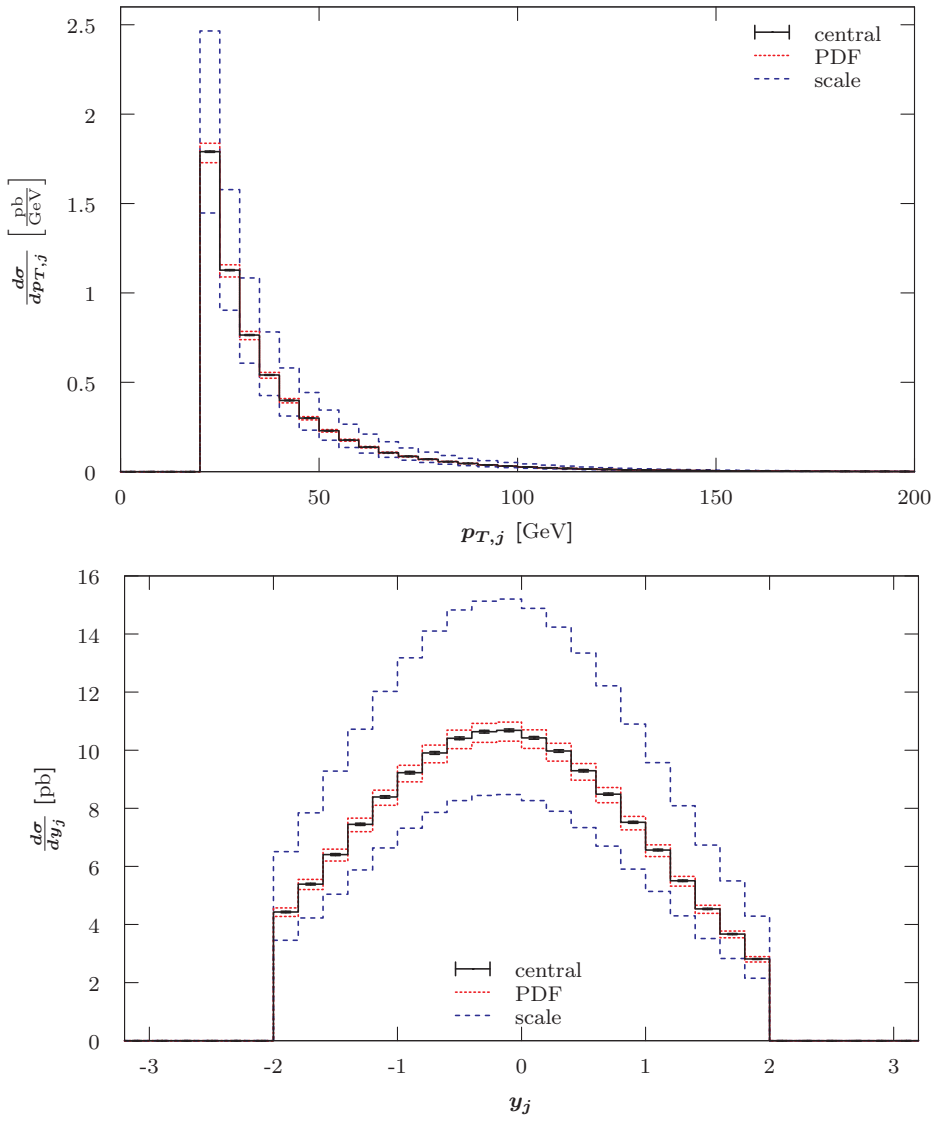

Figure B.5: LO differential cross-section with respect to the jet transverse momentum p_T (top) and the jet rapidity y (bottom) for the $p\overline{p} \to (W^+ \to \ell^+\nu_\ell) + 1\ jet$ process at the Tevatron Run II using a fixed scale of $\mu_0 = M_W$. Additional details are given in the caption of Figure 7.1.

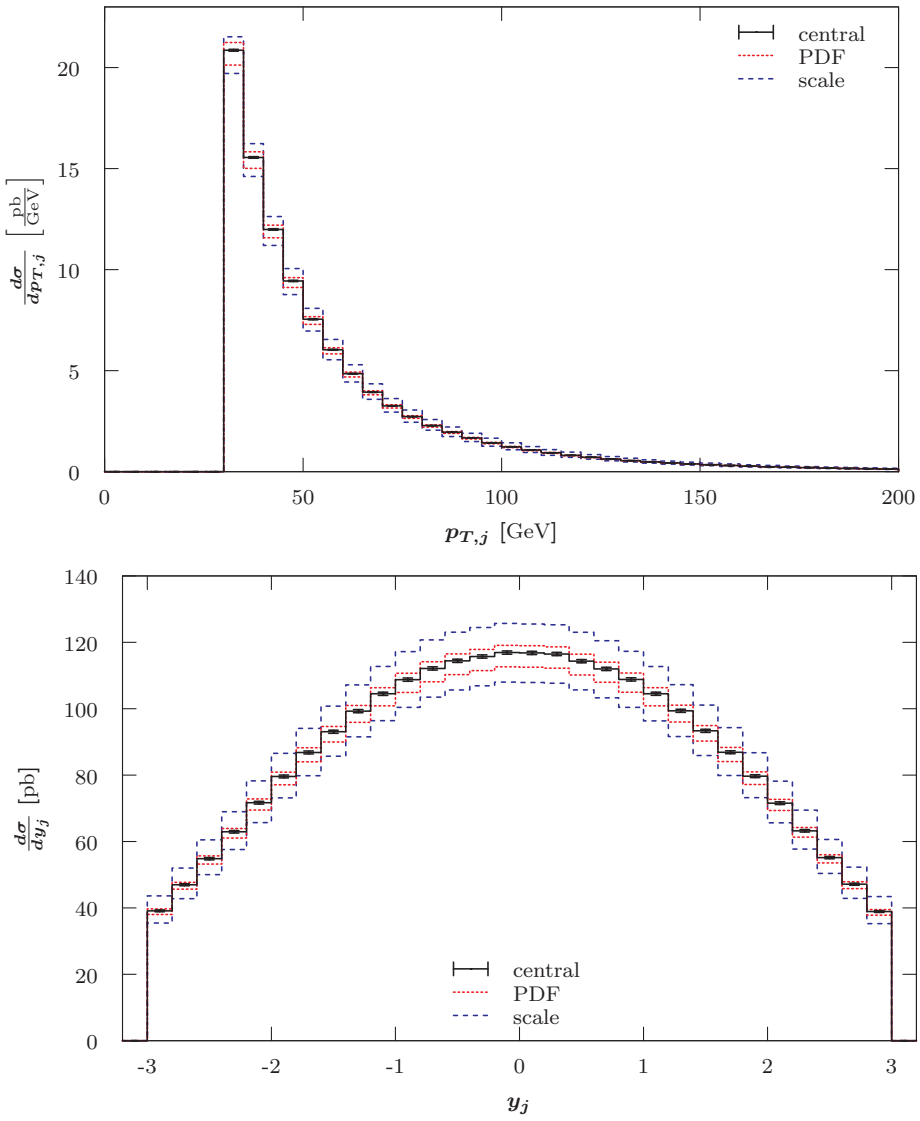

Figure B.6: LO differential cross-section with respect to the jet transverse momentum (top) and the jet rapidity (bottom) for the pp $\to (W^+ \to \ell^+\nu_\ell)$+1 *jet* process at the LHC with 14 TeV using a fixed scale of $\mu_0 = M_W$. Additional details are given in the caption of Figure 7.1.

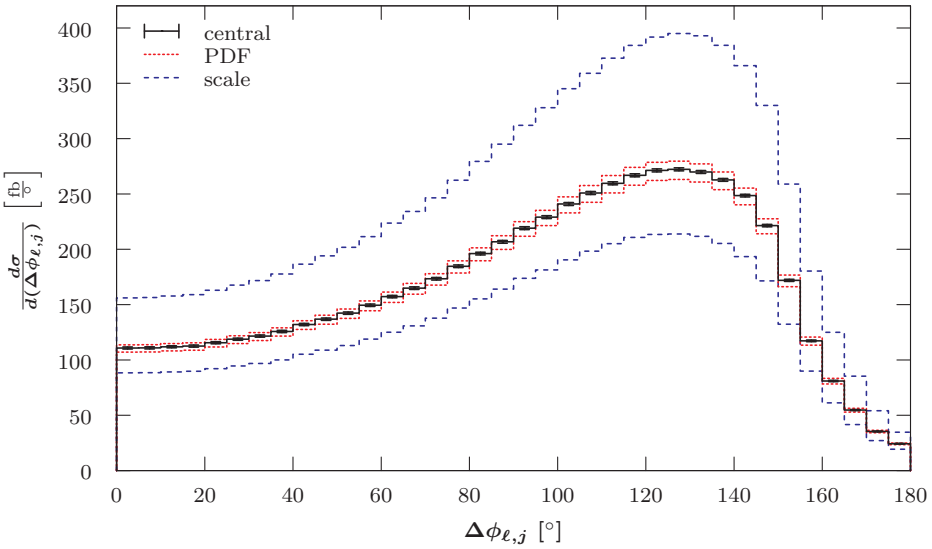

Figure B.7: LO differential cross-section with respect to the azimuthal angle ϕ between the charged lepton and the jet for the $p\overline{p} \to (W^+ \to \ell^+\nu_\ell) + 1\ jet$ process at the Tevatron Run II using a fixed scale of $\mu_0 = M_W$. Additional details are given in the caption of Figure 7.1.

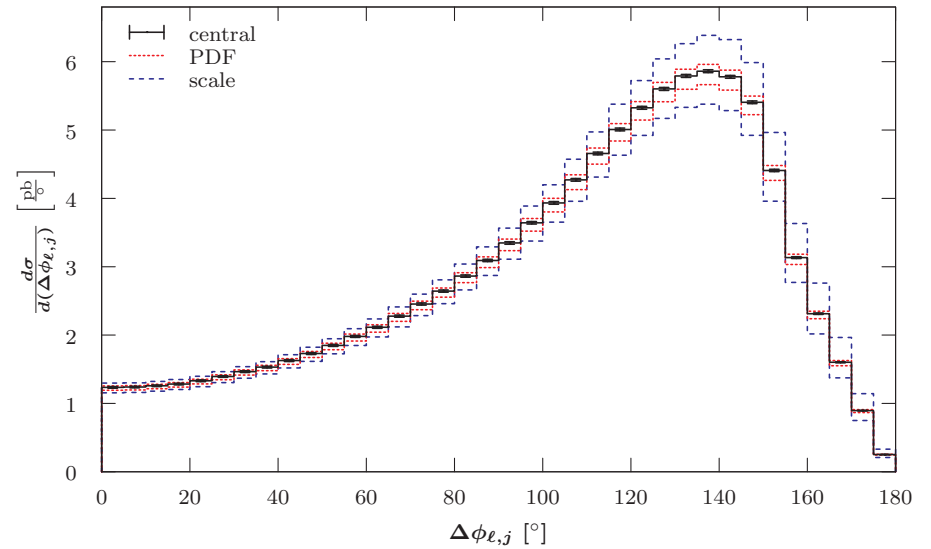

Figure B.8: LO differential cross-section with respect to the azimuthal angle ϕ between the charged lepton and the jet for the $pp \to (W^+ \to \ell^+\nu_\ell) + 1\ jet$ process at the LHC with 14 TeV using a fixed scale of $\mu_0 = M_W$. Additional details are given in the caption of Figure 7.1.

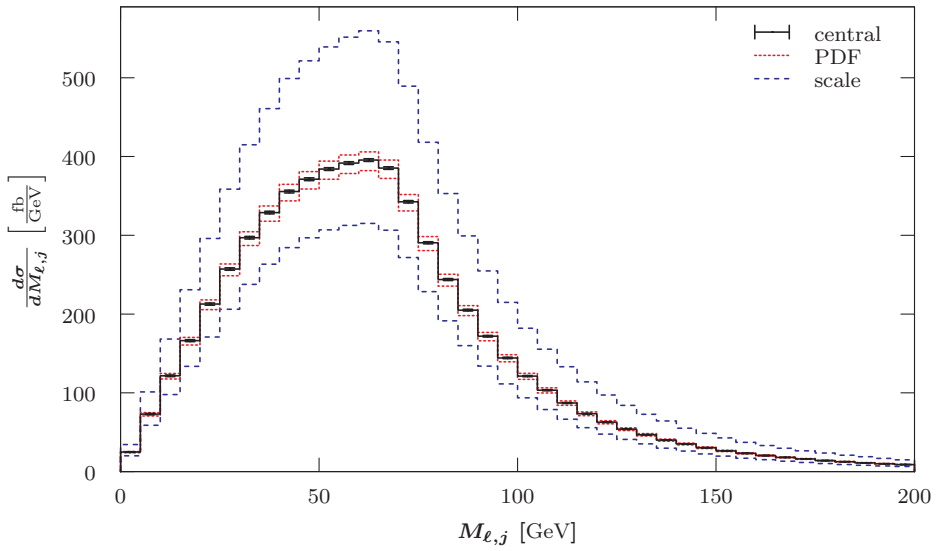

Figure B.9: LO differential cross-section with respect to the invariant mass between the charged lepton and the jet for the $p\overline{p} \to (W^+ \to \ell^+\nu_\ell) + 1\ jet$ process at the Tevatron Run II using a fixed scale of $\mu_0 = M_W$. Additional details are given in the caption of Figure 7.1.

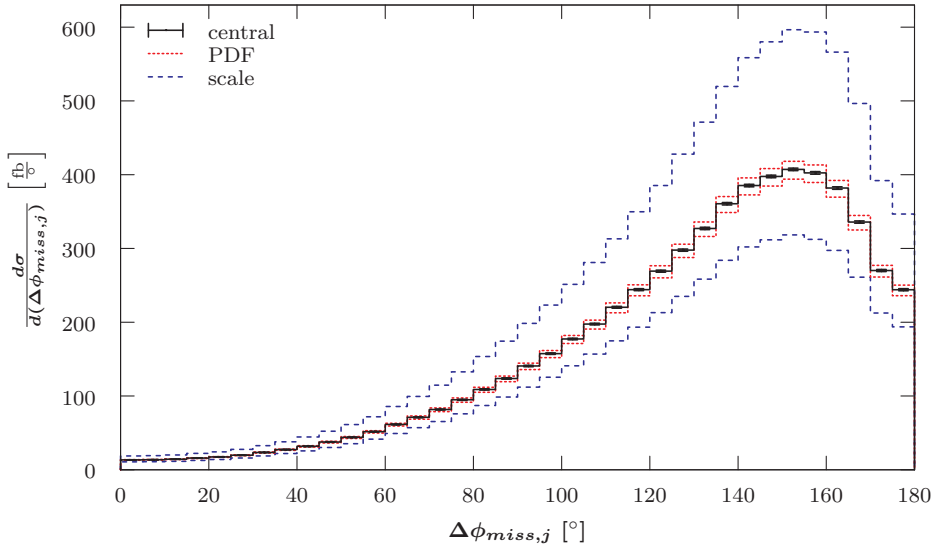

Figure B.10: LO differential cross-section with respect to the azimuthal angle ϕ between the missing transverse momentum and the jet for the $p\overline{p} \to (W^+ \to \ell^+\nu_\ell) + 1\ jet$ process at the Tevatron Run II using a fixed scale of $\mu_0 = M_W$. Additional details are given in the caption of Figure 7.1.

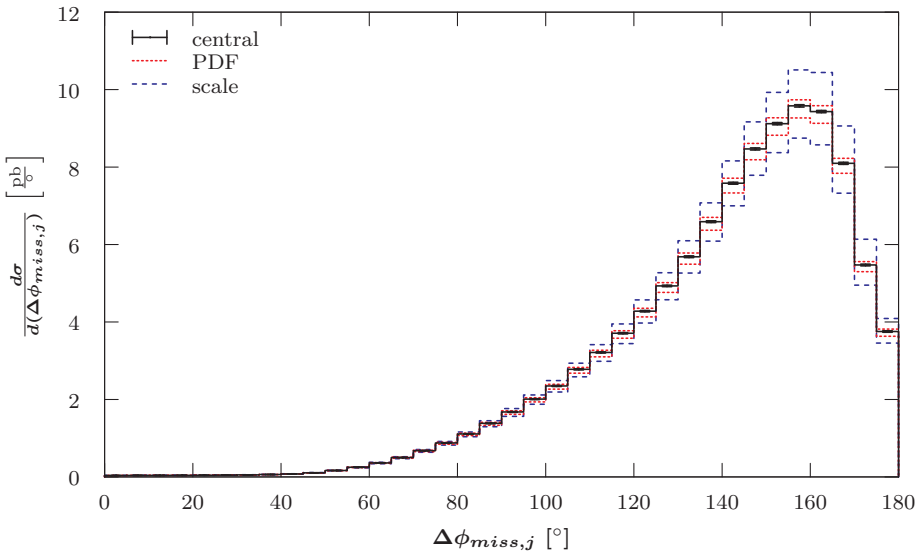

Figure B.11: LO differential cross-section with respect to the azimuthal angle ϕ between the missing transverse momentum and the jet for the $pp \to (W^+ \to \ell^+\nu_\ell) + 1\ jet$ process at the LHC with 14 TeV using a fixed scale of $\mu_0 = M_W$. Additional details are given in the caption of Figure 7.1.

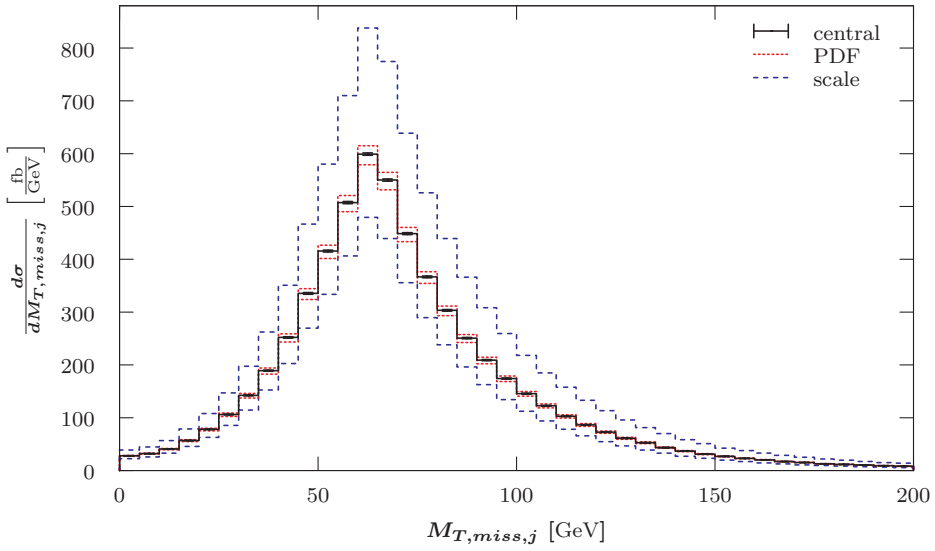

Figure B.12: LO differential cross-section with respect to the transverse mass between the jet and missing transverse momentum vector for the $p\bar{p} \to (W^+ \to \ell^+\nu_\ell) + 1\ jet$ process at the Tevatron Run II using a fixed scale of $\mu_0 = M_W$. Additional details are given in the caption of Figure 7.1.

B.2.1.3 $p^{(}\overline{p}^{)} \to (W^+ \to \ell^+\nu_\ell) + 2$ jets

This section provides some additional graphs for the $p^{(}\overline{p}^{)} \to (W^+ \to \ell^+\nu_\ell)+2\,jets$ process, which were mentioned in Section 7.4.1.3.

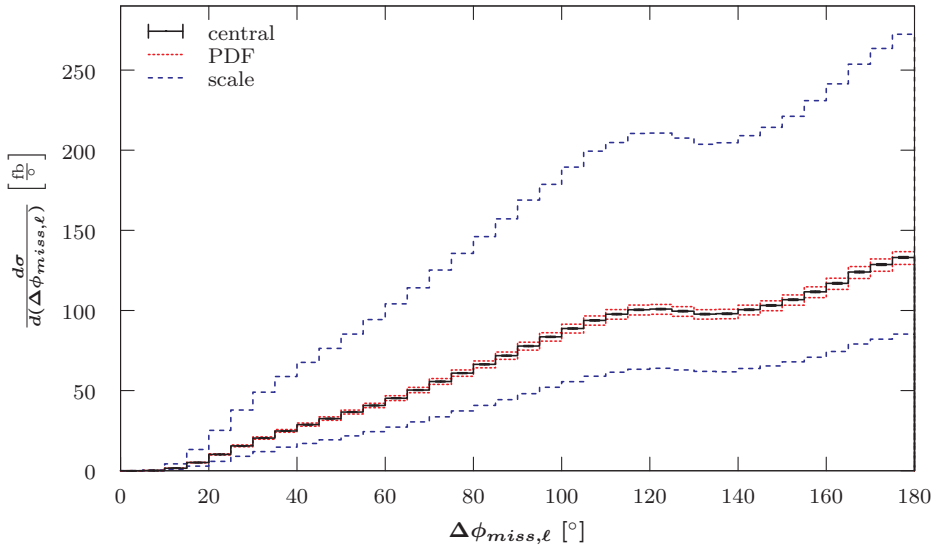

Figure B.13: LO differential cross-section with respect to the transvers angle ϕ between the charged lepton and the missing trensverse momentum for the $p\overline{p} \to (W^+ \to \ell^+\nu_\ell) + 2\,jets$ process at the Tevatron Run II using a fixed scale of $\mu_0 = M_W$. Additional details are given in the caption of Figure 7.1.

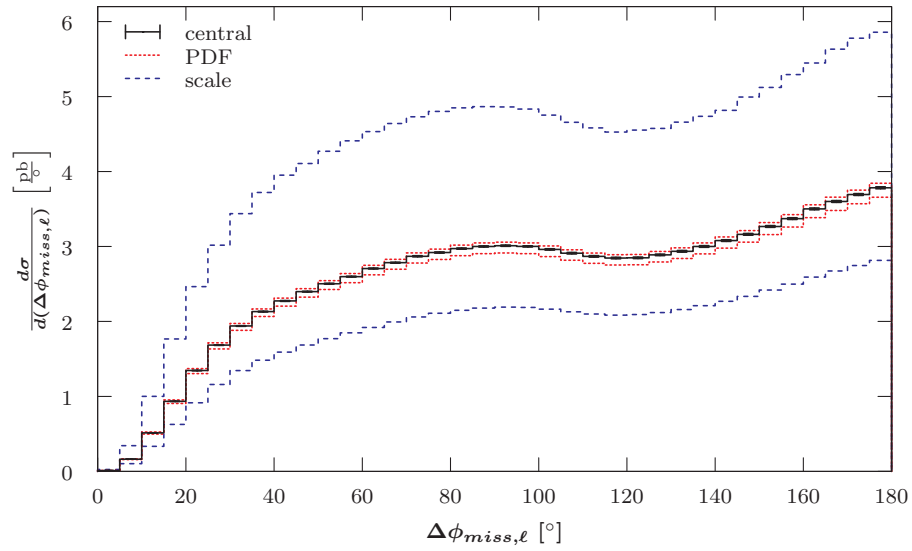

Figure B.14: LO differential cross-section with respect to the azimuthal angle ϕ between the charged lepton and the missing transverse momentum for the $pp \to (W^+ \to \ell^+\nu_\ell) + 2\,jets$ process at the LHC with 14 TeV using a fixed scale of $\mu_0 = M_W$. Additional details are given in the caption of Figure 7.1.

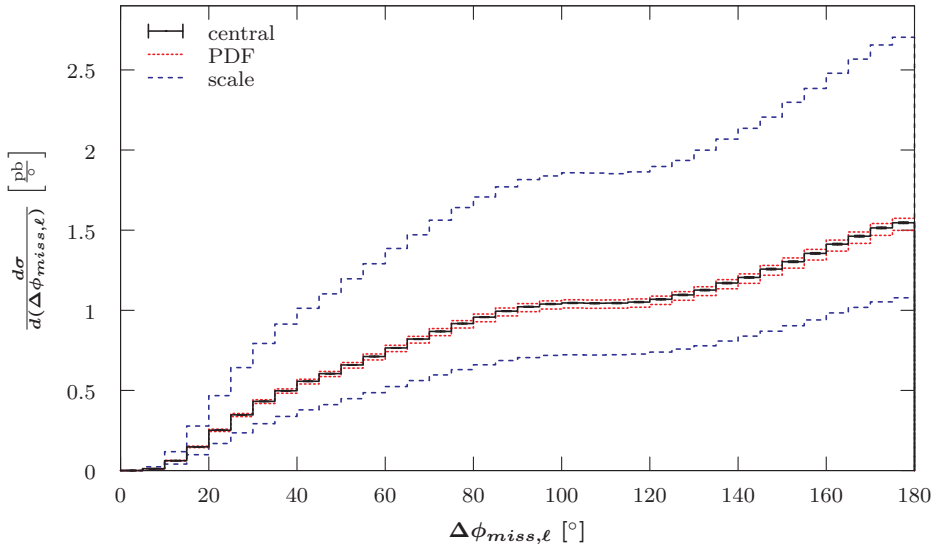

Figure B.15: LO differential cross-section with respect to the azimuthal angle ϕ between the charged lepton and the missing transverse momentum for the pp $\rightarrow$ ($W^+ \rightarrow \ell^+\nu_\ell$) + 2 *jets* process at the LHC with 7 TeV using a fixed scale of $\mu_0 = E_T^V$. Additional details are given in the caption of Figure 7.1.

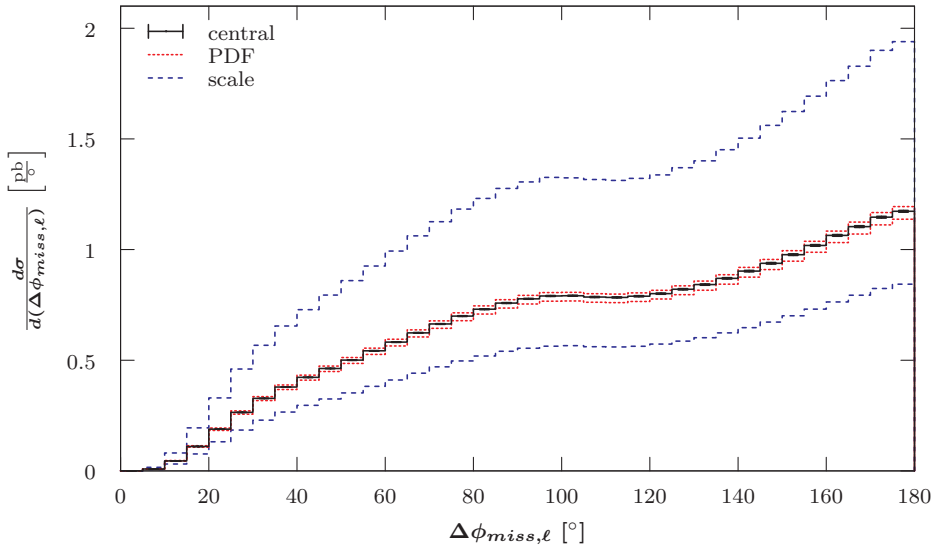

Figure B.16: LO differential cross-section with respect to the azimuthal angle ϕ between the charged lepton and the missing transverse momentum for the pp $\rightarrow$ ($W^+ \rightarrow \ell^+\nu_\ell$) + 2 *jets* process at the LHC with 7 TeV using a fixed scale of $\mu_0 = \hat{H}_T$. Additional details are given in the caption of Figure 7.1.

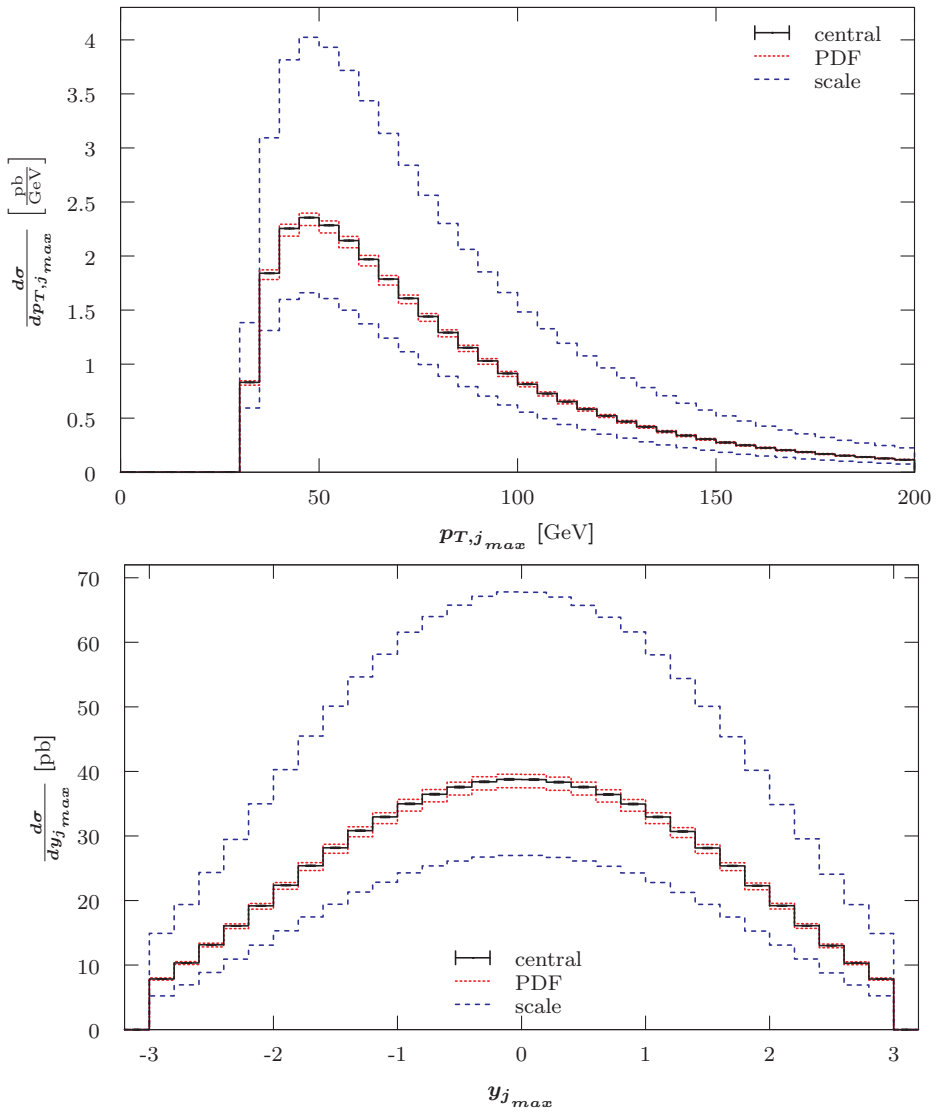

Figure B.17: LO differential cross-section with respect to the transverse momentum (top) and the rapidity (bottom) of the harder jet j_{max} for the $pp \to (W^+ \to \ell^+\nu_\ell) + 2\ jets$ process at the LHC with 7 TeV using a fixed scale of $\mu_0 = E_T^W$. Additional details are given in the caption of Figure 7.1.

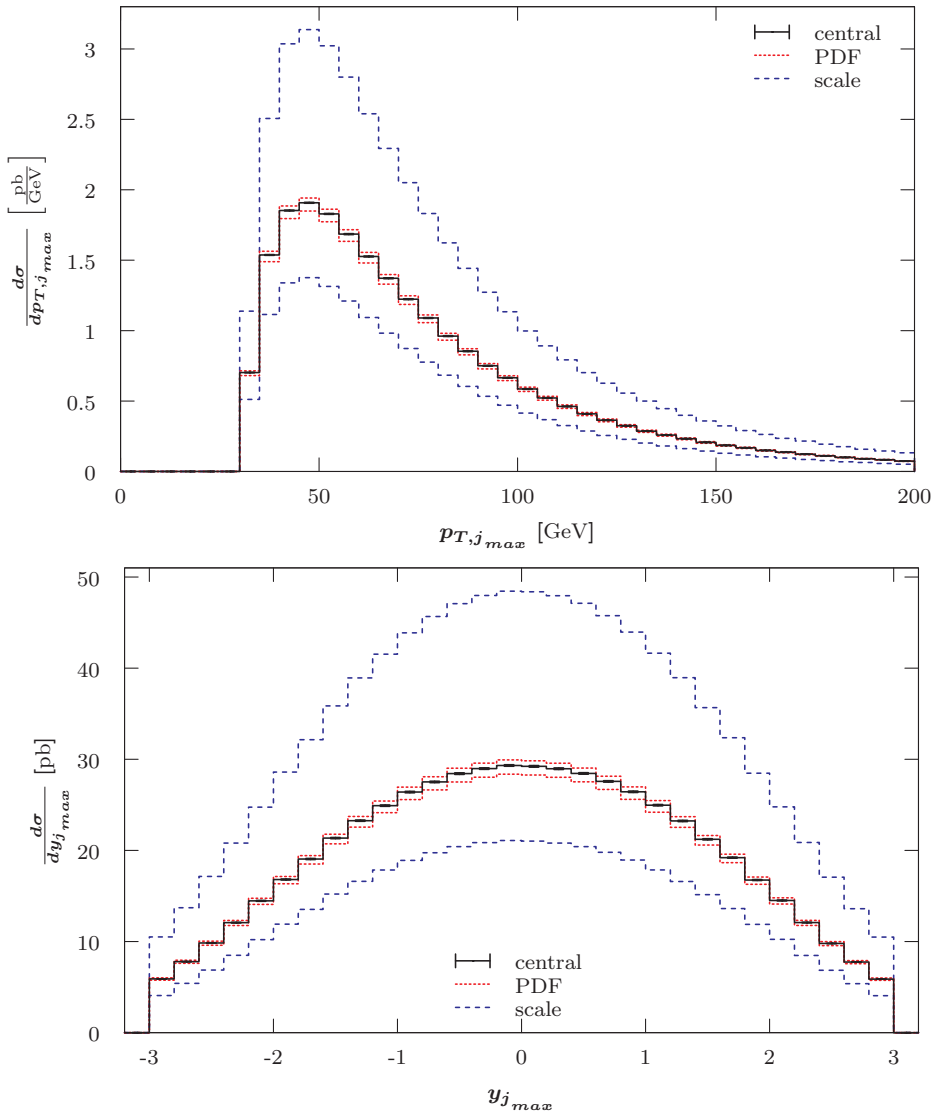

Figure B.18: LO differential cross-section with respect to the transverse momentum (top) and the rapidity (bottom) of the harder jet j_{max} for the $pp \to (W^+ \to \ell^+\nu_\ell) + 2\ jets$ process at the LHC with 7 TeV using a fixed scale of $\mu_0 = \hat{H}_T$. Additional details are given in the caption of Figure 7.1.

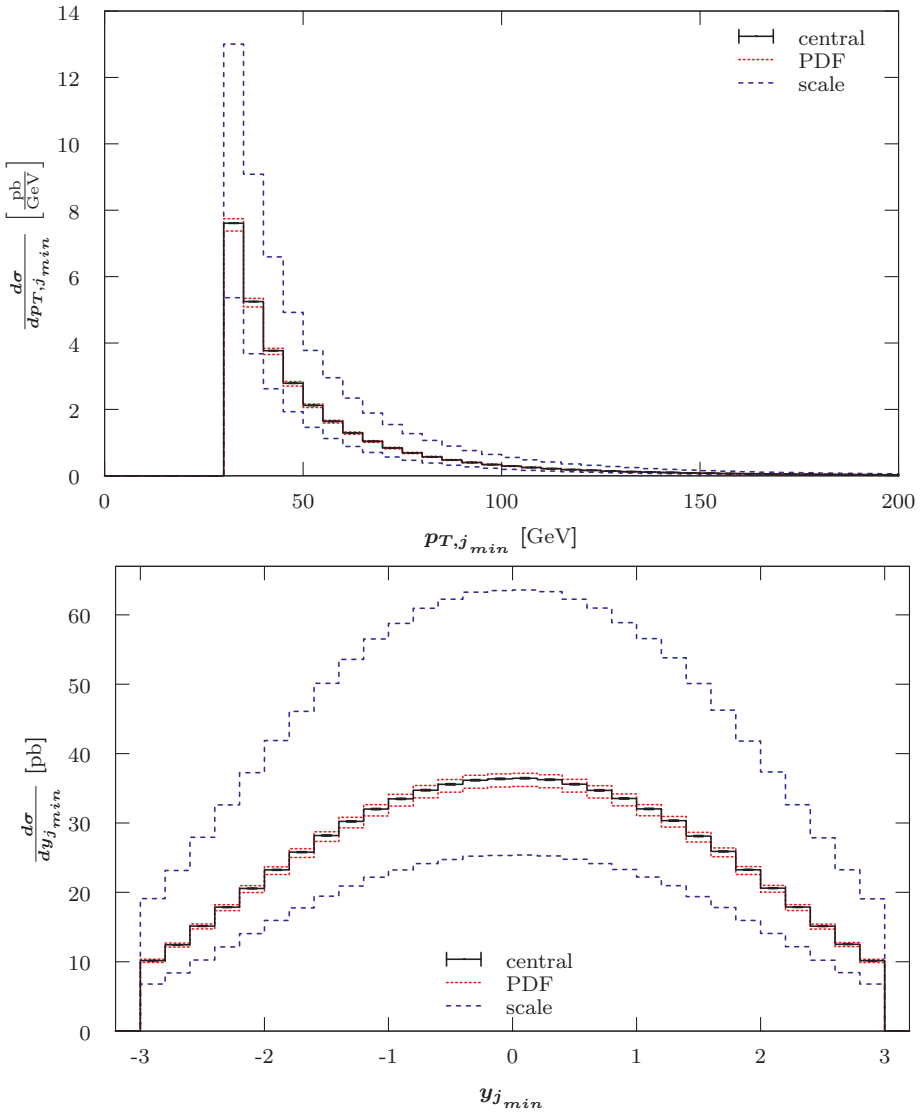

Figure B.19: LO differential cross-section with respect to the transverse momentum (top) and the rapidity (bottom) of the softer jet j_{min} for the pp $\to (\mathrm{W}^+ \to \ell^+\nu_\ell) + 2\ jets$ process at the LHC with 7 TeV using a fixed scale of $\mu_0 = E_T^{\mathrm{W}}$. Additional details are given in the caption of Figure 7.1.

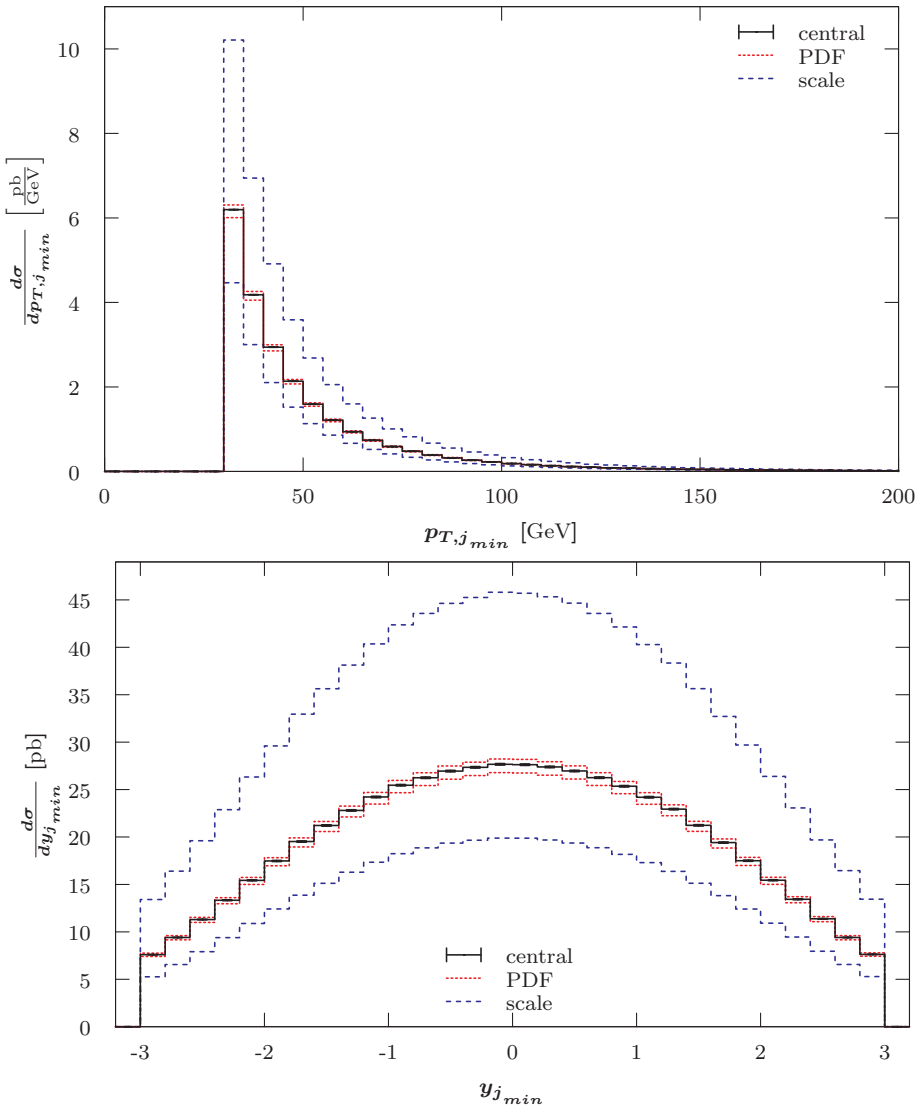

Figure B.20: LO differential cross-section with respect to the transverse momentum (top) and the rapidity (bottom) of the softer jet j_{min} for the $pp \to (W^+ \to \ell^+\nu_\ell) + 2\ jets$ process at the LHC with 7 TeV using a fixed scale of $\mu_0 = \hat{H}_T$. Additional details are given in the caption of Figure 7.1.

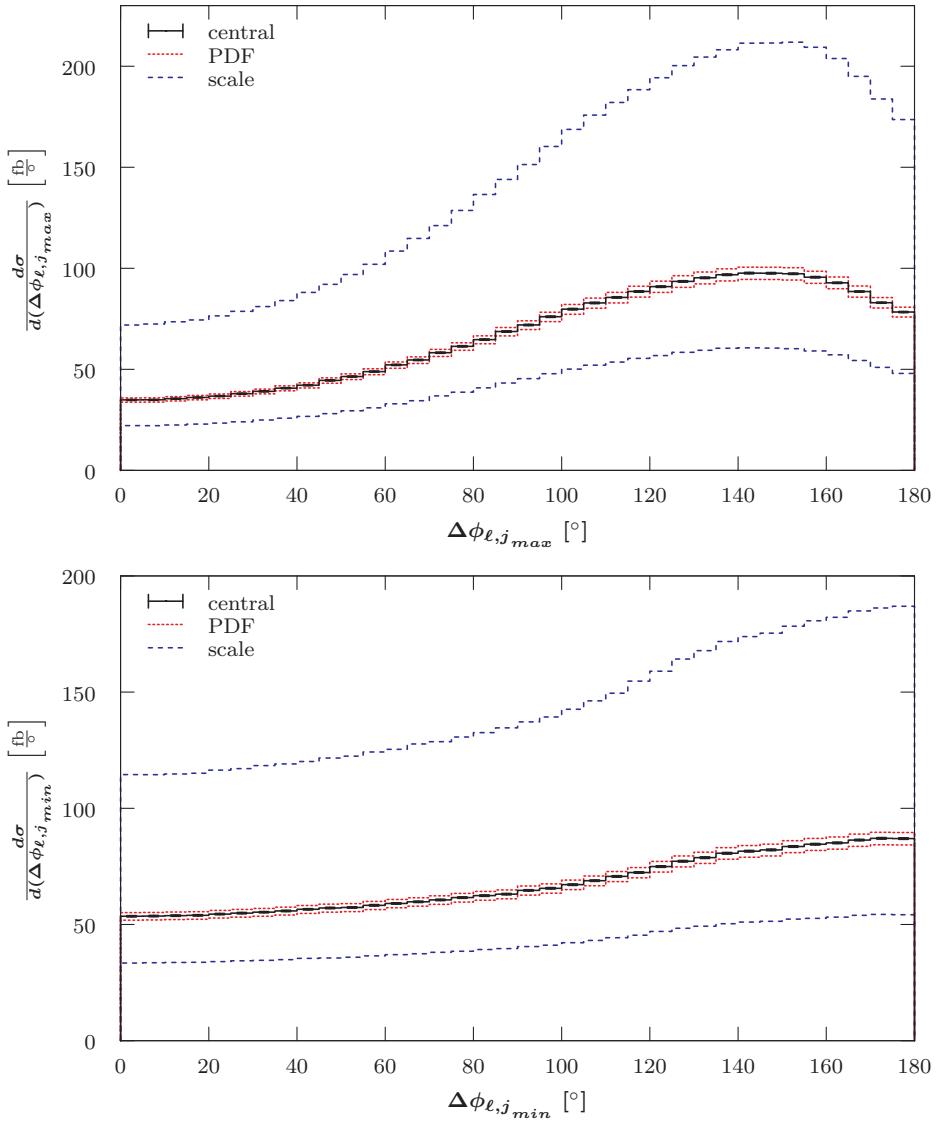

Figure B.21: LO differential cross-section with respect to the azimuthal angle ϕ between the charged lepton and the harder (top) as well as the softer (bottom) jet for the $p\overline{p} \to (W^+ \to \ell^+\nu_\ell) + 2\ jets$ process at the Tevatron Run II using a fixed scale of $\mu_0 = M_W$. Additional details are given in the caption of Figure 7.1.

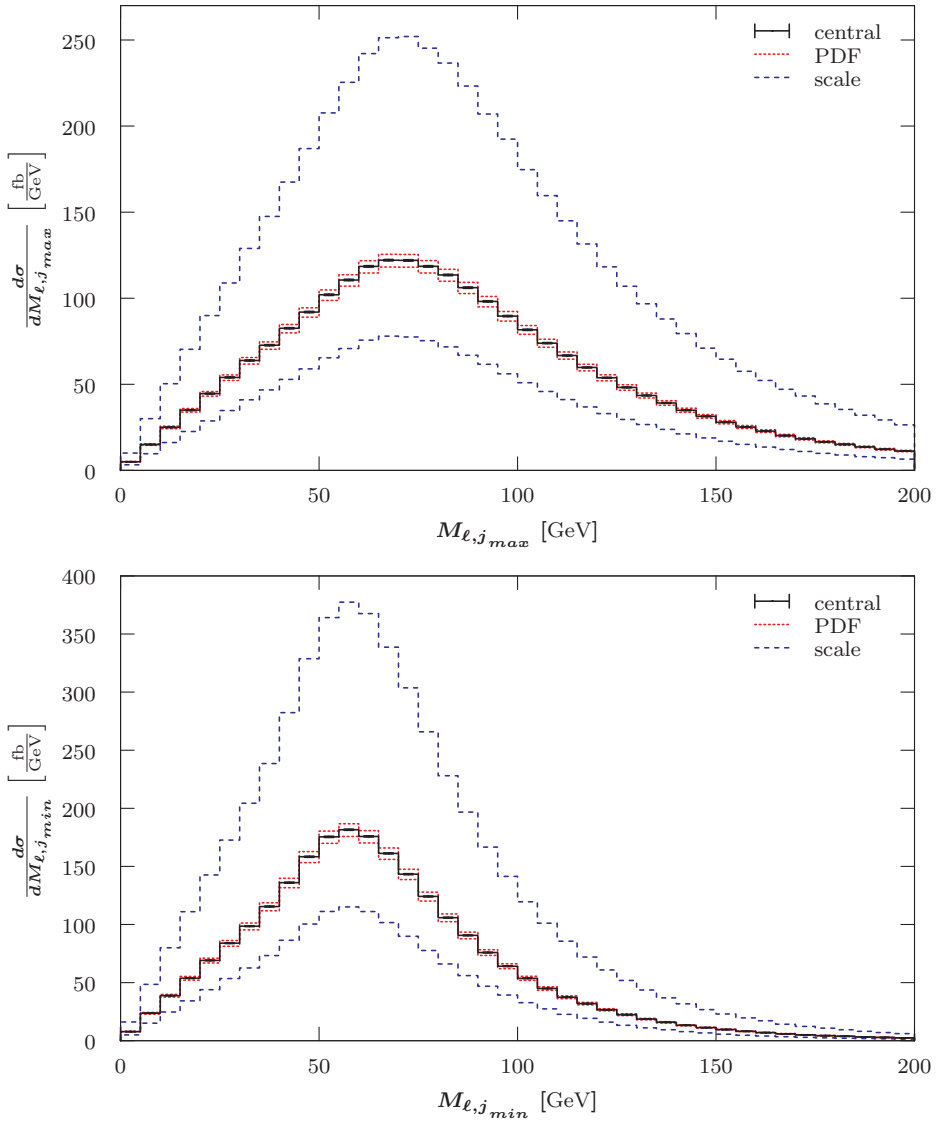

Figure B.22: LO differential cross-section with respect to the invariant mass of the charged lepton and the harder (top) as well as softer (bottom) jet for the $p\overline{p} \to (W^+ \to \ell^+\nu_\ell) + 2\ jets$ process at the Tevatron Run II using a fixed scale of $\mu_0 = M_W$. Additional details are given in the caption of Figure 7.1.

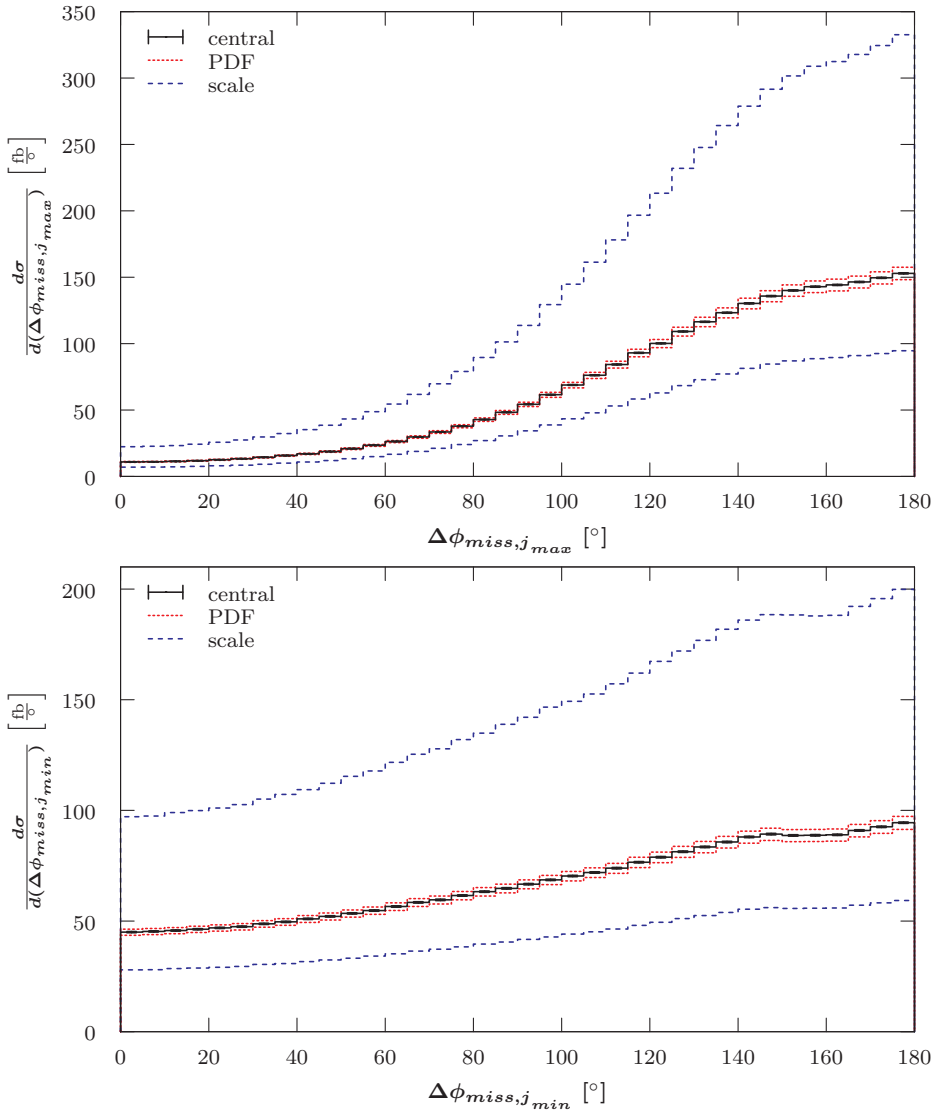

Figure B.23: LO differential cross-section with respect to the azimuthal angle ϕ between the missing transverse momentum and the harder (top) as well as softer (bottom) jet for the $p\overline{p} \to (W^+ \to \ell^+\nu_\ell)+2\,jets$ process at the Tevatron Run II using a fixed scale of $\mu_0 = M_W$. Additional details are given in the caption of Figure 7.1.

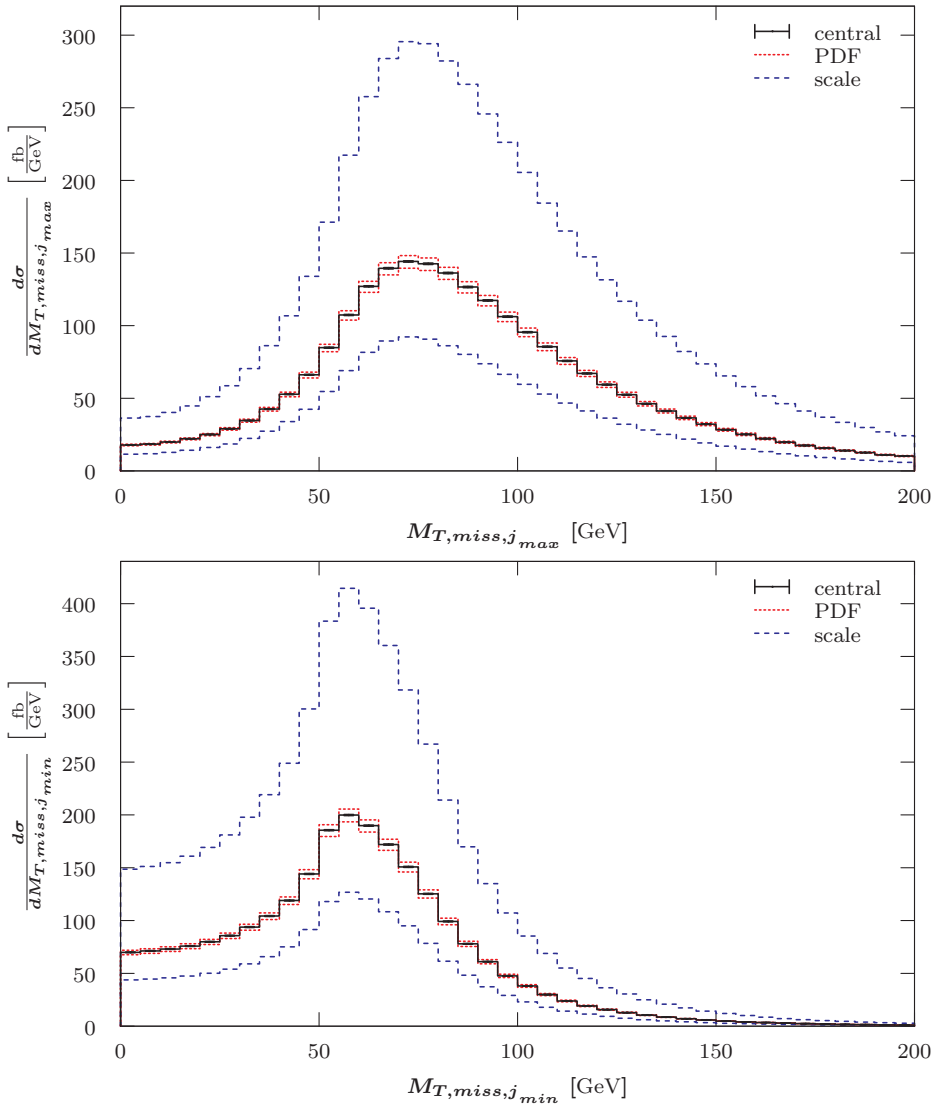

Figure B.24: LO differential cross-section with respect to the transverse mass of the missing transverse momentum vector and the harder (top) as well as softer (bottom) jet for the $p\overline{p} \to (W^+ \to \ell^+\nu_\ell)+2\,jets$ process at the Tevatron Run II using a fixed scale of $\mu_0 = M_W$. Additional details are given in the caption of Figure 7.1.

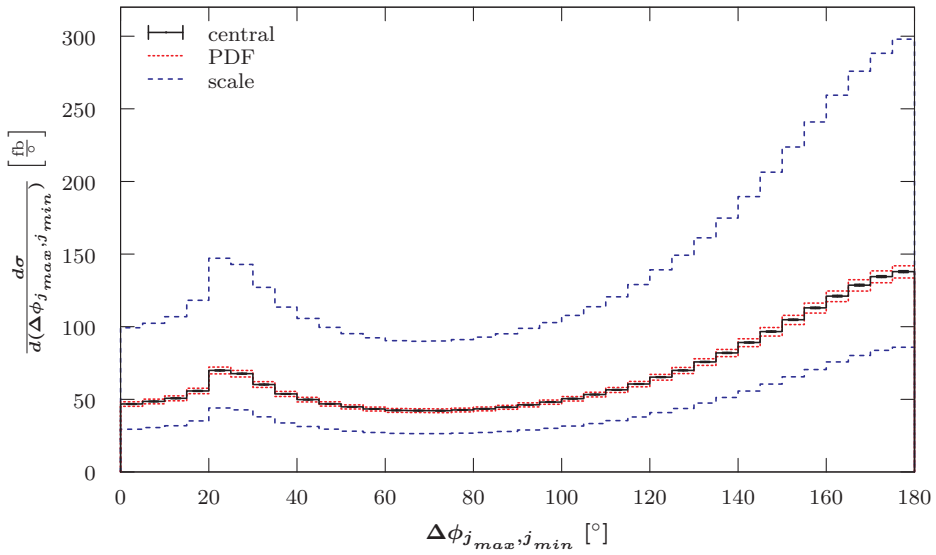

Figure B.25: LO differential cross-section with respect to the azimuthal angle ϕ between the harder j_{max} and the softer jet j_{min} for the $p\overline{p} \to (W^+ \to \ell^+\nu_\ell) + 2\ jets$ process at the Tevatron Run II using a fixed scale of $\mu_0 = M_Z$. Additional details are given in the caption of Figure 7.1.

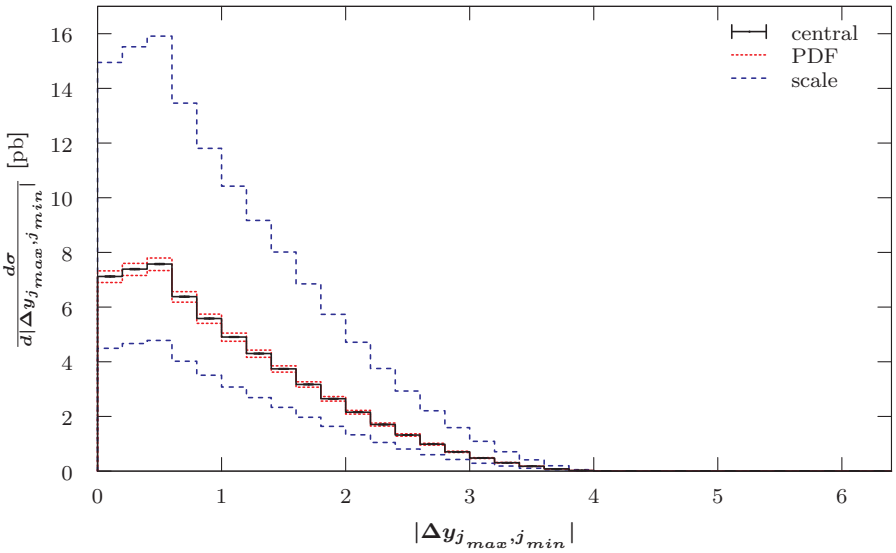

Figure B.26: LO differential cross-section with respect to the difference in rapidity between the harder j_{max} and the softer jet j_{min} for the $p\overline{p} \to (W^+ \to \ell^+\nu_\ell) + 2\ jets$ process at the Tevatron Run II using a fixed scale of $\mu_0 = M_Z$. Additional details are given in the caption of Figure 7.1.

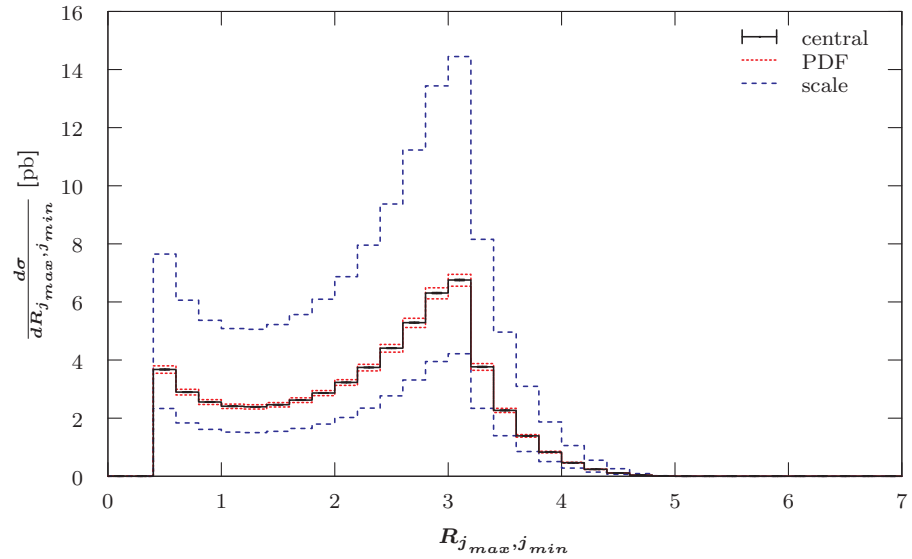

Figure B.27: LO differential cross-section with respect to separation between the harder j_{max} and the softer j_{min} jet for the $p\overline{p} \to (W^+ \to \ell^+\nu_\ell) + 2\ jets$ process at the Tevatron Run II using a fixed scale of $\mu_0 = M_Z$. Additional details are given in the caption of Figure 7.1.

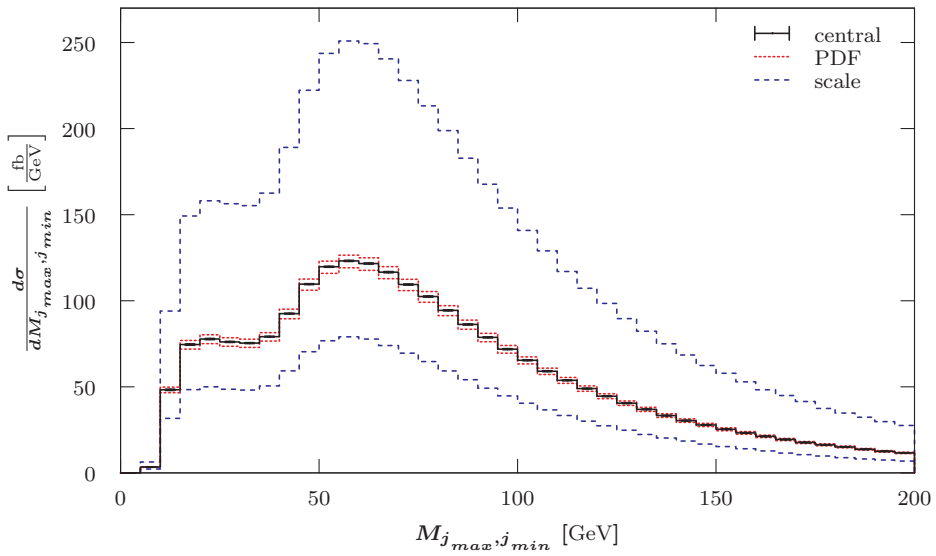

Figure B.28: LO differential cross-section with respect to the inavaraitn mass of the harder j_{max} and the softer j_{min} jet for the $p\overline{p} \to (W^+ \to \ell^+\nu_\ell) + 2\ jets$ process at the Tevatron Run II using a fixed scale of $\mu_0 = M_Z$. Additional details are given in the caption of Figure 7.1.

B.2.2 $p^{(}\overline{p}^{)} \to (W^- \to \ell^-\overline{\nu}_\ell) + n$ jets

B.2.2.1 $p^{(}\overline{p}^{)} \to (W^- \to \ell^-\overline{\nu}_\ell)$

This section provides an additional rapidity distribution and an additional azimuthal angle distribution for the $pp \to (W^- \to \ell^-\overline{\nu}_\ell)$ process. Both were mentioned in Section 7.4.2.1.

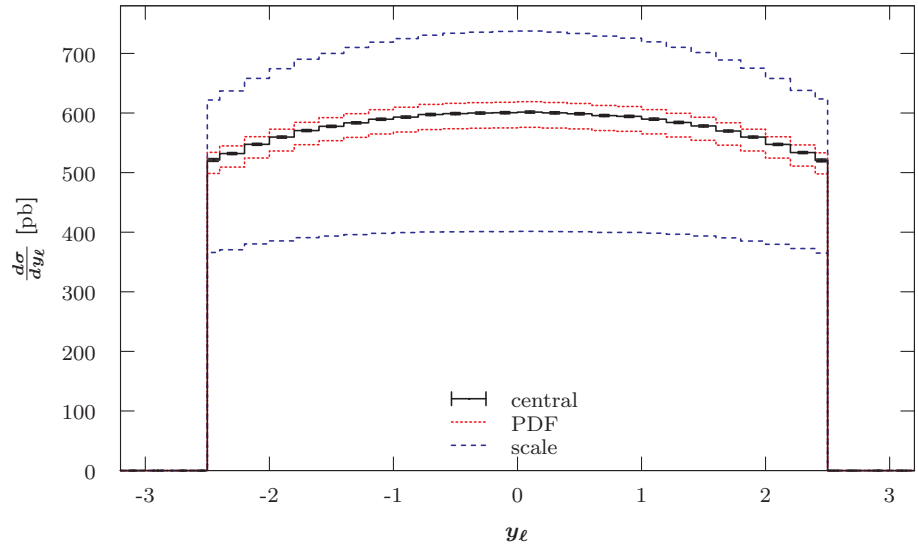

Figure B.29: LO differential cross-section with respect to the charged lepton rapidity for the $pp \to (W^- \to \ell^-\overline{\nu}_\ell)$ process at the LHC with 14 TeV using a fixed scale of $\mu_0 = M_W$. The first and last filled bin are half-width due to the applied selection cut, $|y_\ell| < 2.5$. Additional details are given in the caption of Figure 7.39.

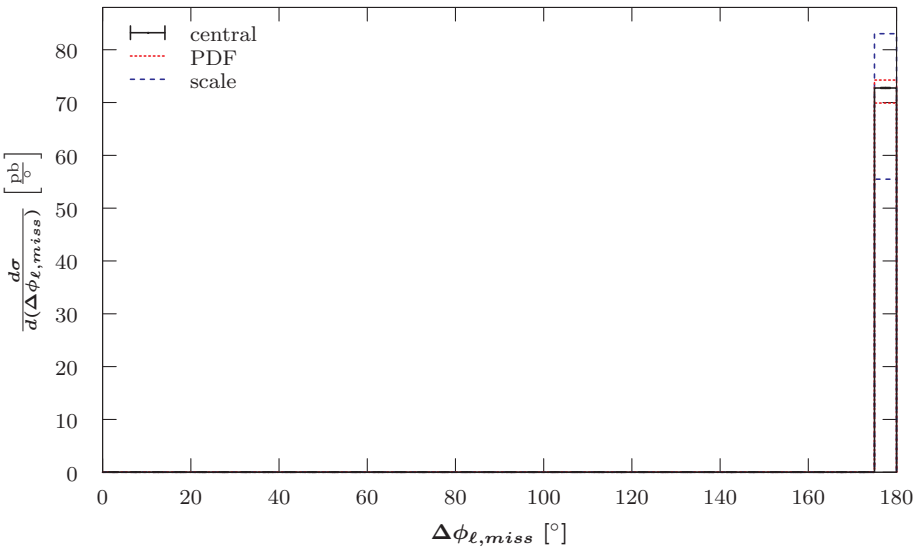

Figure B.30: LO differential cross-section with respect to the azimuthal angle ϕ between the charged lepton and the missing trensverse momentum for the $pp \to (W^- \to \ell^-\overline{\nu}_\ell)$ process at the LHC with 7 TeV using a fixed scale of $\mu_0 = M_W$. Additional details are given in the caption of Figure 7.39.

B.2.2.2 $p^{(}\overline{p}^{)} \to (W^- \to \ell^- \overline{\nu}_\ell) + 1$ jet

This section provides some additional graphs for the $p^{(}\overline{p}^{)} \to (W^- \to \ell^- \overline{\nu}_\ell) + 1\ jet$ process, which were mentioned in Section 7.4.2.2.

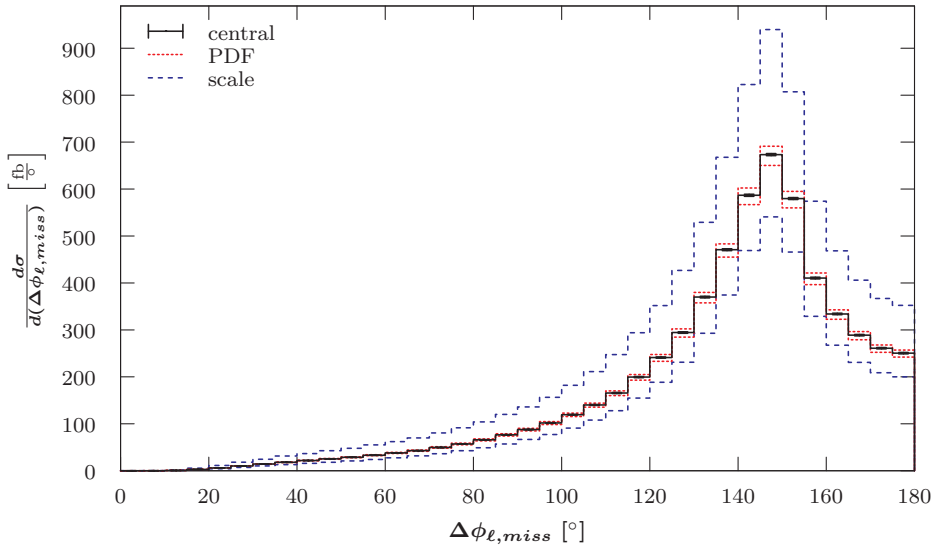

Figure B.31: LO differential cross-section with respect to the transvers angle ϕ between the charged lepton and the missing trensverse momentum for the $p\overline{p} \to (W^- \to \ell^- \overline{\nu}_\ell) + 1\ jet$ process at the Tevatron Run II using a fixed scale of $\mu_0 = M_W$. Additional details are given in the caption of Figure 7.39.

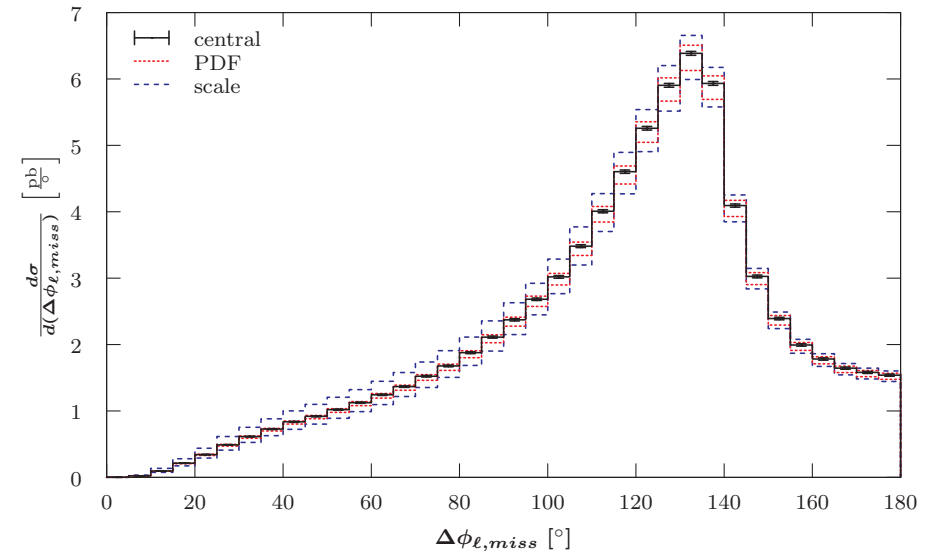

Figure B.32: LO differential cross-section with respect to the azimuthal angle ϕ between the charged lepton and the missing transverse momentum for the $pp \to (W^- \to \ell^- \overline{\nu}_\ell) + 1\ jet$ process at the LHC with 14 TeV using a fixed scale of $\mu_0 = M_W$. Additional details are given in the caption of Figure 7.39.

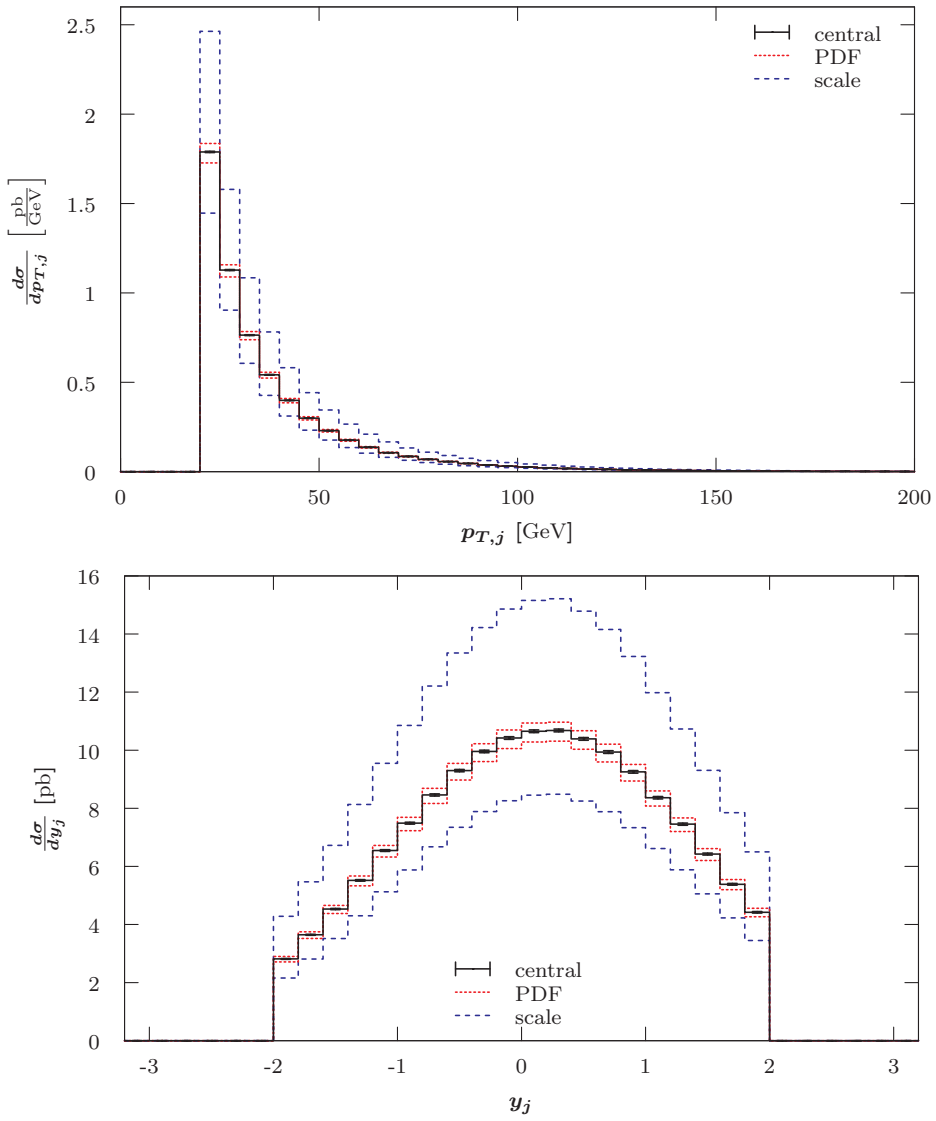

Figure B.33: LO differential cross-section with respect to the jet transverse momentum p_T (top) and the jet rapidity y (bottom) for the $p\overline{p} \to (W^- \to \ell^- \overline{\nu}_\ell) + 1\ jet$ process at the Tevatron Run II using a fixed scale of $\mu_0 = M_W$. Additional details are given in the caption of Figure 7.39.

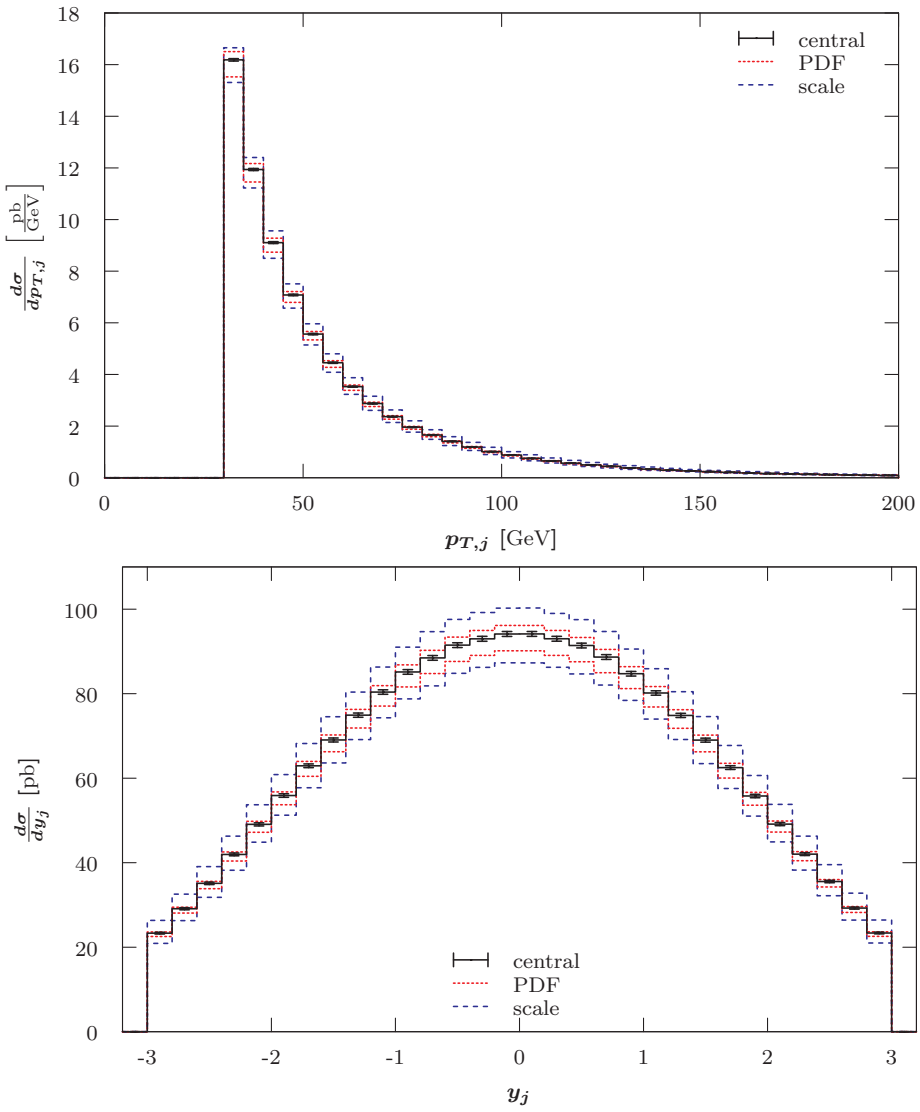

Figure B.34: LO differential cross-section with respect to the jet transverse momentum (top) and the jet rapidity (bottom) for the pp $\to (\mathrm{W}^- \to \ell^- \overline{\nu}_\ell)$+1 *jet* process at the LHC with 14 TeV using a fixed scale of $\mu_0 = M_\mathrm{W}$. Additional details are given in the caption of Figure 7.39.

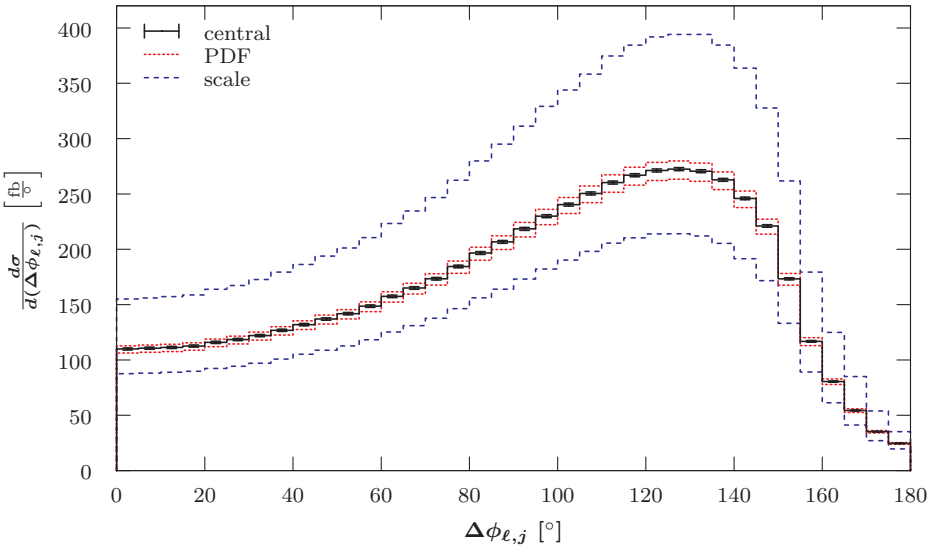

Figure B.35: LO differential cross-section with respect to the azimuthal angle ϕ between the charged lepton and the jet for the $p\overline{p} \to (W^- \to \ell^-\overline{\nu}_\ell) + 1\ jet$ process at the Tevatron Run II using a fixed scale of $\mu_0 = M_W$. Additional details are given in the caption of Figure 7.1.

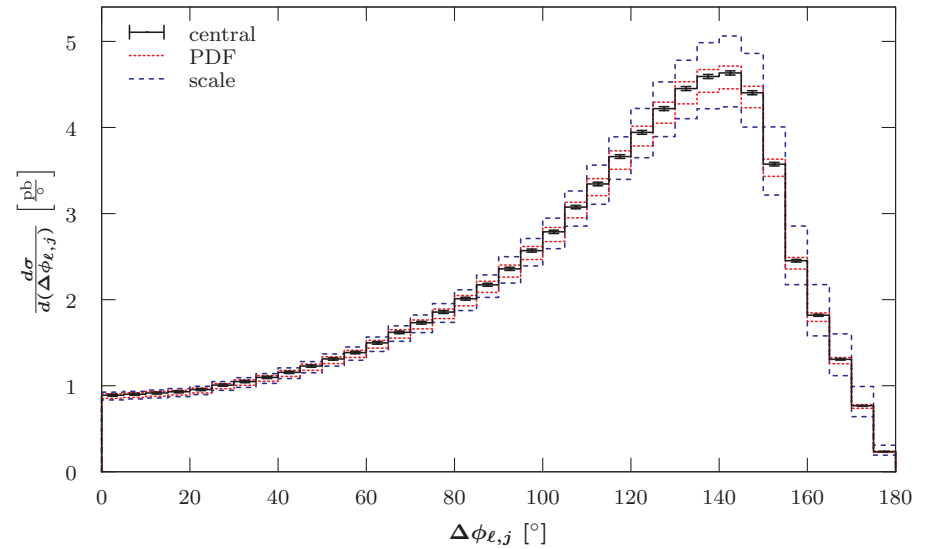

Figure B.36: LO differential cross-section with respect to the azimuthal angle ϕ between the charged lepton and the jet for the $pp \to (W^- \to \ell^-\overline{\nu}_\ell) + 1\ jet$ process at the LHC with 14 TeV using a fixed scale of $\mu_0 = M_W$. Additional details are given in the caption of Figure 7.1.

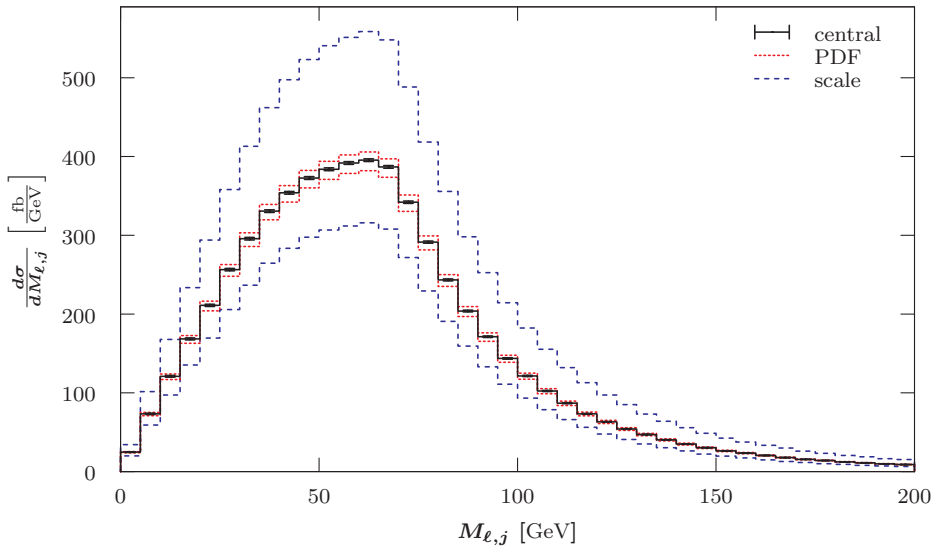

Figure B.37: LO differential cross-section with respect to the transverse mass of the charged lepton and the jet for the $p\overline{p} \to (W^- \to \ell^- \overline{\nu}_\ell) + 1\ jet$ process at the Tevatron Run II using a fixed scale of $\mu_0 = M_W$. Additional details are given in the caption of Figure 7.39.

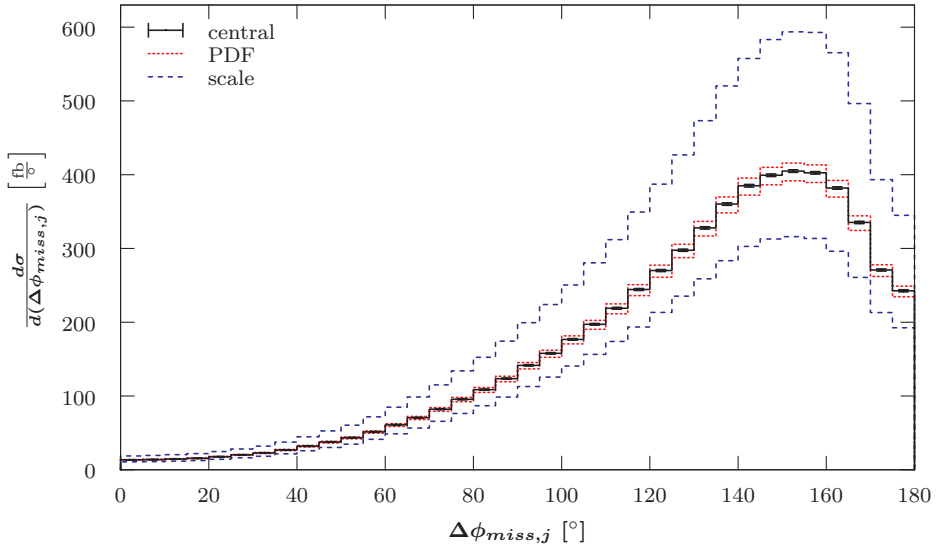

Figure B.38: LO differential cross-section with respect to the transvers angle ϕ between the missing transverse momentum and the jet for the $p\overline{p} \to (W^- \to \ell^- \overline{\nu}_\ell) + 1\ jet$ process at the Tevatron Run II using a fixed scale of $\mu_0 = M_W$. Additional details are given in the caption of Figure 7.1.

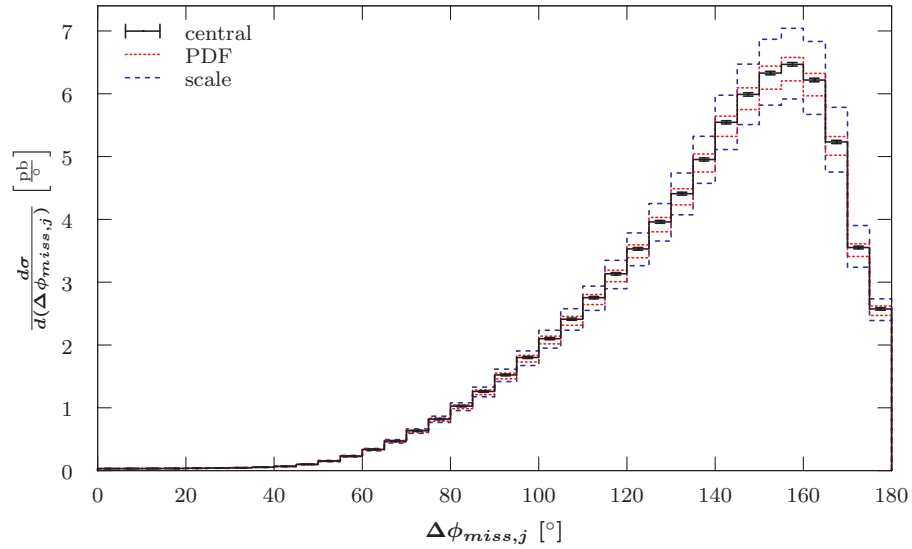

Figure B.39: LO differential cross-section with respect to the transvers angle ϕ between the missing transverse momentum and the jet for the pp $\to (\mathrm{W}^- \to \ell^- \overline{\nu}_\ell) + 1\ jet$ process at the LHC with 14 TeV using a fixed scale of $\mu_0 = M_\mathrm{W}$. Additional details are given in the caption of Figure 7.1.

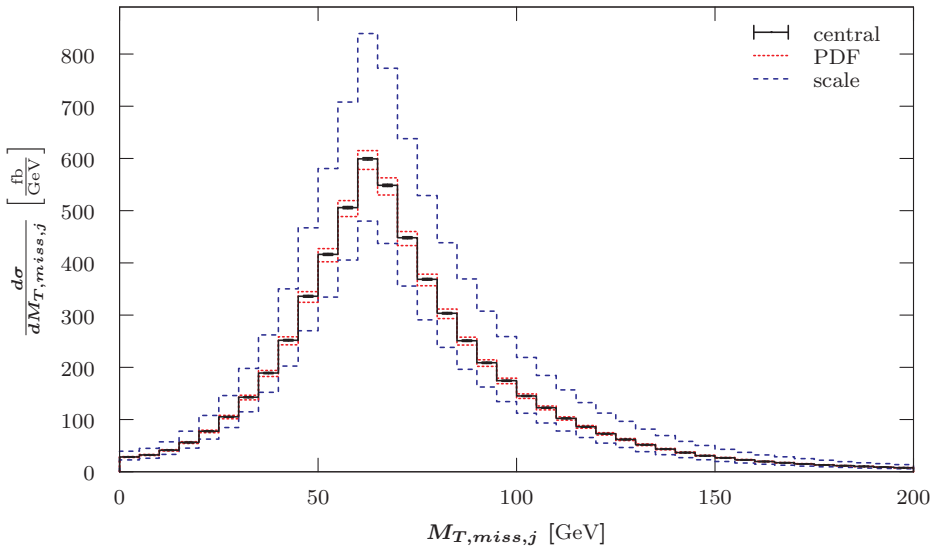

Figure B.40: LO differential cross-section with respect to the transverse mass between the jet and missing transverse momentum vector for the $\mathrm{p\overline{p}} \to (\mathrm{W}^- \to \ell^- \overline{\nu}_\ell) + 1\ jet$ process at the Tevatron Run II using a fixed scale of $\mu_0 = M_\mathrm{W}$. Additional details are given in the caption of Figure 7.39.

B.2.2.3 $p^{(}\overline{p}^{)} \to (W^- \to \ell^- \overline{\nu}_\ell) + 2$ jets

This section provides some additional graphs for the $p^{(}\overline{p}^{)} \to (W^- \to \ell^- \overline{\nu}_\ell) + 2\ jets$ process, which were mentioned in Section 7.4.2.3.

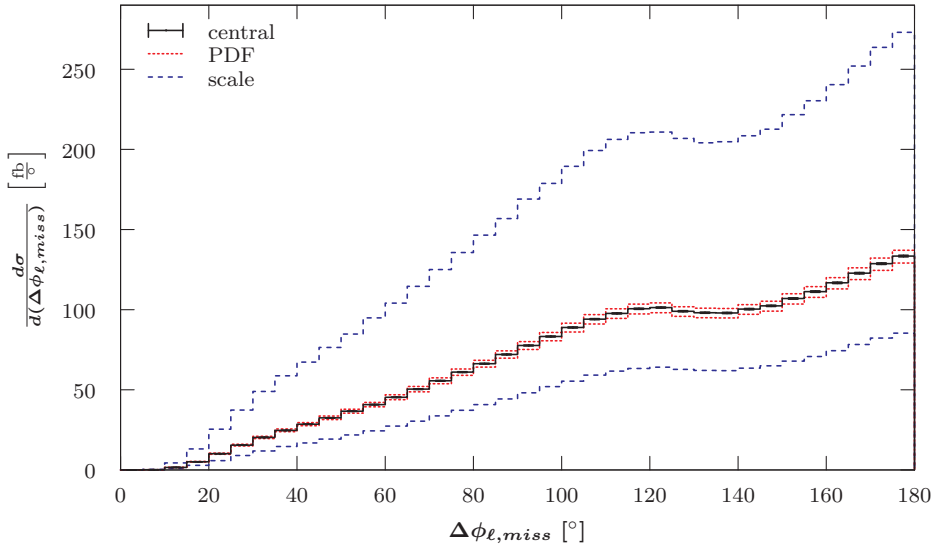

Figure B.41: LO differential cross-section with respect to the transvers angle ϕ between the charged lepton and the missing trensverse momentum for the $p\overline{p} \to (W^- \to \ell^- \overline{\nu}_\ell) + 2\ jets$ process at the Tevatron Run II using a fixed scale of $\mu_0 = M_W$. Additional details are given in the caption of Figure 7.39.

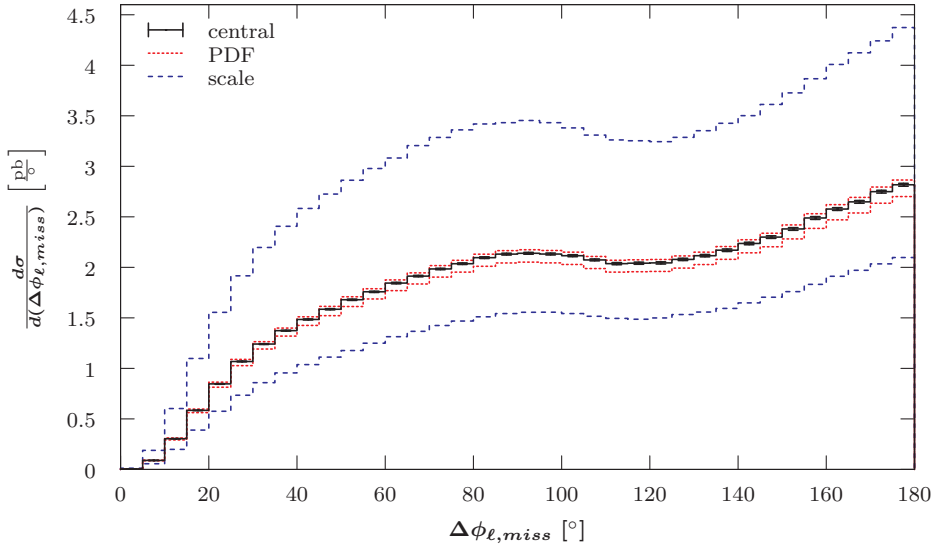

Figure B.42: LO differential cross-section with respect to the azimuthal angle ϕ between the charged lepton and the missing transverse momentum for the $pp \to (W^- \to \ell^- \overline{\nu}_\ell) + 2\ jets$ process at the LHC with 14 TeV using a fixed scale of $\mu_0 = M_W$. Additional details are given in the caption of Figure 7.39.

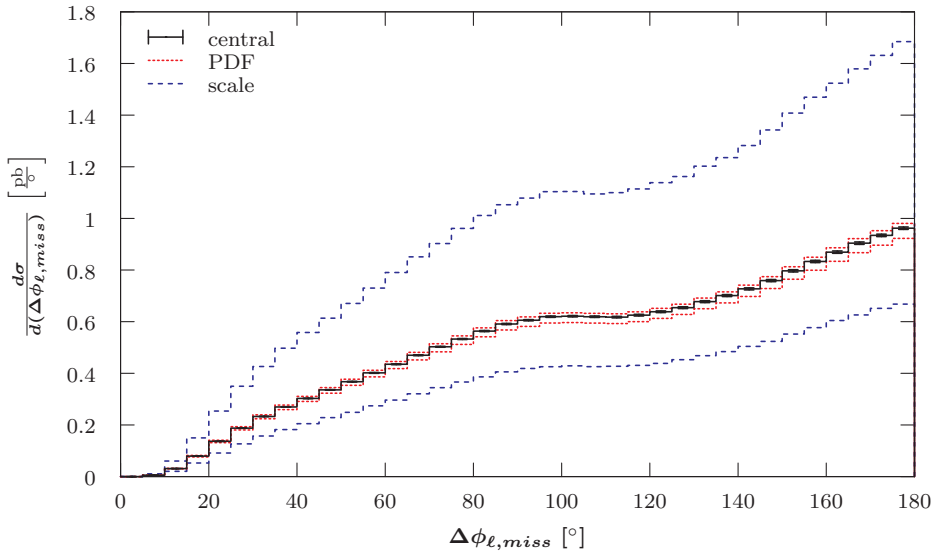

Figure B.43: LO differential cross-section with respect to the transvers angle ϕ between the charged lepton and the missing trensverse momentum for the pp $\to$ ($W^- \to \ell^-\overline{\nu}_\ell$) + 2 *jets* process at the LHC with 7 TeV using a fixed scale of $\mu_0 = E_T^V$. Additional details are given in the caption of Figure 7.1.

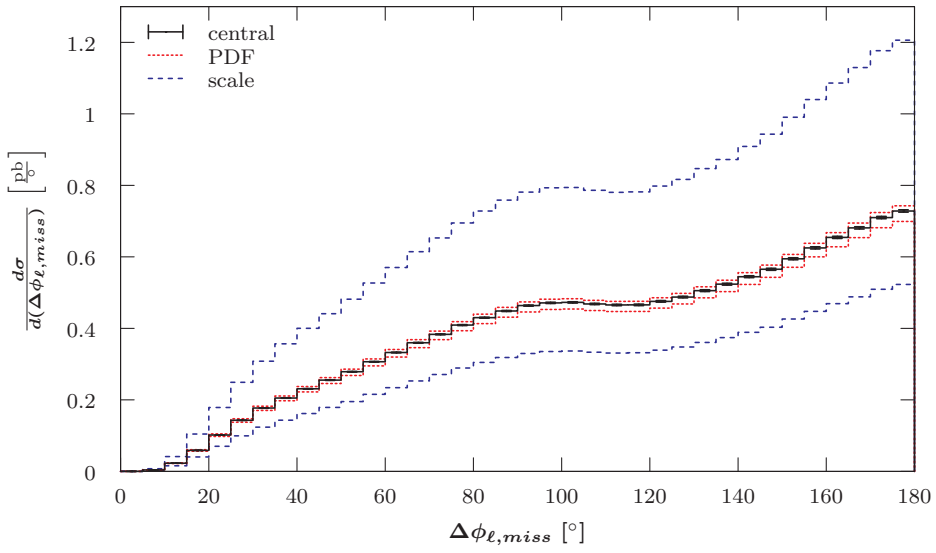

Figure B.44: LO differential cross-section with respect to the transvers angle ϕ between the charged lepton and the missing trensverse momentum for the pp $\to$ ($W^- \to \ell^-\overline{\nu}_\ell$) + 2 *jets* process at the LHC with 7 TeV using a fixed scale of $\mu_0 = \hat{H}_T$. Additional details are given in the caption of Figure 7.1.

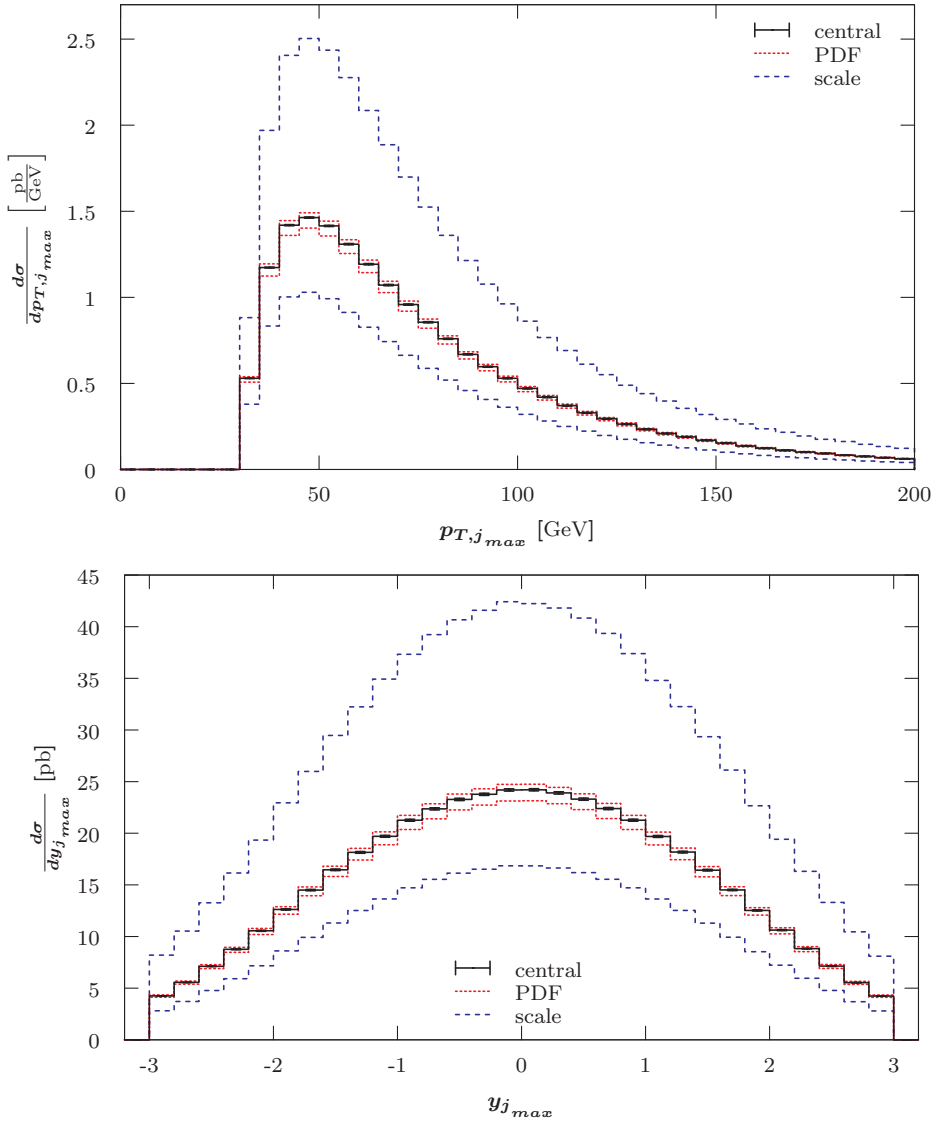

Figure B.45: LO differential cross-section with respect to the transverse momentum (top) and the rapidity (bottom) of the harder jet j_{max} for the pp $\to (\mathrm{W}^- \to \ell^- \overline{\nu}_\ell) + 2\ jets$ process at the LHC with 7 TeV using a fixed scale of $\mu_0 = E_T^{\mathrm{W}}$. Additional details are given in the caption of Figure 7.1.

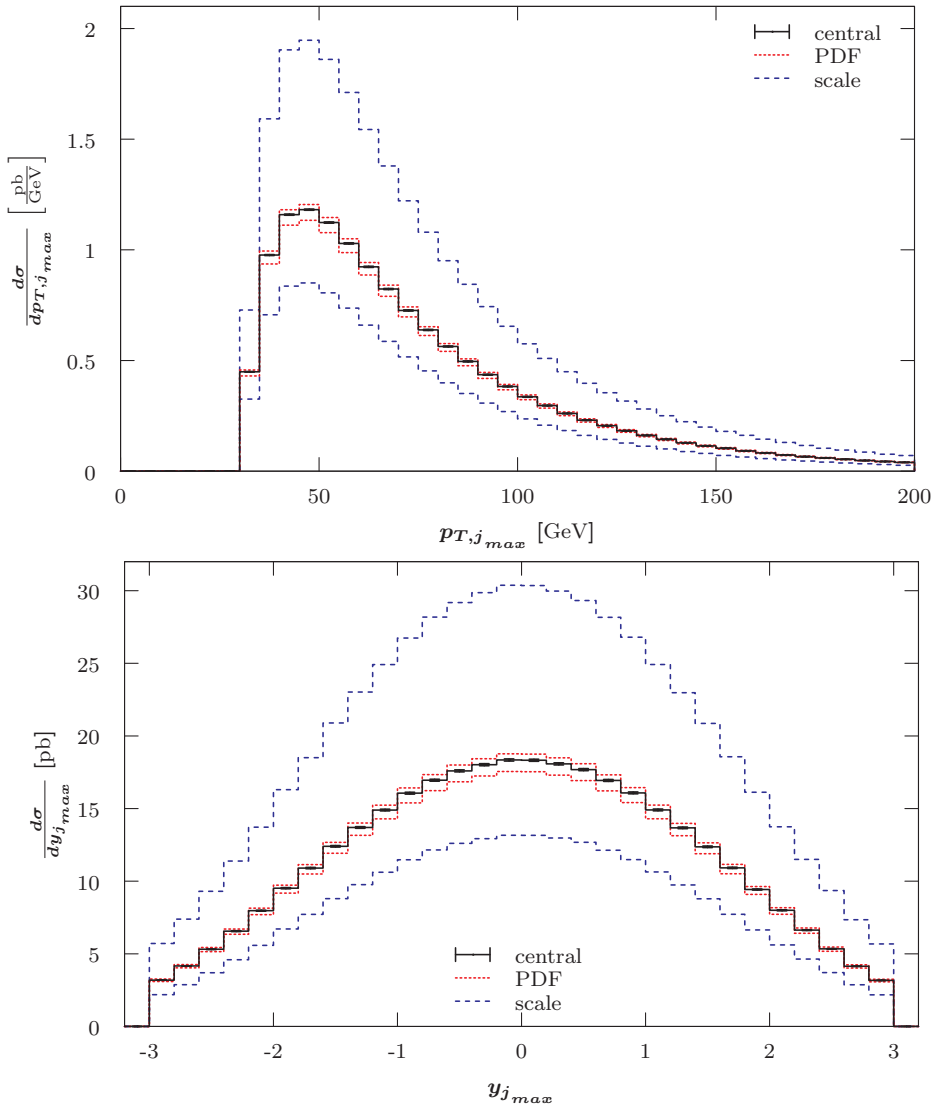

Figure B.46: LO differential cross-section with respect to the transverse momentum (top) and the rapidity (bottom) of the harder jet j_{max} for the $pp \to (W^- \to \ell^- \overline{\nu}_\ell) + 2\ jets$ process at the LHC with 7 TeV using a fixed scale of $\mu_0 = \hat{H}_T$. Additional details are given in the caption of Figure 7.1.

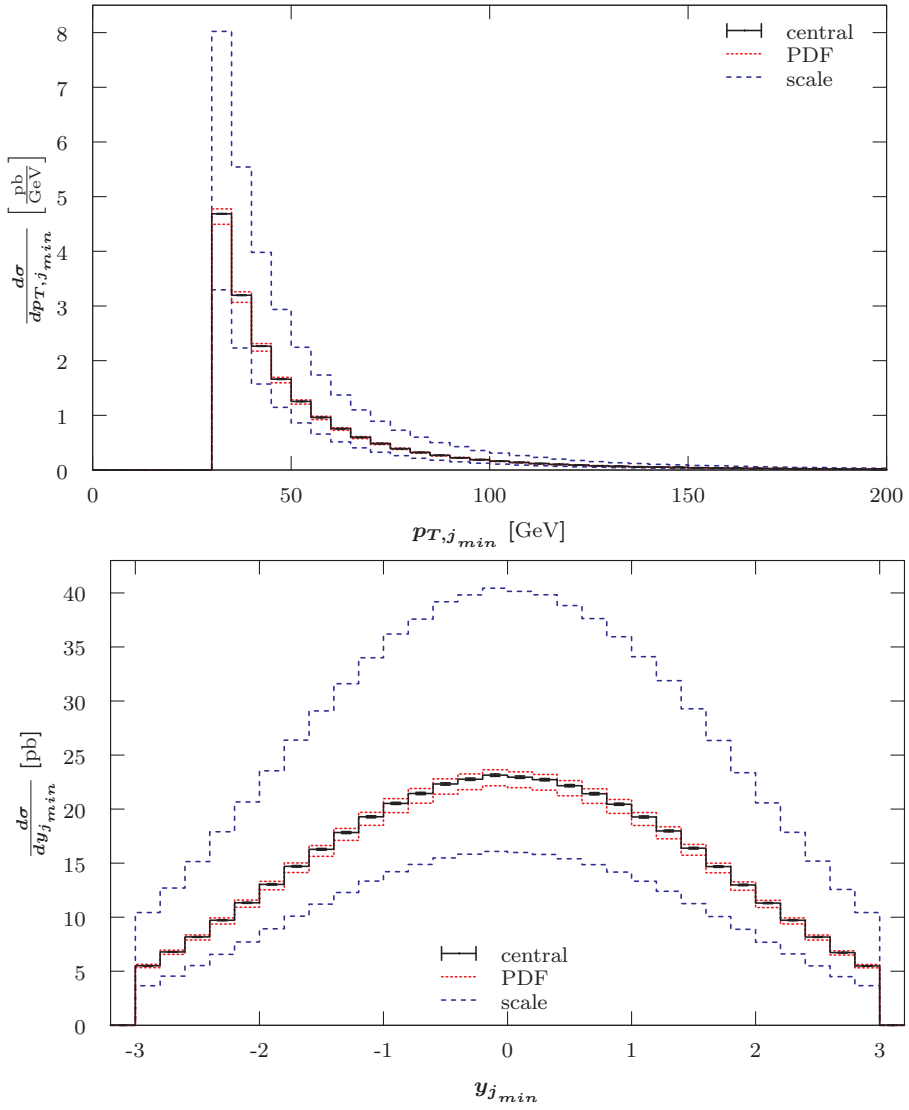

Figure B.47: LO differential cross-section with respect to the transverse momentum (top) and the rapidity (bottom) of the softer jet j_{min} for the pp $\to (\mathrm{W}^- \to \ell^- \overline{\nu}_\ell) + 2\ jets$ process at the LHC with 7 TeV using a fixed scale of $\mu_0 = E_T^{\mathrm{W}}$. Additional details are given in the caption of Figure 7.1.

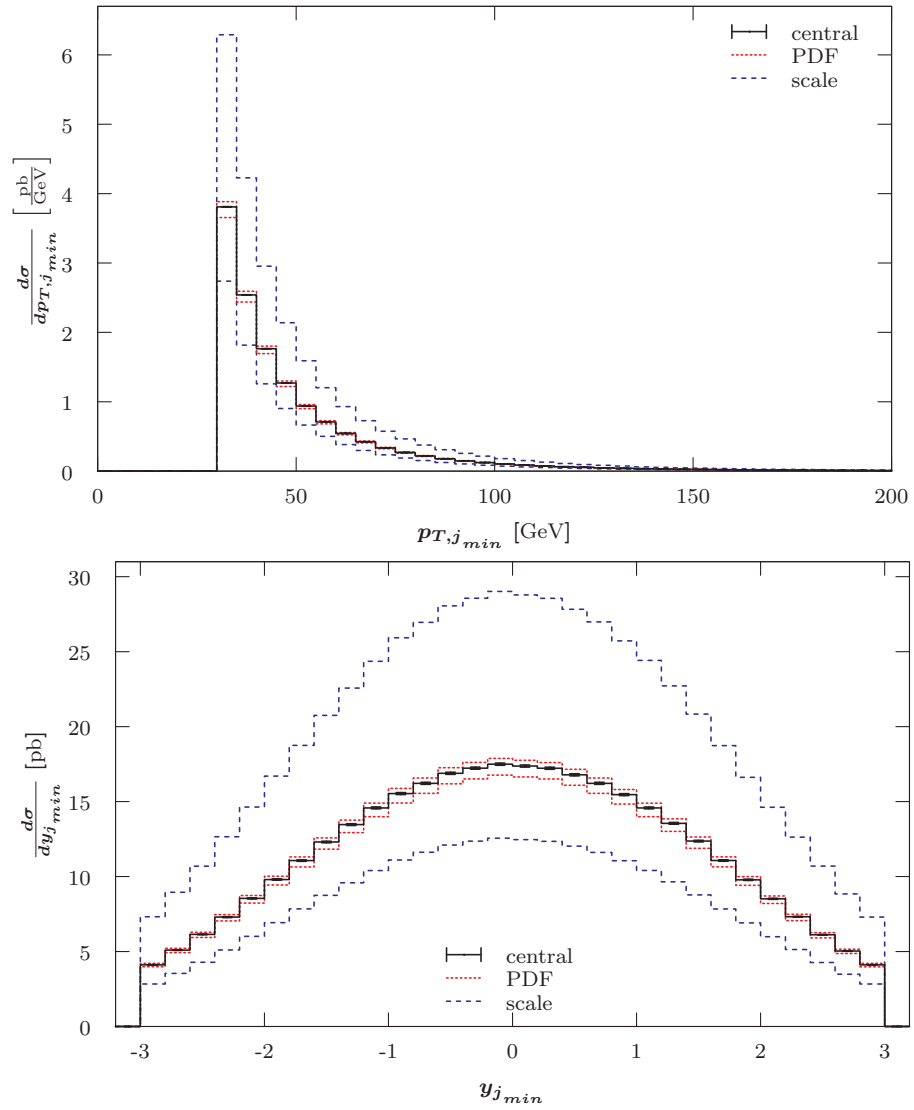

Figure B.48: LO differential cross-section with respect to the transverse momentum (top) and the rapidity (bottom) of the softer jet j_{min} for the pp $\to (\mathrm{W}^- \to \ell^- \overline{\nu}_\ell) + 2\ jets$ process at the LHC with 7 TeV using a fixed scale of $\mu_0 = \hat{H}_T$. Additional details are given in the caption of Figure 7.1.

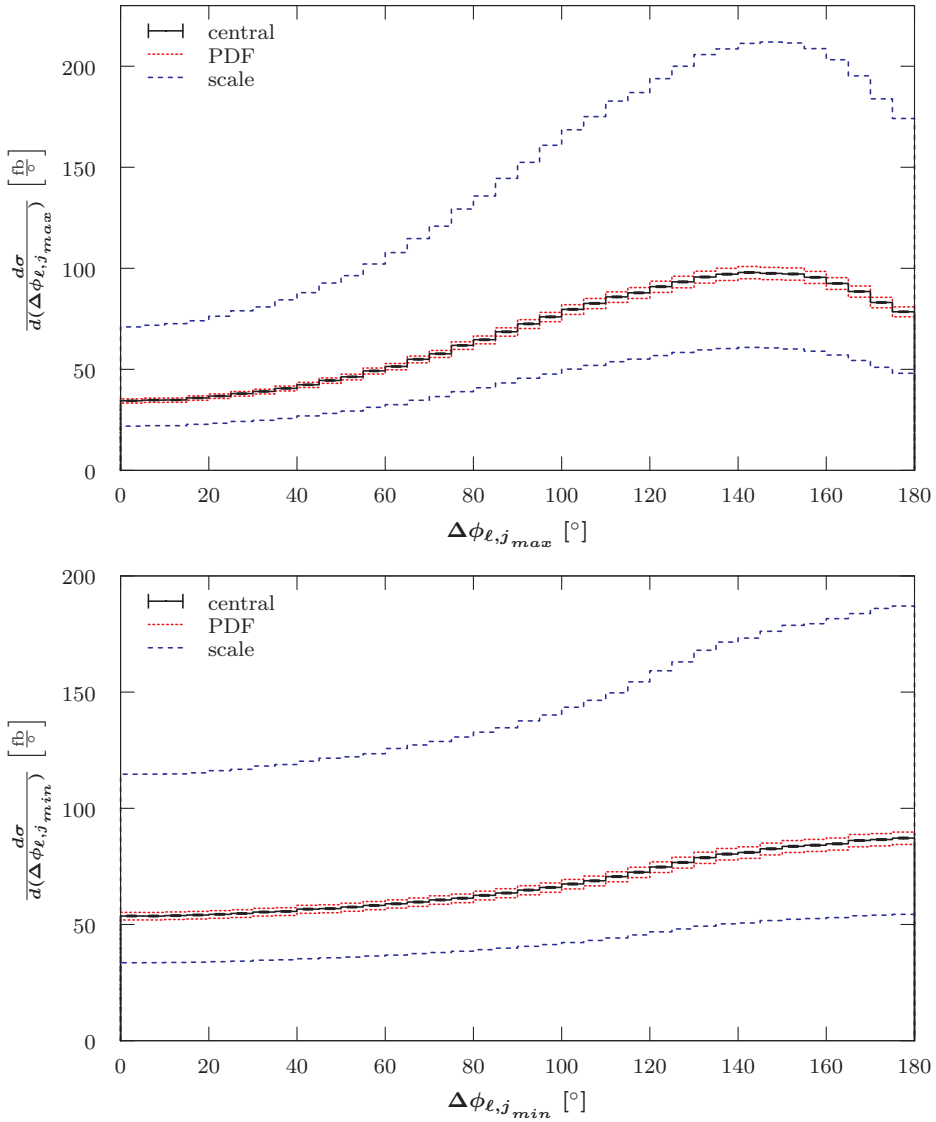

Figure B.49: LO differential cross-section with respect to the azimuthal angle ϕ between the charged lepton and the harder (top) as well as the softer (bottom) jet for the $p\overline{p} \to (W^- \to \ell^-\overline{\nu}_\ell)+2\,jets$ process at the Tevatron Run II using a fixed scale of $\mu_0 = M_W$. Additional details are given in the caption of Figure 7.39.

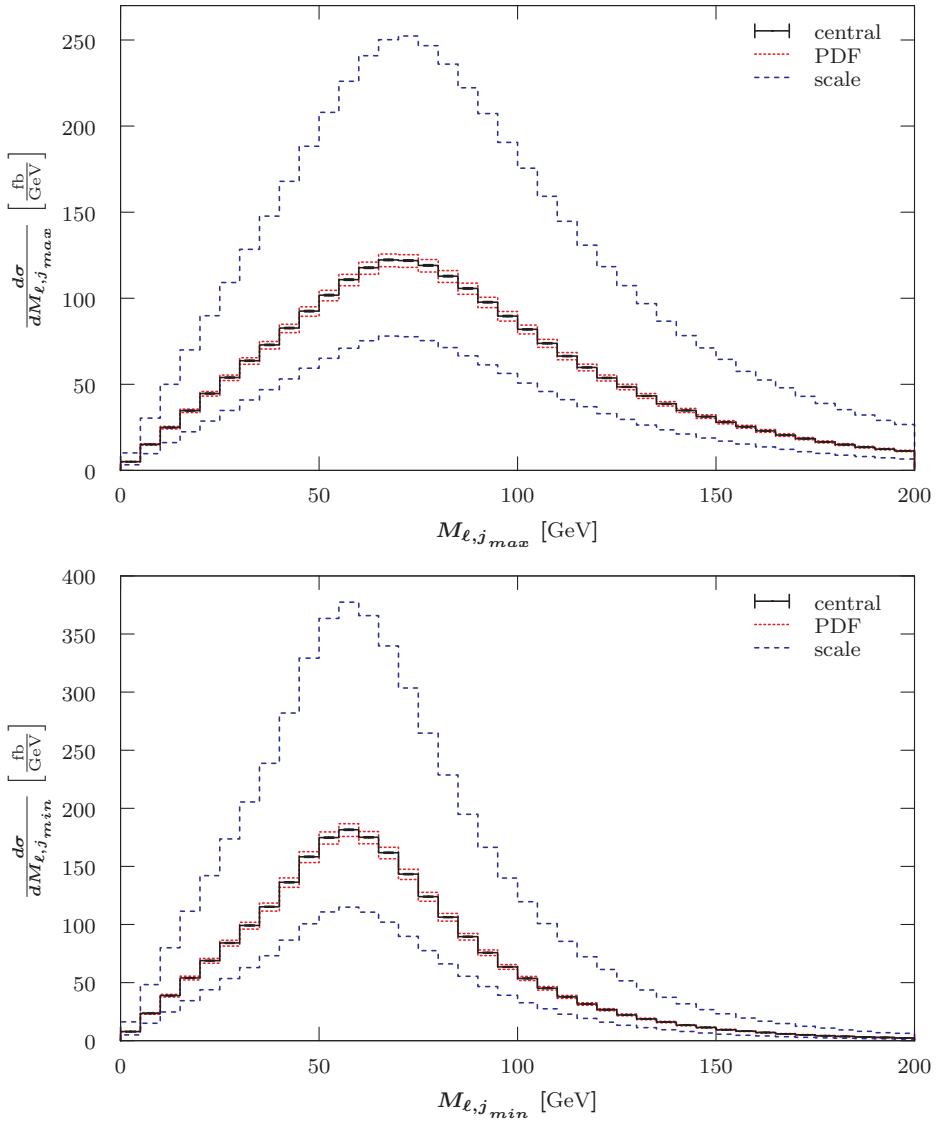

Figure B.50: LO differential cross-section with respect to the invariant mass of the charged lepton and the harder (top) as well as softer (bottom) jet for the $p\overline{p} \to (W^- \to \ell^- \overline{\nu}_\ell) + 2\ jets$ process at the Tevatron Run II using a fixed scale of $\mu_0 = M_W$. Additional details are given in the caption of Figure 7.46.

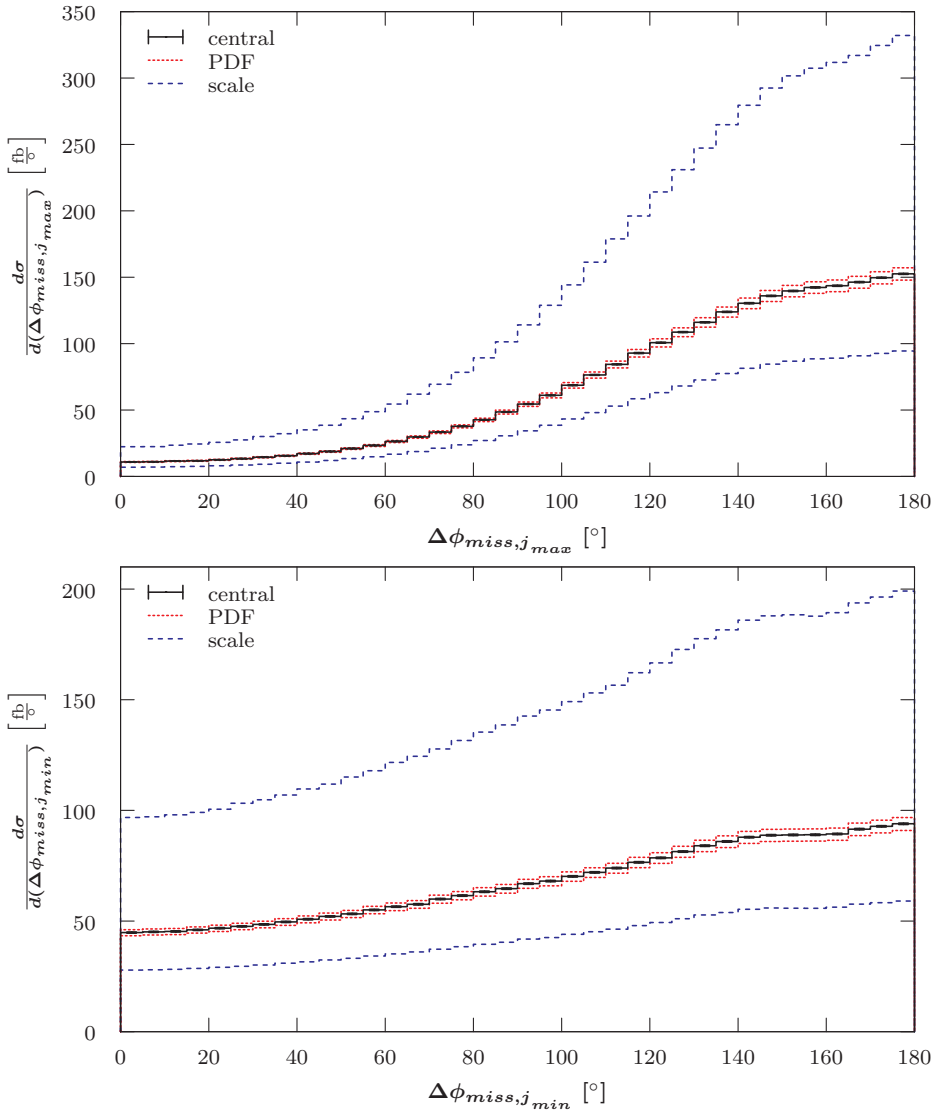

Figure B.51: LO differential cross-section with respect to the azimuthal angle ϕ between the missing transverse momentum and the harder (top) as well as softer (bottom) jet for the $p\overline{p} \to (W^- \to \ell^- \overline{\nu}_\ell)+2\ jets$ process at the Tevatron Run II using a fixed scale of $\mu_0 = M_W$. Additional details are given in the caption of Figure 7.39.

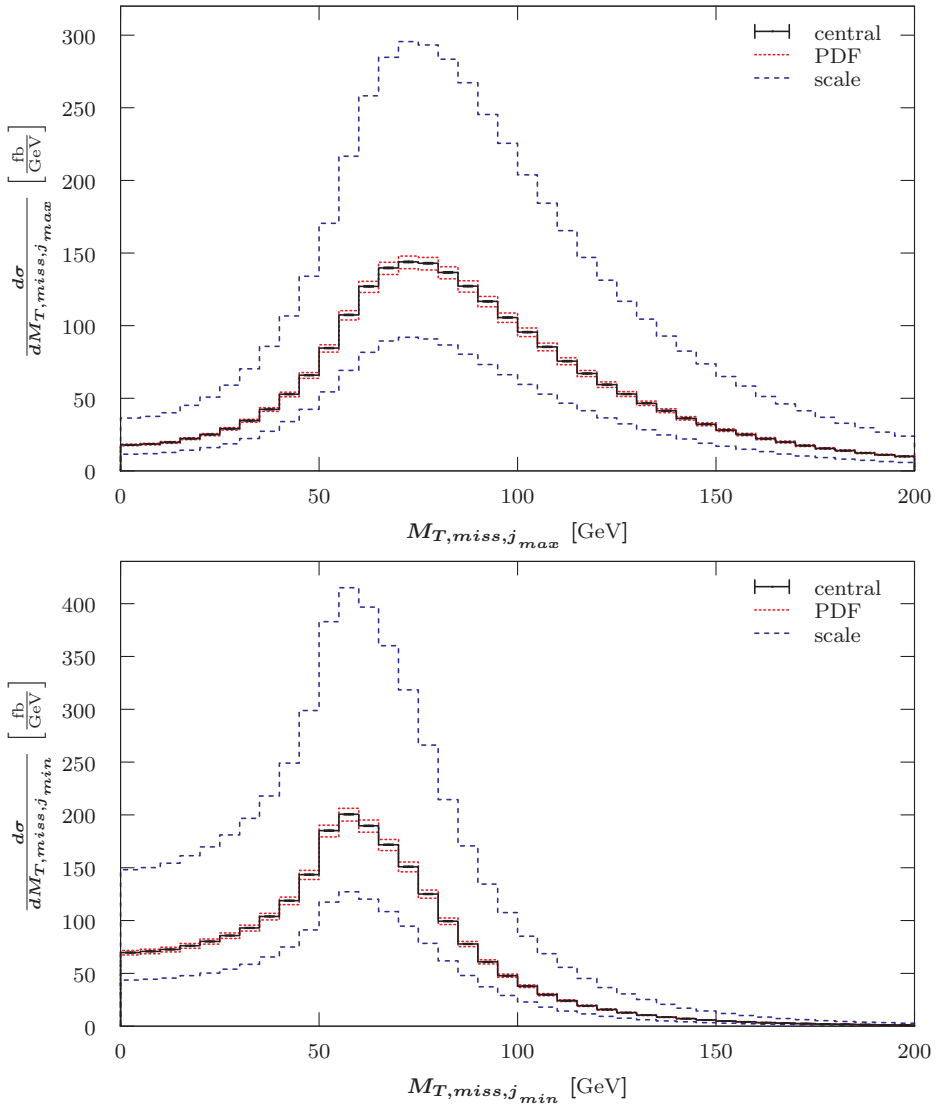

Figure B.52: LO differential cross-section with respect to the transverse mass of the missing transverse momentum vector and the harder (top) as well as softer (bottom) jet for the $p\overline{p} \to (W^- \to \ell^- \overline{\nu}_\ell)$+2 *jets* process at the Tevatron Run II using a fixed scale of $\mu_0 = M_W$. Additional details are given in the caption of Figure 7.39.

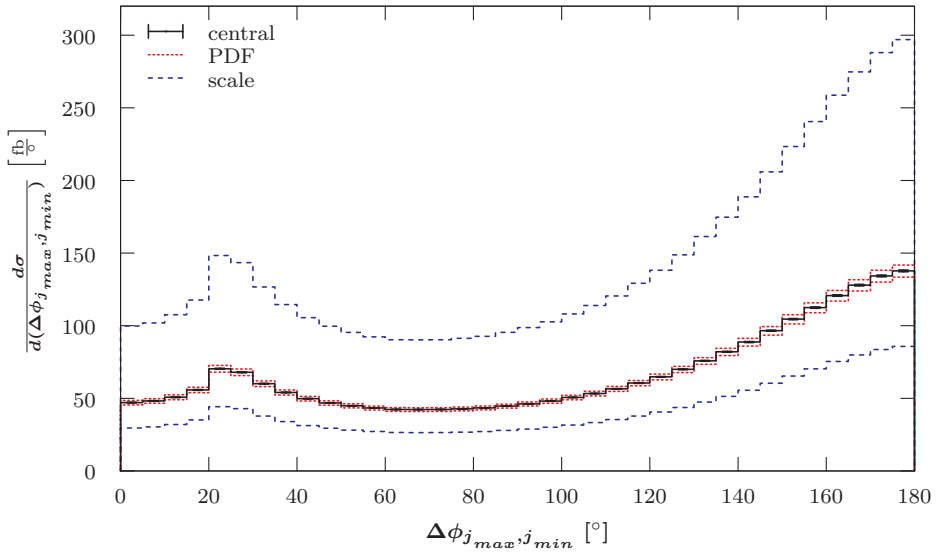

Figure B.53: LO differential cross-section with respect to the azimuthal angle ϕ between the harder j_{max} and the softer jet j_{min} for the $p\overline{p} \to (W^- \to \ell^-\overline{\nu}_\ell) + 2\ jets$ process at the Tevatron Run II using a fixed scale of $\mu_0 = M_Z$. Additional details are given in the caption of Figure 7.39.

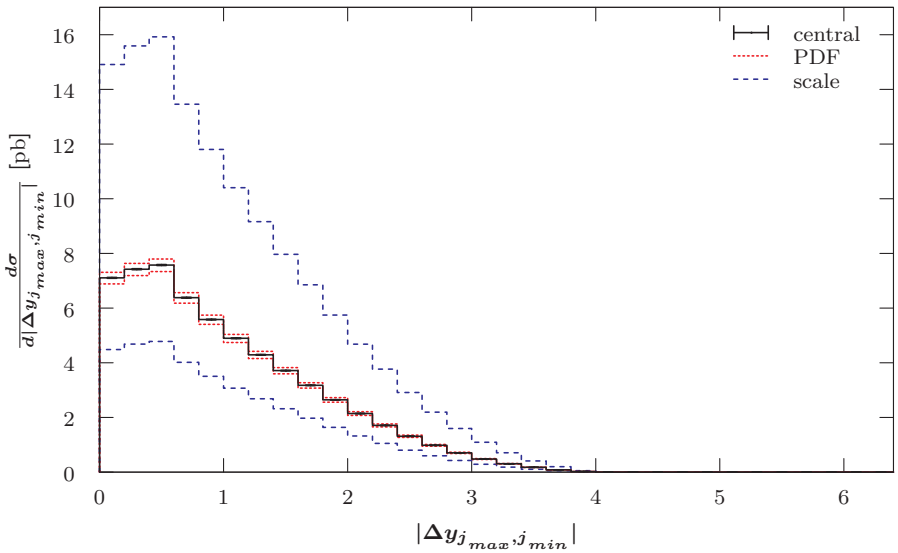

Figure B.54: LO differential cross-section with respect to the difference in rapidity between the harder j_{max} and the softer jet j_{min} for the $p\overline{p} \to (W^- \to \ell^-\overline{\nu}_\ell) + 2\ jets$ process at the Tevatron Run II using a fixed scale of $\mu_0 = M_Z$. Additional details are given in the caption of Figure 7.39.

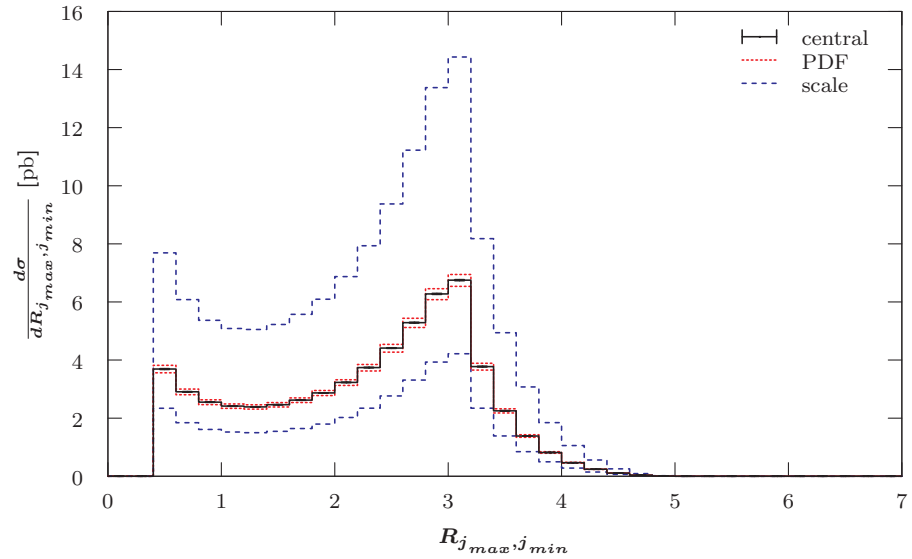

Figure B.55: LO differential cross-section with respect to separation between the harder j_{max} and the softer j_{min} jet for the $p\overline{p} \to (W^- \to \ell^- \overline{\nu}_\ell) + 2\ jets$ process at the Tevatron Run II using a fixed scale of $\mu_0 = M_Z$. Additional details are given in the caption of Figure 7.39.

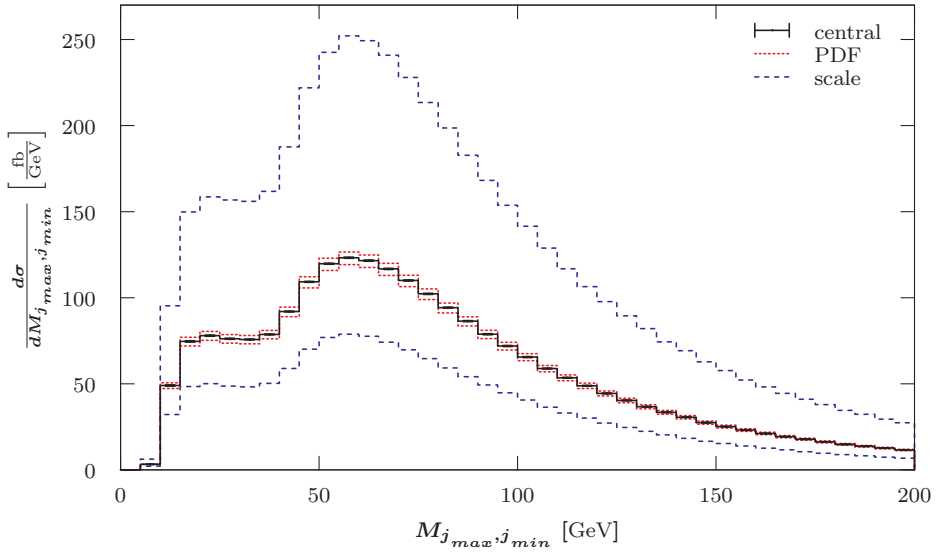

Figure B.56: LO differential cross-section with respect to the inavaraitn mass of the harder j_{max} and the softer j_{min} jet for the $p\overline{p} \to (W^- \to \ell^- \overline{\nu}_\ell) + 2\ jets$ process at the Tevatron Run II using a fixed scale of $\mu_0 = M_Z$. Additional details are given in the caption of Figure 7.39.

B.2.3 $p^{(}\overline{p}^{)} \to (Z \to \ell^-\ell^+) + n$ jets

B.2.3.1 $p^{(}\overline{p}^{)} \to (Z \to \ell^-\ell^+)$

This section provides some additional graphs for the $p^{(}\overline{p}^{)} \to (Z \to \ell^-\ell^+)$ process, which were mentioned in Section 7.4.3.1.

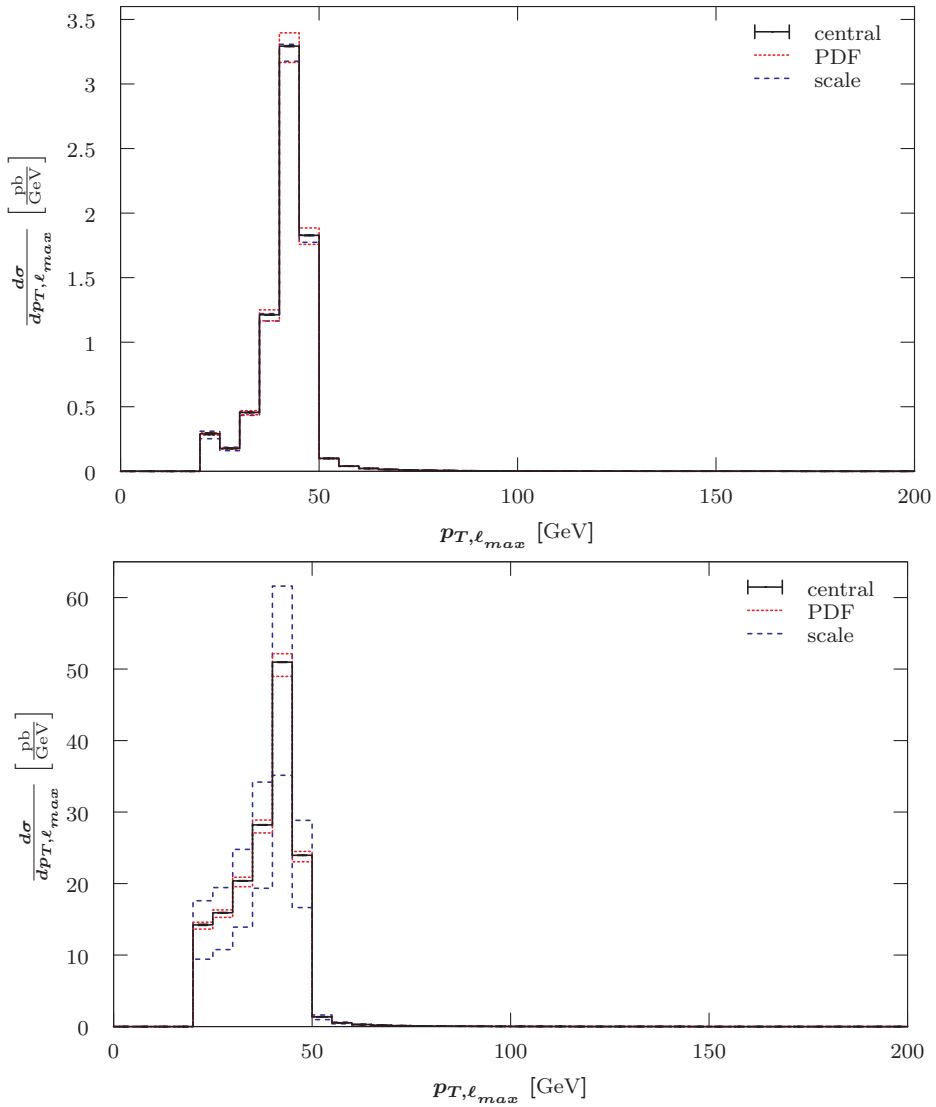

Figure B.57: LO differential cross-section with respect to the harder charged lepton ℓ_{max} transverse momentum for the $p^{(}\overline{p}^{)} \to (Z \to \ell^-\ell^+)$ process at the Tevatron Run II (top) and the LHC with 14 TeV (bottom) using a fixed scale of $\mu_0 = M_Z$. Additional details are given in the caption of Figure 7.77.

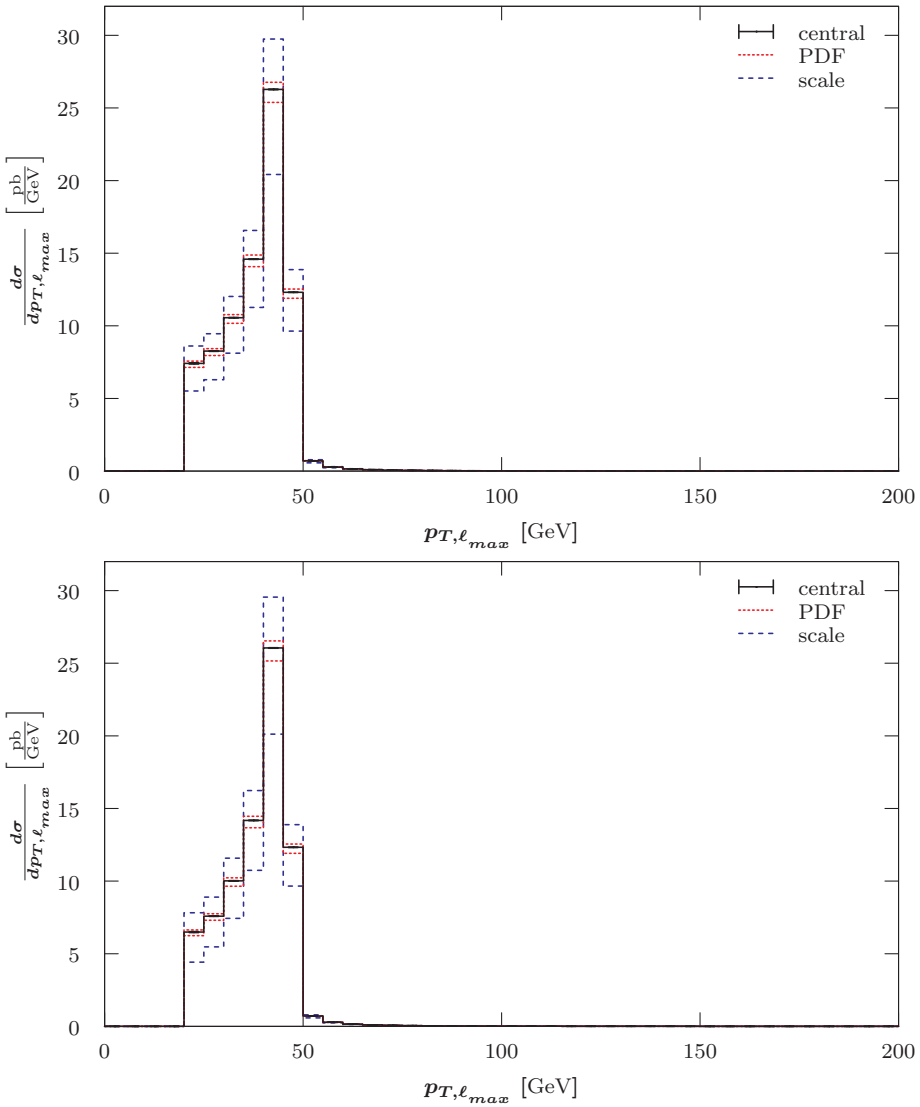

Figure B.58: LO differential cross-section with respect to the harder charged lepton ℓ_{max} transverse momentum for the pp $\to$ (Z $\to \ell^-\ell^+$) process at the LHC with 7 TeV using the dynamic scales of $\mu_0 = E_T^{\text{Z}}$ (top) and $\mu_0 = \hat{H}_T$ (bottom). Additional details are given in the caption of Figure 7.77.

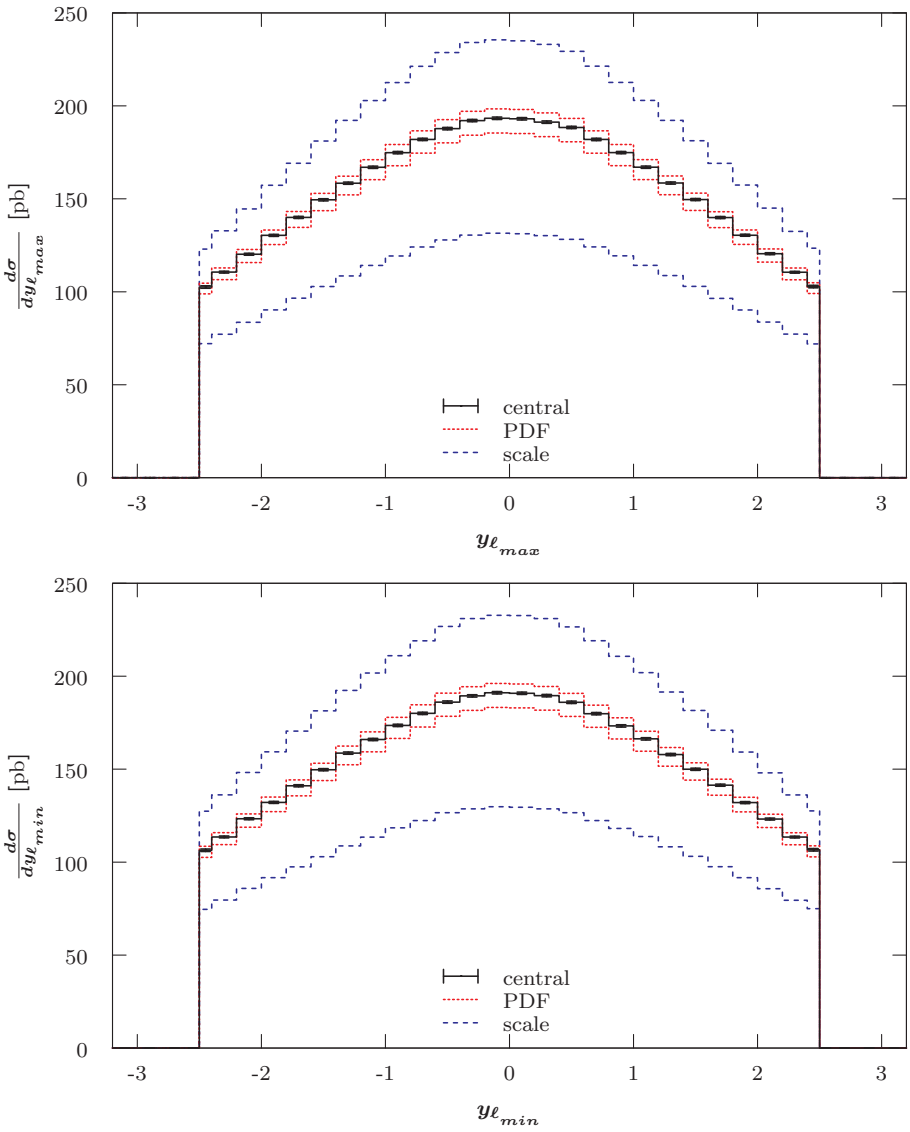

Figure B.59: LO differential cross-section with respect to the rapidity of the harder ℓ_{max} (top) and the softer ℓ_{min} (bottom) charged lepton for the pp $\to$ (Z $\to \ell^-\ell^+$) process at the LHC with 14 TeV using a fixed scale of $\mu_0 = M_{\mathrm{Z}}$. The first and last filled bin are half-width due to the applied selection cut, $|y_\ell| < 2.5$. Additional details are given in the caption of Figure 7.77.

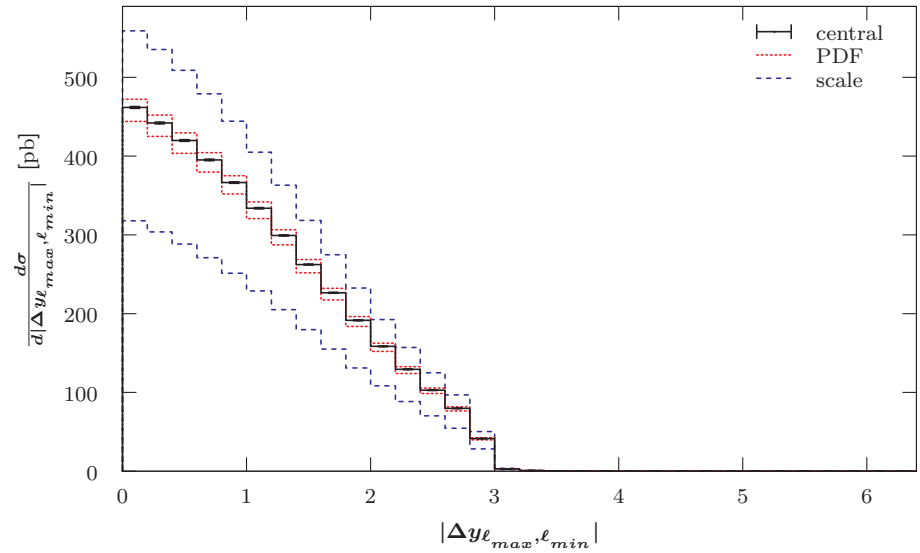

Figure B.60: LO differential cross-section with respect to the difference in rapidity between the two charged leptons for the pp $\to$ (Z $\to \ell^-\ell^+$) process at the LHC with 14 TeV using a fixed scale of $\mu_0 = M_{\mathrm{Z}}$. Additional details are given in the caption of Figure 7.77.

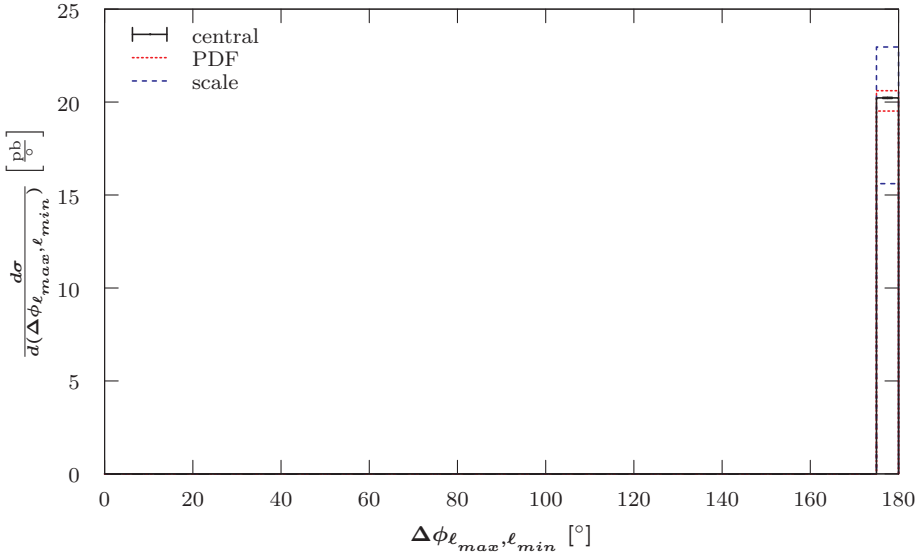

Figure B.61: LO differential cross-section with respect to the transvers angle ϕ between the harder ℓ_{max} and the softer ℓ_{min} charged lepton for the pp $\to$ (Z $\to \ell^-\ell^+$) process at the LHC with 7 TeV using a fixed scale of $\mu_0 = M_{\mathrm{Z}}$. Additional details are given in the caption of Figure 7.77.

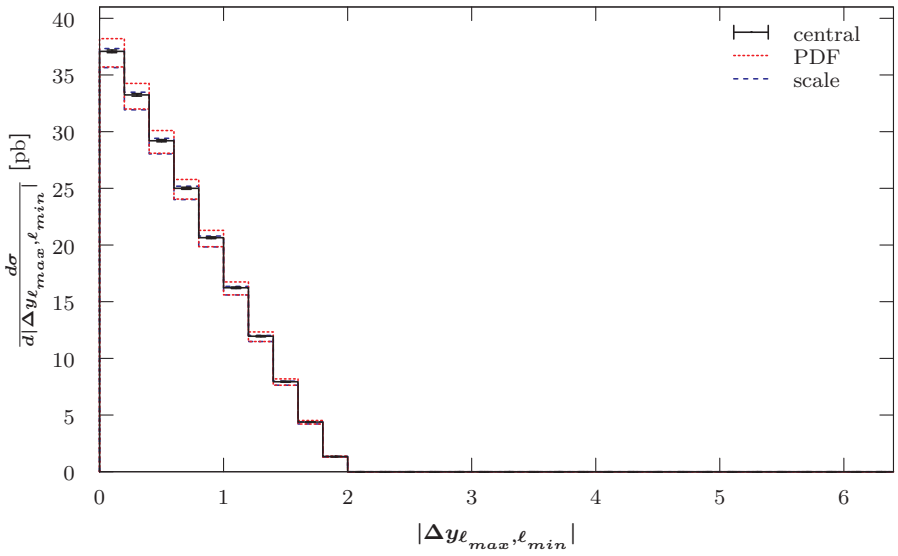

Figure B.62: LO differential cross-section with respect to the difference in rapidity between the harder ℓ_{max} and the softer ℓ_{min} charged lepton for the $p\overline{p} \to (Z \to \ell^-\ell^+)$ process at the Tevatron Run II using a fixed scale of $\mu_0 = M_Z$. Additional details are given in the caption of Figure 7.77.

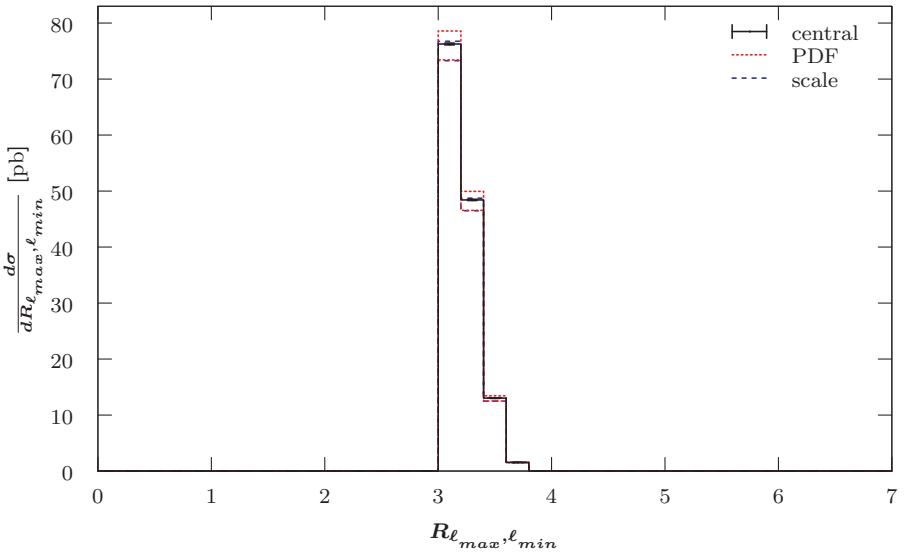

Figure B.63: LO differential cross-section with respect to distance R between the harder ℓ_{max} and the softer ℓ_{min} charged lepton for the $p\overline{p} \to (Z \to \ell^-\ell^+)$ process at the Tevatron Run II using a fixed scale of $\mu_0 = M_Z$. Additional details are given in the caption of Figure 7.77.

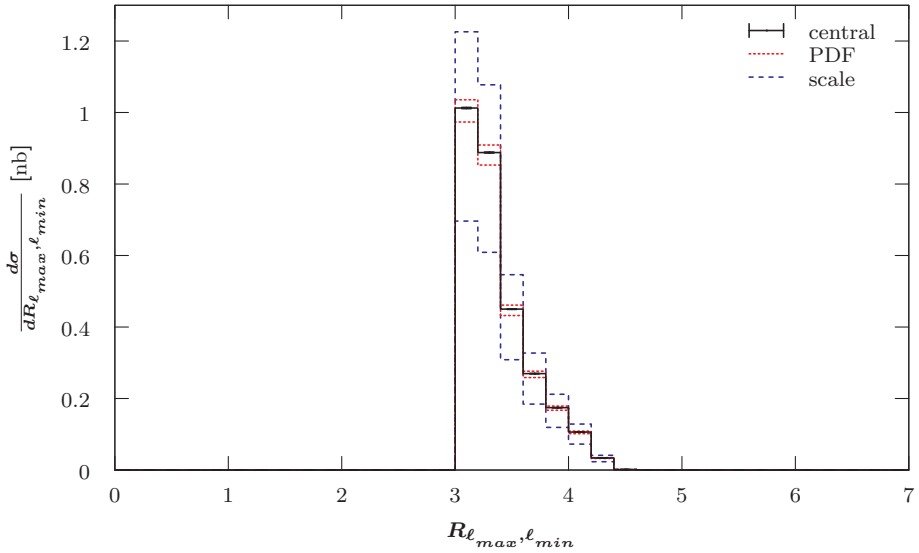

Figure B.64: LO differential cross-section with respect to distance R between the two charged leptons for the $pp \to (Z \to \ell^-\ell^+)$ process at the LHC with 14 TeV using a fixed scale of $\mu_0 = M_Z$. Additional details are given in the caption of Figure 7.77.

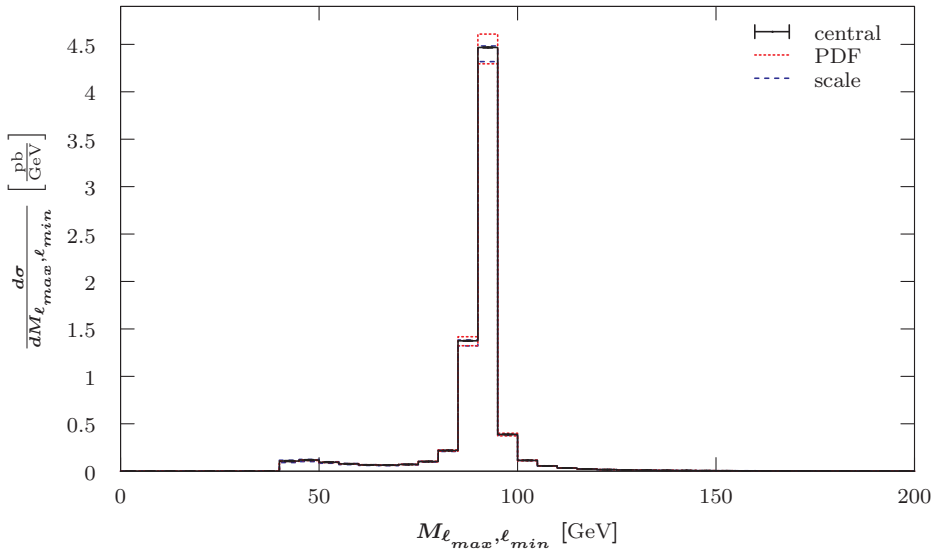

Figure B.65: LO differential cross-section with to the invariant mass of the two charged leptons for the $p\bar{p} \to (Z \to \ell^-\ell^+)$ process at the Tevatron Run II using a fixed scale of $\mu_0 = M_Z$. Additional details are given in the caption of Figure 7.77.

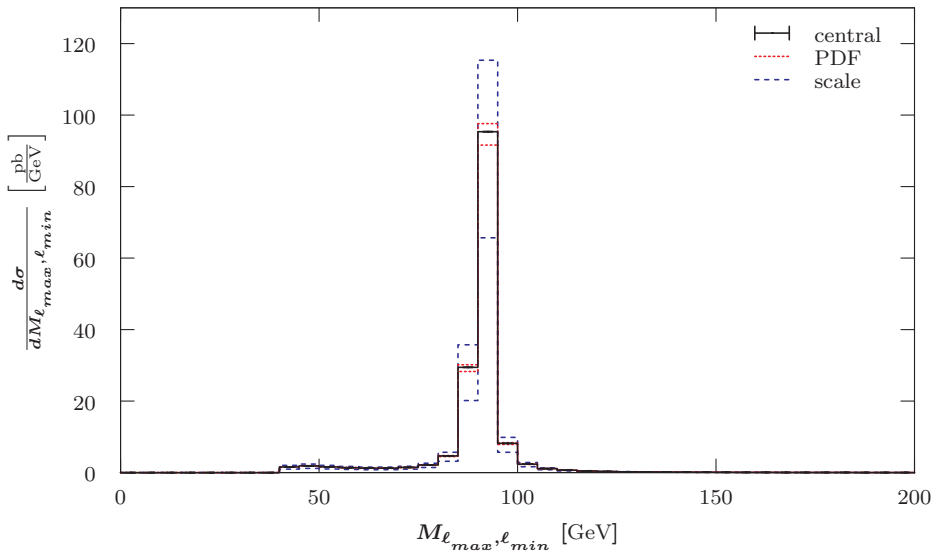

Figure B.66: LO differential cross-section with to the invariant mass of the two charged leptons for the pp $\to$ (Z $\to \ell^-\ell^+$) process at the LHC with 14 TeV using a fixed scale of $\mu_0 = M_{\text{Z}}$. Additional details are given in the caption of Figure 7.77.

B.2.3.2 $p^{(}\overline{p}^{)} \to (Z \to \ell^-\ell^+) + 1$ jet

This section provides some additional graphs for the $p^{(}\overline{p}^{)} \to (Z \to \ell^-\ell^+) + 1\ jet$ process, which were mentioned in Section 7.4.3.2.

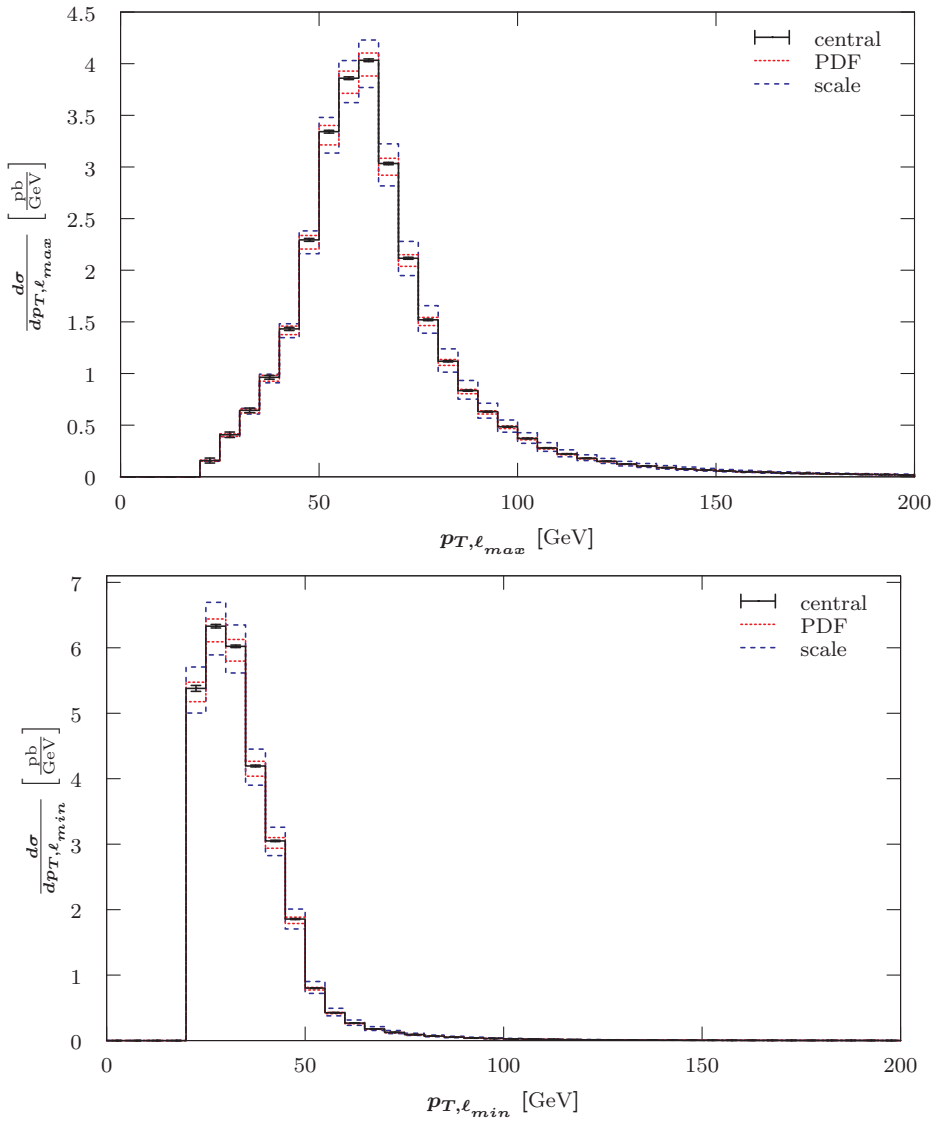

Figure B.67: LO differential cross-section with respect to the harder ℓ_{max} (top) and the softer ℓ_{min} (bottom) charged lepton transverse momentum for the $pp \to (Z \to \ell^-\ell^+) + 1\ jet$ process at the LHC with 14 TeV using a fixed scale of $\mu_0 = M_Z$. Additional details are given in the caption of Figure 7.77.

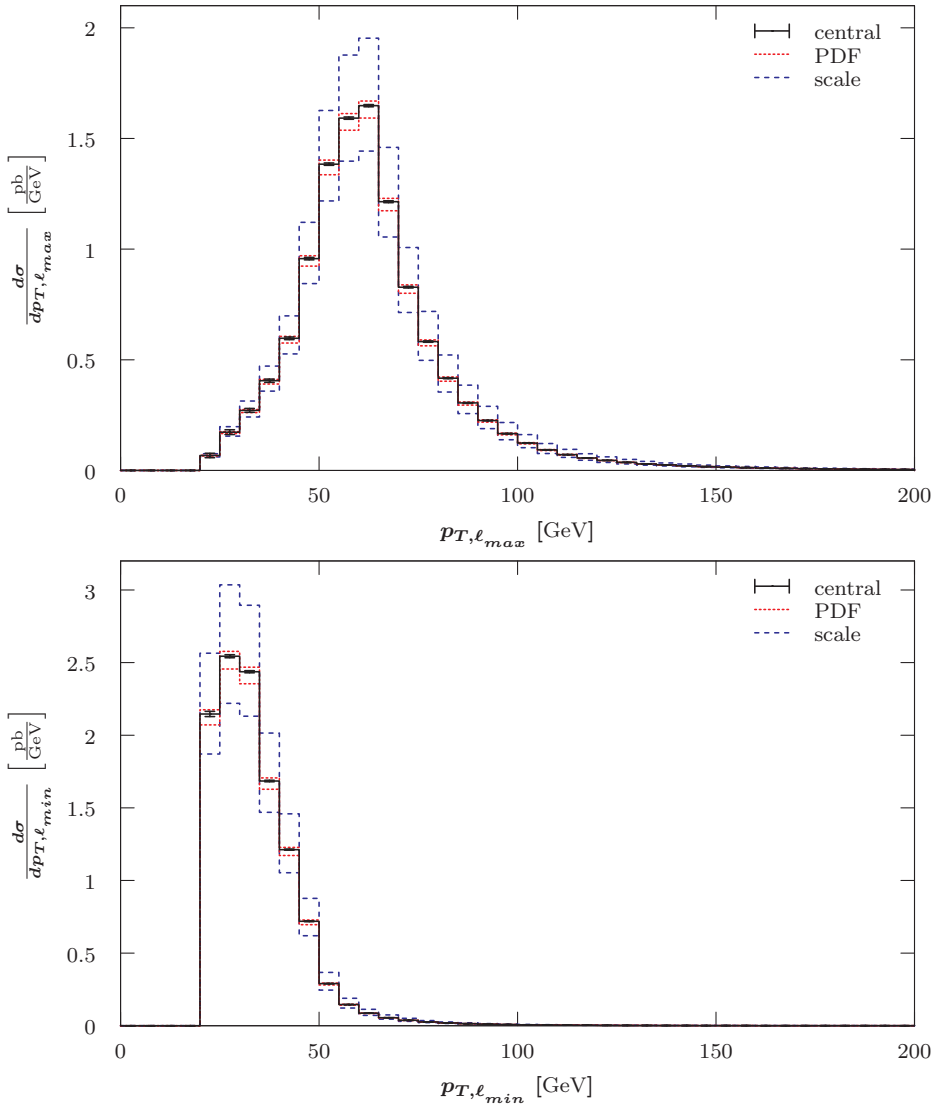

Figure B.68: LO differential cross-section with respect to the harder ℓ_{max} (top) and the softer ℓ_{min} (bottom) charged lepton transverse momentum for the pp $\to$ (Z $\to \ell^-\ell^+$) + 1 *jet* process at the LHC with 7 TeV using the dynamic scale of $\mu_0 = E_T^{\text{Z}}$. Additional details are given in the caption of Figure 7.77.

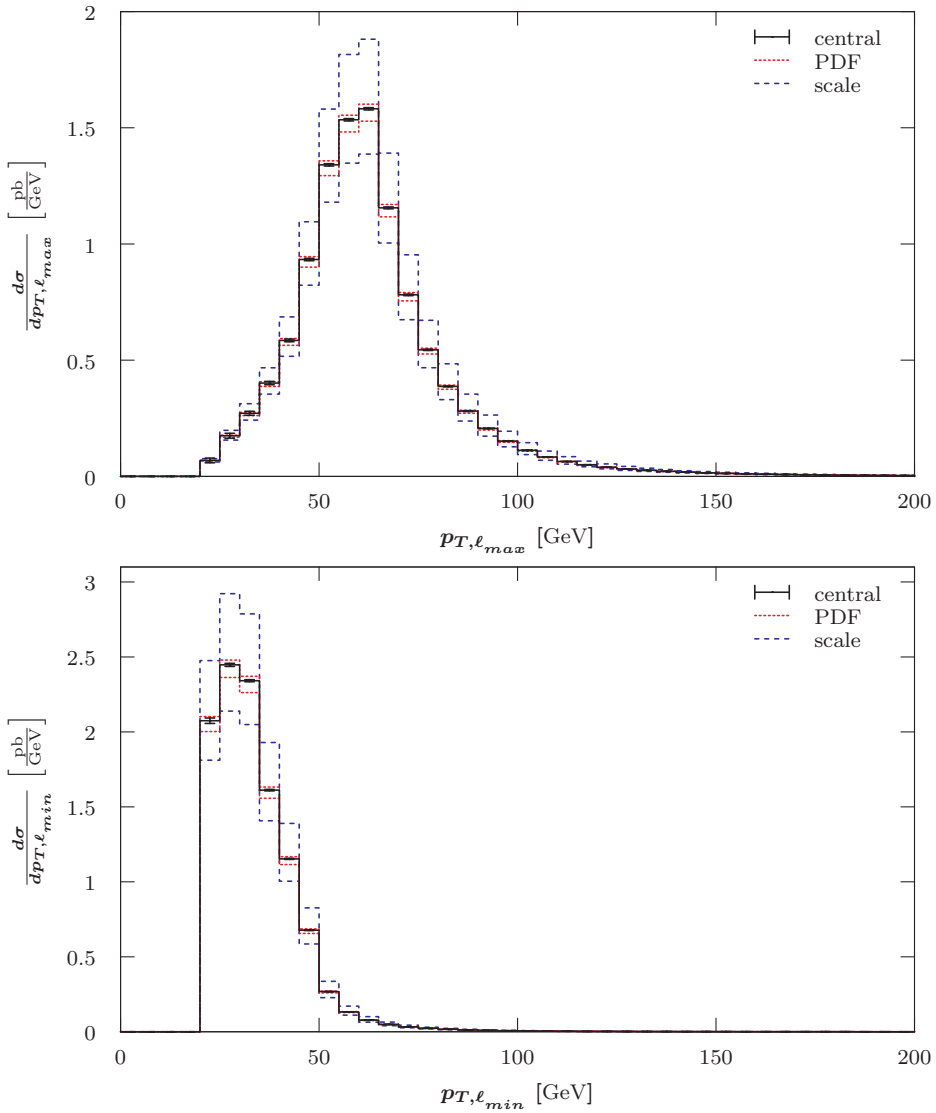

Figure B.69: LO differential cross-section with respect to the harder ℓ_{max} (top) and the softer ℓ_{min} (bottom) charged lepton transverse momentum for the pp $\to$ (Z $\to \ell^-\ell^+$) + 1 *jet* process at the LHC with 7 TeV using the dynamic scale of $\mu_0 = \hat{H}_T$. Additional details are given in the caption of Figure 7.77.

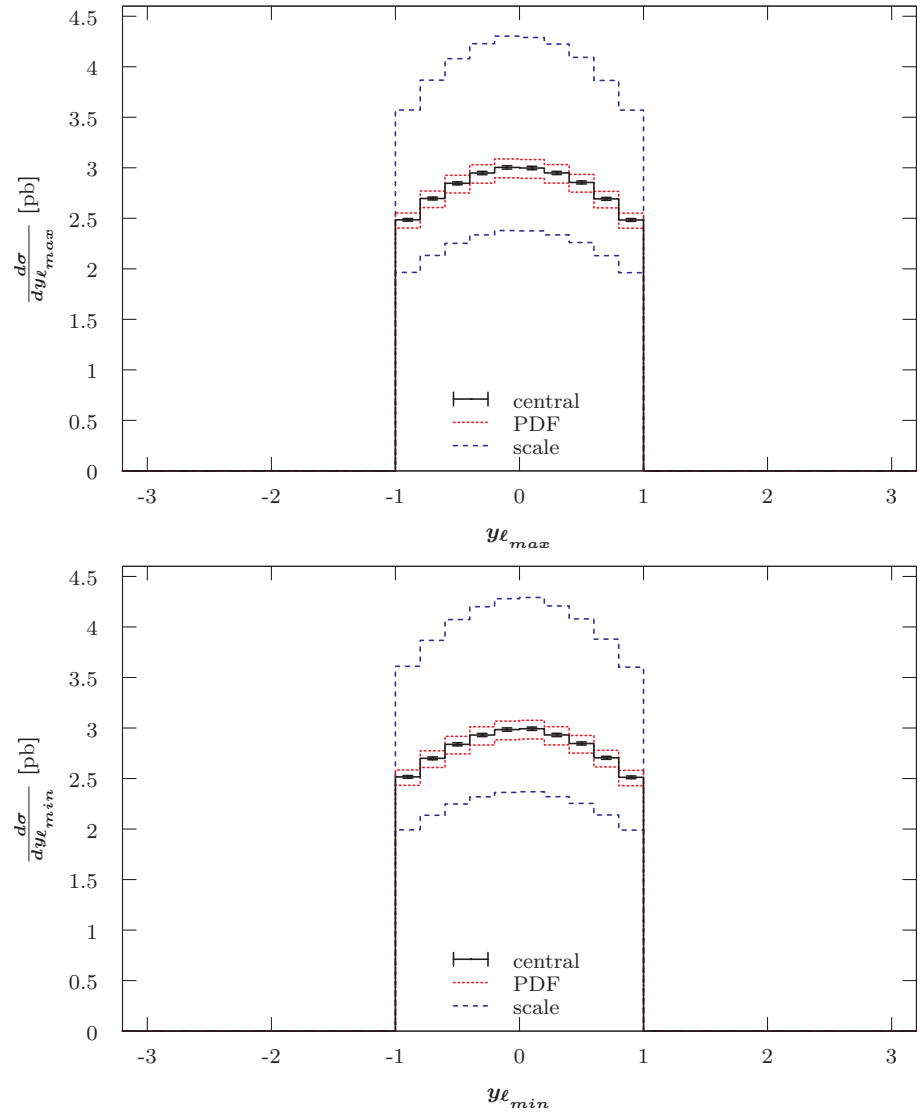

Figure B.70: LO differential cross-section with respect to the harder ℓ_{max} (top) and the softer ℓ_{min} (bottom) charged lepton rapidity for the $p\overline{p} \to (Z \to \ell^-\ell^+) + 1\ jet$ process at the Tevatron Run II using a fixed scale of $\mu_0 = M_Z$. Additional details are given in the caption of Figure 7.77.

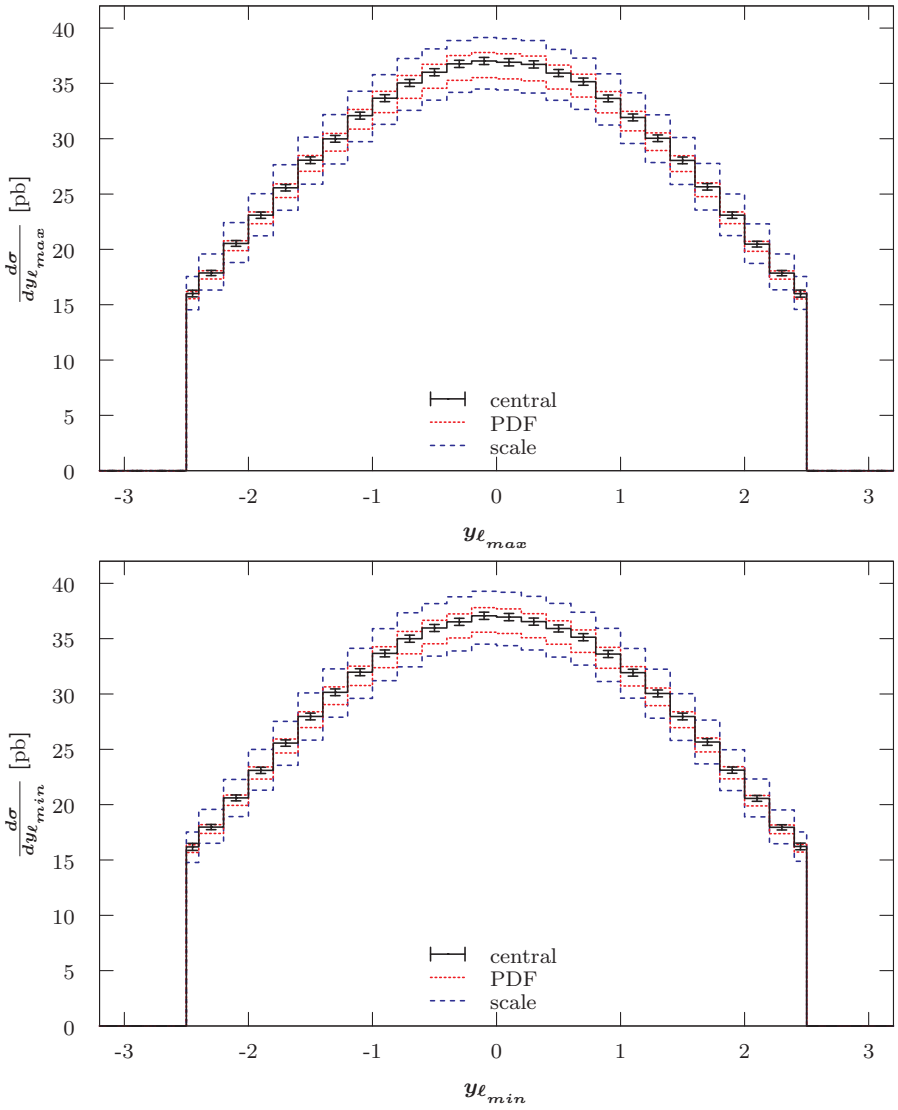

Figure B.71: LO differential cross-section with respect to the harder ℓ_{max} (top) and the softer ℓ_{min} (bottom) charged lepton rapidity for the pp $\to$ (Z $\to \ell^-\ell^+$) + 1 *jet* process at the LHC with 14 TeV using a fixed scale of $\mu_0 = M_{\mathrm{Z}}$. The first and last filled bin are half-width due to the applied selection cut, $|y_\ell| < 2.5$. Additional details are given in the caption of Figure 7.77.

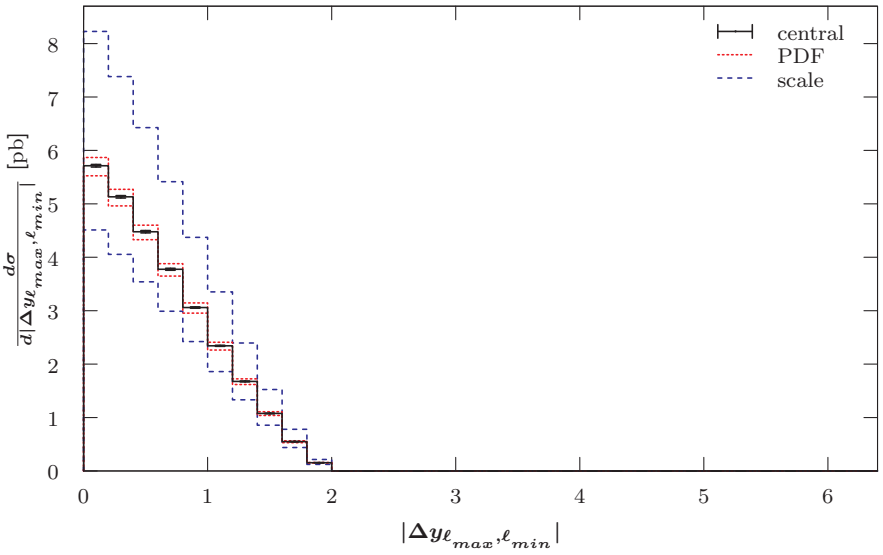

Figure B.72: LO differential cross-section with respect to the difference in rapidity between the harder ℓ_{max} and the softer ℓ_{min} charged lepton for the $p\overline{p} \to (Z \to \ell^-\ell^+) + 1\ jet$ process at the Tevatron Run II using a fixed scale of $\mu_0 = M_Z$. Additional details are given in the caption of Figure 7.77.

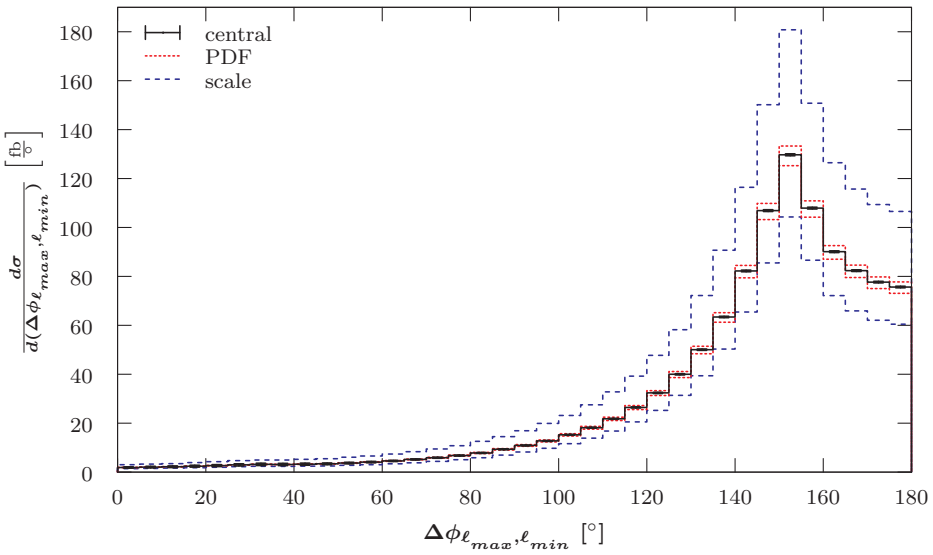

Figure B.73: LO differential cross-section with respect to rapidity difference between the two charged leptons for the $p\overline{p} \to (Z \to \ell^-\ell^+) + 1\ jet$ process at the Tevatron Run II using a fixed scale of $\mu_0 = M_Z$. Additional details are given in the caption of Figure 7.77.

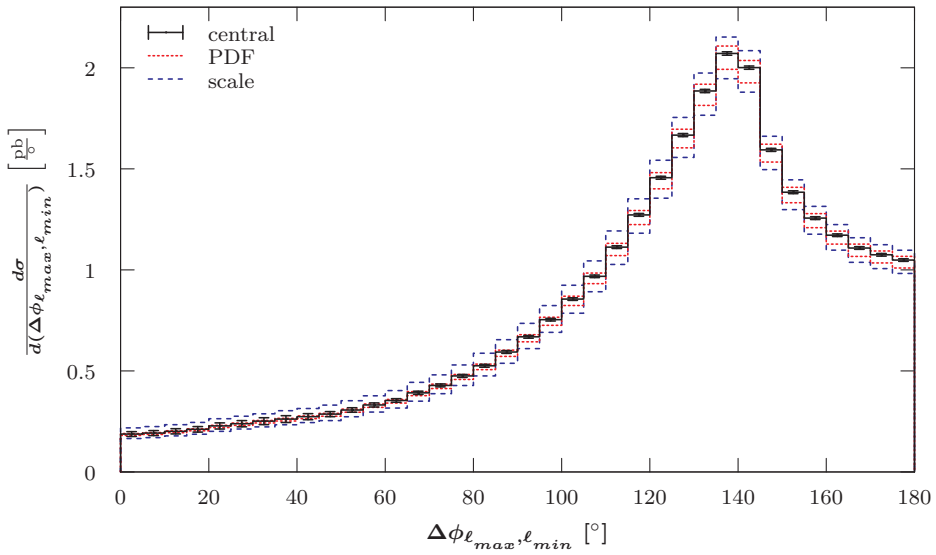

Figure B.74: LO differential cross-section with respect to rapidity difference between the two charged leptons for the pp $\to (\text{Z} \to \ell^-\ell^+) + 1\ jet$ process at the LHC with 14 TeV using a fixed scale of $\mu_0 = M_\text{Z}$. Additional details are given in the caption of Figure 7.77.

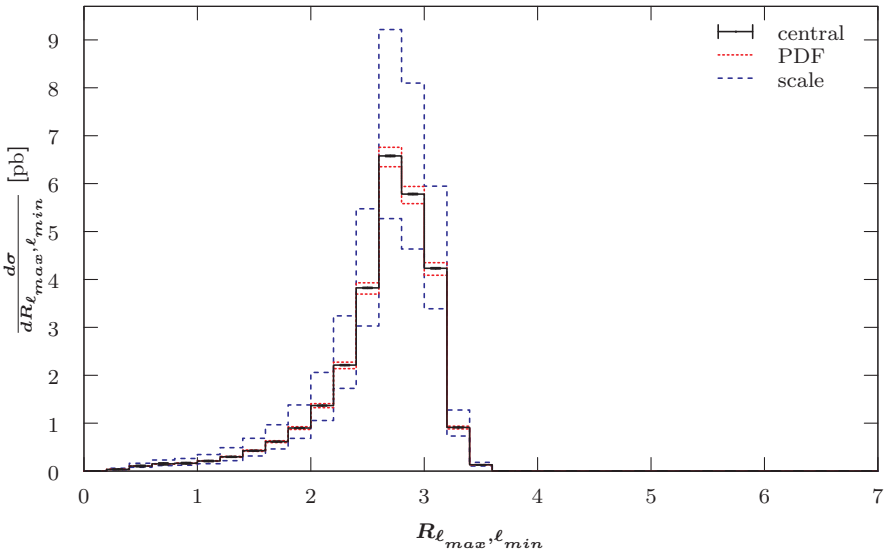

Figure B.75: LO differential cross-section with respect to the separation between the two charged leptons for the pp $\to (\text{Z} \to \ell^-\ell^+) + 1\ jets$ process at the Tevatron Run II using a fixed scale of $\mu_0 = M_\text{Z}$. Additional details are given in the caption of Figure 7.77.

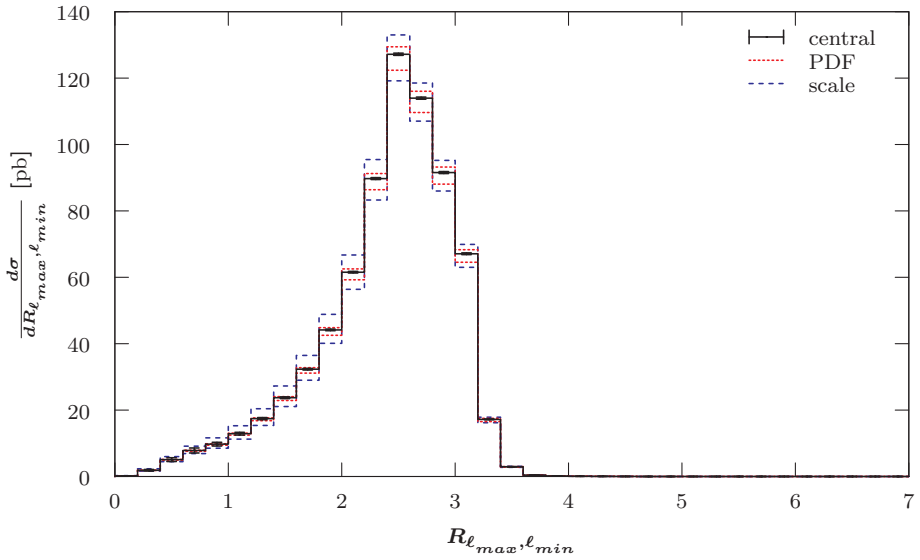

Figure B.76: LO differential cross-section with respect to the separation between the two charged leptons for the $pp \to (Z \to \ell^-\ell^+) + 1\ jets$ process at the LHC with 14 TeV using a fixed scale of $\mu_0 = M_Z$. Additional details are given in the caption of Figure 7.77.

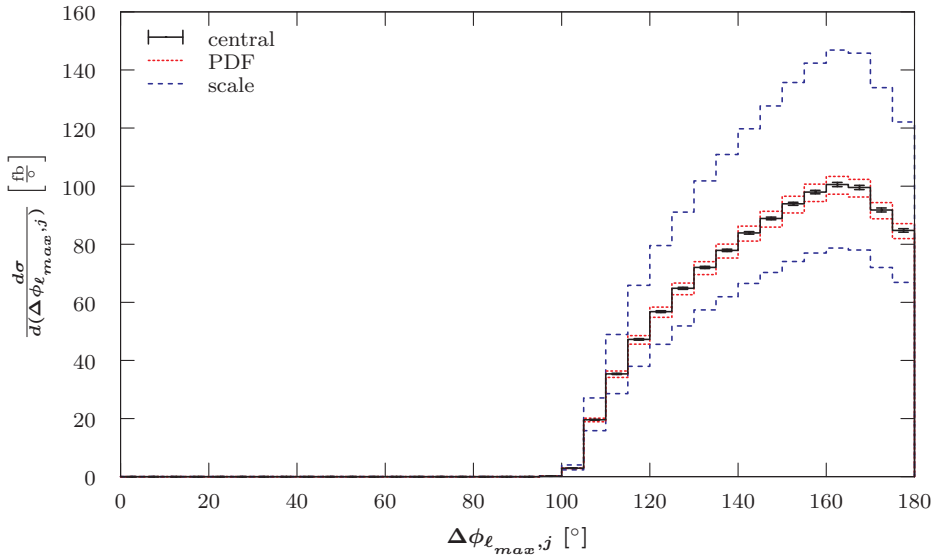

Figure B.77: LO differential cross-section with respect to the rapidity difference between the harder charged lepton ℓ_{max} and the jet j for the $p\bar{p} \to (Z \to \ell^-\ell^+) + 1\ jet$ process at the Tevatron Run II using a fixed scale of $\mu_0 = M_Z$. Additional details are given in the caption of Figure 7.77.

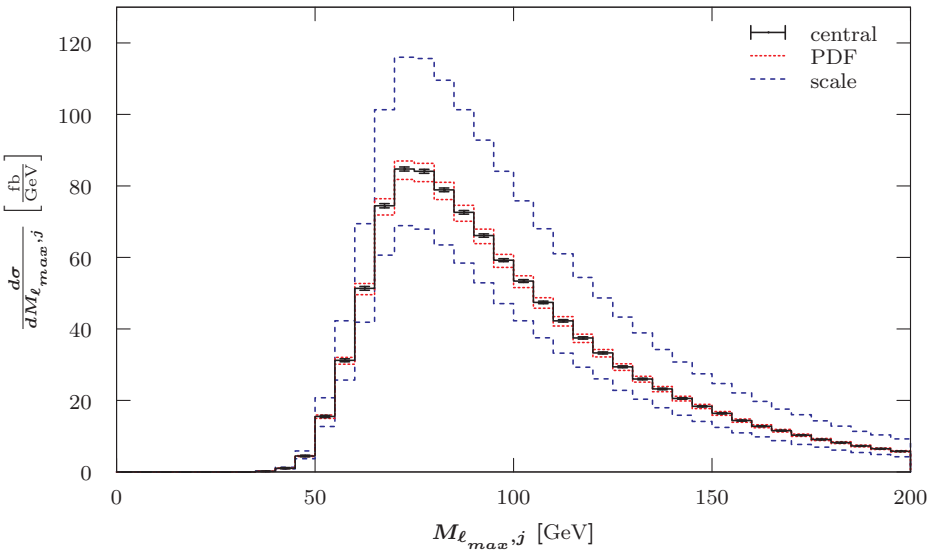

Figure B.78: LO differential cross-section with respect to the inavaraitn mass of the harder charged lepton ℓ_{max} and the jet j for the $p\overline{p} \to (Z \to \ell^-\ell^+) + 1\ jet$ process at the Tevatron Run II using a fixed scale of $\mu_0 = M_Z$. Additional details are given in the caption of Figure 7.77.

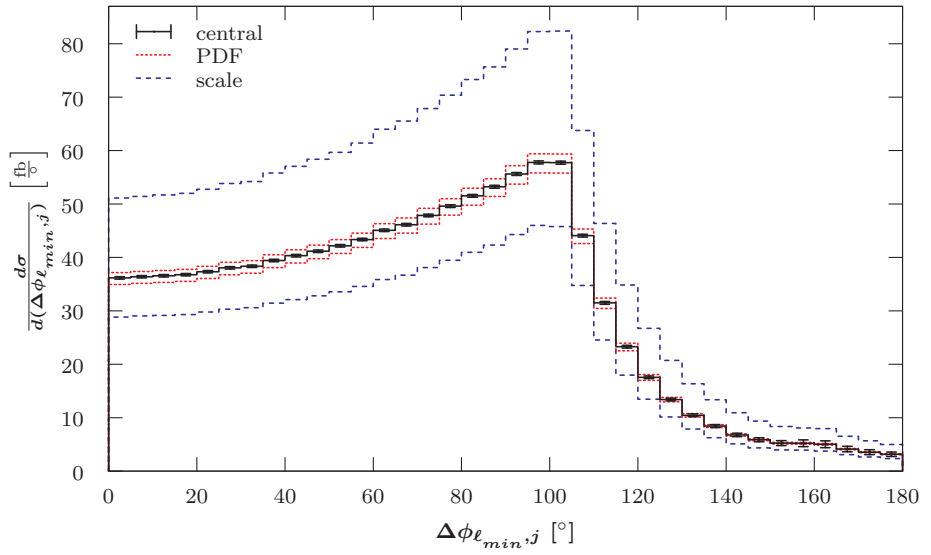

Figure B.79: LO differential cross-section with respect to the rapidity difference between the softer charged lepton ℓ_{min} and the jet j for the $p\overline{p} \to (Z \to \ell^-\ell^+) + 1\ jet$ process at the Tevatron Run II using a fixed scale of $\mu_0 = M_Z$. Additional details are given in the caption of Figure 7.77.

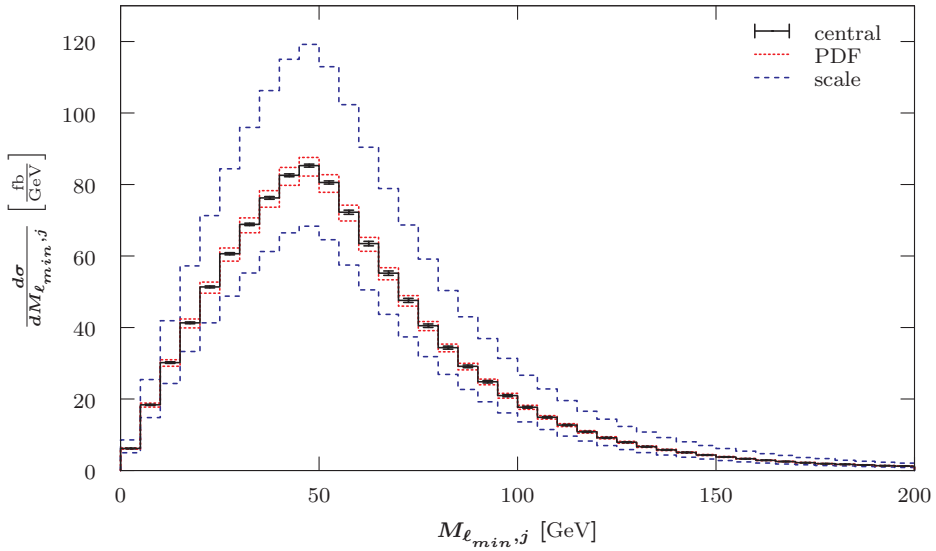

Figure B.80: LO differential cross-section with respect to the inavaraitn mass of the softer charged lepton ℓ_{min} and the jet j for the $p\overline{p} \to (Z \to \ell^-\ell^+) + 1\ jet$ process at the Tevatron Run II using a fixed scale of $\mu_0 = M_Z$. Additional details are given in the caption of Figure 7.77.

B.2.3.3 $p^{(}\overline{p}^{)} \to (Z \to \ell^-\ell^+) + 2$ jets

This section provides some additional graphs for the $p^{(}\overline{p}^{)} \to (Z \to \ell^-\ell^+) + 2\ jets$ process at the Tevatron Run II, which were mentioned in Section 7.4.3.3.

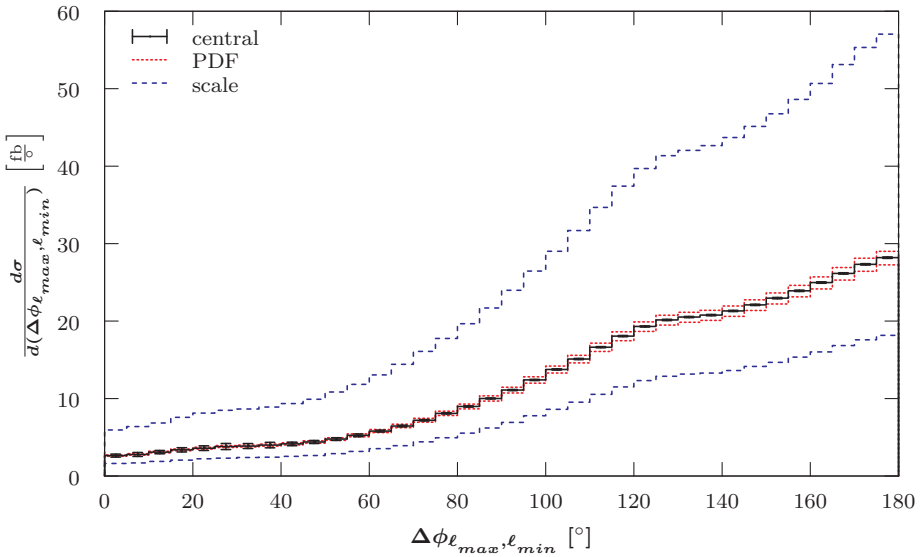

Figure B.81: LO differential cross-section with respect to the rapidity difference between the two charged leptons for the $p\overline{p} \to (Z \to \ell^-\ell^+) + 2\ jets$ process at the Tevatron Run II using a fixed scale of $\mu_0 = M_Z$. Additional details are given in the caption of Figure 7.77.

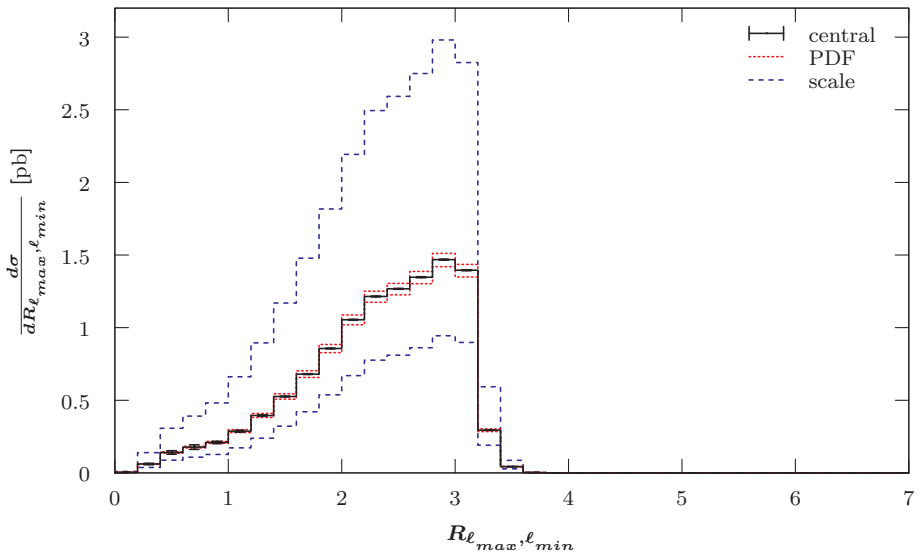

Figure B.82: LO differential cross-section with respect to the separation between the harder ℓ_{max} and the softer ℓ_{min} charged lepton for the $p\overline{p} \to (Z \to \ell^-\ell^+) + 2\ jets$ process at the Tevatron Run II using a fixed scale of $\mu_0 = M_Z$. Additional details are given in the caption of Figure 7.77.

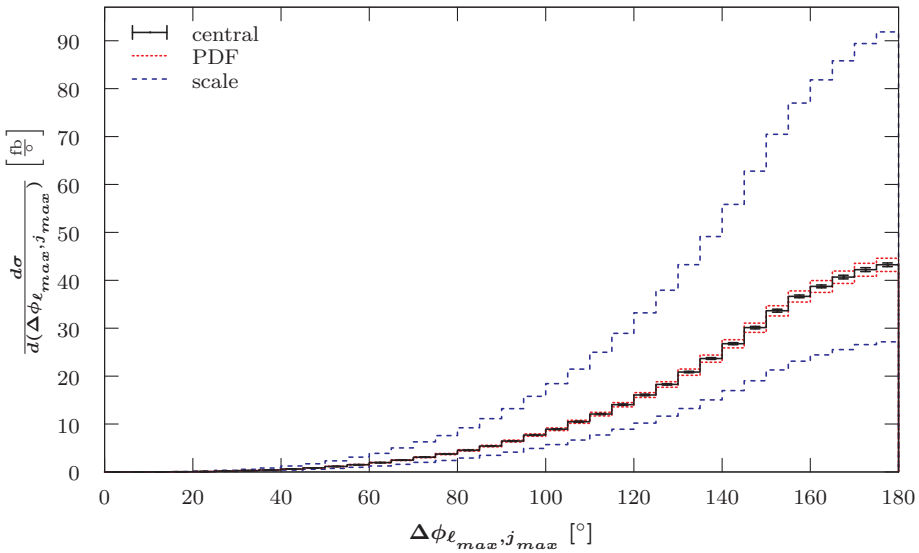

Figure B.83: LO differential cross-section with respect to the azimuthal angle ϕ between the harder charged lepton ℓ_{max} and the harder jet j_{max} for the $p\overline{p} \to (Z \to \ell^-\ell^+) + 2\ jets$ process at the Tevatron Run II using a fixed scale of $\mu_0 = M_Z$. Additional details are given in the caption of Figure 7.77.

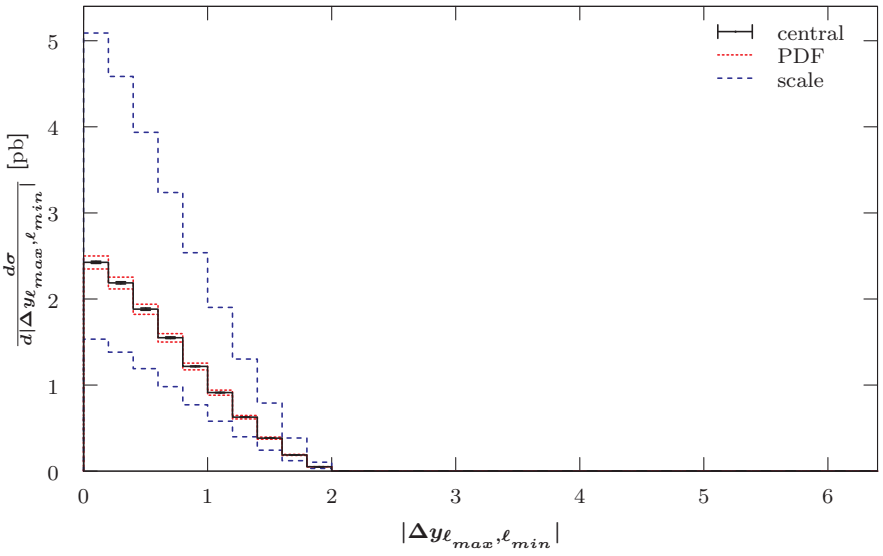

Figure B.84: LO differential cross-section with respect to the difference in rapidity between the harder ℓ_{max} and the softer ℓ_{min} charged lepton for the $p\overline{p} \to (Z \to \ell^-\ell^+) + 2\ jets$ process at the Tevatron Run II using a fixed scale of $\mu_0 = M_Z$. Additional details are given in the caption of Figure 7.77.

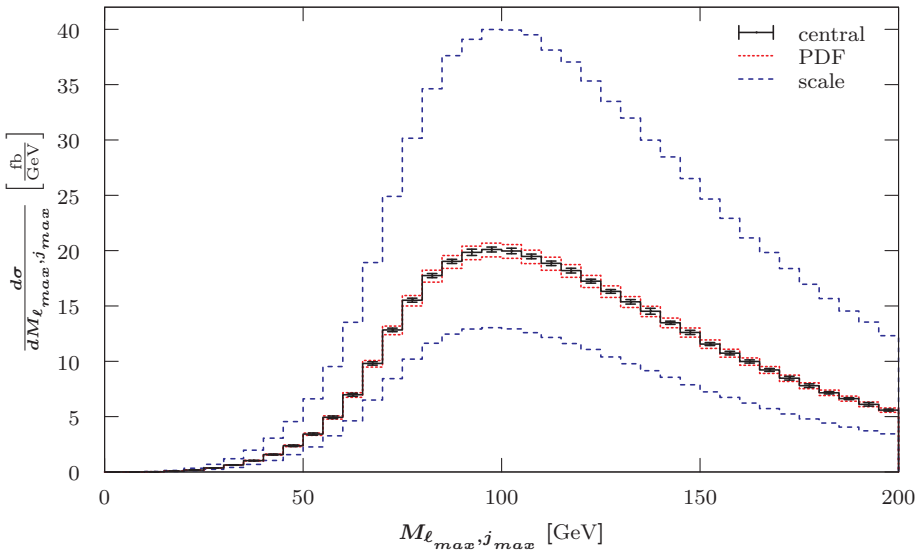

Figure B.85: LO differential cross-section with respect to the inavaraitn mass of the harder charged lepton ℓ_{max} and the harder jet j_{max} for the $p\overline{p} \to (Z \to \ell^-\ell^+) + 2\ jets$ process at the Tevatron Run II using a fixed scale of $\mu_0 = M_Z$. Additional details are given in the caption of Figure 7.77.

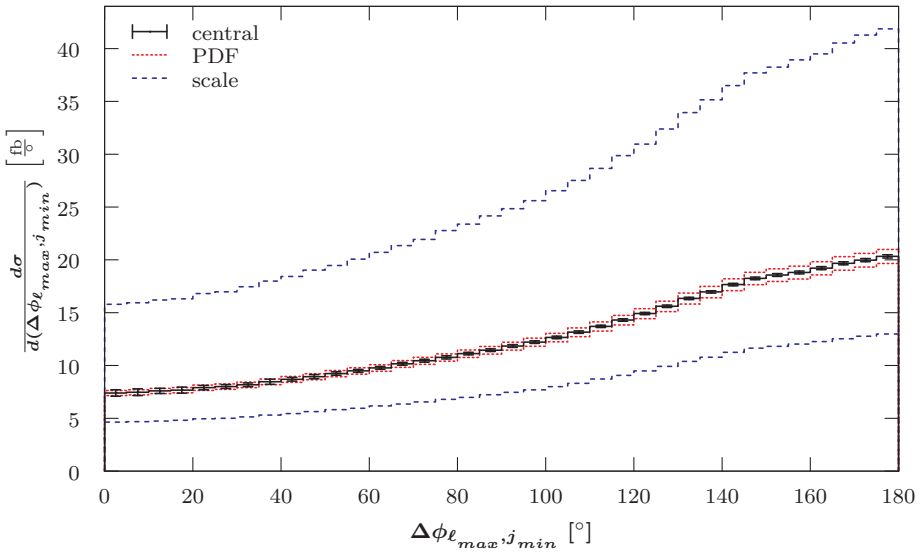

Figure B.86: LO differential cross-section with respect to the azimuthal angle ϕ between the harder charged lepton ℓ_{max} and the softer jet j_{min} for the $p\overline{p} \to (Z \to \ell^-\ell^+) + 2\ jets$ process at the Tevatron Run II using a fixed scale of $\mu_0 = M_Z$. Additional details are given in the caption of Figure 7.77.

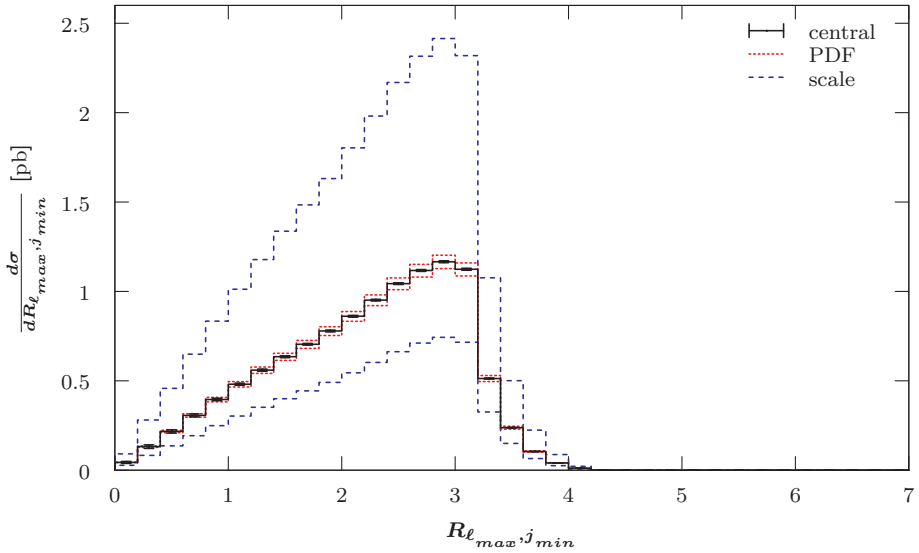

Figure B.87: LO differential cross-section with respect to the separation between the harder charged lepton ℓ_{max} and the softer jet j_{min} for the $p\overline{p} \to (Z \to \ell^-\ell^+) + 2\ jets$ process at the Tevatron Run II using a fixed scale of $\mu_0 = M_Z$. Additional details are given in the caption of Figure 7.77.

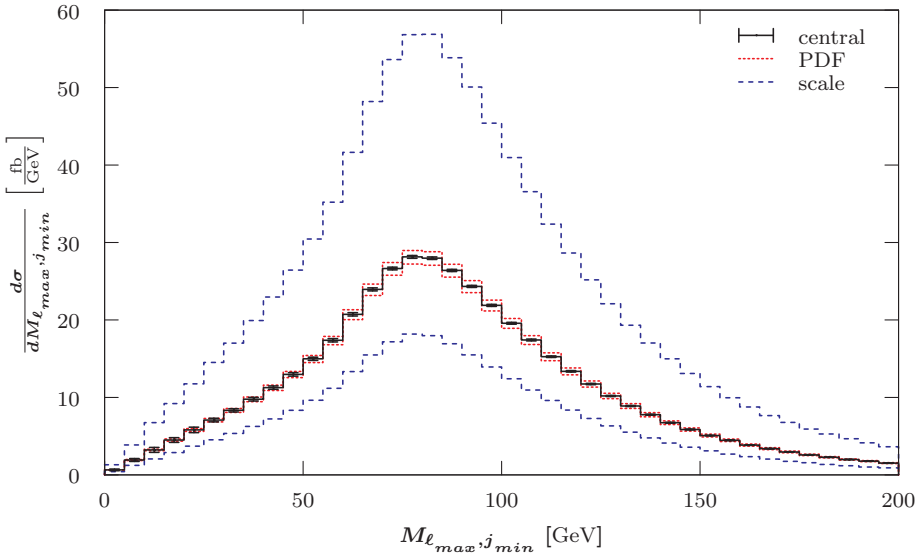

Figure B.88: LO differential cross-section with respect to the inavaraitn mass of the harder charged lepton ℓ_{max} and the softer jet j_{min} for the $p\overline{p} \to (Z \to \ell^-\ell^+) + 2\ jets$ process at the Tevatron Run II using a fixed scale of $\mu_0 = M_Z$. Additional details are given in the caption of Figure 7.77.

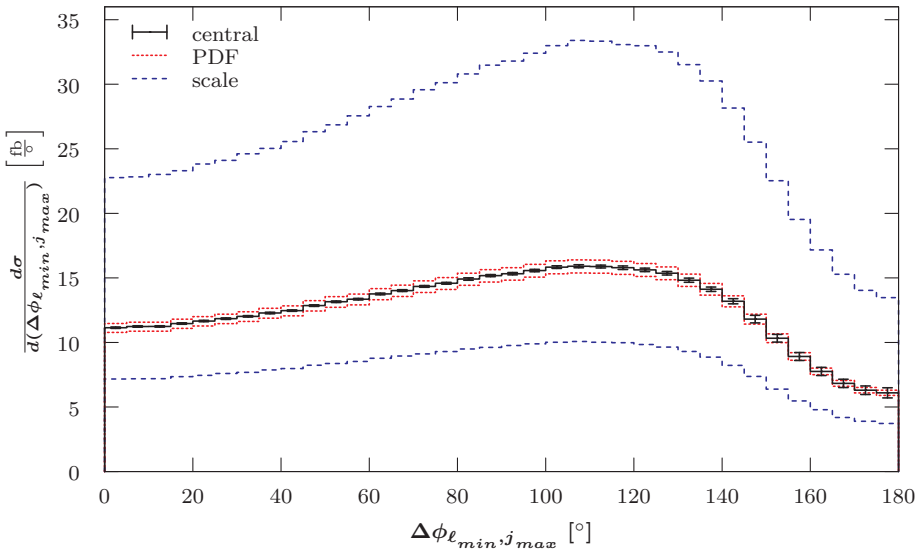

Figure B.89: LO differential cross-section with respect to the azimuthal angle ϕ between the softer charged lepton ℓ_{min} and the harder jet j_{max} for the $p\overline{p} \to (Z \to \ell^-\ell^+) + 2\ jets$ process at the Tevatron Run II using a fixed scale of $\mu_0 = M_Z$. Additional details are given in the caption of Figure 7.77.

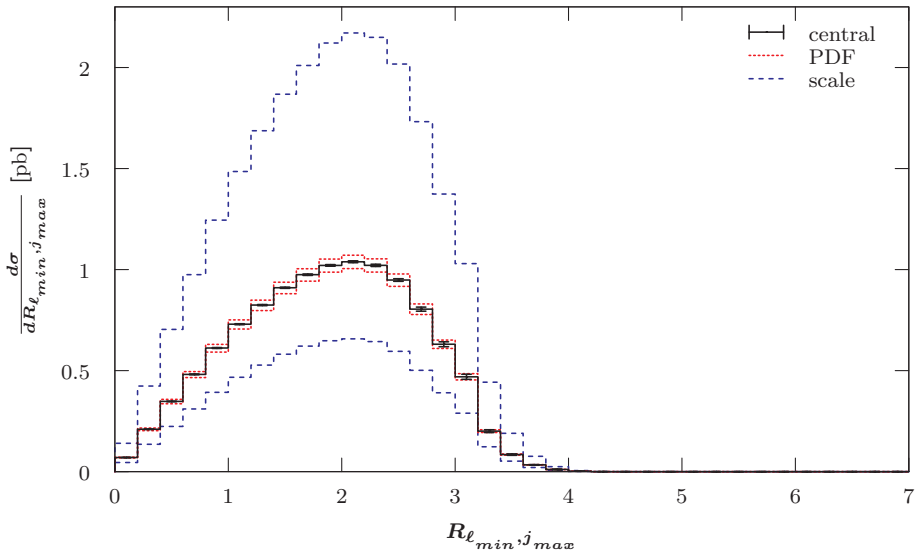

Figure B.90: LO differential cross-section with respect to the separation between the softer charged lepton ℓ_{min} and the harder jet j_{max} for the $p\overline{p} \to (Z \to \ell^-\ell^+) + 2\ jets$ process at the Tevatron Run II using a fixed scale of $\mu_0 = M_Z$. Additional details are given in the caption of Figure 7.77.

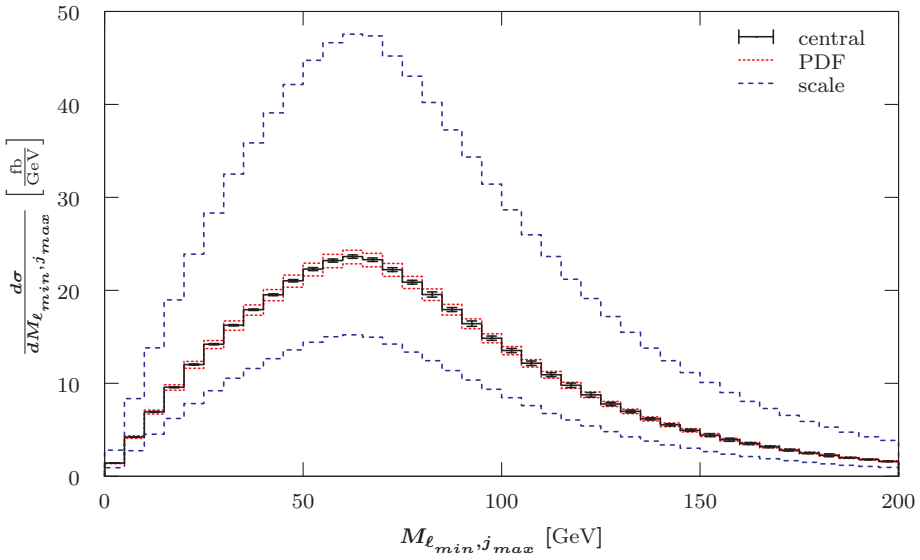

Figure B.91: LO differential cross-section with respect to the inavaraitn mass of the softer charged lepton ℓ_{min} and the harder jet j_{max} for the $p\overline{p} \to (Z \to \ell^-\ell^+) + 2\ jets$ process at the Tevatron Run II using a fixed scale of $\mu_0 = M_Z$. Additional details are given in the caption of Figure 7.77.

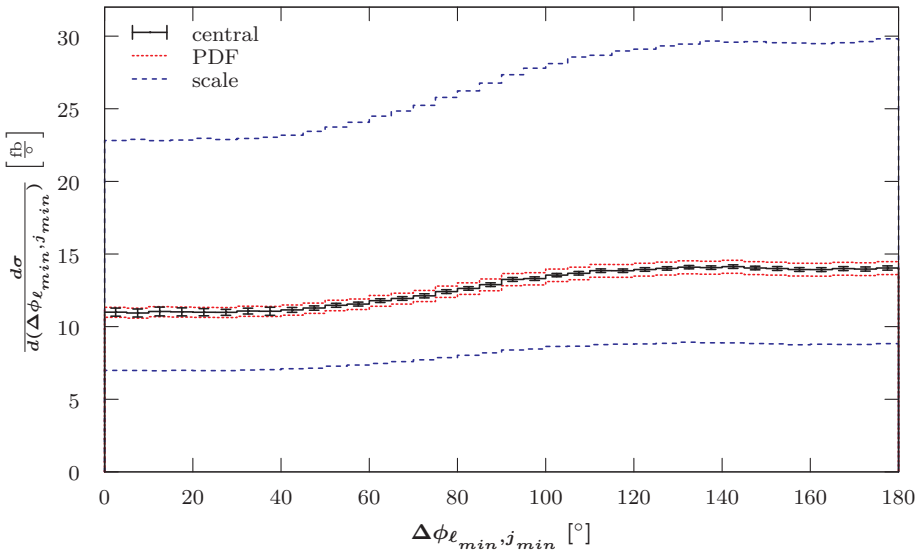

Figure B.92: LO differential cross-section with respect to the azimuthal angle ϕ between the softer charged lepton ℓ_{min} and the softer jet j_{min} for the $p\overline{p} \to (Z \to \ell^-\ell^+) + 2\ jets$ process at the Tevatron Run II using a fixed scale of $\mu_0 = M_Z$. Additional details are given in the caption of Figure 7.77.

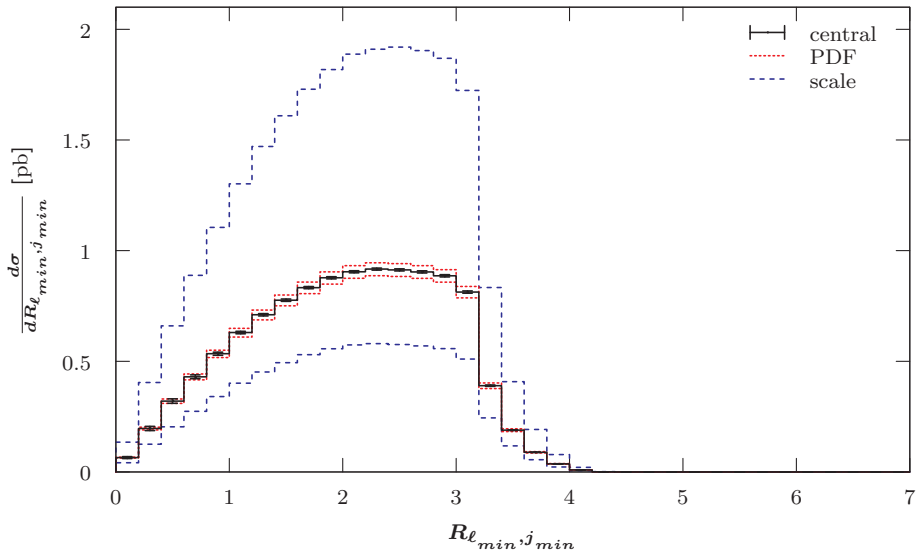

Figure B.93: LO differential cross-section with respect to the separation between the softer charged lepton ℓ_{min} and the softer jet j_{min} for the $p\bar{p} \to (Z \to \ell^-\ell^+) + 2\ jets$ process at the Tevatron Run II using a fixed scale of $\mu_0 = M_Z$. Additional details are given in the caption of Figure 7.77.

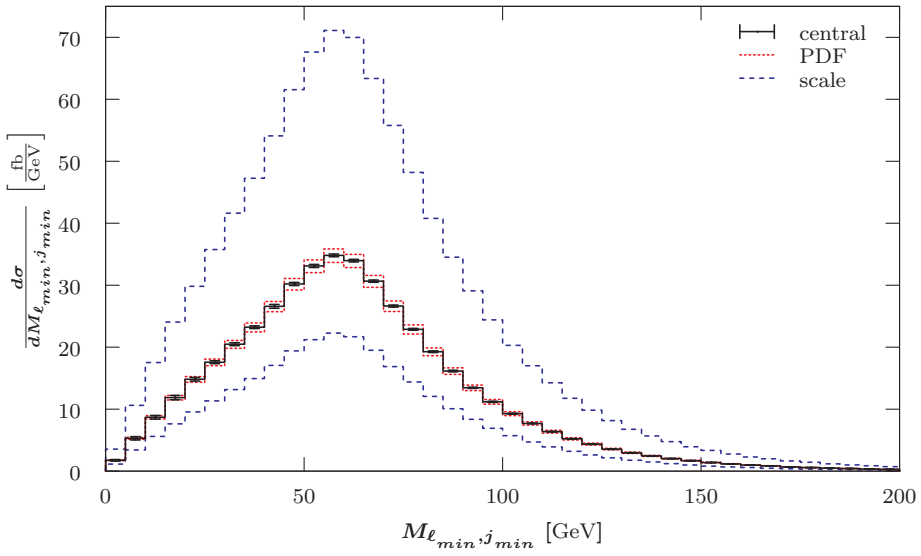

Figure B.94: LO differential cross-section with respect to the inavaraitn mass of the softer charged lepton ℓ_{min} and the softer jet j_{min} for the $p\bar{p} \to (Z \to \ell^-\ell^+) + 2\ jets$ process at the Tevatron Run II using a fixed scale of $\mu_0 = M_Z$. Additional details are given in the caption of Figure 7.77.

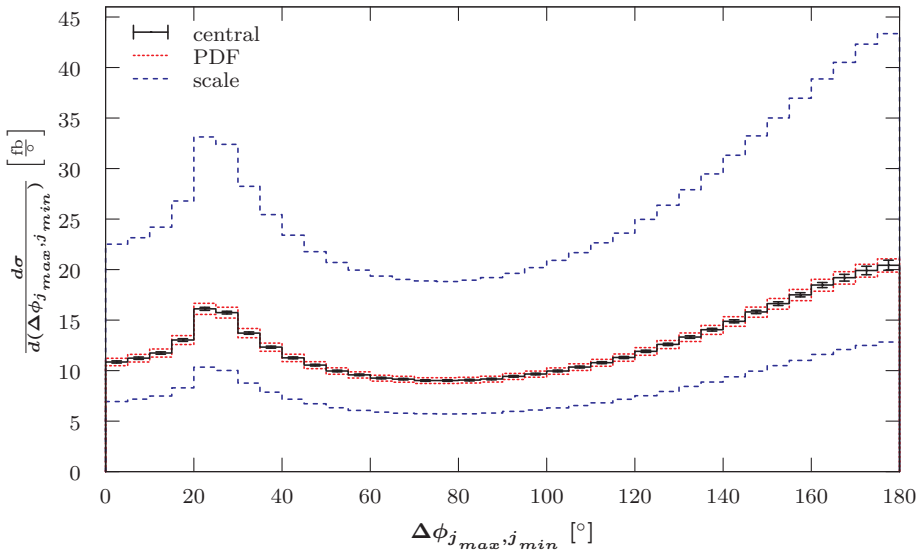

Figure B.95: LO differential cross-section with respect to the azimuthal angle ϕ between the harder j_{max} and the softer jet j_{min} for the $p\overline{p} \to (Z \to \ell^-\ell^+) + 2\ jets$ process at the Tevatron Run II using a fixed scale of $\mu_0 = M_Z$. Additional details are given in the caption of Figure 7.77.

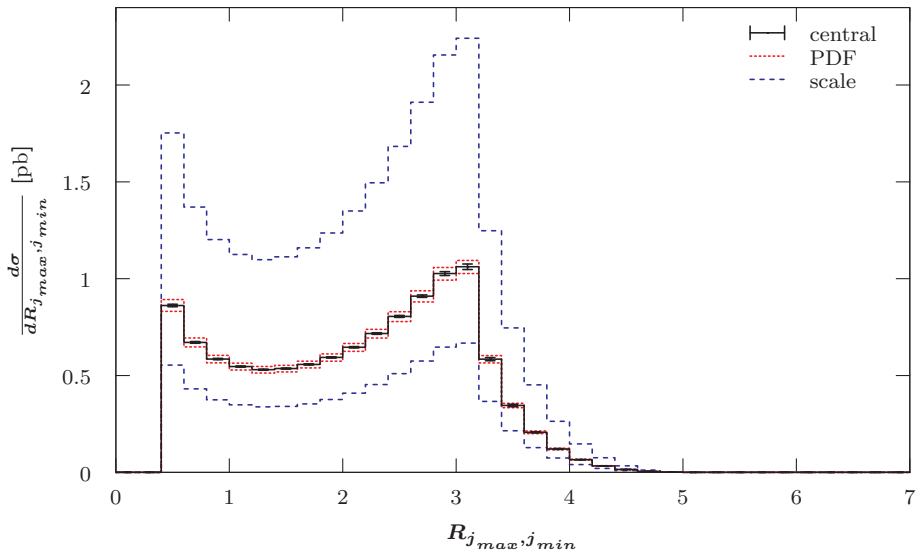

Figure B.96: LO differential cross-section with respect to the separation between the harder j_{max} and the softer j_{min} jet for the $p\overline{p} \to (Z \to \ell^-\ell^+) + 2\ jets$ process at the Tevatron Run II using a fixed scale of $\mu_0 = M_Z$. Additional details are given in the caption of Figure 7.77.

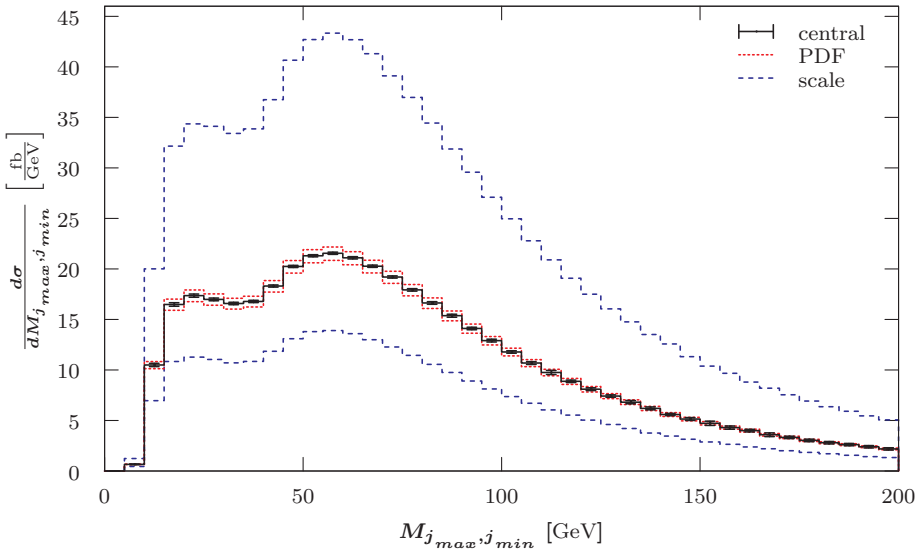

Figure B.97: LO differential cross-section with respect to the inavaraitn mass of the harder j_{max} and the softer j_{min} jet for the $p\overline{p} \to (Z \to \ell^-\ell^+) + 2\ jets$ process at the Tevatron Run II using a fixed scale of $\mu_0 = M_Z$. Additional details are given in the caption of Figure 7.77.

B.2.4 $p^{(}\overline{p}^{)} \to (Z \to \sum_{\ell=e,\mu,\tau} \nu_\ell \overline{\nu}_\ell) + n$ jets

B.2.4.1 $p^{(}\overline{p}^{)} \to (Z \to \sum_{\ell=e,\mu,\tau} \nu_\ell \overline{\nu}_\ell)$

This section gives the missing transverse momentum graph for the $pp \to (Z \to \sum_{\ell=e,\mu,\tau} \nu_\ell \overline{\nu}_\ell)$ process at the LHC with 7 TeV, which was mentioned in Section 7.4.4.1.

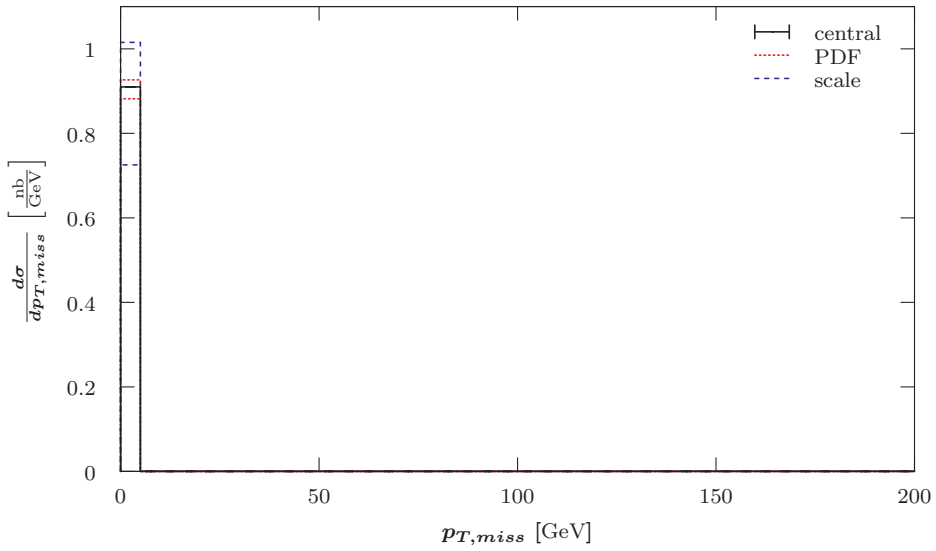

Figure B.98: LO differential cross-section with respect to missing transverse momentum for the $pp \to (Z \to \sum_{\ell=e,\mu,\tau} \nu_\ell \overline{\nu}_\ell)$ process at the LHC with 7 TeV using a fixed scale of $\mu_0 = M_Z$. Additional details are given in the caption of Figure 7.127.

B.2.4.2 $p^{(}\overline{p}^{)} \to (Z \to \sum_{\ell=e,\mu,\tau} \nu_\ell \overline{\nu}_\ell) + 1$ jet

This section provides some additional graphs for the $p^{(}\overline{p}^{)} \to (Z \to \sum \nu\overline{\nu}) + 1\ jet$ process, which were mentioned in Section 7.4.4.2.

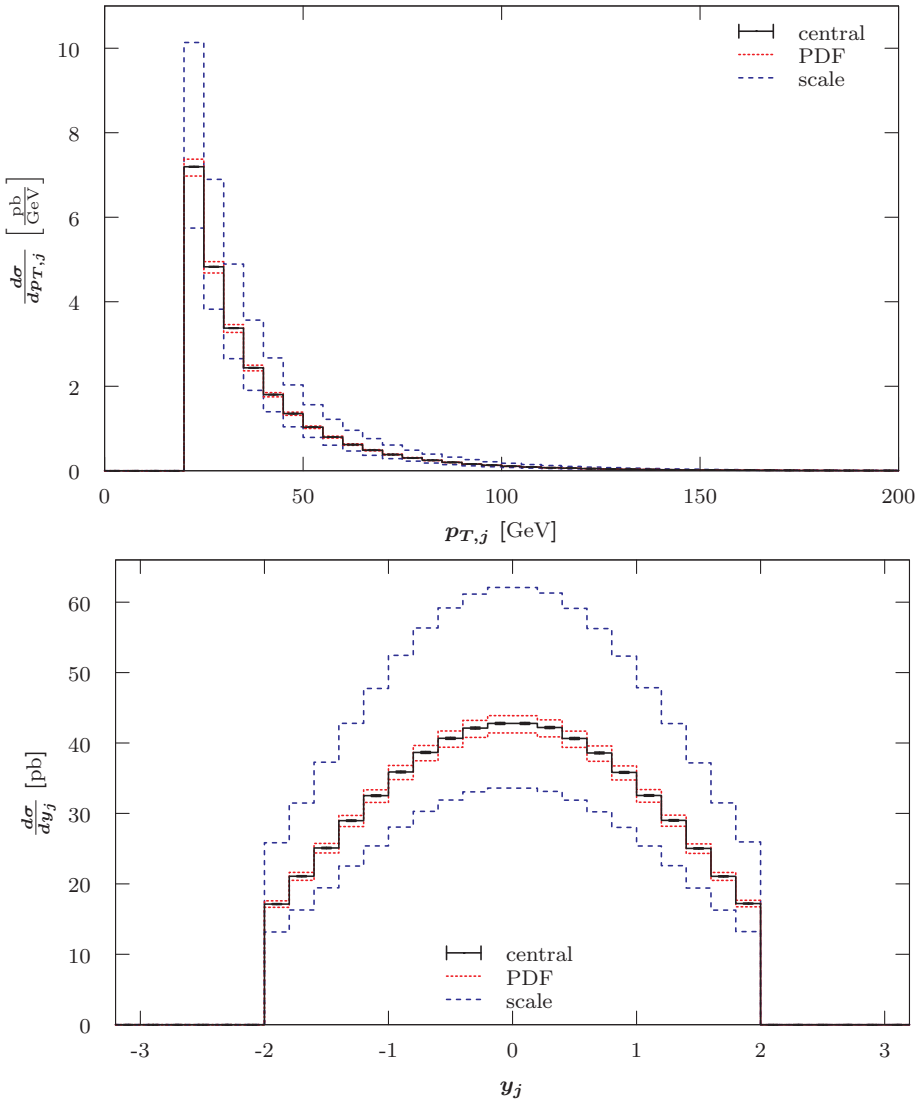

Figure B.99: LO differential cross-section with respect to the transverse momentum (top) and the rapidity (bottom) of the jet for the $p\overline{p} \to (Z \to \sum \nu\overline{\nu}) + 1\ jet$ process at the Tevatron Run II using a dynamic scale of $\mu_0 = M_Z$. Additional details are given in the caption of Figure 7.127.

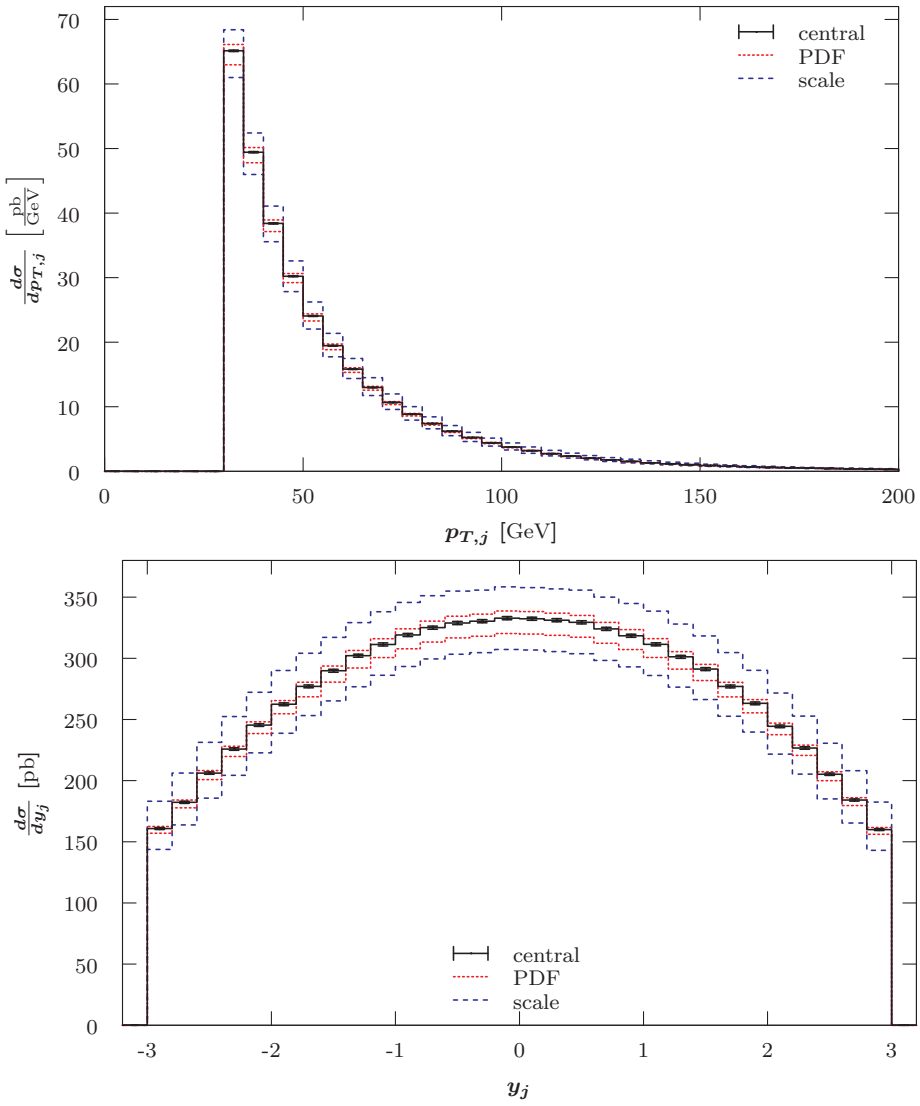

Figure B.100: LO differential cross-section with respect to the transverse momentum (top) and the rapidity (bottom) of the jet for the pp $\to$ (Z $\to \sum \nu\overline{\nu}$) + 1 *jet* process at the LHC with 14 TeV using a dynamic scale of $\mu_0 = M_{\text{Z}}$. Additional details are given in the caption of Figure 7.127.

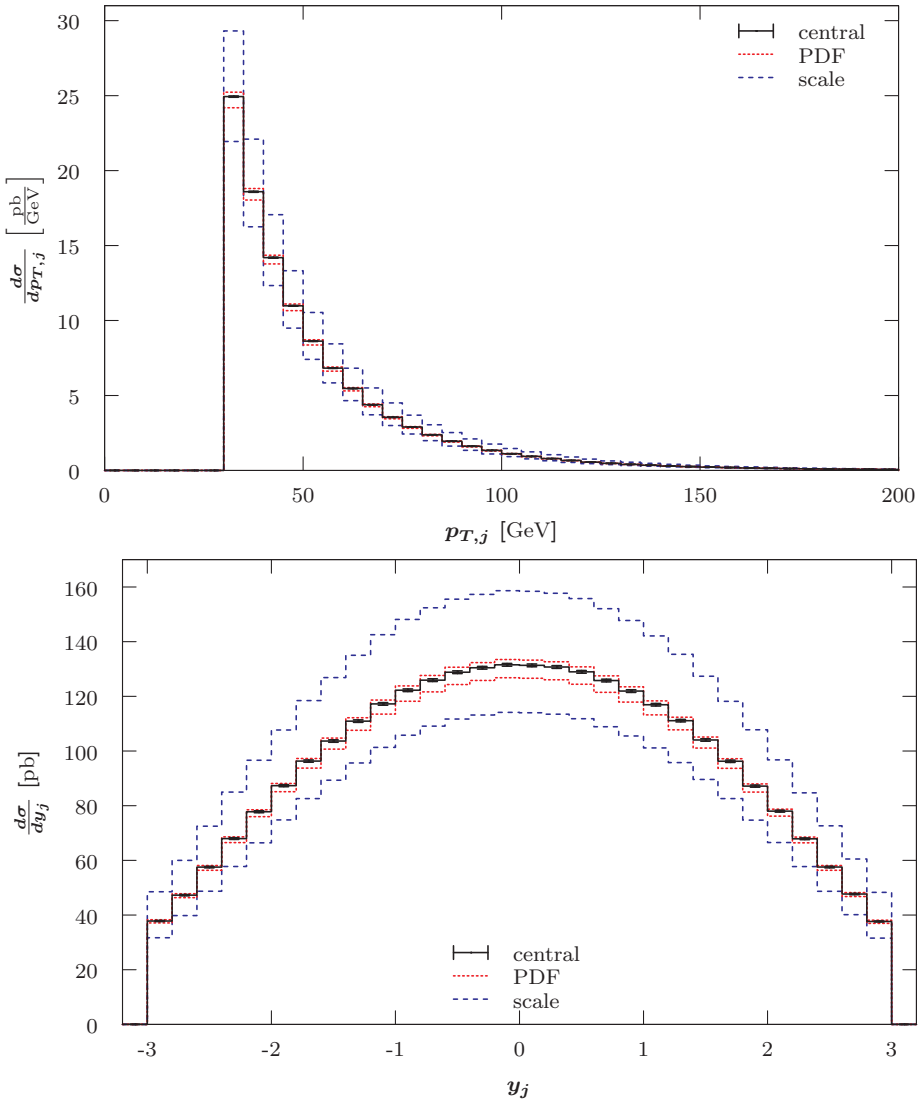

Figure B.101: LO differential cross-section with respect to the transverse momentum (top) and the rapidity (bottom) of the jet for the pp $\to$ (Z $\to \sum \nu\overline{\nu}$) + 1 *jet* process at the LHC with 7 TeV using a dynamic scale of $\mu_0 = E_T^{\text{Z}}$. Additional details are given in the caption of Figure 7.127.

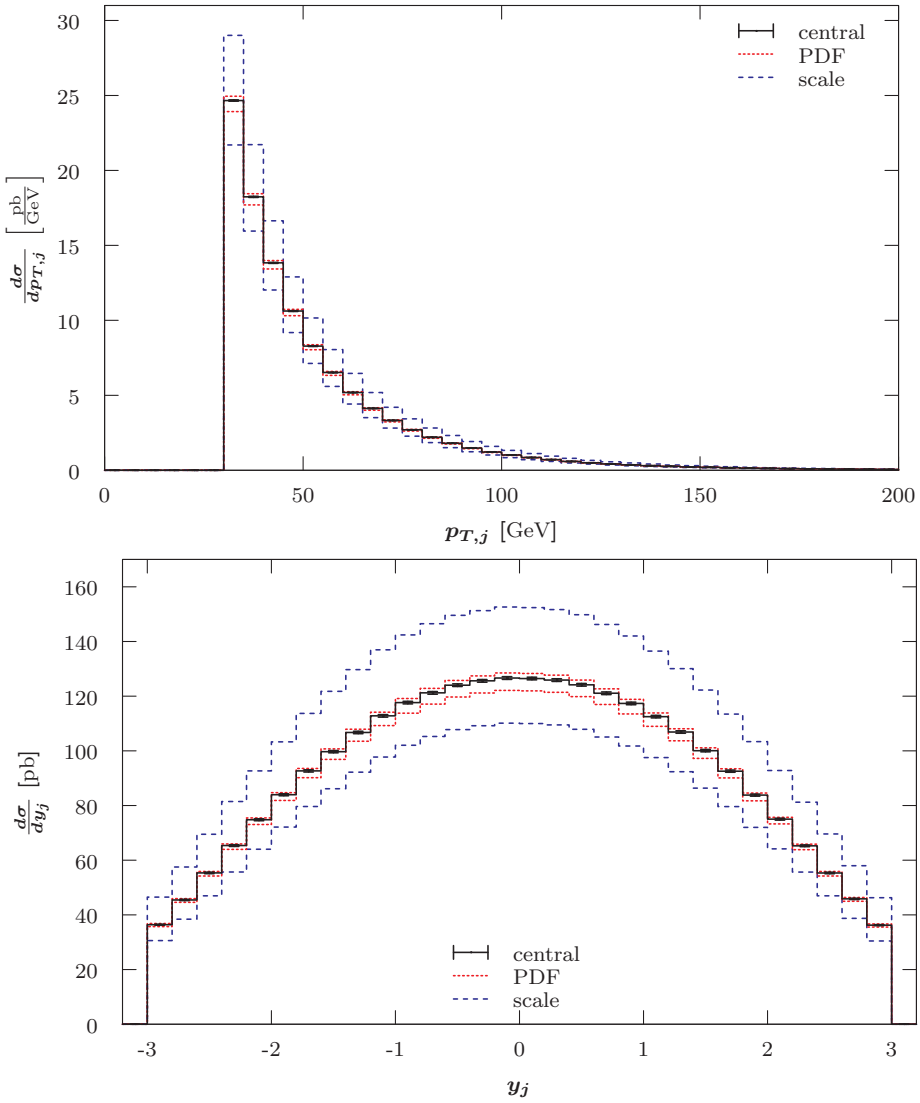

Figure B.102: LO differential cross-section with respect to the transverse momentum (top) and the rapidity (bottom) of the jet for the pp $\to$ (Z $\to \sum \nu\overline{\nu}$) + 1 *jet* process at the LHC with 7 TeV using a dynamic scale of $\mu_0 = \hat{H}_T$. Additional details are given in the caption of Figure 7.127.

B.2.4.3 $p^{(}\overline{p}^{)} \to (Z \to \sum_{\ell=e,\mu,\tau} \nu_\ell \overline{\nu}_\ell) + 2$ jets

This section provides some additional graphs for the $p^{(}\overline{p}^{)} \to (Z \to \sum \nu\overline{\nu}) + 2\ jets$ process at the Tevatron Run II and the LHC with 14 TeV, which were mentioned in Section 7.4.4.3.

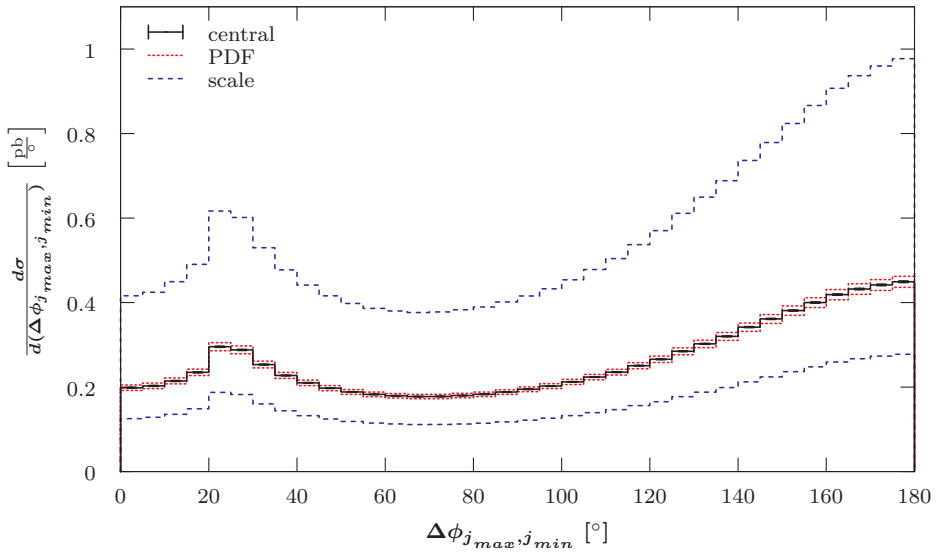

Figure B.103: LO differential cross-section with respect to the azimuthal angle ϕ between the harder j_{max} and the softer jet j_{min} for the $p\overline{p} \to (Z \to \sum \nu\overline{\nu}) + 2\ jets$ process at the Tevatron Run II using a fixed scale of $\mu_0 = M_Z$. Additional details are given in the caption of Figure 7.127.

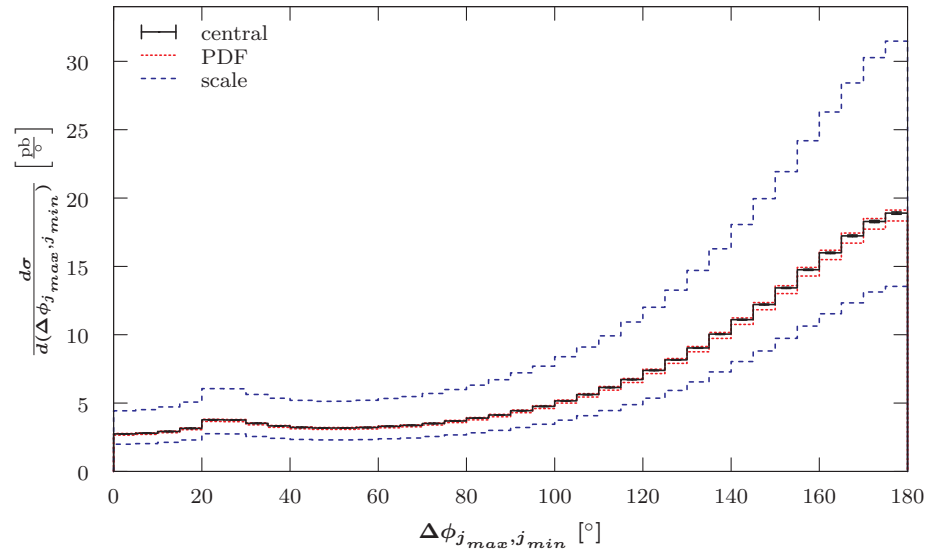

Figure B.104: LO differential cross-section with respect to the azimuthal angle ϕ between the harder j_{max} and the softer jet j_{min} for the $pp \to (Z \to \sum \nu\overline{\nu}) + 2\ jets$ process at the LHC with 14 TeV using a fixed scale of $\mu_0 = M_Z$. Additional details are given in the caption of Figure 7.127.

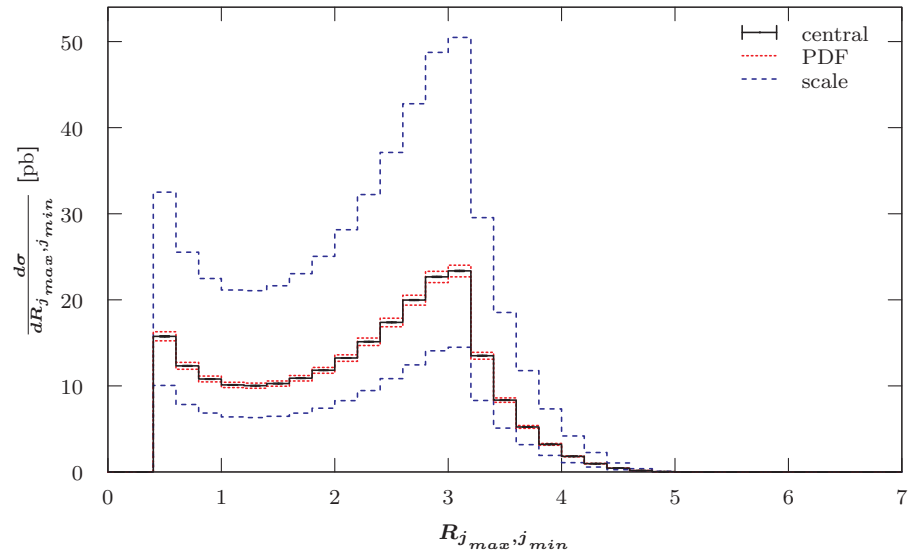

Figure B.105: LO differential cross-section with respect to separation between the harder j_{max} and the softer j_{min} jet for the $p\overline{p} \to (Z \to \sum \nu\overline{\nu}) + 2\ jets$ process at the Tevatron Run II using a fixed scale of $\mu_0 = M_Z$. Additional details are given in the caption of Figure 7.127.

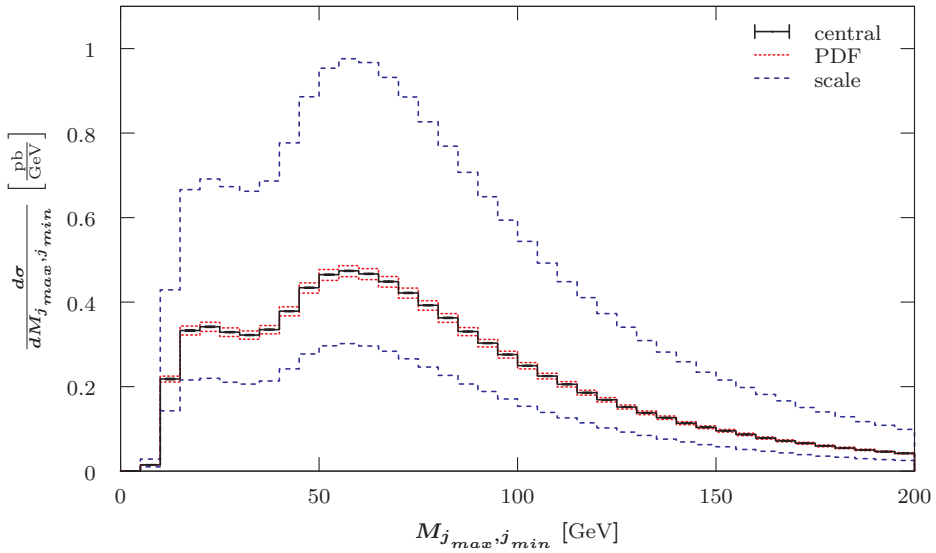

Figure B.106: LO differential cross-section with respect to the inavaraitn mass of the harder j_{max} and the softer j_{min} jet for the $p\overline{p} \to (Z \to \sum \nu\overline{\nu}) + 2\ jets$ process at the Tevatron Run II using a fixed scale of $\mu_0 = M_Z$. Additional details are given in the caption of Figure 7.127.